NATIONAL CENTER FOR COMPUTATIONAL
HYDROSCIENCE AND ENGINEERING
THE UNIVERSITY OF MISSISSIPPI

Phase I Report for SERRI Project No. 80037:

Investigation of Surge and Wave Reduction by Vegetation

Weiming Wu (PI)

March 2011

This material is based upon work supported by the U.S. Department of Homeland Security under U.S. Department of Energy Interagency Agreement 43WT10301. The views and conclusions contained in this document are those of the authors and should not be interpreted as necessarily representing the official policies, either expressed or implied, of the U.S. Department of Homeland Security.

SERRI Report 80037-01

SERRI Project: Investigation of Surge and Wave Reduction by Vegetation

FINAL REPORT OF PHASE I

Weiming Wu (PI)
National Center for Computational Hydroscience and Engineering
The University of Mississippi, MS 38677

Yavuz Ozeren (Stationed at UM) and *Daniel Wren* (Co-PI)
National Sedimentation Laboratory, USDA-ARS, Oxford, MS 38655

Qin Chen (Co-PI) and *Guoping Zhang* (Co-PI)
Civil and Environ.Engineering Dept., Louisiana State Univ., Baton Rouge, LA 70803

Marjorie Holland (Co-PI)
Biology Department, The University of Mississippi, MS 38677

Yan Ding, *Soumendra N. Kuiry* and *Mingliang Zhang*
National Center for Computational Hydroscience and Engineering
The University of Mississippi, MS 38677

Ranjit Jadhav and *James Chatagnier*
Civil and Environ. Engineering Dept., Louisiana State Univ., Baton Rouge, LA 70803

Ying Chen and *Leili Gordji*
Biology Department, The University of Mississippi, MS 38677

Date Published:
March 2011

Prepared for
U.S. Department of Homeland Security
under U.S. Department of Energy Interagency Agreement 43WT10301
Southeast Regional Research Initiative (SERRI)
Basic Ordering Agreement 4200000224, Task Order Number 4000075852

Prepared by
OAK RIDGE NATIONAL LABORATORY
Oak Ridge, Tennessee 37831-6283
managed by UT-BATTELLE, LLC
for the U.S. DEPARTMENT OF ENERGY
under contract DE-AC05-00OR22725

ACKNOWLEDGEMENTS

Funding for this project was provided by the Department of Homeland Security-sponsored Southeast Region Research Initiative (SERRI) managed by the Department of Energy's Oak Ridge National Laboratory (ORNL). The program manager Mr. Michael Mathews at the DHS Science and Technology (S&T) Directorate, Mr. Benjamin Thomas, Jr. and Ms. Berky A. Wagner at ORNL are acknowledged for their guidance, insight and timely handling of technical and business affairs related to this project. The present research would not have been so successful without their supervision and support.

Thanks to Dr. Sam Wang, Dr. Mustafa Altinakar, Ms. Kathy McCombs, and Mr. Paul Smith at NCCHE and colleagues at the Office of Research and Sponsored Programs and the Accounting Office of The University of Mississppi for their support for this research.

Jeffrey Diers, Glenn Gray, and Will Simpson are acknowledged for their technical assistance during preparation of the laboratory setup and throughout the experiments.

We greatly appreciate the cooperation extended by Bobbie Chauvin and Frank Ellender of the Louisiana Land and Exploration Company in granting us permission to access the marsh field site and letting us deploy instrumentation. The Field Support Group of the Coastal Studies Institute of the Louisiana State University is thanked for assembling marsh sensor array and assistance in deployment, data acquisition and retrieval of the instruments. Assistance from the LUMCON is appreciated for providing boats and personnel during initial reconnaissance trips. Special thanks to T. Baker Smith, LLC of Houma, LA for providing boat and personnel during sensor deployment for Tropical Storm Ida, sensor recovery during Tropical Storm Bonnie and for carrying out topographic surveys of the marsh site. We also want to thank Dr. Andrew Kennedy of the University of Notre Dame for lending us pressure sensors and Uriah Gravois of the University of Florida for assistance in sensor and data retrieval during Tropical Storm Ida. We appreciate WAVCIS station data provided by Dr. Greg Stone of the CSI-LSU and tidal data provided by Maria Suarez of LUMCON. Input from several professionals from various state and federal agencies was sought in the early stages of the project to select appropriate field site because of their extensive field experience on the Louisiana coast. In this regard we want to thank Quin Kinler and Cindy Steyer of the USDA-NRCS in Baton Rouge, LA, Ronnie Paille of the USFWS in Lafayette, LA and Darin Lee of the Office of Coastal Protection and Restoration in Thibodaux, LA. Sincere thanks to Quin for helping us identify and locate the landowners of the field sites.

Thanks to Sam Testa, Lisa Brooks, and Matt Moore at the USDA-ARS National Sedimentation Laboratory for their guidance and insight for the lab analyses carried out by UM-Biology team. Thanks to Dave Ruple and Dr. Mark Woodrey at Grand Bay National Estuarine Research Reserve (GNDNERR), for helping find suitable research sites, obtain data needed and for taking us where we needed to be despite the weather. Gratitude to UM Department of Biology for supporting this study. Thanks to Rani Menon for helping with logistical aspects of our experiment. Thanks to Jeffery Cannon, Mark Winkler, Patrick Hourguettes, Jessica Landrum, Sarah Magee, Melissa Baskin and Steven Nelson for helping us collecting soil and plant samples in the MS field sites.

CONTENTS

LIST OF FIGURES

LIST OF TABLES

NOTATIONS

The most significant parameters and their dimensions used in this report are listed as follows:

A_v	Projected area of vegetation stem [L^2]
C_D	Drag coefficient [-]
C_M	Inertia coefficient [-]
D_v	Stem diameter [L]
d	Water depth [L]
F	Force in vegetation [MLT^{-2}]
F_D	Drag force in vegetation [MLT^{-2}]
F_I	Inertia force in vegetation [MLT^{-2}]
g	Gravitational acceleration [LT^{-2}]
H	Wave height [L]
H_i	Incident wave height [L]
H_{rms}	Root-mean-square wave height [L]
H_s	Significant wave height [L]
h	Still water depth [L]
h_v	Vegetation height [L]
K_c	Keulegan-Carpenter number [-]
L	Wave length [L]
L_v	Vegetation span [L]
N_v	Vegetation density [L^{-2}]
Re	Reynolds number [-]
T	Wave period [T]
U and V	Depth-averaged flow velocities in x and y directions [LT^{-1}]
u	Characteristic or local horizontal flow velocity [LT^{-1}]
v	Local vertical flow velocity [LT^{-1}]
η	Water surface elevation [L]
λ	Spacing between vegetation elements [L]
μ	Dynamic viscosity of water [$ML^{-1}\ T^{-1}$]
ν_t	Turbulent viscosity of water [$ML^{-1}\ T^{-1}$]
ρ, ρ_ω	Mass density of water [ML^{-3}]

ACRONYMS

CARRI	Community and Regional Resilience Initiative
DHS	Department of Homeland Security
DOE	Department of Energy
LA	Louisiana
LSU	Louisiana State University
MS	Mississippi
NCCHE	National Center for Computational Hydroscience and Engineering
NSL	National Sedimentation Laboratory, USDA-ARS
ORNL	Oak Ridge National Laboratory
SERRI	Southeast Region Research Initiative
UM	The University of Mississippi
VOF	Volume-of-Fluid
1-D	One-dimensional
2-D	Two-dimensional
3-D	Three-dimensional

SOUTHEAST REGION RESEARCH INITIATIVE

In 2006, the U.S. Department of Homeland Security commissioned UT-Battelle at the Oak Ridge National Laboratory (ORNL) to establish and manage a program to develop regional systems and solutions to address homeland security issues that can have national implications. The project, called the Southeast Region Research Initiative (SERRI), is intended to combine science and technology with validated operational approaches to address regionally unique requirements and suggest regional solutions with potential national implications. As a principal activity, SERRI will sponsor university research directed toward important homeland security problems of regional and national interest.

SERRI's regional approach capitalizes on the inherent power resident in the southeastern United States. The project partners, ORNL, the Y-12 National Security Complex, the Savannah River National Laboratory, and a host of regional research universities and industrial partners, are all tightly linked to the full spectrum of regional and national research universities and organizations, thus providing a gateway to cutting-edge science and technology unmatched by any other homeland security organization.

Because of its diverse and representative infrastructure, the state of Mississippi was chosen as a primary location for initial implementation of SERRI programs. Through the Mississippi Research Initiative, SERRI plans to address weaknesses in dissemination and interpretation of data before, during, and after natural disasters and other mass-casualty events with the long-term goal of integrating approaches across the Southeast region.

As part of its mission, SERRI supports technology transfer and implementation of innovations based upon SERRI-sponsored research to ensure research results are transitioned to useful products and services available to homeland security responders and practitioners. Concomitantly, SERRI has a strong interest in supporting the commercialization of university research results that may have a sound impact on homeland security and encourages university principal investigators to submit unsolicited proposals to support the continuation of projects previously funded by SERRI.

For more information on SERRI, go to the SERRI Web site: www.serri.org.

EXECUTIVE SUMMARY

Surge and waves generated by hurricanes and other severe storms can cause devastating damage of property and loss of life in coastal areas. Vegetation in wetlands, coastal fringes and stream floodplains can reduce storm surge and waves while providing ecological benefits and complementing traditional coastal defense approaches such as permanent levees, seawalls and gates. However, little is known regarding the necessary scales and arrangements of vegetation needed to maximize surge and wave reduction benefit. Existing storm surge and wave models utilize the conventional quadratic law for bed shear stress and cannot realistically account for the mechanism of surge and waves through vegetation. Thus, it is highly desirable to develop more realistic parameterizations of the vegetation-dependent bottom drag coefficient. Hence, the main objective of Phase I of this research project was to conduct laboratory experiments, field measurements and computational modeling to investigate the effectiveness of wetland vegetation in mitigating hurricane and storm surges.

Extensive laboratory experiments were carried out to investigate wave attenuation by rigid and flexible model vegetation as well as live vegetation under monochromatic and random wave conditions in a flat-bottom wave flume. The live vegetation species include Spartina alterniflora (dormant and green) and Juncus roemerianus (green). The total number of wave and vegetation combinations was 1,041 for regular waves and 476 for irregular wave experiments. A total of 320 experimental configurations were utilized, with each configuration repeated three times for regular waves and up to five times for irregular waves to obtain more reliable data sets. Drag coefficients of all the tested vegetation species were derived from the collected wave gage data and video images, and regression equations were derived for the drag coefficient as functions of the Reynolds number, Keulegan-Carpenter number and vegetation submergence ratio. Laboratory experiments were also conducted to assess the effect of rigid model vegetation on wave setup over a sloping beach. The experiments demonstrated the reduction of wave setup and runup by vegetation over a sloping beach.

Field investigations of surge and wave attenuation by vegetation included two campaigns under tropical storm and winter cold front conditions. Considerable effort was devoted to select sites at Terrebonne Bay, LA, where permission was obtained to access a privately-owned wetland suitable for the project. An array of instruments, including 9 wave gages and one water level gage, was developed and deployed at a fixed location in Terrebonne Bay to measure wave attenuation over shallow water and salt marshes during the hurricane and cold-front seasons of 2009 and 2010. In addition to the instrument array at the fixed location, five portable, self-recording wave gages were successfully deployed twice in Breton Sound and Terrebonne Bay in rapid response to Tropical Storm Ida in 2009 and Tropical Storm Bonnie in 2010, even though no hurricanes made landfall on the Mississippi and Louisiana coast in the project period of 2009-2010. The data collected at the fixed site at Terrebonne Bay was not conclusive because of unexpected factors which could not be controlled. However, valuable surge and wave attenuation data during the two tropical storms were collected.

Field investigations also included measurements of vegetation and soil properties. In addition to the field sites at Terrebonne Bay and Breton Sound on the Louisiana coast, eight transects were established at Graveline Bayou in Gautier, MS and the Grand Bay National Estuarine Research Reserve in Pecan, MS. Biomechanical properties Spartina alterniflora

and Juncus roemerianus and related soil properties were measured at the selected marsh sites. The relationship of the stiffness and height/diameter ratio of these vegetation species was established using the measured data. Vegetation height, diameter, coverage, and biomass in the lower and higher marshes as well as in coastal and inland marshes were compared. Seasonal vegetation growth was quantified.

Four typical numerical models were developed or adopted for quantifying the effects of vegetation on surge and waves. The models included a depth-averaged two-dimensional shallow water model for long waves such as tsunami wave, a one-dimensional Boussinesq model for short waves such as wind waves, a vertical two-dimensional model based on the Navier-Stokes equations for both long and short waves, and a wave-action model for wave energy spectra. The first three models are phase-resolving models that compute the wave dynamic deformation processes, and the fourth model is a phase-averaging model that determines the characteristic wave heght, period and spectrum distribution. All four models can handle both non-breaking and breaking waves. The models were tested using data from the present laboratory experiments and from the literature. The model results demonstrated the reduction of surge and waves by vegetation.

In the course fulfilling the goals of this project, the research team has devoted tremendous efforts that have resulted in the completion of all the planned tasks for Phase I. The laboratory and field data, the empirical formulas developed from the data, and the numerical models are all significant contributions to better understanding and ability t predict surge and wave attenuation by vegetation. It is anticipated that these results will find broad application in coastal management and planning for areas with existing coastal marshlands as well for marsh restoration and establishment efforts.

1. INTRODUCTION

1.1 General Information

This is the final report of the research project entitled "Investigations of Surge and Wave Reduction by Vegetation", Basic Ordering Agreement 4200000224, Task Order Number 4000075852, Project Number 80037, funded through the Southeast Regional Research Initiative (SERRI), managed by Oak Ridge National Laboratory (ORNL) and operated by UT-Battelle, LLC. The Agreement period was from January 1, 2009, to December 31, 2010, with a three-month no-cost extension to March 31, 2011.

1.2 Background and Objectives

As evidenced during Hurricane Katrina, surges and waves generated by hurricanes and other severe storms can cause devastating damage of property and loss of life in coastal areas. Traditional engineering approaches to mitigating these severe impacts include permanent levees, seawalls and gates. Despite considerable advances in these technologies, coastal regions are becoming increasingly and alarmingly vulnerable to natural and man-made disasters due to rapid urbanization, subsidence, wetland loss and potential sea level rise. According to 1998 statistics, the narrow coastal fringe comprising 17% of the contiguous U. S. land area is inhabited by more than 53% of the nation's population (Crowell et al. 2007). It is estimated that by the year 2020, 80% of the U. S. population will reside within 200 miles of ocean and lake coastlines, which are subjected to flooding caused by hurricanes and other strong storms. Therefore, improved measures for mitigating the impact of hurricane and storm surge are needed.

It is generally acknowledged that coastal features such as wetlands, coastal ridges, barrier islands, dunes, reefs, and coastal stream floodplain complexes can reduce surges and waves, complementing the previously noted traditional engineering approaches. However, little is known regarding the necessary scales and arrangements of these features to maximize surge and wave reduction benefits. Because these features also provide significant ecological and economical benefits, tools are needed to assess trade-offs between ecological and storm mitigation benefits and to support decisions that will balance these benefits with the need for improved coastal protection.

Vegetation in wetlands, coastal fringes and stream floodplains can effectively reduce the flow speed, modify turbulence structure, attenuate surge and wave energy, and affect sediment dynamics. In the past, the potential of wetlands to dampen storm surge has been expressed by empirical rules of thumb based on informal observation. For example, the U. S. Army Corps of Engineers (1965) indicated that storm surge could be reduced by 1 m over an inland length of 14.5 km. However, recent studies point out that such constant rates do not account for transient forcing and local topography (Resio and Westerink 2008).

Existing storm surge and wave models utilize the conventional quadratic law for bed shear stresses. For flows over flooded areas with vegetation, the bottom drag coefficient is not only a function of water depth, but also depends on the type and density of the vegetation as well as the flow speed, which may generate a drag force exceeding the bending strength of the seagrass blades and result in a sharp reduction in bed resistance at high speeds associated with storm surge. Thus, it is highly desirable to develop new parameterizations of the bottom drag coefficient that reflect realistic flow conditions over

vegetated low-lying lands. New formulations of the vegetation-dependent bottom drag coefficient rely on careful laboratory and field experiments for accurate delineation.

This study aimed to investigate interactions among surge, wave and vegetation through laboratory experiments and field observations, and to develop and validate methods to quantify the reduction of surge and waves by vegetation. The objectives of the studies are to:

- Provide field and laboratory datasets of surge and wave attenuation by wetland vegetation for validation of numerical models and improved estimates of frictional resistance algorithms and coefficients;
- Demonstrate quantification of surge and wave reduction by vegetation using a variety of computational models typically used in coastal engineering practice;
- Develop guidance for characterizing the attenuation of surge and waves as a function of vegetation type, density, and height (Information will be limited to the types of vegetation measured in the field and laboratory studies);
- Characterize each experimental site with respect to soil classification, sediment bulk density, organic matter content, texture, salinity, pH, elevation, and plant growth form;
- Establish relationships between attenuation of surge and waves, botanical characteristics, and site characteristics; and
- Identify field demonstration site(s) and generate online video clip(s), with quantitative information relating vegetation to wave and surge attenuation, for illustrating the value of natural landscape features.

1.3 Planned Tasks

The project was divided into three interrelated tasks: laboratory experiments, field investigations, and computational modeling, as described below.

Task 1: Conduct laboratory experiments to assess the dissipation of wave energy and water level changes induced by vegetation

Laboratory experiments were carried out in the wave flume facility at the USDA-ARS National Sedimentation Laboratory (NSL), Oxford, Mississippi to investigate wave attenuation by rigid and flexible model vegetation as well as live vegetation under monochromatic and random wave conditions in a flat-bottom wave flume. The live vegetation species include *Spartina alterniflora* (dormant and green) and *Juncus roemerianus* (green). Laboratory experiments were also conducted to assess the effect of rigid model vegetation on wave setup over a sloping beach installed in the same wave flume.

Task 2: Conduct field investigations to assess surge and wave reduction by vegetation

Field investigations covered hydrodynamic and biomechanical aspects of wave/surge and vegetation. The hydrodynamic program consisted of two subtasks: 1) wave and surge attenuation field experiments under winter storm conditions, and 2) surge attenuation under tropical storm conditions. The first subtask was conducted at fixed locations, while the second subtask depended on the predicted landfall location of a tropical storm or hurricane. The rationale for having two separate field programs was to account for the fact that winter cold fronts occur much more frequently than tropical storms. Waves and water level changes caused by frequent cold fronts (about 24 per year) increase the probability of

making adequate numbers of field observations to understand the physics of fluid-vegetation interactions. The second subtask provided valuable datasets under realistic hurricane and field conditions.

The biomechanical program was directed towards the measurement of coastal vegetation and soil properties during various seasonal conditions. The collected data included vegetation height, diameter, density, stiffness and above/belowground biomass, as well as soil moisture, composition, and grain size at several sites located on the Louisiana and Mississippi coasts.

Task 3: Data compilation and model validation of surge and wave reduction by vegetation

The data collected in the present laboratory/field experiments and in other investigations published in the literature were synthesized and applied to validate and develop algorithms and models to account for the effects of vegetation on storm surge, current and waves. The drag coefficients of selected vegetation species were related to wave and vegetation parameters. A depth-averaged 2-D shallow water model, a 1-D Boussinesq model, a vertical 2-D RANS (Reynolds-Averaged Navier-Stokes) flow model, and a wave-action energy balance model were applied to simulate the wave and surge attenuation by vegetation.

1.4 Project Team Organization

This project was conducted by a multidisciplinary research team consisting of researchers and professors in the fields of Computational Hydroscience and Engineering, Coastal engineering, Geotechnical engineering, Biology and Ecology, and from universities and government agencies. The institutes participating in this project were the National Center for Computational Hydroscience and Engineering (NCCHE) and the Biology Department, The University of Mississippi (UM); the USDA-ARS National Sedimentation Laboratory (NSL), Oxford, MS; and the Department of Civil and Environmental Engineering, Louisiana State University (LSU), Baton Rouge, LA. The research project was led by Dr. Weiming Wu (PI). Corresponding to the three research tasks mentioned above, three teams were established as follows:

Computational modeling team (NCCHE):

Dr. Weiming Wu (PI), Research Associate Professor
Dr. Yan Ding, Research Assistant Professor
Dr. Soumendra N. Kuiry, Research Scientist
Dr. Mingliang Zhang, Postdoctoral Research Associate (left in Sept. 2010)
National Center for Computational Hydroscience and Engineering (NCCHE)
The University of Mississippi, MS 38677

Laboratory experiment team (NSL):

Dr. Daniel Wren (Co-PI), Research Hydraulic Engineer
National Sedimentation Laboratory, USDA-ARS, Oxford, MS 38655

Dr. Yavuz Ozeren, Research Scientist
Stationed at Biology Department and NCCHE, The University of Mississippi, MS 38677

Field investigation team (LSU and UM-Biology):

Dr. Qin Chen (Co-PI), Associate Professor
Dr. Guoping Zhang (Co-PI), Assistant Professor
Mr. Ranjit Jadhav, PhD Student
Mr. James Chatagnier, MS Student
Civil Engineering Dept., Louisiana State University, Baton Rouge, LA 70803

Dr. Marjorie Holland (Co-PI), Professor
Miss Ying Chen, MS Student
Ms. Leili Gordji, Research Assistant (Jan.-July, 2009)
Biology Department, The University of Mississippi, MS 38677

1.5 Research Approaches

The project was conducted through field investigations, laboratory experiments and computational modeling. These three approaches complemented one other, resulting in a much more successful effort than would be possible using only one of these approaches. The field investigations provide understanding and description of surge and wave attenuation under realistic prototype conditions with winter storm and tropical storm seasons. The laboratory experiments provide systematic physical insight into the problem in a well-controlled environment that reliably covers a wider range of wave and vegetation parameters than the field sites. The field investigations and laboratory experiments provided a large number of data sets for developing and validating formulas and models to quantify surge and wave attenuation by vegetation. The numerical analysis, after validation by experimental data, complements the laboratory and field experiments by extending the range of wave conditions and vegetation properties and by providing more comprehensive understanding and description of the phenomena.

The project was carried out across multidisciplinary research fields, including Computational Hydroscience and Engineering, Civil Engineering, Coastal Engineering, Geotechnical Engineering, Biology and Ecology. Even though we have focused more on the hydrodynamic aspect of the problem, we considered the biomechanical properties of vegetation and geotechnical properties of soils, as well as seasonal growth form of vegetation species under study.

1.6 Project Progress and Difficulties

Since January 2009, our research team has made significant progress in field measurements, laboratory experiments and computational modeling for attenuation of waves and surges by vegetation. We devoted considerable effort to select sites at Terrebonne Bay, LA and obtain permission to access the privately-owned wetland suitable for this project. We also established eight transects at Graveline Bayou in Gautier, MS and the Grand Bay National Estuarine Research Reserve in Pecan, MS, and measured the biomechanical properties of *Spartina alterniflora* and *Juncus roemerianus* and the related soil properties at selected marsh sites. We developed and deployed an array of instruments, including 9 wave gages and one water level gage, at a fixed location in Terrebonne Bay to measure wave attenuation over shallow water and over salt marshes in hurricane and cold-front active seasons in 2009 and 2010. In addition to the instrument array at the fixed

location, we also successfully deployed five portable, self-recording wave gages twice in Breton Sound and Terrebonne Bay in rapid response to Tropical Storm Ida in 2009 and Tropical Storm Bonnie in 2010, respectively. We carried out laboratory experiments to investigate the effectiveness of wave attenuation by rigid and flexible model vegetation as well as live vegetation under monochromatic and random wave conditions. The live vegetation species include *Spartina alterniflora* (dormant and green) and *Juncus roemerianus* (green). We developed or adopted a depth-averaged 2-D shallow water model for long waves, a 1-D Boussinesq-type model for short waves, and a vertical 2-D RANS model for both long and short waves, and a wave-action model for wave energy spectra to account for the effects of vegetation on surges and waves, tested these models using measurement data from the literature and through the present experiment work. These accomplishments demonstrate that we fulfilled the goals of the project.

We encountered difficulties during field experiments, which were affected by many factors out of our control. Data collection during tropical storms and hurricanes is quite dangerous and required careful planning, preparation and execution. Some devices that were installed at the fixed Terrebone Bay field site were damaged by passing boats or severe weather. Although the hurricane season in 2010 has been very active, none of the hurricanes has made landfall on the Mississippi and Louisiana coast. These difficulties resulted in only two measurements for the tropical storm conditions.

1.7 Technology Innovation and Advantages Gained

This research project has carefully addressed high-priority needs in the areas of coastal protection, wetland management and erosion control. Field and laboratory data on wave and surge reduction by vegetation of different coastal species, at different depths, and at different times of the year have been collected to refine existing models and develop new models. The species studied, *Spartina alterniflora* and *Juncus roemerianus*, are common to the Gulf Coast where hurricanes often occur, and they may be effective in holding wetland soils because their roots and rhizomes are not easily moved by wave action. Their effectiveness of dissipating wave energy and reducing wave setup has been quantified through field and laboratory observations and computational modeling. The flexibility of aboveground plant parts as well as the resilience and resistance of belowground plant parts to wave effects shall be investigated. The research has generated very valuable datasets that can be exploited by coastal restoration and disaster mitigation organizations and authorities, such as the U. S. Army Corps of Engineers, Federal Emergency Management Agency, National Oceanic and Atmospheric Administration, Mississippi and Louisiana Departments of Natural Resources, and the U. S. Department of Agriculture, as well as academic communities.

1.8 Outline of the Report

This report is organized into seven chapters. Chapter 1 provides a general introduction of this project. Chapter 2 provides a comprehensive literature review on surge and wave attenuation by vegetation, including the role of vegetation in coastal protection, quantification of vegetation effects on current and waves, past laboratory experiments, field investigation and numerical modeling, as well as coastal marsh features related to the present topic. Chapter 3 details the laboratory experiments, including the experimental setup, laboratory measurement technologies, and data analysis, including the calculation of

drag coefficients. Chapter 4 describes the field investigations of surge and wave attenuation, focusing on hydrodynamics, while Chapter 5 presents measurements of coastal vegetation and soils at the field sites located on the Louisiana and Mississippi Gulf coasts. The vegetation species studied are *Spartina alterniflora* and *Juncus roemerianus*. Field site selection, field measurement technologies, and analysis methods are described, and the collected data are synthesized. Chapter 6 describes the computational models for simulating effects of vegetation on surge and waves. The models include a depth-averaged 2-D shallow water model for long waves, a 1-D Boussinesq-type model for short waves, a vertical 2-D RANS model for both long and short waves, and a wave-action model for wave energy spectra. Chapter 7 gives conclusions and planned future work. Finally, references are listed, and four appendices contain data sets and synthesized figures. Appenix A presents the laboratory experiment data. Appendix B includes the field data of surge and wave collected during tropical storms and winter cold fronts. Appendix C covers the field data of vegetation and soil propteries. Appendix D shows the demonstration wave flume.

2. LITERATURE REVIEW

A considerable number of research efforts have been devoted to conduct laboratory experiments and field investigations and develop analytical and numerical models to understand and simulate attenuation of surges and waves by vegetation. A comprehensive literature review is presented in the following sections to highlight these studies over the the last decades.

2.1 Hurricane Disaster and Coastal Protection

The northern Gulf of Mexico coast of Louisiana and Mississippi annually experiences tropical storms. In the last 50 years, the region was impacted by 14 major hurricanes. According to some estimates, the region is more than twice as likely to see major hurricanes compared to the Texas and Florida coast (Resio 2007). The recent hurricanes Katrina (2005), Rita (2005), Gustav (2008) and Ike (2008) have shown the enormity of the devastation caused by the hurricane surge and waves to human life and property along the coast. For example, in 2005, after Hurricane Katrina, more than a quarter million people were displaced, more than 1,500 people lost their lives, and the property damage exceeded $100 billion (Graumann et al. 2005).

Until recently, coastal protection typically involved construction of hard structures, such as levees, floodgates, jetties and breakwaters. These measures may alter nearshore hydrodynamic and circulation patterns, disrupt regional and local morphodynamic processes, and cause unintended ecosystem consequences. The latest trends in coastal engineering are focusing more and more on sustainable, non-intrusive forms of coastal protection, such as natural wetland vegetation. Vegetation plays an important role in the sustainable development of aquatic environment. Aquatic vegetation can help to dissipate incoming wave energy, regulate water levels, enhance deposition of sediment near coastal zones, improve water quality, reduce flood and storm damages, provide important fish and wildlife habitats, and support recreational activities.

Different types of vegetation along coasts can protect the shoreline from surge and wave attacks during severe hydrological conditions. There are numerous examples showing the importance of vegetation on shoreline stability: the harvesting of Kelp *Laminaria hyperborea* in the Norwegian coast (Dubi and Torum 1995, Mork 1996), the kelp beds of *Macrocystis pyrifera* on the Californian coast (Elwany et al. 1995, Elwany and Flick 1996), seagrass meadows of *Posidonia oceanica* along the Mediterranean coast (Gacia and Duarte 2001), the *Spartina* canopies (Möller et al. 1996, 1999) or *Zostera marina* (Fonseca and Calahan 1992) fields in English salt marshes. Magi et al. (1996) and Mazda et al. (1997) studied the quantitative effects of vegetation species, *Rhizophora stylosa* and *Kandelia candel*, respectively, on the reduction of sea waves, based on field observations. Massel et al. (1999) discussed the effect of *Rhizophora species* on the reduction of sea waves.

Coastal marshes are typically protected by barrier islands. When the barrier islands disappear, so do the marshes mainly because of the wave-induced damage and erosion. Previous studies (e.g. Roland and Douglass 2005) have found a strong correlation between the level of wave energy and the survival of wetland marshes.

2.2 Quantification of Vegetation Effects on Current and Waves

2.2.1 Resistance of Vegetation to Current

Vegetation is classified to be either flexible or rigid based on whether it is subject to deformation under flow. Herbaceous species such as grasses usually are flexible, whereas woody species such as trees usually are rigid. However, it is recognized that different portions of the plant and the same plant in different stages of its life cycle can behave in significantly different ways.

As an approximation, a vegetation stem (such as tree trunk) is often conceptualized as a cylinder. The total force exerted on a vegetation element is the sum of a drag force and an inertia force, as expressed by the Morison equation (Morison et al. 1950):

$$\vec{F} = \frac{1}{2} C_D \rho A_v |\vec{u}| \vec{u} + C_M \rho V_v \frac{d\vec{u}}{dt} \tag{2.1}$$

where $\vec{F}$ is the total force on the vegetation element, C_D is the drag coefficient, C_M is the inertia coefficient, ρ is the water density, A_v is the projected area defined as the frontal area of a vegetation element projected to the plane normal to the streamwise flow direction, V_v is the volume of a vegetation element, and $\vec{u}$ is the vector of flow velocity acting on the vegetation element. Because the inertia force is usually smaller than the drag force, the inertia force has been ignored in many studies (Dalrymple et al. 1984, Shimizu and Tsujimoto 1994, Wu 2007).

The drag coefficient is the key parameter in Eq. (2.1). The drag coefficient for a single cylinder in an ideal two-dimensional flow is related to the Reynolds number. Li and Shen (1973) investigated the drag coefficient for a group of cylinders with various set-ups. They identified four factors that need to be considered to determine the drag coefficient: (1) turbulence of the flow, (2) non-uniform velocity profile, (3) free surface, and (4) blockage. Lindner (1982) suggested that in densely vegetated channels, the first two of these factors are of minor importance and can be neglected. Lindner extended the work of Li and Shen, and established a method to compute the drag coefficient C_D for a single rigid plant in a group.

Nepf (1999) explored the drag of vegetation on steady currents using arrays of rigid cylinders to be represented as vegetation. The study concluded that the bulk drag coefficient is a function of vegetation density as represented by the occupied fractional volume. A similar conclusion was made by Bokaian and Geoola (1984). They showed that the bulk drag coefficient is relatively constant for fractional volume up to 0.01 and declines steadily beyond this density.

Ghisalberti and Nepf (2004) considered the effects of canopy submergence on flow, turbulence and drag. They observed significant reduction in drag relative to the Nepf (1999) expression when the top of the canopy was submerged, attributed to vortex shedding by the free end of the submerged grass blades. The bulk drag coefficient was approximately 64% of its value for emergent plants, depending weakly on the depth of the shear layer inside the canopy. They did not explore the effects by changing the degree of submergence.

As an alternative approach, the resistance introduced by vegetation can be incorporated into the Manning coefficient. Consider a steady, uniform flow in a channel with rigid vegetation distributed nearly uniformly over the bed. The total resistance is a combination of the bed shear and the vegetation drag. Thus, the following relation exists (Wu 2007)

$$n^2 = n_b^2 + \frac{1}{2g(1-c_{v0})} C_D N_v A_v \eta_v^2 \min(\frac{h_v}{h}, 1.0) R_s^{1/3} \quad (2.2)$$

where n is the Manning coefficient corresponding to the total roughness, n_b is the Manning coefficient corresponding to the bed roughness, N_v is the number of plants per unit bed area, h is the flow depth, h_v is the vegetation height, η_v is a coefficient of about 1.0 (Stone and Shen 2002), and R_s is the hydraulic radius of the bed with vegetation. Many models simply set R_s as the flow depth h, while Barfield et al. (1979) and Wu (2007) considered the effect of emergent and submerged vegetation on the flow "eddy size". Eq. (2.2) is similar to the approach proposed by Petryk and Bosmajan (1975), which was applied to mangroves, using an increased Manning friction values for mangrove field sites derived from stem densities and diameters (Furukawa et al. 1997, Mazda et al. 1995, Wolanski et al. 1980).

One may also use Eq. (2.1) to compute the drag force on flexible vegetation, but the projected area should be computed using the deformed height or the drag coefficient that has to be related to flow conditions. For vegetation with limbs and leaves, the conceptual model of single cylinder is no longer realistic. In this case, the projected area is often defined as the blockage area of the limbs and leaves. However, the limbs and leaves deform under flow shear so that the blockage area changes with flow conditions.

For vegetation submerged in intermediate flow, Ree and Palmer (1949) presented a set of curves for the Manning n as a function of UR. For both submerged and emergent vegetation, Wu et al. (1999) related the drag coefficient and the Manning n to the Reynolds number and the bed (or friction) slope. The obtained relations of $n \sim UR$ or $n \sim (Re, S)$ vary with vegetation species.

According to Kouwen et al. (1969), the resistance to the flow by flexible vegetation can be determined using a relative roughness approach similar to the widely accepted resistance relationships developed for rigid roughness in pipes and channels. Because flexible vegetation bends when subjected to shear, its roughness height is a function of vegetation properties and flow parameters. The significant vegetation properties are the stem density M and the flexural rigidity in bending, given by $J=EI$. Here, E is the stem's modulus of elasticity and I is the second moment of inertia of the stem area. Based on laboratory experiments on flow over flexible plastic strips, Kouwen and Li (1980) obtained

$$k_s = 0.14 h_v \left[\frac{(MEI/\tau)^{0.25}}{h_v} \right]^{1.59} \quad (2.3)$$

where h_v is the local height of the strips (m), τ is the local bed shear stress (N/m^2), and MEI is the flexural rigidity (Nm^2). The parameter MEI can be measured directly for different species using the "board drop" test (Kouwen 1988). Based on laboratory experiments for alfalfa, Bermuda grass, buffalo grass, blue grass, weeping love grass, Kentucky grass, Serica lespezeda, Sudan grass, and Rhodes grass, Kouwen (1988) (also see Temple 1987) related MEI with the vegetation height for growing and dormant grass species, respectively, as

$$MEI = 319 h_v^{3.3}, \quad MEI = 25.4 h_v^{2.26} \quad (2.4)$$

Application of Eq. (2.4) should be restricted to those grasses that have been tested. These grasses (e.g. alfalfa, Bermuda grass) are not as rigid as Spartina grasses. Its validity to other grasses such as Spartina grasses should be confirmed by experiments.

For flexible vegetation such as trees and bushes, the foliage, whether broad or needle-like, is the major contributor to the total drag. Reconfiguring or reshaping of the foliage is a critical process in generating drag. Considering this fact, Jarvela (2004) suggested the use of the leaf area index (i_{la}) in determining the friction factor. The leaf area index is conventionally defined as the ratio of the upper-side projected area of the leaves in canopy to the area of the surface under the canopy. The developed relation of the Darcy-Weisbach friction factor, λ, for partially submerged vegetation is

$$\lambda = 4C_{Dx} i_{la} \left(\frac{U}{U_x} \right)^x \frac{h}{h_v} \tag{2.5}$$

where C_{Dx} is a species-specific drag coefficient, U is the flow velocity, U_x is a reference velocity, and x is an exponent. Jarvela (2004) validated his formula against the experimental data of Kouwen and Fathi-Maghadam (2000) using coniferous trees.

Freeman et al. (2000) conducted experiments on the resistance due to shrubs and woody vegetation in a large 2.44-m-wide flume and a small 0.46-m-wide flume. A total of 20 different species of broadleaf deciduous vegetation commonly found in floodplains and riparian zones were evaluated. It was observed that the plant leaf mass trailed downstream forming a streamlined, almost teardrop-shaped profile. The leaf shape changed with velocity and became more streamlined with increasing velocity, yielding a significant decrease in the drag coefficient and resistance coefficient with velocity. Regression equations for the Manning n were obtained by Freeman et al. (2000) using these experiment data.

Other vegetation resistance mechanisms were investigated, e.g. depth-dependent vegetation effects (Fathi-Maghadam and Kouwen 1997, Kutija and Hong 1996) and the spatial distribution and hydraulic interaction between vegetation elements (Naot et al. 1997). Kutija and Hong (1996) studied flow through submerged, non-submerged, flexible and rigid vegetation and applied the cantilever beam theory (Timoshenko 1955) to the bending of flexible vegetation. The model used the one-dimensional horizontal momentum equation solved in the vertical direction.

2.2.2 Wave Attenuation by Vegetation

The theory of wave energy dissipation due to viscous boundary layer friction, permeability and the viscous nature of the sea bed in shallow water has been developed in great detail (Sleath 1984) since the early works of Putman and Johnson (1949), Bretschneider and Reid (1954) and others. Price et al. (1968) developed a hydrodynamic model that simulates the effects of seaweed as a high viscous layer. Camfield (1983) considered vegetation as a high friction area and studied wind-wave growth over shallow flooded regions.

Numerous models predict wave attenuation using time-averaged conservation equation of wave energy and account for vegetation effects in an energy dissipation term (Dalrymple et al. 1984, Mendez and Losada 2004), while others use the conservation of momentum approach (Kobayashi et al. 1993, Lima et al. 2006). These models were expressed in terms of

a wave shear stress friction coefficient (Teeter et al. 2001) or the drag force acting on the vegetation (Dalrymple et al. 1984, Kobayashi et al. 1993).

A popular approach for predicting wave attenuation by vegetation is the solution of the time-averaged conservation equation of wave energy in which the local flow field is estimated using linear wave theory. The effects of the vegetation are included only in the dissipation term in the energy equation used to obtain the local wave height. Theoretically, the depth-integrated energy dissipation rate per unit bed area is defined as

$$\varepsilon_v = \int_0^{h_v} N_v \left(F_x u_x + F_y u_y + F_z u_z \right) dz \tag{2.6}$$

where F_i and u_i are the components of force $\vec{F}$ and velocity $\vec{u}$ (i=x, y, and z).

Dalrymple et al. (1984) examined wave diffraction due to localized areas of energy dissipation, such as dense stands of kelp, pile clusters, or submerged trees, and derived an energy dissipation factor based on the Morison equation (2.1). Mendez and Losada (2004) provided a wave transformation model for submerged and emergent vegetation which includes an energy dissipation term similar to that proposed by Dalrymple et al. (1984). Assuming that the wave heights have an invariant Rayleigh distribution, Mendez and Losada (2004) obtained the following expression for the wave energy dissipation per horizontal unit area

$$\varepsilon_v = \frac{1}{2\sqrt{\pi}} \rho C_D N_v D_v \left(\frac{gk}{2\omega} \right)^3 \frac{\sinh^3 kh_v + 3\sinh kh_v}{3k \cosh^3 kh} H_{rms}^3 \tag{2.7}$$

where D_v is the diameter of the vegetation element, k is the wave number, ω is the wave angular frequency, and H_{rms} is the root-mean-squared wave height.

Kobayashi et al. (1993) presented a different approach based on the continuity and linearized momentum equations, and developed an analytical model to predict wave attenuation over vegetation by assuming an exponential decay of incoming irregular waves and adopting the quadratic friction law for the resistance due to vegetation. The drag coefficient is related to the Reynolds number. Their analytical solution was compared with 60 test runs conducted by Asano et al. (1988) using deeply submerged artificial kelp.

Mork (1996) extended the idea of high viscous layer and developed a theory to take into account the form drag for the canopy layer and the lower vegetative area. Massel et al. (1999) described sea wave reduction based on a mathematical model. Their study focused on the wave energy dissipation by bottom friction and vegetation density, where the vegetation impact was incorporated by an extra amount of the drag force.

Mazda et al. (1995) made an important observation from their numerical simulation that water flow in tidal creek is mainly driven by the drag force due to mangrove swamps. Based on this observation, Mazda et al. (1997) established a simple mathematical relation that balances water surface slope with the drag force caused by mangrove swamps. The detailed numerical study and comparison with the measured values confirmed that tidal flow in the swamps depends on the effective length of the vegetation which is a function of projected length and volume of mangrove vegetation. The study also showed that the drag coefficient increases with increasing value of the Reynolds number and tends to converge to a value 0.4 when the Reynolds number crosses the limit 5×10^4. Their suggested values of drag coefficient lie in the range of 0.4–10.

Mendez et al. (1999) developed a simplified model using potential flow and an eigenfunction expansion to analyze wave induced kinematics and dynamics of a submerged or emerged vegetation field. The model successfully predicted wave damping, vegetation and fluid motion and forces and moments on the vegetation.

A study carried out by Möller et al. (1999) reveals that wave attenuation does not vary linearly with distance across the salt marshes, but that most wave energy is dissipated or reflected over the first 10 to 50 meters of the salt marsh surface.

Lovas (2000) developed a wave transformation model incorporating the effect of kelp for the surf zone. The model was implemented considering variable depth to simulate wave breaking. However, due to the linearization of the force on the vegetation by the current, potential application of the model was limited (Mendez and Losada 2004).

The initial models were developed neglecting the plant motion in the flowing current. Later on, Mendez and Losada (2004) presented an empirical model for wave transformation through a vegetation field to predict wave damping and wave breaking on variable depths. The nonlinear expression of drag force was modified to take into account the swaying motion of vegetation such as seagrass by changing the characteristic velocity to the relative velocity between plant and current. Asano at el. (1993) also extended their earlier study to include the vegetation motion in flowing water.

Dean and Bender (2006) applied linear wave theory to illustrate wave set up caused by momentum transfer from breaking waves and energy dissipation due to vegetation. The study examined different features of the static setup component including effects of beach slope, wave nonlinearities and energy dissipation resulting from internal drag forces caused by vegetation and surface forces due to bottom friction.

2.3 Laboratory Experiments and Field Investigations

Different types of vegetation offer different amount of resistance to the shoreward propagating waves. Therefore, a number of laboratory experiments and field measurements on different vegetation species have been carried out by many investigators over time. The laboratory and field measurements are used to understand the physical processes and to validate mathematical models. Some examples are given below.

Asano et al. (1988) conducted experiments on wave attenuation due to vegetation in a 27 m long, 0.5 m wide and 0.7 m deep flume using flexible polypropylene strips of 0.25 m in length as model vegetation.

Gambi et al. (1990) studied flow speed reduction by *Zostera marina L.* (eelgrass) in a seawater flume, with the seagrass bed occupying only 20 percent of the width of the flume.

Dubi (1995) and Dubi and Torum (1997) presented laboratory experiments to investigate wave energy dissipation in a coastal kelp field of artificial *Laminaria hyperborean*, analyzing the sensitivity of the damping rate to several parameters. Experimental regular wave data were compared to previously existing theoretical work.

Li and Yan (2007) conducted experiments on wave-current-vegetation interaction in a flume of 15 m in length, 0.31 m in width, and 0.4 m in height, using semirigid rubber rods as model vegetation.

Schutten et al. (2004) measured the hydraulic forces on submerged aquatic vegetation by waves. The experiments were carried out in a wave-flume (5 m long, 0.6 m wide and 1 m deep), and replicas and real plants were used.

Augustin et al. (2009) conducted laboratory experiments on wave attenuation using synthetic vegetation under a range of wave conditions and plant stem densities. The bulk drag coefficient was determined using linear wave theory and the friction factor using a nonlinear Boussinesq model (COULWAVE). The drag coefficient obtained using linear theory showed a higher dependence on Reynolds number during emergent conditions than during near-emergent conditions. However, drag coefficients during near-emergent conditions exhibited somewhat higher correlation with the Keulegan–Carpenter number. The experiments proved that emergent conditions lead to a higher amount of wave attenuation compared to near-emergent conditions.

Knutson et al. (1982) conducted a field study on wave damping in two *Spartina alterniflora* marshes located on the eastern shore of Chesapeake Bay in Virginia. They found that the wave energy absorption is dependent upon the width and overall condition of the marsh and the severity of wave condition impinging on the shoreline; marshes are most effective in damping waves when water depth is less than plant height; during extreme coastal storms and hurricanes, wind set up may elevate water depth to a level several times higher than the plants, and under such conditions the wave damping accomplished by the plants will be relatively small.

Elwany et el. (1995) carried out experiments on *Macrocystis pyrifera* kelp forest on the propagating waves at Carlsbad, California to measure wave reduction. The measurements were continued for about 67-day period. Their study concluded that when the average vegetation density is about 10 plants per 100 m^2, the vegetation does not have a significant effect on waves. Such information can be important for mathematical models and as indication of limitation using coastal vegetation to protect shorelines.

Field observations of wave attenuation by seagrass were carried out in Duck Point Cove, near Bishop's Head Point, MD, in mesohaline Chesapeake Bay (Newell and Koch 2004). Time series of wave height and seagrass parameters were measured in different months at two adjacent sites parallel to the shoreline, one vegetated with *R. maritima* and the other non-vegetated. The size of *R. maritima* bed was about 600 m in the alongshore direction and 200 m in the cross-shore direction.

A field research of wave attenuation through vegetation at the Paulina Marsh was conducted in 2002 by WL/Delft Hydraulics (2003), in association with Netherlands Institute for Ecology. The waves and vegetation characteristics over a 26 meter long, straight transect of the marsh in August and September were measured.

Lightbody and Nepf (2006) conducted field investigation to test a simple method for estimating the velocity profile and longitudinal dispersion in emergent salt marsh canopies from knowledge of stem shape and the distribution of vegetation biomass. They measured the stem frontal area, flow velocity, vertical diffusion, and small scale longitudinal dispersion in a field of a monoculture of the tall form of *S. alterniflora* (smooth, relatively rigid leaves and culms having 5-15 mm diameter) on a bar in the middle of the Rowley River located at the Plum Island Estuary in Rowley, MA. The local tide was about 1.5 m and velocities on the nearby river channel reached 2-4 m/s.

Quartel et al. (2007) conducted field measurements in the Red River Delta, Vietnam. The field experiments were used to quantify wave reduction and wave energy dissipation using a model based on linear wave theory.

2.4 Numerical Modeling

Section 2.2 has included a significant number of mathematical models which are mostly based on the linear wave theory. This type of models can be categorized as phase-averaged models, which directly compute wave spectral variations in space and time by using a time-averaged wave energy equation and output wave energy spectra and statistical wave parameters such as significant wave heights, mean directions etc. (e.g. Dalrymple et al. 1984, Kobayashi et al. 1993). The energy dissipation due to vegetation expressed in Eq. (2.7) is often used in the wave energy equation as a sink term. Such models have been used in many coastal hydrodynamic models that compute current and waves separately with either considering or ignoring the interactions of current and waves. For example, Meijer (2005) implemented a capability of simulating wave attenuation by vegetation in the 2-D nearshore model SWAN.

In the last decades, due to the enormous advancement in computing capability, numerical models that directly simulate dynamic wave shape deformations have received much attention. This type of models can be categorized as phase-resolving models. The complete Navier-Stokes equations or the shallow water equations simplified from the Naver-Stokes equations are solved depending upon the complexity of the physical processes and the desirable level of accuracy. The shallow water equations require less computing resources and thus are more often used than the full Navier-Stokes equations. The drag force and inertia force are included in the governing equations as a sink term. Different discretization techniques such as finite-difference, finite-element and finite-volume methods are utilized to solve the system of equations. The phase-resolving models can give detailed wave phase information as waves propagate through vegetation zones but need more extensive computing efforts than the phase-averaging models.

The depth-averaged shallow water models (1-D and 2-D) have been extensively applied to simulate open-channel flows over both non-vegetated and vegetated beds (e.g. Wu et al. 2005). In the coastal context, such models can be used to simulate propagation of long waves. Notable analytical results include the one-dimensional solution of solitary wave on a sloping beach obtained by Carrier and Greenspan (1958). Synolakis (1986) conducted a series of experiments to understand the physical processes and proposed analytical solutions to compute runup on a sloping beach. However, the existing analytical runup models based on the non-linear shallow water equations (NSWEs) are restricted to the propagation of non-breaking waves on simple beach geometries (Carrier and Greenspan 1958, Synolakis 1986, Li and Raichlen 2001). In more general situations, numerical solutions of the NSWEs have become more and more popular. For example, Wolanski et al. (1980) developed a 2-D depth-integrated numerical model called 2DSWAMP to model flows in mangrove creeks. It was found that mangrove creeks experienced an asymmetry in the tidal current structure due to vegetation-induced resistance in mangrove reaches. Furukawa et al. (1997) used the model 2DSWAMP and a lake model in their study of tidal currents, cohesive sediment and organic carbon transport in a highly vegetated mangrove swamp in Australia.

The effects of mangrove forests on the flow structure in estuaries was also studied by Wu et al. (2001) using a two-dimensional depth-integrated model. The hydrodynamic model was modified to include both the effects of drag force induced by mangrove trees and the blockage effects on the mass fluxes through mangrove forests. Two idealized tests were considered and it was found that the velocities were significantly reduced by mangroves in the forested area, and correspondingly a significant increase occurred in the

velocities in the main channel. The model developed by Wu et al. (2001) was enhanced by Struve et al. (2003). They conducted experiments in a laboratory flume and further validated the numerical model considering additional resistance and blockage created by mangrove model trees. Drag coefficient values obtained from calibrating the hydrodynamic model with the experimental data ranged from 0 to 4.5. Teo et al. (2009) applied the two-dimensional numerical model of Wu et al. (2001) to an idealized estuary to study the impact of mangroves on tsunami waves. The vegetation was represented by rigid circular cylinders. The numerical experiments showed that the vegetation significantly impacted the wave height and velocity inside the vegetated area. Harada and Imamura (2005) performed numerical simulations, including an evaluation of the quantitative effects of coastal forests in controlling tsunami reduction and damage. They found that an increase in forest width can reduce not only inundation depth, but also the currents and hydraulic forces behind the coastal forest. Thuy et al. (2010) also applied a depth-averaged 2-D shallow water model for simulating tsunami wave runup on a vegetated beach, and explored the influence of coastal forest gap on tsunami inundation.

Erduran and Kutija (2003) introduced a quasi-three-dimensional model, which coupled the finite volume solution of the two-dimensional shallow water equations with a finite difference solution of Navier–Stokes equations for the vertical velocity distribution. The drag forces were included in both sets of equations, and a cantilever beam theory was used to deal with flexible vegetation. Hall and Cratchley (2006) tested a number of numerical models based on finite element and finite volume methods to study tidal wave movements in the vegetated Mawddach estuary. The models simulated the physical processes of energy dissipation and transient water storage within different wetland vegetation communities.

As a long wave approaches shallow water, its wavelength and energy are compressed and its amplitude increases. In this region nonlinearities lead to steepening waves, propagating bores or even breaking waves. Only the integral form of the NSWEs is valid near discontinuities and modeling this regime accurately requires numerical scheme that can handle steep gradients and discontinuities. When dealing with steep gradients, volume conservation becomes an important factor for models based on non-conservative, differential form of the shallow water equations. The finite volume method has the advantage of solving integral form of the equations as a fully conservative scheme. The Godunov-type formulation with Riemann solver can handle steep gradients through shock-capturing ability. Dodd (1998) investigated wave run-up, overtopping and regeneration problem using the approximate Riemann solver of Roe (1981) and resolved the moving boundary value problem by imposing a minimum water depth criteria in the dry area. Hu et al. (2000) presented a similar model based on the Harten, Lax and van Leer (HLL) approximate Riemann solver (Harten et al. 1983). Brocchini et al. (2001) applied finite volume method to two-dimensions using weighted average flux method with an exact Riemann solver and the moving shoreline was treated as a cavitation problem. Wei et al. (2006) presented a run-up model in two-dimensions using an exact Riemann solver. Delis et al. (2008) developed one- and two-dimensional run-up models based on Roe's Riemann solver and improved wet/dry algorithm. Mahdavi and Talebbeydokhti (2009) proposed a one-dimensional wave runup model using a first-order centered scheme (FORCE). These finite volume based numerical models can also be used to simulate wave propagation through vegetation field by considering the resistance force induced by vegetation.

Unfortunately, the numerical models based on the shallow water equations are not suitable for modelling waves propagating from relatively deep water to shallow water and

when the propagating waves are short in nature. In these circumstances, another class of numerical models based on the solution of the extended Boussinesq equations is a suitable choice. The pioneering work of Peregrine (1967) established the foundation for many Boussinesq-type models used today. Madsen et al. (1991), Madsen and Sørensen (1992), Madsen et al. (1997) and Nwogu (1993) enhanced the classical Boussinesq equations. The former introduced third-order terms with a free parameter into the momentum equation, while the latter derived a new set of governing equations from the three-dimensional Euler equations with the horizontal velocity evaluated at a reference depth. The two approaches have identical dispersion characteristics that show good agreement with linear wave theory. Tonelli and Petti (2009, 2010) proposed a hybrid scheme based on the extended Boussinesq equations of Madsen and Sørensen (1992) for slowly varying bathymetry. The numerical code combines the finite volume technique, applied to solve the advective part of the equations, with the finite difference method, used to discretize dispersive and source terms. Shiach and Mingham (2009) studied the accuracy of a second-order discretization of the unsteady term in the extended Boussinesq equations unlike the fourth-order discretization of the term presented in Erduran et al. (2005). In these Boussinesq-type numerical models the effects of vegetation were not considered. The authors primarily focused on wave propagation from deep to shallow water. In the later years the Boussinesq-type models have been used to simulate decay in wave height due to vegetation. For example, Chen et al. (2007) studied the effects of seagrass bed geometry on wave attenuation and suspended sediment transport using a modified Nearshore Community Model (NearCoM), which uses the Boussinesq-type equations proposed by Wei et al. (1995). They found that when wave orbital velocities and the seagrass canopy interact, increasing seagrass bed width in the direction of wave propagation results in higher wave attenuation, and increasing incoming wave height results in higher relative wave attenuation.

With advancement of computer technologies in recent years, the computation of flow through vegetation zones based on the Navier-Stokes equations has gained more and more attentions. For flow in vegetated open channels, numerical modeling has been performed by Shimizu and Tsujimoto (1994), Lopez and Garcia (2001), and Neary (2003) using Reynolds-averaged Navier-Stokes (RANS) equations with two-equation isotropic turbulence models, as well as by Naot et al. (1996) and Choi and Kang (2001) using multi-equation anisotropic turbulence models. All these RANS models include the drag force terms in the momentum equations and consider the generation of turbulence by vegetation. Su and Li (2002) and Cui and Neary (2002) conducted large eddy simulations (LES) of flow through vegetated open channels. Li and Yan (2007) investigated interactions among current, waves and vegetation using 3-D Reynolds-averaged Navier-Stokes equations with a one-equation isotropic turbulence model. Physical experiments were also carried out to verify the model. The unsteady fluid force on vegetation was described by a time dependent inertia component and a drag component. The model was applied to different wave and flow conditions such as pure waves, pure current, as well as wave-current. The model successfully reproduced the laboratory measurements on the turbulence and velocity profiles induced by vegetation–current interaction.

However, those RANS models mentioned above did not consider breaking waves. In order to simulate breaking waves, one of the choices is to use the VOF (volume of fluid) method in vertical 2-D and 3-D models. For example, Kothe and Mjolsness (1992) proposed a two-dimensional (2D) model (called RIPPLE) of incompressible fluid flows based on the VOF method. Iwata et al. (1996) used a modified version of the SOLA-VOF model for

numerical analysis of breaking and post-breaking wave deformation due to submerged impermeable structures. Lin and Liu (1998) coupled the RIPPLE model with the $k-\varepsilon$ turbulence model and applied it to calculate breaking waves on a sloping beach. Troch and Rouck (1999) discussed the implementation of an active wave generating–absorbing boundary condition for a numerical model (VOFbreak2) based on the VOF method. Hieu et al. (2004) simulated breaking waves in a surf zone using a VOF-based two-phase flow model. Lin and Xu (2006) developed a Numerical Water FLUME called NEWFLUME to simulate wave propagation and different hydraulic problems. Ketabdari et al. (2008) and Xiao and Huang (2008) described the development of a numerical model based on RANS and $k-\varepsilon$ equations to estimate the impact of wave propagation on a sloped beach.

2.5 Features of Coastal Marshes

2.5.1 Estuarine Characteristics

An estuary is a partially enclosed body of water where fresh water from rivers and streams mixes with salt water from the ocean, and supports communities such as tidal fresh water, brackish and salt marshes. Tidal inundation is the main factor shared by salt, brackish and fresh marshes, with dissimilarity in major floristic elements and physiognomy correlated to variations in salinity. Areas with salinities greater than 15 ppt (parts per thousand) will support salt marshes and less than 0.5 ppt will support fresh marshes. Brackish marshes occupy the salinity zone between the fresh and salt marsh zones (Metzler and Rosza 1982, Odum 1978, Odum et al. 1978).

Estuarine wetlands are in the mid and lower portion of the estuary nearer marine conditions while tidal fresh water wetlands are usually located at the head of estuaries. Tidal fresh water wetlands are ecosystems characterized by fresh water conditions which maintain low salinities, plant communities dominated by fresh water species, but experience a daily ocean-induced tidal fluctuation (Odum 1978). Although tidal fresh water wetlands occur in virtually every U.S. coastal state, they are a distinctive type of ecosystem located between tidal estuarine wetlands and non-tidal fresh water wetlands. These wetlands appear to have a greater number of potential ecological niches and present a more diverse habitat than estuarine wetlands because of a high species diversity of plants (Odum et al. 1978).

Salt marshes, which are coastal wetlands rich in marine life, can be found throughout the world on protected temperate shorelines and at the edges of estuaries where fresh water mixes with seawater. A salt marsh, which is a unique environment, is classified as being the intertidal coastal area of fine sediment that has been transported by water and is stabilized by vegetation (Edwards and Proffitt 2003, Tiner 2005). Salt marshes are also called nurseries because many species of fish and shellfish spend their early stages of life in the marshes as the marshes provide abundant food and shelter for their young. In addition, salt marshes serve to shield and protect coastal areas from floods and storms because they can take the brunt of storm surges, buffering the shoreline from flood and storm damage (Weis and Butler 2009).

Wetlands in many coastal areas are threatened by sea level rise. Although the effects of salinity and water level on coastal marsh vegetation have been widely investigated, there are few studies (Baldwin and Mendelssohn 1998) about the role of disturbance in causing shifts in vegetation due to changes in salinity or water level. Baldwin and Mendelssohn

(1998) examined interactions of disturbance with salinity and water level treatments. Their results suggest that disturbance is an important component of vegetation change in response to rising sea level, catalyzing rapid shifts in vegetation structure or accelerating wetland loss. Sandy sediment deposition results in increased marsh plain elevation and bulk density. Soil nitrogen is also decreased with sandy sediment deposition. These changes create a strong wetland-upland gradient and influence the development of well-defined vegetation zones from wetland to upland (Byrd and Kelly 2006).

2.5.2 Vegetation in the U.S. Coasts

Salt marshes are composed of a variety of plants including sedges, rushes, and grasses (Mitsch et al. 2009). *Spartina alterniflora* Loisel. (smooth cordgrass), a perennial emergent grass, is a dominant species in intertidal wetlands, especially in estuarine salt marshes (Fig. 2.1). The salt marsh often grows along sea water, from Quebec and Newfoundland to Florida and Texas. *S. alterniflora* was introduced in oyster culture, in Pacific County, Washington, and spread along the Atlantic coast of Europe (Hitchcock and Chase 1950). It is often prolific in areas exposed to moderate waves such as coastal marsh edges. The stems, which are often 1 cm wide, are soft and spongy or succulent at base. This plant, which has long and extensive roots, can increase belowground production.

Spartina patens (Aiton) Muhl. (saltmeadow cordgrass or Salt Marsh Hay), which is also known as salt hay grass, is a species found in high marsh zones where it is covered at times by high tides or in saline marshes inland (e.g., the inland areas of brackish coastal salt marsh, USDA Plants Database 2010)(Fig. 2.2). *Spartina patens* is the most common indicator species for the highest marsh zone and the high marsh (Adams et al. 2008, Woodrey and Walker 2009). *Juncus roemerianus* Scheele. (black needlegrass rush), a typical emergent marsh plant forming extensive and often dense stands, is primarily restricted to coastal marshes and estuaries of the South Atlantic and Gulf Coasts of the United States (Fig. 2.3). The leaves which can grow to 2 m tall are longer than the stems (culms). The species is one of about thirty rhizomatous perennials which persist as major vegetational components of these temperate and subtropical salt marshes (Eleuterius 1975).

In addition, Pennings et al. (2005) investigated the factors producing zonation patterns of the dominant plants in salt marshes in south-eastern U.S.A. They found that *Juncus roemerianus* dominates the high marsh and *Spartina alterniflora* dominates the middle and low marsh. Although *Spartina* occurred naturally at low densities in the *Juncus* zone, it performed well if transplanted there only if neighbors were removed, indicating that its lower limit was set by physical stress (Pennings et al. 2005). However, *Juncus roemerianus* dominates the low, middle and high marsh zones in inland marshes and *Spartina alterniflora* dominates the low marsh in coastal marshes at the Grand Bay and Graveline Bayou along the Gulf Coast of Mississippi. The middle and high marsh zones in coastal marshes also support *Distichlis spicata* and/or *Scirpus robustus* (GNDNERR website, Woodrey and Walker 2009).

Fig. 2.1. Distribution of *Spartina alterniflora* Loisel. on the U. S. Coasts
(http://plants.usda.gov/maps/)

Fig. 2.2. Distribution of *Spartina patens* (Aiton) Muhl. on the U. S. Coasts
(http://plants.usda.gov/maps/)

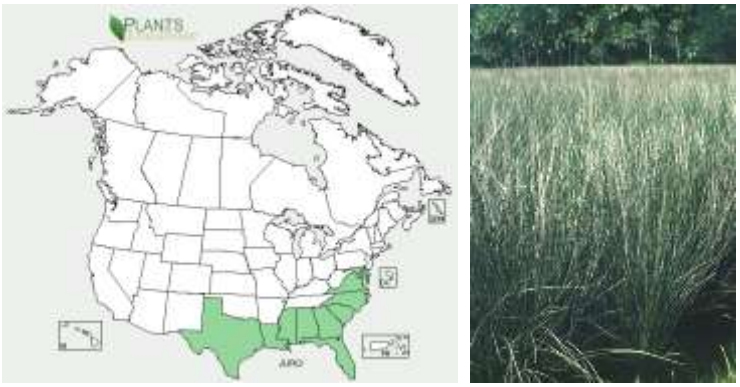

Fig. 2.3. Distribution of *Juncus roemerianus* Scheele. on the U. S. Coasts
(http://plants.usda.gov/maps/)

2.5.3 Marsh Zonation

With the reduction in sea level rise in northeastern U.S.A., *Spartina* stands were able to perpetuate themselves, moving outward over tidal flats and landward over gradually

flooding upland or fresh water wetlands instead of being submerged and lost. The elevation was raised just above mean high water because of sufficient sedimentation in the landward portions of the newly developing marshes. In northeastern U.S.A. marshes, the raised elevation allowed the establishment of less flood-tolerant species, especially *Spartina patens* (saltmeadow cordgrass). The process of seaward and landward development caused the existing low and high marsh vegetation pattern (Fig. 2.4, Niering and Warren 1980).

Throughout southeastern U.S.A. marshes, there is a two-way penetration of species into the estuarine marsh area; those which extend downward from fresh water into the low salinity, mid salinity and high salinity regions which are dominated by *Juncus roemerianus* and those which extend from high salinity into low salinity and fresh water areas. Moreover, there is a lateral distribution of plant species in the saline and brackish marshes to upland areas. The lateral distribution of plants exhibits distinct zonation which represents sharp delineation of a particular species or group of species from other species. In salt or brackish marshes, *Spartina alterniflora* normally forms a fringe border between *Juncus roemerianus* and the open water of bays, rivers, creeks and bayous. *S. alterniflora*, which extends into the salt water, is apparently controlled in part by the tides. In addition, the *S. alterniflora* zone, which occurs as a pure stand, is not associated or intermixed by other vascular plants. The *S. alterniflora* habitat normally occurs in protected bays, bayous (tidal creeks), rivers and behind sand spits and on leeward sides of islands instead of on high energy sand beaches where wind and waves form dunes (Fig. 2.5, Christmas et al. 1973).

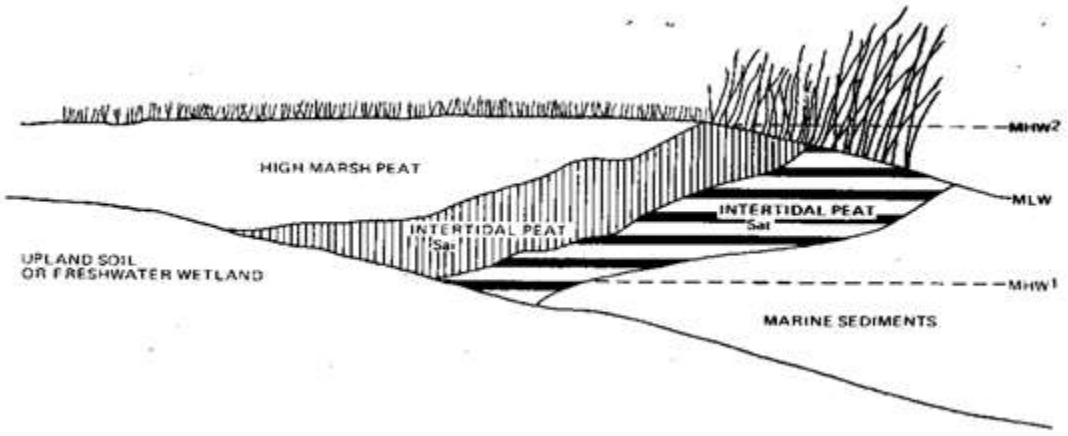

Fig. 2.4. Bisect showing southern New England marsh development oceanward with intertidal Spartina alterniflora tall (Sat) and intermediate (Sai) peat being replaced by high marsh peat; Key: MHW= mean high water when marsh development began; MHW= mean high water at present; MLW= mean low water at present (Niering and Warren 1980)

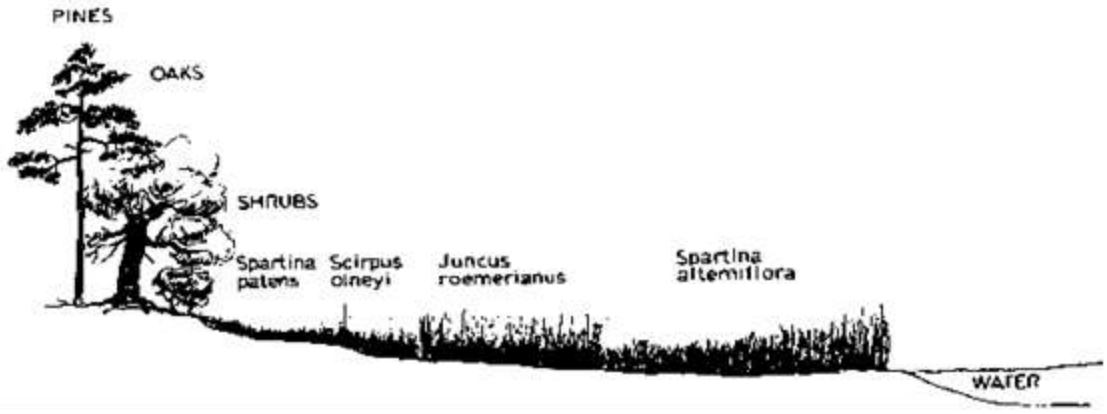

Fig. 2.5. Bisect which shows the zonation of vegetation of a salt marsh along the Davis Bay, Gulf Coast of Mississippi (Christmas et al. 1973)

2.5.4 Productivity

The effectiveness of marsh vegetation in reducing soil erosion depends on the productivity of the vegetation. The more productive marsh vegetation is, presumably the better it will be at reducing wave energy aboveground and consolidating sediments belowground. Some studies indicate that microbial processes involving assimilatory coupling of elemental cycles are responsible for nutrient fluxes in biogeochemical cycles. Although phosphorus also contributes to eutrophication, primary production in most temperate estuaries and coastal marine ecosystems is nitrogen limited. When elements such as carbon, nitrogen and phosphorus are incorporated into biomass or released through decomposition, these different inorganic elements provide varying amounts of energy yield and the interaction of these processes creates a microbial energy economy by assimilatory coupling of elemental cycles (Burgin et al. 2011, Howarth et al. 2011). Besides microbial processes and elemental limits for the primary production in estuaries and coastal areas, several researchers have observed productivity among marshes along salinity gradients (De la Cruz 1973, Eleuterius 1972, 1976, 1990, Foster 1968, Howes et al. 1986, Morgan 1961, Odum 1971, Odum and Fanning 1973, Odum et al. 1995, Schelske and Odum 1961, Table 2.1). In general, but not always, productivity tends to decrease with increasing salinity, presumably because of energy costs associated with salt stress adaptations (De la Cruz 1973, De la Cruz and Hackney 1977, Howes et al. 1986, Mendelssohn and Burdick 1988, Odum 1971, Odum et al. 1995). In addition, other researchers have previously observed significant differences in productivity between lateral and medial portions within coastal marshes (De la Cruz 1973, Eleuterius 1975, 1976). These differences appear to be due primarily to anoxia gradients and nutrient gradients (Darby and Turner 2008, De la Cruz and Garbriel 1973, De la Cruz and Hackney 1977, Howes et al. 1986, Mendelssohn and Burdick 1988). Such differences in productivity could translate into differences in erosion between lateral and medial portions of the marsh. Although there are some studies comparing plant primary production between the fresh water and salt marshes due to salinity gradients (Atkinson et al. 2010, De la Cruz 1973, Eleuterius 1990, Holland and Burk 1990, Metzler and Rosza 1982, Odum 1978, Odum et al. 1995, Table 2.2) and at different elevations within marshes (Mendelssohn and Burdick 1988, Mendelssohn and McKee 1989) relatively few studies have

compared plant primary production between low marsh zones and high marsh zones between coastal marshes and inland marshes along salinity gradients.

Table 2.1. Estimates of annual net primary production (g · dry wt · m^{-2}) of above-ground materials of selected salt marsh communities (De La Cruz 1973, Eleuterius 1990)

Marsh community	Annual Net Production	Geographic Location	Reference
Mixed vegetation	992-1108	Bay St. Louis, MS	De la Cruz & Gabriel (1973)
Mixed vegetation	1246	Patuxent Estuary, MD	Johnson (1970)
Spartina alterniflora	445-2883	Patuxent Estuary, MD; Bay Estuary, LA; Canary Creek Estuary, DE; .Sapelo Is., GA.;Barataria Beaufort, NC;	Johnson (1970), Kirby (1971), Morgan (1961), Odum & Fanning (1973), Teal (1962), Williams & Murdoch (1969), Schelske & Odum (1961), Smalley (1959)
Juncus roemerianus	560-2000	Ocean Springs, MS; Cape Fear River, NC; Everglades, FL; Bodie Is., NC; Cape Lookout, NC;	Eleuterius (1972, 1976, 1990), Foster (1968), Heald (1969), Waits (1967), Williams & Murdoch (1972), Stroud & Cooper (1968)
Spartina cynosuroides	1028	Altamaha River Estuary, GA	Odum & Funning (1973)
Spartina patens	993-1296	Long Is., NY; Bodie Is., NC	Harper (1918), Waits (1967)

Table 2.2. Estimates of annual net primary production (g · dry wt · m^{-2}) of below ground materials of selected salt marsh communities

Marsh community	Annual Net Production	Geographic Location	Reference
Mixed vegetation	586-746	Wise County, VA	Atkinson et al. (2010)
Spartina alterniflora	370-603	Cocodrie, LA	Darby and Turner (2008)
Juncus roemerianus	9700-12400	Bay St. Louis, MS	De La Cruz (1973)

2.6 Research Needs

Wave- and current-related processes in coastal vegetated systems are little understood and still need extensive investigations. As Wolanski et al. (2001) pointed out, each species has a unique configuration of trunks, prop roots and pneumatophores that works as a different drag force and therefore results in a different reduction rate of waves. For examples, with regard to *Spartina alterniflora* and *Juncus roemerianus* that commonly exist in the Louisiana and Mississippi Gulf coast, as well as in other U.S. coasts, we do not have much information either on their quantitative hydrological functions or their qualitative physical behaviours. Hence, for useful and effective vegetation planting, we firstly need to accumulate quantitative knowledge of each vegetation species based on field observations

and laboratory experiments. The vegetation characteristics can be utilized to formulate drag force which in turn can be used in numerical models.

Modeling of waves through vegetation has seen much progress in recent years (e.g. Wamsley et al. 2009, 2010) but a lot of uncertainties still exist in quantification of vegetation resistance to current and waves. The bottom drag coefficient is one of the key parameters of the current storm surge and wave models that are used for planning natural resource management and emergency response. The current modeling practice (e.g. Bunya et al. 2010) accounts for wetland frictional effects by specifying Manning's *n* coefficients using land-cover definitions from the USGS GAP data (Hartley et al. 2000, Villea 2005). The current literature has scarce field data sets, which are mostly limited to relatively small waves (Augustin et al. 2009, Moller 2006, Smith et al. 2010). Research is needed to provide laboratory and field measurements of surge and wave attenuation by wetland vegetation. These data can be used to develop a more realistic and physically based parameterization of vegetation-dependent bottom drag coefficient. Some of the high-priority research needs are identified below:

(1) The past investigations mostly focused on rigid and flexible model elements, yet real vegetation species should be further investigated.
(2) The drag or friction coefficient of flexible vegetation is related to the vegetation type, density, geometry, and flexural rigidity, as well as the flow conditions. Such relationship may have a different formulation for a different type of vegetation, and has to be determined by laboratory and field experiments.
(3) Drag force of vegetation is determined using the depth-averaged velocity in 1-D and depth-averaged 2-D models but the local velocity in vertical 2-D and 3-D models, perhaps requiring different values of drag coefficient in these models. Moreover, the drag coefficient in wave and current models might also have different values. Such differences need to be clarified.
(4) Real vegetation grows and dies, resulting in seasonal change of surge and wave attenuation. This needs to be further investigated experimentally.
(5) Theoretical analysis shows that vegetation may significantly affect wave setup (Dean and Bender 2006); however, this needs to be validated by laboratory and field experiments.
(6) The survival of vegetation under surge and wave stress is the key to the success of coastal wetland restoration. This needs to be studied using integrated approaches in hydrodynamics, geomorphology, biology, ecology, etc.
(7) Vegetation may be damaged by strong surge and waves under severe storm conditions and thus lose its effectiveness in surge and wave attenuation. How to quantify this mechanism need to be investigated in-depth.
(8) The required on-shore distance/area of vegetation for effective wave/surge reduction needs to be studied systematically.
(9) More research needs to be conducted for the effect of vegetation on current and waves coexisted.
(10) The attenuation of combined wave and surge by marshes on the Mississippi and Louisiana Gulf Coasts needs to be further investigated, because of high hurricane risk and wetland loss in these areas.

3. LABORATORY EXPERIMENTS ON WAVE ATTENUATION BY VEGETATION

The goal of the work described in this chapter was to investigate and quantify, through laboratory experiments, the ability of vegetation to reduce wave energy. Experiments were conducted by the NSL team in a wave flume at the USDA-ARS National Sedimentation Laboratory in Oxford, Mississippi (Figs. 3.1-3.3).

Physical model studies rely on the assumption that the model behaves in a manner similar to the prototype, making it possible to generate conditions that can be used to predict prototype behavior. In order to correctly replicate the prototype, the model is required to satisfy geometric and dynamic similarity conditions. Geometric similarity requires the ratios of the linear dimensions to be equal and dynamic similarity requires the ratios of the forces to be the equal between the prototype and the model. The former can easily be satisfied by matching the length scales of the model and prototype with constant ratio. Dynamic similarity mainly requires the Froude number ($\mathrm{Fr} = u/\sqrt{gh}$) and Reynolds number ($\mathrm{Re} = \rho u D_v / \mu$) to be equal for the model and the prototype. Yet, it is rarely possible to satisfy both when the model is scaled down. For modeling of wave phenomena, Froude scaling is commonly used by assuming the bottom friction is small and Reynolds number is high enough to assume that the drag coefficient is constant (Dalrymple 1985, Huges 1993). These assumptions may not be valid for waves interacting with vegetation and Re= O(10^3-10^4) (Kobayashi et al. 1993, Mazda et al. 1997).

Natural wetlands contain a random distribution of plants (in micro-scale) with variable stem diameter and height and can only be characterized by spatially averaged quantities. In the current study, the model setup is designed to match natural conditions as closely as possible in order to eliminate scaling effects and the limitations described above. The first group of laboratory experiments included testing full scale rigid and flexible model plants along with two live grass species, *Spartina alterniflora* and *Juncus roemerianus,* which are commonly found along the U.S. coasts. The second set of experiments focused on the influence of vegetation on wave breaking and static wave setup over a plane sloping beach.

3.1 Wave Tank Setup

At the beginning of the project, the existing wave flume was modified and upgraded in order to accommodate higher and longer waves, as specified in the original proposal. These changes were necessary to provide relatively high water depths to conduct full scale experiments with live plants such as *Spartina alterniflora* and *Juncus roemerianus.* These upgrades included:

- Higher and transparent sidewalls,
- False floor,
- Improved wave generator with higher power output,
- Improved wave absorber,
- Enhanced data acquisition system,
- User interface improvements.

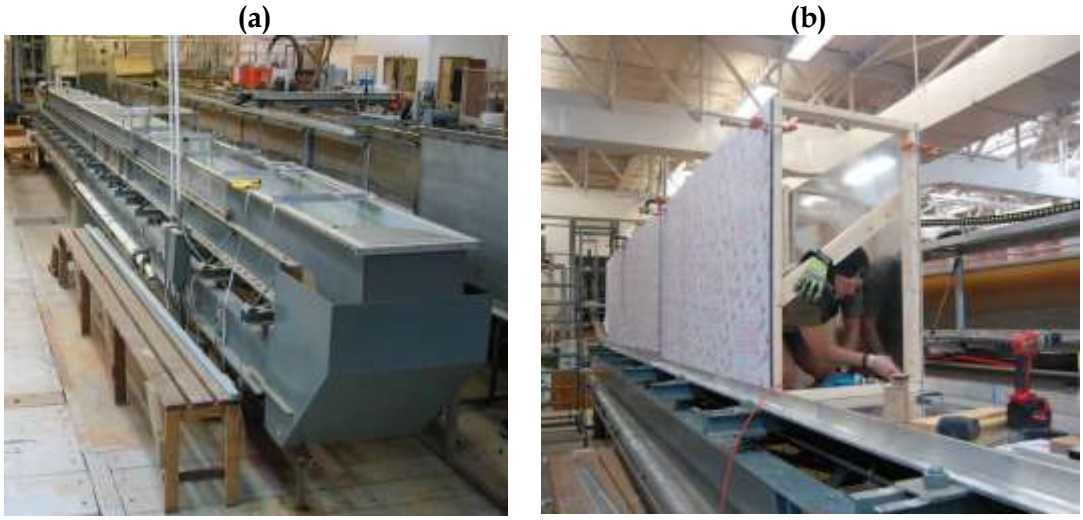

Fig. 3.1. (a) The original wave tank before the improvements and (b) new side wall construction.

The existing wave flume was 19 m long, 0.55 m wide and 0.59 m deep with epoxy coated plywood sidewalls, as shown in Fig. 3.1 (Ozeren et al. 1999). It was upgraded to be 20.6 m long, 0.69 m wide and 1.22 m deep for the present project (Ozeren and Wren 2011). One side and the bottom of the flume are constructed with aluminum sheets that have been coated with epoxy based paint. The other side is made out of polycarbonate sheets to provide transparency. The walls are supported by 1.28 cm (0.5") diameter stainless steel threaded rods which also allow fine adjustment for wall alignment. The wave generator was located 1.2 m from the upwave end of the flume. The bottom of the wave tank was elevated 0.29 m by a plywood false floor to facilitate the placement of model and live vegetation. A ramp with a slope of 1/7 was built in front of the wave generator to provide a gradual transition up to the false floor. A porous, parabolic wave absorber was constructed at the downwave end of the tank to minimize wave reflection. The effective length of the flume from the paddle to the toe of the absorber was 16.9 m (55.4 feet). The test section was placed 11.5 m away from the wave generator and was 3.6 m long.

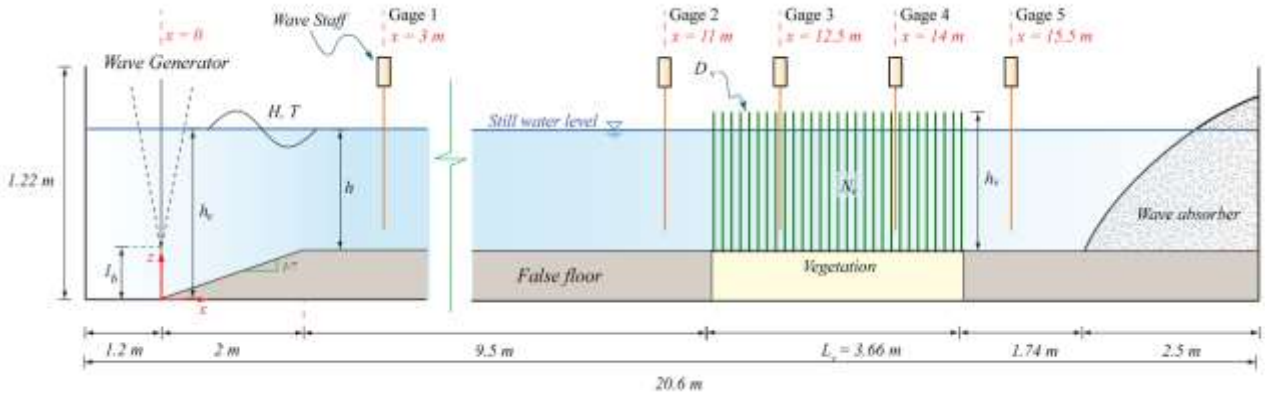

Fig. 3.2. Definition sketch of the experimental setup.

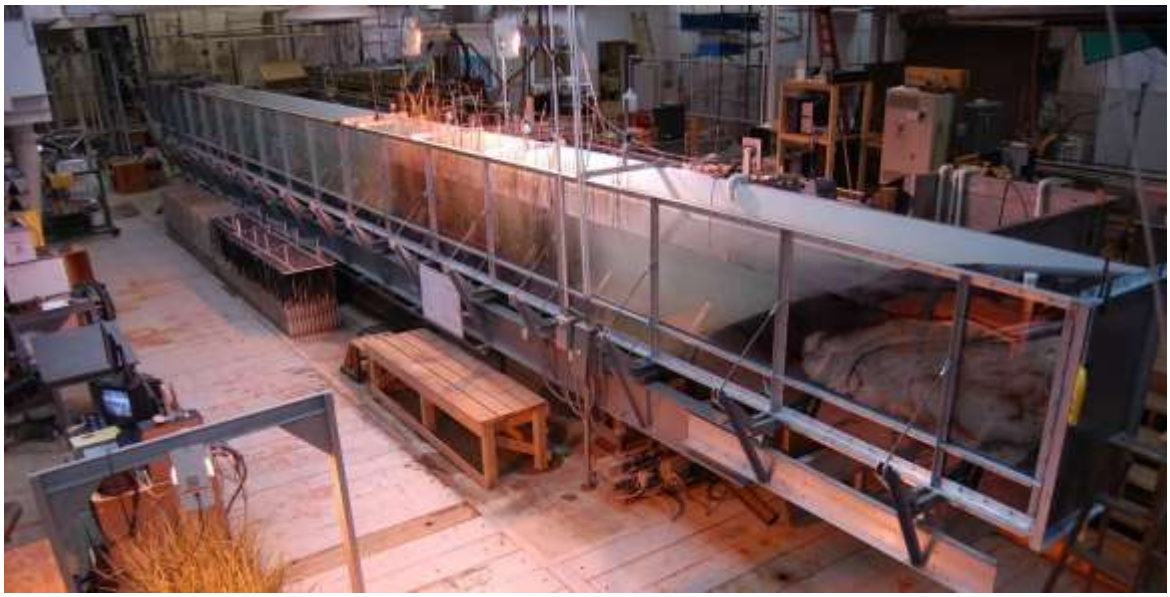

Fig. 3.3. Flume with dormant *S. alterniflora* under growing lights.

3.1.1 Wave Generator

A common method for wave generation in hydraulic facilities is to use a moving board with an established transfer function that relates motion to wave properties. The ideal wavemaker should move as closely as possible to water particle motion in progressive waves. Therefore, a flap type wave generator is usually suited for deepwater wave generation since water particle velocities decrease exponentially with depth, while a piston type wavemaker is more suitable for shallow water wave generation. Therefore, two types of paddles, one a variable-draft flap-type and the other a piston-type, were used interchangeably during the experiments to generate waves at different water depths. The floor in front of the wave paddle was elevated to enable progressive wave generation at shallower water depths. The wave generator (Fig. 3.4) was driven by a stepper motor that was controlled by a custom computer program.

An electromechanical positioner was used to control the sinusoidal motion of the paddle. The generalized solution of the linearized problem was obtained to handle both arrangements. Only the lateral boundary conditions differ from the wave propagation solution (Huges 1993, Ozeren et al. 1999). On the open end, the waves propagate outward by radiation condition. The kinematic condition should be satisfied along the wavemaker boundary. This boundary condition can be derived from the function that defines the boundary, which is written as

$$x(t) = \frac{S(z)}{2}\sin\omega t \tag{3.1}$$

where $S(z)$ is the stroke of the paddle, x is boundary geometry and ω is the wave angular frequency ($\omega = 2\pi/T$). If the governing two-dimensional equations are solved with first order boundary conditions, the ratio of wave height to stroke, S, can be found as

$$\frac{H}{S_0} = \frac{4\sinh kh}{\sinh 2kh + 2kh}\left(\sinh kh + \frac{c_1 - \cosh kh}{k(h - l_b)}\right) \tag{3.2}$$

where k is the wave number ($k = 2\pi / L$), L is the wavelength, l_b is the offset distance of the variable draft wavemaker (Fig. 3.5) and c_1 is a parameter defined by

$$c_1 = \begin{cases} \cosh(-kl_b) & l_b < 0 \\ 1 & l_b \geq 0 \end{cases} \tag{3.3}$$

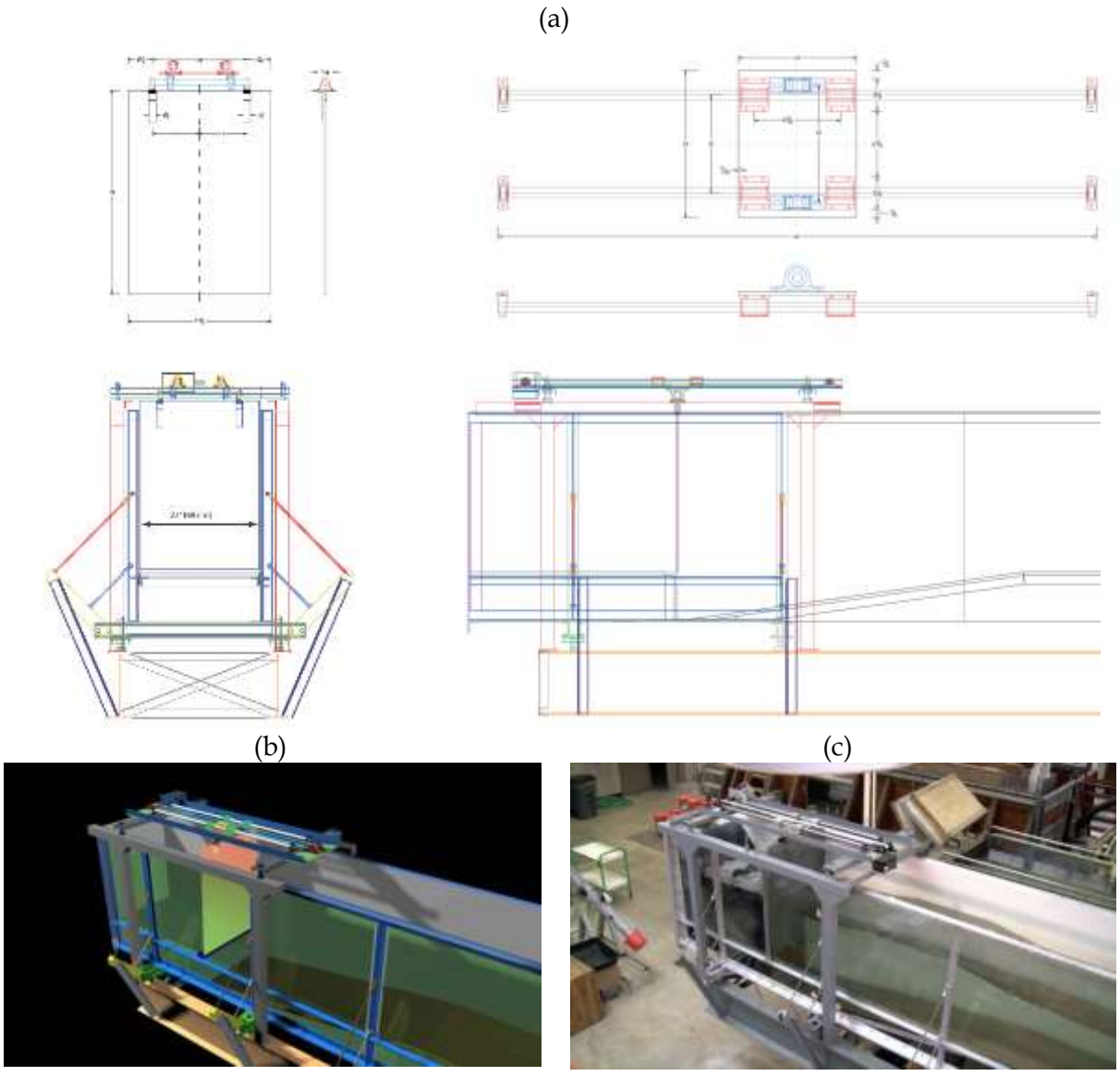

Fig. 3.4. Flap type generator (a&b) CAD drawings and (c) a photo after construction.

It can be seen from Fig. 3.6 that in deep water, for the same wave height, it is easier to generate waves with a flap-type generator ($l_b = 0.28m$), while the piston-type ($l_b = -\infty$) is more efficient in shallow water. Also, it should be noted that more power is needed to

generate waves with a piston type wave maker at the same depth. Therefore, it was more reasonable to use both flap and piston type wave generators to efficiently provide the necessary power with the same motor for various water depths.

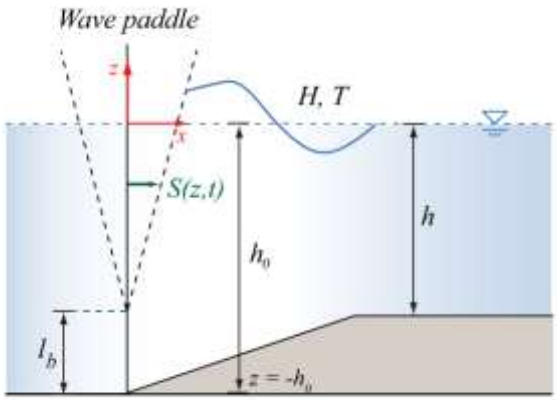

Fig. 3.5. Definition of parameters for a variable draft wavemaker.

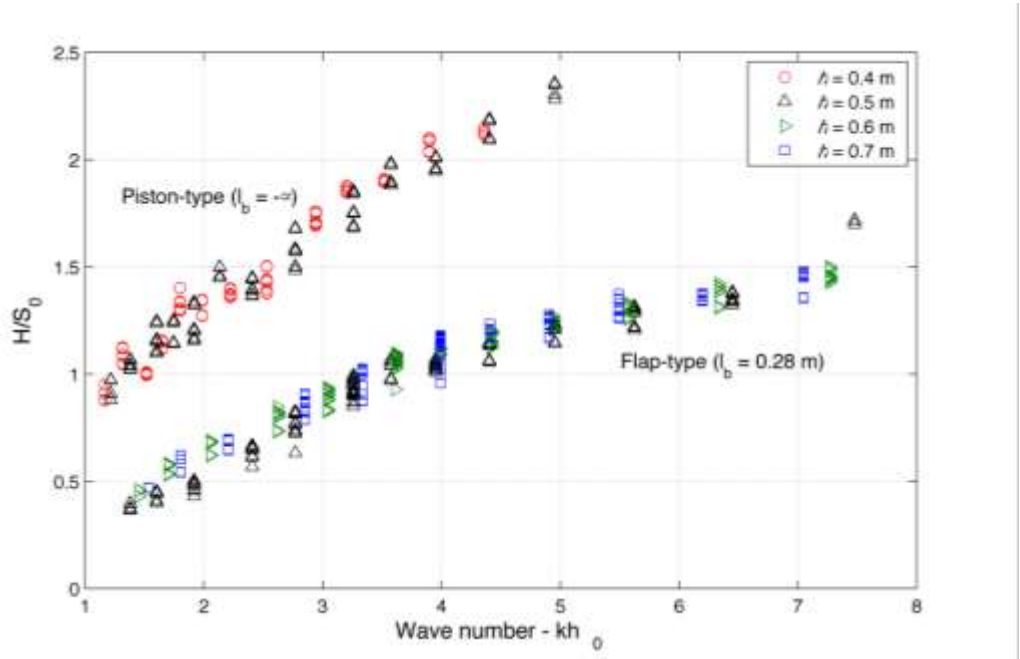

Fig. 3.6. Wave height to stroke ratio for variable draft wavemaker measured in the wave tank (gage at 3 m) at various water depths.

3.1.2 Wave Absorber

A major problem of laboratory wave tank is reflection from the boundaries; mainly from the downwave end of the wave tank. The reflected waves result in an irregular and complex

wave pattern, which makes it difficult to control the model parameters. The most common method is a beach of constant mild slope (<1:10) which is constructed using sand, gravel or stones. These wave absorbers are designed for an effective reflection of less than 10%. The use of a mild slope consumes a considerable fraction of the tank, creating a problem for limited tank lengths. Increasing the roughness of the surface or using porous materials with different geometric arrangements can help to reduce the length of the absorber. Straub et al. (1956) experimentally showed that for the same absorber length, permeable absorbers are more efficient than impermeable ones. For slopes greater than 15^{o}, wire mesh absorbers have higher efficiency than crushed rock absorbers. The length of a wave absorber should not be less than roughly half of the wavelength. Wave reflection from a parabolic beach is less than the reflection from a plane beach with the same length. Although the amount of reflection depends on the absorber length, some reflection will occur even when the absorber is very long (Madsen 1983).

Progressive wave absorbers are utilized to spread the wave energy dissipation along the absorber length. When the waves are transmitted from one medium to another with different properties, there will always be some reflection in response. The idea for an optimum wave progressive absorber is to minimize the overall reflection from the system (Le Mehaute 1972). For larger waves, the absorber will act as a solid wall, while the smaller waves will penetrate freely into the absorber to be reflected from the impervious vertical wall at the end of the absorber. Therefore, higher porosities are more efficient for steeper waves while low porosities are efficient for milder waves. The maximum absorption will occur for an intermediate height at a specific porosity and grain size. Similarly, greater friction will result in reflection from the front face with no penetration, while zero friction will cause reflection from the back wall. To increase the efficiency of the absorber, the porosity may be reduced successively along the absorber.

For the current setup, a progressive, porous and parabolic wave absorber was designed to efficiently minimize wave reflection (Fig. 3.7).

(a) (b)

Fig. 3.7. (a) The wave generator and (b) wave absorber.

The length of the absorber was 2.5 m and the height was 0.8 m from the top of the false floor. The absorber had a parabolic profile composed of three layers of different porosities gradually decreasing in the direction of wave propagation. The first two layers were made of polyethylene plastic mesh with 1.1 cm and 0.5 cm openings and the third layer was made of polyester air filter. The absorber was tested for the range of wave conditions and water

depths to identify its efficiency. The reflection coefficient is defined as the ratio of reflected wave height to incident wave height:

$$K_r = \frac{H_r}{H_i} \tag{3.4}$$

where K_r is estimated for a range of wave parameters through video analysis to validate the wave absorber performance. Fig. 3.8 shows that the reflection was less than 10% for the range of water depths and wave steepnesses tested here.

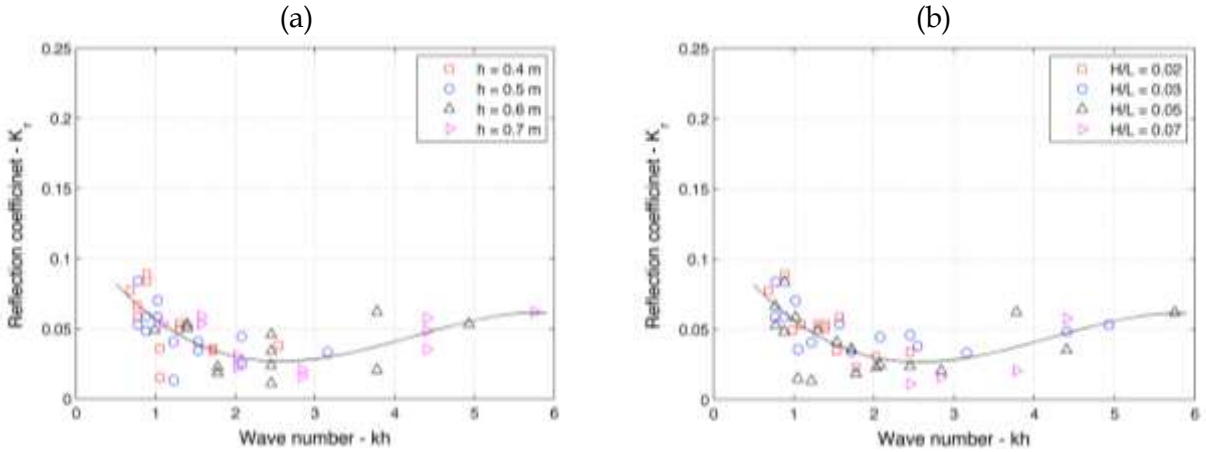

Fig. 3.8. Reflection coefficient for (a) different water depths and (b) different wave steepness.

3.1.3 Sloping Beach

A plane wooden beach (Figs. 3.9 and 3.10) with a 1:21 slope was constructed over the existing false floor to investigate wave setup. The toe of the beach was at x = 7.2 m. The piston type wavemaker was used to generate regular and irregular waves. The water depth at the toe of the beach was 0.4 m for all the experiments.

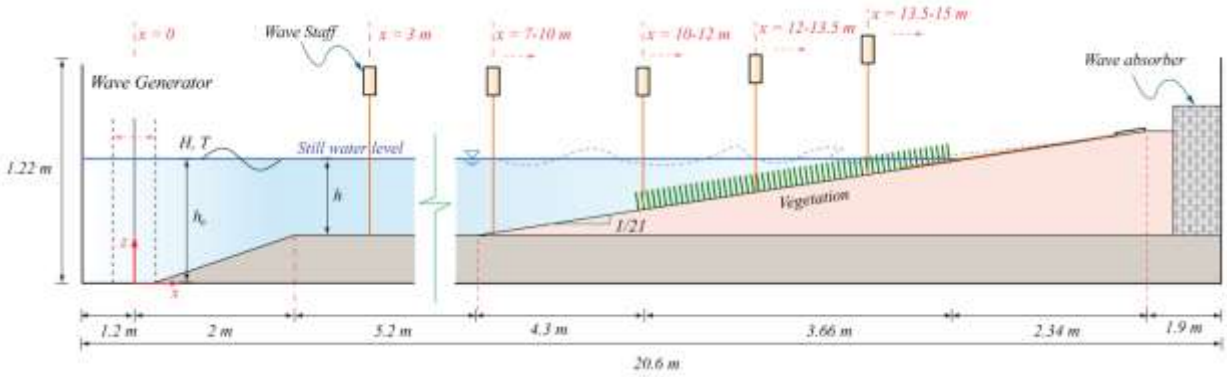

Fig. 3.9. Definition sketch of sloping beach flume configuration.

Fig. 3.10. Photograph of the wave flume with a sloping beach.

3.2 Vegetation Types

Three different types of vegetation were used: rigid, flexible and live. The range of vegetation parameters is shown in Table 3.1. The first four configurations of rigid model vegetation were used in the full-scale flat-bottom experiments, covering three different stem densities (N_v = 156, 350 and 623 stems/m^2) and two different stem heights for N_v = 350 stems/m^2. The fifth rigid model vegetation configuration was used for wave setup experiments, which was scaled with a ratio of 1:3, and the density was 3,182 stems/m^2, corresponding to a full-scale density of 350 stems/m^2. The following sections describe the preparation and use of each type of vegetation.

Table 3.1. Ranges of vegetation parameters (Mean and standard deviations are given for live vegetation stem height and diameter values)

Ref. #	Vegetation type	Density N_v (m^{-2}) / Spacing λ (mm)	Stem height h_v (m)	Stem diameter D_v (mm)	Fractional coverage a = $N_v A_c$
12236301	Rigid model	156 / 86.1	0.63	9.4	0.011
12436301		350 / 57.4	0.63		0.024
12435001		350 / 57.4	0.48		0.024
12636301		623 / 43.1	0.63		0.043
15232003	Rigid model (beach)	3,182 / 19.1	0.20	3.2	0.024
22435001	Flexible model	350 / 57.4	0.48	9.4	0.024
43435005	*S. alterniflora* (Dormant)	545	0.62±0.23	5.1±1.53	0.011
43635005	*S. alterniflora* (Green)	405	0.59± 0.21	6.5±0.9	0.013
45040003	*J. roemerianus* (Green)	2857	1.03±0.27	2.4±0.6	0.013

3.2.1 Rigid Model Vegetation

Rigid vegetation models were constructed from 9.5 mm diameter birch dowels by sliding them in a staggered pattern through the holes of two perforated 6.4 mm thick PVC sheets (Figs. 3.11–3.13). The top sheet was leveled with the false floor and the remaining holes were sealed. Shortly after being immersed, the dowels swelled and locked in place without using any adhesive. Fig. 3.11 shows some spacing and size parameters. The stems were arranged in a staggered pattern with equal spacing between them. With this arrangement, the spacing between the stems, λ, can be related to the vegetation density with the following relation:

$$N_v = \frac{2}{\sqrt{3}}\lambda^{-2} \tag{3.5}$$

Model vegetation for wave setup experiments had the same staggered arrangement. The dowels were hammered in and the PVC sheets were attached to the plywood beach (Fig. 3.13).

Fig. 3.11. Model vegetation stem configuration (λ is the center-to-center distance between individual stems and D_v is the stem diameter).

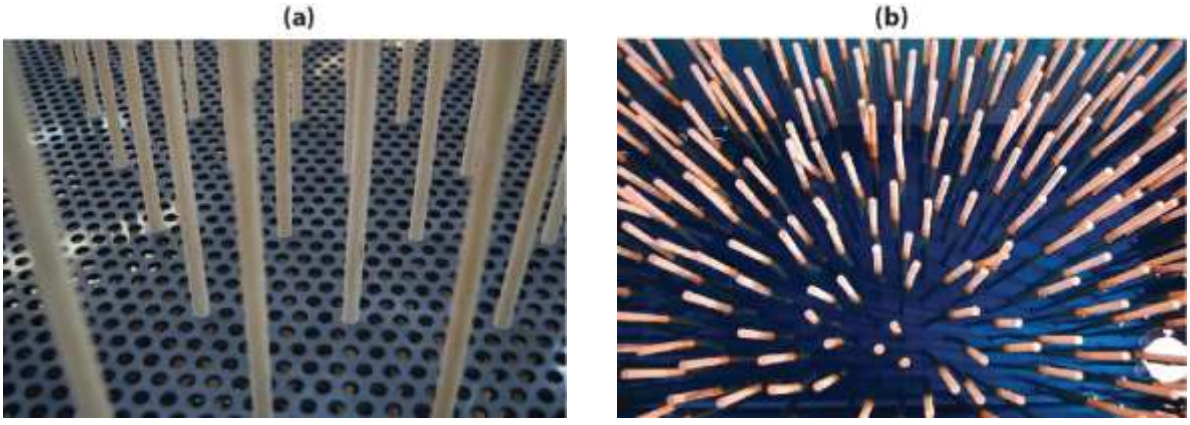

Fig. 3.12. Rigid model vegetation: (a) side view and (b) top view.

Fig. 3.13. Construction of the rigid vegetation elements

3.2.2 Flexible Model Vegetation

Ethylene propylene diene Monomer (EPDM) foam rubber with a 9.5 mm diameter was used to construct flexible model vegetation. The EPDM foam rubber had a density of 368 kg/m^3 and a modulus of elasticity of 4 MPa. Strips of foam rubber 630 mm long were glued into the holes of the PVC sheets in a manner similar to that used for the rigid model vegetation (Fig. 3.14), and the rest of the holes were again sealed. Each PVC sheet was 4′ long and 27″ wide. Three sections of PVC sheets were used to cover a 12′ (3.66 m) long area along the wave tank.

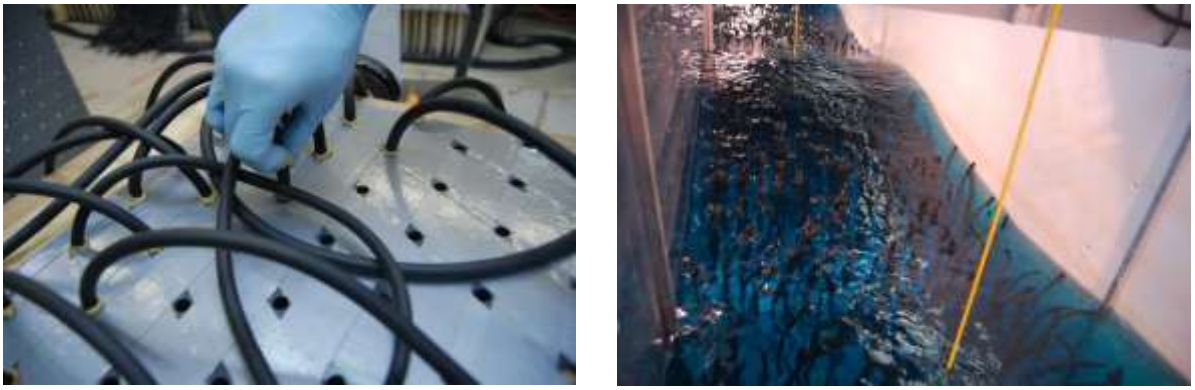

Fig. 3.14. EPDM foam rubber: (a) being assembled and (b) in flume.

3.2.3 Live Vegetation

Dormant and green *Spartina alterniflora* and green *Juncus roemerianus* plants were collected from an outdoor nursery near Houma, LA (Figs. 3.15 and 3.16) and transferred on site into six custom-built PVC boxes (Fig. 3.17). The boxes were 686 mm wide, 610 mm long, 210 mm deep, and 286 mm high. Each box was divided into sixteen 170 mm by 152 mm cells. Plugs of vegetation with an approximately equal number of stems were placed into each cell to provide an even distribution and to control the stem density. The remaining gap around the plugs was filled with native soil. After being transferred into the wave tank, the plants were left under three 750 W growing lights 10 hours a day for 30 days. The wave tank was filled with fresh water up to just above the soil level during this recovery period. The temperature varied between 20–24°C during the experiments.

Samples of *S. alterniflora* from Terrebonne Bay, LA and Grand Bay, MS were collected to measure plant properties and provide preliminary data in addition to data from the LSU field team. The stem length (h_v), thickness, plan volume ($\forall$) and wet weight were measured for each plant. Fig. 3.18 summarizes some of these measurements. Stem diameter, D_v, is calculated by averaging the measured stem thicknesses at approximately 0.25 h_v and 0.756 h_v. The volume of each stem was estimated by completely immersing them into water and immediately measuring the volume of the displaced water. Fig. 3.18a shows mass density distribution defined by $\rho_v = W_s / \forall$. Plan volume can alternatively be estimated if each stem is assumed to be a cylinder of diameter D_v and height h_v. In Fig. 3.18b, the measured and estimated plant volumes are compared.

Fig. 3.15. Plant collection sites.

Fig. 3.16. (a) *S. alterniflora* plugs at a nursary and (b) *J. reomerianus* in Grand Bay, MS.

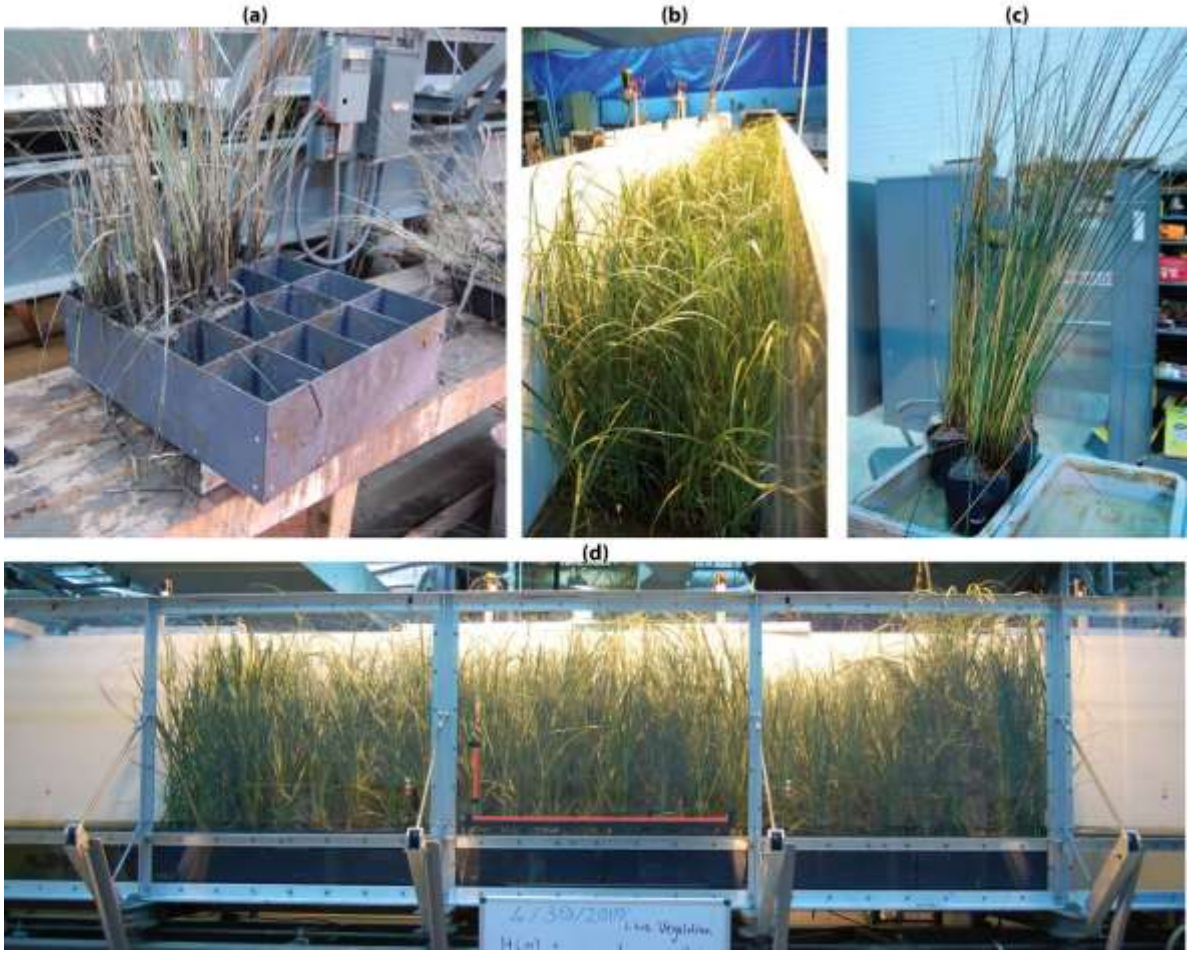

Fig. 3.17. Live vegetation samples at the laboratory; (a, b and d) *S. alterniflora* and (c) *J. roemerianus*.

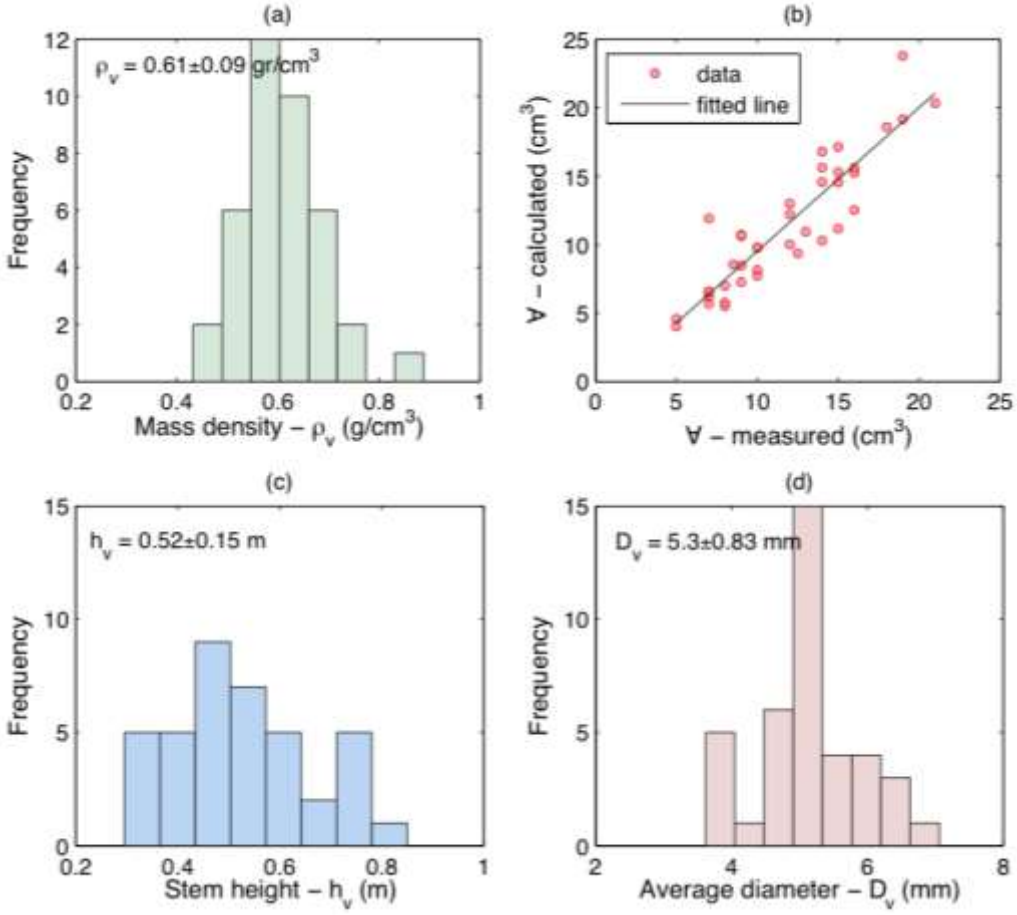

Fig. 3.18. The distribution of (a) mass density, (b) measured and calculated volumes of vegetation and the distribution of (c) vegetation height and (d) average diameter of dormant *S. alterniflora*..

For each live vegetation species tested in the flume, vegetation density (N_v), stem length (h_v) and diameter (D_v) were measured following the same procedure described above. The results are summarized in Table 3.1, and the height and average diameter histograms for live vegetation species are shown in Fig. 3.19.

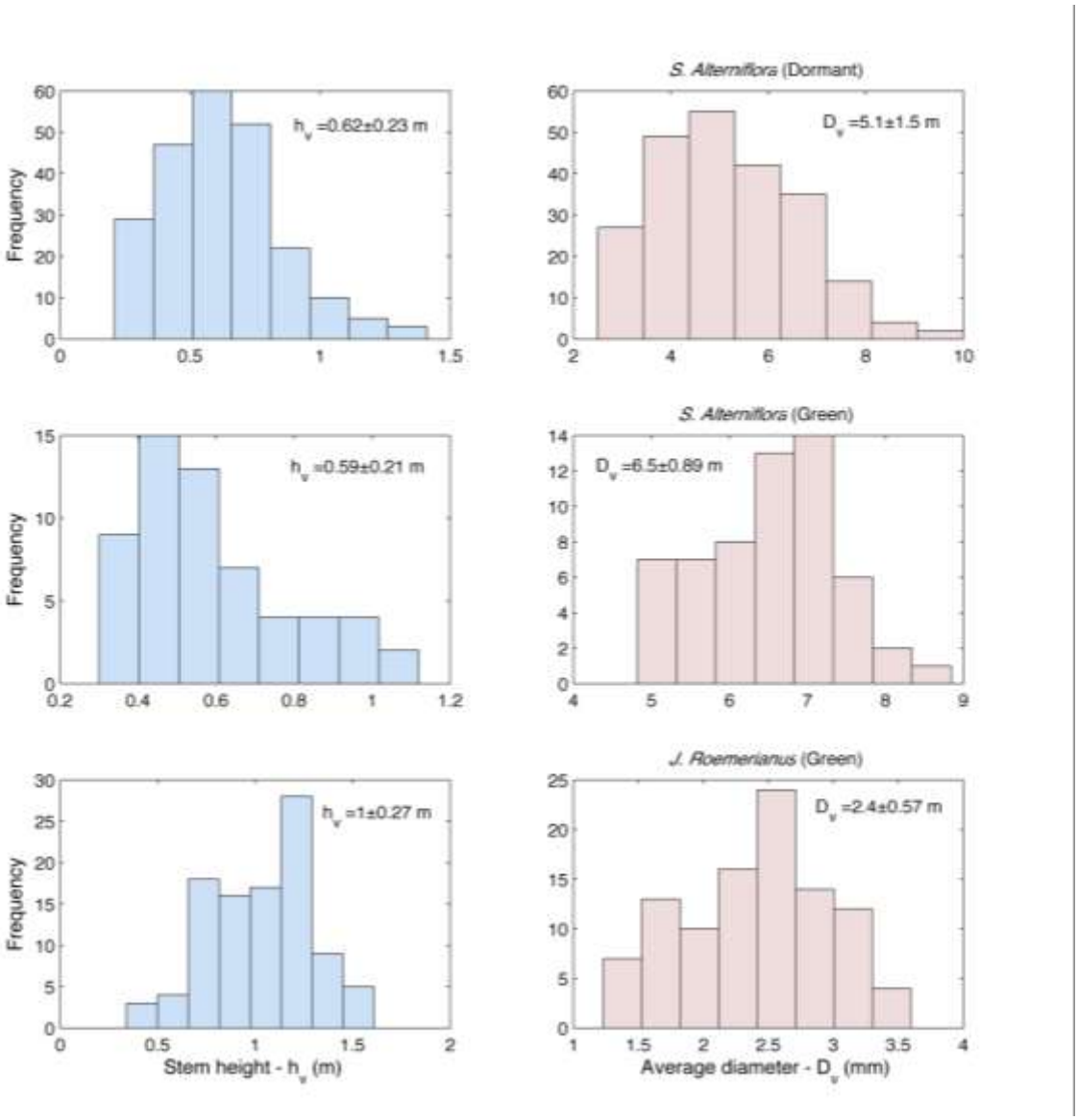

Fig. 3.19. The distribution of vegetation height and average diameter of *S. alterniflora* and *J. roemerianus*.

3.3 Data Collection

3.3.1 Wave Gages

Five one-meter-long capacitance-type wave probes (Ocean Sensor systems Wave Staff, Fig. 3.20) were used to measure water surface displacement. One of the probes was placed 3 m away from the paddle to measure the incident wave height, and the remaining four were distributed along the test section at 1.5 m intervals starting 0.5 m ahead of the vegetation field (Fig. 3.2). The sampling rate of the wave probes was 30 Hz, and the resolution was 0.24 mm. Each staff was clamped to aluminum angle stock mounted on the walls of the wave tank and grounded to the aluminum sidewalls. The flume itself was also grounded on the

laboratory floor through a copper rod. For the wave setup experiments, the wave probes were originally mounted at 3 m, 7.5 m, 11 m, 12.5 m and 14 m away from the wave paddle. In some experiments, the wave staffs were moved downwave during repeated experiments to increase the spatial resolution of the gage data.

The probes were calibrated in the wave tank to ensure accurate water level measurements. The calibrations were checked several times during the project to ensure their proper operation. Fig. 3.21 shows the calibration curve for each gage.

Fig. 3.20. Level sensors mounted on wave tank.

3.3.2 Video Imaging

For a subset of the experimental runs, a digital video camera was used to capture the water surface displacement along the test section through the clear polycarbonate sidewall. The camera had a 29.97 Hz frame rate and 1920 x 1080 pixel resolution. It was positioned 6 m away from the wave tank wall and leveled with the free surface elevation. The field-of-view was 5.82 m along the wave tank, yielding approximately 3 mm/pixel resolution. Blue dye was added to the water to increase contrast with the white wall of the tank. Colored markers were placed on the flume wall to locate the wave probes and scale the data during the video analysis.

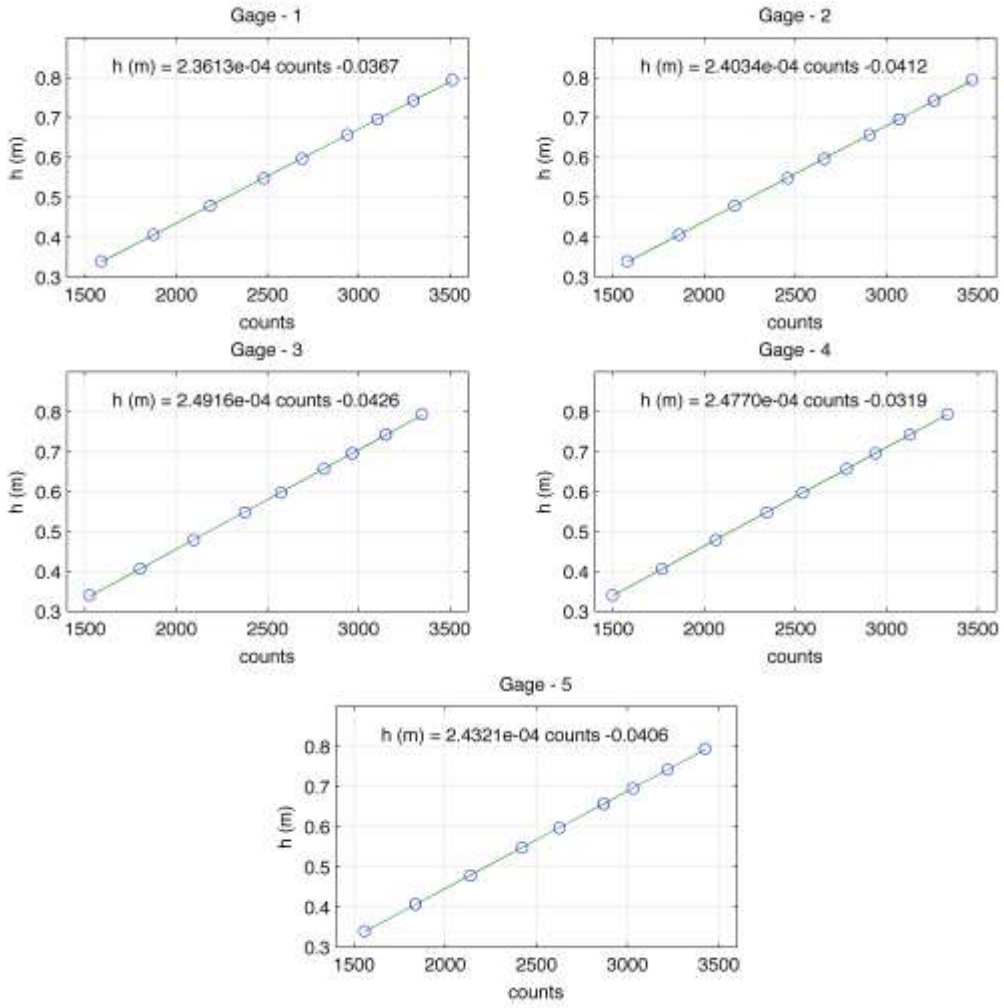

Fig. 3.21. Calibration curves for the level sensors.

3.4 Experiment Procedures

Regular wave experiments were run for at least 100 wave cycles and repeated three times. Control runs with no vegetation in the flume were also performed for the same wave properties that are used in vegetation model experiments. Irregular waves were generated using the JONSWAP spectrum. Five $100T_p$ long time series signals were generated for each spectrum for each vegetation configuration and for control runs to avoid uncertainties. Each of the five repeated runs had the same spectrum but a different irregular signal.

A computer program was written in Labview to conduct multiple experiments and store the data. The GUI allowed the user to populate the set of experiments to be conducted. The list of experiments was generated with the desired wave parameters of water depth, h, wave period, T, and wave height H (or wave steepness H/L). A unique reference number was assigned to each experiment. The tasks of the computer program for a single experiment can be summarized as follows:

- At the beginning of each experiment the program checked the water surface through two level sensors and kept the system idle until the water surface became still.
- Data acquisition started automatically when the standard deviation of the water surface fluctuations was below a threshold value (0.5 counts or 0.125 mm). The wave generator was initiated 10 s after the beginning of the data recording in order to record the still water level.
- The program stored the collected data and waited on idle for the next experiment.

3.5 Data Analysis

The data for each set of experiments were analyzed by computer codes developed in LabVIEW and MATLAB. A Bandpass Butterworth filter was used to remove unwanted frequency components due to local disturbances and noise in the recorded signal. The flowchart in Fig. 3.22 shows the complete gage and video data analysis procedures.

3.5.1 Gage Data

3.5.1.1 Regular waves

The data analysis involved the time series and spectral analysis of water surface elevations (Fig. 3.23) at the gages. Each time series water surface displacement (wave profile) received from the wave gages were calibrated using the corresponding calibration curve described in Fig. 3.21. The water surface was still during the first 10 s of each signal and was used to estimate the still water level. Each wave profile was normalized with the still water level and the steady portion was trimmed from the signal. Two conditions were imposed to identify the steady portion of the signal. The first one required the signal to be steady after the wave front passed all the wave gages, and the second one required the variation of the individual wave heights to be small compared to the variation of the water surface. Assuming the wave front travels with group wave speed, C_g, is defined as

$$C_g = \frac{C}{2}\left(1 + \frac{2kh}{\sinh 2kh}\right) \tag{3.6}$$

and the wave celerity, C, is:

$$C = \sqrt{\frac{g}{k}\tanh\left(kh\right)} \tag{3.7}$$

The periods of the wave profile measured by the sensors was obtained through spectral analysis by using a Fast Fourier Transform routine. Peak period, which is the reciprocal of the spectral frequency with maximum spectral density, was used as the wave period. The wave heights were estimated from the time series signal recorded at each gage by two independent techniques: peak detection and zero-crossing. The former method is applied by fitting a quadratic equation to five data points around each peak. The peaks and valleys were found from the zero-points for the first derivative of the fitted equation. Wave height was defined by the difference between two successive peaks and valleys. The transmitted wave height was obtained by averaging the estimated wave heights within the steady portion of the transmitted wave signal.

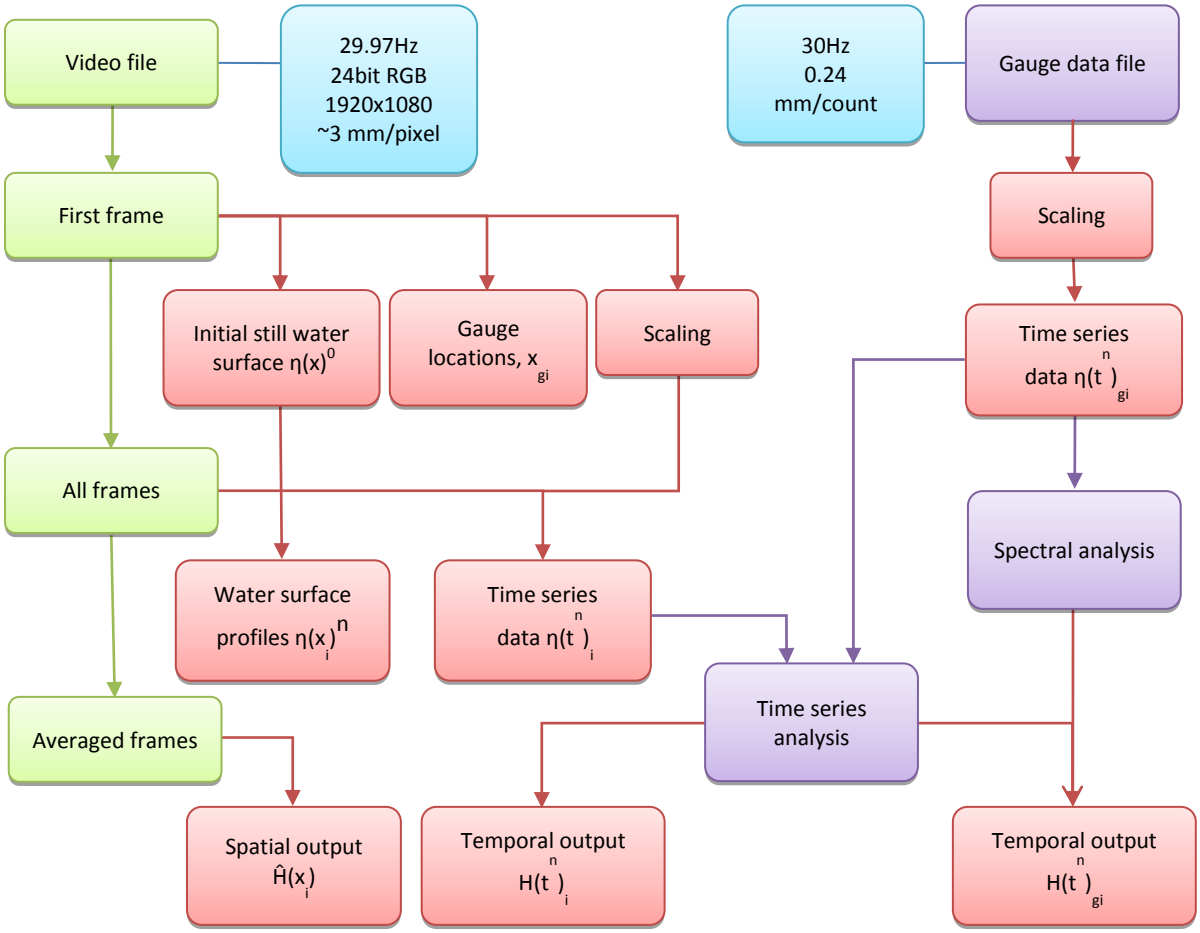

Fig. 3.22. Data analysis procedure.

The zero-crossing method was also used as an alternative method to estimate the wave heights for regular waves (Fig. 3.24). The individual wave heights are defined as the difference between the highest and lowest values of water surface readings between two zero down-crossing points and wave periods are the time span between two successive zero down-crossings. The local peak values are discarded in this analysis. The profile can cross the zero line either with a positive slope or a negative slope. If it crosses with a positive slope it is referred as up-crossing and if the slope is negative then it is called down-crossing. Although both down-crossing and up-crossing methods yield similar results, the down-crossing method is recommended by IAHR/PIANC (1986) due to the definition of wave height.

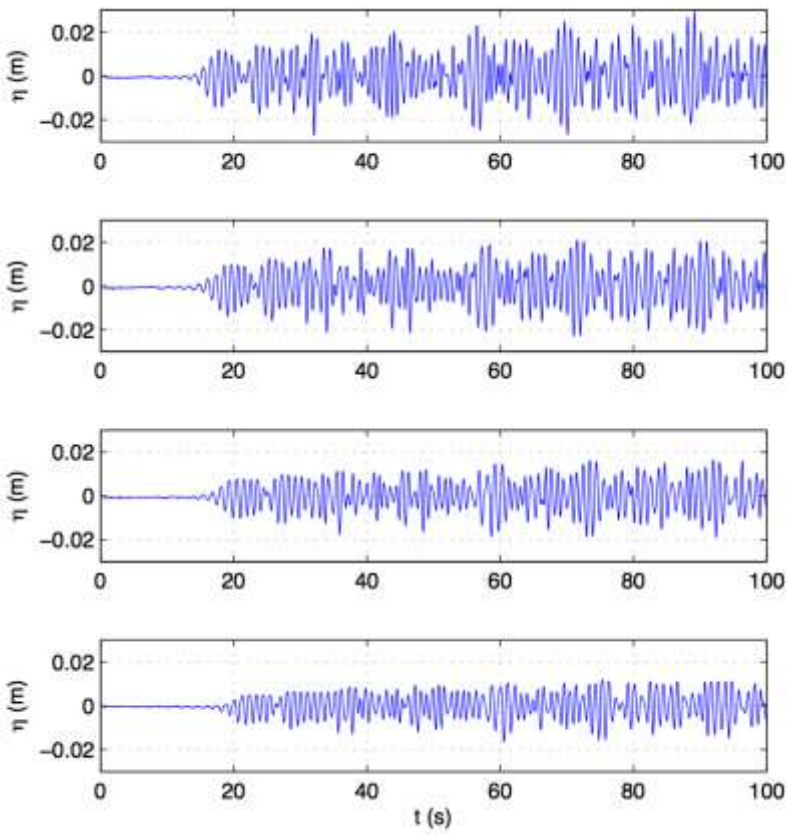

Fig. 3.23. A sample time series signal recorded at four gages.

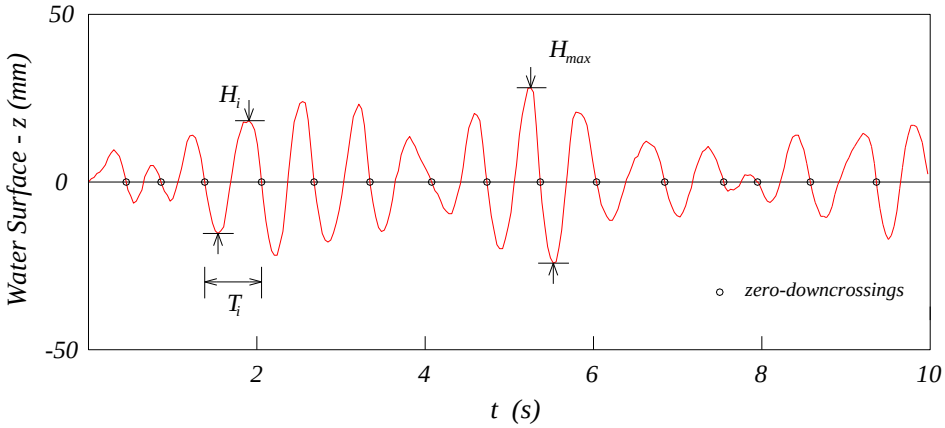

Fig. 3.24. Definition sketch for zero-downcrossing method.

3.5.1.2 **Irregular waves**

Significant wave heights for irregular waves were calculated using spectral analysis by assuming the spectrum to be narrow banded and that the wave heights satisfied the Rayleigh distribution (Longuet-Higgins 1952). The wave statistical parameters used to

define the sea state for irregular wave experiments are obtained by processing all the individual waves in a wave record. The wave record should include several hundred individual waves to ensure statistical accuracy. For most practical purposes, it is common to neglect very small waves and measure the highest waves. It is found that wave heights estimated by visual observations correspond to the average of the highest 30 percent of the waves. The most frequently used parameter obtained by this approach is significant wave height, H_s, which is defined as the average of the highest one-third of the waves in a wave record.

$$H_s = \frac{1}{N/3}\sum_{i=1}^{N/3} H_i \qquad (H_n < H_{n-1} < \ldots < H_1) \tag{3.8}$$

where N is the number of individual waves in the record ranked highest to lowest H_i and i is the rank number.

Root-mean-square (H_{rms}) wave height was computed as follows:

$$H_{rms} = \sqrt{\frac{1}{N}\sum_{i=1}^{N} H_i^{\,2}} \tag{3.9}$$

It has been proven that individual wave heights follow the Rayleigh distribution, assuming the random water surface elevation follows a Gaussian distribution (Longuet-Higgins 1952). It is called the "narrow-band condition" when the wave energy is concentrated in a very narrow range of wave periods. Theoretical values obtained from the Rayleigh distribution are generally in agreement with a narrow-banded sea. Yet, shallow-water waves differ from the Rayleigh distribution due to wave breaking and bathymetric effects.

Irregular waves from water surface recordings can be considered as a combination of a series of regular waves with different periods (or frequencies) and a certain amount of energy is transmitted by each component. Spectral analysis determines the distribution of the energy for each wave frequency by transforming the wave record from the time domain to the frequency domain. This is usually done by the Fast Fourier Transform (FFT) technique. If the wave heights of the random sea follow the Rayleigh distribution, the significant wave height can be approximated by the standard deviation (square root of the variance of the signal) (Longuet-Higgins 1952).

$$H_{mo} = 4.01\sqrt{m_o} \tag{3.10}$$

where m_o is the zero-th moment of the spectrum. This approximation requires the spectrum to be narrow-banded to satisfy the Rayleigh distribution. The i-th moment of the continuous spectrum is obtained by,

$$m_i = \int_0^{\infty} f^i S(f)\,df \tag{3.11}$$

where $S(f)$ is the wave energy spectral density and designates the distribution of variance with frequency, f, assuming that the function is continuous in the frequency domain. The variance of the water surface elevation around the mean water level can be written as

$$\sigma^2 = \frac{1}{T}\int_0^{T} \eta^2(t)\,dt = \frac{1}{2}a^2 \tag{3.12}$$

where σ^2 is the variance, T is the wave period, a is the wave amplitude, and $\eta(t)$ is the time series of the water surface elevation. For a discrete time series signal, the integrals are replaced with summations. The time series of the surface elevation of an irregular wave can be written as the infinite sum of sinusoidal waves of amplitude a, angular frequency, ω, and phase, δ, as follows

$$\eta(t) = \sum_{i=1}^{\infty} a_i \cos(\omega_i t + \delta_i) \tag{3.13}$$

The distribution of variance with frequency is usually designated by $S(f)$, f being the wave frequency, assuming that the function is continuous in the frequency domain. Due to the above relation between variance and wave energy, $S(f)$ is called the "wave energy spectral density" or simply the "wave spectrum". From Eqs. 3.11 and 3.12, the variance of the random signal around the mean water level becomes

$$\sigma^2 = \sum_{i=1}^{\infty} \frac{a_i^2}{2} = \int_0^{\infty} S(f_i)\, df \tag{3.14}$$

The above equation yields the area under the wave spectrum which is referred as the zero-th moment of the spectrum and designated by m_o.

The frequency corresponding to the maximum value of the wave spectrum is defined as the "peak frequency":

$$f_p = f\big|_{S_{\max}(f)} \tag{3.15}$$

and the peak period is the inverse of peak frequency:

$$T_p = \frac{1}{f_p} \tag{3.16}$$

The Joint North Sea Wave Project (JONSWAP) was started in 1967 to investigate the growth of waves under fetch-limited conditions and wave transformation from sea to shallower water area. It is a five-parameter spectrum with three parameters usually held constant. The parameterized JONSWAP spectrum is expressed in terms of H_{m0} and T_p as

$$S(f) = \alpha_s H_{mo}{}^2 f_p{}^4 f^{-5} \gamma^{\beta} \exp\left[-\frac{5}{4}\left(\frac{f_p}{f}\right)^4\right] \tag{3.17}$$

where

$$\alpha_s \approx \frac{0.0624}{0.230 + 0.0336\gamma - \left(\frac{0.185}{1.9+\gamma}\right)}$$

$$\beta = \exp\left[-\frac{(f - f_p)^2}{2\sigma_J{}^2 f_p{}^2}\right]$$

$$\sigma_J \approx \begin{cases} 0.07 & f \le f_p \\ 0.09 & f \ge f_p \end{cases}$$

and γ is the peak enhancement coefficient which controls the sharpness of the spectral peak. $1 \le \gamma \le 7$, and the mean value of γ is 3.3.

3.5.2 Video Data

A subset of the experiments was recorded with a video camera. Each video recording began just before the wave generation and continued for 50 s for vegetation experiments and 100 s for wave setup experiments. The recorded videos were analyzed in three main steps: (1) video preprocessing, wherein the first few frames were analyzed to identify the still water level, wave gage locations, and scaling parameters; (2) video processing, wherein the remaining frames were analyzed to identify the water surface; and (3) video postprocessing, wherein the water surface data were analyzed. Each step is described in more detail below.

3.5.2.1 **Video preprocessing**

The first ten frames of the video were averaged and the red channel of the averaged frame was separated. This frame was cropped around the water surface and scale markers, which were on the flume sidewall as described previously. The red channel was converted into a black and white (binary) image with a user defined threshold and enhanced by removing unwanted imperfections though morphological operations. Background illumination was estimated by a series of smoothing operations. The probe locations were identified and scaling values were calculated using colored markers on the wave tank wall. It was observed that lens distortion error in the vertical direction was negligible for the area covered during the video recording. Therefore, only horizontal lens distortion was corrected using the known locations of the wave probe markers. Camera alignment was corrected using the initial free surface line (still water level) as the datum. Third order polynomials were fitted to the free surface line and the wave probe markers, to be used for camera distortion and alignment correction.

3.5.2.2 **Video processing**

The remaining frames were cropped around the still water level, and the red channel was separated. The estimated background from the preprocessing step was subtracted from each frame to obtain a uniform background. Each frame was then converted to a binary image with the previously defined threshold. The free surface was identified after enhancing the binary image through a series of morphological operations (Fig. 3.25). The binary images were accumulated and averaged after the waves became steady. Free surface elevation data were scaled, normalized with the still water curve, and transformed along the horizontal axis to correct for curvature induced by the camera optics. Water surface displacements at the wave probe locations were interpolated from the estimated water surface profiles for each frame. Fig. 3.26 shows a comparison of video and wave gage data.

3.5.2.3 **Video postprocessing**

Each pixel value of the average frame, **I**, represents the fraction of time that the pixel was dry. White regions in Fig. 3.27 were always dry and black regions were always wet during the averaging period. The summation of the pixel values along a vertical line yields

the variation of the mean water level along the horizontal axis. The vertical sums were normalized with respect to the still water level and scaled to calculate the mean water level. The average binary frame was transformed using the relation: $\mathbf{J} = \mathbf{I} \cdot (1 - \mathbf{I})$ to filter out the stationary pixels and capture the wave height envelope. The resulting matrix, **J**, had values between 0 and 1 if the pixel value changed from frame to frame while it had zero values where there was no change. Lower pixel values represent areas near wave crest and trough while higher pixel values represent areas near mean water level. The average frame was then converted to a binary image with a threshold equal to:

$$e = \frac{1 - fT}{(fT)^2} \tag{3.18}$$

where f is the frame rate, which ensures that any change less frequent than the wave frequency is ignored. An example average frame is given in Fig. 3.28. The region of non-zero values shows the wave height envelope.

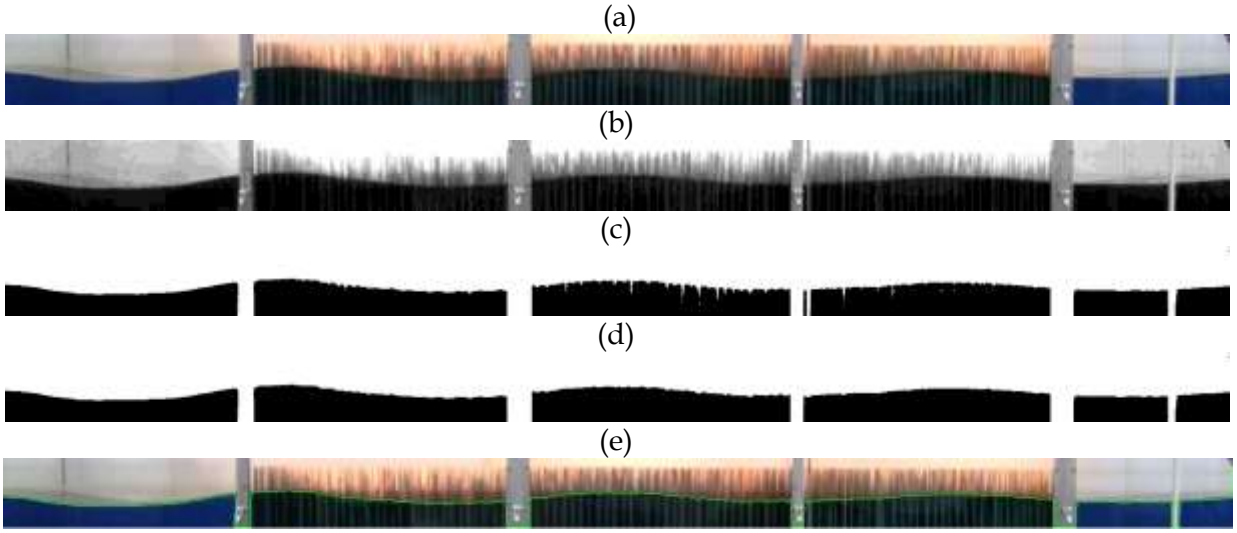

Fig. 3.25. Summary of the video analysis procedure: (a) RGB image, (b) red channel, (c) binary image, (d) enhanced binary image and (e) the captured interface (green line).

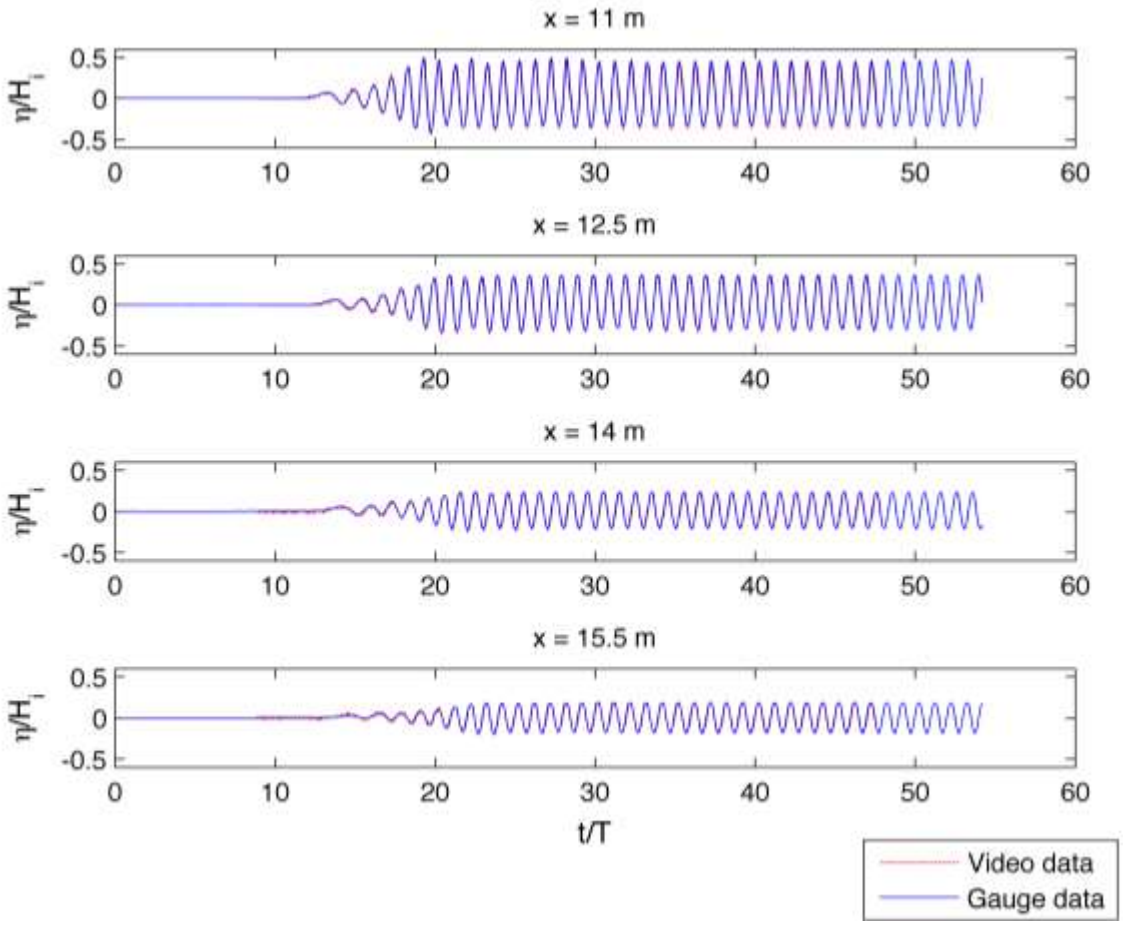

Fig. 3.26. The wave probe time series data compared with the video data for rigid model vegetation (T = 1.2 s, H_i = 0.1 m, h = 0.5 m, D_v = 623 stems/m² and l_s = 0.63 m).

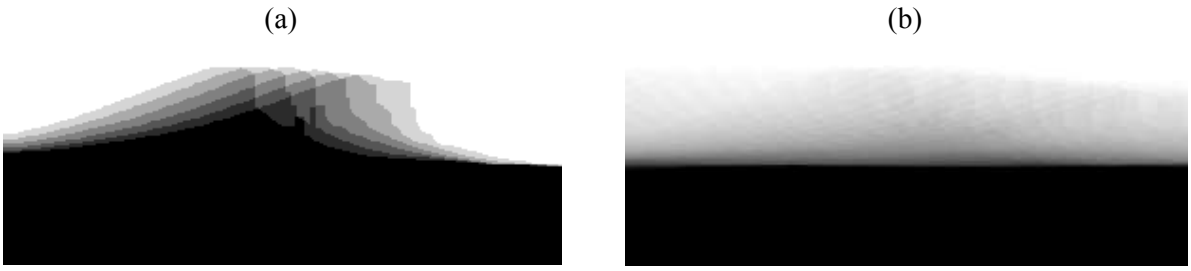

Fig. 3.27. A portion of the average (a) 5 frames and (b) 48 frames for breaking waves over the sloping beach (T = 1.6 s, H = 0.14 m and h = 0.4 m.

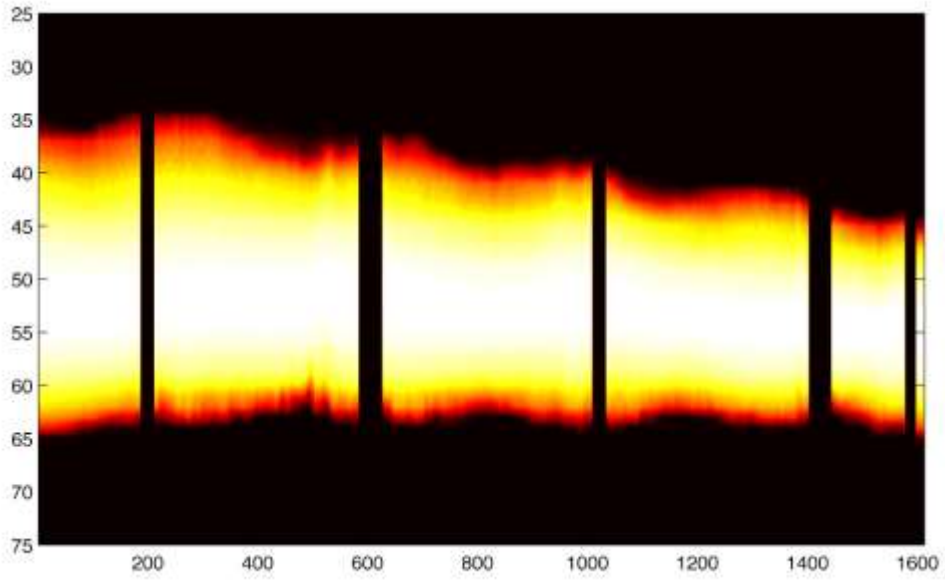

Fig. 3.28 A sample transformed average frame for rigid model vegetation (T = 1.2 s, H = 0.1 m, h = 0.5 m and Dv = 350 stems/m² and ls = 0.63 m). Vertical stripes are the supports of the wave tank, which blocked the camera's view of the water surface. Lower pixel values (darker) represent areas near wave crest and trough while higher pixel values (lighter) represent areas near mean water level.

3.6 Results of Flat-Bed Experiments

As the waves travel through the vegetation, they lose their energy by doing work on the vegetation. The interaction between the vegetation and the waves is complex due to the dynamic nature of the forcing and the spatial variation of both the individual and bulk properties of the plants. Nevertheless, with some approximations, it is possible to estimate a drag coefficient that will represent the bulk of the plants in terms of mean quantities. For a flat-bed and assuming linear wave theory is valid, constant quantities over the depth, and rigid vegetation, a relationship can be established between wave parameters and the vegetation properties (Dalrymple et al. 1984).

According to this relationship, the wave height evolution can be written as:

$$\frac{H}{H_i} = \frac{1}{1+\alpha x} \tag{3.19}$$

where H and H_i are the incident wave height and wave height within the vegetation, and α is the damping factor defined by:

$$\alpha = \frac{4}{9\pi} H_i C_D D_v N_v k \frac{\sinh^3 kah + 3\sinh kah}{\sinh kh(\sinh 2kh + 2kh)} \tag{3.20}$$

where C_D is the bulk drag coefficient and $a = h_v / h$ for submerged vegetation and unity for emergent vegetation. A similar relation can be established for irregular waves (Mendez and Loasada 2004):

$$\frac{H_{rms}}{H_{rmsi}} = \frac{1}{1+\tilde{\alpha}x} \tag{3.21}$$

and

$$\tilde{\alpha} = \frac{1}{3\sqrt{\pi}} H_{rmsi} C_D D_v N_v k_p \frac{\sinh^3 k_p ah + 3\sinh k_p ah}{\sinh k_p h(\sinh 2k_p h + 2k_p h)} \tag{3.22}$$

H_{rmsi} and H_{rms} are the root-mean-square heights of the incident waves and the waves inside the vegetation, k_p is the wave number associated with peak period, ($k_p = 2\pi/L_p$). Reynolds number is defined as

$$R_e = \frac{u_c D_v}{\nu} \tag{3.23}$$

where ν is the kinematic viscosity and u_c is the characteristic velocity defined as the maximum horizontal velocity just before the vegetation zone at mid-height of the plants (x = 0 and $z = -h(1-a)$)

$$u_c = \frac{H}{2}\omega \frac{\cosh(kah)}{\sinh(kh)} \tag{3.24}$$

Another commonly used dimensionless quantity is the Keulegan-Carpenter number:

$$K_c = \frac{u_c T}{D_v} \tag{3.25}$$

The results are organized in two main sections: flat-bed (Section 3.6) experiments and sloping beach (Section 3.7) experiments. Section 3.6.1 and 3.6.2 describe the methodology that is followed to estimate drag coefficient through wave gage data for regular and irregular waves and video data for regular waves. Both of the measuring techniques seek to identify bulk drag coefficients of the vegetation using the idealized analytical models described above. The estimated drag coefficient for each vegetation type is compared in Section 3.6.3. In Section 3.7, the effect of vegetation on wave setup is investigated.

3.6.1 Drag Coefficient Estimation Using Wave Gage Data

The complete list of experiments with regular waves is presented in Table 3.2, and the list of irregular wave experiments is presented in Table 3.3. The first column of the tables includes a reference number that is unique for each experiment. Each experiment with regular waves was repeated three times to minimize uncertainties. The same experiments that were run with the vegetation models were also run for the non-vegetated control case. The results of the control experiments were used to identify some of the other sources of uncertainty. The most important ones are:

- Reflected waves, mainly from the wave absorber and/or the vegetation models,

- Transient (evanescent) waves created during wave generation,
- Resonance with the longitudinal and lateral seiche period of the wave tank,
- Friction losses.

Evanescent waves decay exponentially as they propagate away from the paddle. Hence, their influence is minimal close to the vegetation zone. The resonant periods are avoided during the experiments.

As shown in Section 3.1.2, the wave reflection was minimized with the wave absorber for a wide range of waves. However, when the wave attenuation through vegetation was low (<5%), the reflection became important relative to the amount of dissipation. Higher transmission rates also increased reflected wave height from the absorber. Likewise, for the cases with lower wave transmission, the wave reflection through the vegetation created another source of uncertainty that affected the wave height measurements at the first and second gages. In order to eliminate the errors introduced by the reflected waves and correctly estimate the incident wave height, a curve was fitted to the measured wave heights at five gages of those experiments with no vegetation installed (control case). Depending on the nature of energy dissipation, wave height decay can be exponential or in the form of a rational function (Dalrymple et al. 1984). Here, a rational function ($H = H_i/(1+cx)$) similar to Eq. 3.19 was fitted to the wave heights at five gages for all three runs. Figs. A.1 – A.8 in Appendix A shows the fitted curves (dashed lines) together with the wave height measurements at each gage for the control experiments. The wave height was interpolated at x = 11.5 m (beginning of vegetation zone) and used as the reference incident wave height (H_i) for the vegetated experiments and is presented in the second column of Table 3.2. In Fig. 3.29 the interpolated wave height is compared with the wave height measured at x = 11 m. There is a slight deviation from the fitted line for larger wave heights.

For each run with rigid, flexible and live vegetation, the model defined by Eq. 3.21 was fitted to the wave heights using a nonlinear least squares method and the bulk drag coefficient, C_D, was calculated from Eq. 3.22. The complete list of estimated drag coefficients is in Table 3.2 and fitted curves are presented in Figs. A.1 – A.8 (solid lines) together with the wave height measurements. Note that the wave heights are normalized with H_i and the distance is normalized with the vegetation span, L_v. The beginning of the vegetation zone was set as the origin.

Reflected waves were less pronounced for irregular waves compared to regular waves. Therefore, the incident wave heights calculated at Gage 2 (x = 11 m) were accepted as the reference incident wave heights, H_{m0i} and H_{rmsi}, for irregular waves. Fig. 3.30 compares H_{m0} and H_{rms} for the range of random wave experiments. The model described by Eq. 3.21 was fitted to the data and the bulk drag coefficient C_D was calculated using Eq. 3.22. H_{rms} at four gages for non-vegetated and vegetated runs can also be found in Figs. A.9 – A.16 in Appendix A. Some of the experiments with irregular waves had relatively high wave attenuation due to the damping of the high frequency components. Those cases are not included in the results.

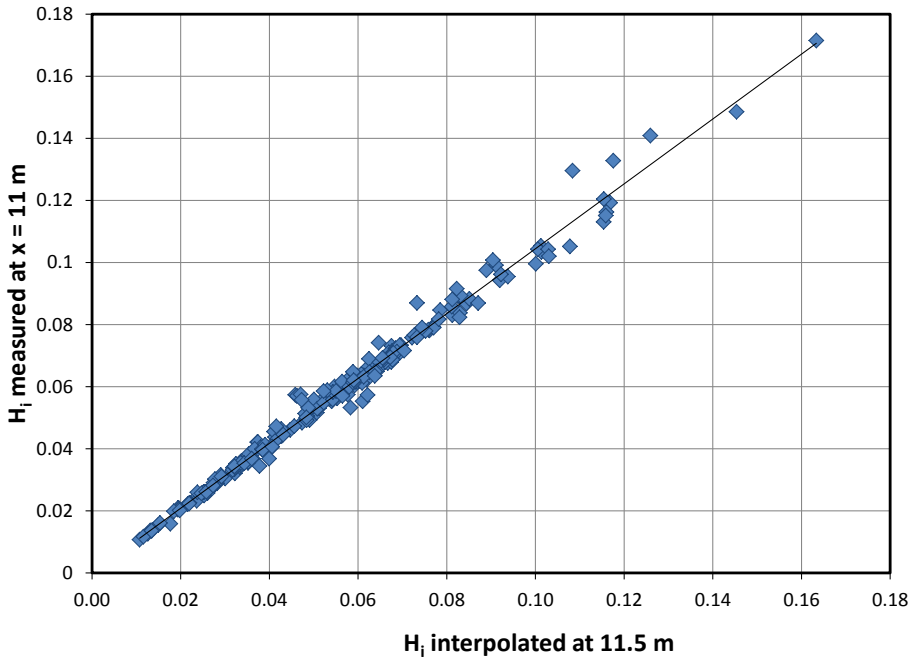

Fig. 3.29. Comparison of interpolated H_i with the measured ones at 11.5 m

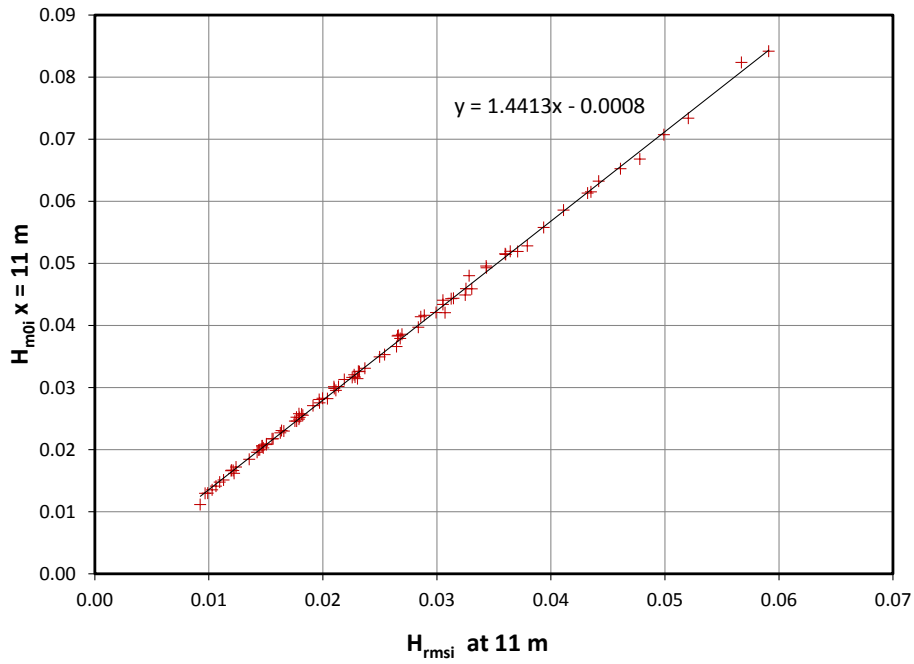

Fig. 3.30. Comparison of H_{rms} and H_{mo}. Wave heights are calculated form the time series signals recorded at x = 11 m.

Table 3.2. Estimated drag coefficients, C_D, from regular wave experiments.

Wave ref. No.	H_i (m)	T (s)	L (m)	h (m)	Rigid model	Rigid model	Rigid model	Rigid model	Flexible model	*S. alterniflora* (Dormant)	*S. alterniflora* (Green)	*J. roemerianus* (Green)
				Veg. ref. No.	12236301	12436301	12435001	12636301	22435001	43435005	43635005	45040003
				Density - N_v (stems/m²)	156	350	350	623	350	545	405	2857
				Stem height - h_v (m)	0.63	0.63	0.48	0.63	0.48	0.62	0.59	1.03
				Stem diameter- D_v (mm)	9.4	9.4	9.4	9.4	9.4	5.1	6.5	2.4
500151101	0.0107	1.10	1.781	0.5				4.915			39.378	7.797
500201201	0.0132	1.20	2.483	0.5						7.124	14.475	6.994
500230701	0.0193	0.70	0.765	0.5	2.617	3.459		3.356	3.971	10.122	24.233	6.467
500260751	0.0216	0.75	0.877	0.5	2.034	2.817		2.840	3.563	10.925	20.916	6.884
500261401	0.0177	1.40	2.580	0.5								
500300801	0.0239	0.80	0.996	0.5	2.423	2.966		2.895	3.489	8.495	18.147	6.549
500301001	0.0236	1.00	1.513	0.5		3.297		3.638	6.206	8.636	16.674	5.775
500311601	0.0194	1.60	3.778	0.5								
500340851	0.0268	0.85	1.120	0.5	1.866	2.456		2.871		6.458	16.705	6.029
500361101	0.0261	1.10	1.781	0.5				3.850			15.328	5.518
500361801	0.0255	1.80	3.572	0.5								4.137
500370901	0.0301	0.90	1.248	0.5	2.269	2.583		2.723	2.813	6.317	15.206	5.266
500380701	0.0322	0.70	0.765	0.5	2.257	2.571		2.578	1.990	4.672	11.940	4.046
500401001	0.0322	1.00	1.513	0.5		2.559		2.964	3.954	6.400	11.472	4.642
500410951	0.0334	0.95	1.380	0.5	1.314	2.201		2.374	2.803	5.657	13.543	4.521
500411201	0.0283	1.20	2.483	0.5							9.393	5.328
500440751	0.0374	0.75	0.877	0.5	2.511	2.577		2.583	2.021	4.622	11.340	3.795
500450601	0.0373	0.60	0.563	0.5						4.472		3.954
500451001	0.0363	1.00	1.513	0.5	1.022	2.796		2.804	3.545	6.083	14.295	4.533

Table 3.2. Estimated drag coefficients, C_D, from regular wave experiments.

Wave ref. No.	H_i (m)	T (s)	L (m)	h (m)	Rigid model	Rigid model	Rigid model	Rigid model	Flexible model	*S. alterniflora* (Dormant)	*S. alterniflora* (Green)	*J. roemerianus* (Green)
500500801	0.0413	0.80	0.996	0.5	2.447	2.454		2.508	1.760	3.683	10.613	3.694
500501001	0.0405	1.00	1.513	0.5		2.661		2.941	3.067	5.197	9.912	3.860
500511401	0.0378	1.40	2.580	0.5								
500530651	0.0459	0.65	0.660	0.5						3.644		
500531101	0.0402	1.10	1.781	0.5							11.087	
500560851	0.0473	0.85	1.120	0.5	2.393	2.270		2.467	1.409	3.259	8.987	3.486
500601001	0.0491	1.00	1.513	0.5		2.589		2.923	2.473	4.334	8.528	3.264
500610701	0.0520	0.70	0.765	0.5	2.288	2.571		2.504	1.370	3.153	9.197	2.621
500611201	0.0426	1.20	2.483	0.5								3.473
500620901	0.0507	0.90	1.248	0.5	2.476	2.399		2.417	1.654	3.188	7.882	2.742
500621601	0.0411	1.60	3.778	0.5								
500690951	0.0574	0.95	1.380	0.5	1.725	2.388		2.376	1.680	3.208	7.408	2.530
500700751	0.0599	0.75	0.877	0.5	2.181	2.327		2.356	1.212	2.777	7.881	2.293
500701001	0.0577	1.00	1.513	0.5		2.550		2.862	2.093	3.791	7.430	2.748
500711801	0.0553	1.80	3.572	0.5								
500761001	0.0620	1.00	1.513	0.5	1.239	2.485		2.552	1.826	3.394	7.284	2.406
500771401	0.0583	1.40	2.580	0.5								
500800701	0.0675	0.70	0.765	0.5		2.443		2.596	1.016	2.287	5.849	1.732
500800751	0.0677	0.75	0.877	0.5		2.324		2.614	1.070	2.332	6.333	1.940
500800801	0.0669	0.80	0.996	0.5	2.150	2.235			1.099	2.377	5.899	1.978
500800851	0.0670	0.85	1.120	0.5		1.984			0.866	2.083	5.564	2.043
500800901	0.0658	0.90	1.248	0.5		2.294		2.542	1.234	2.672	5.936	2.136
500801001	0.0667	1.00	1.513	0.5		2.459		2.848	1.705	3.208	6.682	2.297
500801101	0.0619	1.10	1.781	0.5		2.554		2.738		3.343	6.422	2.562

Table 3.2. Estimated drag coefficients, C_D, from regular wave experiments.

Wave ref. No.	H_i (m)	T (s)	L (m)	h (m)	Rigid model	Rigid model	Rigid model	Rigid model	Flexible model	*S. alterniflora* (Dormant)	*S. alterniflora* (Green)	*J. roemerianus* (Green)
500801201	0.0557	1.20	2.483	0.5								2.581
500801401	0.0610	1.40	2.580	0.5								
500801601	0.0547	1.60	3.778	0.5								
500891101	0.0688	1.10	1.781	0.5	1.724	2.472		2.479	1.836	3.304	6.488	2.225
500900851	0.0739	0.85	1.120	0.5	2.017	1.994		2.153	0.702	1.969	5.180	1.789
500901001	0.0761	1.00	1.513	0.5		2.516		2.709	1.665	3.032	6.324	2.096
501000901	0.0813	0.90	1.248	0.5	1.919				0.879	2.045	4.915	1.615
501001001	0.0846	1.00	1.513	0.5		2.444		2.638	1.392	2.667	5.517	1.758
501021201	0.0722	1.20	2.483	0.5								1.984
501100951	0.0911	0.95	1.380	0.5	1.689	2.207		2.223	1.059	1.957	4.569	1.419
501201001	0.1012	1.00	1.513	0.5		2.327		2.519	1.006	2.110	4.476	1.293
501211001	0.1014	1.00	1.513	0.5	1.359	2.298		2.335	0.994	2.096	4.369	1.280
600151001	0.0126	1.00	1.538	0.6								5.920
600181101	0.0135	1.10	1.829	0.6			5.902				40.597	6.409
600211201	0.0150	1.20	2.123	0.6			4.472					6.034
600230701	0.0196	0.70	0.765	0.6	4.662	3.184	6.453	3.317		6.636	24.784	3.899
600260751	0.0220	0.75	0.878	0.6	3.432	2.924	4.102	2.957	5.573	6.101	22.503	4.161
600271401	0.0197	1.40	2.749	0.6								
600300801	0.0250	0.80	0.998	0.6	3.175	3.034	3.986	2.710	8.602	5.297	18.116	4.115
600311001	0.0254	1.00	1.538	0.6		2.917	2.576	2.941	10.548	6.920	13.750	4.049
600331601	0.0238	1.60	3.271	0.6								
600340851	0.0282	0.85	1.125	0.6	3.091	3.110	4.248	3.021	5.043	4.304	13.892	3.713
600371101	0.0281	1.10	1.829	0.6		3.760	2.834	3.378	9.798	7.222	13.472	4.053
600380701	0.0335	0.70	0.765	0.6	2.968	2.802	4.950	2.702	6.235	3.056	12.381	2.334

Table 3.2. Estimated drag coefficients, C_D, from regular wave experiments.

Wave ref. No.	H_i (m)	T (s)	L (m)	h (m)	Rigid model	Rigid model	Rigid model	Rigid model	Flexible model	*S. alterniflora* (Dormant)	*S. alterniflora* (Green)	*J. roemerianus* (Green)
600380901	0.0322	0.90	1.258	0.6	2.735	2.683	2.992	2.491	4.719	4.185	12.070	3.364
600381801	0.0274	1.80	3.823	0.6			2.253	2.761	7.939	5.206		3.243
600401001	0.0342	1.00	1.538	0.6		2.670	3.416	2.876	7.615	4.977	10.510	2.859
600420951	0.0352	0.95	1.396	0.6	2.839	2.720	2.522	2.705	5.126	3.976	10.560	3.107
600421201	0.0318	1.20	2.123	0.6			2.485				7.891	3.828
600440751	0.0383	0.75	0.878	0.6	2.883	2.724	3.109	2.623	5.686	2.977	10.135	2.280
600461001	0.0389	1.00	1.538	0.6	3.080	2.739	2.696	2.581	6.747	4.214	9.983	2.786
600500801	0.0428	0.80	0.998	0.6	2.605	2.630	2.822	2.445	4.097	2.558	7.797	2.074
600501001	0.0425	1.00	1.538	0.6		2.632	2.638	2.682	5.561	3.765	8.628	2.367
600541401	0.0431	1.40	2.749	0.6								
600551101	0.0428	1.10	1.829	0.6	2.692	3.033	2.628	2.735	5.414	4.240	8.040	2.564
600560851	0.0485	0.85	1.125	0.6	2.538	2.571	2.967	2.521	2.763	2.412	6.133	1.810
600601001	0.0512	1.00	1.538	0.6		2.597	2.578	2.485	4.641	3.374	6.670	1.897
600630901	0.0541	0.90	1.258	0.6	2.454	2.418	2.446	2.450	2.755	2.282	5.863	1.626
600641201	0.0485	1.20	2.123	0.6		1.797	2.297				5.268	2.292
600651601	0.0501	1.60	3.271	0.6								
600700951	0.0592	0.95	1.396	0.6	2.258	2.405	2.317	2.394	2.871	2.285	5.356	1.501
600701001	0.0598	1.00	1.538	0.6		2.544	2.647	2.394	3.697	2.859	5.674	1.563
600761801	0.0575	1.80	3.823	0.6			2.006	2.323	3.985	2.418	3.866	
600771001	0.0653	1.00	1.538	0.6	2.488	2.534	2.260	2.220	3.347	2.511	5.133	1.416
600800701	0.0685	0.70	0.765	0.6		2.403	2.116	2.333		1.397	4.896	1.046
600800751	0.0697	0.75	0.878	0.6		2.410	2.627	2.441	2.841	1.451	4.818	1.144
600800801	0.0685	0.80	0.998	0.6		2.228	2.430	2.246	1.798	1.426	4.110	1.151
600800851	0.0695	0.85	1.125	0.6		2.243	2.460	2.281	1.642	1.545	4.146	1.177

Table 3.2. Estimated drag coefficients, C_D, from regular wave experiments.

Wave ref. No.	H_i (m)	T (s)	L (m)	h (m)	Rigid model	Rigid model	Rigid model	Rigid model	Flexible model	*S. alterniflora* (Dormant)	*S. alterniflora* (Green)	*J. roemerianus* (Green)
600800901	0.0675	0.90	1.258	0.6		2.227	2.236	2.330	1.882	1.635	4.289	1.166
600801001	0.0684	1.00	1.538	0.6		2.507	2.386	2.314	2.956	2.418	4.966	1.337
600801101	0.0634	1.10	1.829	0.6		2.524	2.387	2.517	3.074	2.679	4.870	1.585
600801201	0.0618	1.20	2.123	0.6			2.559			1.654	4.021	1.741
600801401	0.0651	1.40	2.749	0.6								
600801601	0.0625	1.60	3.271	0.6				2.674			4.462	
600811401	0.0661	1.40	2.749	0.6								
600901001	0.0768	1.00	1.538	0.6		2.446	2.573	2.253	2.678	2.168	4.299	1.186
600911101	0.0727	1.10	1.829	0.6	2.206	2.481	2.317	2.324	2.789	2.409	4.435	1.394
600981601	0.0785	1.60	3.271	0.6	2.414			2.697			3.978	1.910
601001001	0.0844	1.00	1.538	0.6		2.298	2.129	2.135	1.940	1.809	3.605	1.016
601061201	0.0825	1.20	2.123	0.6		1.837	2.235			1.530	3.476	1.325
601201001	0.1006	1.00	1.538	0.6		2.156	2.064	2.068	1.653	1.381	3.078	0.826
601401001	0.1169	1.00	1.538	0.6		1.973	1.791	2.010	1.369	1.174	2.622	0.683
610450601	0.0374	0.60	0.563	0.6		2.633		2.665		2.579	13.578	2.314
610530651	0.0462	0.65	0.660	0.6							9.923	
610610701	0.0536	0.70	0.765	0.6	2.577	2.707	2.002	2.530	3.262	1.775	7.230	1.537
610700751	0.0613	0.75	0.878	0.6	2.459	2.442	2.710	2.413	3.376	1.730	5.668	1.355
610800801	0.0686	0.80	0.998	0.6	2.199	2.269	2.434	2.198	1.974	1.450	4.557	1.187
610900851	0.0770	0.85	1.125	0.6	1.958	2.144	2.167	2.173	1.491	1.347	3.665	1.010
611010901	0.0830	0.90	1.258	0.6	1.765	2.012	2.005	1.984	1.553	1.277	3.563	0.893
611231001	0.1029	1.00	1.538	0.6	1.888	2.122	1.881	1.990	1.559	1.346	3.124	0.817
611461101	0.1154	1.10	1.829	0.6		1.932	1.911		1.664	1.241	2.578	0.786
700161001	0.0116	1.00	1.556	0.7		7.892		7.647			120.848	5.523

Table 3.2. Estimated drag coefficients, C_D, from regular wave experiments.

Wave ref. No.	H_i (m)	T (s)	L (m)	h (m)	Rigid model	Rigid model	Rigid model	Rigid model	Flexible model	*S. alterniflora* (Dormant)	*S. alterniflora* (Green)	*J. roemerianus* (Green)
700191101	0.0134	1.10	1.856	0.7		4.553		5.624			86.243	4.901
700221201	0.0153	1.20	2.171	0.7		2.801					50.614	5.199
700230701	0.0185	0.70	0.765	0.7		7.448		7.217		19.950	184.064	3.253
700260751	0.0219	0.75	0.878	0.7		3.577	48.221	4.645		12.053	122.164	3.377
700281401	0.0198	1.40	2.853	0.7							32.754	
700300801	0.0252	0.80	0.999	0.7		3.941	23.852	3.871	14.739	7.933	76.404	2.867
700340851	0.0278	0.85	1.127	0.7		2.750	18.099	3.570		6.700	50.095	2.699
700341601	0.0253	1.60	3.427	0.7								
700380701	0.0324	0.70	0.765	0.7	2.932	3.134		2.867		9.819	92.778	1.855
700380901	0.0318	0.90	1.262	0.7		2.396	8.568	2.858	10.293	5.149	37.045	2.558
700401001	0.0335	1.00	1.556	0.7		2.677	5.967	3.599	10.668	5.180	29.715	2.115
700401801	0.0284	1.80	4.327	0.7				2.573	6.584		8.815	
700420951	0.0353	0.95	1.437	0.7	1.206	2.544	6.008	3.003		4.983	26.941	2.303
700440751	0.0381	0.75	0.878	0.7	2.986	2.843		2.637		6.531	57.191	1.672
700471001	0.0387	1.00	1.556	0.7	1.640	3.056	4.530	3.090	12.177	5.095	21.906	2.056
700500801	0.0428	0.80	0.999	0.7	1.690	2.129	9.147	1.979	8.815	4.127	33.145	1.372
700501001	0.0418	1.00	1.556	0.7		2.705	4.384	2.809	8.656	4.242	21.966	1.722
700530651	0.0470	0.65	0.660	0.7	5.697						108.074	
700560851	0.0481	0.85	1.127	0.7	1.036	2.199	8.050	1.993		3.161	23.124	1.342
700561101	0.0447	1.10	1.856	0.7	1.087	2.719	3.456	2.653	8.736	4.410	15.814	1.835
700601001	0.0508	1.00	1.556	0.7		2.518	4.169	2.522	8.113	3.605	17.436	1.388
700610701	0.0523	0.70	0.765	0.7	2.283	2.319	15.104	2.123		5.242	54.136	1.229
700630901	0.0543	0.90	1.262	0.7	1.944	2.340	3.795	2.143	4.926	2.875	17.411	1.212
700651201	0.0484	1.20	2.171	0.7		1.819	3.066	2.025	3.753		9.864	1.628

Table 3.2. Estimated drag coefficients, C_D, from regular wave experiments.

Wave ref. No.	H_i (m)	T (s)	L (m)	h (m)	Rigid model	Rigid model	Rigid model	Rigid model	Flexible model	*S. alterniflora* (Dormant)	*S. alterniflora* (Green)	*J. roemerianus* (Green)
700700751	0.0608	0.75	0.878	0.7	2.284	2.450	12.316	2.055	14.778	3.344	31.406	0.938
700700951	0.0603	0.95	1.437	0.7	2.123	2.527	4.088	2.161	6.104	2.757	13.985	1.084
700701001	0.0593	1.00	1.556	0.7		2.312	3.822	2.294	5.703	2.940	14.206	1.126
700781001	0.0659	1.00	1.556	0.7	2.334	2.487	3.093	2.162	5.956	2.789	11.801	0.967
700800701	0.0679	0.70	0.765	0.7		2.013		1.866		3.157	38.965	0.878
700800751	0.0694	0.75	0.878	0.7		2.422	9.055	2.096	15.249	3.124	28.082	0.848
700800801	0.0688	0.80	0.999	0.7	1.874	2.200	6.523	1.761	7.384	2.249	18.277	0.758
700800851	0.0682	0.85	1.127	0.7		1.871	6.705	1.884		1.568	15.103	0.897
700800901	0.0678	0.90	1.262	0.7		2.132	2.674	1.985	2.607	1.856	13.256	0.851
700801001	0.0680	1.00	1.556	0.7		2.419	3.211	2.172	4.211	2.476	11.690	0.958
700801101	0.0649	1.10	1.856	0.7		2.436	3.109	2.242	4.083	2.573	10.060	1.116
700801201	0.0596	1.20	2.171	0.7		1.565	2.773	1.933		1.761	7.621	1.266
700801401	0.0609	1.40	2.853	0.7								
700801601	0.0626	1.60	3.427	0.7				2.502	5.125	1.782	5.901	1.226
700841401	0.0643	1.40	2.853	0.7								
700900851	0.0759	0.85	1.127	0.7	1.344	1.696	5.582	1.657		1.725	12.012	0.733
700901001	0.0771	1.00	1.556	0.7		2.466	3.499	2.184	4.299	2.461	10.524	0.867
700931101	0.0752	1.10	1.856	0.7	1.660	2.484	2.821	2.135	4.336	2.361	8.347	0.934
701001001	0.0851	1.00	1.556	0.7		2.392	2.744	2.068	4.237	2.209	8.995	0.742
701010901	0.0829	0.90	1.262	0.7	1.251	1.731	2.955	1.588	3.687	1.802	9.458	0.604
701031601	0.0811	1.60	3.427	0.7		2.599	1.930	2.374	4.828	1.589	4.266	0.974
701091201	0.0831	1.20	2.171	0.7		1.935		1.961	2.301	1.890	5.771	0.907
701201001	0.1001	1.00	1.556	0.7		2.204	2.221	1.982	3.170	2.022	6.755	0.579
701241001	0.1030	1.00	1.556	0.7	2.102	2.146	2.367	1.861	3.961	2.098	6.629	0.567

Table 3.2. Estimated drag coefficients, C_D, from regular wave experiments.

Wave ref. No.	H_i (m)	T (s)	L (m)	h (m)	Rigid model	Rigid model	Rigid model	Rigid model	Flexible model	*S. alterniflora* (Dormant)	*S. alterniflora* (Green)	*J. roemerianus* (Green)
701401001	0.1154	1.00	1.556	0.7		2.033	2.481	1.871	3.159	1.846	5.640	0.481
701491101	0.1160	1.10	1.856	0.7	1.126	1.711	2.417	1.638	2.174	1.590	4.180	0.531
400291001	0.0253	1.00	1.464	0.4			3.892				22.458	5.427
400300801	0.0290	0.80	0.987	0.4			3.170				23.494	5.392
400330851	0.0322	0.85	1.145	0.4			2.928				2.973	5.275
400341101	0.0247	1.10	1.718	0.4							2.930	
400370901	0.0335	0.90	1.224	0.4			3.117				18.779	4.993
400391201	0.0278	1.20	1.936	0.4			3.240				17.988	5.391
400400951	0.0354	0.95	1.344	0.4			3.168				16.953	4.753
400441001	0.0388	1.00	1.464	0.4			2.812				14.457	4.176
400481401	0.0367	1.40	2.393	0.4			3.320				11.158	3.922
400490801	0.0488	0.80	0.987	0.4			2.680				13.156	3.818
400511101	0.0383	1.10	1.718	0.4			3.460				13.398	
400550851	0.0543	0.85	1.145	0.4			2.625				11.327	3.746
400571601	0.0390	1.60	2.836	0.4								
400581201	0.0427	1.20	1.936	0.4			3.126				11.320	
400610901	0.0563	0.90	1.224	0.4			2.718				1.343	
400651301	0.0483	1.30	2.166	0.4			2.978				8.967	3.317
400651801	0.0473	1.80	3.269	0.4								
400670951	0.0589	0.95	1.344	0.4			2.786				9.266	
400721401	0.0564	1.40	2.393	0.4			2.816				7.338	2.936
400731001	0.0639	1.00	1.464	0.4			2.355				8.548	2.847
400742001	0.0531	2.00	3.695	0.4							5.428	
400781501	0.0580	1.50	2.616	0.4								

Table 3.2. Estimated drag coefficients, C_D, from regular wave experiments.

Wave ref. No.	H_i (m)	T (s)	L (m)	h (m)	Rigid model	Rigid model	Rigid model	Rigid model	Flexible model	*S. alterniflora* (Dormant)	*S. alterniflora* (Green)	*J. roemerianus* (Green)
400851101	0.0673	1.10	1.718	0.4			2.882				7.421	
400851601	0.0594	1.60	2.836	0.4								
400971201	0.0733	1.20	1.936	0.4			2.489				5.949	2.653
400981801	0.0733	1.80	3.269	0.4								
401081301	0.0813	1.30	2.166	0.4			2.343				4.773	2.312
401081401	0.0889	1.40	2.393	0.4			2.330				4.527	2.229
401112001	0.0823	2.00	3.695	0.4			2.114				3.514	
401201501	0.0920	1.50	2.616	0.4			2.242					
401311601	0.0938	1.60	2.836	0.4								
401421801	0.1084	1.80	3.269	0.4								
401632001	0.1259	2.00	3.695	0.4			1.963				2.620	1.367
500300801	0.0321	0.80	0.996	0.5			2.619				15.768	4.358
500301001	0.0258	1.00	1.513	0.5			2.499				14.954	4.836
500340851	0.0344	0.85	1.120	0.5			2.470				13.747	4.387
500361101	0.0273	1.10	1.781	0.5			2.818				12.343	
500370901	0.0360	0.90	1.248	0.5			2.540				11.721	4.674
500410951	0.0385	0.95	1.380	0.5			2.181				1.645	3.796
500411201	0.0292	1.20	2.483	0.5			2.737				11.565	4.640
500451001	0.0406	1.00	1.513	0.5			2.429				8.756	4.166
500500801	0.0551	0.80	0.996	0.5			2.289				7.474	2.532
500511401	0.0399	1.40	2.580	0.5							7.553	
500531101	0.0431	1.10	1.781	0.5			2.491					
500560851	0.0589	0.85	1.120	0.5			2.174				6.435	2.499
500611201	0.0456	1.20	2.483	0.5			2.457				7.946	3.398

Table 3.2. Estimated drag coefficients, C_D, from regular wave experiments.

Wave ref. No.	H_i (m)	T (s)	L (m)	h (m)	Rigid model	Rigid model	Rigid model	Rigid model	Flexible model	*S. alterniflora* (Dormant)	*S. alterniflora* (Green)	*J. roemerianus* (Green)
500620901	0.0613	0.90	1.248	0.5			2.259				5.675	2.298
500621601	0.0416	1.60	3.778	0.5								
500690951	0.0655	0.95	1.380	0.5			1.894				5.143	2.196
500691301	0.0522	1.30	2.312	0.5			2.264				6.326	2.835
500711801	0.0565	1.80	3.572	0.5								
500761001	0.0704	1.00	1.513	0.5			1.974				4.612	2.268
500771401	0.0621	1.40	2.580	0.5							5.175	
500812001	0.0590	2.00	4.561	0.5			1.954				3.758	2.175
500851501	0.0638	1.50	2.826	0.5								
500891101	0.0745	1.10	1.781	0.5			2.367				4.715	2.813
500921601	0.0646	1.60	3.778	0.5								
501021201	0.0782	1.20	2.483	0.5			1.879				3.392	1.916
501071801	0.0871	1.80	3.572	0.5								
501161301	0.0904	1.30	2.312	0.5			1.969				3.744	1.753
501222001	0.0922	2.00	4.561	0.5			1.848				2.923	1.750
501291401	0.1078	1.40	2.580	0.5			1.774				2.827	1.523
501411501	0.1159	1.50	2.826	0.5							3.129	
501541601	0.1176	1.60	3.778	0.5			2.679				2.527	1.416
501791801	0.1453	1.80	3.572	0.5								
502032001	0.1634	2.00	4.561	0.5			1.716				2.179	1.929

Table 3.3. Estimated drag coefficients, C_D, from irregular wave experiments

Exp. ref. No.	H_{rms} (m) @11m	H_{mo} (m) @11m	T_p (s)	L (m)	h (m)	Rigid model	Rigid model	Rigid model	Rigid model	Flexible model	*S. alterniflora* (Dormant)	*S. alterniflora* (Green)	*J. roemerianus* (Green)
					Veg. ref. No.	12236301	12436301	12435001	12636301	22435001	43435005	43635005	45040003
					Density - N_v (stems/m²)	156	350	350	623	350	545	405	2857
					Stem length - h_v (m)	0.63	0.63	0.48	0.63	0.48	0.62	0.59	1.03
					Stem diameter - D_v (mm)	9.4	9.4	9.4	9.4	9.4	5.1	6.5	2.4
r500151005	0.0092	0.0111	1.00	1.513	0.5								
r500181105	0.0103	0.0135	1.10	1.781	0.5					9.111	8.502	18.344	5.784
r500200805	0.0122	0.0162	0.80	0.996	0.5					4.726			
r500201205	0.0113	0.0151	1.20	2.048	0.5					9.571	7.684	17.071	5.872
r500230705	0.0142	0.0196	0.70	0.765	0.5	2.674	2.448		2.357	3.201	5.645	16.529	4.095
r500250905	0.0147	0.0206	0.90	1.248	0.5					4.634	8.697		
r500260755	0.0156	0.0217	0.75	0.877	0.5	3.524	2.347		2.382	3.835	6.234	20.351	4.999
r500261405	0.0135	0.0184	1.40	2.571	0.5					11.142			
r500300805	0.0177	0.0246	0.80	0.996	0.5	3.401	2.676		2.756	3.427	6.295	15.020	4.792
r500301005	0.0166	0.0230	1.00	1.513	0.5					5.478	7.551		
r500311605	0.0156	0.0217	1.60	3.078	0.5	8.914	4.214		4.247	11.858	5.717	12.008	4.707
r500340855	0.0197	0.0281	0.85	1.120	0.5	3.140	2.686		2.652	3.666	6.304	14.969	4.867
r500361105	0.0191	0.0271	1.10	1.781	0.5					5.610	7.565		
r500361805	0.0180	0.0252	1.80	3.572	0.5								
r500370905	0.0219	0.0313	0.90	1.248	0.5	2.598	2.500		2.618	3.508	5.706	13.800	4.571
r500380705	0.0226	0.0316	0.70	0.765	0.5	3.412	2.505		2.312	2.937	5.035	11.136	3.736
r500411205	0.0211	0.0295	1.20	2.048	0.5					5.960	6.374		
r500440755	0.0250	0.0349	0.75	0.877	0.5	2.967	2.714		2.449	2.738	4.835	11.450	3.880
r500451005	0.0254	0.0353	1.00	1.513	0.5	4.193	3.050		2.731	4.026	5.314	12.839	4.562

Table 3.3. Estimated drag coefficients, C_D, from irregular wave experiments

Exp. ref. No.	H_{rms} (m) @11m	H_{mo} (m) @11m	T_p (s)	L (m)	h (m)	Rigid model	Rigid model	Rigid model	Rigid model	Flexible model	*S. alterniflora* (Dormant)	*S. alterniflora* (Green)	*J. roemerianus* (Green)
r500500805	0.0284	0.0397	0.80	0.996	0.5	2.713	2.471		2.309	2.554	4.435	10.593	3.463
r500511405	0.0266	0.0383	1.40	2.571	0.5								
r500531105	0.0289	0.0416	1.10	1.781	0.5	3.154	2.529		2.509	3.879	5.083	10.071	
r500560855	0.0325	0.0449	0.85	1.120	0.5	2.745	2.600		2.460	2.588	4.303	9.737	3.271
r500611205	0.0328	0.0480	1.20	2.048	0.5	3.265	2.665		2.655	3.733	4.921	8.842	3.654
r500620905	0.0360	0.0514	0.90	1.248	0.5	3.574	2.828		2.627	2.612	4.096	9.193	3.134
r500621605	0.0305	0.0441	1.60	3.078	0.5								
r500690955	0.0394	0.0558	0.95	1.380	0.5	2.712	2.514		2.469	2.250	3.883	8.380	2.824
r500761005	0.0411	0.0586	1.00	1.513	0.5	2.802	2.617		2.398	2.313	3.646	8.009	2.804
r500891105	0.0478	0.0668	1.10	1.781	0.5	2.678	2.502		2.453		3.794	7.034	2.544
r600151005	0.0097	0.0130	1.00	1.538	0.6					17.432	10.534	30.467	4.956
r600181105	0.0110	0.0148	1.10	1.829	0.6		4.403	4.083		17.122	10.488	22.546	4.810
r600200805	0.0124	0.0172	0.80	0.998	0.6						7.410	27.845	4.665
r600211205	0.0120	0.0167	1.20	2.123	0.6		3.480	3.429		12.881	9.868	22.795	4.468
r600230705	0.0148	0.0203	0.70	0.765	0.6	4.489	2.767		2.896		6.009	20.994	3.016
r600250905	0.0147	0.0206	0.90	1.258	0.6			6.355			7.890	22.721	4.701
r600260755	0.0163	0.0227	0.75	0.878	0.6	3.998	3.109	6.853	2.948	14.085	5.864	19.492	3.370
r600271405	0.0145	0.0200	1.40	2.705	0.6								4.576
r600300805	0.0179	0.0258	0.80	0.998	0.6	4.377	3.151	7.104	2.978	10.389	5.693	18.860	3.341
r600311005	0.0176	0.0246	1.00	1.538	0.6			4.828			6.866	19.248	3.873
r600331605	0.0177	0.0252	1.60	3.271	0.6								3.388
r600340855	0.0197	0.0275	0.85	1.125	0.6	3.943	3.193	5.283	3.095	11.879	5.670	16.724	3.266
r600371105	0.0214	0.0302	1.10	1.829	0.6			3.685			5.624	16.027	3.383
r600380705	0.0237	0.0331	0.70	0.765	0.6	3.107	2.600		2.407	7.981	3.820	12.137	2.328
r600380905	0.0230	0.0314	0.90	1.258	0.6	3.298	2.680	3.906	2.813	7.388	4.550	13.465	2.924
r600381805	0.0204	0.0282	1.80	3.823	0.6	8.012	3.385	3.566	3.531	8.583	4.711	9.086	2.862

Table 3.3. Estimated drag coefficients, C_D, from irregular wave experiments

Exp. ref. No.	H_{rms} (m) @11m	H_{mo} (m) @11m	T_p (s)	L (m)	h (m)	Rigid model	Rigid model	Rigid model	Rigid model	Flexible model	*S. alterniflora* (Dormant)	*S. alterniflora* (Green)	*J. roemerianus* (Green)
r600421205	0.0232	0.0326	1.20	2.123	0.6			2.669			5.656	11.739	3.134
r600440755	0.0268	0.0379	0.75	0.878	0.6	2.859	2.616	4.601	2.334	7.409	3.064	10.866	2.291
r600461005	0.0266	0.0384	1.00	1.538	0.6	2.814	2.417	1.705	2.368	4.103	3.875	11.110	2.697
r600500805	0.0299	0.0421	0.80	0.998	0.6	3.152	2.543	4.203	2.288	4.140	2.922	9.668	2.232
r600541405	0.0286	0.0414	1.40	2.705	0.6								
r600551105	0.0313	0.0443	1.10	1.829	0.6	2.972	2.637	2.458	2.561	5.210	3.696	8.819	2.514
r600560855	0.0326	0.0459	0.85	1.125	0.6	2.485	2.426	2.666	2.372	3.792	2.841	9.456	2.096
r600630905	0.0379	0.0528	0.90	1.258	0.6	2.818	2.548	3.456	2.447	3.405	2.479	7.271	1.838
r600641205	0.0343	0.0496	1.20	2.123	0.6	3.685	2.946	2.685	2.715	5.152	3.895	7.679	2.562
r600651605	0.0344	0.0493	1.60	3.271	0.6								
r600771005	0.0442	0.0632	1.00	1.538	0.6	2.465	2.444	2.014	2.336	2.714	2.249	6.293	1.682
r600811405	0.0432	0.0613	1.40	2.705	0.6								
r600911105	0.0521	0.0734	1.10	1.829	0.6	2.488	2.498	2.492	2.229	2.943	2.228	5.235	1.474
r601061205	0.0591	0.0842	1.20	2.123	0.6	2.969	2.520	2.388	2.385	2.778	2.207	4.570	1.474
r700161005	0.0099	0.0130	1.00	1.551	0.7			23.064	2.868	18.805	16.860	53.498	4.403
r700191105	0.0106	0.0141	1.10	1.856	0.7			12.971		19.748	13.666	46.641	4.348
r700200805	0.0121	0.0166	0.80	0.999	0.7			48.737			20.087	94.314	3.394
r700221205	0.0120	0.0166	1.20	2.171	0.7			10.839		23.776	14.469	39.399	4.570
r700230705	0.0144	0.0199	0.70	0.765	0.7	8.051	4.610		3.123		20.107	148.362	2.499
r700250905	0.0151	0.0208	0.90	1.262	0.7						11.574		3.195
r700260755	0.0164	0.0231	0.75	0.878	0.7	6.921	5.588		3.502		14.246	104.191	2.687
r700281405	0.0151	0.0209	1.40	2.805	0.7	5.499	3.714	6.155	3.373	15.629	10.242	21.976	3.959
r700300805	0.0179	0.0249	0.80	0.999	0.7	5.942	3.183	39.988	2.618	15.849	10.196	73.076	2.653
r700311005	0.0181	0.0257	1.00	1.551	0.7			10.392			9.659		3.117
r700340855	0.0200	0.0283	0.85	1.127	0.7		3.649	22.774	2.601	29.474	9.141	57.345	2.609
r700341605	0.0182	0.0255	1.60	3.427	0.7			3.687		13.089		16.239	3.112

Table 3.3. Estimated drag coefficients, C_D, from irregular wave experiments

Exp. ref. No.	H_{rms} (m) @11m	H_{mo} (m) @11m	T_p (s)	L (m)	h (m)	Rigid model	Rigid model	Rigid model	Rigid model	Flexible model	*S. alterniflora* (Dormant)	*S. alterniflora* (Green)	*J. roemerianus* (Green)
r700371105	0.0210	0.0301	1.10	1.856	0.7			7.555			7.869		2.869
r700380705	0.0228	0.0317	0.70	0.765	0.7		3.526		2.846	80.029	11.390	96.832	1.858
r700380905	0.0228	0.0321	0.90	1.262	0.7	4.550	2.660		2.610	16.937	7.784	41.493	2.389
r700401805	0.0210	0.0299	1.80	4.033	0.7	5.985	2.816	3.910	2.669	10.412	5.022	13.170	2.483
r700431205	0.0231	0.0326	1.20	2.171	0.7			4.314			6.911	25.955	2.780
r700440755	0.0265	0.0366	0.75	0.878	0.7	2.911	2.801		2.419	25.232	8.749	60.205	1.759
r700471005	0.0269	0.0386	1.00	1.551	0.7	3.071	3.112	6.078	2.143	9.487	5.634	25.087	2.131
r700500805	0.0307	0.0421	0.80	0.999	0.7		3.085	38.348	2.471		7.015	38.881	1.740
r700560855	0.0331	0.0459	0.85	1.127	0.7		2.769	14.751	2.332	18.066	5.473	28.831	1.604
r700561105	0.0315	0.0444	1.10	1.856	0.7	3.477	2.891	4.915	2.335	9.560	5.088	16.568	2.002
r700561405	0.0305	0.0434	1.40	2.805	0.7							14.345	2.413
r700630905	0.0371	0.0519	0.90	1.262	0.7	2.601	2.265	6.681	2.035	9.504	4.428	20.908	1.390
r700651205	0.0364	0.0519	1.20	2.171	0.7	3.352			2.395	7.940	4.576	12.641	1.909
r700691605	0.0360	0.0516	1.60	3.427	0.7							8.179	1.740
r700781005	0.0435	0.0615	1.00	1.551	0.7	2.563	2.289		1.969	6.399	3.509	13.660	1.239
r700841405	0.0461	0.0652	1.40	2.805	0.7				2.688	6.120		8.693	
r700931105	0.0499	0.0707	1.10	1.856	0.7	2.038	2.078	3.028	1.846	3.854	3.154	9.869	1.241
r701091205	0.0567	0.0824	1.20	2.171	0.7	2.255	2.377		1.917	4.551	3.075	7.236	1.160

3.6.2 Drag Coefficient Estimation through Video Analysis

Fig. 3.31 shows the flume arranged for video data collection, with blue dye for contrast, dots to locate gages, and orange lines for scaling. Fig. 3.32 shows video analysis and wave gage data for six different vegetation configurations. The solid lines in these plots are the smoothed time-averaged wave heights estimated from average frame analysis. The plots correspond to the runs of the exact same wave conditons (T = 1.2 s amd h = 0.5 m). The results of the remaining runs can be found in Figs. A.17 - A.22 in Appendix A. It can be seen that the wave heights based on video analysis were similar to wave gage data at fixed locations. The estimated incident wave heights, H_i varies slightly between the experiments due the wave reflection.

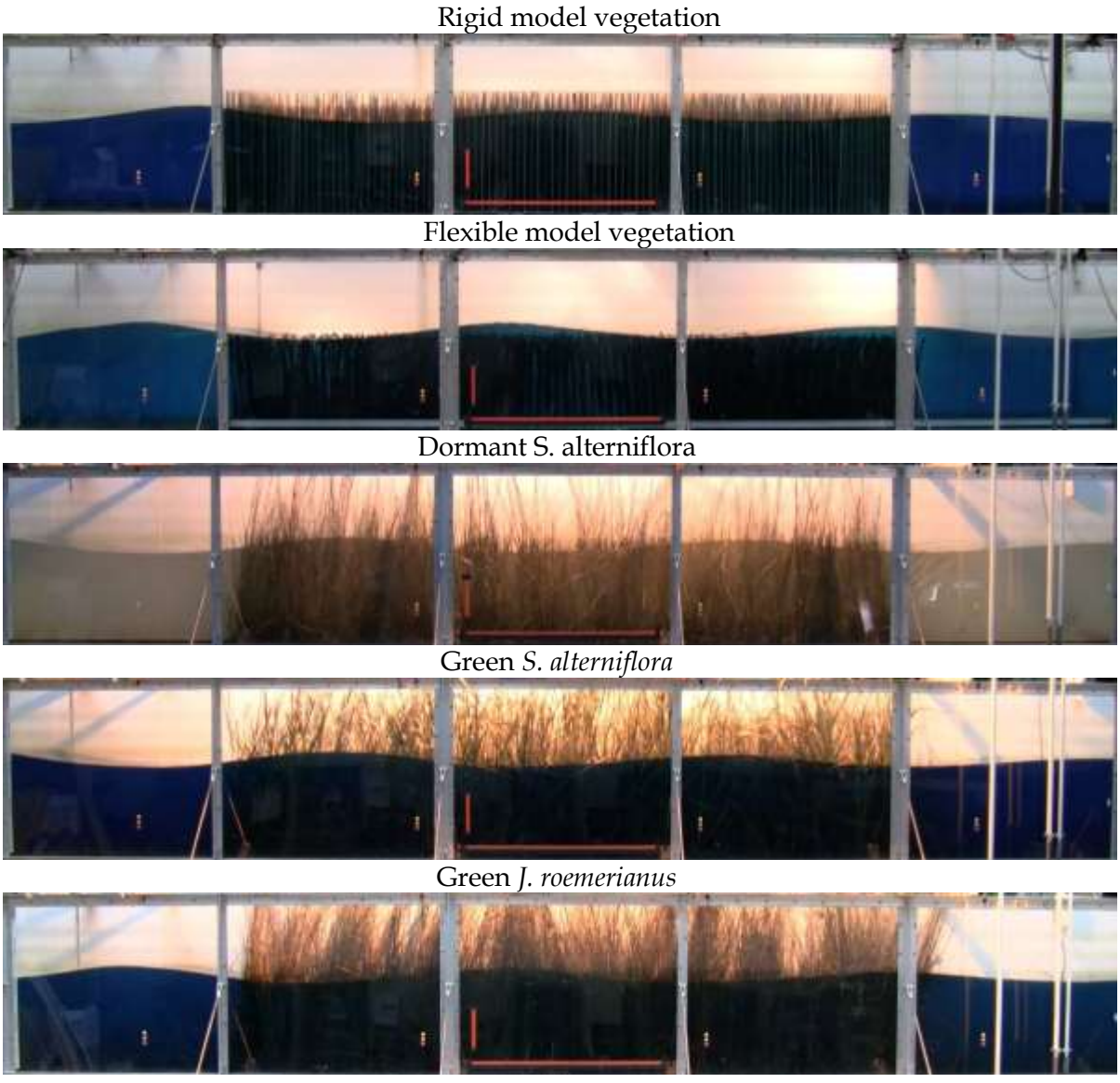

Fig. 3.31. Example images of each vegetation type in flume.

The least agreement between gage data and video analysis was observed in flexible model and *J. roemerianus.* Black foam rubber was used to construct the flexible vegetation model which blended in with the dark blue color of the water and made it harder to identify the free surface at low water depths. Likewise, *J. roemerianus* was relatively darker compared to the other plants resulting in higher errors. Nevertheless, the average error was less than 5% for the runs presented here.

The primary cause of uncertainty in the video data is due to the cross-tank variations in the water surface, mainly cross-tank seiche. The water surface considered in the video recordings was the interface visible to the camera along the side wall, while the wave gages were mounted at the tank's centerline. The cross-tank resonant frequency was avoided in order to minimize this source of error. Other sources of uncertainty include camera alignment and distortion errors. However, the water surface displacement comparison given in Fig. 3.26 shows that there was no phase shift between the two signals which indicates that uncertainty due camera distortion and alignment was minimized with the camera correction procedure.

The model defined by Eq. 3.19 was fitted to the experimental data and plotted in Fig. 3.32 and Figs. A.17 – A.22 with a dashed line. The list of drag coefficients is in Table 3.4. As described earlier, two important external effects had to be considered while evaluating the wave attenuation through the vegetation field inside the wave tank. One is the partial standing wave due to the reflected waves from the wave absorber at the end of the wave tank and/or the vegetation itself, and the other is wave attenuation due to the wave tank itself, such as sidewalls, geometric imperfections, and nonlinearities. The oscillations around the fitted curve indicate the existence of reflected waves. It is not possible to estimate the wave reflection from the wave gage data, but the video data clearly show the nodes and antinodes of the partially standing waves. This difference should be expected since wave height readings at a limited number of fixed points can lead to unrealistic results due to aliasing and the presence of standing waves. For example, in Fig. 3.32 some of the gage reading coincide with nodes while some of them coincide with ati-nodes.

Since the video recording procedure was carried out manually and video data analysis took a considerably longer time compared to the gage data analysis, only selected experiments were recorded with the camera. Yet, the procedure provides valuable information in identifying major features of the wave transformation through vegetation with a consumer-grade video camera. The procedure provides a continuous distribution of wave heights along the vegetation zone with a reasonable precision. The modulation of wave height, which was considered in previous studies (Mendez et al. 1999), can be clearly observed.

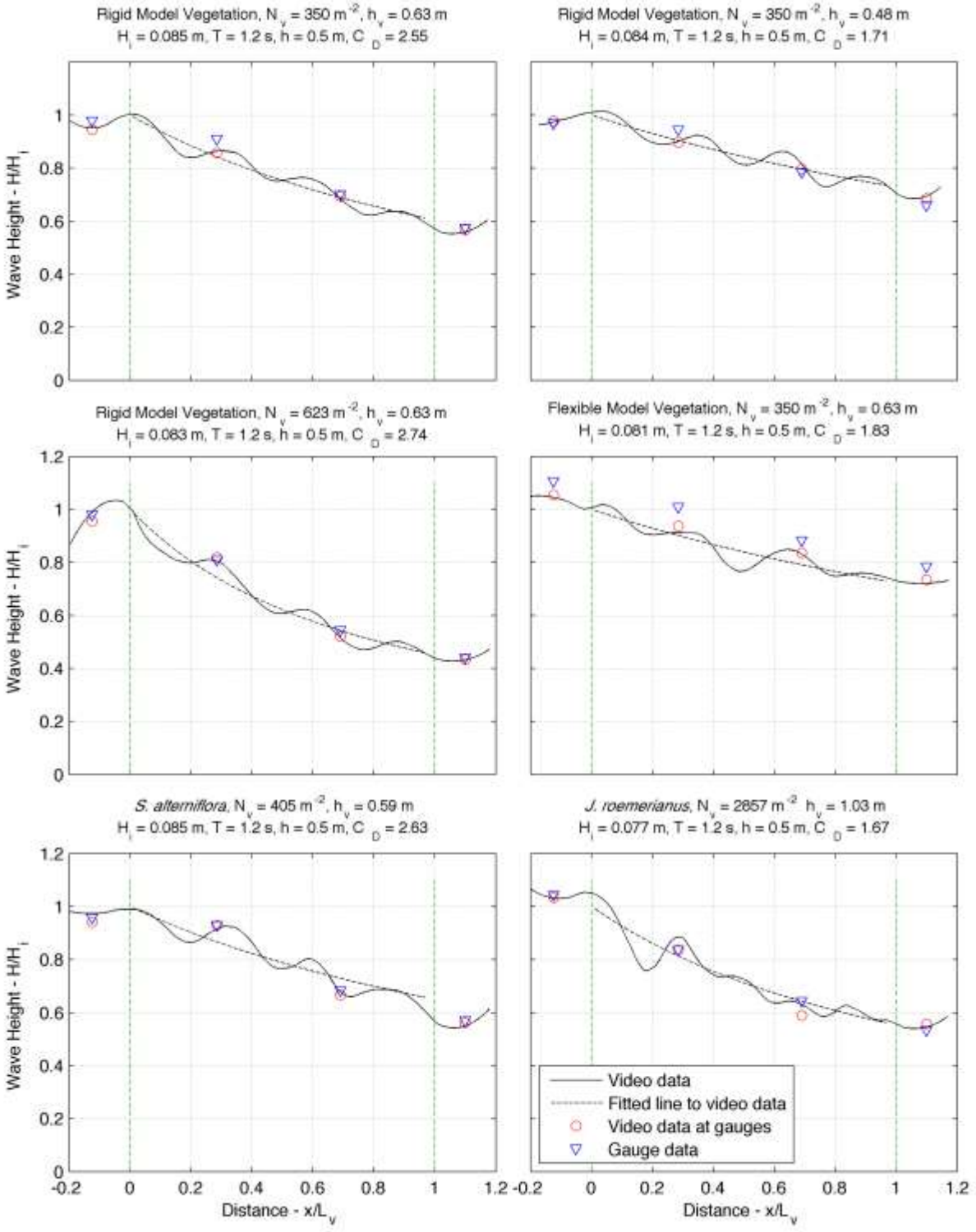

Fig. 3.32. Wave height evolution over model and live vegetation.

Table 3.4. Estimated drag coefficients, C_D, from regular wave experiments through video analysis.

Wave ref. No.	H_i (m)	T (s)	L (m)	h (m)	Rigid model	Rigid model	Rigid model	Rigid model	Flexible model	*S. alterniflora* (Dormant)	*S. alterniflora* (Green)	*J. roemerianus* (Green)
				Veg. ref. No.	**12236301**	**12436301**	**12435001**	**12636301**	**22435001**	**43435005**	**43635005**	**45040003**
				Density – N_v (stems/m²)	**156**	**350**	**350**	**623**	**350**	**545**	**405**	**2857**
				Stem height - h_v (m)	**0.63**	**0.63**	**0.48**	**0.63**	**0.48**	**0.62**	**0.59**	**1.03**
				Stem diameter - D_v (mm)	**9.4**	**9.4**	**9.4**	**9.4**	**9.4**	**5.1**	**6.5**	**2.4**
400300801	0.031	0.8	0.987	0.4			2.723				18.348	
400441001	0.039	1.0	1.464	0.4			2.806				12.241	
400581201	0.045	1.2	1.936	0.4			2.965				7.893	
400721401	0.061	1.4	2.393	0.4			2.764				5.314	
400731001	0.065	1.0	1.464	0.4			2.267				5.561	
400851601	0.070	1.6	2.836	0.4			2.332				3.988	
400971201	0.077	1.2	1.936	0.4			2.269				4.225	
400981801	0.084	1.8	3.269	0.4			2.039				3.416	
401112001	0.090	2.0	3.695	0.4			2.090				3.436	
401201401	0.106	1.4	2.393	0.4			2.196				3.392	
401421601	0.120	1.6	2.836	0.4			2.004				2.758	
401631801	0.146	1.8	3.269	0.4			1.812				2.350	
401852001		2	3.695	0.4			1.805				2.473	
500300801	0.034	0.8	0.996	0.5		2.402	2.375	3.295	2.465		9.848	3.503
500451001	0.042	1.0	1.513	0.5		3.423	2.225	2.460	3.476		6.643	3.002
500500801		0.8	0.996	0.5		3.253		3.061	2.222			
500611201	0.050	1.2	2.048	0.5		2.945	2.021	3.040	3.384		4.753	2.853
500711801		1.8	3.572	0.5		2.666		2.891	2.952			
500761001	0.071	1.0	1.513	0.5		2.395	1.587	2.777	2.037		3.436	1.762
500771401	0.069	1.4	2.571	0.5		2.805	2.566	2.975	2.899		3.355	1.724

Table 3.4. Estimated drag coefficients, C_D, from regular wave experiments through video analysis.

Wave ref. No.	H_i (m)	T (s)	L (m)	h (m)	Rigid model	Rigid model	Rigid model	Rigid model	Flexible model	*S. alterniflora* (Dormant)	*S. alterniflora* (Green)	*J. roemerianus* (Green)
500800801		0.8	0.996	0.5		2.195		2.379	0.934			
500921601	0.078	1.6	3.078	0.5			2.129				2.692	1.610
501000801		0.8	0.996	0.5		2.131		2.555	0.903			
501021201	0.084	1.2	2.048	0.5		2.551	1.712	2.742	1.833		2.627	1.672
501071801	0.096	1.8	3.572	0.5			2.009				2.374	1.218
501190801		0.8	0.996	0.5		1.907		2.409				
501211001		1	1.513	0.5		2.333		2.616	1.212			
501222001	0.103	2.0	4.056	0.5			1.997				2.688	1.363
501291401	0.119	1.4	2.571	0.5			1.607				2.085	1.265
501511001		1	1.513	0.5		2.174		2.458	0.826			
501541601	0.134	1.6	3.078	0.5			1.530				1.772	1.094
501791801	0.162	1.8	3.572	0.5			1.519					0.940
502032001	0.176	2.0	4.056	0.5			1.581				2.013	0.992
700300801	0.027	0.8	0.999	0.7		4.114		0.172	64.844			2.250
700380701	0.034	0.7	0.765	0.7								
700471001		1	1.551	0.7		3.256		2.464	7.431			1.999
700500801	0.045	0.8	0.999	0.7		2.202		2.131	10.407			
700561401	0.049	1.4	2.805	0.7								
700651201	0.052	1.2	2.171	0.7		2.617	3.199	2.428	4.455			1.571
700781001	0.068	1.0	1.551	0.7		2.045	2.142	1.799	5.532			0.969
700800801	0.067	0.8	0.999	0.7		1.572		1.326	0.973			0.808
700811801	0.067	1.8	4.033	0.7		2.757	3.550	3.096	4.338			1.778
700841401	0.075	1.4	2.805	0.7		2.358	2.537	2.444	4.803			1.175
701000801		0.8	0.999	0.7		1.473	6.635	1.657	7.510			0.666
701091201	0.087	1.2	2.171	0.7		2.088	2.124	2.114	3.100			0.870
701200801						1.392		1.330				

Table 3.4. Estimated drag coefficients, C_D, from regular wave experiments through video analysis.

Wave ref. No.	H_i (m)	T (s)	L (m)	h (m)	Rigid model	Rigid model	Rigid model	Rigid model	Flexible model	*S. alterniflora* (Dormant)	*S. alterniflora* (Green)	*J. roemerianus* (Green)
701241001	0.107	1.0	1.551	0.7		1.699	3.684	1.594	3.642			0.516
701551001		1	1.551	0.7		1.446	3.143	1.419	3.785			0.437

3.6.3 Regression Equations of Drag Coefficient

Drag coefficients, C_D are plotted against Reynolds number, Re and Keulegan-Carpenter number, K_c for regular waves in Figs. 3.33–3.41 and irregular waves in Figs. 3.42–3.50. Note that the parameter h_v/h in these plots are different than a since it can be greater than zero. The video data analysis results are also included in these plots when available. Figs. 3.35 and 3.39 are plotted on a semi-log scale to better view the relation. Two empirical relationships, one rational and one exponential, are fitted to the data in Figs. 3.33–3.41, but only the rational fit is shown. The models fitted to the data and their confidence intervals are given in Tables 3.12–3.13. In general, the correlation was reasonable for all of the vegetation models except for the rigid model vegetation with N_v = 156 (Ref. No. = 12236301). The plot for this vegetation model shown in Fig. 3.33 is highly scattered due to very low wave attenuation along the vegetation zone. The scattering is less pronounced when the waves are irregular in Fig. 3.42.

Basic results from the drag coefficient plots (Figs. 3.31-3.49) are below:

- Gage data analysis and video analysis yield similar results
- For both regular and random waves:
    - Drag coefficients at different water depths ($h_v/h = a$) seem to collapse for model vegetation.
    - There is a slight dependency of C_D on plant height relative to the water depth.
    - Submerged vegetation appears to have very high drag coefficients at low Reynolds numbers.
    - The drag coefficient approaches a constant value at high Re or K_c.
    - In general, the relationship with K_c provided a better fit with both of the models used compared to the one with Re.
    - Flexible model vegetation had higher drag coefficients at low Re compared to the rigid model.
    - Live vegetation appears to have more dependency on relative plant height due to density and biomass distributions along the depth.

The derivation of the wave attenuation relation takes relative plant high into account, the properties of the vegetation which were assumed constant along the vegetation height may actually vary. N_v and D_v commonly decrease with elevation along the vegetation while wave energy increase. For this reason in Figs. 3.37 (Dormant *S. alterniflora*) and 3.39 (*J. roemerianus*) the data that correspond to the different relative stem heights are separated. The separation is less pronounced in Fig. 3.38 for green *S. alterniflora* which is possibly due to the fact that the leaves were denser closer to the top of the plant.

A better relation can be obtained by introducing the relative plant height into the fitted empirical model. Fig. 3.40 presents the new curve fitted to *J. roemerianus* and Table 3.11 shows the modified empirical relation. With the same modification, new empirical relations are obtained with irregular waves for *J. roemerianus*. These results are shown in Fig. 3.50 and Table 3.12. With this modified relationship, the coefficient of determination (R^2) ranged between 0.85 - 0.95 for the tested model fits.

Table 3.5. The parameters and estimated drag coefficients from the regular wave experiments for the model $C_D = a + \left(b/\mathrm{Re}\right)^c$.

Ref. No.	Vegetation Type	*a*	*b*	*c*	R^2	C_D (Re = 10^3)	C_D (Re = $2x10^3$)
12236301	Rigid model	0.423	9,307	0.325	0.09	2.489	2.072
12436301	Rigid model	1.933	845	1.257	0.57	2.743	2.272
12435001	Rigid model	2.557	565	3.284	0.84	2.712	2.573
12636301	Rigid model	1.983	831	1.401	0.69	2.755	2.275
22435001	Flexible model	-	4,020	0.851	0.62	3.269	1.812
43435005	*S. alterniflora* (Dormant)	-	2,623	1.013	0.68	2.657	1.316
43635005	*S. alterniflora* (Green)	-	6,066	1.301	0.58	10.43	4.235
45040003	*J. roemerianus* (Green)	-	1,269	0.744	0.65	1.194	0.713

Table 3.6. The parameters and estimated drag coefficients from the regular wave experiments for the model $C_D = a + \left(b/K_c\right)^c$.

Ref. No.	Vegetation Type	*a*	*b*	*c*	R^2	C_D (K_c = 10)	C_D (K_c = 30)
12236301	Rigid model	1.886	7.531	2.219	0.21	2.419	1.933
12436301	Rigid model	2.272	6.000	2.382	0.72	2.569	2.294
12435001	Rigid model	2.347	6.937	2.506	0.89	2.747	2.372
12636301	Rigid model	2.231	6.732	2.089	0.77	2.668	2.275
22435001	Flexible model	-	64.06	0.673	0.46	3.492	1.667
43435005	*S. alterniflora* (Dormant)	0.883	53.42	1.283	0.83	9.464	2.979
43635005	*S. alterniflora* (Green)	1.767	76.04	1.641	0.84	29.664	6.367
45040003	*J. roemerianus* (Green)	0.772	202.7	0.782	0.673	10.52	4.455

Table 3.7. The parameters and estimated drag coefficients from the regular wave experiments for the model $C_D = a + b\exp(c\,\mathrm{Re})$.

Ref. No.	Vegetation Type	*a*	*b*	*c*	R^2	C_D (Re = 10^3)	C_D (Re = $2x10^3$)
12236301	Rigid model	-0.177	3.117	-1.577E-04	0.09	2.486	2.097
12436301	Rigid model	2.237	7.830	-2.822E-03	0.57	2.702	2.264
12435001	Rigid model	2.856	716.3	-1.564E-02	0.81	2.856	2.856
12636301	Rigid model	2.259	10.11	-3.149E-03	0.70	2.693	2.278
22435001	Flexible model	0.778	11.57	-1.504E-03	0.66	3.351	1.350
43435005	*S. alterniflora* (Dormant)	1.787	21.85	-3.510E-03	0.69	2.440	1.807
43635005	*S. alterniflora* (Green)	4.705	172.2	-3.904E-03	0.58	8.179	4.775
45040003	*J. roemerianus* (Green)	0.411	8.110	-3.466E-03	0.71	0.665	0.419

Table 3.8. The parameters and estimated drag coefficients from the regular wave experiments for the model $C_D = a + b\exp(cK_c)$.

Ref. No.	Vegetation Type	*a*	*b*	*c*	R^2	C_D (K_c = 10)	C_D (K_c = 30)
12236301	Rigid model	1.999	12.40	-0.346	0.21	2.387	1.999
12436301	Rigid model	2.370	27.49	-0.579	0.69	2.454	2.370
12435001	Rigid model	2.732	267.1	-1.195	0.87	2.734	2.732
12636301	Rigid model	2.345	17.57	-0.431	0.76	2.581	2.345
22435001	Flexible model	1.310	9.07	-0.137	0.49	3.609	1.458
43435005	*S. alterniflora* (Dormant)	2.093	27.63	-0.125	0.80	9.980	2.736
43635005	*S. alterniflora* (Green)	6.469	326.6	-0.261	0.82	30.402	6.597
45040003	*J. roemerianus* (Green)	0.883	8.53	-0.026	0.71	7.460	4.794

Table 3.9. The parameters and estimated drag coefficients from the irregular wave experiments for the model $C_D = a + \left(b/\mathrm{Re}\right)^c$.

Ref. No.	Vegetation Type	*a*	*b*	*c*	R^2	C_D (Re = 10^3)	C_D (Re = $2x10^3$)
12236301	Rigid model	2.569	673.7	2.717	0.82	2.910	2.621
12436301	Rigid model	2.134	556.9	1.447	0.5	2.562	2.291
12435001	Rigid model	2.587	662.7	2.047	0.52	3.017	2.691
12636301	Rigid model	0.713	9,370	0.240	0.33	2.422	2.160
22435001	Flexible model	-	2,923	1.122	0.46	3.332	1.531
43435005	*S. alterniflora* (Dormant)	-	2,620	0.912	0.77	2.407	1.279
43635005	*S. alterniflora* (Green)	-	5,683	1.168	0.43	7.613	3.387
45040003	*J. roemerianus* (Green)	-	1,291	0.562	0.56	1.155	0.783

Table 3.10. The parameters and estimated drag coefficients from the irregular wave experiments for the model $C_D = a + \left(b/K_c\right)^c$.

Ref. No.	Vegetation Type	*a*	*b*	*c*	R^2	C_D (K_c = 10)	C_D (K_c = 30)
12236301	Rigid model	2.628	6.118	2.231	0.77	2.962	2.656
12436301	Rigid model	2.404	4.369	2.160	0.65	2.572	2.420
12435001	Rigid model	-	12.83	1.541	0.71	1.469	0.270
12636301	Rigid model	2.056	2.669	0.738	0.35	2.433	2.223
22435001	Flexible model	3.502	8.326	2.021	0.62	4.192	3.577
43435005	*S. alterniflora* (Dormant)	2.396	27.94	1.540	0.89	7.264	3.292
43635005	*S. alterniflora* (Green)	5.934	32.33	1.955	0.78	15.847	7.092
45040003	*J. roemerianus* (Green)	-	178.2	0.624	0.58	6.037	3.041

Table 3.11. Modified models fitted to the *J. roemerianus* data for regular waves.

Fitted model	*a*	*b*	*c*	R^2
$C_D = a + \left(\frac{b}{\mathrm{Re}\left(h/h_v\right)^2} \right)^c$	-	352.6	0.7604	0.85
$C_D = a + \left(\frac{b}{K_c\left(h/h_v\right)^2} \right)^c$	-	55.22	0.8166	0.92
$C_D = a + b\exp(c\,\mathrm{Re})$	0.6097	8.117	-0.0131	0.90
$C_D = a + b\exp(cK_c\left(h/h_v\right)^2)$	0.8508	8.981	-0.0928	0.95

Table 3.12. Modified models fitted to the *J. roemerianus* data for irregular waves.

Fitted model	*a*	*b*	*c*	R^2
$C_D = a + \left(\frac{b}{\mathrm{Re}\left(h/h_v\right)^2} \right)^c$	-	383.9	0.6081	0.86
$C_D = a + \left(\frac{b}{K_c\left(h/h_v\right)^2} \right)^c$	-	58.50	0.6410	0.85
$C_D = a + b\exp(c\,\mathrm{Re})$	0.72159	6.440	-0.01556	0.90
$C_D = a + b\exp(cK_c\left(h/h_v\right)^2)$	1.19302	6.550	-0.1183	0.87

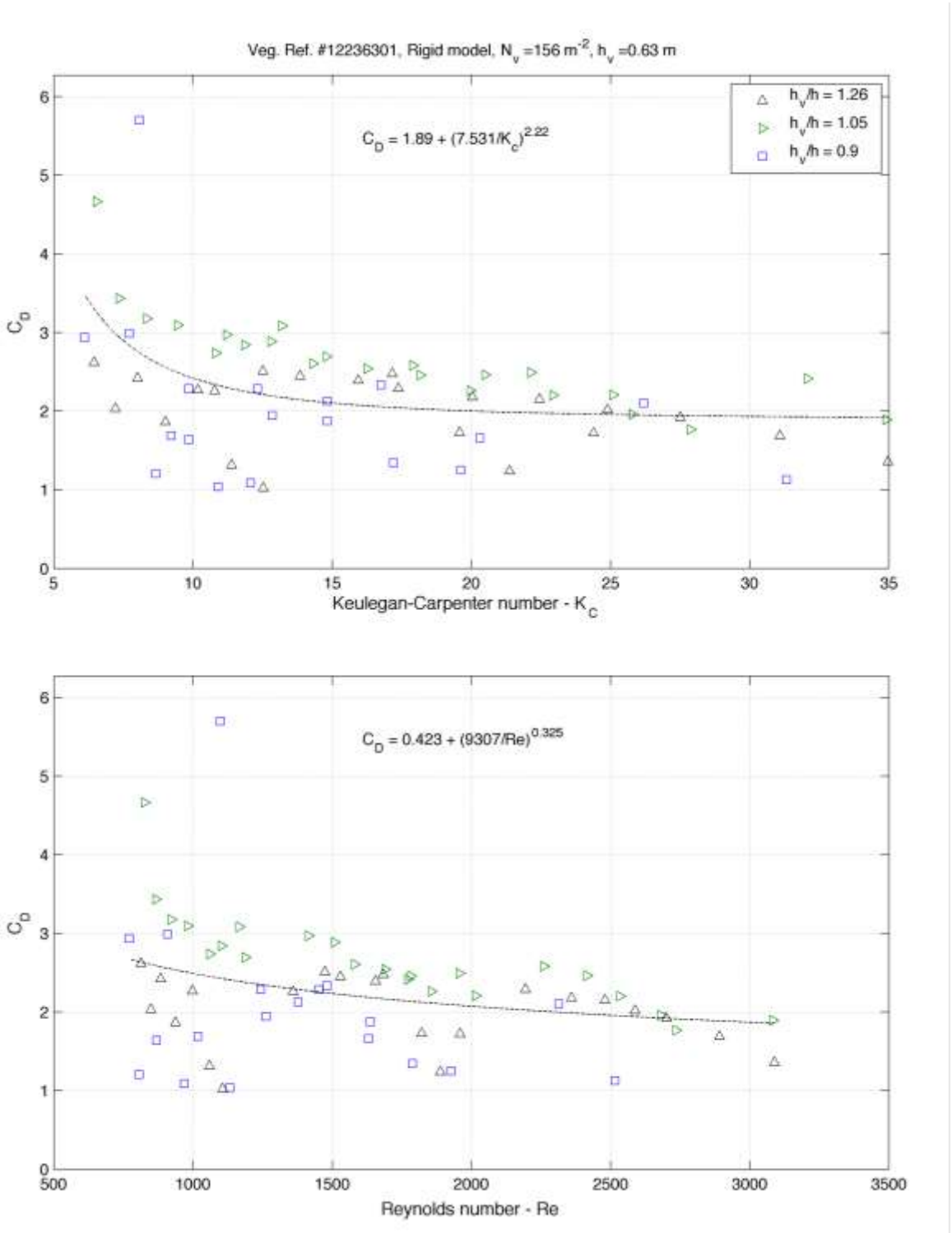

Fig. 3.33. Drag coefficients for rigid model vegetation with N_v = 156 and h_v = 0.63 m.

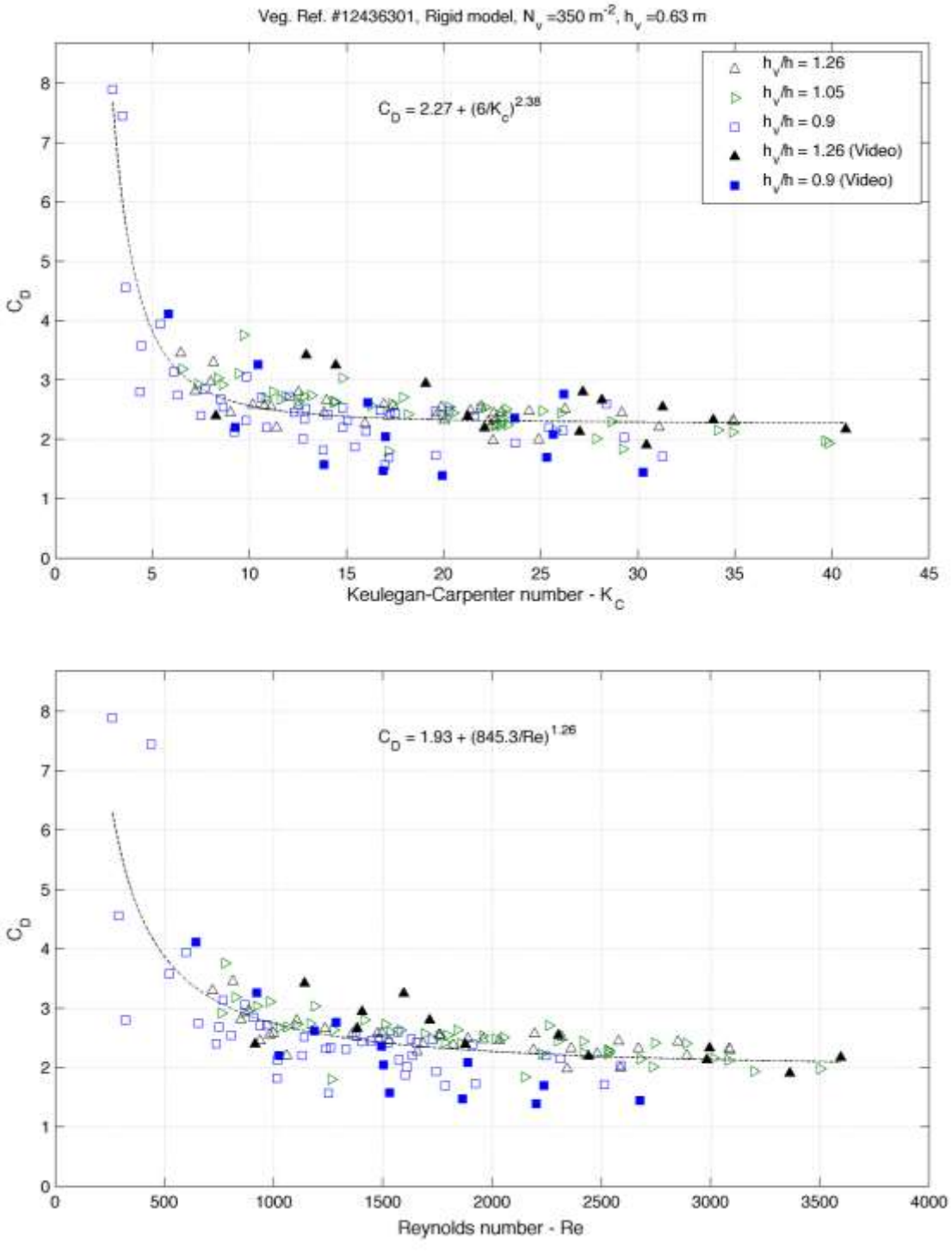

Fig. 3.34. Drag coefficients for rigid model vegetation with N_v = 350 and h_v = 0.63 m.

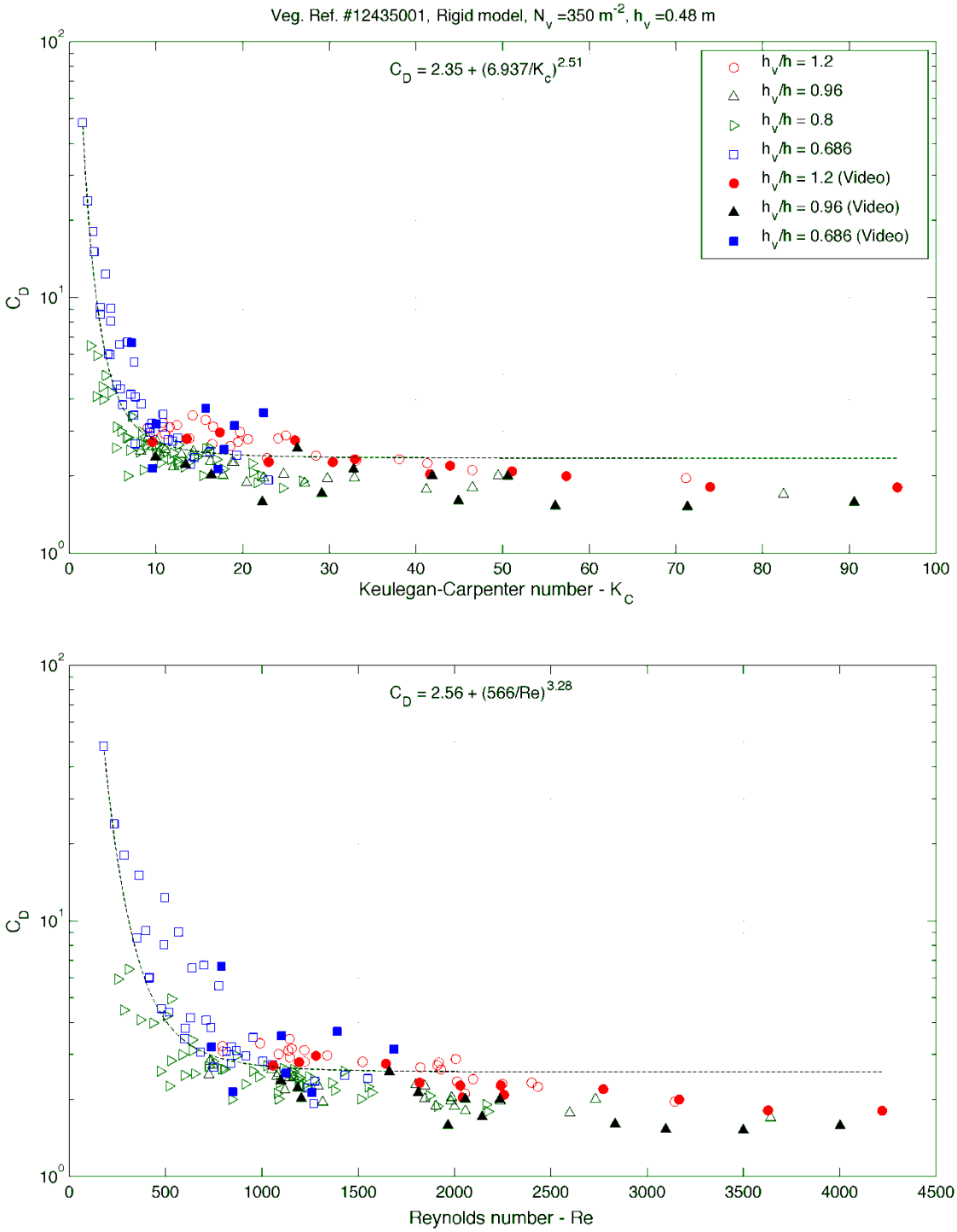

Fig. 3.35. Drag coefficients for rigid model vegetation with N_v = 350 and h_v = 0.48 m.

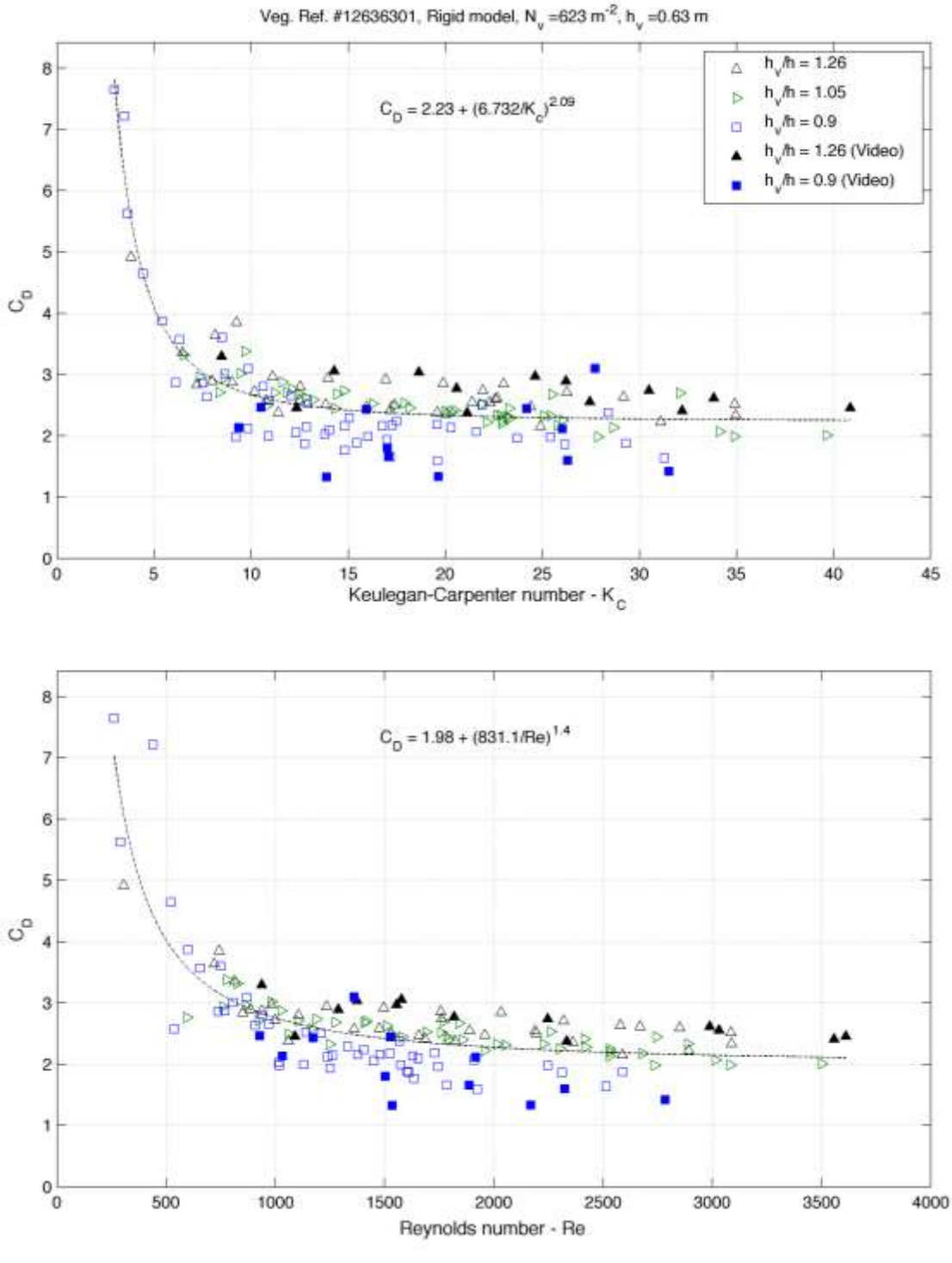

Fig. 3.36. Drag coefficients for rigid model vegetation with N_v = 623 and h_v = 0.63 m.

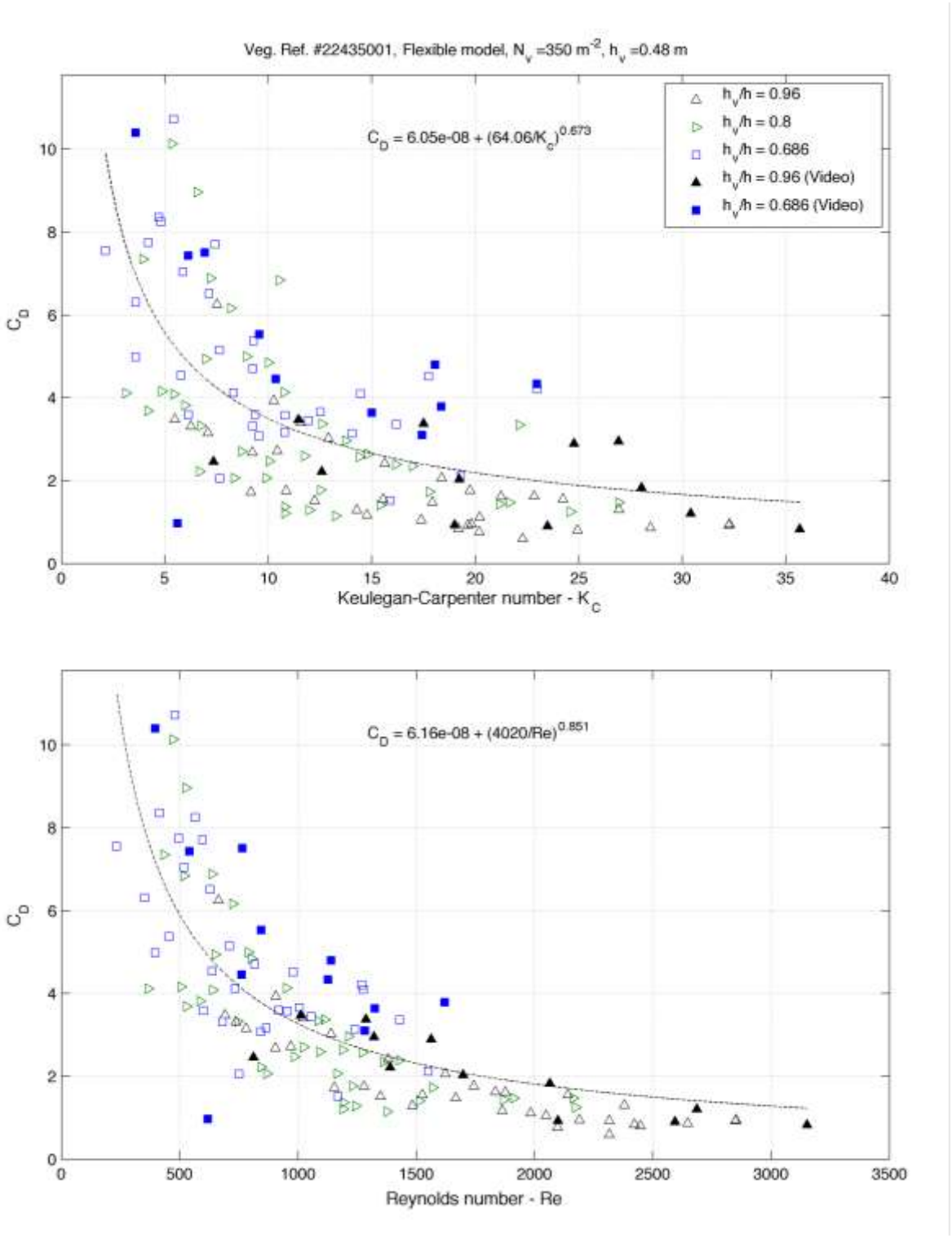

Fig. 3.37. Drag coefficients for flexible model vegetation with N_v = 350 and h_v = 0.48 m.

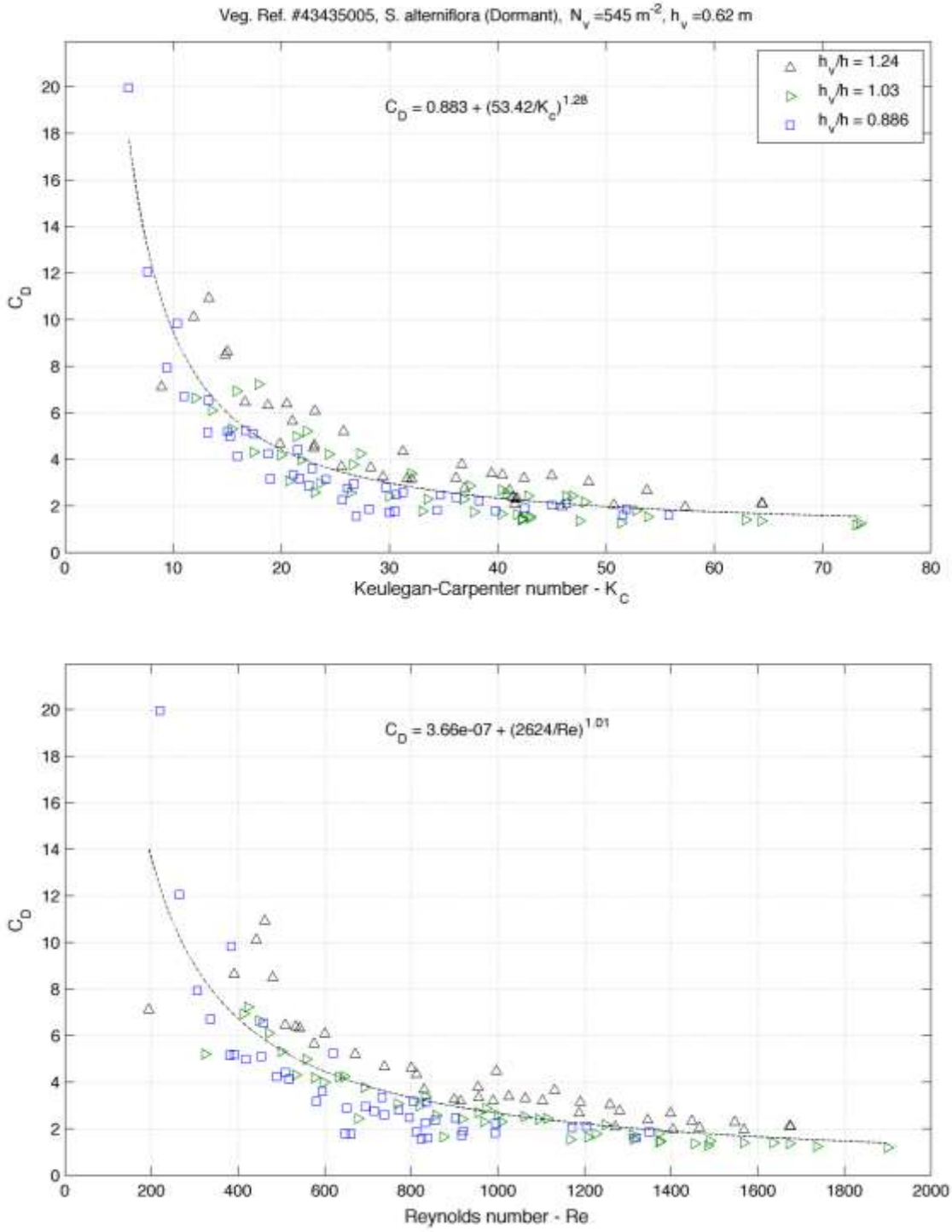

Fig. 3.38. Drag coefficients for dormant *S. alterniflora* with N_v = 545 and h_v = 0.62 m.

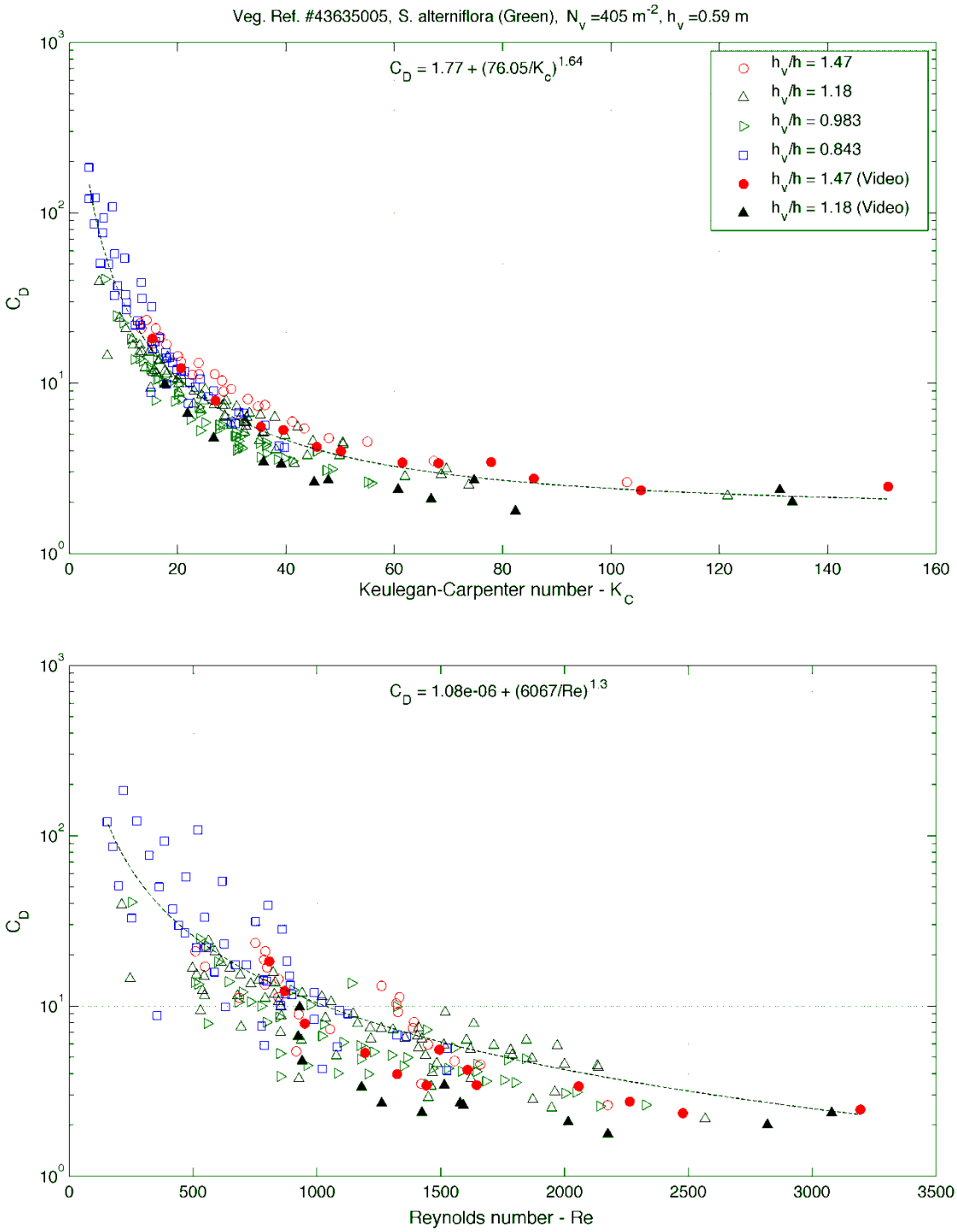

Fig. 3.39. Drag coefficients for green *S. alterniflora* with N_v = 405 and h_v = 0.59 m.

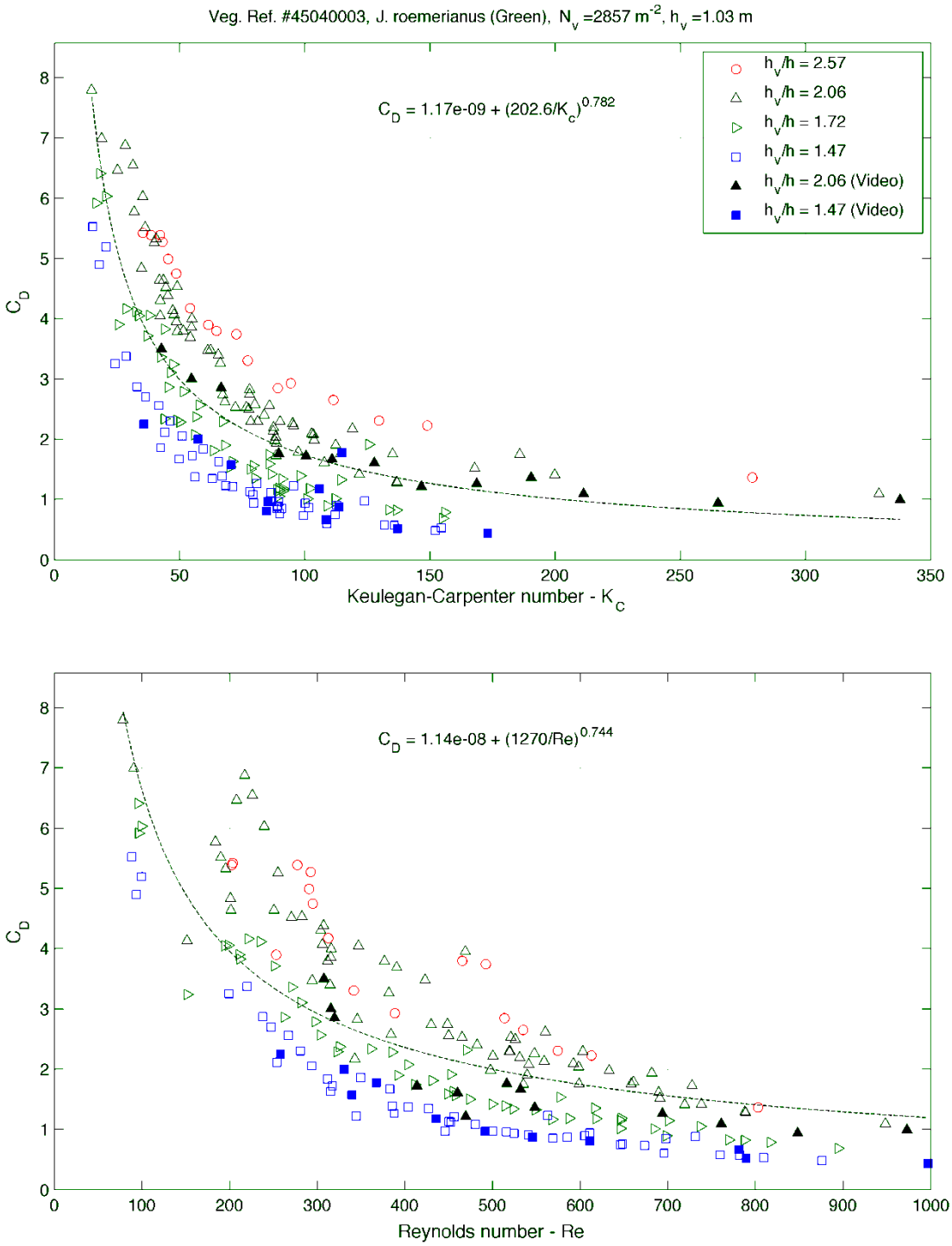

Fig. 3.40. Drag coefficients for *J. roemerianus* with N_v = 2857 and h_v = 1.03 m.

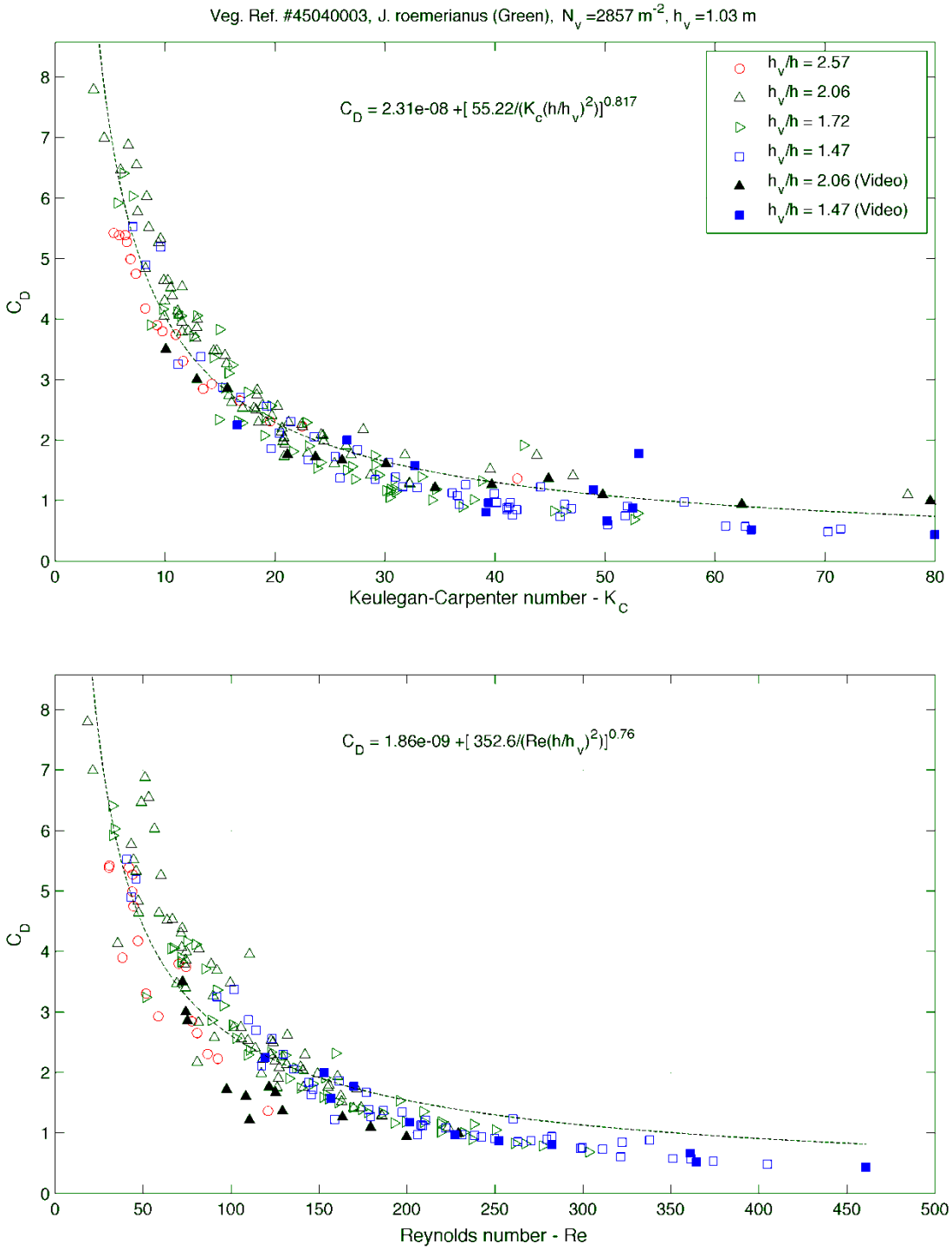

Fig. 3.41. Drag coefficients for *J. roemerianus* with N_v = 2,857 and h_v = 1.03 m (Modified).

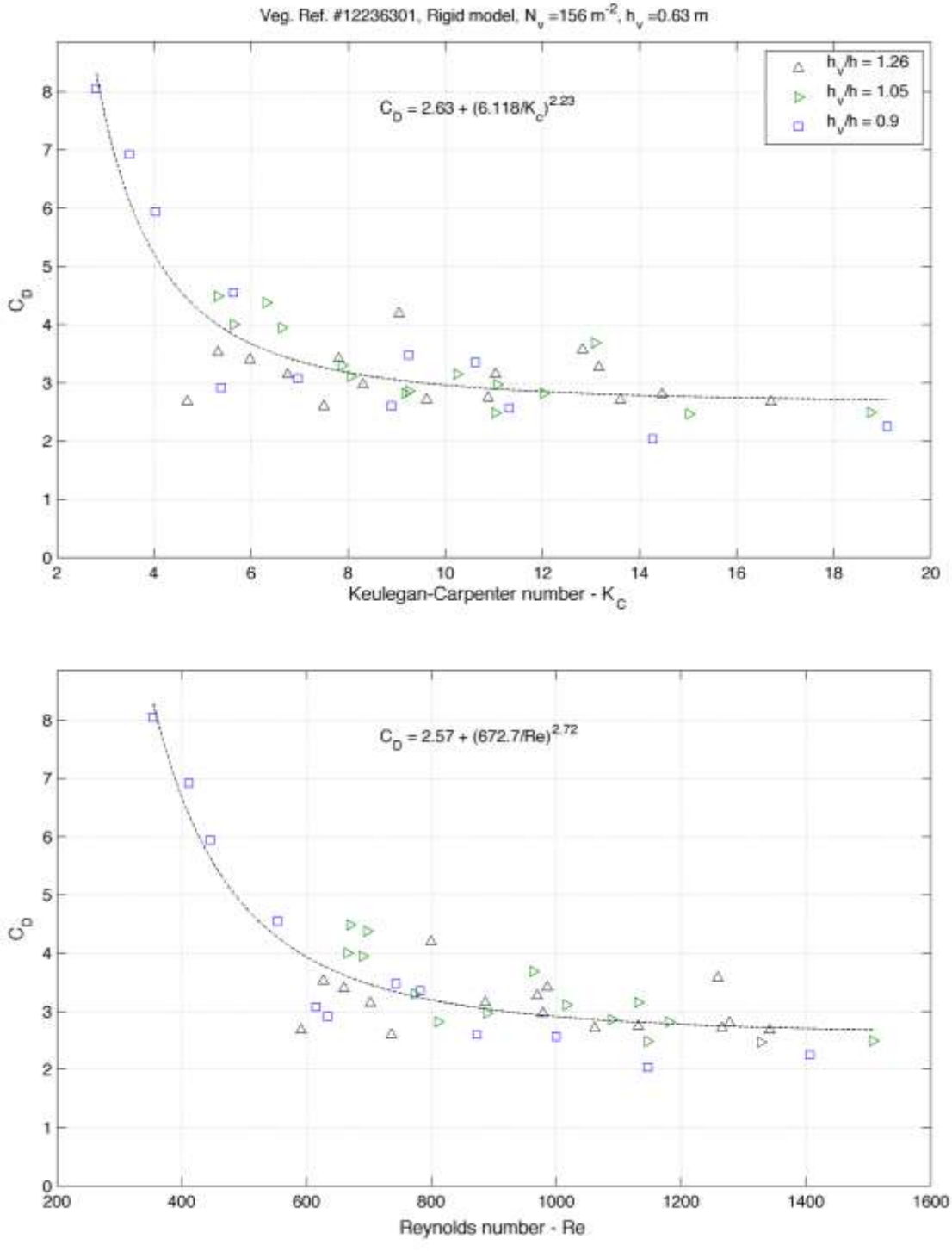

Fig. 3.42. Drag coefficients for rigid model vegetation with N_v = 156 and h_v = 0.63 m (Irregular).

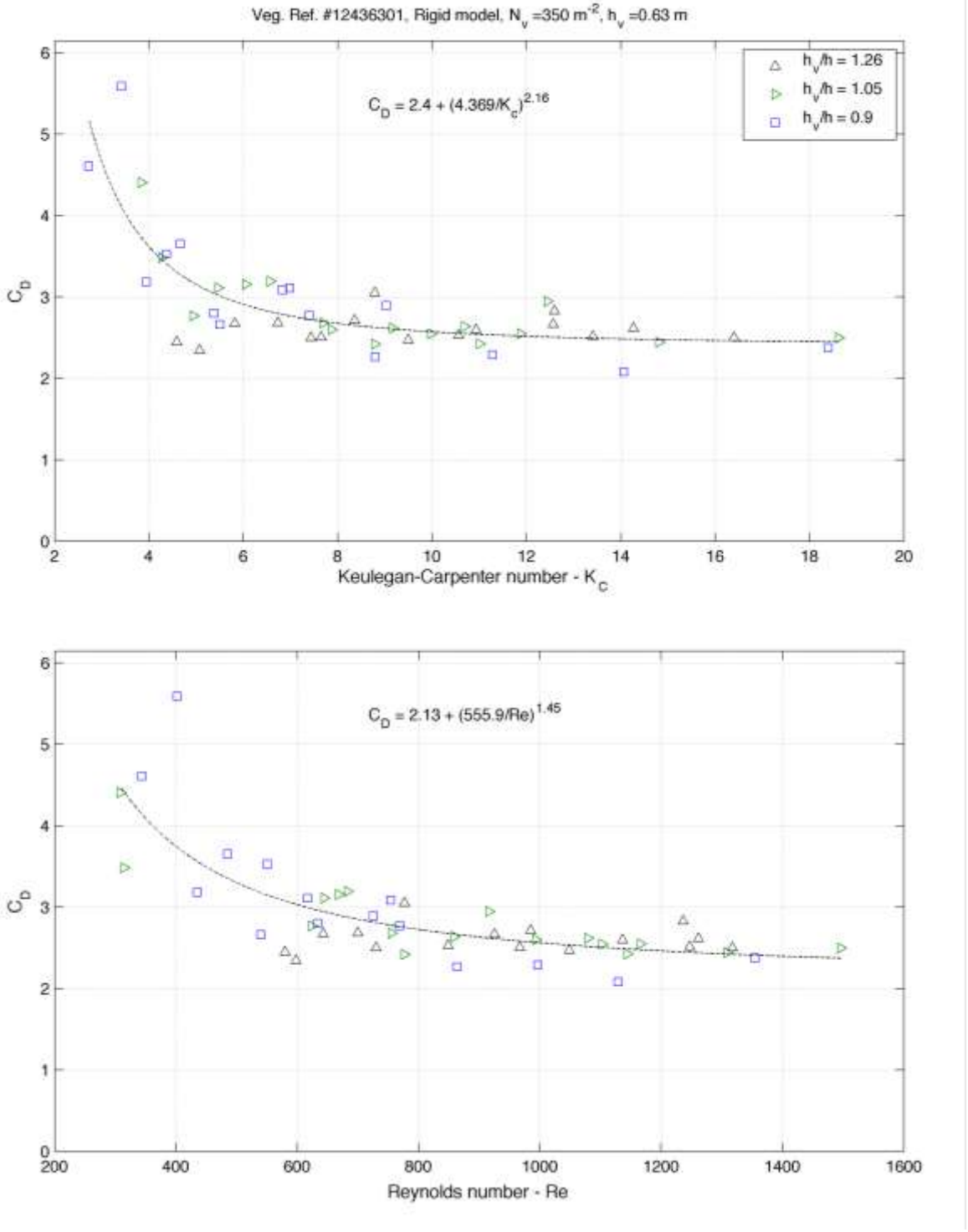

Fig. 3.43. Drag coefficients for rigid model vegetation with N_v = 350 and h_v = 0.63 m (Irregular).

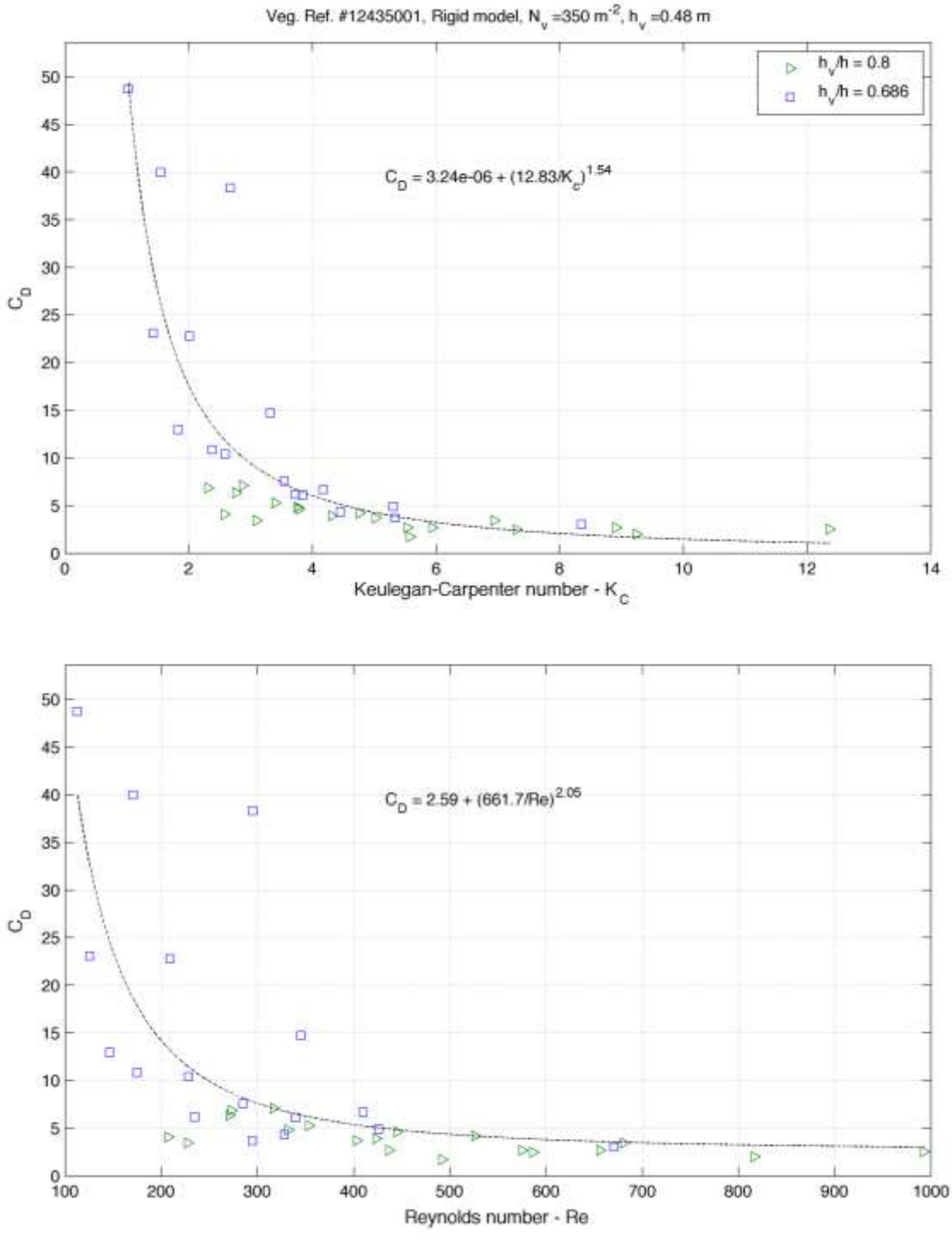

Fig. 3.44. Drag coefficients for rigid model vegetation with N_v = 350 and h_v = 0.48 m (Irregular).

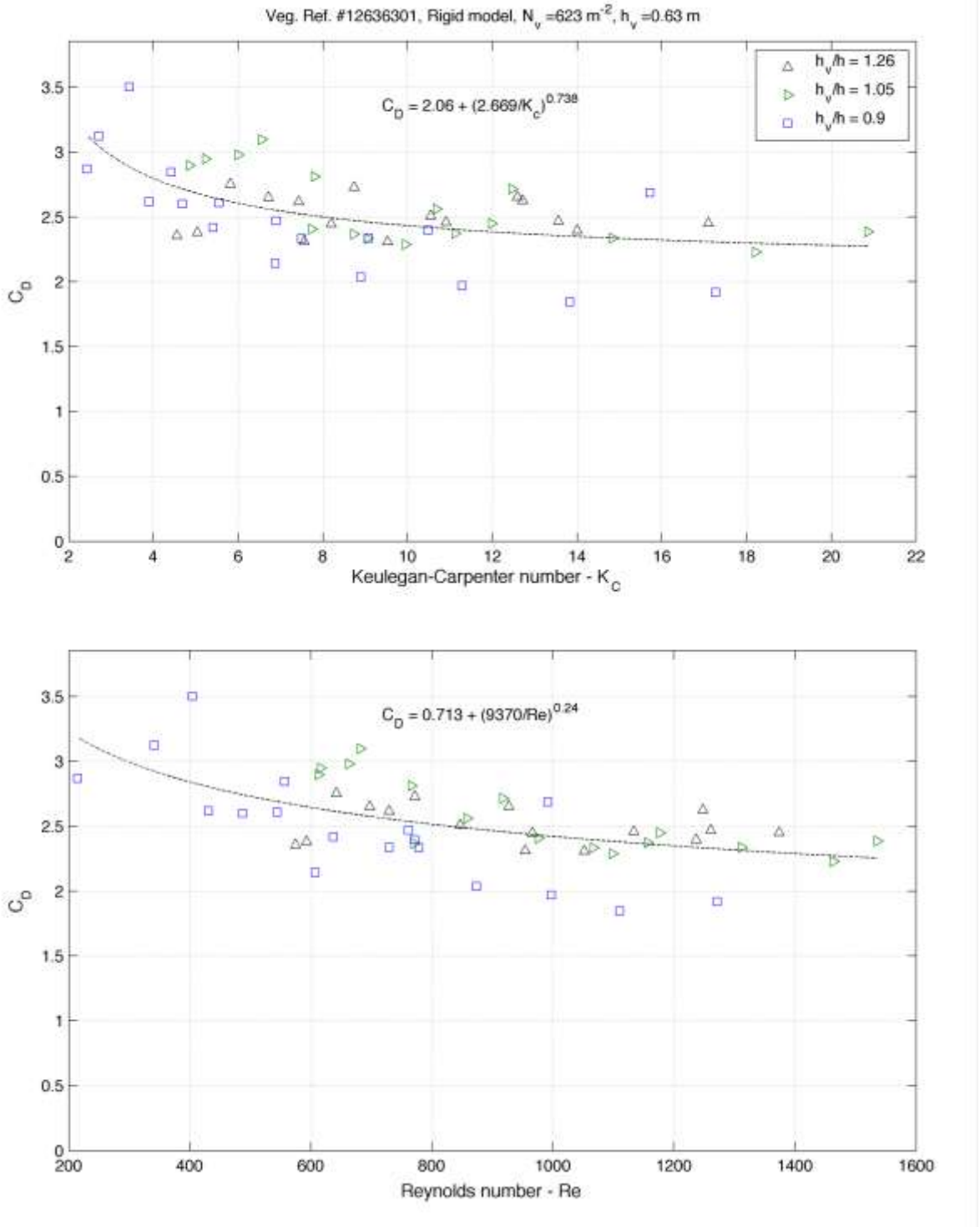

Fig. 3.45. Drag coefficients for rigid model vegetation with N_v = 623 and h_v = 0.63 m (Irregular).

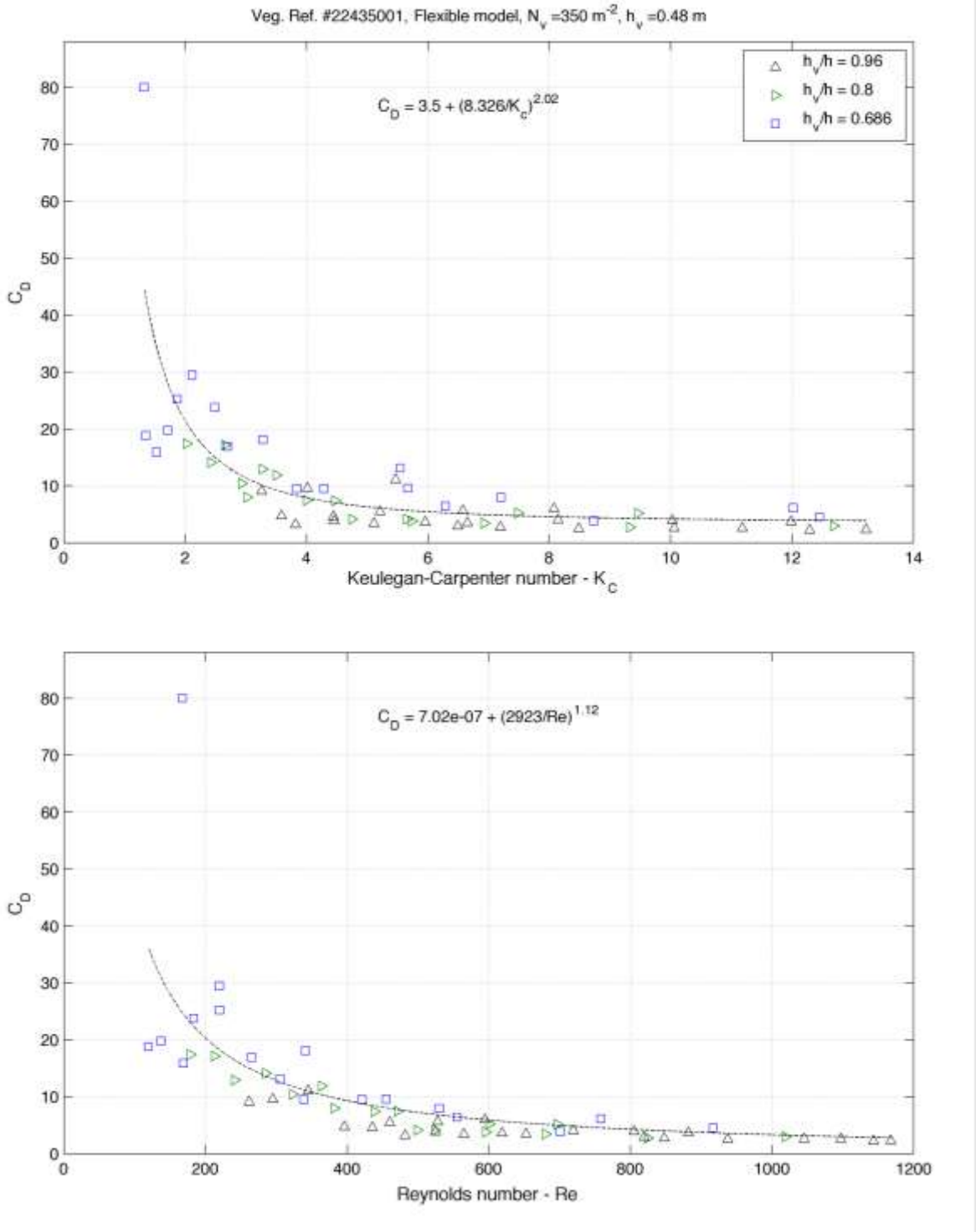

Fig. 3.46. Drag coefficients for flexible model vegetation with N_v = 350 and h_v = 0.48 m (Irregular).

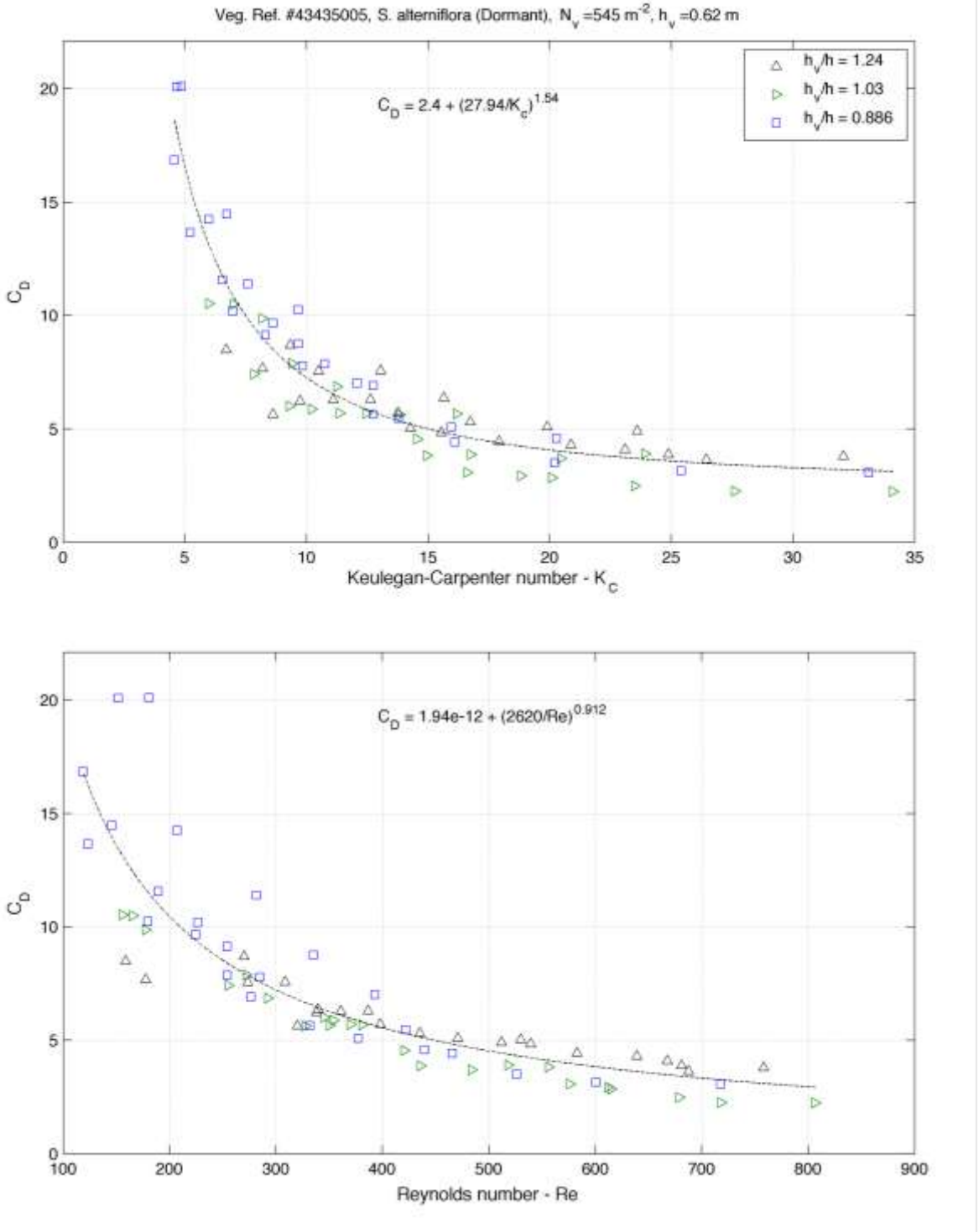

Fig. 3.47. Drag coefficients for dormant *S. alterniflora* with N_v = 545 and h_v = 0.62 m (Irregular).

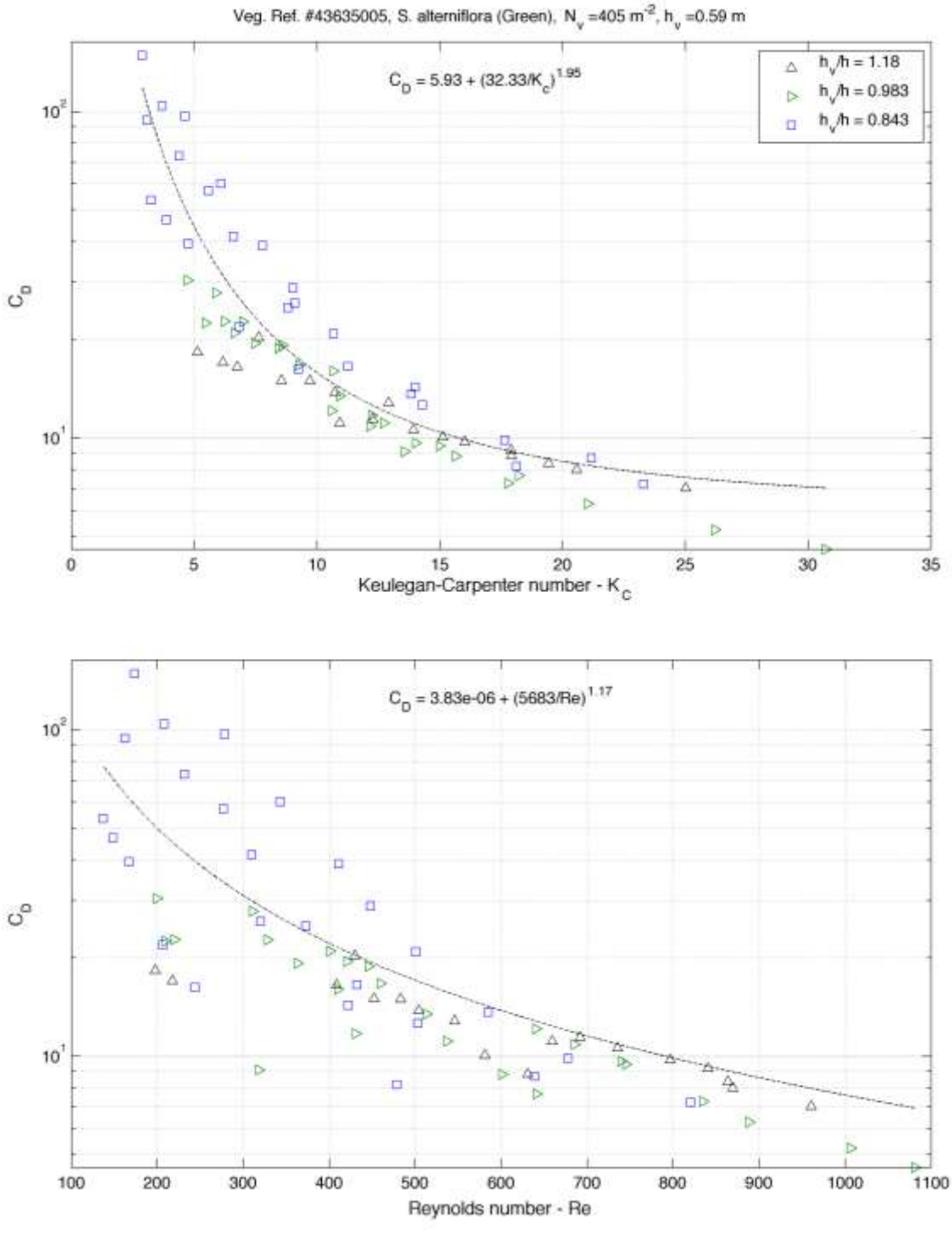

Fig. 3.48. Drag coefficients for green *S. alterniflora* with N_v = 405 and h_v = 0.59 m (Irregular).

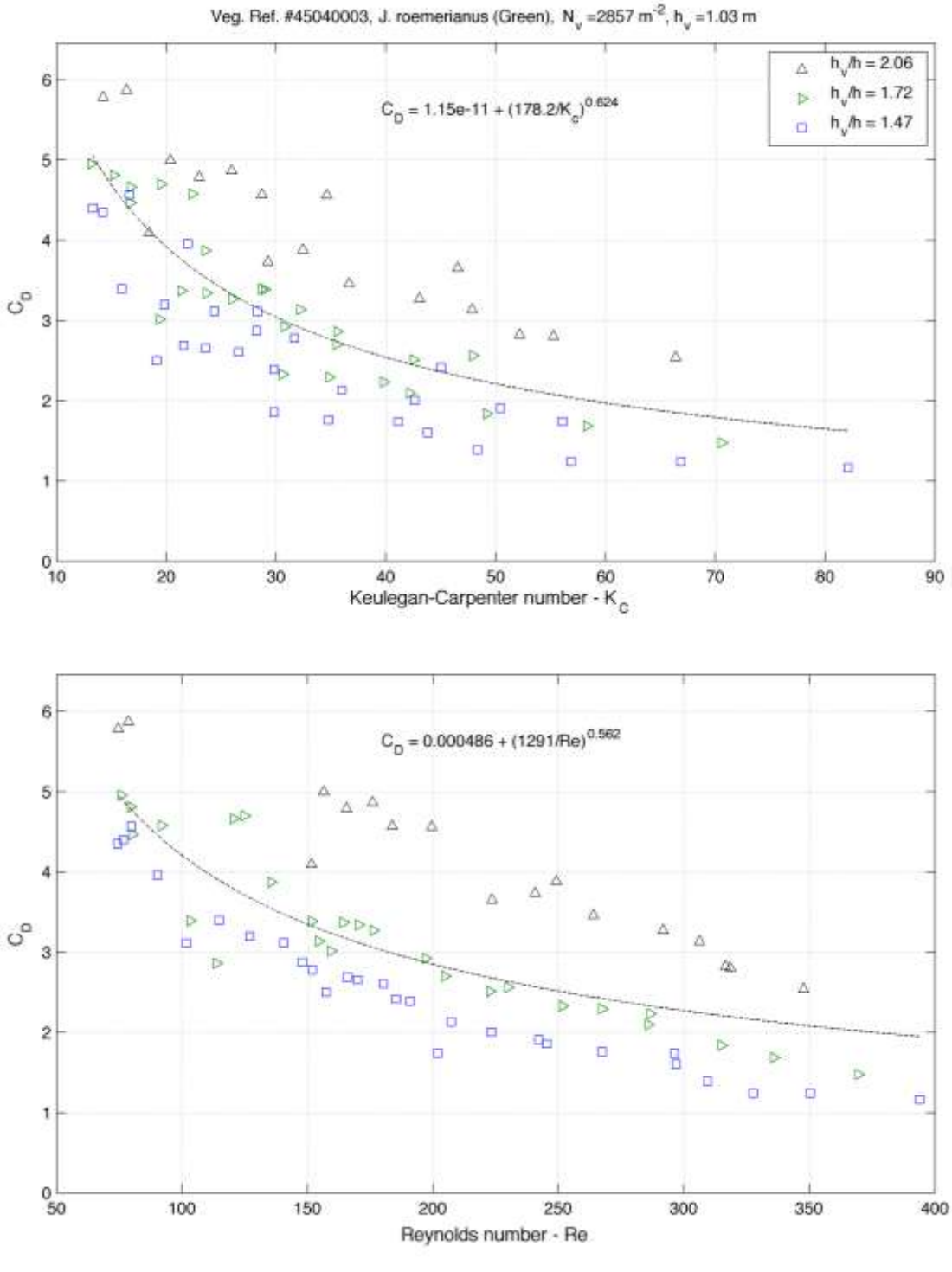

Fig. 3.49. Drag coefficients for *J. roemerianus* with N_v = 2,857 and h_v = 1.03 m (Irregular).

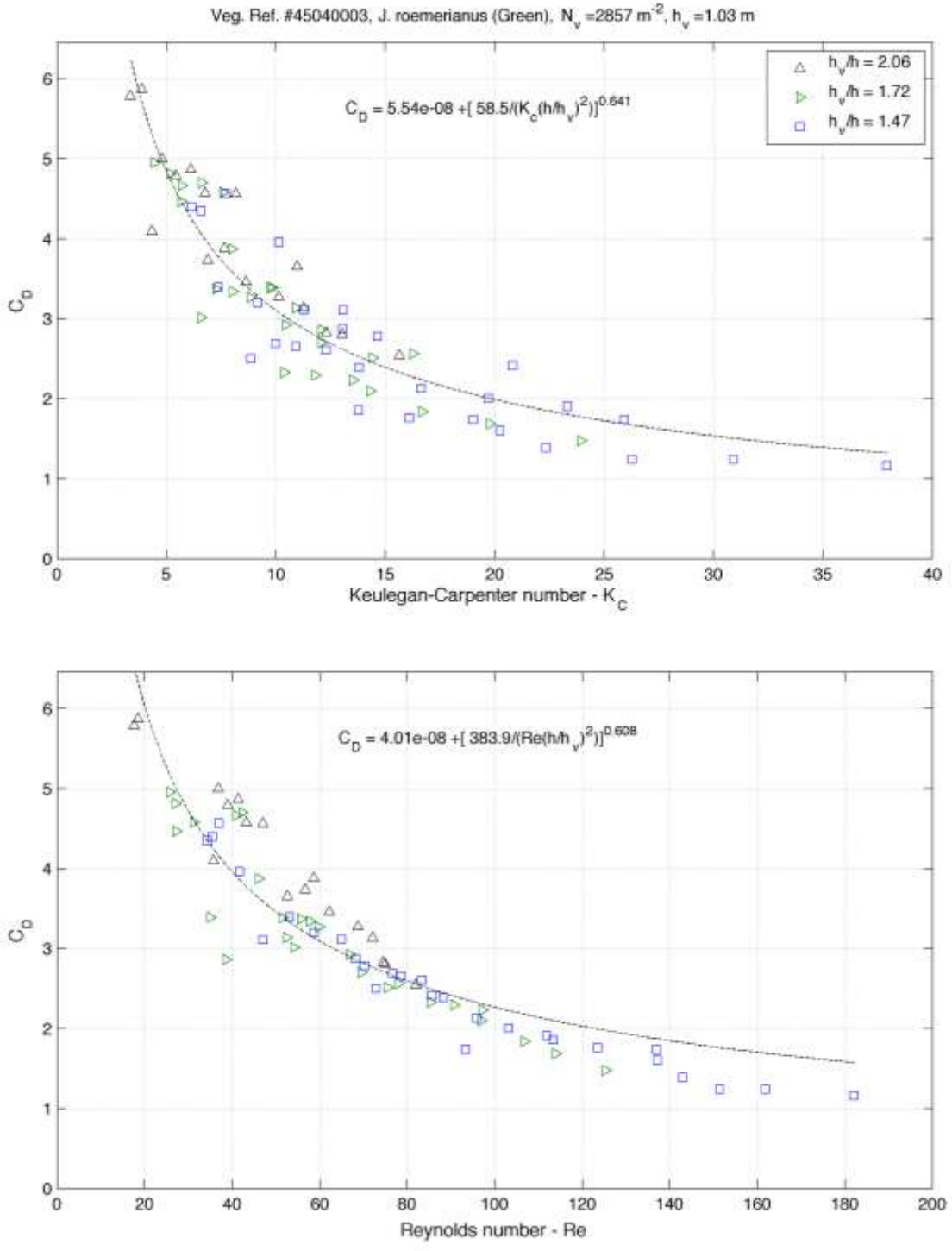

Fig. 3.50. Drag coefficients for *J. roemerianus* with N_v = 2,857 and h_v = 1.03 m (Irregular, modified).

3.7 Results of Sloping Beach Experiments

The waves start breaking as they approach the shoreline and dissipate most of their energy due to the turbulence generated. However, their momentum is transferred to the water column, resulting in a water surface slope. Wave setup is the water level rise due to the momentum transfer to the water column during the wave-breaking process, and wave runup is the time varying fluctuation of the water surface elevation at the shoreline due to wave breaking. Wave setup can contribute several feet to the elevated water levels and can almost double the elevation of water at the coast during extreme storm events. It is theoretically shown that vegetation can substantially reduce wave setup (Dean and Bender 2006). A series of experiments with regular and irregular waves were conducted to investigate and quantify the effect of vegetation on wave setup and shoaling. The gage locations for the conducted experiments are listed in Table 3.14. The list of experiments can be found in Tables 3.14 and 3.15. Water depth, *h*, was 0.4 m for all of the test cases. The same wave gages in flat-bed experiments were used to measure water surface displacement during these experiments. The video analysis procedure was also tested for wave setup experiments.

The camera was positioned at the same location as it was in the flat-bed experiments. The interface between the sloping beach and the water was also captured in addition to the water surface during the video pre-processing. A different threshold had to be used to make it possible to recognize the two interfaces simultaneously. If [IW] is the binary image that defines the water surface and [IS] is the image that defines the slope, then water boundaries can be calculated from:

$$[W] = [IS] - [IW] \tag{3.26}$$

This procedure is illustrated in Fig. 3.51. The still water line was located by fining the interaction of two interfaces as shown in the figure. Part of the beach above the still water line was removed in order to locate the free surface during shoaling.

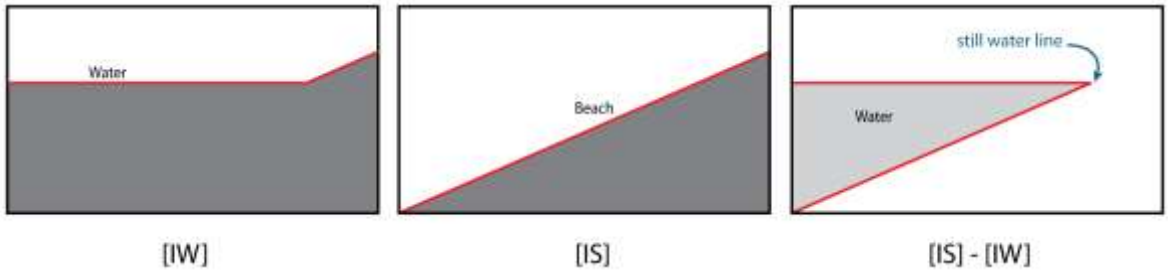

Fig. 3.51. Video analysis procedure to capture the water boundaries.

The same analysis procedure described in Section 3.5.2 was used to acquire an average frame over the steady portion of the recording. A sample average frame is given in Fig. 3.52. Similar to Fig. 3.28, darker colors indicate lower pixel values which translated into areas less frequently occupied by water. Note that the image is recolored to better identify the gradients. An important advantage in this analysis is that the mean water level can easily be calculated by simply summing the average pixel values along each column. The peak pixel value in Fig. 3.52 along each column is the median at each section along the

horizontal axis. Recalling the expression $\mathbf{J} = \mathbf{I} \cdot (1 - \mathbf{I})$ from Section 3.5.2, the average frame is defined by:

$$\mathbf{I} = \bar{p}_{ij} = \frac{1}{f \Delta t} \sum_{\Delta t} p_{ij}^{\ t} \tag{3.27}$$

where f is the frame rate, Δt is the duration of the video and p_{ij} is the pixel value of each binary frame at time t. The mean water level is calculated as

$$\bar{\eta}_{i,vid} = \sum_{j=1}^{M_p} \bar{p}_{ij} \tag{3.28}$$

in which M_p is the number of pixels in the vertical direction. $\bar{\eta}_{i,vid}$ is the mean water level in units of pixels. The wave height can be estimated by summing the number of pixels that exceed the threshold value defined by Eq. (3.18) along each column of **J** shown in Fig. 3.52. With this method the mean water level and wave height is calculated only up to the still water line.

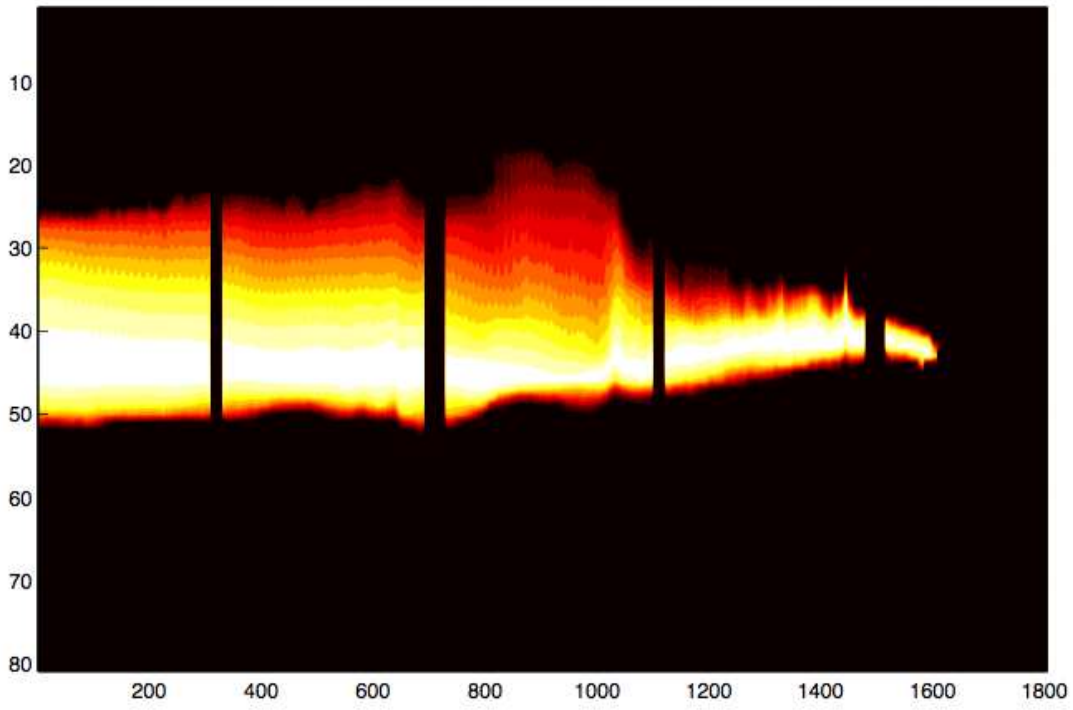

Fig. 3. 52. (a) A sample transformed average frame for wave breaking along the non-vegetated plane sloping beach (T = 1.2 s, H_i = 0.09 m, h = 0.4 m and slope = 1:20).

The estimated wave height transformation along the plane beach is compared with gage data in Fig. 3.53a. The solid line is the smoothed time-averaged wave height profile estimated from the transformed average frame (**J**). The mean and maximum differences between wave heights estimated through video data and wave gage data were 4 mm and 5 mm, respectively, which shows a good agreement between the two measurement techniques. Fig. 3.53b shows the mean water level and wave height envelope along the

beach profile. The breaking point is assumed to be the station where the wave crest line in Fig. 3.53b reaches a maximum value. The mean and maximum differences between the wave gage and video analysis results for mean water level were 1.2 mm and 3 mm, respectively.

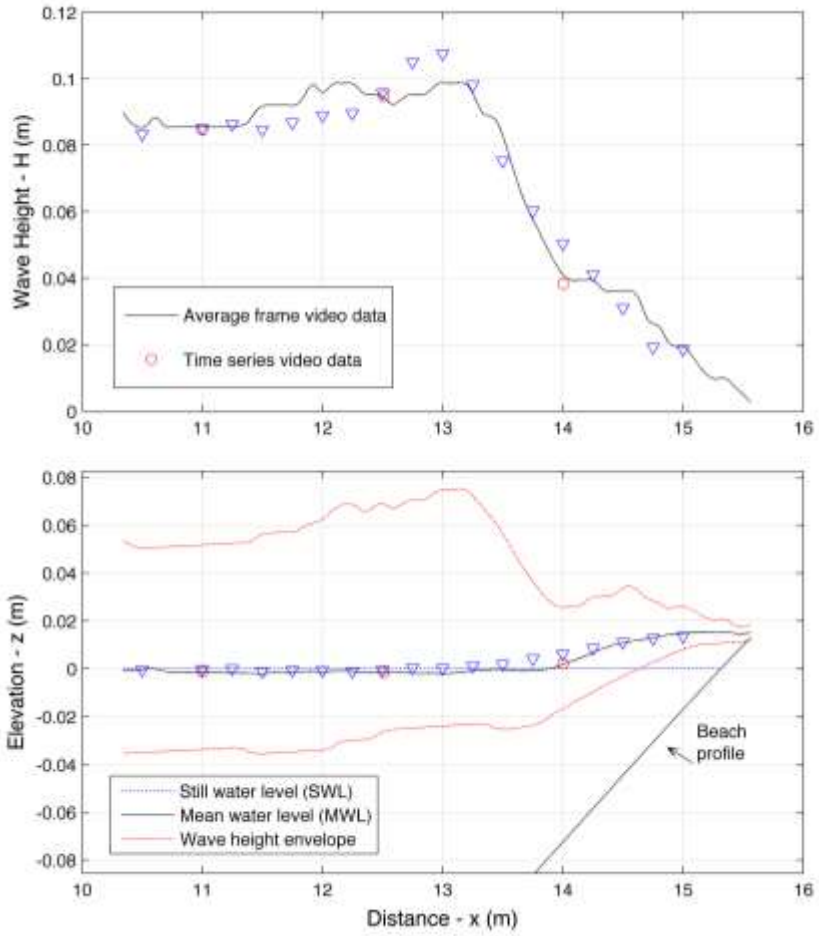

Fig. 3. 53. (a) Wave height transformation and (b) mean water level along the plane sloping beach (T = 1.2 s, H_i = 0.09 m, h = 0.4 m and slope = 1:20).

The video analysis procedure can provide valuable information to identify some key features during wave breaking. Although the resolution (~3 mm/pixel) of the video data was low compared to the scales on which mean water level varied (O(1 mm -10 mm)), the results shown in Fig. 3.53 are promising. The resolution can be increased by moving the camera to a closer position, and multiple cameras can be synchronized to improve the quality of the data.

For the remaining wave setup experiments, including the vegetated beach profile, data recording was carried out using only the wave gages. When the wave generation started in the wave tank a long wave system associated with the wave front was created. The measurements have to be carried out after the initial surge dissipates. It was observed that the wave setup became steady in less than 100 s after beginning the wave generation. Each

regular and irregular wave experiment was 300 s long and the first 100 s was not used during the analysis.

Since only five gages were available, the locations of the gages were varied, and the experiments were repeated for the same conditions with the gages in the new positions. In addition, each experiment at a certain gage location was repeated three times for regular waves and 5 times for irregular waves. The final position of each gage overlapped with the next gage to ensure repeatability (Table 3.13). Water displacement was measured at 34 different locations for each wave condition over vegetated and non-vegetated beach profiles. Only one model vegetation type was tested during the wave setup experiments, as described previously (Table 3.1). Fig. 3.54 shows synchronized photographs of waves moving up non-vegetated and vegetated sloping beach profiles. Note the significant increase in wave runup for the non-vegetated case and the lack of wave breaking in the vegetated case. The same procedure described in Section 3.5 was followed to analyze the data. Wave setup was calculated as the difference between the still water elevation and the time averaged water surface displacements within the steady portion of the recording at each gage. The averaging interval was adjusted to multiples of wave period T. Some common parameters associated with wave breaking and setup are shown in Fig. 3.55. Wave height and mean water level variation along the beach profile are plotted in Fig.3.56 for regular waves. The vertical axis is normalized with the wave height measured at gage 1, which is accepted as the incident wave height. Breaking point is defined as the location where the wave height reaches a maximum value. For irregular wave experiments (Fig. 3.57), the breaking point is assumed to be the station where significant wave height H_s reaches its maximum value. However, the data are presented in terms H_{mo}.

As the waves get steeper during shoaling, the water particle velocities in the wave crest exceed the wave celerity and the waves break. The results are summarized in Table 3.15 for regular waves and 3.16 for irregular waves. The type of breaking is described by the surf similarity parameter which is defined as:

$$\xi_o = \frac{\tan\beta}{\sqrt{H_o / L_o}} \tag{3.29}$$

where $\tan\beta$ is the beach slope and H_o and L_o are deepwater wave height and length. Here, H_i and L are used instead of the deepwater values and the subscript is replaced with "i". The breaker index is defined as:

$$\gamma_b = \frac{H_b}{h_b} \tag{3.30}$$

and the breaker height index is:

$$\Omega_b = \frac{H_b}{H_o} \tag{3.31}$$

where H_b is the wave height and h_b is the water depth during breaking. The slope of the mean water level is related to the beach slope with:

$$\frac{d\eta}{dx} = -K\frac{dh}{dx} \tag{3.32}$$

where K is a constant (Bowen 1968).

Table 3.13. Gage locations for sloping beach experiments for different test cases (each test case was repeated three times)

	Test cases						
x (m)	I	II	III	IV	V	VI	VI
3.00	1	1	1	1	1	1	1
7.00	2						
7.25							
7.50		2					
7.75							
8.00			2				
8.25							
8.50				2			
8.75							
9.00					2		
9.25							
9.50						2	
9.75							
10.00	3						2
10.25							
10.50		3					
10.75							
11.00			3				
11.25				3			
11.50					3		
11.75						3	
12.00	4						3
12.25		4					
12.50			4				
12.75				4			
13.00					4		
13.25						4	
13.50	5						4
13.75		5					
14.00			5				
14.25				5			
14.50					5		
14.75						5	
15.00							5

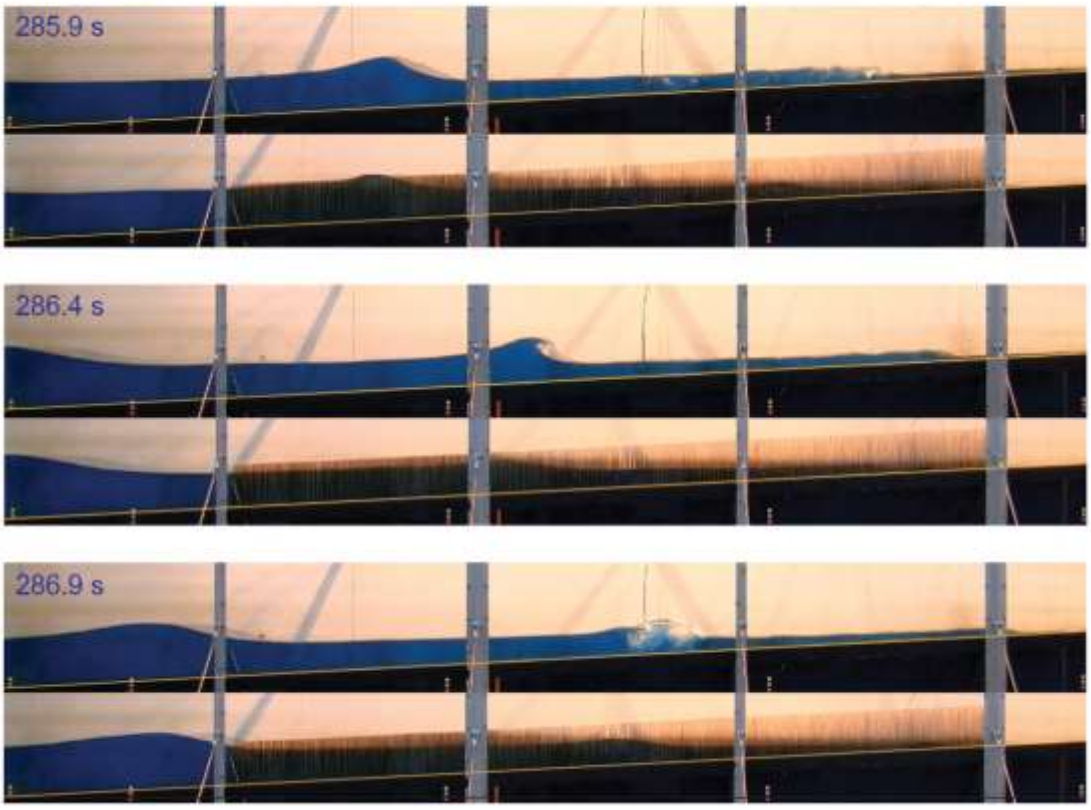

Fig. 3.54. Wave setup over a non-vegetated and vegetated beach.

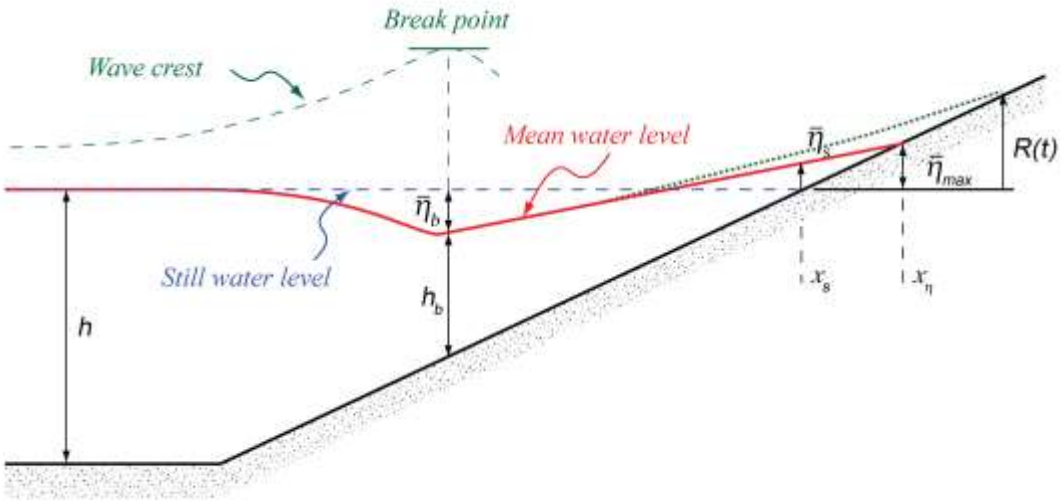

Fig. 3.55. Wave setup along a typical beach with some common parameters.

To estimate the location of maximum wave setup, $\bar{\eta}_{max}$, the line passing through gage locations x = 14.75 m and x =15 m was linearly extrapolated to where it intersected the beach. Although the time averaging was over the multiples of wave period, it is not required for the beach to be 'wetted' at all times during averaging intervals. Yet, all of the

measuring stations were on the offshore side of the still water line. Other parameters given in Tables 3.15 and 3.16 are:

$\overline{\eta}_{\min}$: Minimum setup (maximum setdown)
$\overline{\eta}_b$: Setup at break point
$\overline{\eta}_{15m}$: Setup at x = 15 m
x_s : The location of the shore line during wave setup (x = 0 at wave paddle)
x_{SWL} : The location of the still water line (x_{SWL} = 15.56 m at h = 0.4 m)

Two major conclusions can be drawn from Figs. 3.56 and 3.57: One is that wave heights are significantly reduced during shoaling over the vegetated beach compared to the plain beach. The other conclusion is that for both regular and irregular waves, the setup due to vegetation was considerably less compared to the plane beach. In some cases (i.e ref. = 40100180) a setdown was observed rather than a setup which is in consistent with the findings of Dean and Bender (2006). In most of these plots, mean water level was greater than the still water level in the constant depth part of the flume, which is due to the finite volume of water in the wave tank. The reflection from the beach and vegetation resulted in modulation of the wave heights in some of the figures. Reflection from the vegetated beach was larger than for the plain beach, which also indicates that energy dissipation by wave breaking over the vegetated beach was low compared to that of the plain beach. It was also observed that the location of the break point relative the vegetation zone affected the setup profile.

In Figs. 3.58 and 3.59, dimensionless wave profiles of the experiments are platted against wave phase for regular waves for Ref. No. 40058120 and 40098180. The remaining experiments are presented in Fig. A.23 in Appendix A. In each plot, ten waves within the steady portion of the times series water surface displacements were combined for vegetated and non-vegetated experiments. These figures clearly show the effect of vegetation on the wave pattern during the shoaling process. As the waves progress over the plain beach, they get steeper and the crest gets narrower. But, for the vegetated beach, the waves preserve their shape and attenuate along the vegetated section of the beach (i.e. Ref. No. = 40058120).

Together with the plots in Figs. 3.56 and 3.57 the phase plots show that the setdown due to the vegetation along the shoreline is more pronounced when the waves showed nonlinear properties (steeper crest and wider troughs, i.e. Ref. No. 4098180). As the wave height further increased, the break point moved towards offshore, outside the vegetation zone. For these experiments, the wave height variation along the vegetated beach was almost the same as that of the plain beach, yet, wave setup was less than half (Ref. No. 40155120). For this case, wave attenuation due to breaking matches wave attenuation by vegetation but, over the vegetated beach, drag force counteracts the radiational stresses and reduces wave setup.

In Figs. 3.60 and 3.61, measured wave spectra are compared for plain and vegetated beach experiments. The the complete list of plots can be found in Appendix A, Fig. A.24. An important difference between the spectra is that, during wave breaking, the energy is transferred to the high frequency components, while for vegetated beach experiments, most of the high frequency waves are dissipated.

Table 3.14. Wave setup measurements with regular waves

Ref. No.	T (s)	h (m)	L (m)	H_i (m)	H_b (m)	h_b (m)	$\overline{\eta}_b$ (mm)	$\overline{\eta}_{\min}$ (mm)	$\overline{\eta}_{15m}$ (mm)	$\overline{\eta}_{\max}$ (mm)	$\overline{\eta}_{15m}$ (mm) (veg.)	$\overline{\eta}_{\max}$ (mm) (veg.)	ξ_o (mm)	K	γ_b	Ω_b	x_s (m) x_s = 15.56 m	$\frac{\eta_{\max}}{H_i}$
40019120	1.20	0.4	1.936	0.0136	0.0302	0.038	0.230	-0.340	1.593	5.368	0.349	-0.372	0.553	0.118	0.785	2.223	15.692	0.395
40028160	1.60	0.4	2.836	0.0235	0.0540	0.062	0.231	-0.476	4.223	10.620	0.330	-0.684	0.508	0.172	0.876	2.293	15.806	0.451
40033180	1.80	0.4	3.269	0.0243	0.0598	0.061	-0.016	-0.484	4.808	10.815	0.268	-0.650	0.536	0.160	0.975	2.459	15.810	0.445
40039120	1.20	0.4	1.936	0.0300	0.0533	0.062	0.197	-0.395	4.860	10.974	0.379	-0.497	0.371	0.162	0.866	1.774	15.813	0.365
40045240	2.40	0.4	4.532	0.0362	0.0741	0.084	-0.446	-0.824	7.165	16.094	0.352	0.137	0.518	0.209	0.882	2.047	15.924	0.444
40057160	1.60	0.4	2.836	0.0490	0.0875	0.085	0.781	-0.834	9.470	17.831	0.652	-0.700	0.352	0.188	1.026	1.784	15.962	0.364
40058120	1.20	0.4	1.936	0.0465	0.0724	0.085	0.079	-0.694	8.005	16.298	0.311	-0.665	0.299	0.193	0.856	1.558	15.929	0.351
40058300	3.00	0.4	5.765	0.0407	0.0949	0.084	-0.317	-0.821	8.997	20.083	0.645	-1.285	0.550	0.237	1.127	2.329	16.010	0.493
40065180	1.80	0.4	3.269	0.0529	0.0909	0.096	0.013	-1.180	10.786	21.862	0.623	-1.402	0.364	0.228	0.946	1.718	16.049	0.413
40085160	1.60	0.4	2.836	0.0748	0.1091	0.119	-0.035	-1.251	14.859	23.366	1.336	-1.579	0.285	0.170	0.915	1.457	16.081	0.312
40091240	2.40	0.4	4.532	0.0789	0.1296	0.130	-0.408	-2.206	15.731	25.742	0.725	-0.237	0.351	0.191	0.994	1.643	16.133	0.326
40097120	1.20	0.4	1.936	0.0848	0.1076	0.119	0.190	-1.200	13.580	17.135	1.453	-0.609	0.221	0.081	0.901	1.268	15.947	0.202
40098180	1.80	0.4	3.269	0.0847	0.1291	0.131	0.237	-1.167	17.030	28.039	1.807	-2.254	0.287	0.201	0.986	1.524	16.182	0.331
40100120	1.20	0.4	1.936	0.0873	0.1112	0.120	0.382	-1.317	13.744	15.862	1.833	-0.359	0.218	0.050	0.930	1.273	15.919	0.182
40100140	1.40	0.4	2.393	0.0909	0.1283	0.132	1.058	-0.940	17.300	24.930	2.818	-0.559	0.237	0.148	0.973	1.411	16.115	0.274
40100160	1.60	0.4	2.836	0.0917	0.1342	0.131	0.710	-1.621	18.016	29.365	2.311	-1.565	0.257	0.203	1.021	1.464	16.211	0.320
40100180	1.80	0.4	3.269	0.0866	0.1302	0.131	0.360	-1.242	17.293	27.621	1.914	-2.006	0.284	0.190	0.993	1.504	16.173	0.319
40100240	2.40	0.4	4.532	0.0896	0.1406	0.130	-0.536	-2.712	17.574	25.627	1.092	0.139	0.329	0.154	1.079	1.568	16.130	0.286
40100300	3.00	0.4	5.765	0.0741	0.1398	0.131	0.323	-1.198	15.550	29.690	1.780	-2.676	0.408	0.251	1.066	1.887	16.218	0.401
40115300	3.00	0.4	5.765	0.0843	0.1684	0.177	0.162	-1.331	18.159	33.135	2.055	-2.808	0.383	0.250	0.950	1.998	16.292	0.393
40136240	2.40	0.4	4.532	0.1206	0.1669	0.163	-2.053	-3.389	22.479	28.596	3.092	0.582	0.284	0.111	1.021	1.384	16.194	0.237
40142160	1.60	0.4	2.836	0.1322	0.1687	0.177	-0.285	-1.023	23.886	30.652	4.260	-1.344	0.214	0.118	0.954	1.276	16.239	0.232
40155120	1.20	0.4	1.936	0.1328	0.1567	0.212	0.627	-0.195	18.239	23.511	5.096	0.881	0.177	0.105	0.738	1.180	16.084	0.177
40163180	1.80	0.4	3.269	0.1531	0.1986	0.188	-0.174	-1.787	26.568	36.184	5.580	0.199	0.214	0.153	1.054	1.297	16.358	0.236

Table 3.15. Wave setup measurement with irregular waves

Ref. No.	T_p (s)	h (m)	L_p (m)	H_{m0} (m)	H_{rms} (m)	H_b (m)	h_b (m)	$\overline{\eta}_b$ (mm)	$\overline{\eta}_{\min}$ (mm)	$\overline{\eta}_{15m}$ (mm)	$\overline{\eta}_{\max}$ (mm)	$\overline{\eta}_{15m}$ (mm) (veg.)	$\overline{\eta}_{\max}$ (mm) (veg.)	ξ_o (mm)	K	γ_b	Ω_b	x_s (m) (x_{SWL}= 15.56 m)	$\frac{\eta_{\max}}{H_{m0}}$
r40039120	1.2	0.4	1.936	0.037	0.025	0.039	0.061	-0.053	-0.752	2.708	6.604	1.0909	-0.344	0.343	0.117	0.636	1.105	15.719	0.181
r40057160	1.6	0.4	2.836	0.047	0.032	0.051	0.084	-0.805	-1.053	4.702	10.560	0.8165	-0.573	0.363	0.157	0.607	1.115	15.804	0.225
r40058120	1.2	0.4	1.936	0.054	0.037	0.053	0.096	-0.046	-0.952	4.659	9.730	0.5257	0.5784	0.280	0.139	0.554	1.009	15.787	0.179
r40065180	1.8	0.4	3.269	0.055	0.037	0.060	0.096	0.133	-1.189	6.018	13.365	0.1554	-0.224	0.361	0.184	0.624	1.118	15.865	0.244
r40085160	1.6	0.4	2.836	0.074	0.049	0.078	0.130	-1.053	-1.517	8.189	15.814	0.3471	0.2929	0.289	0.180	0.595	1.068	15.918	0.213
r40091240	2.4	0.4	4.532	0.067	0.048	0.073	0.119	0.075	-1.949	8.217	18.317	0.4314	-0.25	0.386	0.225	0.612	1.120	15.972	0.272
r40098180	1.8	0.4	3.269	0.079	0.054	0.082	0.130	-1.019	-1.75	9.072	16.755	0.1623	0.051	0.301	0.177	0.627	1.063	15.938	0.213

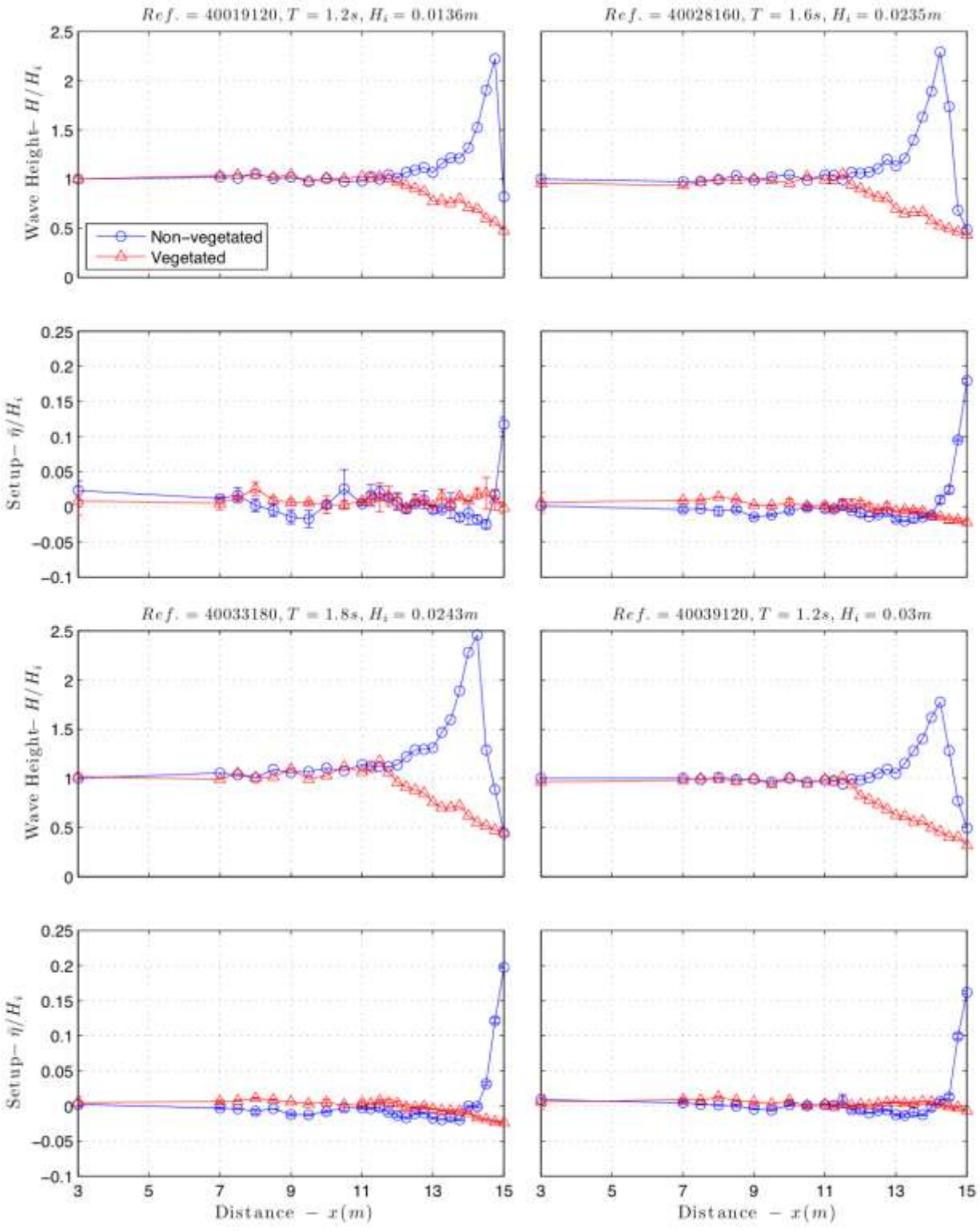

Fig. 3.56. Wave height transformation and mean water level along the plane sloping beach (regular waves)

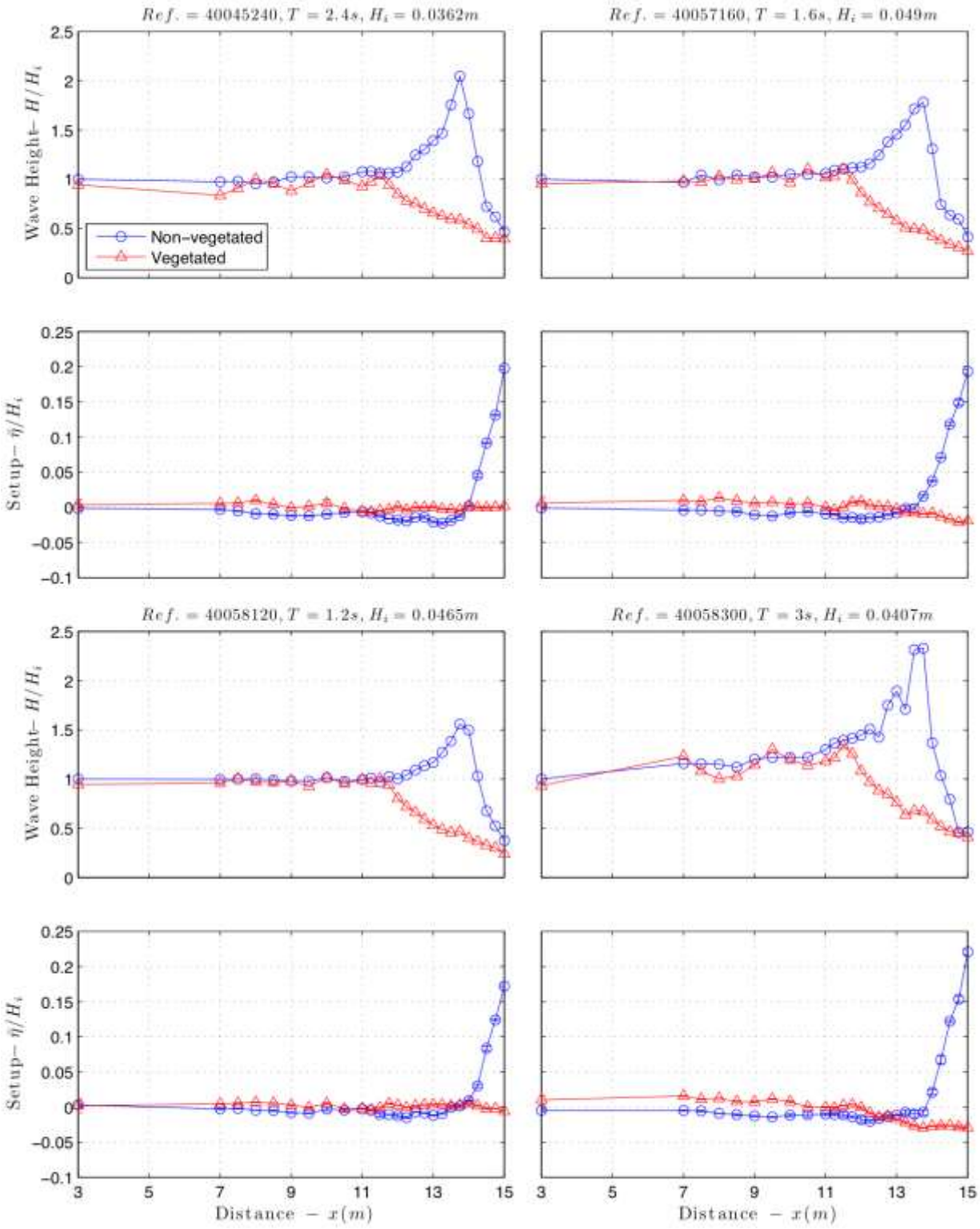

Fig. 3.56. Wave height transformation and mean water level along the plane sloping beach (regular waves, continued).

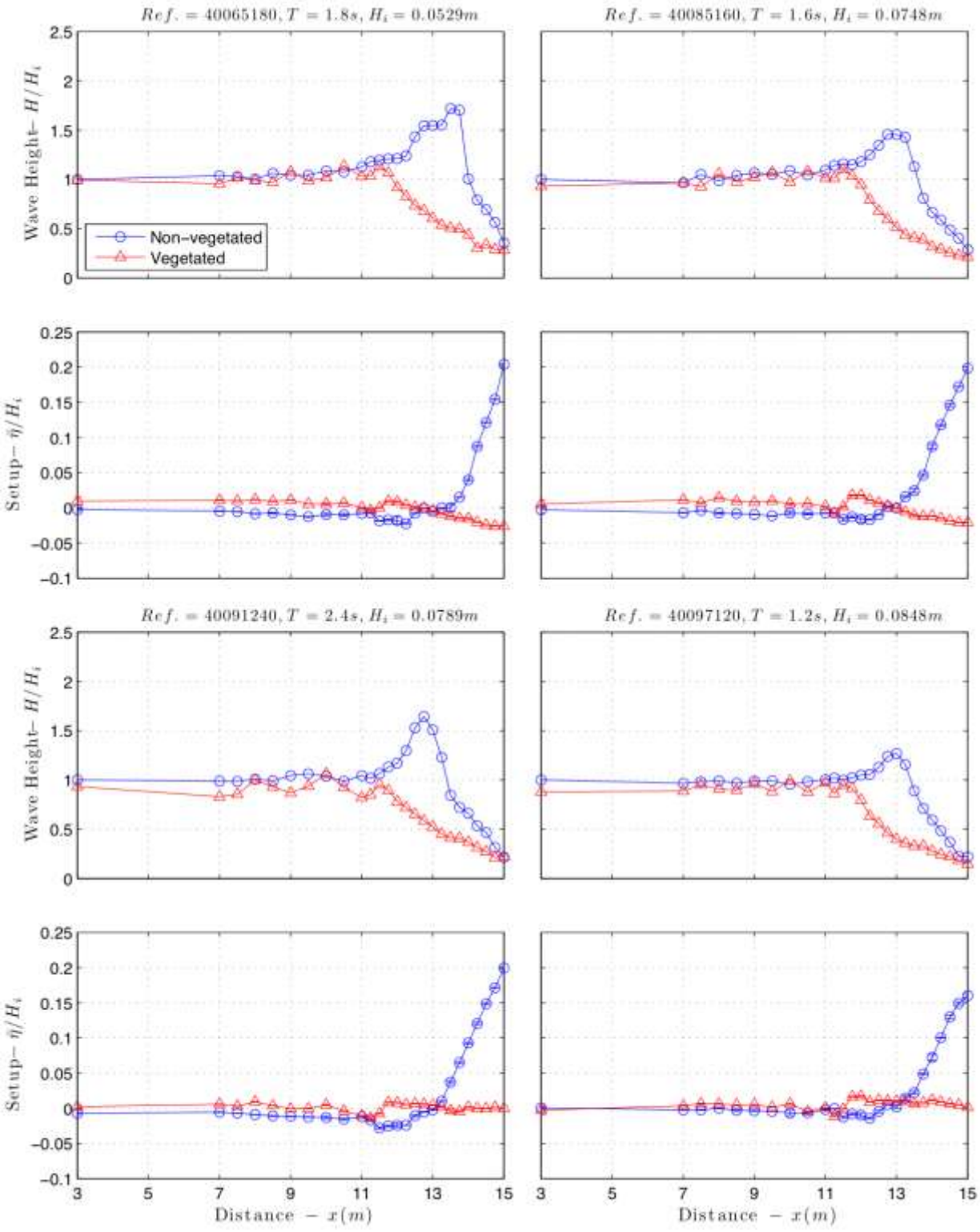

Fig. 3.56. Wave height transformation and mean water level along the plane sloping beach (regular waves, continued)

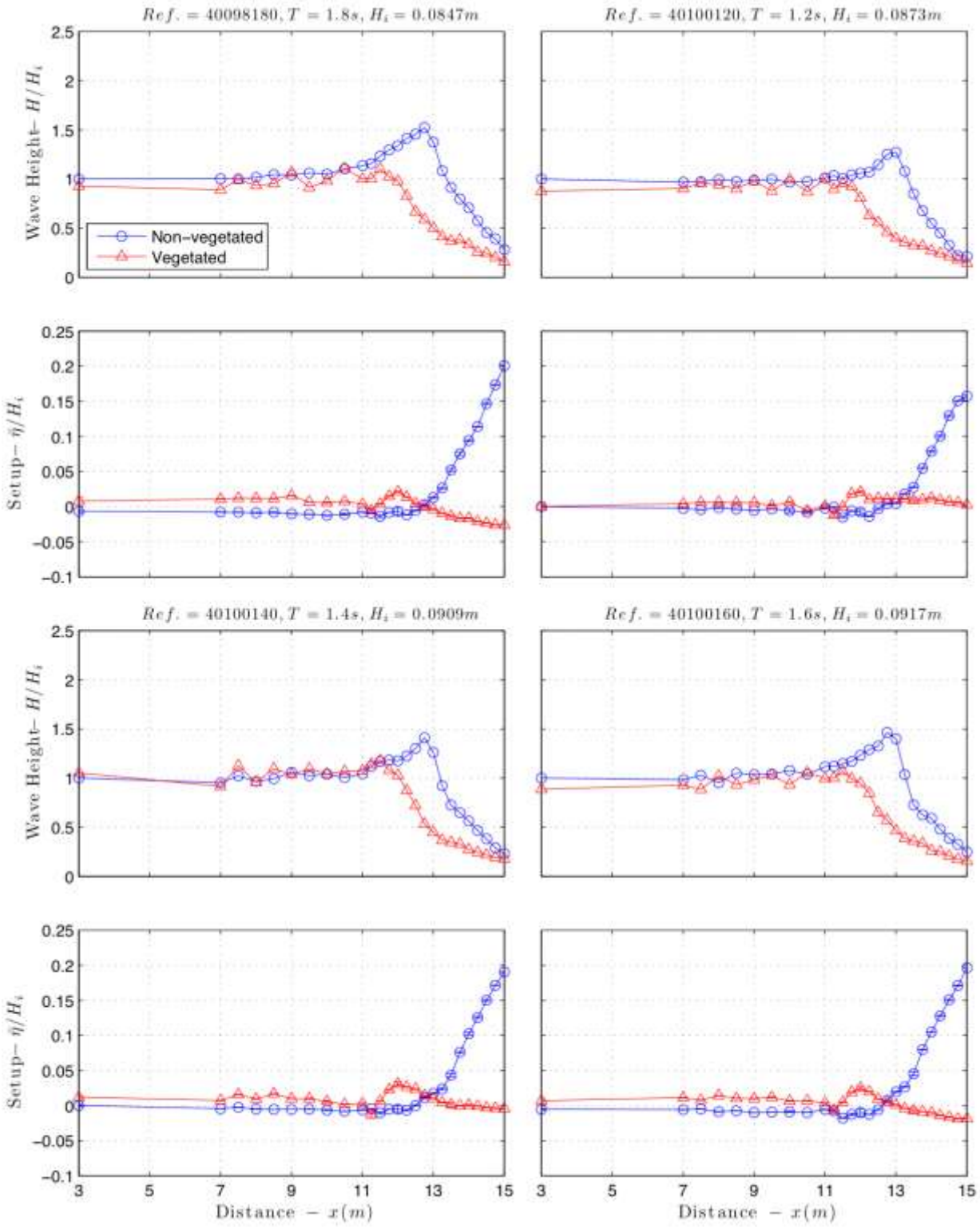

Fig. 3.56. Wave height transformation and mean water level along the plane sloping beach (regular waves, continued)

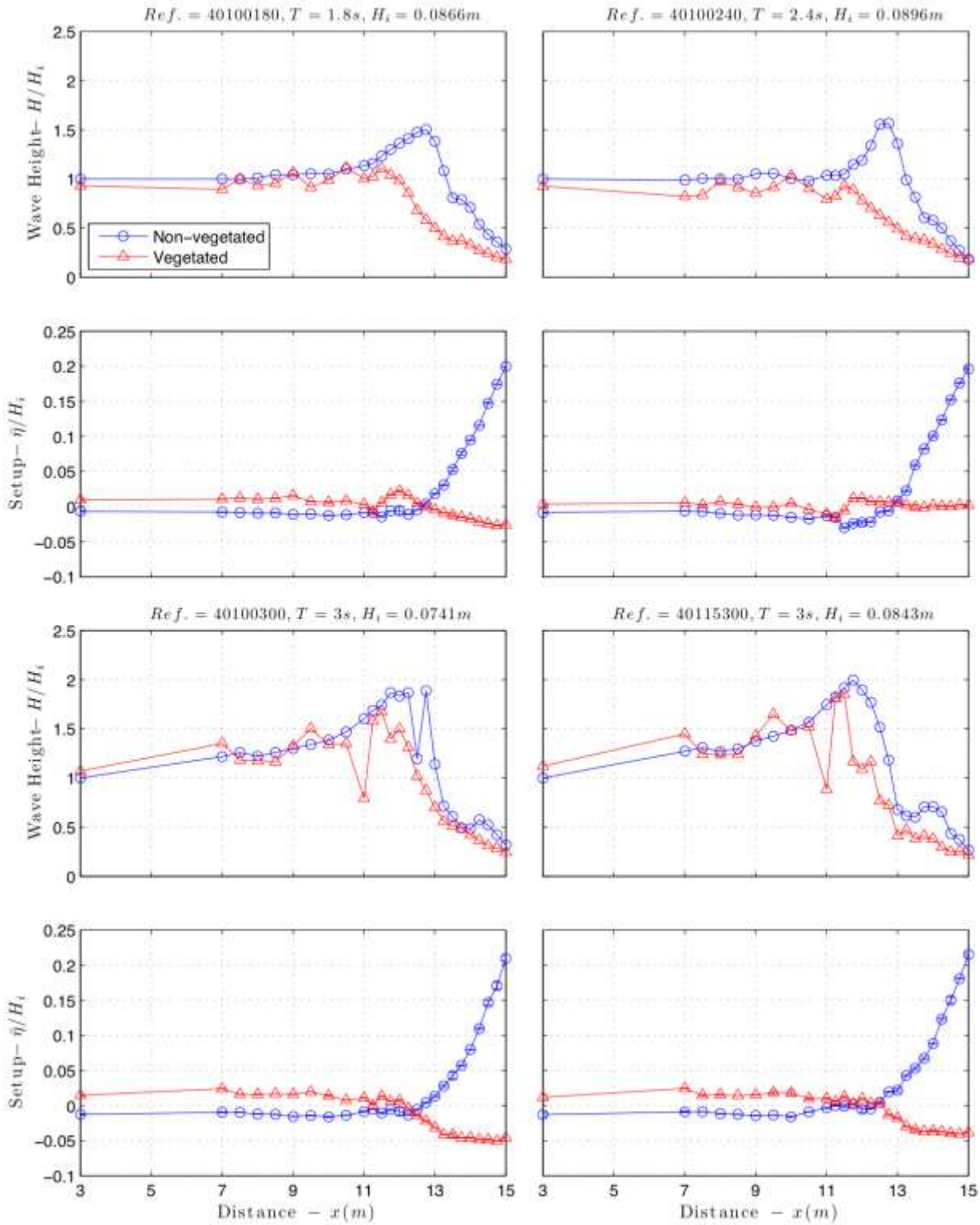

Fig. 3.56. Wave height transformation and mean water level along the plane sloping beach (regular waves, continued)

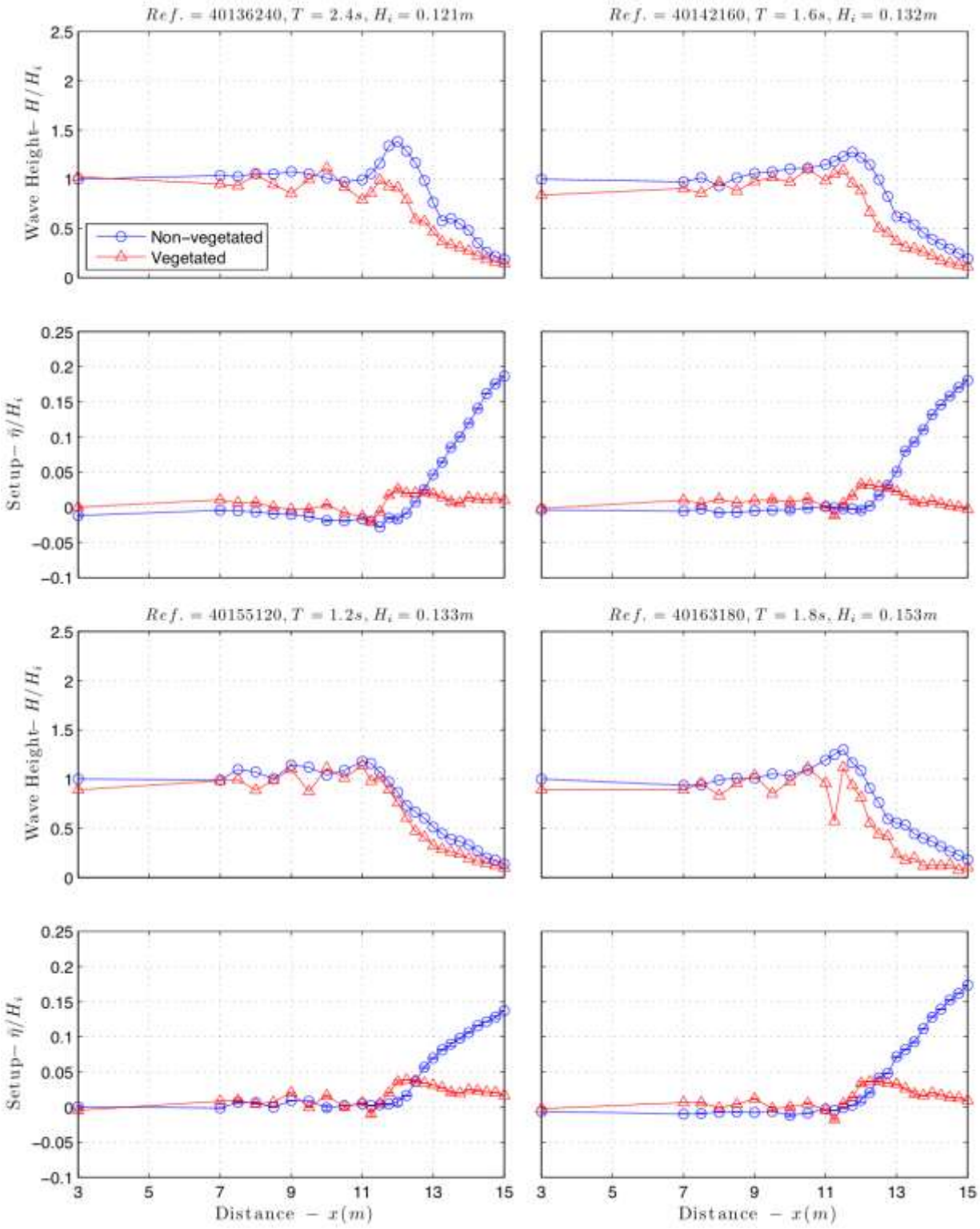

Fig. 3.56. Wave height transformation and mean water level along the plane sloping beach (regular waves, continued)

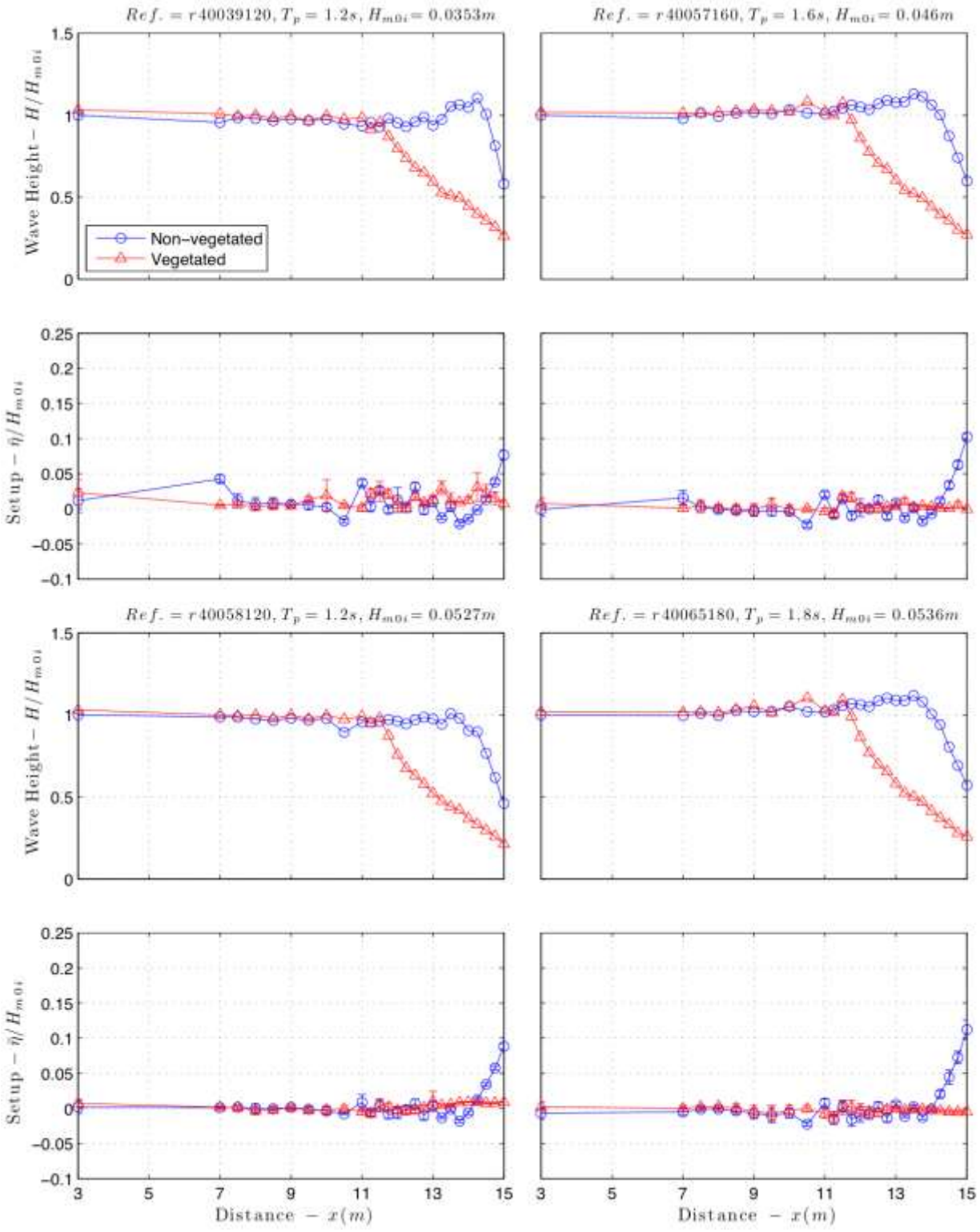

Fig. 3.57. Wave height transformation and mean water level along the plane sloping beach (irregular waves).

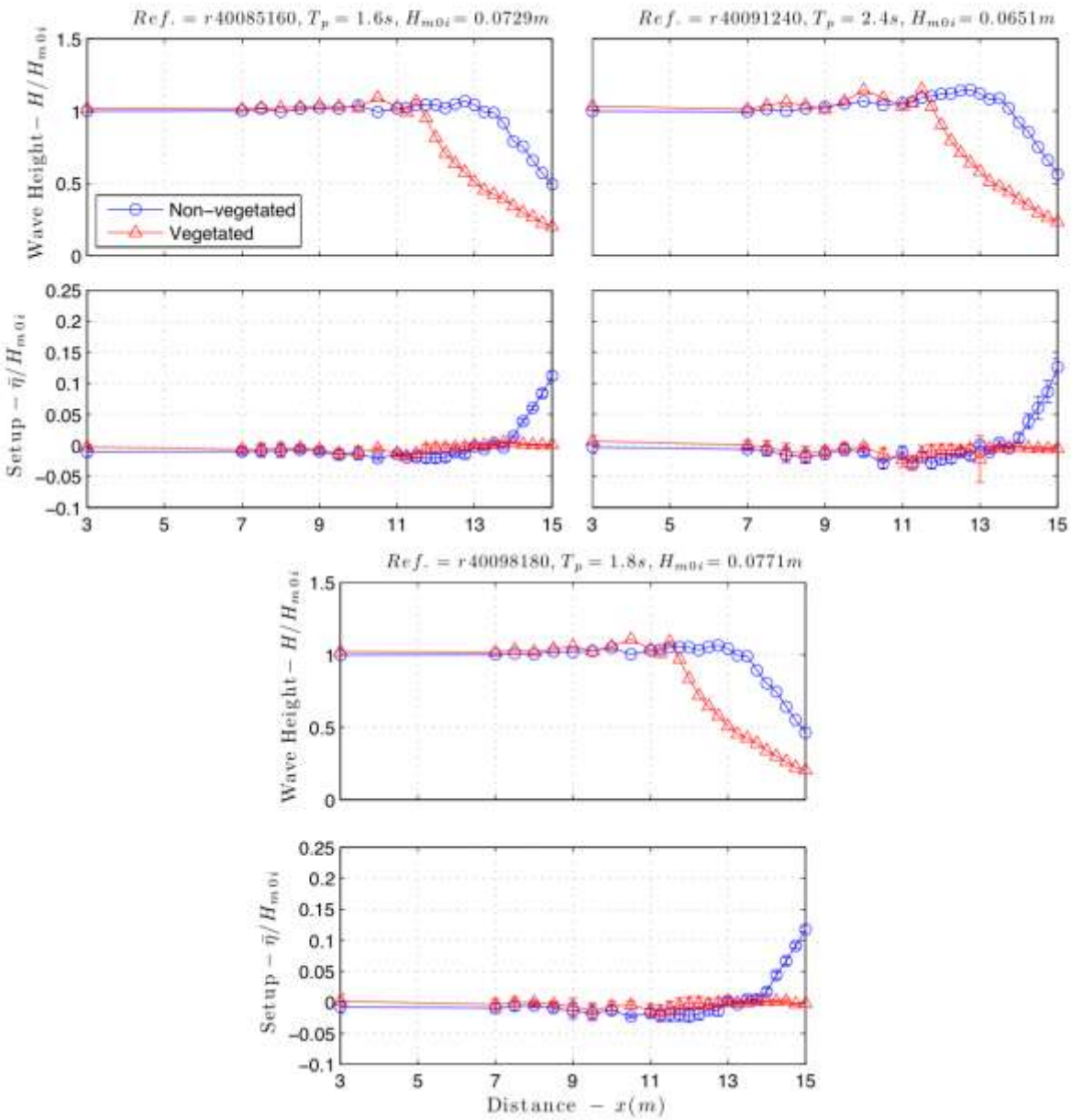

Fig. 3.57. Wave height transformation and mean water level along the plane sloping beach (irregular waves).

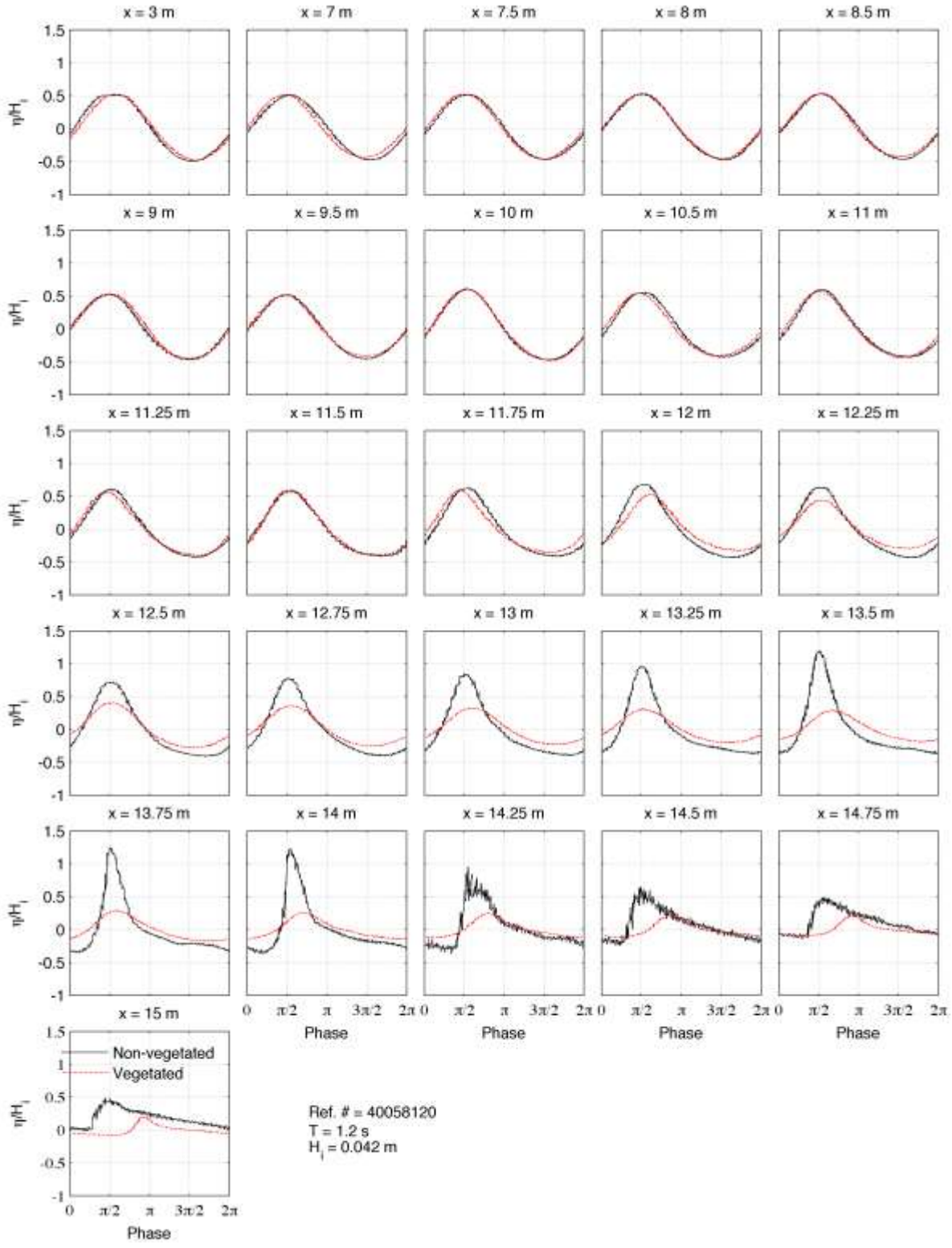

Fig. 3.58. Times series wave profile for vegetated and non-vegetated sloping beach. Each plot contains ten waves starting from 200 seconds.

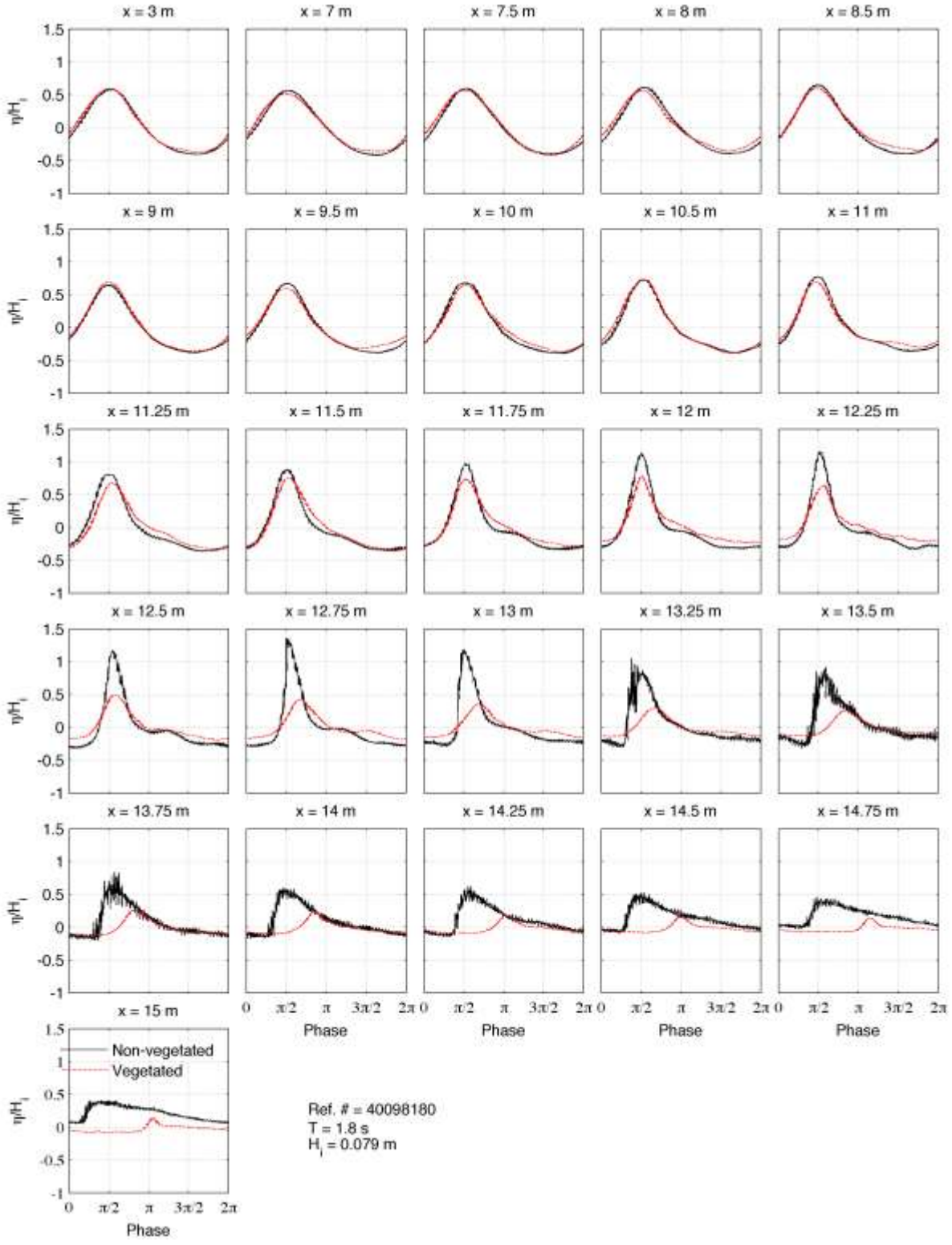

Fig. 3.59. Times series wave profile for vegetated and non-vegetated sloping beach. Each plot contains ten waves starting from 200 seconds.

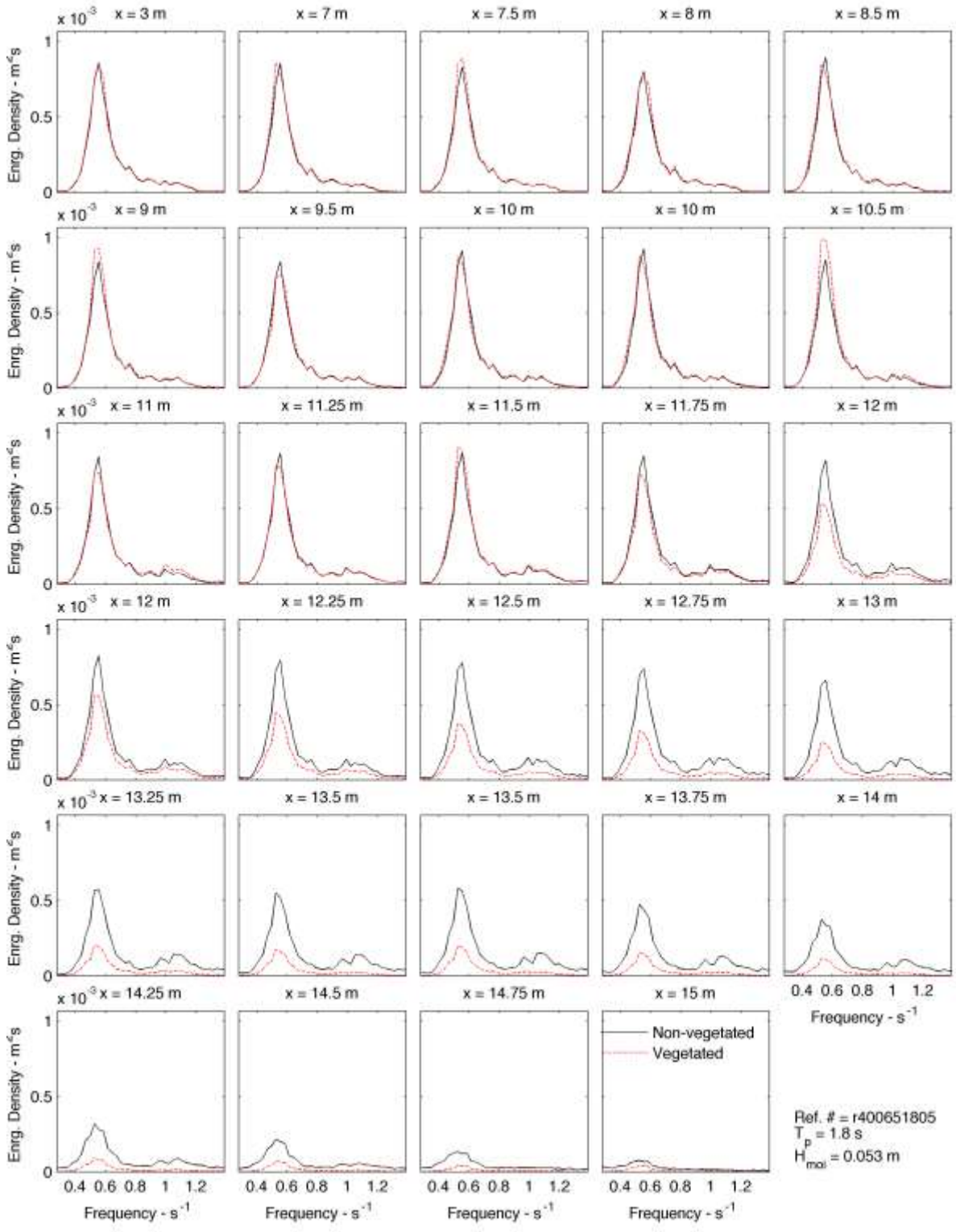

Fig. 3.60. Wave spectrum results of vegetated and non-vegetated sloping beach experiments with irregular waves.

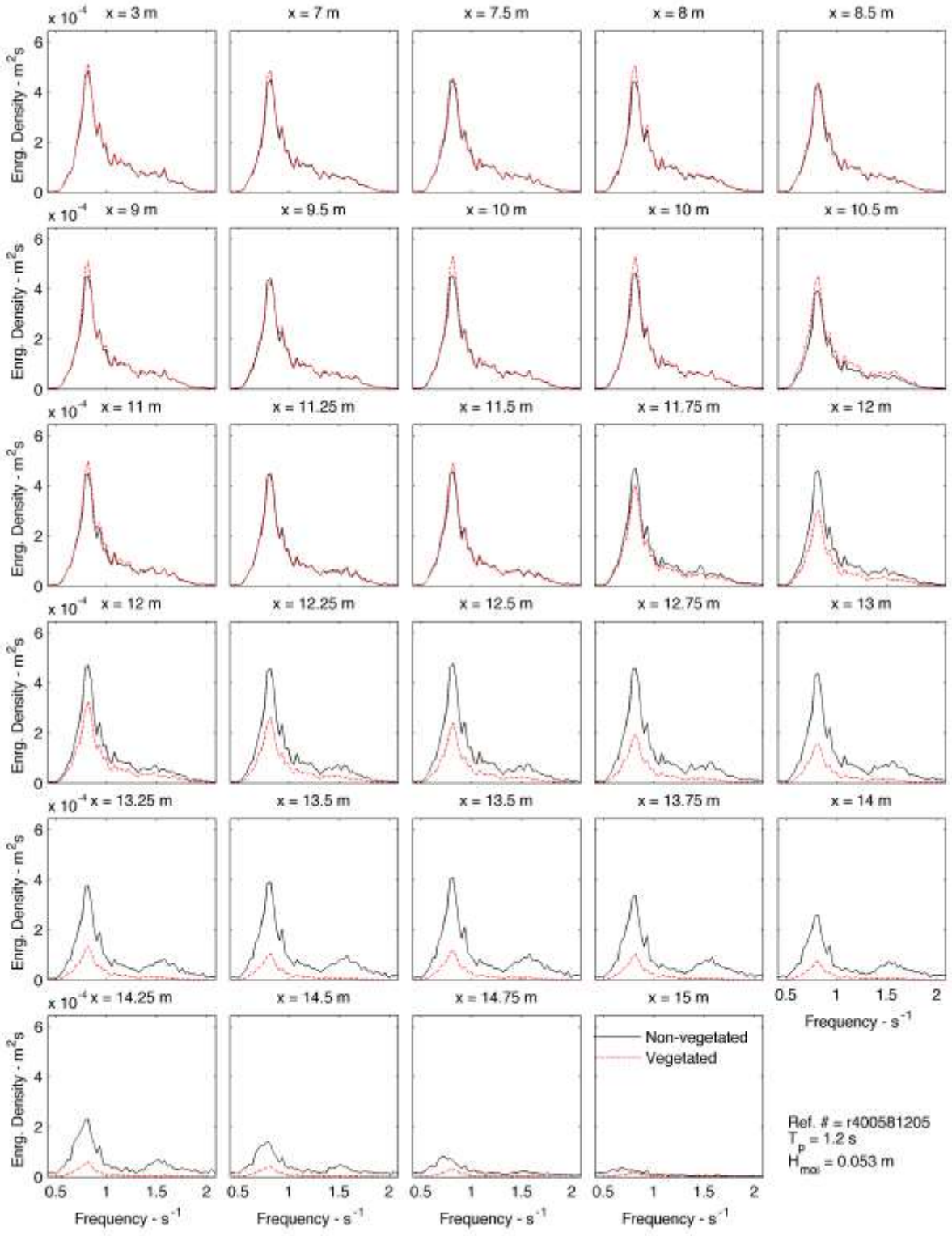

Fig. 3.61. Wave spectrum results of vegetated and non-vegetated sloping beach experiments with irregular waves (Experiment Ref. No. r400581205).

3.8 Summary

The main objectives of the laboratory experiments in this project were: (1) to assess the effect of vegetation on wave attenuation through model and live vegetation, and (2) to measure wave setup over a sloping beach with and without model vegetation. The wave tank at the USDA-ARS National Sedimentation Laboratory in Oxford, Mississippi, was improved to make this series of experiments possible. The completed wave tank was 20.6 m long, 0.69 m wide and 1.22 m deep. The wave flume utilized, when appropriate, a flap-type or a piston-type wave generator, both of which were controlled by a computer that also handled data collection. Capacitive wave probes were used to measure, at 30 Hz, the water surface elevation at 5 locations along the wave flume.

The first set of experiments included the testing of full-scale rigid model vegetation, full-scale flexible model vegetation, live and dormant *Spartina alterniflora,* and live *Juncus roemerianus* in both regular and irregular wave fields on a flat-bottom flume. A total of 3,123 regular wave experiments and 1,987 irregular wave experiments were carried out, including repeated runs of 231 different regular wave conditions and 89 different irregular wave conditions. The total number of wave and vegetation combinations was 1,041 for regular waves and 476 for irregular wave experiments. The results of the flat-bottom experiments were used to analyze wave attenuation as a function of vegetation type and density. Bulk drag coefficients (C_D) were estimated for all vegetation models and live species using theories described in Dalrymple et al. (1984) and Mendez and Losada (2004). Empirical relations were established for C_D as a function of Reynolds number and Keulegen-Carpenter number for each vegetation type. In addition, a new technique was developed for measuring water surface profiles through the vegetation field with a consumer grade digital video camera. There were 206 regular wave experiments (47 of which were the non-vegetated case) recorded with the camera and analyzed frame by frame.

In the second part of the experimental work, the effect of vegetation on wave breaking and setup was investigated. Rigid vegetation models with a 1:3 model to prototype scale were placed on a plane sloping beach and tested under regular and irregular waves. There were 144 experiments covering 24 different regular wave conditions and 70 experiments covering 24 different irregular wave conditions. Water surface elevation measurements were augmented by repeating experiments with the wave staffs at different locations. Video data analysis was also used to obtain complete water surface profiles during the sloping beach phase of the experimental work. Time series of water surface elevations, average wave heights, mean water levels, and wave spectra for vegetated and non-vegetated plain beach experiments were compared to identify the influence of vegetation on wave breaking and wave setup. The experiments showed that the wave setup and runup are reduced significantly by vegetation.

4. FIELD INVESTIGATIONS OF WAVE AND SURGE ATTENUATION BY VEGETATION

This chapter presents the field campaigns conducted on the Lousiana coastal marshes by the Louisiana State University (LSU) team as part of the SERRI project "Investigations of Surge and Wave Reduction by Vegetation," and describes the collected data sets of surge and wave attenuation by wetland vegetation.

Opportunities to collect required data sets on the Louisiana coast existed under two types of weather events: cold fronts and tropical storms. In an average year, the Louisiana coast experiences 20 to 30 cold fronts (Georgiou et al. 2005). These fronts can generate measurable wind waves over wetlands, while storm surge generated by tropical storms or hurricanes may not occur every year at a specific location. Therefore, the field experiments were focused on the wave attenuation under cold front conditions at fixed locations and surge reduction at locations determined by the forecasted landfall location. Therefore, the research plan included two separate data collection campaigns. The first campaign was directed towards measurements of waves and surge during a hurricane, referred to hereafter as "hurricane deployment". The second campaign was focused on the measurement of waves during winter fronts, referred to hereafter as "winter front deployment." For both campaigns, suitable wetland sites were identified and appropriate instrumentation was deployed to carry out measurements, as described in the following sections.

4.1 Site Selcetion

To ensure reasonable accessibility to the study site, only the Louisiana coast was considered for experimental sites. The coast consists of approximately 9,715 km^2 of marshes that vary in width from 20 to 75 km. Fig. 4.1 shows various marsh types in coastal Louisiana.

The large marsh patches are not uniform fields of grass but are scattered with low lying areas of varying sizes, plant types, densities and topography (Fig. 4.2). Often the marshes are segmented by bayous, canals and trenasses. This is far from a grassy field with dimensions on the order of several kilometers consisting of healthy stands of uniform marsh vegetation that would be an ideal setting for the proposed investigation.

Two sets of sites were required for field investigations based on whether hurricane deployment or winter front deployment was to be used.

4.1.1 Sites for Hurricane Deployment

The locations of the gages to be deployed depended on the forecasted track of the hurricane. In preparation, several potential deployment locations were planned using the information from various sources. Maps of aerial vegetation coverage of the coastal region were reviewed to identify regions of relatively continuous marsh. Information on access to these remote areas via primary and secondary roads, bayous and canals was obtained from Louisiana GIS databases. Personnel at the various local, state, federal agencies who have been active in coastal restoration efforts were contacted to gain valuable information on the quality of marsh, required means of access (e.g. boat, airboat) and to explore the possibility of taking advantage of the existing scientific monitoring efforts in the region. Fig. 4.3 shows

the alignments of gages that were planned in anticipation of hurricane surge measurements. Note the gages were never deployed because of absence of hurricanes during the study period.

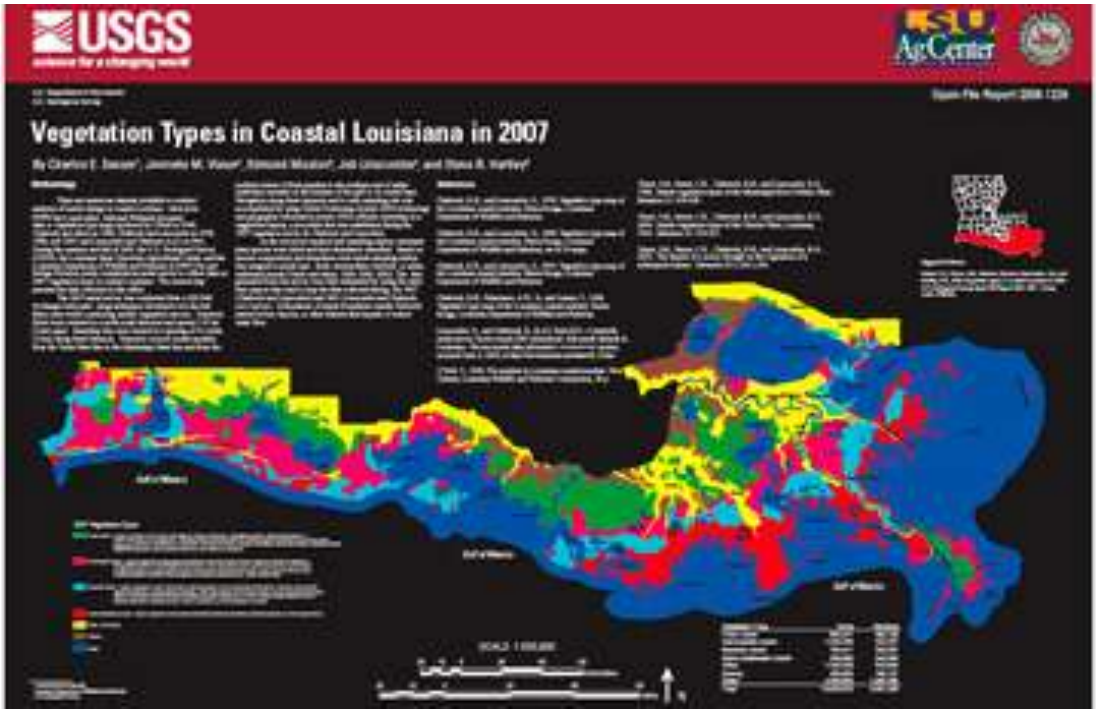

Fig. 4.1. Marsh types of coastal Louisiana (Source: USGS).

Fig. 4.2. Aerial view of typical marsh on the Louisiana coast (Source: OCPR).

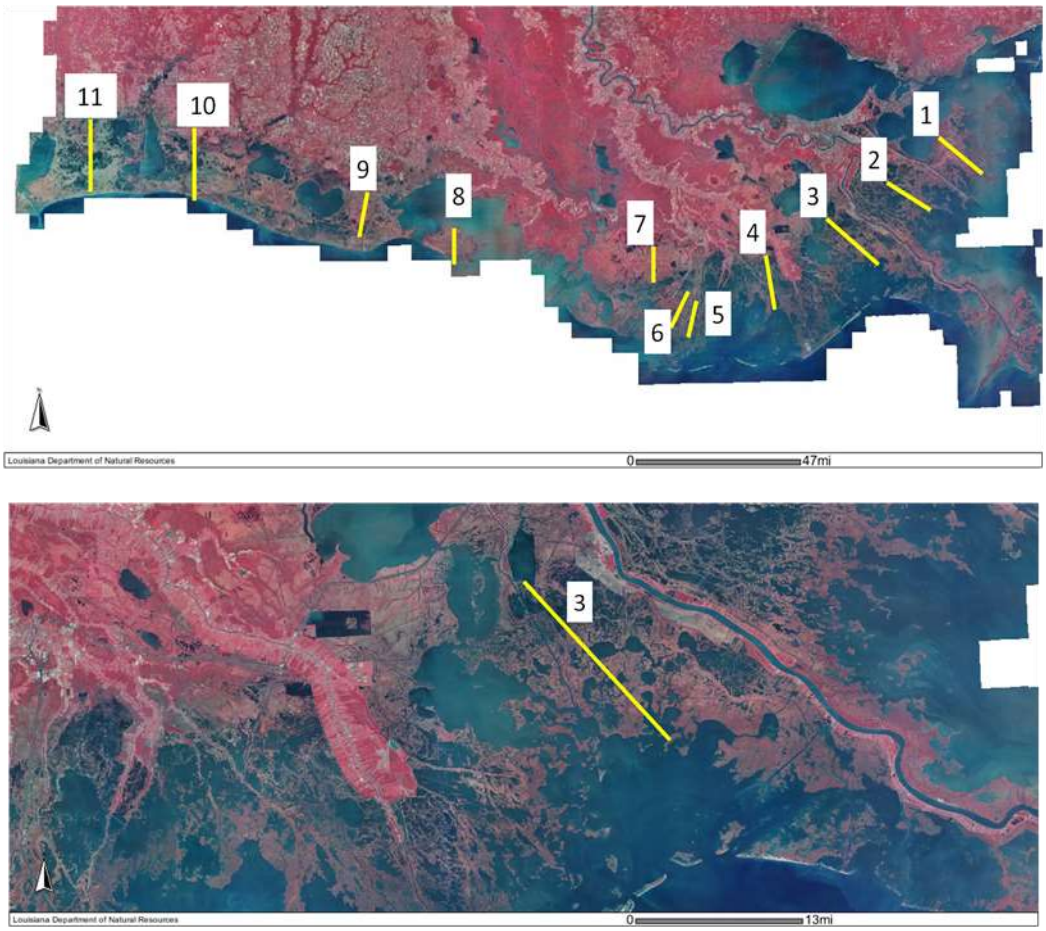

Fig. 4.3. Planned alignments of gages for surge measurements: (upper) All transects, (lower) Closer view of Transect 3 on the Louisiana coast (Source: OCPR).

4.1.2 Sites for Winter Front Deployment

To capture waves through marsh during the winter fonts, a relatively long term deployment site was envisioned. Required features were a healthy stand of vegetation and presence of measurable wave environment. Unfortunately, under normal (non-storm) weather conditions, vegetation and waves were not found to coexist on the Louisiana coast. Healthier marsh exists in the northern portions of the bays and estuaries but is sheltered from the waves. In contrast, the southern portions have measurable waves but the constant lapping of waves under normal conditions erodes away most of the healthy marsh vegetation. Therefore, finding a proper site turned out to be very critical to the success of the project.

It would have been cost and time prohibitive to reconnoiter the vast coastal marshes of Louisiana to identify experimental sites. Therefore, several meetings were undertaken with field scientists from state and federal agencies involved in the marsh restoration work to review field photographs and discuss potential sites. Based on this information, two regions were identified for the field work. The first site was in the Breton Sound and the second was

in Terrebonne Bay (Fig. 4.4). The research team reconnoitered both the locations before deploying instruments.

Fig. 4.4. Shortlisted sites for wave measurements during winter fronts and the research team on the reconnaissance trip.

4.1.2.1 **Breton Sound site**

The Breton Sound estuary covers about 270,000 km^2 in Plaquemines and St. Bernard parishes (www.lacoast.gov). It is bounded on the west by the Mississippi River, on the east by the Mississippi River Gulf Outlet (MRGO), and on the north by Bayou La Loutre. Chandeleur barrier island chain is located about 35 km from the marshes. A southernmost marsh area known as the Mozambique Point was also identified. The research team carried out reconnaissance of the location by boat to observe the state of the vegetation and physical setting (Fig. 4.5). The common vegetation communities in the marshes are smooth cordgrass (*Spartina alterniflora*) and saltmarsh meadow (*Spartina patens*). The health of the vegetation

varies with elevation, exposure to the waves, and salinity regime. The plant density is seasonal, with maximum density during the summer months.

After several weeks of communications to acquire permission to install marsh gage array on this site, the landowner did not allow the use of the wetland.

Fig. 4.5. Vegetation at the Breton Sound site (August 2009).

4.1.2.2 **Terrebonne Bay site**

Terrebonne Bay is located on the west side of Barataria Bay. It is bounded by Bayou Terrebonne on the east and the Houma Navigation canal on the west. It is bordered on the south by a series of narrow, low-lying barrier islands, called the Isles Dernieres and the Timbalier Islands that are approximately 15 km south of the selected site (Figs. 4.4 and 4.6). The common vegetation communities in these marshes are smooth cordgrass (*Spartina alterniflora*) and saltmarsh meadow (*Spartina patens*) as shown in Fig. 4.7.

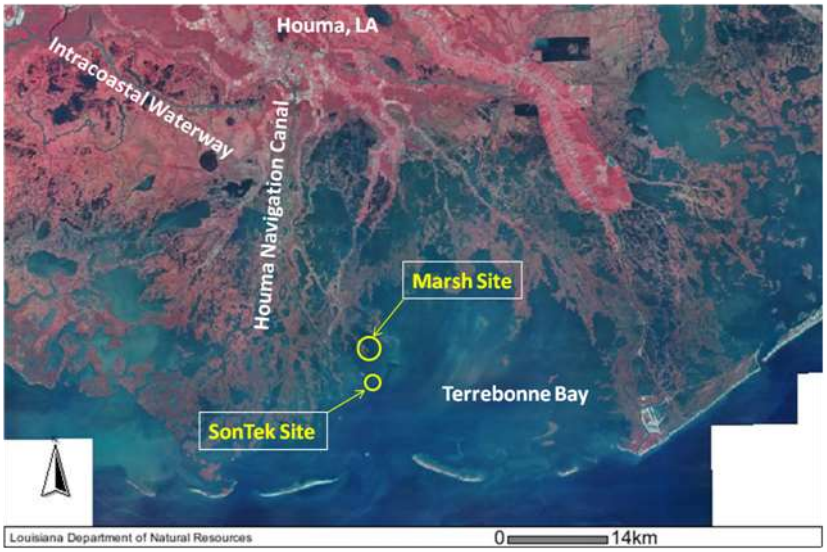

Fig. 4.6. Terrebonne Bay marsh site.

Fig. 4.7. Vegetation at the Terrebonne site (September 2010).

It was estimated that under normal weather conditions, the proposed site would not likely have waves passing through vegetation because of the low tidal range (approx. 0.3 m) in the bay. It would take a favorable combination of sustained southerly winds at high tide to produce measurable waves through the vegetation. To ascertain the suitability of this location to meet the goals of the proposed experiment, it was essential to examine the probability of such flooding occurrences in a typical year using long term water level records in the vicinity.

The daily water level data recorded at the LUMCON Marine Center during the six non-hurricane months (January through May and December) were analyzed to determine frequency of exceedance of specific water levels. Results are shown in Table 4.1. Each row indicates the number of times in which the given water level was exceeded in each year.

Table 4.1. Frequency distribution of daily water levels recorded at LUMCON Marine Center for the 2000-2007 period (non-hurricane months)

Water Level (m, NAVD88)	2000	2001	2002	2003	2004	2005	2006	2007
-0.8	0	0	0	0	0	0	0	0
-0.7	0	0	0	0	0	1	0	0
-0.6	0	0	0	0	2	0	0	0
-0.5	0	0	0	0	2	0	0	0
-0.4	0	0	0	0	3	0	0	0
-0.3	0	0	0	0	3	0	0	0
-0.2	0	0	0	0	1	1	1	0
-0.1	2	0	0	1	4	2	1	2
0	5	10	3	3	3	4	5	1
0.1	5	23	13	11	12	13	17	10
0.2	7	32	41	45	29	26	27	42
0.3	9	46	43	42	36	45	32	62
0.4	3	54	43	49	45	57	16	24
0.5	0	15	30	22	20	16	4	18
0.6	0	0	9	8	14	3	3	11
0.7	0	0	0	0	2	0	0	0
Total	31	180	182	181	176	168	106	170

The table shows that in a typical year one may expect 30 to 40 days of water level exceeding 0.3 m, which is an average marsh elevation on the coast. Days with high winds offer opportunities for waves to flow through marsh vegetation.

There are no historic long-term wave measurements records in the bay. An expedited STWAVE model of the bay was setup to estimate wave heights inside the bay resulting from south winds under no bottom friction. This provided estimates of the best possible wave heights. Fig. 4.8 shows the model domain. Results for predicted wind waves under various likely wind conditions are summarized in Table 4.2.

Based on this exercise, it was expected that the opportunities for measuring waves through vegetation under non-hurricane conditions existed under two circumstances: 1) when the marsh is continuously flooded over several hours due to high water level pushed in by sustained southerly winds, and 2) once every day at high tide, if the winds are higher. During a reconnaissance trip on March 30, 2009, waves of maximum height of about 0.3-0.5 m and time periods of 2-3 s were observed approaching one of the marsh islands with wind speed of around 10 m/s (20 knots). The waves shoaled and broke at the edge or slightly inside the marsh and traveled across through vegetation. The vegetation was thin and flooding depth was about 0.1 m. Similar conditions were observed during a field visit on May 3, 2009, when the winds were out of south at around 8 m/s (15 knots). Both of these locations did not have healthy, uniform variety of vegetation, but a patchy, weedy growth was observed.

Based on the above analysis and information, the Terrebonne Bay site was selected. Importantly, the landowner granted permission to access the area and deploy instruments.

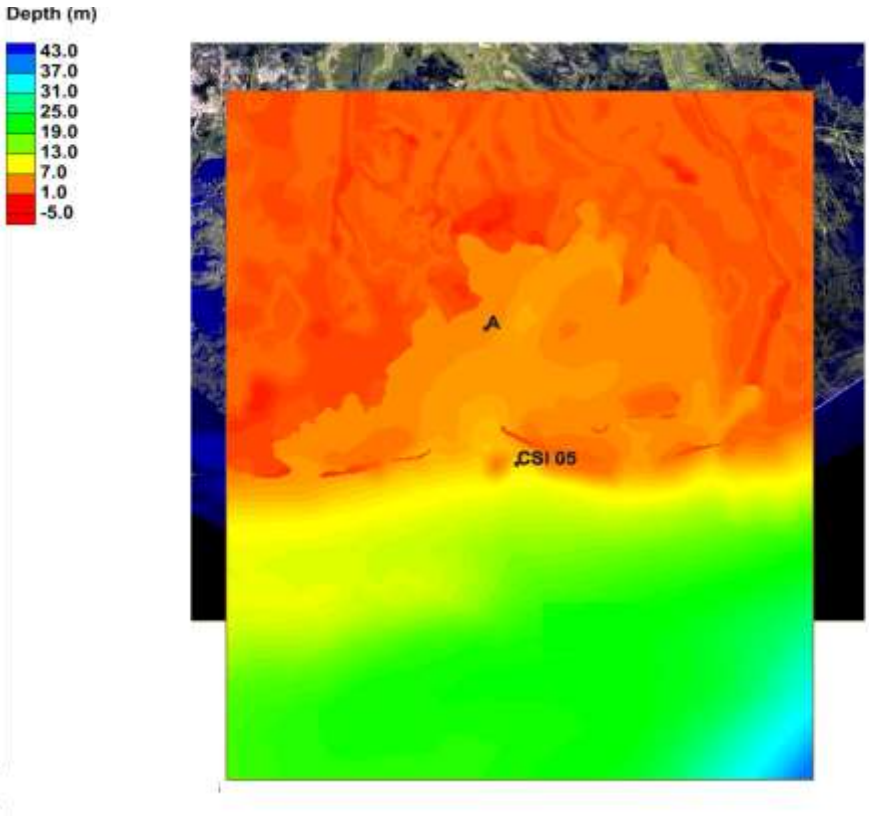

Fig. 4.8. STWAVE model domain and bathymetry.

Table 4.2. STWAVE predicted wave heights at the field site for various wind speeds and direction

Run ID	Wind Direction (degrees)	Wind Speed (m/s)	Tidal Elevation (m, NAVD88)	Offshore Input Spectrum	Wave Height at Point A (m)	Wave Period at Point A (sec)
1	180	8	0.3048	Zero	0.55	4.6
2	180	10	0.3048	Zero	0.66	5.0
3	180	12	0.3048	Zero	0.77	5.3
4	180	14	0.3048	Zero	0.87	5.6
5	180	16	0.3048	Zero	0.94	5.9
6	202.5	8	0.3048	Zero	0.32	4.6
7	202.5	10	0.3048	Zero	0.43	5.0
8	202.5	12	0.3048	Zero	0.53	5.3
9	202.5	14	0.3048	Zero	0.60	5.6
10	202.5	16	0.3048	Zero	0.67	5.9
11	225	8	0.3048	Zero	0.40	4.4
12	225	10	0.3048	Zero	0.53	4.8
13	225	12	0.3048	Zero	0.65	5.0
14	225	14	0.3048	Zero	0.75	5.3
15	225	16	0.3048	Zero	0.85	5.6

4.2 Instrumentation

The choice of the wave and surge measuring gages depended on the type of deployment, as described in the following sections.

4.2.1 Gages for Hurricane Deployment

The goal of this deployment was to collect surge as well as waves produced during a hurricane. The general characteristics desired in a gage were: relatively small size to allow quick manual deployment in front of an impending hurricane, sufficient memory and battery capacity to record and store continuous measurements for up to 7 days, rugged housing to withstand strong currents and reasonable cost to afford deployment of a 5-6 gages along 2-3 alignments. Two different types of gages were selected for surge and wave measurements during hurricanes as described below.

For surge measurements, HOBO U20 Water Level Data Loggers (U20-001-01) were procured. The durable ceramic pressure sensor and electronics have a stainless steel housing (Fig. 4.9) and can measure water level, barometric pressure and temperature. The sensor has an operational range of 0 to 9 m, water level accuracy of 0.5 cm, and a resolution of 0.21 cm. It uses a factory-replaceable 3.6 Volt battery and has 64 K memory. The sensor is 15 cm long, has a diameter of 2.46 cm, and weighs 210 g. Data logging can be set at single or multiple intervals, with up to 8 user-defined logging intervals and durations. Intervals from 1 second to 18 hours can be set. HOBOware Pro software provides easy conversion to accurate water level reading, fully compensated for barometric pressure, temperature, and water density.

Note that these sensors were never deployed because of the absence of hurricane during the study period.

Fig. 4.9. Photo of gage used to measure hurricane surge.

For wave measurements, the gages were custom-built around a low power Onset Tattletale TFX-11 v2 data-logger with 2MB of non-volatile memory (Kennedy et al. 2010). The gage consists of a 100 PSI absolute (689 kPa) piezoelectric silicon pressure sensor, and a data-logger interface board. All these parts were housed in a commercial Schedule 40 PVC pipe. The length of the instruments was less than 30 cm (Fig. 4.10). The gages were attached to 25 kg square steel bases to hold them in place during strong storm generated currents. An acoustic beacon and a small float were added to the assembly to facilitate retrieval.

The sampling frequency was set to 1.67, 2 and 4 Hz depending on the deployment and availability of sensors. The gages sampled either continuously or in a burst mode for approximately 7 days until the memory became full.

Fig. 4.10. Gage used to measure hurricane waves.

4.2.2 Gages for Winter Front Deployment

A total of 9 gages were deployed for wave measurements during winter cold fronts. One of them was a directional ADV (Acoustic Doppler Velocimeter) with an integrated pressure sensor and the rest were non-directional pressure transducers.

The Sontek Triton-ADV Wave/Tide/Current Gauge (Fig. 4.11) accomplishes directional wave measurements via PUV processing. The 3.2 kg instrument features a 10-MHz, 3-D ADV sensor (with 10-cm distance to sampling volume) mounted on a 15-cm stem attached to a self-contained electronics package that includes internal compass/2-axis tilt, pressure and temperature sensors, and 12 V DC alkaline battery pack. Electronics are housed in a Delrin pressure case with wet-mateable connector. The standard 128 MB compact flash memory was augmented to 2 GB.

The specification for velocity measurements were: range 0.1-4.8 m/s, resolution 0.01 cm/s and accuracy of 0.1 cm/s. The strain gage type pressure sensor has an accuracy of 0.1% and operational depth of 30 m. It can sample 1-, 2- or 4-Hz bursts with sample length of 128 to 8192. The temperature sensor has an accuracy of 0.1 0C and resolution of 0.01 0C.

The Sontek collected data at 4 Hz sampling frequency, every 30 min. The memory and battery capacity lasted for about 5 weeks allowing monthly maintenance trips.

The non-directional wave gages (Fig. 4.12) were built by the Field Support Group of the Coastal Studies Institute at LSU. Each gage is a Model PX309-005G strain gauge type pressure transducer from Omega Engineering with a ±0.25% typical accuracy. Excitation is continuous during any given sampling period, so the sampling frequency is determined by the data logger. The pressure transducers are not vented. Pressure measurements are made relative to the internal pressure within the housing. The five gages were connected to a central data logger by a four-conductor cable. Two conductors provided excitation voltage from the data logger, and two conductors returned the milli-volt signal to the data logger in a differential mode.

Fig. 4.11. Sontek Triton-ADV.

The data logger is a Campbell Scientific CR1000. It has a memory capacity of 2 GB, which is sufficient for recording for more than one month for the five marsh sensors. Battery capacity is matched to the deployment duration dictated by the sample data and data storage capacity, i.e. a month or more.

The data-logger housings were custom built using 6 inch I.D. schedule 80 PVC pipe which was turned to incorporate dual static o-ring glands and a bonded cap. The marsh array was constructed in the same manner as the open water data-loggers, with the exception of four external inputs to accommodate four self-contained pressure sensors housed in 1 ½ inch I.D. Schedule 80 PVC pipe, again turned to incorporate dual static o-ring glands and a bonded connector end. The three open water sensors and the main housing of the marsh array were all powered by a 12v source which consisted of 16-1.5v non-rechargeable alkaline cells.

The open water sensors were installed using three 21'-1 ½ "I.D. galvanized steel pipes driven into the sea floor in a 6' equilateral triangle formation. These three uprights were then bound together using three 8'galvanized steel pipes and scaffolding clamps. The sensor itself was attached to a 1 ¾ " galvanized steel pipe "sleeve" with a steel disk welded to the bottom, and this sleeve was placed over one of the three legs of the support structure. The final scaffold clamp was then attached over this sleeve to lock everything into place.

The marsh array involved constructing several mud dams to reduce the possibility of clogging the pressure sensor diaphragm. These were made of schedule 20 PVC tubing with a wire bottom which was then inserted into a hole that was bored into the marsh, the main housings mud dam was made of polyester resin and fiberglass cloth.

Fig. 4.12. (top)Marsh gages housing with pressure transducer inside, and (bottom) Inside of the data logger assembly with integrated pressure transducer.

4.3 Data Collection

Wave measurements were made during the short term hurricane deployment and the long term winter front deployments with varying degrees of success. Fig. 4.13 summarizes the inventory of the collected data and subsequent sections describe the details of the data collection effort.

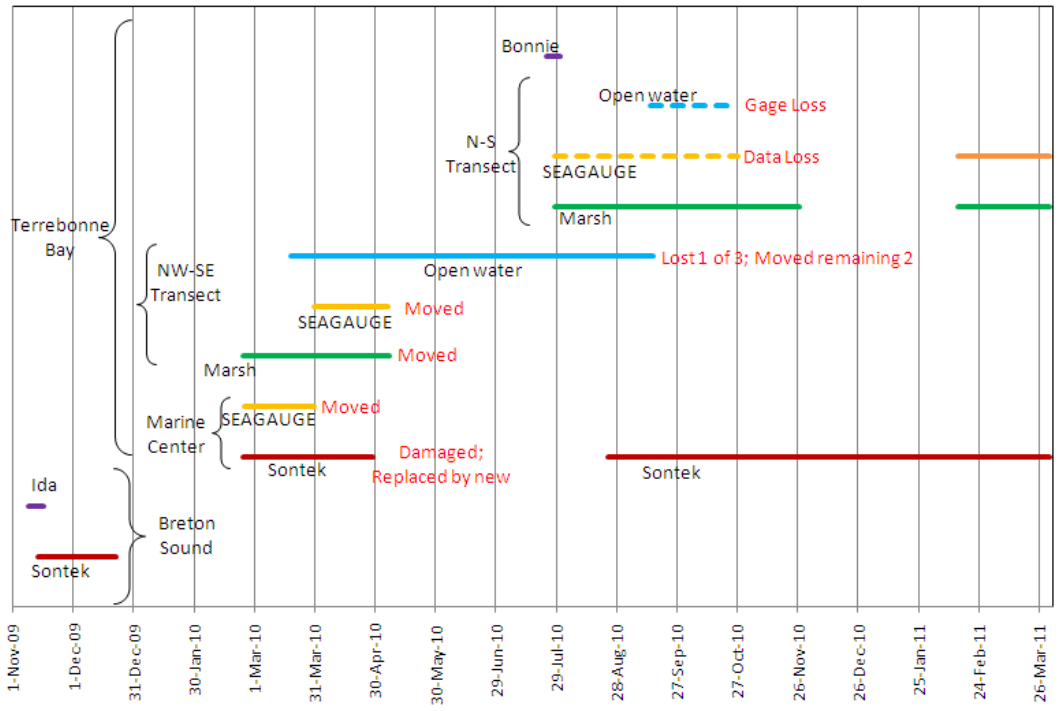

Fig. 4.13. Timeline of data collection.

4.3.1 Tropical Storms and Hurricanes

During the study period, the Louisiana Gulf coast experienced no hurricanes and only two tropical storms. Tropical Storm Ida made landfall on November 10, 2009 and Tropical Storm Bonnie made landfall on July 25, 2010. Based on the track of the impending tropical storm, gages were deployed several hours before landfall.

4.3.1.1 Tropical Storm Ida

Ida was a late season (4-10 November 2009) hurricane. It was the first November hurricane in the Gulf of Mexico since Kate of 1985 (Avila and Cangialosi 2009). Ida's path is shown in Fig. 4.14.

On Monday November 9, 2009 at 9:00 AM (15:00 UTC) National Hurricane Center Advisory Number 23, Ida was located about 300 km south-southwest of the mouth of Mississippi River. It was moving toward the north-northwest at about 28 km/hr. The center was expected to make landfall along the northern Gulf on Tuesday morning.

On the morning of November 9, 2009 between 10 AM to 2 PM CST, four gages were deployed by boat in the marshes near Mozambique Point in the upper Breton Sound. The locations of the gages are shown in Fig. 4.15 along with the other existing monitoring stations in the area. Gage J was deployed at a location as far south as possible to travel safely in the face of wind and waves. Then moving northwards Gages F, I and E were placed on the adjoining marshes. Finally, Gage G was deployed in Lake Lery. Fig. 4.16 shows close-up

of the locations of gages J, F, I and E. The coordinates of all the deployed gages are listed in Table 4.3.

Fig. 4.14. Path of Tropical Storm Ida (November 2009).

All four gages were retrieved on November 16, 2009, several days after the surge receded. This deployment provided approximately 7 days of continuously recorded water levels at 1.67 Hz sampling frequency. As an example, Fig. 4.17 shows the location of one of the gages (Gage I) photographed during gage deployment and retrieval.

Fig. 4.15. Locations of USGS and gages deployed for Ida.

Fig. 4.16. Close-up view of the locations of the gages deployed for Ida.

Table 4.3. Coordinates of the gages deployed during Tropical Storm Ida

Gage	Northing	Easting	Comments
J	29 39.7065'	89 34.0103'	Southernmost; in open water at a depth of 5.25 ft
F	29 39.7354'	89 34.0438'	At the edge of the marsh; nearest to open water
I	29 39.5458'	89 33.6793'	On the marsh
E	29 40.0340'	89 34.9766'	On the marsh
G	29 47.9250'	89 48.1544'	Northernmost; in Lake Lery

Fig. 4.17. Location of Gage I photographed during deployment (top) and during retrieval (bottom) for Tropical Storm Ida.

4.3.1.2 **Tropical Storm Bonnie**

Bonnie was a small and weak tropical storm. The path of the storm is shown in Fig. 4.18. Before landfall, Bonnie began to weaken and made landfall along the southeastern coast of Florida near Elliot Key at around 1430 UTC on July 23, 2010. Late on July 24, Bonnie degenerated into a non-convective remnant low pressure system at 0000 UTC on July 25 about 60 mi southeast of the mouth of the Mississippi River. The remnant circulation made landfall 4 hr later near the southeastern tip of Louisiana, and continued inland and dissipated over east-central Louisiana after 1800 UTC that same day (Stewart 2010).

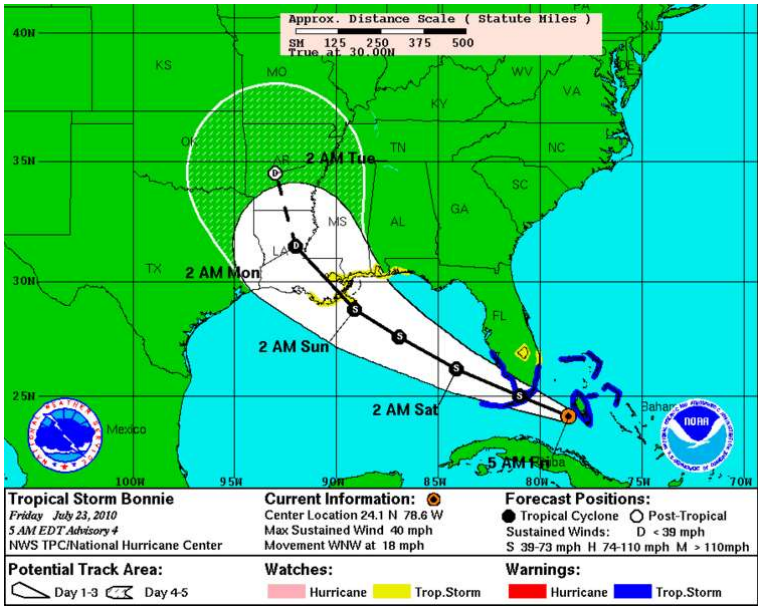

Fig. 4.18. Path of Tropical Storm Bonnie (July 2010)

Fig. 4.19. Location of gages deployed for Tropical Storm Bonnie.

Four gages were deployed on the marsh in Terrebonne Bay on July 24, 2010, Saturday just after 9:30 AM CDT (Fig. 4.19). The coordinates of the gages are in Table 4.4.

Gage D sampled 15 min bursts at 4 Hz on every hour. Rest of the gages sampled 30 min bursts at 2 Hz on every hour.

Gage A location was selected by judging the bottom topography with a staff, such that the slope from the bay floor had a relatively flat slope. All gages were retrieved after 3 days on July 27, 2010. Gages C and D were never inundated.

Gage A float

Gage B (at the marsh edge)

Gage C

Gage D

Fig. 4.20. Gages deployed for Tropical Storm Bonnie.

Table 4.4. Coordinates of the gages deployed during Tropical Storm Bonnie

Gage ID	Northing	Easting	Distance from B (m)	Elevation m, NAVD88	Comments
A	263613.808	3512568.383	112.0	Water level at 0.59	Southernmost In open water at a depth of 1.6 m
B	263971.38	3512484.323	0	0.48	At the edge of the marsh, nearest to the open water
C	263982.305	3512478.719	3.7 3	0.74	
D	263990.242	3512475.29	6.4	0.65	Northernmost

4.3.2 Winter Fronts

As stated previously, for long term winter front deployment, two potentially favorable sites were identified, one in Breton Sound and the other in Terrebonne Bay.

4.3.2.1 **Breton Sound deployment for winter fronts**

Data collection during winter season started as soon as the first gage, the Sontek Triton-ADV, was received and deployed on November 13, 2009 in Breton Sound. It was deployed at 29°31'46.30"N and 89°24'42.20"W, approximately 14 km south of the site identified for the deployment of the marsh gage array (Fig. 4.21). Unfortunately, after several requests and communications, the land owner did not grant permission to access to the site for experiment set up, so no data could be collected from the marsh. The Sontek Triton ADV was subsequently retrieved on December 22, 2009. During this period 17 min bursts were sampled at 4 Hz frequency every 30 minutes to record puv (pressure, x-component of velocity and y-component of velocity) time series.

A wave monitoring station (CSI-16) exists approximately 40 km to the south of the selected ADV site. The station is maintained by the WAVCIS program of LSU. It collects directional wave parameters along with wind speed and direction.

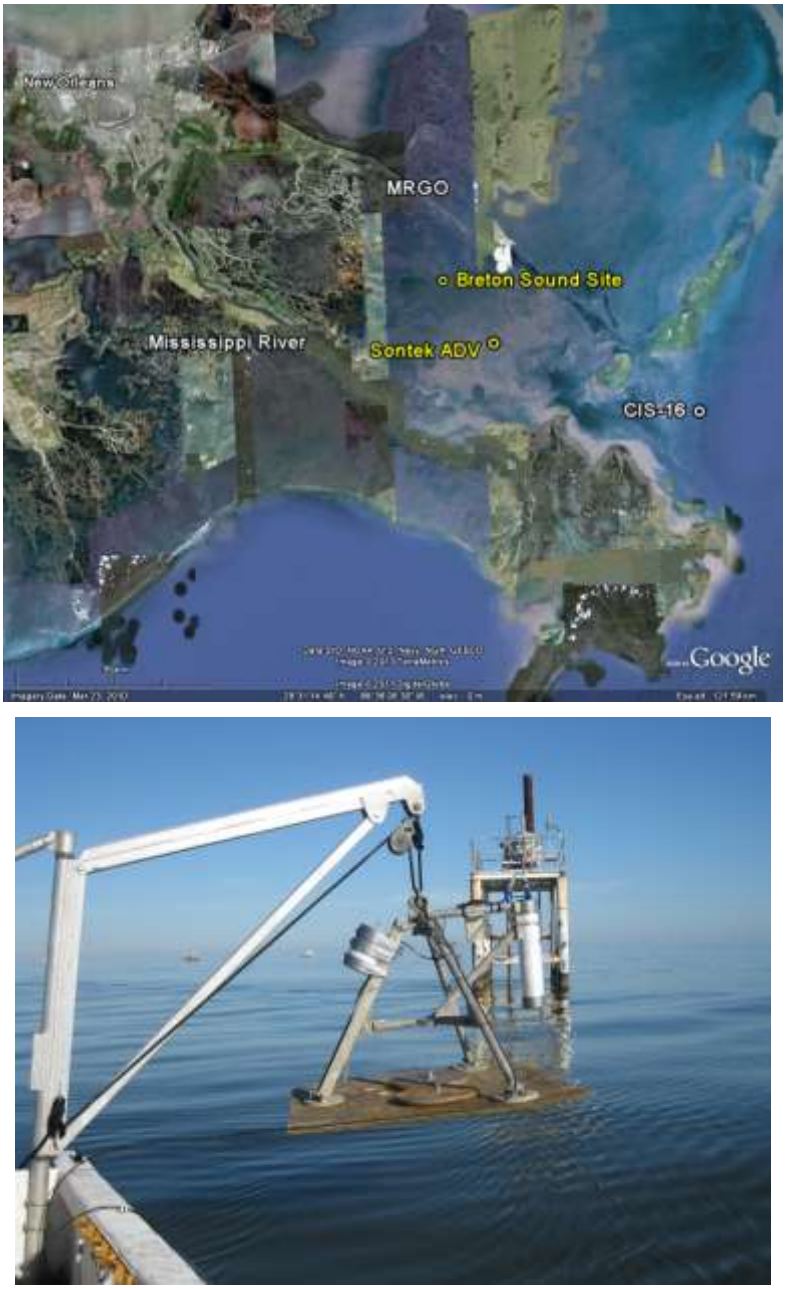

Fig. 4.21. Sontek-ADV deployment for winter fronts in Breton Sound. Location (top) and deployment from a boat (bottom).

4.3.2.2 **Terrebonne Bay deployment for winter fronts**

A wetland site was selected in Terrebonne Bay with access permission for winter front deployment. On February 23, 2010, the Sontek Triton ADV was deployed in Terrebonne Bay near a U. S. Coast Guard platform (Fig. 4.22). The platform also supports LUMCON instrumentation that records continuous tide levels, salinity, turbidity and meteorological parameters. To the south of this location, outside the barrier island chain, at approximately

15 km, a WAVCIS station CSI-05 is present. It collects hourly non-directional wave parameters.

The ADV collected data continuously until April 29, 2010 when it was found damaged. During this period 17 min bursts were sampled at 4 Hz frequency every 30 minutes to record puv (pressure, x-component of velocity and y-component of velocity) time series.

The damaged ADV was replaced with a new ADV of with the same specifications and deployed on July 24, 2010. To date this gage has collected 17 min bursts of puv time serried every 30 minutes at 4 Hz sampling frequency. The sampling frequency was inadvertently set to 2 Hz at the time of damaged sensor replacement in July 2010. It was reset to 4 Hz on February 14, 2011. The ADV continues to collect wave data.

The ADV provides valuable information on the wave field travelling a distance of 4 km northwards to the marsh site (Fig. 4.22) where the marsh array and open water gages are located.

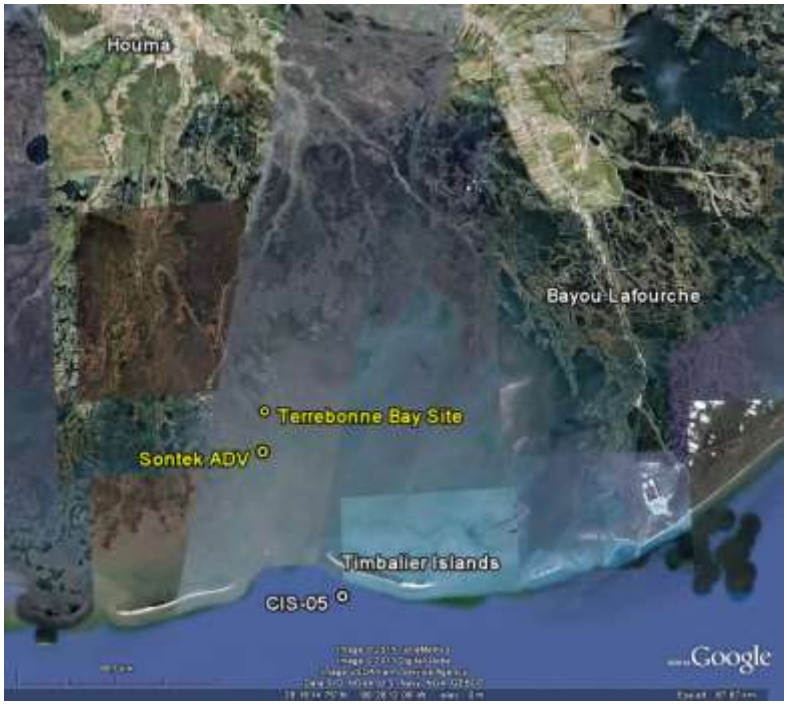

Fig. 4.22. Marsh site and Sontek-ADV location for winter fronts deployment in Terrebonne Bay.

At the marsh site, two parallel arrays of gages were deployed as shown in the schematic in Fig. 4.23. The first array consisted of 5 gages placed in the marsh grass to measure propagation of waves through the marsh. Fig. 4.24 shows photographs of the site, gages M1, M2 immediately after the deployment and gage M1 found washed off during retrieval.

The second array of 3 gages was placed in the adjacent open water to measure the same wave field without the attenuation caused by the marsh. The three open water gages were deployed on March 18, 2010 (Fig. 4.25). All the marsh and open water gages recorded pressure bursts at 4 Hz frequency on every hour. During the collection period, the middle gage was first found missing and subsequently some of the remaining gages were found

missing. As a result of the response to the BP oil spill, the area witnessed increased boat traffic increasing risk of loss.

In preparation for the hurricane season, it was decided to increase the length of the transect on the marsh. The new North-South alignment of the 5-gage marsh array and 2-gage open water array is shown in a schematic in Fig. 4.26. The gages sampled 17 min burst of 4 Hz every hour from July 24, 2010 to December 16, 2010.

Due to signal issues, the marsh gages were brought back to the FSG workshop on LSU campus, and, after correcting the problems, were deployed at the same north south alignment but over a much shorter distance. The configuration of the gages is shown in a schematic in Fig. 4.27.

Fig. 4.23. Arrays of marsh and open water gages in Terrebonne Bay during Feb-May, 2010 (Northwest to Southeast alignment).

Fig. 4.24. Clockwise from top left: Marsh site looking northwest; gage M1 at deployment; gage M2 at deployment; washed off gage M1.

Fig. 4.25. Open water gages W1, W2 and W3.

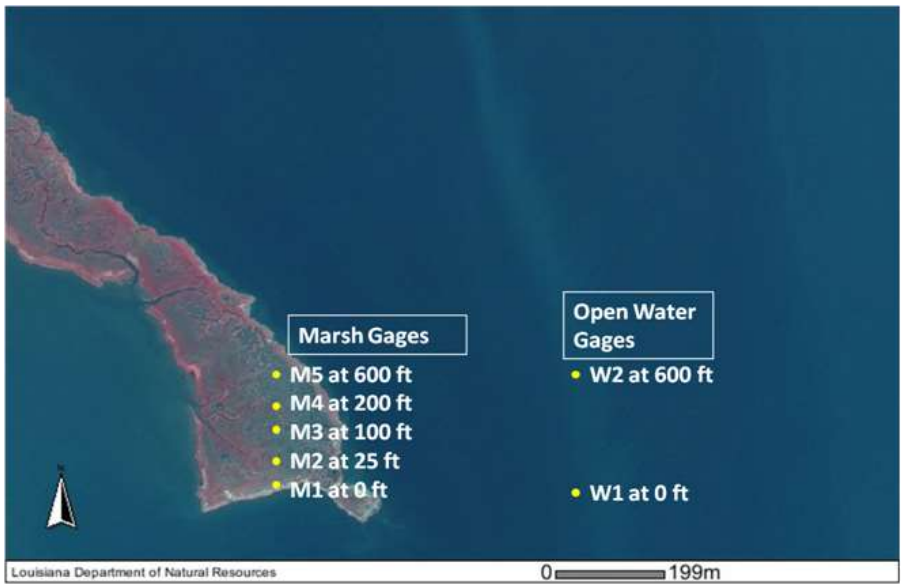

Fig. 4.26. Arrays of marsh and open water gages in Terrebonne Bay during Jul-Dec, 2010 (North-South alignment).

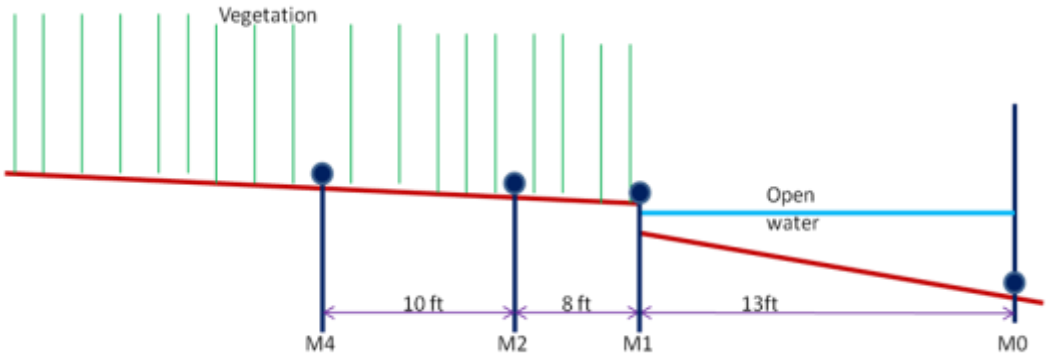

Fig. 4.27. Marsh array deployment over a shorter stretch during Feb-Mar, 2011 (North- South alignment). Not to scale.

4.3.3 Topography

After the placement of north-south marsh array, a topographic survey of the marsh site was carried out on September 2, 2010. The spot elevation measurements are shown in Fig. 4.28.

Bathymetry in the open water in front of the marsh was also surveyed. The north-south profile is shown in Fig. 4.29.

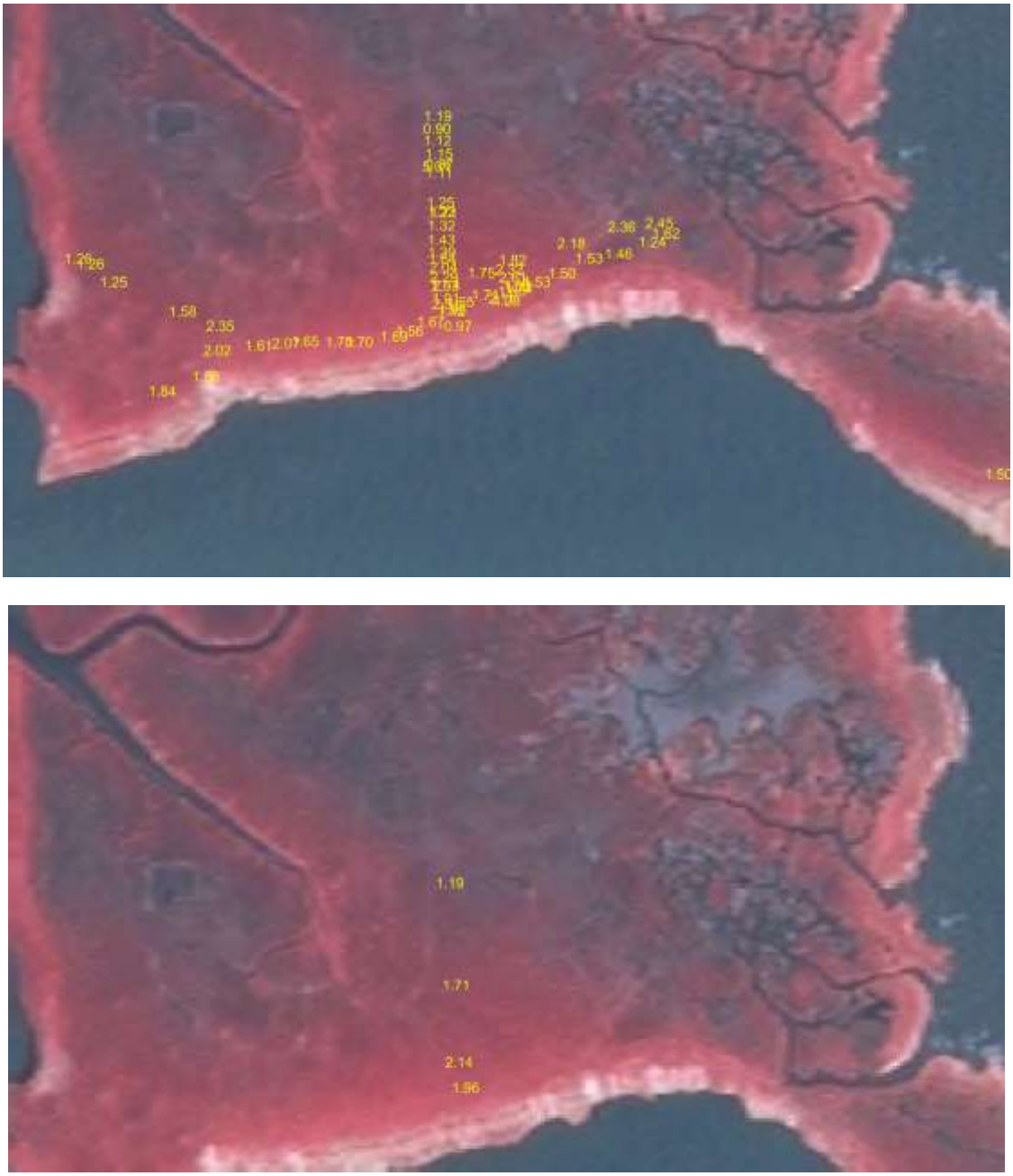

Fig. 4.28. Topographic survey of the field site. (Elevations in ft, NAVD88, Louisiana State Plane South Coordinate System). All survey data (top); Gage elevations (bottom).

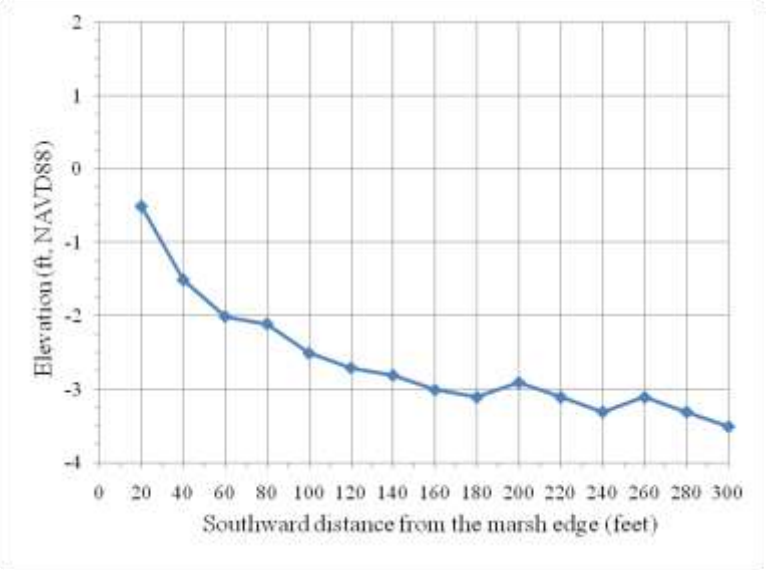

Fig. 4.29. Bathymetric profile of the open water to the south of marsh.

4.4 Analyses and Results

4.4.1 Surge Attenuation

Winds during Ida peaked at midnight on November 9, 2009 as shown by the record (Fig. 4.30) at the NOAA meteorological station (SHBL1 No. 8761305) at Shell Beach, LA. The pressure transducers rapidly deployed on the morning of November 9 provided approximately 7 days of continuous record of water levels at 4 gage locations (Fig. 4.30).

In the early hours the surge in Breton Sound marsh rose against the north, north-easterly winds and receded within hours once the center of the storm moved northwards. As seen from the records, the marsh in the Breton Sound basin experienced surge of over marsh for about 12 hr. At its peak the surge depth over marsh was about 1 m. At the northernmost gage G, the surge peaked 14.5 hours later than the southernmost gage J. As noticed by the research team during deployment, during this time the water was above marsh and gradually raising through the vegetation. Comparatively, the normal tidal peak (as measured after November 15) took approximately 8 hours to peak at gage G. The relative lags in time to peak can be seen in Fig. 4.31.

During the normal tidal cycle, the water propagates northwards only through bayous (major being Bayou Terre aux Boeufs) and small rivulets and connecting ponds. This is an efficient route for water to propagate through open water bodies devoid of any vegetation. In contrast, during storm surge, once the water rises above canal banks and starts propagating as an increasingly deepening sheet flow, it encounters more resistance due to the marsh vegetation which slows its northwards movements. It should be noted that, this slow movement cannot be entirely attributed to the vegetation resistance. During this period, winds out of north must have offered some resistance. Additionally, decreasing average head differential between the northern and southern ends of the basin must have played some role in slowing down the northwards propagation of surge.

Water level data from three USGS monitoring gages (Fig. 4.32) were also available during this period. The stations are USGS No. 07374527 (Northeast Bay Gardene near Point-a-La-Hache, LA), USGS No. 073745257 (Crooked Bayou Northwest of Little Cuatro Caballo near Delacroix) and USGS No. 073745253 (Reggio Canal near Wills Point, LA). Out of these stations, datum for the Crooked Bayou station could not be confirmed, so that station was not considered for plotting. Water level records from Bay Gardene and Reggio Canal stations are plotted in Fig. 4.32. Plot shows that the surge heights and peak times compare well with records at gages J and G.

Gage records also show that a surge of 1.7 m in the bay, reduced to 0.7 m as it propagated through the wetlands northwards.

The behavior of the storm surge during rising and falling hours, is analyzed further to examine the influence of marsh. Fig. 4.33 shows water depth record during falling limb of surge. Recall that gage J is situated in open water whereas gages F and I are on the marsh. In the figure, water depth at gage J is plotted relative to the marsh surface which is 2.1 m above the bottom where Gage J was located.

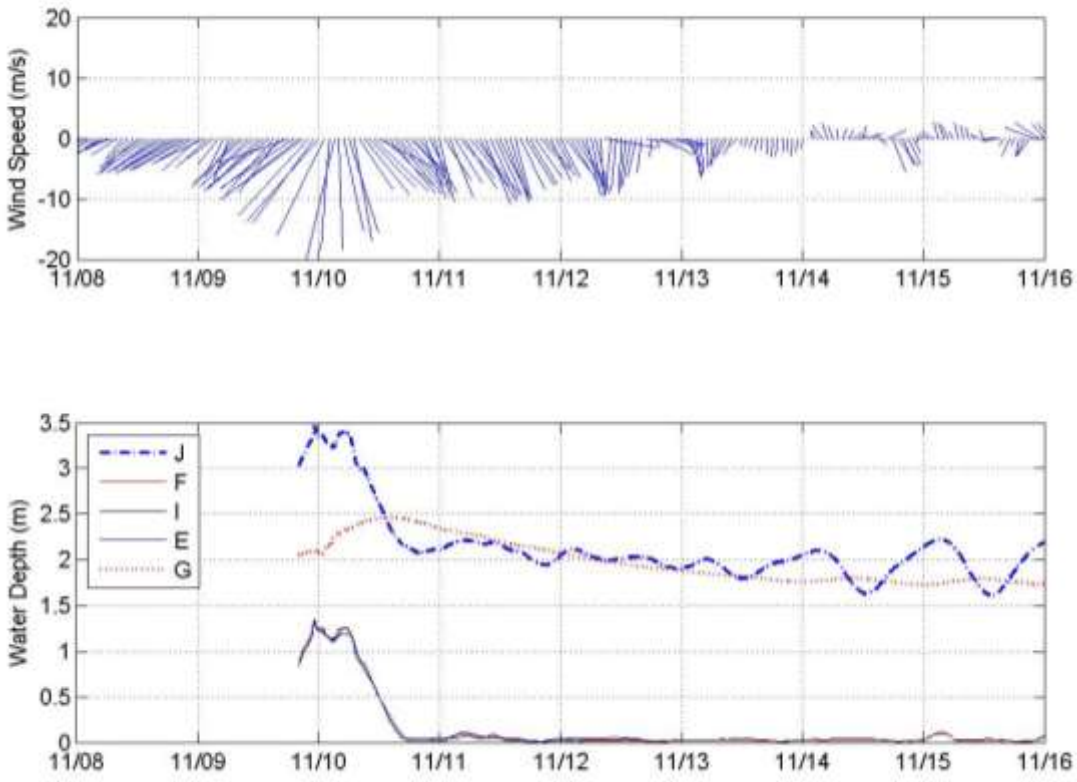

Fig. 4.30. Wind recoded at Shell Beach, LA NOAA station (SHBL1 No. 8761305) and water levels recorded during Tropical Storm Ida (November 2009).

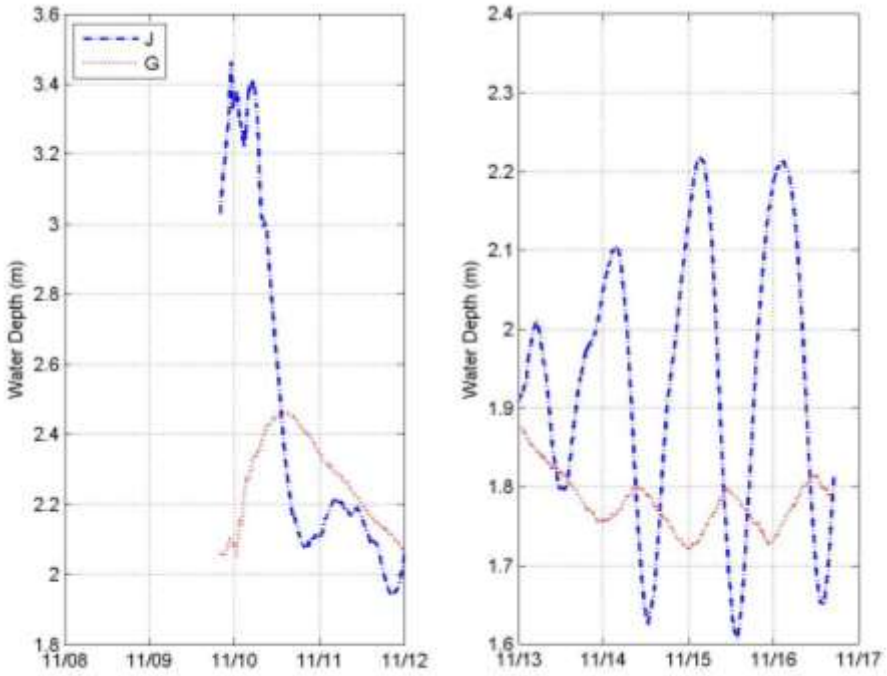

Fig. 4.31. Comparison of surge (left) and normal tide (right) peaks in open water (J) at the southern end and marsh (G) at the northern end of the basin recorded during Tropical Storm Ida (November 2009).

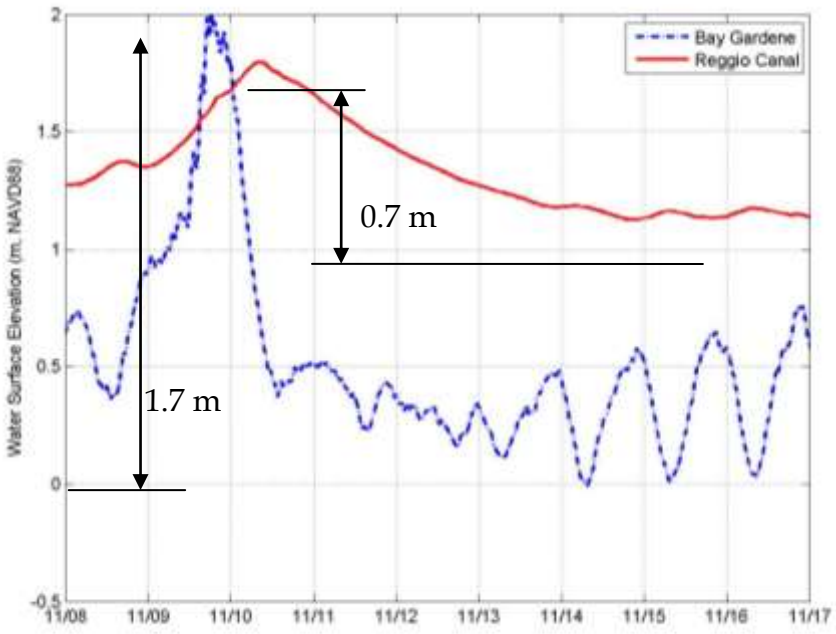

Fig. 4.32. Surge recorded at the USGS gages during Tropical Storm Ida (November 2009).

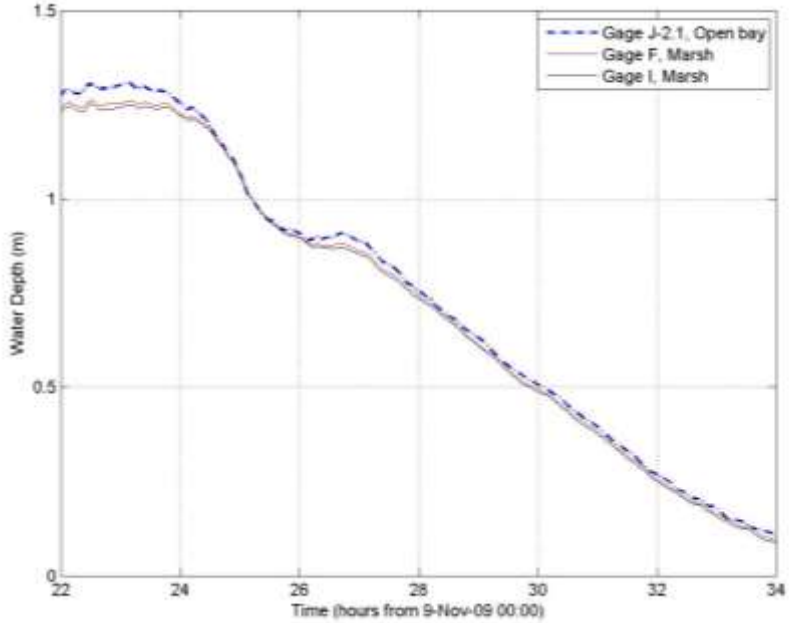

Fig. 4.33. Receding portion of the surge recorded during Tropical Storm Ida.

For each gage record, the rate at which the surge receded after the peak is examined further in Fig. 4.34. The figure shows how the rate of water level drop changed with respect to the prevailing water depth. From the peak to about 0.8 m depth, the rate of water level drop diminished rapidly. The rate of drop slowed down relatively during the depths 0.8 to 0.4 m. Below 0.4 m depth, the rate of water level drop decreased faster. This can be related to the characteristics of the vegetation canopy experienced by the receding waters. Above 0.8 m water depth, the vegetation was completely submerged and offered relatively smaller resistance to the flow. In water depth range of 0.8 to 0.4 m, vegetation was partially emergent and water started passing through flexible leafy upper portions of the vegetation without any significant change in the vegetation friction magnitude as suggested by somewhat uniform characteristics of the canopy structure. Below the water depth of 0.4 m, the vegetation became largely emergent and receding waters experienced stiff stalks of vegetation offering frictional resistance. This reduced the rate of water level drop relatively quickly. As noted before, one should also consider other simultaneous active forcing during this time and that is northerly wind. Wind speed reduced as the water dropped and its impact cannot be separated based on observed data sets.

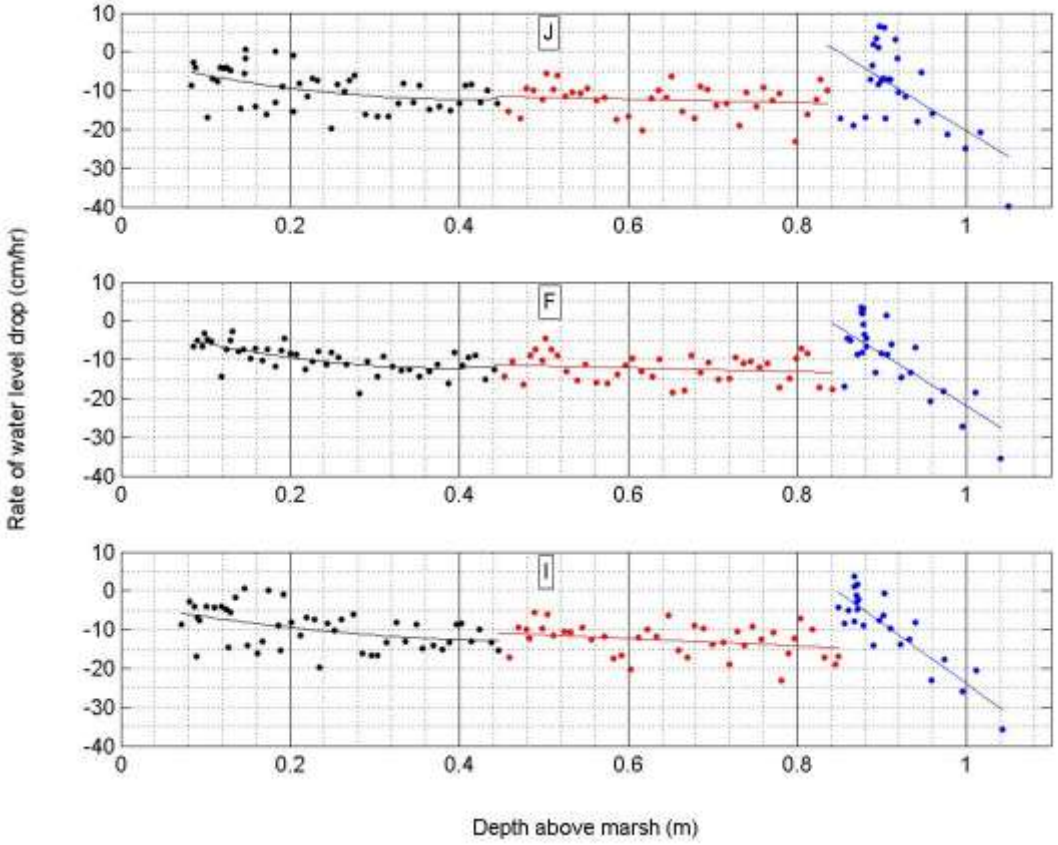

Fig. 4.34. Variation of rate of water level drop with depth during Tropical Storm Ida.

4.4.2 Wave Attenuation

The wave records collected during the hurricane and winter front deployments were analyzed using linear wave theory (e.g. Svendsen 2006). After adjusting for atmospheric pressure, pressure spectra were calculated for the 17 min duration pressure burst time series using standard procedures. Each burst was divided into 16 equal segments with 50% overlap. Each segment was linearly detrended, a Hanning window was applied, and the pressure spectrum was calculated using standard Fast Fourier Transform method. The spectral estimates from 31 overlapping segments were ensemble averaged to produce final spectral estimates.

4.4.2.1 **Wave environment in Breton Sound and Terrebonne Bay**

To measure the wave parameters travelling northwards to the experimental marsh site, an acoustic Doppler velocimeter, Sontek Triton-ADV, was deployed in the southern portion of the bay. As a first deployment, the ADV was placed in Breton Sound (Fig. 4.21). Although, no marsh wave measurements were carried out in this bay due to unavailability of the desired site, the ADV measurements show the nature of wave conditions in this bay.

Fig. 4.35 shows time series of measured significant wave height and peak period over the data collection period. For reference, data from wave gage CSI-16 are plotted to show the simultaneous wave conditions outside the bay. CSI-16 has a considerable open water fetch from northeast all the way to the southwest. Winds in these directions result in significant waves at this site. To the north of CSI-16 lies a barrier island chain, so not all the wave energy is transported into the northerly marshes. In fact, scatter plots of significant wave height (H_{mo}) and peak perod (T_p) in Fig. 4.36 indicate that there is no strong correlation between the wave environment outside the bay (CSI-16) and inside it (ADV). However, some swell energy does propagate inside the bay. This can be seen in the bottom panel of Fig. 4.35 with dark reddish brown areas in the low frequency band. The T_p scatter plot (Fig. 4.36) also shows correlation at higher peak periods.

As stated previously, the research team was not granted permission by the landowners for the field deployment site in Breton Sound, so the ADV was moved to Terrebonne Bay. The Terrebonne Bay deployment was of much longer duration as this where the marsh site is located. Figs. 4.37 and 4.38 show wave parameters collected during the years 2009 and 2010, respectively, and Fig. 4.39 shows the scatter plot.

Terrebonne Bay is more enclosed bay than Breton Sound. The south and southeast fetch is not as extensive as in Breton Sound. The ADV location had limited fetch from northeast to southeast. However, the ADV location is directly to the north of Cat Island Pass which provides a break in the barrier island chain. This allows low energy swells to propagate northwards in the bay.

This is the first study to measure and document the relatively long term wave environment inside a Louisiana bay. It was noted that during non-tropical conditions, the wave heights generally stay below 0.5 m and mostly around 20 cm. The environment is dominated by local seas with low energy swells from the Gulf of Mexico.

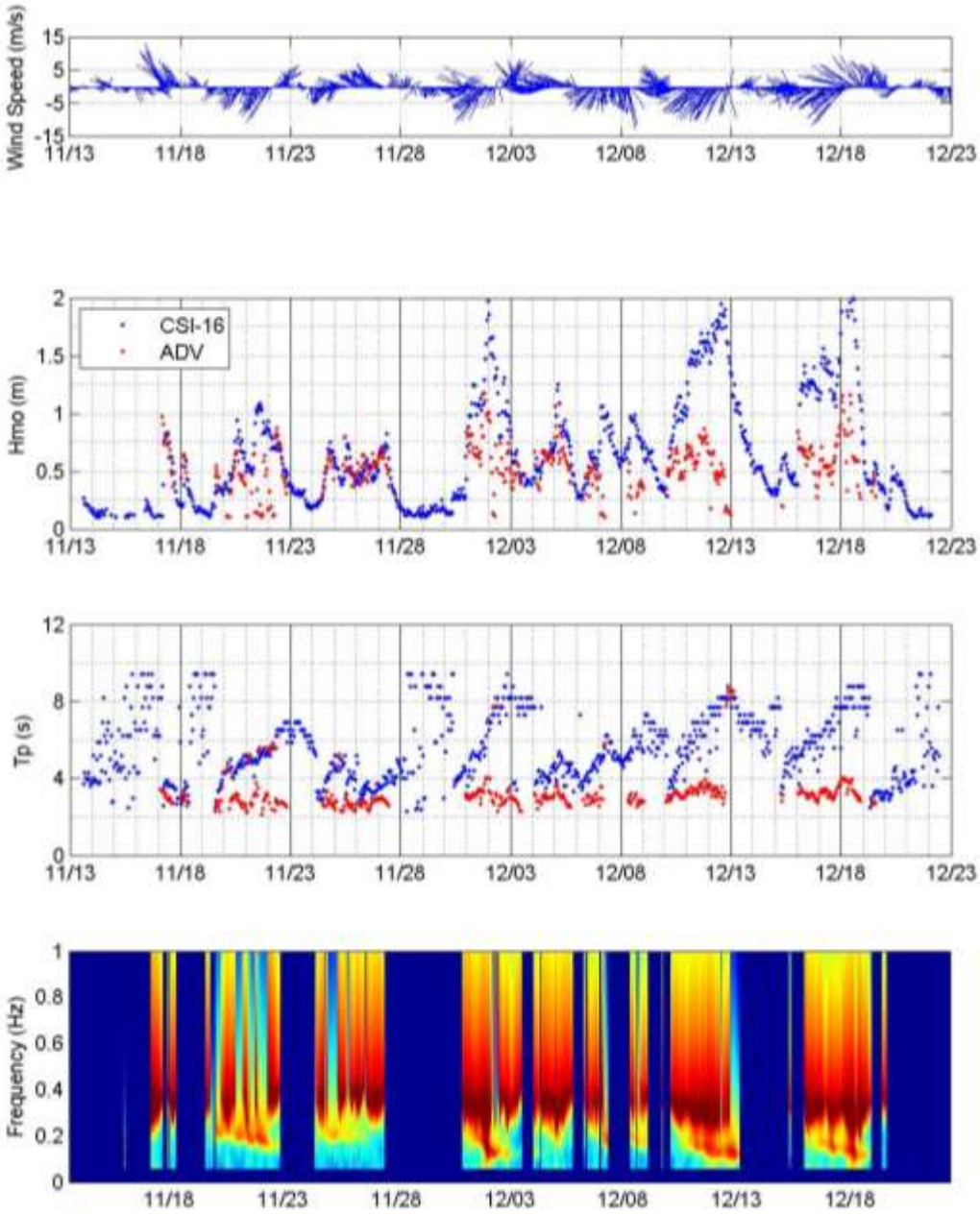

Fig. 4.35. Measured wave heights and periods at ADV and CSI-16 in Breton Sound (2009). Bottom panel shows wave energy spectra time series at ADV.

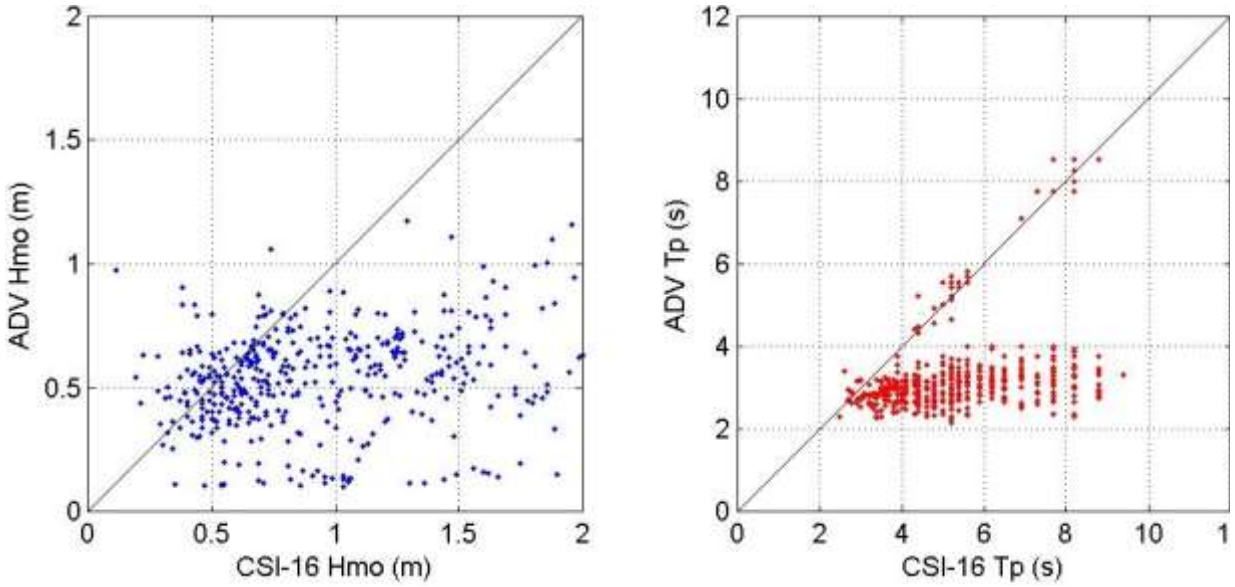

Fig. 4.36. Scatter plots of measured wave heights and periods at ADV and CSI-16 in Breton Sound.

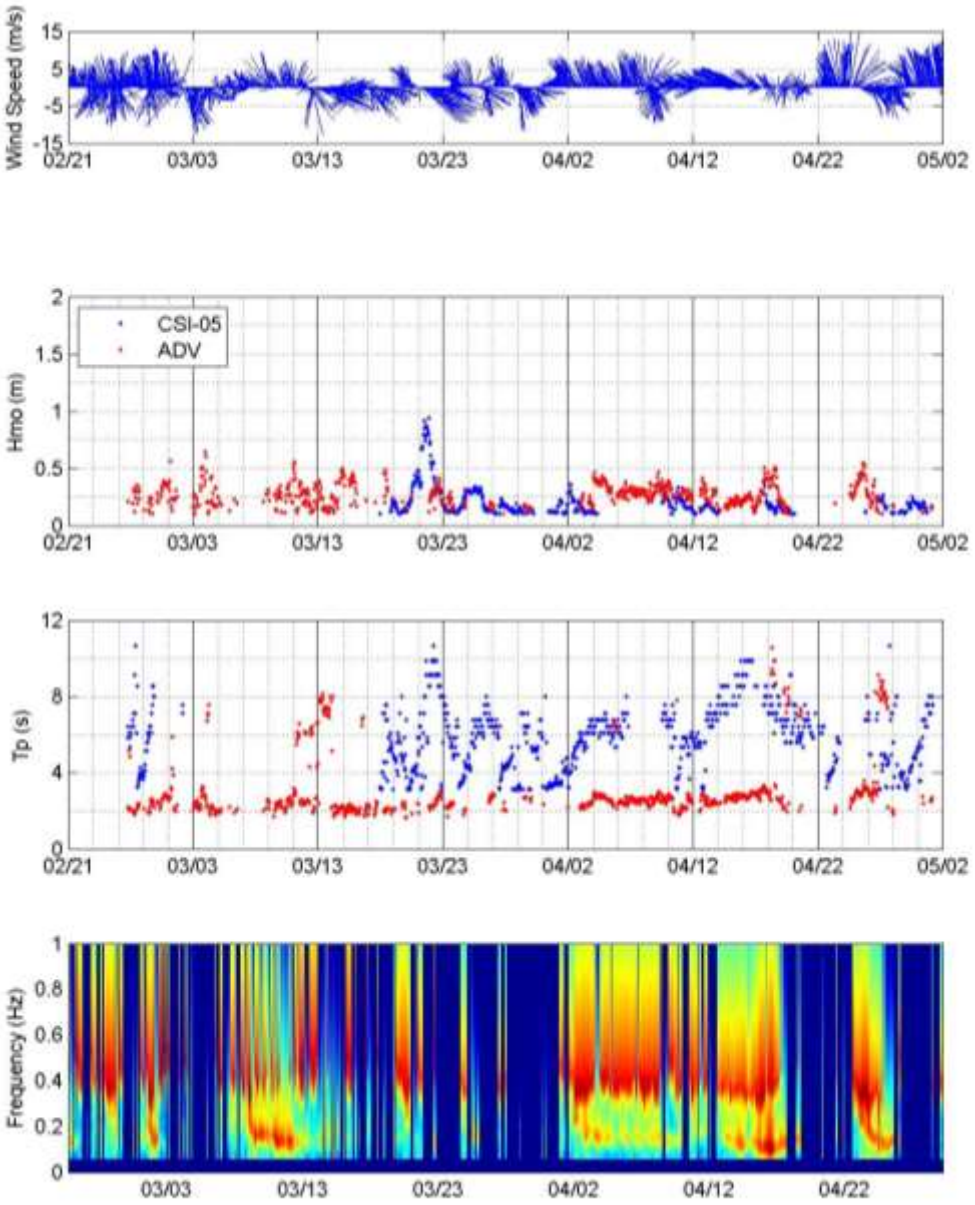

Fig. 4.37. Measured wave heights and periods at ADV and CSI-05 in Terrebonne Bay (2009). Bottom panel shows wave energy spectra time series at ADV.

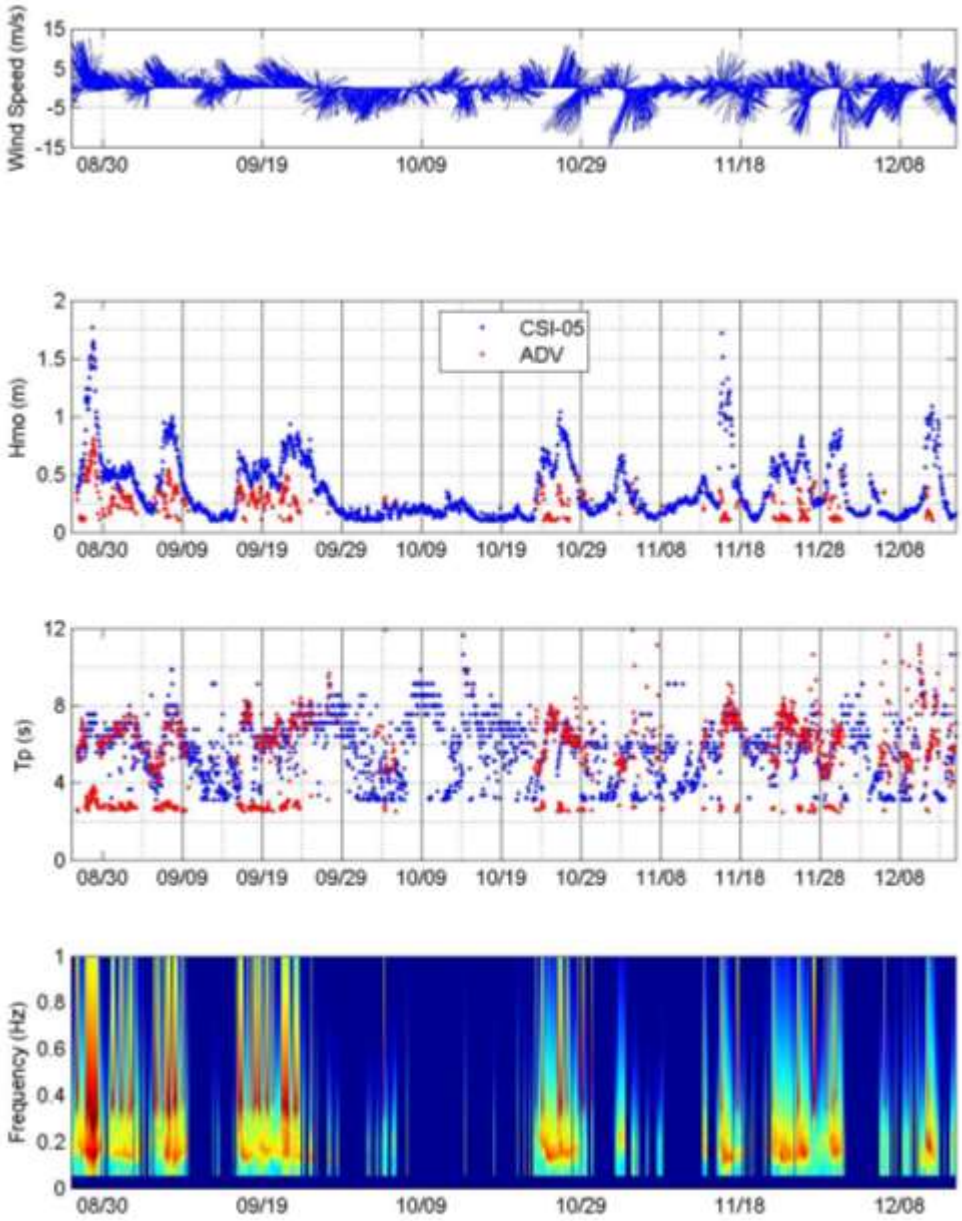

Fig. 4.38. Measured wave heights and periods at ADV and CSI-05 in Terrebonne Bay (2010).). Bottom panel shows wave energy spectra time series at ADV.

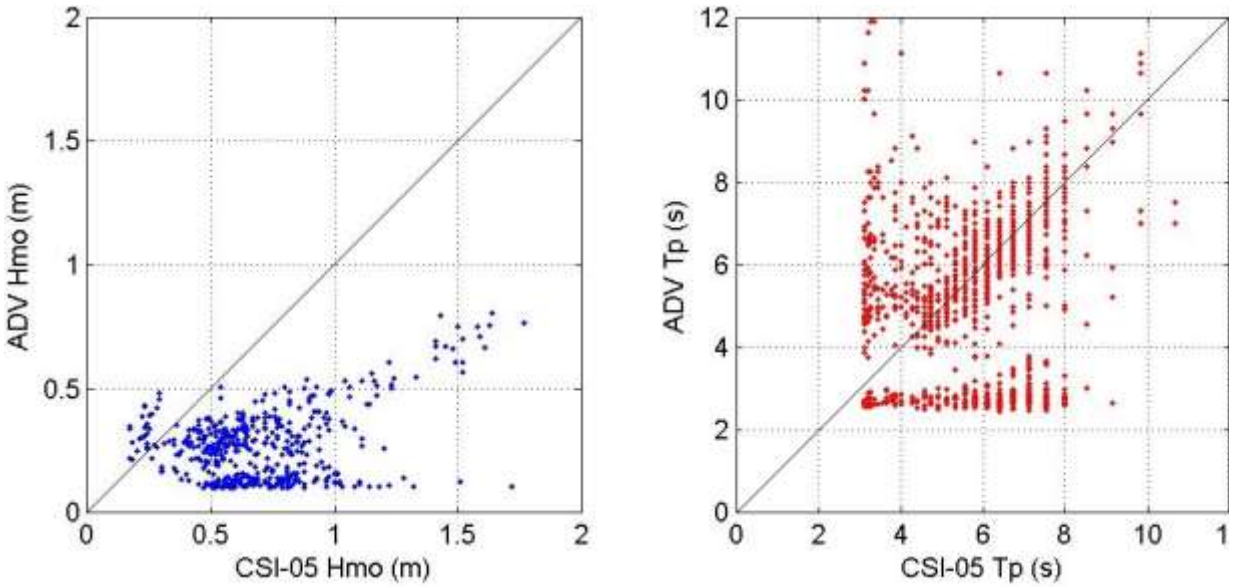

Fig. 4.39. Scatter plots of measured wave heights and periods at ADV and CSI-05 in Terrebonne Bay.

4.4.2.2 **Winter front wave attenuation**

An array of five gages was deployed on the salt-marsh in Terrebonne Bay for approximately 7 months during 2010 (Fig. 4.13) along two different transects. The first transect, NW-SE, was oriented in the northwest-southeast direction (Fig. 4.23). It was deployed from February 23, 2010 through May 6, 2010 at which point the marsh was found to be severely eroded loosening Gage M1 to sink in the open water. A Seagauge was also deployed 6.1 m (20 ft) away in the open water in front of the marsh. The entire setup was serviced on March 30, 2010 and data was downloaded. Fig. 4.40 shows weekly average of the Seagage tide record in comparison with tidal record at LUMCON Terrebonne Bay station. LUMCON data is shifted to align with the Seagauge record. Evidence of erosion can be seen in the records deviating from April 1 onwards. On March 31, Seagauge was removed for data download and attached to the pole at the same location.

During this deployment, gages M3, M4 and M5 did not get inundated. Gages M1 and M2 were inundated on several instances as shown in Fig. 4.41. Sometime around mid-April, an estimated 1.8 m (6 ft) of marsh edge was washed off leaving gage M1 in the open water and making M2 more prone to inundation. Therefore, M2 shows more spikes during the end of April and May. Notice the concurrent high tides and strong south wind.

When intact in position, gages M1 and M2 were inundated to a depth less than 20 cm and no measurable waves were recorded. At the end of April and during May, after being washed off, gage M2 was inundated to a depth of about 40 cm.

This field campaign showed the dynamic nature of the Louisiana wetland landscape even over a short period of a couple of months. During February and March, when gage M1 was intact, water depths seldom rose over 15 cm. Gage M2 experienced minor inundation on some of these events. However, no significant flooding and associated waves were present to provide any useful datasets for the purpose of this project. Starting from April the winds seem to be persistent from the south with a strong period in the third week of April. Wave generated during this sustained wind period along with a strong third week

wind, appears to have eroded marsh gradually. Although, not the primary purpose of the present study, this phenomenon shows how even without any significant inundation a constant wave action can severly cause erosion and wetland loss within a short period.

The marsh array was pulled out in the first week of May, 2010 and redeployed at the end of July-2010 on a 183 m (600 ft) long North-South transect at the start of the hurricane season. The longer configuration was aimed at capturing tropical storm data. Measurements during this deployment are shown in Fig. 4.42. The wind and the tidal water level record is from LUMCON Marine Center monitoring station.

The marsh gage M1 and M2 were inundated on several occasions with M1 water depths mostly at or below 20 cm. On a few instances depths close to 40 cm were recorded. Except the event during the last week of August, the wave signal was too weak to be able to distinguish from the noise of the pressure transducers that make up these gages. During the August event, wave signal was weak, however, it was sufficient to compute peak time periods of 3-4 seconds. During this short period, sustained southeast winds pushed water into the bay and onto marsh.

Marsh gage M2, which is 6.3 m (25 ft) northwards of M1 shows some inundation. However, based on visual observations, and bathymetry, it should be noted that this is not a continuous sheet of water from M1. A small (~10 cm) ridge separates M1 and M2. Water pushed over this relatively higher elevation ponds in the vicinity of M2.

To correct the persistent problems with signal in the marsh array gages, they were brought back to FSG workshop on campus and were deployed after correcting the issues. The deployment was over a much shorter distance (Fig. 4.27). Gage M0 was deployed in the water just to the south of marsh edge. On the marsh, only gage M1 was experienced waves and M2 recorded sporadic minor inundation during this deployment.

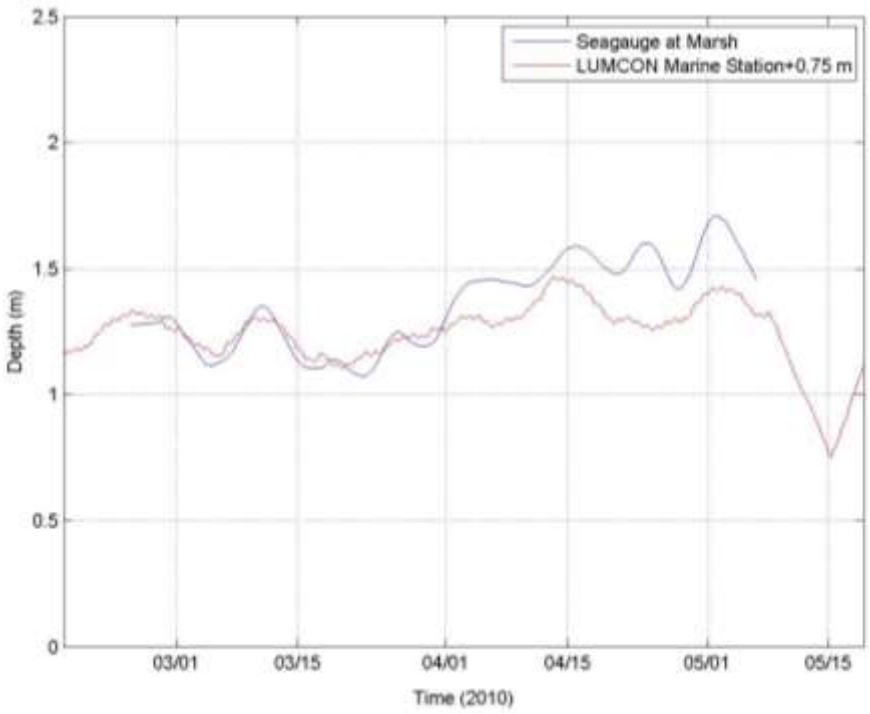

Fig. 4.40. Comparison of tidal records at Seagauge and LUMCON Terrebonne Bay station.

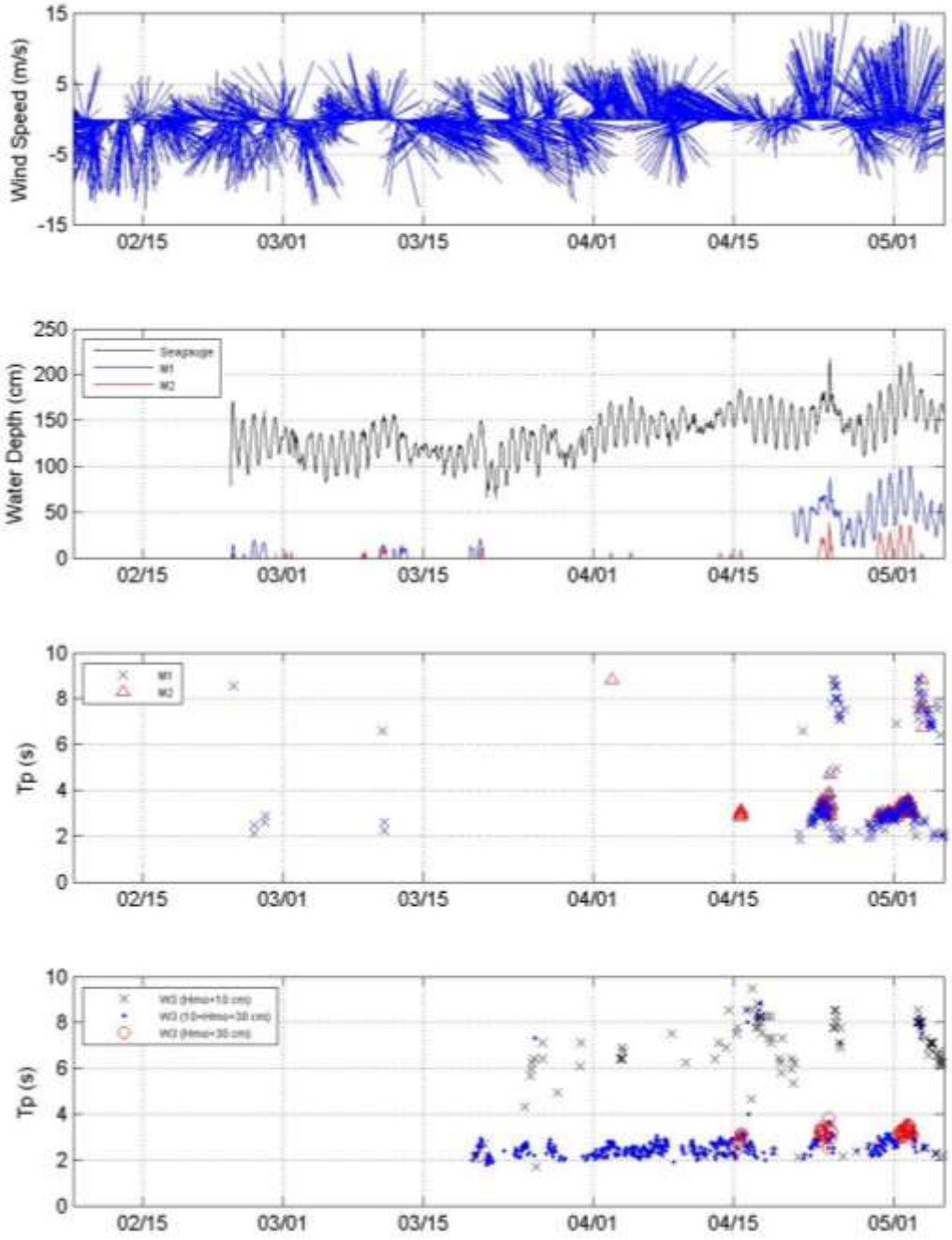

Fig. 4.41. Measurements along the NW-SE marsh array (2010).

During this deployment, the waves approaching the marsh were generally in the 10-25 cm range with corresponding peak periods of 2-3 sec (Gage M0). The higher wave heights coincided with the high tide accompanied by higher southerly winds. When the tide was sufficiently high, some of the high waves propagated on to the marsh and were recorded at gage M1 which is located at the water's edge of the marsh. Since there was no sufficient inundation water depth, the wave heights recorded at M1 were 5-7 cm. Peak time periods of

these waves virtually remained unchanged. The wave propagation over marsh was in the form of uprush and downrush. On a few occasions, the waves travelled over the marsh at least 8 feet (2.4 m) and minor inundation at gage M2 was recorded. No measureable wave signal could be retrieved at this location.

Out of all the deployments during the entire research study period, only this deployment provided an error-free signal at the marsh sensors enabling calculations of the wave height as reported in Fig. 4.43.

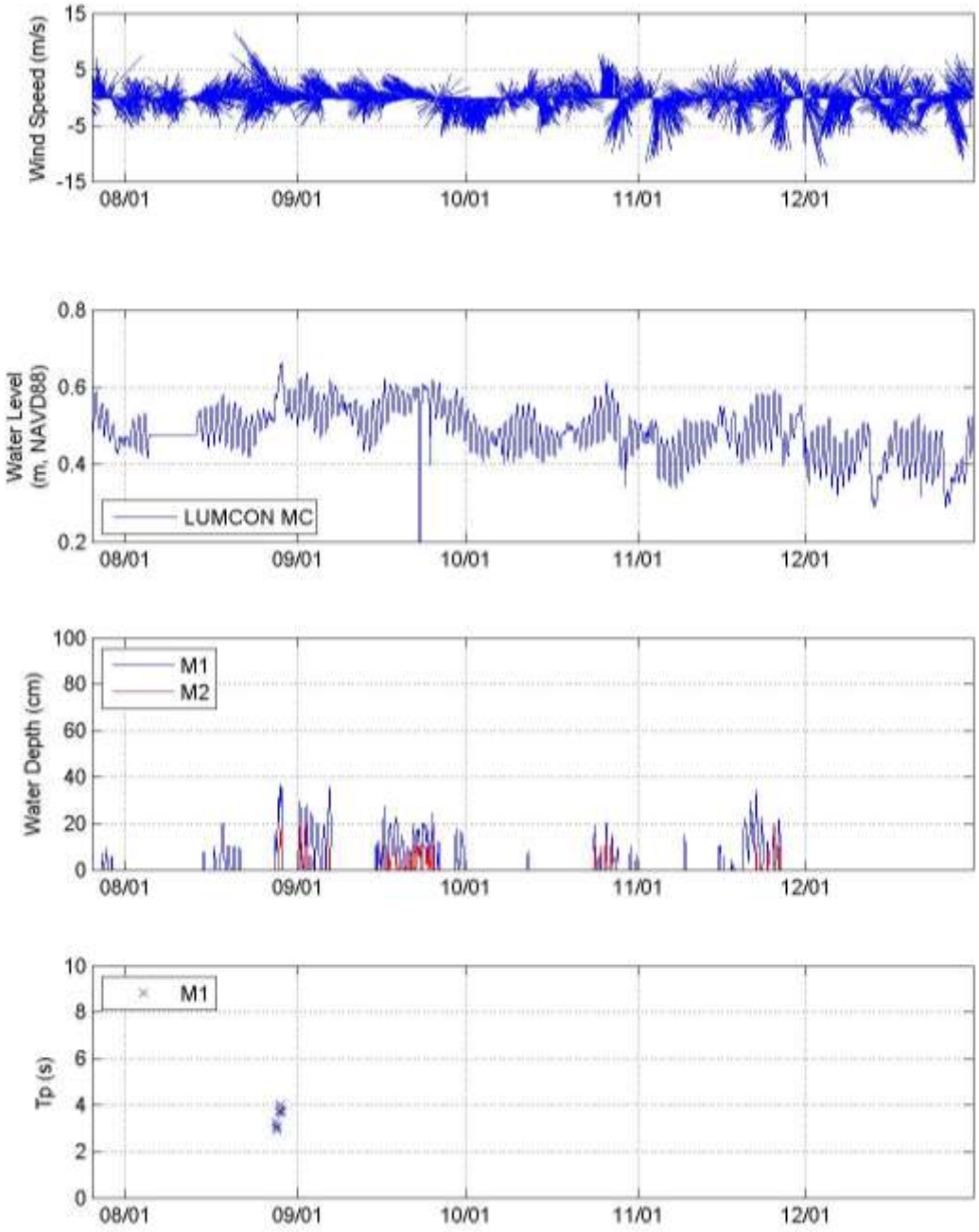

Fig. 4.42. Measurements along the N-S marsh array (2010).

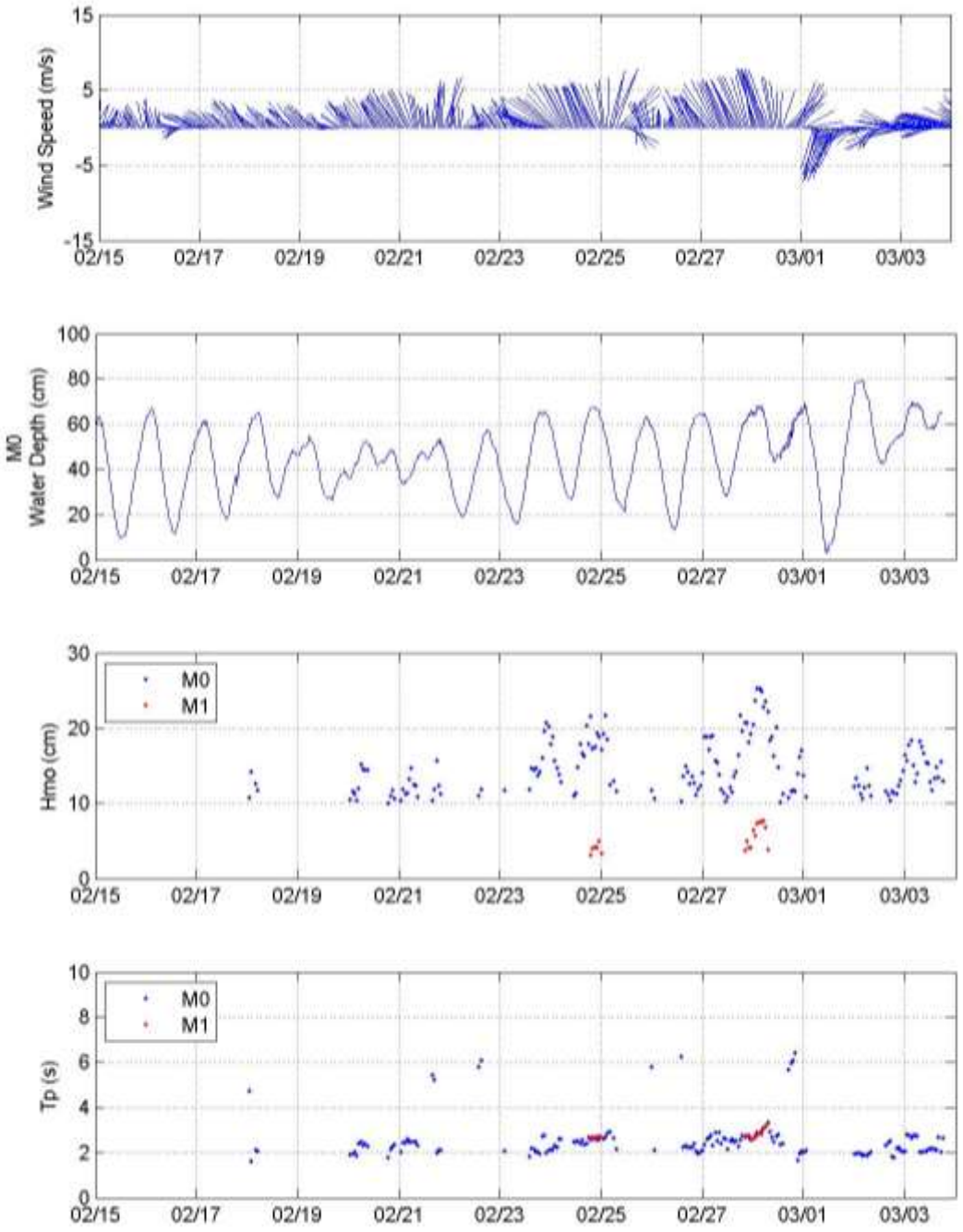

Fig. 4.43. Measurements from the marsh array deployment over a shorter stretch during Feb-Mar, 2011 (North- South alignment).

4.4.2.3 **Tropical storm wave attenuation**

To investigate waves in open water and over wetland during TS Ida, continuous pressure recorded at gages J, F and I were analyzed with the standard spectral technique. The deployment locations of these gages are shown in Figs. 4.15 and 4.16. Gages J, F and I are in the region where open water area starts to the south of wetlands. Wave parameters at these 3 gages are compared in Fig. 4.44.

The gages were on the west, weaker, side of the storm. Though the wetlands experienced surge producing water depths over a meter, the winds were mostly from north and northeast during the recording period, i.e. from wetlands towards open water. In the open water, at about 3 m depth, highest waves close to 0.45 m were recorded at gage J, in spite of the short fetch. As the surge rose, gage J experienced waves above 0.3 m, peaking up to 0.45 m. As the surge started receding around November 9, 2009, 1700 hours, wave heights started diminishing gradually. Around this time winds started gradually shifting out of east. The wave energy moved from higher to lower frequencies as evidenced by gradually increasing peak wave periods.

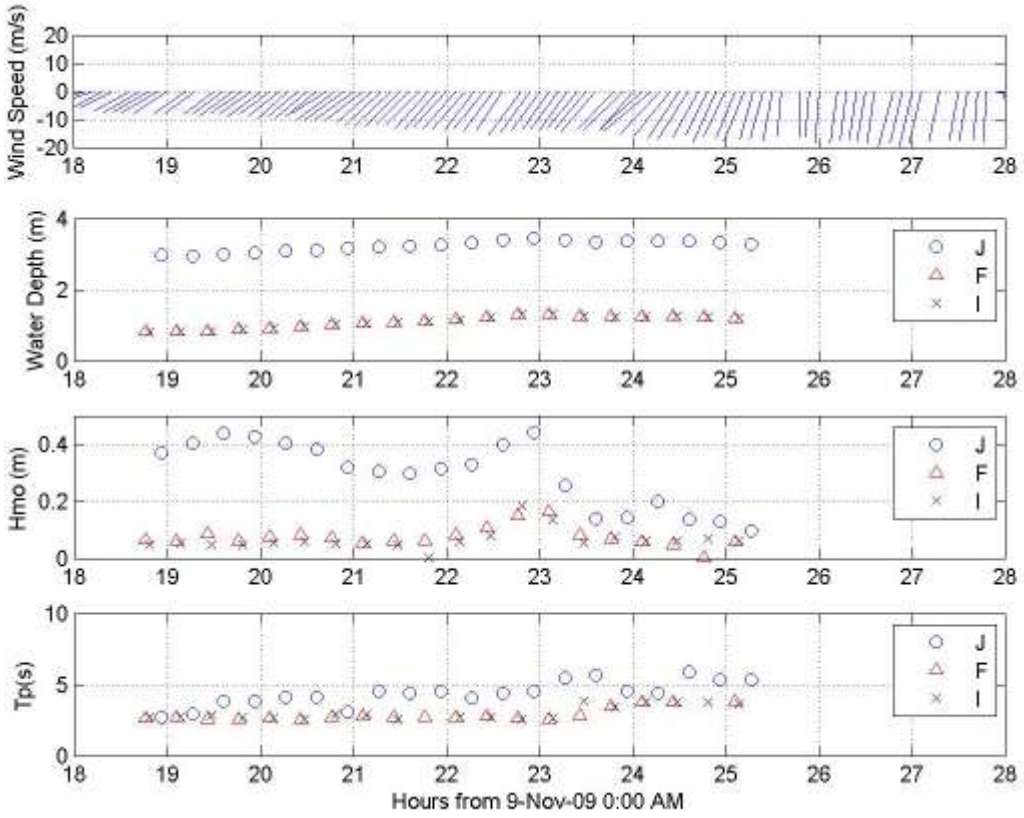

Fig. 4.44. Wave Measurements during Tropical Storm Ida (Nov. 2009).

Trends similar to those observed in open water were recorded at the gages F and E on wetlands. While open water waves peaked at 0.45 m, on the wetlands, wave heights did not exceed 0.2 m. As the surge receded, wave energy moved from higher to lower frequencies.

Owing to the seaward wind, open water waves propagating from open water over to the wetlands were not observed, the data did show that the highest wave heights present in the

marsh were below 0.2 m. This finding is in agreement with waves in wetlands measured during Hurricane Gustav (Smith et al. 2010). These waves indicated a peak periods around 2 sec in 3 m depth of water.

4.5 Summary

The primary goal of this study was to provide field datasets of surge and wave attenuation by wetland vegetation for validation of numerical models and to develop improved estimates of frictional resistance algorithms and coefficients. An additional goal was to develop guidance that characterizes the attenuation of surge and waves as a function of vegetation type, density, and height.

To this end, two field data collection programs were planned and implemented. In the first program, pressure sensor gages were deployed during Tropical Storm Ida in 2009 and Tropical Storm Bonnie in 2010. The study period did not see any other major tropical storm and no opportunities to fully implement the plan became available. Because the storm tracks of Ida and Bonnie fell much eastward of the major marsh areas, the data collected was useful but in a limited range of wave heights and peak periods. Surge levels recorded during Ida showed that surge receded in distinct speed that could be related to the depth above the marsh floor. At higher depths, vegetation was fully submerged and offered relatively lower frictional resistance. At medium depths, vegetation was emergent and receding waters experienced resistance from the leafy flexible canopy producing relatively stable receding rate. When water depths lowered further, it encountered stiff stalks of the marsh vegetation that offered relatively higher friction diminishing water level drop relatively rapidly. Northerly winds also made some contribution to this phenomenon, but those contributions cannot be isolated based on the available measurements only.

Successful wave measurements were carried out during TS Ida. At the peak of the storm and associated surge, wave heights of 45 cm with peak period of 4-5 sec were measured in open water depths of 3 m in the vicinity of the marsh. Most of these were local seas. Simultaneously recorded waves in the marsh were less than 20 cm with a peak periods around 2-3 sec. Due to the seaward wind direction, waves measured in the marsh were not the ones coming from the open water measurements; the data showed that significant waves did not exist in the inundated vegetation even at the depth of over 1 m.

The second field program was designed to collect parameters of the waves through marsh vegetation during winter storms. The setup in Terrebonne Bay consisted of an ADV system in the open water providing the incoming wave environment and a marsh site with a linear array of 5 wave gages. Parallel to this array, another set of 3 gages were deployed in the adjacent open water for comparison. The ADV collected a useful data set over several months providing, for the first time, information on the wave environment inside this bay with rapidly eroding marshes. During the study period, the wave heights were generally found to be below 50 cm and mostly around 20 cm. The environment is dominated by local seas; however, persistent low energy swells from the Gulf were recorded inside the bay. Further north in the bay, the marsh gages also recorded swells. The data suggests that the potential for intrusion of increased wave energy from the Gulf exists if the barrier island chain is deteriorated.

The marsh gage array, unfortunately, did not record any winter front waves strong enough to measure. The primary reason for this is the low topographic elevation of the marsh edge. On rare occasions, the water level reached high enough to produce measurable

depths (10-20 cm) over the gages; however, the gage records were found to have substantial noise levels compared to the high energy spectral peaks. Whatever measurements were recorded at the marsh gage right at the edge indicated an uprush and downrush movement similar to that in swash zones. During one period (April 2010) when winds were strong, sustained and in alignment with the array (NW-SE) on the relatively lower region of the marsh edge, the erosion was so rapid that the marsh gage became detached resulting in loss of data collection opportunity.

4.6 Lessons Learned

Current scientific literature provides very little data on wave measurements through marshes. For the northern Gulf coast, no such data exists in spite of some efforts such as those documented by Smith et al. (2010), and it is for a reason. As experienced firsthand by this research team, such an endeavor is fraught with many challenges. They pertain to the scarcity of weather windows, unique physical environment, logistics, instrumentation, access issues, scheduling and budgetary constraints.

Selecting a suitable field site is at the foundation of such a unique data collection project. Successful data collection with waves passing through marsh vegetation requires the confluence of several opportune factors. The ambient water level needs to be high enough to produce marsh inundation of at least 30-50 cm with simultaneous southerly winds strong enough to produce waves. Further, when this happens, the marsh needs to have a healthy stand of uniform vegetation species as opposed to an assortment of weeds, creepers and open patches. As we found over the past 2 years, such a situation is difficult to come by at least in the coastal marshes of Louisiana and Mississippi for a couple of reasons. First is the microtidal environment of the region. Under normal meteorological conditions, an average tidal range of about 0.3 m does not inundate marshes to the level useful for the research goals, so one has to depend on the occurrence of sustained winds along with high tide. Moreover, to improve chances of data capture, one has to look for high tide during spring tides. As noted by the research team during several field work and reconnaissance trips, marsh areas with breaking waves passing through do exist, albeit very few and only when all factors mentioned above coincide. However, due to the constant battering by the waves, these selective marshes typically do not support dense healthy uniform vegetation. Over time, the vegetation gets decimated by the constant wave action and subsequently the marsh erodes away. The waves move on to batter the next level of vegetation and the process continues. These issues prevent researchers from choosing a "fixed" site for "long-term" deployment. The plan needs to be flexible to allow shorter deployments, e.g. 2-3 days during spring tides or during high sustained winds so that the wave gages can be moved to suitable location. Taking into account the rarity of such events, a thought should be given to making use of northerly high winds during the fronts to increase data collection opportunities. Unfortunately, northerly winds push the water out of the bays, making these weather windows less desirable. However, sites such as the south shore of Lake Pontchartrain could be promising. During high tides, this region may provide useful field sites, under northerly winds.

It is important to identify an array of field sites, because in most cases availability of the site is contingent upon permission to access it from the land owners. Large parts of the Louisiana and Mississippi Gulf coast marshes are owned by numerous private landowners who may not have standard access agreements in place nor may they be willing to permit

access. It can be very difficult to locate the landowner and even after that the access permission paperwork can take an excessively long time. This can detrimentally affect data collection due to lost weather windows, seasons and delay timely completion of the project.

Selecting appropriate wave gages is critical to the success of wave data collection. For winter fronts scenarios, it is unlikely one can get waves over 30 cm in the marsh on the Gulf coast. In this setting, the waves on the marsh tend to be nonlinear and use of pressure sensors becomes problematic (Wang et al. 1986, Tsai et al. 2001). The problem arises because, to derive water levels from a measured pressure record, a transfer function based on the linear wave theory is applied as standard practice. This introduces large errors in the estimates of wave height. Considering the anticipated wave environment, a wave staff gage is recommended with proper mounting to reduce movement of the staff.

Selecting sampling burst frequency high enough to resolve wave periods to be studied is essential. Based on the collected data, the anticipated wave periods in the marsh would be 2-3 sec. To be able to have the wave spectrum peak frequency at least an order of magnitude away from the noise floor, a sampling frequency of at least 8 Hz is recommended.

If the wave gages are built in-house from components, it is extremely important to test all features of the system. Sometimes a gage may be able to measure steady water depth correctly, but it may not correctly record a fluctuating water level as in a wave form. The system has to be tested in wave tank with known input waves. A range of wave heights and periods need to be tested to ensure that there is enough excitation voltage in the system to produce the entire output signal without any clipping of the crests or troughs. It is important to carry such tests during different times of the day and on different days to examine the influence of ambient temperature, pressure and resulting drift. The instruments need to be carefully calibrated in the beginning and the calibration should be checked periodically.

As stated earlier, collecting wave parameters in vegetation requires targeted, customized deployment in terms of site and weather window. This requires availability of field crew and boat on short notice. It also means several field trips that may require overnight stay near the site. A typical schedule of monthly field visits will not suffice. This fact should be considered while planning budget and schedule for such research activity.

The Louisiana and Mississippi coastal areas experience high boat traffic related to the recreational and commercial fishing and the oil and gas industries. Such traffic increases the risk of damage to the deployed instrumentation. During the present study, this risk was increased highly due to the traffic responding to the BP oil spill resulting in damage and/or loss of three sensors. While such incidents cannot be completely prevented, subsurface deployment for open water is highly recommended on this coast.

Future similar research will be well served by consideration of the aforementioned factors. Since it takes substantial personnel and financial resources to plan, travel and spend time at these remote sites, it may be prudent to support simultaneous related research activities at these sites. For example, the research team observed that the marsh where the wave gages were deployed eroded rapidly over a few weeks. In such cases, systematic measurements of erosion rates would be a useful effort.

5. FIELD INVESTIGATIONS OF COASTAL MARSH VEGETATION AND SOIL PROPERTIES

It is generally acknowledged that vegetation in wetlands, coastal fringes, and stream floodplains can attenuate surge and wave energy and affect sediment dynamics (Baumann et al. 1984, Chapman 1960, Cronk and Fennessy 2001, Mitsch and Gosselink 2009, Nixon and Oviatt 1973). However, field datasets on coastal vegetation type, density and height that could improve quantification of wave attenuation by wetland vegetation received little attention. Therefore, coastal botanical and site characteristics that could affect the attenuation of coastal surges and waves need to be studied more because integrating field datasets into models of wave attenuation by wetland vegetation would be an invaluable contribution to salt marsh restoration and conservation projects (Asano 2006, Augustin et al. 2009, Feagin et al. 2009). The field studies described in this chapter served this purpose.

Two field campaign programs were carried out by the LSU team and the UM-Biology team in several sites along the Louisiana and Mississippi Gulf Coast. The campaign conducted by the LSU team focused more on the biomechanical properties such as stiffness of *Spartina alterniflora, Juncus roemarianus* and several other species, while the campaign by the UM-Biology team focused more on the growth forms and productivities of *Spartina alterniflora* and *Juncus roemarianus*. Both campaigns measured the related site characteristics, including soil properties.

5.1 Biomechanical Properties of *S. alterniflora* and *J. roemarianus*

The objective of this subtask was to study and understand the biomechanical properties of saltwater marsh vegetation on the northern Gulf of Mexico coast, with a special focus on *Spartina alterniflora* and *Juncus roemarianus*. With this base of information, the parameterization of vegetation biomechanical properties can be used to model the attenuation of waves and storm surges as they progress across salt marsh areas.

5.1.1 Research Sites

The main site of study for vegetation biomechanical property measurements is located in Terrebonne Bay area, 4 miles southeast of Louisiana Universities Marine Consortium (LUMCON) in Cocodrie, Louisiana (Fig. 5.1). After several preliminary site trips and surveys of the Louisiana coastal wetlands, the site was chosen from several possible locations in the Terrebonne Bay and Breton Sound areas. This final chosen site proved ideal due to the large open fetch in the southeast direction. Also, the vegetation at this site is comprised almost entirely of *Spartina alterniflora*, which is the main vegetation of focus in this study. Due to its location and orientation, the site is very susceptible to erosion and is eroding quickly. Other team members collected wave data on the marshes during storm events as described in Chapter 4, which can be used to correlate the hydrodynamics to the biomechanics of salt marshes.

In addition to this main site, data have also been collected on other vegetation species, including *Juncus roemarianus, Spartina patens,* and *Scirpus robustus* from Graveline Bayou, MS and Breton Sound and Barataria Bay, LA in hopes of expanding the scope of this study. Table 5.1 shows the number of sample trips and vegetation species measured.

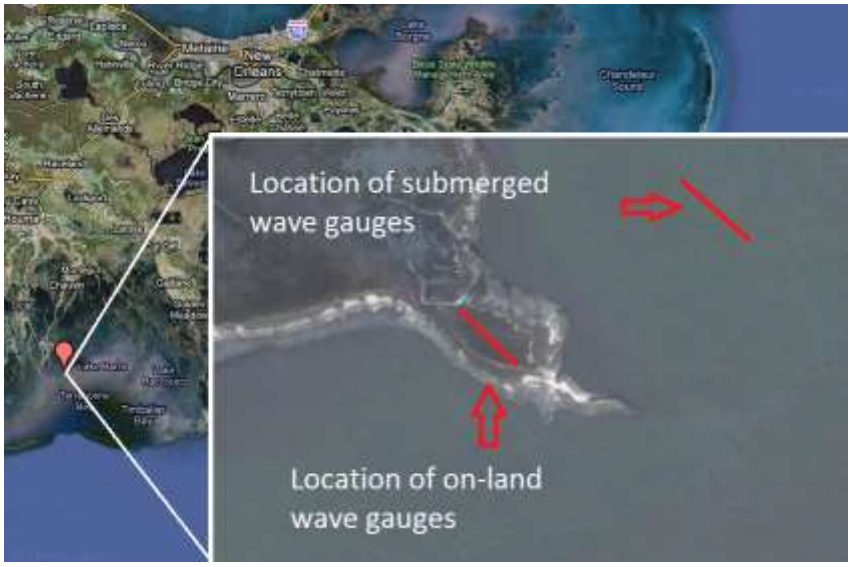

Fig. 5.1. Aerial view of the main site (Google Maps, Imagery Date: 2/12/2006).

Table 5.1. Summary of vegetation property sample trips

Trip	Date	Area	Location	Tested Species[a]	# of Plants	# of Board Drop Tests[b]
1	8/13/2009	Breton Sound	N29°38.065,W89°30.027′	SA	15	2
2	12/22/2009	Terrebonne Bay	N29°11.603',W90°36.794'	SA	15	3
3	4/8/2010	Terrebonne Bay	N29°13.415, W90°36.340	SA	20	6
4	5/12/2010	Graveline Bayou	N30°22.051',W88°41.082'	JR	60	N/A
5	6/19/2010	Breton Sound	N29°39.870',W89°36.611'	SA, JR	30	N/A
6	7/10/2010	Breton Sound	N29°40.069',W89°37.200' N29°42.249',W89°38.683'	SA, JR, SP	60	N/A
7	7/31/2010	Breton Sound	N29°39.820',W89°36.575 N29°42.402',W89°38.473 N29°42.570',W89°40.863	SA, JR, SP	90	6
8	8/20/2010	Barataria Bay	N29°27.785',W89°58.190'	SA, SR	25	4
9	12/2/2010	Terrebonne Bay	N29°13.415, W90°36.340	SA	30	4
10	12/14/2010	Breton Sound	N29°42.402',W89°38.473 N29°42.570',W89°40.863 N29°42.249',W89°38.683	SP	45	N/A

[a]: SA = *Spartina alternaflora*, SP = *Spartina patens*, SR = *Scirpus robustus*, JR = *Juncus roemarianus*.
[b]: Plant population density measurement was also conducted for each board drop test.

5.1.2 Vegetation Bending Test

The method to measure the bending stiffness of vegetation was adapted from the work done by Freeman et al. (2000), which was used to investigate the effects of vegetation, particularly ground cover plants, small trees and shrubs, on flow resistance. Fig. 5.2 shows the plant stiffness measuring tool, and Fig. 5.3 shows the field stiffness measurement using

spring force gages. The tool is made from yard sticks (Fig. 5.2a) to measure the vegetation height and indicate a 45° angle side to align the vegetation during the bending test. A handheld spring gage or a digital load cell is used to measure the pulling force (Fig. 5.3). The measurement procedure is described below.

Plants were randomly selected over each study site during a sampling trip. First, the total plant height and stem height were measured using the tool shown in Fig. 5.2(a). A binder clip was attached to the stem of the plant at half of the stem height. The handheld spring gage or digital load cell was connected to the binder clip. The plant was pulled on a horizontal line to a 45° angle with the horizontal plane as shown in Figs. 5.2b and 5.2c. Accurate 45° angle pulls were achieved by pulling the plant parallel with a member of the plant measuring tool which was mounted at a 45° angle to the base (Fig. 5.3). The bending force was then measured using the spring gage or digital load cell. The plant was cut and brought back laboratory to measure the diameter and other parameters. The plant sampled was assigned a number within a dataset. In the laboratory, the stem diameter was measured at ¼ up from the base. Redundant measurements of similar plants (about 15) were made to address variation of stiffness for plants of the same dimensions and species. The average parameters of the 15 plants composed a data set.

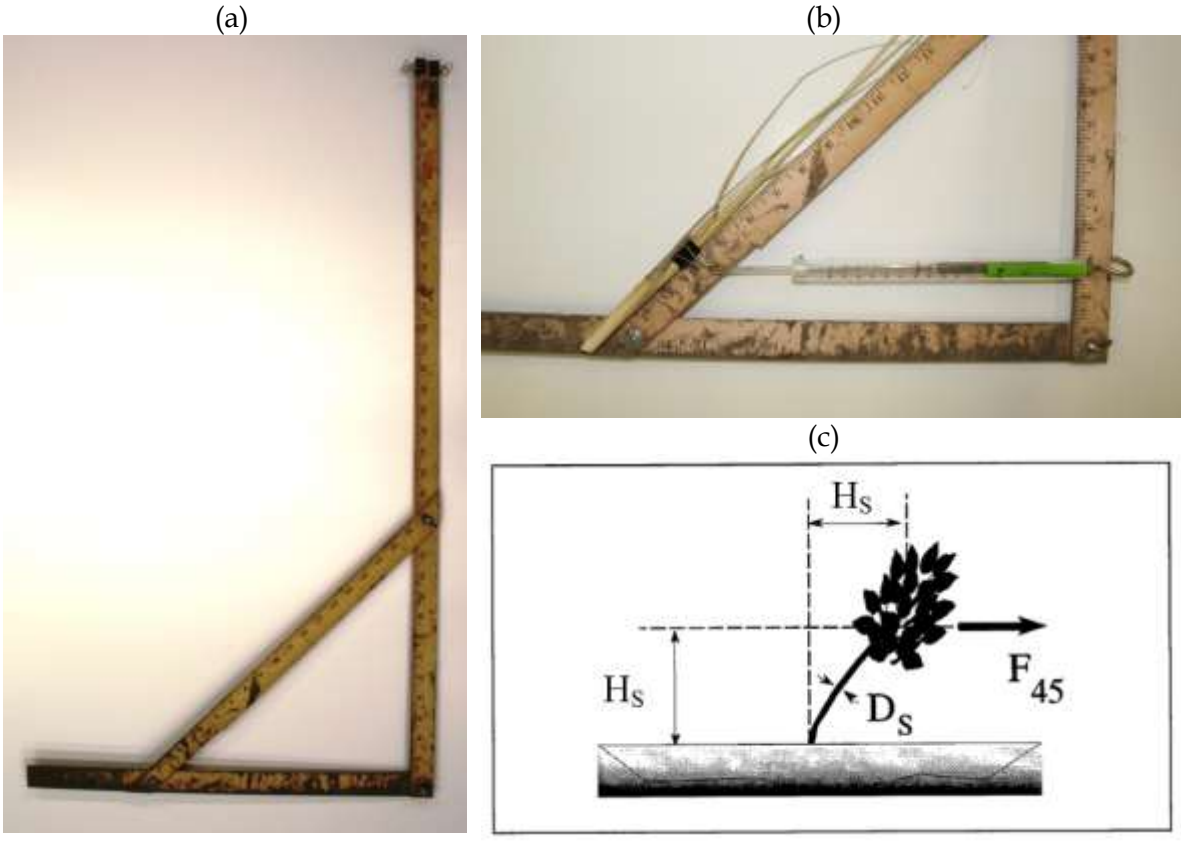

Fig. 5.2. (a) Plant measurement tool, (b) demonstration of spring gage attachment and how the plant measurement tool is used to align plant to a 45° angle, and (c) methodology of bending measurment (adapted from Freeman et al. 2000).

Fig. 5.3. Measuring plant bending force.

The stem was assumed to have a constant circular cross-section, so that its modulus of elasticity, *E,* was calculated using the Euler-Bernoulli beam equation:

$$E = \frac{F_{45} h_s^2}{3I} \tag{5.1}$$

where F_{45} is the horizontal force used to pull the plant stem to an angle of 45°, h_s is the height from the base of the stem at which the force is applied, and I is the second moment of inertia for a circular cross-section which can be obtained from the stem height and diameter.

The modulus of elasticity (E) and second moment of inertia (I), along with the measured plant population density M, were used for the direct computation of *MEI*. Here, M is the relative density defined as a ratio of the stem count to a reference number of stems per unit area. For convenience, the reference number is taken to be 1 stem per unit area. Note that M is considered as a ratio and is dimensionless (Kouwen and Li 1980).

The *MEI* is the flexural rigidity of the vegetation per unit area. It has the units of force times length squared (area). It can be perceived as an "equivalent to plastic stiffness" number (Kouwen 1988). The degree to which vegetation resists bending depends on the flexural rigidity and density of the vegetation (i.e. *MEI*), while the drag force due to the flowing of water determines the bending moments imposed on the vegetation (Kouwen and Li 1980). This parameter has been used in Eq. (2.3) to determine the equivalent roughness height of flexible vegetation.

5.1.3 Board Drop Test

The board drop test was first developed by Eastgate (1966) to estimate the parameter *MEI* for vegetated hydraulic channels. The board drop test consists of 6 ft by 1 ft board weighing 4.85 kg, but the board used in this study was 6 ft by 2 ft and slightly heavier to account for the less uniform and less dense but stiffer coastal marsh vegetation. The board is

stood vertically on one end and allowed to fall rotating about this end in contact with the ground, as shown in Fig. 5.4. When the board hits the vegetation, it slides length-wise in the direction of rotation, imparting a friction force along with the weight of the board. The distance from the ground to the dropped edge of the board (*BH*) is measured. Eastgate found a relationship of board height and *MEI* fitting $MEI = 3122BH^{2.82}$ for several grasses.

The procedure for the board drop test is as follows:

1. An area of visibly uniform vegetation is selected for testing and density over a square meter is hand counted.
2. The drop test board is stood on one edge on the border of the area that is to be tested.
3. From a vertical position the board is allowed to fall over under the weight of gravity.
4. The fall of the board is arrested by the vegetation of the test area, resulting in the board being propped up by the vegetation, with the falling side being more elevated than the side that was in contact with the ground (See Figs. 5.4 and 5.5).
5. The distances from the two high corners of the board to the soil below are measured and then averaged to get the drop height (*BH*) of the test.

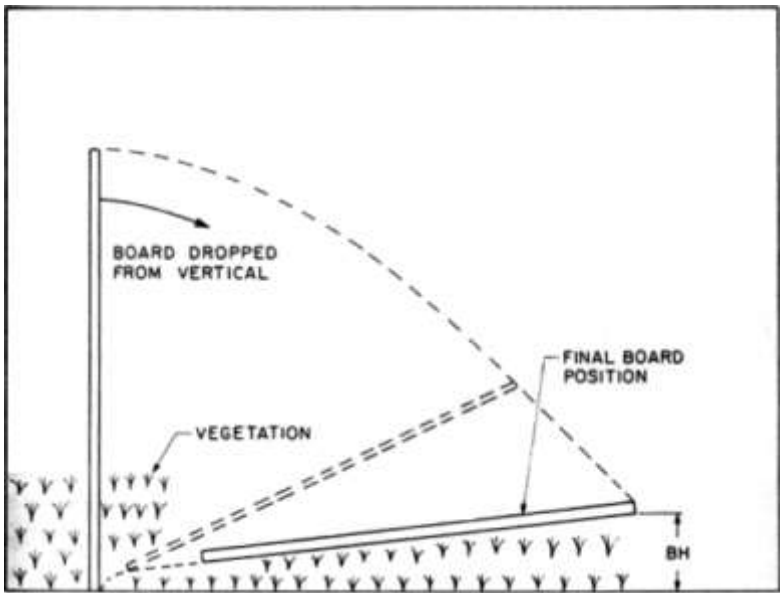

Fig. 5.4. Schematic of the board drop test (Kouwen 1988).

Fig. 5.5. Final position of the board in a board drop test.

5.1.4 Soil Sampling

Soil testing was undertaken to sediment samples carefully selected in the study sites. Soil characterization was performed to inspect the preferable soil characteristics that promote the growth of *S. Alterniflora*. Soil properties, such as grain size distribution, organic matter content, pore water salinity, pore water pH, and Atterberg limits (used for soil classification) were evaluated. Previous studies demonstrate that these properties are closely related to sediment erosion (Feagin et al. 2009). The objective is to characterize soil parameters that promote healthy growth of salt-marsh grasses, and to investigate if there is an optimum soil condition that produces vegetation that outperforms other areas. The tests performed are:

- ASTM D2974 standard tests for moisture, ash, and organic matter of peat and other organic soils.
- ASTM D4318 standard tests for liquid limit, plastic limit, and plasticity index of soils.
- ASTM D422 standard tests for particle-size analysis of soils.
- Pore-water salinity using a centrifuge to separate soil solids from pore water (Fig. 5.6a). Then, salinity is measured using a salinity refractometer (Fig. 5.6b).
- Pore-water pH using a centrifuge to separate soil solids from pore water. Then pH is measured using a bench-top pH meter (Fig. 5.7).

(a) (b)

Fig. 5.6. (a) Centrifuge used to separate soil solids from pore water and (b) handheld salinity refractometer.

Fig. 5.7. Benchtop pH meter.

5.1.5 Analyses and Results

5.1.5.1 Vegetation bending data

Bending data was collected for four different species of salt-marsh vegetation. Species include: *Spartina alterniflora* (Smooth Cordgrass), *Juncus roemerianus* (Black Needlerush), *Spartina patens* (Saltmeadow Cordgrass), and *Scirpus robustus* (Saltmarsh Bullrush). The main focus of the measurements was on the Smooth Cordgrass due to its prevalence in Gulf

of Mexico salt-marshes, its heartiness or resilience, and the wealth of documentation on it. Fig. 5.8 shows a chart of all live plant *E* values plotted against the ratio of stem height over stem diameter. Short stout plants appear on the left while tall slender plants appear on the right. The plant stiffness increases with increase in stem height/stem diameter ratio for all plants sampled. Plotting all live plants together, the trendline can be represented with a power equation:

$$E = 183204\left(\frac{h_s}{D_v}\right)^{1.773} \tag{5.2}$$

where *E* is in N/m². The regression relation has a R^2 value of 0.8518. Surprisingly, this trend seems to continue across all species (*Spartina alterniflora*, *Juncus roemarianus, Spartina patens, and Scirpus robustus*) even though the mechanism of bending may be different between species. For example, short *Spartina alterniflora* bends mostly at the soft base of the plant near the soil, while *Juncus roemarianus* bends more uniformly up the plant to the pull point.

A change is noted between dormant and live vegetation, as shown in Fig. 5.9. Dormant plants of the same stem height to stem diameter ratio have a significantly lower stiffness modulus than their green equivalents. This was also demonstrated in Eq. (2.4) for land grasses. Future work is needed to develop the temporal variation of coastal vegetation biomechanical properties and density.

The seasonal variation of stem heights for *Spartina alterniflora* is shown in Fig. 5.10. As the plant matures the difference between the total height and stem height decreases until the plant becomes dormant. It is also noticed that both stem and total plant heights increase as the growing season progresses.

Fig. 5.11 plots the relations of *MEI* and density for *Spartina alterniflora* and *Juncus roemerianus*. The *MEI* values were calculated using the averaged modulus of elasticity (*E*) and second moment of inertia (*I*) of a data set, and the vegetation density taken during board drop tests at the same site. It appears that *J. roemerianus* would be the preferred ground cover to attenuate waves and storm surge, but this species is not tolerant of high salinity.

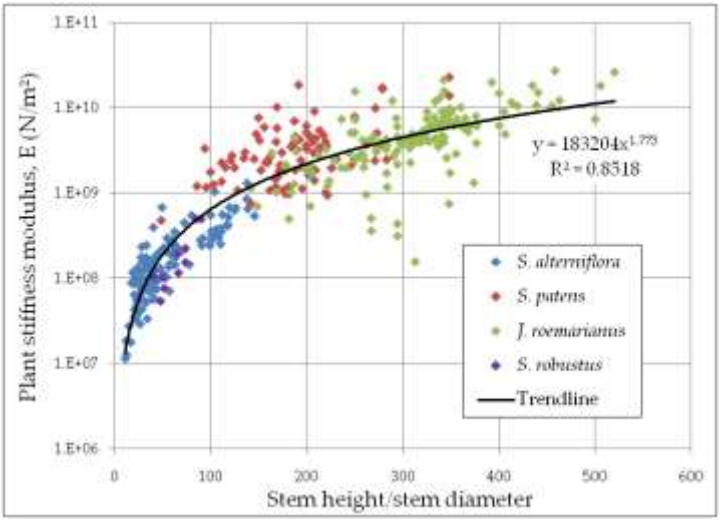

Fig. 5.8. E vs. h_s/D_v for all green vegetation.

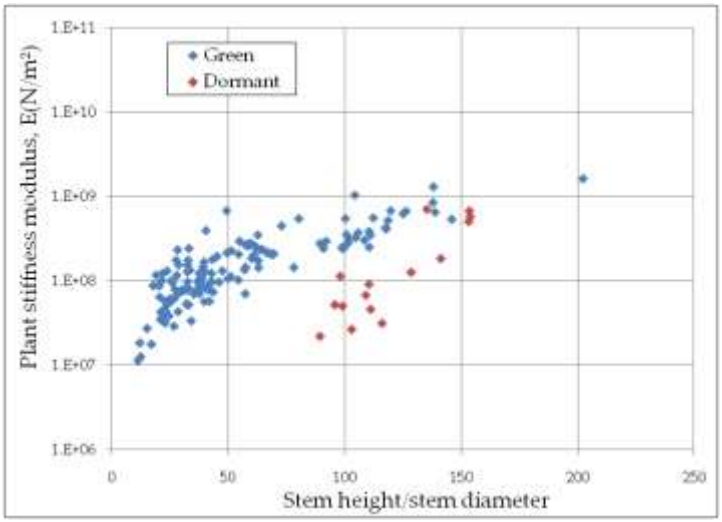

Fig. 5.9. Comparison of stiffness of live and dormant *S. alterniflora.*

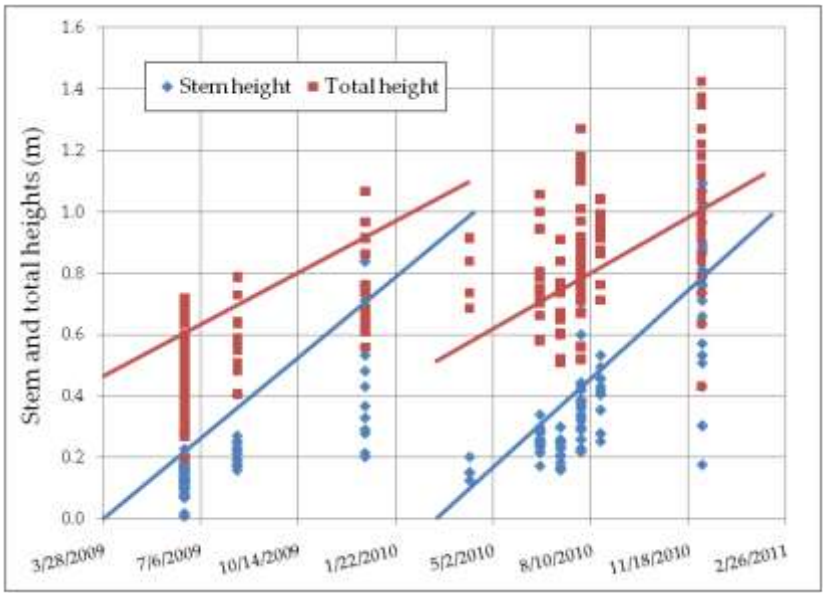

Fig. 5.10. Temporal variation of *S. alterniflora* **total height and stem height.**

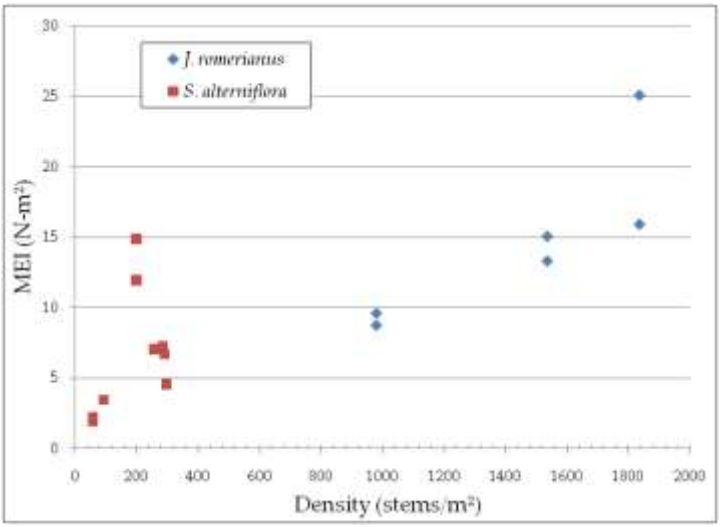

Fig. 5.11. Calculated MEI vs density.

5.1.5.2 **Board drop test results**

The board drop test has proven to be difficult to acquire reliable, consistent data (see Fig. 5.12). This is most likely due to the non-uniformity of salt marsh vegetation. High winds may also influence the board drop velocity when it contacts the vegetation canopy surface. However, a loose correlation between board drop height and density for *Spartina alteriflora* is observed in Figs. 5.12 and 5.13.

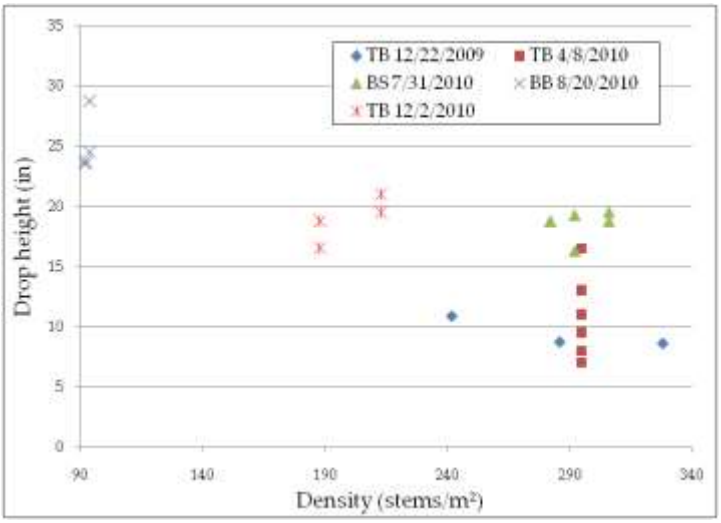

Fig. 5.12. Drop height vs density for *Spartina alterniflora.*

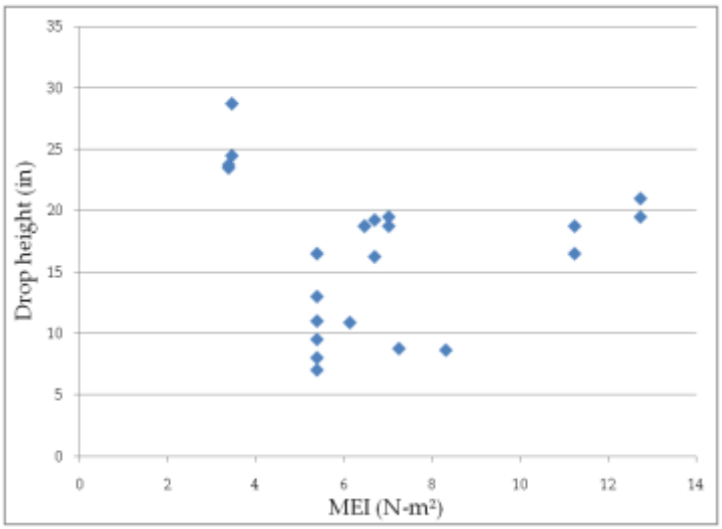

Fig. 5.13. Board drop height vs. observed *MEI* for *Spartina alterniflora.*

5.1.5.3 Soil property data

A summary of soil testing results is shown in Table 5.2. Samples with names starting with BS, CS, TB, and MS were from Breton Sound, Chandeleur Sound, Terrebonne Bay, and Graveline Bayou, Mississippi, respectively. The values PL (plastic limit) and LL (liquid limit) are the Atterberg limits, and the plasticity index, PI, equals LL - PL.

Table 5.2. Summary of soil properties

Sample	Depth (ft)	Water content (wt. %)	Organic matter content (wt. %)	PL	LL	PI	Pore water pH	Salinity (gNaCl/ 100gH_2O)
BS BKT	0-0.5	93.90%	7.40%	22%	59%	37%	5.22	2.9
CS TOP	0-1	132.30%	10.70%	30%	65%	35%	4.29	3.6
CS BOT A	1-1.5	121.60%	10.00%	22%	53%	31%	Sample had dried	
CS BOT B	1-1.5	82.30%	5.60%	22%	50%	28%	3.39	4
TB A	1	165.60%	12.90%	32%	100%	68%	4.18	2.4
TB B	1	149.30%	12.00%	31%	98%	67%	3.97	2.6
MS A	0.5-1.0	84.50%	15.90%	24%	75%	51%	6.89	1.8
MS B	0.5-1.0	163.00%	7.70%	30%	96%	66%	6.86	2.7
TB C	0.5-1	180.90%	10.30%	31%	96%	65%	6.56	2.9

Fig. 5.14 is a Casagrande plasticity chart using the Unified Soil Classification System (USCS). Samples from Terrebonne Bay are consistently of a high plasticity, while samples from Chandeleur Sound are the leanest. These findings are consistent with the results in the particle size distribution chart in Fig. 5.15, which shows that samples from Terrebonne Bay have consistently small particle sizes lending themselves to better cohesion and a larger plastic range. Also, it is widely known that pore water salinity increases the cohesion of soils, thus increasing their plasticity. This could be skewing the classification of these soils of more plasticity.

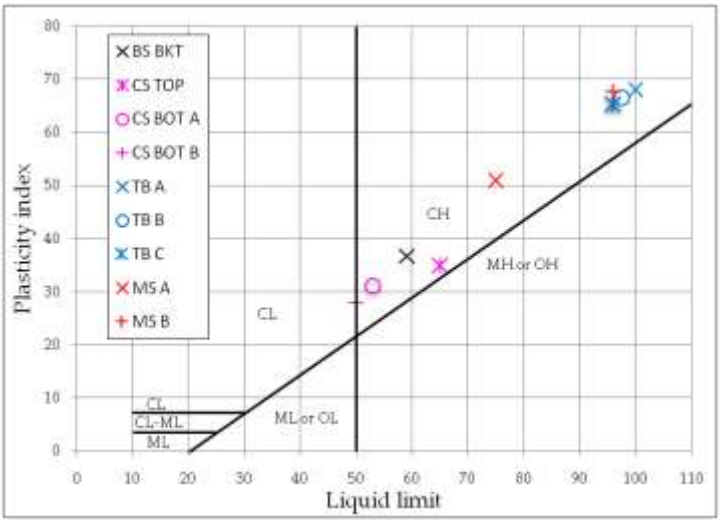

Fig. 5.14. Soil plasticity chart using the Unified Soil Classification System.

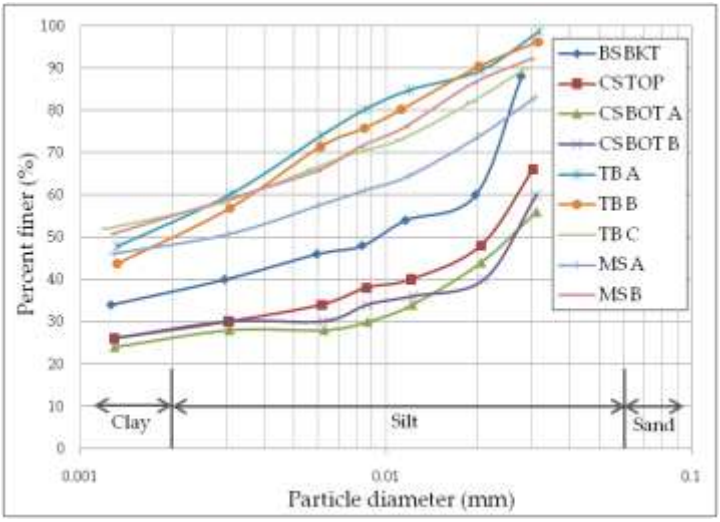

Fig. 5.15. Soil particle size distribution.

5.2 Growth Forms and Productivities of *S. alterniflora* and *J. roemarianus*

The first step in this campaign was to identify field demonstration sites in Mississippi that would complement the sites chosen previously in Louisiana, and then to characterize each sampling site by surveying native plants, characterizing associated sediments in both low and high marsh zones, measuring primary production of native vegetation, and assessing elevation and salinity gradients in coastal and inland marshes vegetated by *Spartina alterniflora* Loisel., *Juncus roemerianus* Scheele., and/or *Spartina patens* (Aiton) Muhl. along the Mississippi Gulf Coast. The field and laboratory datasets collected include soil horizon, sediment bulk density, organic matter content, texture, salinity, pH, elevation, and plant growth form (density, cover, biomass, rhizome thickness, and height).

5.2.1 Research Sites

The Grand Bay National Estuarine Research Reserve in southeast Mississippi provides unique coastal habitats for research because of the great biological significance of the variety of wetland and terrestrial habitats. Yet, Grand Bay had focused on hydrological parameters and ornithological studies, but not on coastal vegetation. Thus, Grand Bay and neighboring Graveline Bayou were chosen as the research sites after reviewing the aerial photographs and historical data available.

The Grand Bay Reserve [30° 21.551'N, 88° 25.202'W] (Figs. 5.16 and 5.17), which is located in Jackson County in southeast Mississippi, is one of the most biologically productive estuarine ecosystems in the Gulf of Mexico region. The Grand Bay National Estuarine Research Reserve (GNDNERR) is a marine protected area comprised of approximately eighteen thousand acres (7287.45 hectares), found chiefly within the Grand Bay National Wildlife Refuge and the Grand Bay Savanna Coastal Preserve (Adams et al. 2008, Woodrey and Walker 2009). This Reserve contains a variety of wetland habitats, both tidal and non-tidal, such as salt marshes, saltpans and bays as well as terrestrial habitats that are unique to the coastal zone such as maritime forests (Cho and May 2006). The fresh water marshes in the Reserves are either tidal or non-tidal depending on where they are located within the landscape and most of these habitats are rarely flooded by saltwater. The estuaries of the Reserves are dominated by the salt marsh community. The salt marshes which are influenced by the rise and fall of the tides are divided into three major wetland zones based on minor differences in elevation. The low marsh (zone closest to open water) which is the narrowest zone along the fringes of many of the Reserves' bayous where the brackish tidal waters reach every day is dominated by *Spartina alterniflora* (Smooth Cordgrass). The mid-marsh (about 20 m inland from the edge) is not covered by water every day because it is located above the mark of mean (average) high water between the low and high marsh. The highest zone (about 40 m inland), which is covered with water only during unusually high water events such as hurricanes, serves as an interface with the adjacent terrestrial habitats (Cho and May 2006, GNDNERR website, Woodrey and Walker 2009).

Graveline Bayou [30° 21.47'N, 88° 41.41'W] (Fig. 5.16) is located between Ocean Springs and Gautier along the Mississippi Gulf Coast. Graveline Bayou has a wetland reserve boundary of 946 hectares (9,472,950 square meters; Gulf Ecological Management Sites website, GEMS 2010). Graveline Bayou represents one of a few relatively undisturbed estuarine bays and small tidal creeks in Mississippi. The area supports salt marsh, brackish marsh, and several oyster beds. The bay, marsh, adjoining upland forest, and undeveloped beach front near the mouth of Graveline Bayou are an important landing area for neotropical migrant birds. The coastal marsh estuarine system receives only local fresh water runoff and consists largely of mid-level *Juncus roemerianus* (needlegrass rush) dominated marsh along its entire length. *Spartina alterniflora* (Smooth cordgrass) occurs largely as narrow (1-3 m) bands along the coast, creeks and bayous.

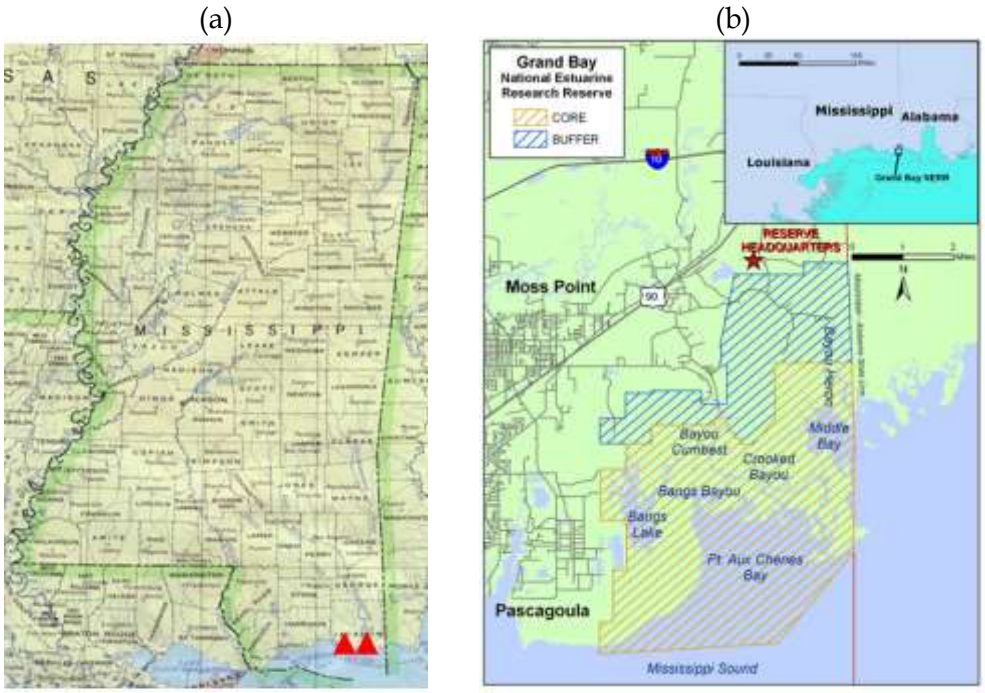

Fig. 5.16. (a) Grand Bay and Graveline Bayou are indicated by red triangles on the Mississippi Coast (Google Map accessed on 17 March 2010); (b) Grand Bay National Estuarine Research Reserve on MS Gulf Coast (GNDNERR Website 2010).

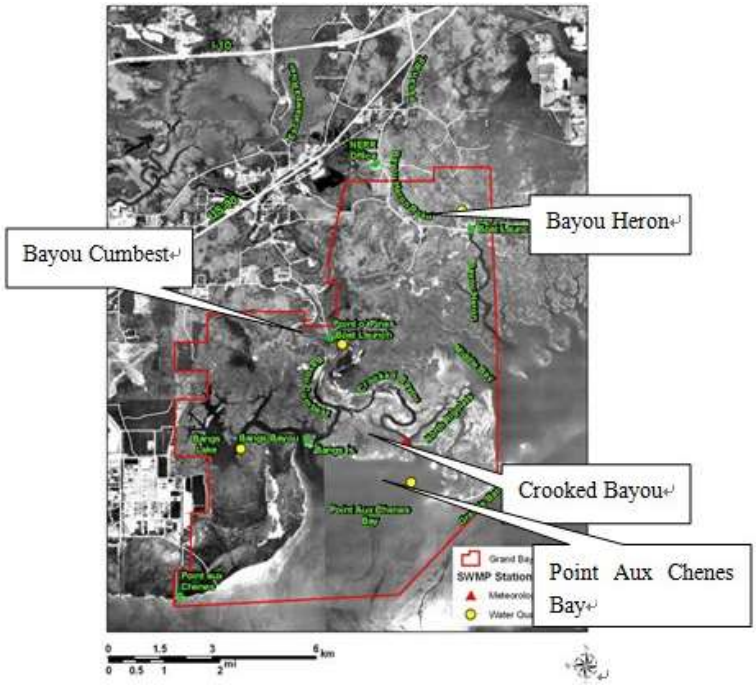

Fig. 5.17. Grand Bay NERR Monitoring Stations (GNDNERR Website 2010).

Fig 5.18. Map of Grand Bay, Bayou Heron, Orange Grove and Graveline Bayou(Google Map accessed on 23 February 2010).

Table 5.3 lists the recent hurricanes affected the two sites. Both Graveline Bayou and Grand Bay sites were inundated by Hurricane Katrina in 2005, and no coastal marshes exist in Mississippi which have not been inundated by hurricanes. Hurricane Katrina (Table 5.3; NOAA Coastal Services Center website) made landfall and damaged marsh vegetation along the Louisiana and Mississippi coast on 29 August 2005 as a Category 5 storm. Katrina's wind speeds peaked at 282 kph, and at its largest, had hurricane force winds extending 193 km from its eye. Storm surge heights were 6 to 10 m in some areas along the coast, the effects of which extended as far east as Mobile, AL. At Grand Bay, the maximum sustained wind speed of Hurricane Katrina was stronger than 205 km/hr and the storm surge was 3.97m. Hurricane Rita followed, on 24 September 2005, and made landfall farther to the west near Sabine Pass, TX, and consequently had less of an impact on Grand Bay compared to Katrina (McKee and Cherry 2009). Physical and chemical parameters were recorded at Grand Bay prior to, during, and subsequent to these major storms (Tables 5.4–5.6).

Table 5.3. The timing of Hurricanes along the MS Gulf Coast from 2004-2010 (Data provided by Dr. Mark Woodrey of GNDNERR; GNDNERR Website)

Date	Name	Description
Sep. 2004	Hurricane Ivan	Category 3, land fall East of the Grand Bay NERR
Jul. 2005	Tropical Storm Cindy	Sustained winds in excess of 55 mph (24.59 m/s)
	Hurricane Dennis	Category 3, light wind and rain
Aug. 2005	Hurricane Katrina	Category 5, storm surge 4.575-5.49 m (15-18ft) and 100 mph (44.704 m/s) winds
Sep. 2005	Hurricane Rita	Category 5, storm surge 0.915-1.525 m (3-5ft)
Aug. 2008	Tropical Storm Fay	Caused unusual water depths
Sep. 2008	Hurricane Gustav	104 mph (46.492 m/s) winds
	Hurricane Ike	Category 2
Aug. 2009	Tropical Storm Claudette	45.36 mph (20.3 m/s) winds
Nov. 2009	Tropical Storm Ida	Category 2, 45 mph (20.12 m/s) winds
Jul. 2010	Tropical Storm Bonnie	45 mph (75 km/h)

Erosion of marsh shoreline in the Grand Bay National Estuarine Research Reserve (GNDNERR) has been occurring steadily throughout the past several hundred to thousands of years. One recent example of marsh erosion occurred with the pirating in the early 1950s of the Escatawpa River by the Pascagoula River (Otvos 1985). This natural process is driven by relative sea-level rise (combination of sea-level rise and land subsidence; Fig. 5.19; NOAA website) and wave attack, and is offset somewhat by the conversion of upland areas to wetlands.

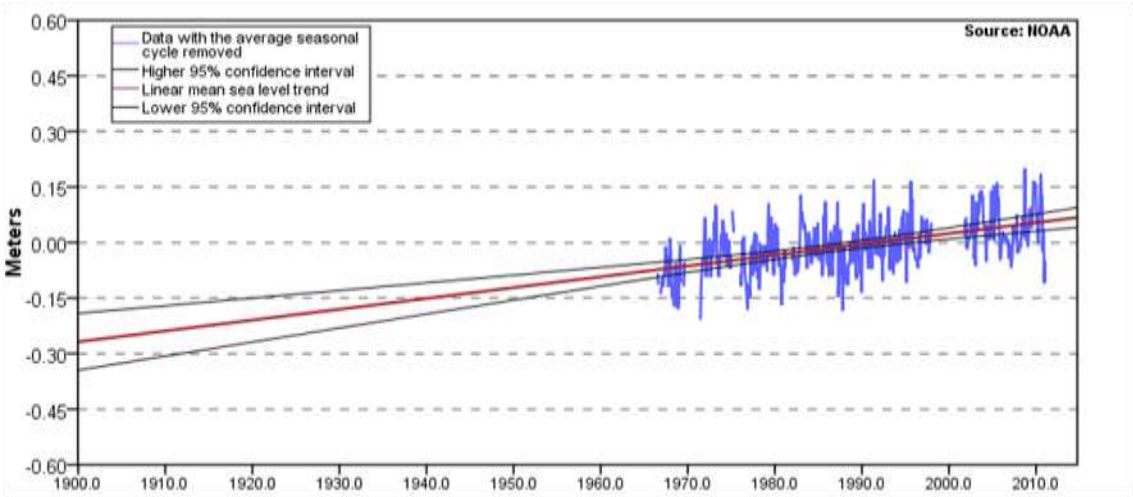

Fig. 5.19. Mean sea level trend in Mississippi

However, the process of upland conversion is limited, and in many cases reversed, by human development, making marsh erosion more problematic. Shoreline positions of the wave-exposed marsh shorelines were surveyed using Global Positioning System (GPS) techniques in 1993 and 1999. The 1993 and 1999 GPS data cover the area from west of Point aux Chenes to the interior of Point aux Chenes Bay, and along the southern shore of South Rigolets Island. Areas of the 1999 surveyed shoreline show more than 2.5 m/yr (8 ft/yr.) of erosion which totals 15 m/6 yr (50ft). The southwestern shoreline of South Rigolets Island has the highest erosion rates, which average 50 m over the six-year period (1993-1999; 8 m/yr, 27 ft/yr). The same 1999 surveyed shoreline show more than 40 m (130 ft) of shoreline loss since 1986 which equals 3 m/yr (10 ft/yr). Of the 11.8 km surveyed, 3.8 km had more than 3 m/yr of loss over a 13-year period (1986-1999; Schmid 2000). The shoreline in areas exposed to high wave energy has been receding 6-10 m/yr since 2003 when GNDNERR began monitoring erosion rates at various locations where geological substrates and exposure to wave energy are different. Moreover, the coastal salt marshes located along the fringe of the Grand Bay are being eroded away at over 9.144 meters (30 feet) per year (GNDNERR website). The highlighted (in yellow) long-term erosion areas shown on the map of GNDNERR (Fig. 5.16b) are associated with the most wave-exposed orientations, notably Point aux Chenes and South Rigolets Island (Schmid 2000).

Crooked Bayou (CR) meteorological station, Point Aux Chenes (PC) water quality station, Bayou Heron (BH) water quality station and Bayou Cumbest (BC) water quality station (Figs. 5.16b, 5.17 and 5.18) are the four monitoring stations at Grand Bay closest to the sample sites. Crooked Bayou (CR) meteorological station and Point Aux Chenes (PC)

water quality station are the two monitoring stations closest to South Rigolets Island (Transects 1 and 2 as described in the next subsection; Figs. 5.16b, 5.17 and 5.18); Bayou Heron (BH) is close to Transect 5, and Bayou Cumbest (BC) is close to Transect 8. Grand Bay was inundated by hurricanes or tropical storms in three seasons from 2004 to 2010 (Table 5.3).

Each storm's winds often caused unusually high or low water depths. Before Hurricane Katrina occurred, the Crooked Bayou site was abandoned and the Point Aux Chenes site designated in order to capture more low tide data. After 2005, the water depth increased by more than five times because the monitoring site was moved from Crooked Bayou (CR) to Point Aux Chenes (PC; Figs. 5.16b and 5.17). For example, Tropical Storm Fay's winds caused water depths to be unusually low as the storm passed east of the Reserve, headed northwest pushing water out of the Reserve on 25 August 2008. Once the storm's track changed to the southwest just west of the Reserve, the water depth readings were unusually high as the storm's winds pushed water back into the Reserve. Hurricane Ike caused unusually high water depths in the Reserve in the days before landfall, as the storm passed south of the Reserve on its way to Texas on 12 September 2008.

The hydrologic, chemical and physical data from 2004 to 2010 (Tables 5.4–5.6) for the coastal areas at Crooked Bayou (CR) and Point Aux Chenes (PC) monitoring stations show that the salinity ranges from 12.4 ppt to 27.2 ppt and the average salinity is 22.67 ppt. The water depth ranges from 0.1 m to 2.0 m and the average water depth is 0.87 m. For the northeastern inland Bayou Heron (BH) monitoring station, the salinity ranges from 8.6 ppt to 24.9 ppt and the average salinity is 18.33 ppt. The water depth ranges from 0.5 m to 1.6 m and the average water depth is 1.27 m. For the northwestern inland Bayou Cumbest (BC) monitoring station, the salinity ranges from 10.5 ppt to 31.1 ppt and the average salinity is 17.41 ppt. The water depth ranges from 0.2 m to 0.7 m and the average water depth is 0.47 m.

The average salinity at Crooked Bayou (CR) and Point Aux Chenes (PC) monitoring stations (23.03 ppt, 2004-2010) is higher than that at Bayou Cumbest (BC) monitoring station (17.81 ppt, 2004-2010). Moreover, the average salinity at Bayou Cumbest (BC) monitoring station is slightly higher than that at Bayou Heron (BH) monitoring station (17.76 ppt, 2004-2010). The average water depth at Crooked Bayou (CR) and Point Aux Chenes (PC) monitoring stations (0.87 m, 2004-2010) is lower than that at Bayou Heron (BH) monitoring station (1.24 m, 2004-2010). But the average water depth at Crooked Bayou (CR) and Point Aux Chenes (PC) monitoring stations is higher than that at Bayou Cumbest (BC) monitoring station (0.44 m, 2004-2010).

Table 5.4 Monitoring Data (2004-2010) for Coastal Sites [Crooked Bayou (CR) and Point Aux Chenes (PC)]

Year	Time	Temperature (°C)	Salinity (ppt)	Dissolved Oxygen (mg/l)	Depth (m)	pH
2004 (CR)	Winter	13.1	20.0	9.4	0.2	7.8
	Spring	20.8	19.9	7.5	0.5	7.7
	Summer	28.2	26.4	5.5	0.1	7.8
	Fall	24.2	23.1	6.7	0.2	7.6
Total year		21.6	22.4	7.3	0.3	7.7
2005 (CR, PC)	Winter	14.2	24.2	8.8	0.5	8.0
	Spring	22.4	17.0	7.6	0.2	7.7
	Summer	29.9	17.2	6.2	0.4	7.7
	Fall	23.3	27.0	7.9	1.1	8.1
Total year		22.5	25.0	7.8	1.2	8.1
2006 (PC)	Winter	14.1	25.1	9.3	0.9	8.1
	Spring	22.9	20.5	7.5	1.0	8.0
	Summer	30.0	27.2	6.3	1.0	7.9
	Fall	22.9	27.1	8.0	2.0	8.2
Total year		22.5	25.0	7.8	1.2	8.1
2007 (PC)	Winter	14.0	26.3	8.9	0.9	8.2
	Spring	22.1	25.9	7.2	0.9	7.9
	Summer	29.8	26.8	6.4	1.0	7.9
	Fall	23.2	24.9	7.6	1.1	8.1
Total year		22.3	26.0	7.5	1.0	8.0
2008 (PC)	Winter	13.1	26.6	10.6	1.0	8.4
	Spring	21.8	18.8	6.5	1.0	8.2
	Summer	29.5	21.0	5.8	1.1	8.0
	Fall	22.0	26.0	7.0	1.2	8.0
Total year		21.6	23.1	7.5	1.1	8.2
2009 (PC)	Winter	14.1	21.5	9.5	1.0	8.3
	Spring	22.3	12.4	7.7	0.8	8.0
	Summer	29.6	23.7	5.6	0.9	7.8
	Fall	25.2	21.0	6.6	1.2	8.0
Total year		22.8	19.7	7.4	1.0	8.0
2010 (PC)	Winter	10.4	19.9	10.7	0.5	8.3
	Spring	21.5	17.3	7.4	0.9	8.0
	Summer	30.4	19.7	4.9	1.1	7.5
	Fall	23.5	25.3	5.8	1.2	7.0
Total year		21.5	20.6	7.2	0.9	7.7

*These water quality data are the average values per year according to the data in monitoring sites Crooked Bayou (CR) [30° 21.594'N, 88° 25.140'W] or Point Aux Chenes (PC) [30° 20.916'N, 88° 25.112'W]. The data are available from Grand Bay Monitoring Data (GNDNERR website). Winter (Dec, Jan, Feb); Spring (Mar, Apr, May); Summer (Jun, Jul, Aug); Fall (Sep, Oct, Nov).Data provided by Dr. Mark Woodrey (GNDNERR Research Coordinator).

Table 5.5 Monitoring Data (2004-2010) for Brackish Sites at Bayou Heron (BH)

Year	Time	Temperature (°C)	Salinity (ppt)	Dissolved Oxygen (mg/l)	Depth (m)	pH
2004 (BH)	Winter	13.2	12.6	6.6	0.8	6.7
	Spring	23.4	17.6	4.8	0.9	7.0
	Summer	29.5	13.8	3.1	0.9	6.7
	Fall	25.0	18.2	3.7	1.0	6.9
Total year		22.8	15.6	4.6	0.9	6.8
2005 (BH)	Winter	14.9	18.5	8.8	0.5	8.0
	Spring	22.5	8.6	4.9	1.0	6.1
	Summer	29.6	11.1	2.6	1.1	6.4
	Fall	24.0	22.5	4.3	1.4	7.0
Total year		22.8	15.2	5.2	1.0	6.9
2006 (BH)	Winter	15.8	20.9	5.8	1.2	7.1
	Spring	23.6	17.8	4.8	1.3	7.0
	Summer	31.0	24.9	2.3	1.3	6.8
	Fall	24.0	24.2	3.5	1.4	7.1
Total year		23.6	22.0	4.1	1.3	7.0
2007 (BH)	Winter	15.1	21.5	5.0	1.3	7.3
	Spring	22.9	23.1	4.7	1.3	7.2
	Summer	30.3	23.9	1.3	1.4	6.9
	Fall	24.3	24.9	3.0	1.5	7.1
Total year		23.2	23.4	3.5	1.4	7.1
2008 (BH)	Winter	14.2	20.9	5.0	1.3	7.2
	Spring	21.4	14.3	3.9	1.4	6.8
	Summer	29.5	17.5	1.0	1.4	6.8
	Fall	22.6	23.8	3.9	1.6	7.0
Total year		21.9	19.1	3.5	1.4	7.0
2009 (BH)	Winter	14.4	14.2	5.7	1.3	7.0
	Spring	21.7	9.1	4.4	1.5	6.5
	Summer	29.9	20.5	0.9	1.4	6.9
	Fall	23.8	17.7	2.5	1.6	7.0
Total year		22.5	15.4	3.4	1.5	6.9
2010 (BH)	Winter	11.5	17.2	7.2	1.2	7.2
	Spring	21.0	15.3	2.7	1.4	6.9
	Summer	29.7	14.8	1.0	1.5	6.8
	Fall	24.2	23.2	3.5	1.3	7.2
Total year		21.6	17.6	3.6	1.4	7.0

*These water quality data are the average values per year according to the data in monitoring sites Bayou Heron [30° 25.068'N, 88° 24.324'W]. The data are available from Grand Bay Monitoring Data (GNDNERR website). Winter (Dec, Jan, Feb); Spring (Mar, Apr, May); Summer (Jun, Jul, Aug); Fall (Sep, Oct, Nov). Data provided by Dr. Mark Woodrey of GNDNERR.

Table 5.6 Monitoring Data (2004-2010) for Brackish Sites at Bayou Cumbest (BC)

Year	Time	Temperature (°C)	Salinity (ppt)	Dissolved Oxygen (mg/l)	Depth (m)	pH
2004 (BC)	Winter	13.9	12.9	9.3	0.2	7.4
	Spring	24.9	22.1	6.4	0.3	7.4
	Summer	30.6	15.6	5.3	0.3	7.3
	Fall	25.0	18.3	5.8	0.4	7.2
Total year		23.6	17.2	6.7	0.3	7.3
2005 (BC)	Winter	14.5	18.6	9.1	0.3	7.4
	Spring	23.5	10.3	6.5	0.3	6.9
	Summer	30.3	10.7	5.1	0.4	7.0
	Fall	23.8	23.7	5.9	0.5	7.0
Total year		23.0	15.8	6.7	0.4	7.1
2006 (BC)	Winter	14.8	18.8	8.8	0.3	7.6
	Spring	24.0	18.8	6.9	0.4	7.2
	Summer	31.0	24.1	5.4	0.4	7.1
	Fall	23.5	21.1	6.2	0.4	7.4
Total year		23.3	20.7	6.8	0.4	7.3
2007 (BC)	Winter	14.5	16.1	8.1	0.3	7.5
	Spring	26.7	28.2	6.6	0.6	7.3
	Summer	30.7	22.1	4.2	0.5	7.3
	Fall	22.6	23.5	5.1	0.6	7.4
Total year		23.6	22.5	6.0	0.5	7.4
2008 (BC)	Winter	13.5	13.5	8.8	0.4	7.4
	Spring	29.4	12.1	6.0	0.5	7.3
	Summer	30.0	14.0	4.4	0.5	7.1
	Fall	14.5	24.0	8.4	0.5	7.5
Total year		21.9	15.9	6.9	0.5	7.3
2009 (BC)	Winter	13.9	17.9	8.7	0.4	7.5
	Spring	26.6	7.3	6.4	0.6	7.3
	Summer	29.9	18.7	4.6	0.6	7.1
	Fall	21.4	15.0	5.5	0.7	7.2
Total year		23.0	14.7	6.3	0.6	7.3
2010 (BC)	Winter	10.5	11.8	10.6	0.6	7.5
	Spring	22.5	13.9	6.8	0.6	7.2
	Summer	31.1	13.1	4.8	0.6	7.1
	Fall	23.9	21.6	5.4	0.4	7.3
Total year		22	15.1	6.9	0.6	7.3

*These water quality data are the average values per year according to the data in monitoring sites Bayou Heron [30° 25.068'N, 88° 24.324'W]. The data are available from Grand Bay Monitoring Data (GNDNERR website). Winter (Dec, Jan, Feb); Spring (Mar, Apr, May); Summer (Jun, Jul, Aug); Fall (Sep, Oct, Nov). Data provided by Dr. Mark Woodrey of GNDNERR.

5.2.2 Field Measurements

Four coastal transect lines and four inland transect lines were established in the research sites based on the different intensity of the storm surges. Initial samples were obtained at the Grand Bay National Estuarine Research Reserve along two coastal transects: one is in the West end of Rigolets Island and the other is in the east end of South Rigolets Island in the north Gulf of Mexico (Figs. 5.18 and 5.20). The dominant vegetation along both transects is *Spartina alterniflora* Loisel. and *Jucus roemerianus* Scheele. Two additional inland transects were established on the North side of Graveline Bayou in Gautier, MS (Figs. 5.18 and 5.21). On the latter two transects, the vegetation is primarily *Juncus roemerianus* Scheele. with some *Spartina alterniflora* Loisel. in low marsh. Transect 5 was established further inland north of the Bayou Heron boat landing at the Grand Bay National Estuarine Research Reserve (Figs. 5.18 and 5.22), and Transect 6 was at the South side of Graveline Bayou along the Gulf Coast (Figs. 5.18 and 5.23). Transect 5 is dominated by *Juncus roemerianus* Scheele. Transect 7 was established at the South side of Graveline Bayou along the Mississippi Gulf Coast east of Transect 6 (Figs. 5.18 and 5.24a). Both Transects 6 and 7 are located in coastal areas. Transect 8 was established inland at Orange Grove north of Point O' Pines boat landing (Figs. 5.18 and 5.24b). Transect 8 is dominated by *Juncus roemerianus* Scheele. Soil and vegetation samples were collected in both low and high marsh zones on each transect established.

The hydrologic and chemical data (salinity, pH, water depth) of these experimental sites have been obtained from monitoring stations of GNDNERR (obtained from GNDNERR website; Tables 5.4–5.6). Soil samples were collected to observe and measure soil properties from the low marsh zone (marsh edge) and at 40 m inland from wave break in the high marsh zone of coastal marshes vegetated by *Spartina alterniflora* Loisel., and/or *Juncus roemerianus* Scheele. On each transect, ten replicate soil cores were collected in the low marsh zone (marsh edge) and another replicate ten soil cores were collected from the high marsh zone. Soil cores were sampled with an 8.5 cm diameter by 30 cm long steel corer device (Art's Manufacturing & Supply; AMS Split Core Sampler). Each soil sample core was removed with a plunger from the top soil layer; thus, the soil sample was extracted from the bottom 5 cm of the soil core. The core samples were each placed in a Freezer Zip-Lock Bag, frozen, and placed in a cooler for transportation to the laboratory. The core samples were kept frozen until processed.

Initial observations were made in December 2009 to characterize the experimental sites as to substrate composition (e.g. classification), plant height (dead and live), and plant growth form (*Spartina alterniflora* Loisel., *Juncus roemerianus* (Scheele)., and/or *Spartina patens* (Aiton) Muhl. No evidence of *Spartina patens* was observed during any marsh visits. The percent cover occupied by each plant species in a 0.25 m^2 quadrat was recorded (Holland and Burk 1990). Aboveground vegetation was clipped within a 0.25 m^2 quadrat (Fig. 5.25a) and rhizomes and roots of vegetation were collected to measure aboveground and belowground biomass from both low and high marsh zones in each transect. The aboveground vegetation and rhizome samples were each placed in carefully labelled 30 gallon trash bags and placed in a cooler for transportation to the laboratory. Then vegetation samples were refrigerated until sorted by species and measured for aboveground and belowground biomass. On each transect, elevation was also measured by a total station (electronic level system, Autolaser 300, David White Instruments), which is a theodolite with an electronic distance measurement device (EDM, Anastasiou and Brooks 2003,

Warren and Niering 1993) in open water, in low marsh zone (marsh edge), at 20 m and at 40 m from open water along each transect (Fig. 5.25b).

(a) (b)

Fig. 5.20. The low marsh zone of (a) Transect 1 and (b) Transect 2 in the Coastal South Rigolets Island West (December 2009)

(a) (b)

Fig. 5.21. (a) The high marsh zone of Transect 3 and (b) the low marsh zone of Transect 4 at the north side of Graveline Bayou (March 2010).

(a) (b)

Fig. 5.22. (a) The low marsh zone of Bayou Heron (Transect 5, 12 March 2010); (b) students in the Aquatic Botany Class working with Dr. Holland in the high marsh zone of Bayou Heron (Transect 5 looking northwest).

(a) (b)

Fig. 5.23. (a) The south marsh edge of Graveline Bayou (Transect 6, 12 March 2010); (b) the high marsh zone of Transect 6 at south side of Graveline Bayou (13 May 2010).

(a) (b)

Fig. 5.24. (a) The low marsh zone of Transect 7 at south side of Graveline Bayou and, (b) the low marsh zone (marsh edge) of Transect 8 at Orange Grove of Grand Bay (13 May 2010).

(a) (b)

Fig. 5.25. (a) Students Steven Nelson and Lauren Melissa Baskin clipping aboveground vegetation in a 0.25 m² quadrat; (b) the elevation laser rod (electronic level system, Autolaser 300, David White Instruments).

5.2.3 Laboratory Analyses

Substrate properties (e.g. particle size distribution, organic carbon, nitrogen, phosphorus, and Total Kjeldahl Nitrogen (TKN)) were measured at the USDA-ARS National Sedimentation Lab in Oxford, MS using standard methods. Laboratory analyses of the soil samples included measurements of soil moisture (105°C for 24 hours), grain size and particle size distribution (HORRIBA LA-910 Particle Size Analyzer Dry Sample Analysis Method; Fig. 5.26), soil percent organic matter by measuring the loss on ignition (LOI

method; 400°C for 1 hour; Black 1965), and of Total Kjeldahl Nitrogen (TKN) and phosphorus (TP), digested by QuikChem Method 10-107-06-2-E (Wendt 1997) and QuikChem Method 10-115-01-1-C (APHA standard methods 1989, Lachat Instrument 1995, Horneck and Miller 1998). The soil bulk density was measured by estimating the volume of the samples and measuring the loss of water in soil samples (60 °C for 48 hours; Heuscher et al. 2005, Center for Applied Research and Environmental Systems, CARES website 2010). The volume of void space in the soil sample is equal to the water mass in the fully saturated collected soil sample since one gm H_2O is equal to one ml H_2O according to the formulas:

Bulk density (g/cm^3) = dry mass (g) / total volume (cm^3);
Total volume = void volume + solid volume;
Solid volume (cm^3) = dry mass / 2.65 (g/cm^3);
Void volume (ml) = wet mass- dry mass = water mass (g)
The solid particle density is assumed as 2.65 g/cm^3 (CARES website 2010).

Aboveground and belowground biomass, soil moisture, sediment bulk density and organic matter content were measured in the laboratory in the UM Biology Department, Oxford, MS. Aboveground vegetation and rhizomes were sorted by species, washed and dried at 105°C for 24 hours (or longer) to measure above- and belowground biomass (Cronk and Fennessy 2001, Howes et al. 1986, Whigham and Simpson 1977). Biomass (g/m^2) is computed as dry weight / quadrat area. Rhizome thickness and stem diameter were also measured with calipers. Plant density was estimated by calculating the stem diameter and multiplying the percent cover in each 0.25 m^2 quadrat. The formulas for soil moisture and LOI are expressed as follows (Black 1965):

Soil moisture % = (1-dry soil weight / wet weight) ×100;
LOI % = (dry weight – ash weight) / dry weight ×100.

Fig. 5.26. Horriba LA-910 Particle Size Analyzer (USDA-ARS National Sedimentation Lab).

5.2.4 Data Analysis

The hydrologic, physical and chemical data (temperature, salinity, dissolved oxygen, water depth, and pH) from GNDNERR meteorological or water quality monitoring stations provided by Dr. Mark Woodrey of GNDNERR have been summarized in four seasons (December, January, and February for winter; March, April, and May for spring; June, July, and August for summer; September, October, and November for fall) each year from 2004 to 2010 (Tables 5.4, 5.5, and 5.6). Both salinity and elevation data were compared to note differences in biomass in low and high marsh zones between coastal and brackish marsh locations.

Soil properties (organic matter content, moisture, mean grain size, particle size distribution and sediment bulk density) and plant parameters (above- and belowground biomass, standing shoot heights, rhizome thickness, stem diameter and density) in the low and high marsh zones in eight transects were analyzed (eight low marsh zones and eight high marsh zones) in order to compare differences in substrate properties and plant parameters between the low marsh and high marsh zones along elevation and salinity gradients. A two way ANOVA was used to test if there were any significant differences in soil properties and plant parameters. In addition, comparisons of soil properties and plant biomass between the Gulf Coast (Transects 1, 2, 6 and 7) and further inland (Transects 3, 4, 5, and 8) in both low and high marsh were made. Comparisons were also made between Graveline Bayou and Grand Bay. Table 5.7 groups the transects in coastal and inland marshes, as well as in Graveline Bayou and Grand Bay.

Table 5.7. The distribution of the transects according to location and type

	Coastal sites	Inland
Grand Bay	1,2	5,8
Graveline Bayou	6,7	3,4

5.2.5 Results

The results are presented in five separate sections: elevation and zonation, soil properties, plant parameters, vegetation heights and plant response.

5.2.5.1 Elevation and zonation

Elevations of the low marsh zone (marsh edge), middle marsh zone (20 m inland from wave break), and high marsh zone (40 m inland from wave break) were measured on eight transects in May and August 2010. Figs. 5.27 and 5.28 show the zonations of all eight transects with the elevations of the low, middle, and high marsh zones (Table C.7). In Transects 1 and 2, the low, middle and high marsh zones are all dominated by *Spartina alterniflora*. In Transects 3 and 4 located at North Graveline Bayou (brackish marsh), the low, middle and high marsh zones are dominated by *Juncus roemerianus*. No plant grows between the low and middle marsh zones on Transects 6 and 7 because of vehicle use.

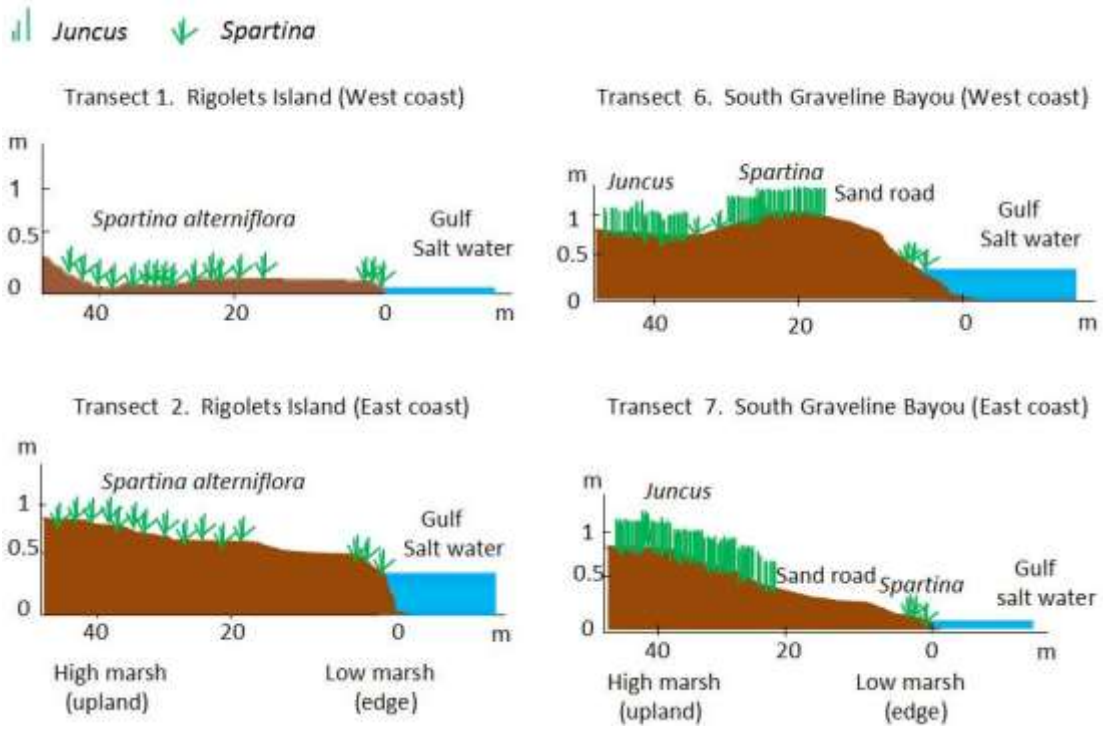

Fig. 5.27. Profile diagrams of coastal sites (Transects 1, 2, 6 and 7) which show the zonation of salt marshes

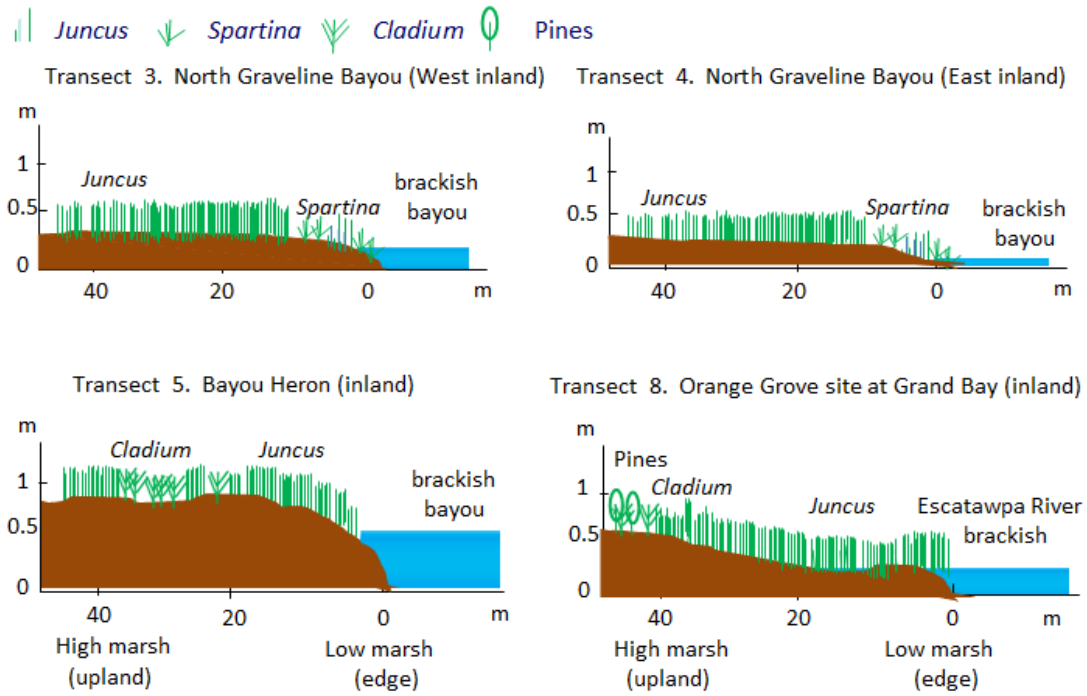

Fig. 5.28. Profile diagrams of inland sites (Transects 3, 4, 5 and 8) which show the zonation of brackish marshes.

In Transect 5 located at Bayou Heron of Grand Bay (brackish marsh), all the low, middle, and high marsh zones are dominated by *Juncus roemerianus*. In Transect 6, a bisect of South Graveline Bayou (West coast), *Spartina alterniflora* is the dominant species in the low marsh zone and *Juncus roemerianus* is the dominant species in both middle and high marsh zones. In Transect 7 at South Graveline Bayou (East coast), the low marsh zone is dominated by *Spartina alterniflora* and both middle and high marsh zones are dominated by *Scirpus robustus*. In Transect 8 at Orange Grove of Grand Bay (brackish marsh), all the low, middle, and high marsh zones are dominated by *Juncus roemerianus*. Both the low and middle marsh zones were inundated by the brackish water in Transect 8 at May 2010 sampling but not at August and November 2010.

5.2.5.2 **Soil properties**

The average moisture, average organic matter, average bulk density and mean grain size of soil samples in eight transects were compared in the low and high marsh zones, as shown in Figs. 5.29, 5.31, 5.33 and 5.35 and Tables C.8-C.11. The soil percentages of sand, silt and clay in the low and high marsh zones in eight transects are shown in Figs. 5.37 and 5.38, respectively. The results combined by low and high marsh zones, coastal and inland marsh zones, and Grand Bay and the Graveline Bayou sites in eight transects are shown in Fig. 5.30, 5.32, 5.34, 5.36 and 5.39. Table 5.8 summarizes the comparison results. For example, the low marsh zones have lower average soil organic matter than the high marsh zones.

Differences in the average soil properties between low and high marshes, between coastal and inland marshes and between Grand Bay and Graveline Bayou were compared using the two-way ANOVA test, and the results are shown in Table 5.9. One can see that there is not significant difference between low and high marshes, but mixed results between Grand Bay and Graveline Bayou.

Table 5.8. Comparison of average soil properties in different marsh zones

Soil property		Location	vs.	Location
Moisture		low marsh zones	<	high marsh zones
		coastal marshes	<	inland marshes
		Grand Bay	<	Graveline Bayou
Organic matter		low marsh zones	<	high marsh zones
		coastal marshes	<	inland marshes
		Grand Bay	>	Graveline Bayou
Bulk density		low marsh zones	<	high marsh zones
		coastal marshes	>	inland marshes
		Grand Bay	>	Graveline Bayou
Mean grain size		low marsh zones	<	high marsh zones
		coastal marshes	>	inland marshes
		Grand Bay	>	Graveline Bayou
Percentage	Sand	low marsh zones	<	high marsh zones
		coastal marshes	>	inland marshes
		Grand Bay	>	Graveline Bayou
	Silt	low marsh zones	>	high marsh zones
		coastal marshes	<	inland marshes
		Grand Bay	<	Graveline Bayou
	Clay	low marsh zones	<	high marsh zones
		coastal marshes	<	inland marshes
		Grand Bay	>	Graveline Bayou

Table 5.9. ANOVA test results of significant difference in soil properties in marsh zones

Soil property	Low vs. high marsh zones	Coastal vs. inland marshes	Grand Bay vs. Graveline Bayou
Moisture	No (p>0.05)	No (p>0.05)	No (p>0.05)
Organic matter	No (p>0.05)	Yes (p=8.556E-06<0.05)	No (p>0.05)
Bulk densituy	No (p>0.05)	Yes (p=3.403E-04<0.05)	No (p>0.05)
Mean grain size	No (p>0.05)	Yes (p=3.2E-05<0.05)	No (p>0.05)
Percentage of sand	No (p>0.05)	Yes (5.92E-14<0.05)	Yes (p=0.0013<0.05))
Percentage of clay	No (p>0.05)	Yes (3.674E-11<0.05)	No (p>0.05)
Percentage of silt	No (p>0.05)	Yes (2E-09<0.05)	Yes (p=0.00049<0.05)

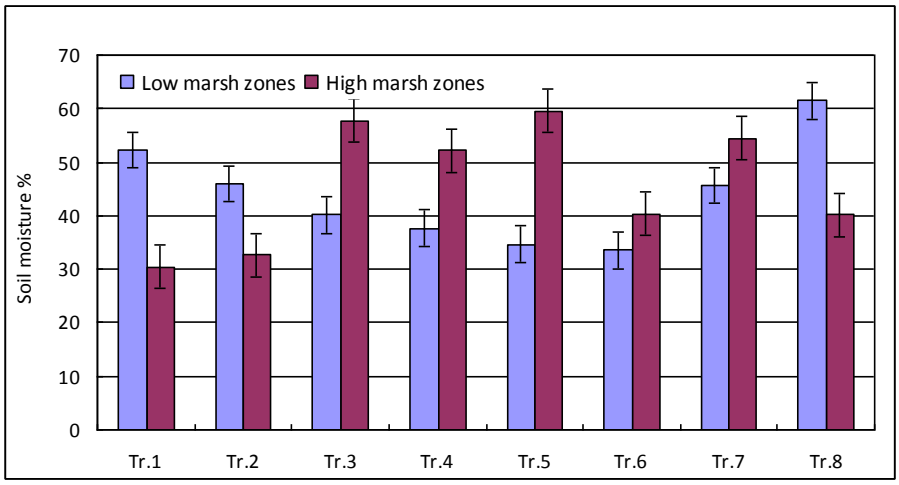

Fig. 5.29. The average soil moisture in the low and high marsh zones in eight transects (±SE, n=120)

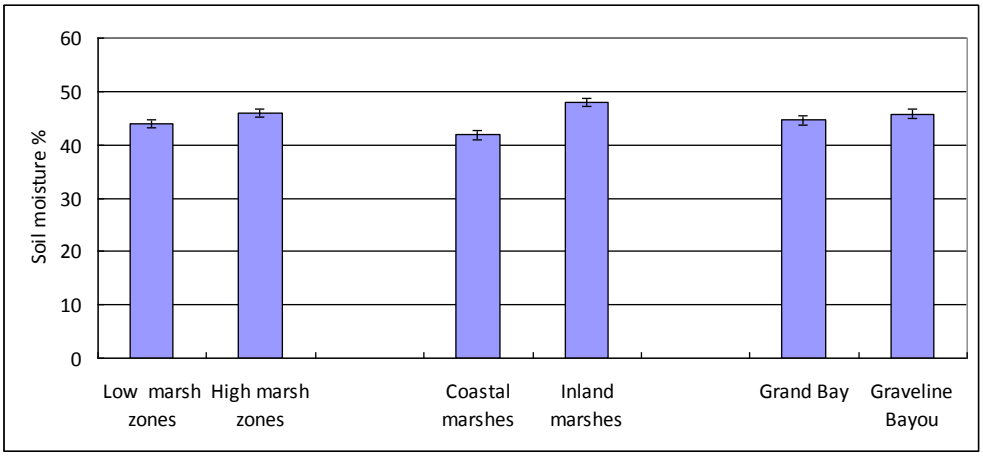

Fig. 5.30. Average soil moisture compared for low marsh zones, high marsh zones, coastal marshes, inland marshes, Grand Bay and Graveline Bayou (±SE, n=120)

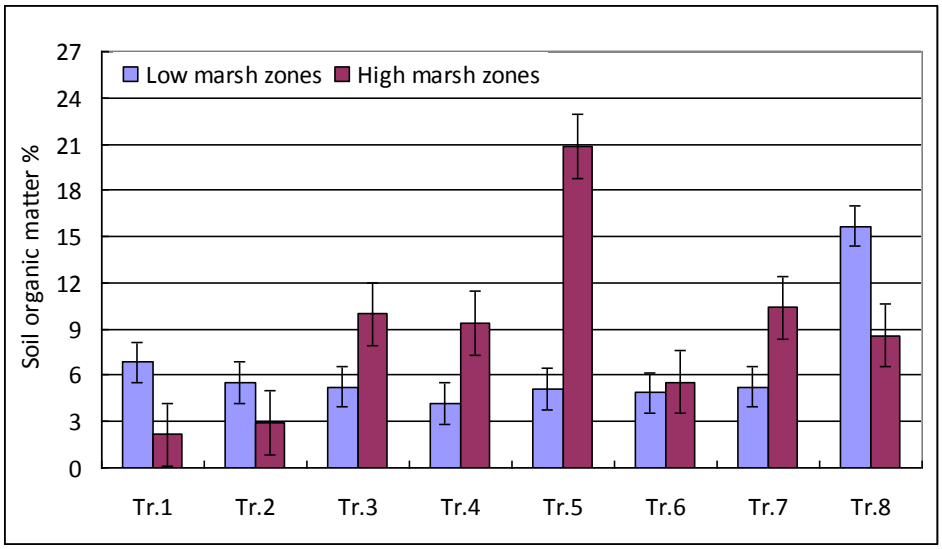

Fig. 5.31 Average soil organic matter in the low and high marsh zones in eight transects (±SE, n=120).

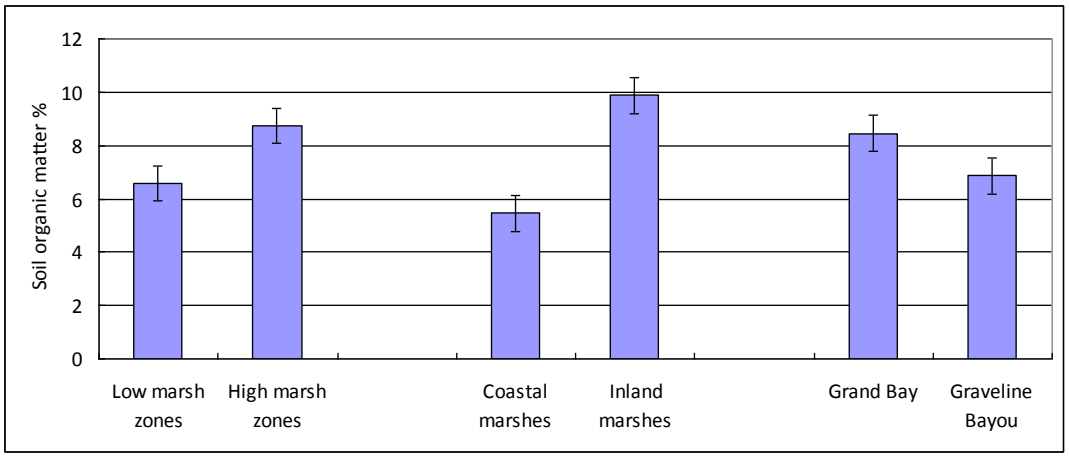

Fig. 5.32. Average soil organic matter compared for low marsh zones, high marsh zones, coastal marshes, inland marshes, Grand Bay and Graveline Bayou (±SE, n=120).

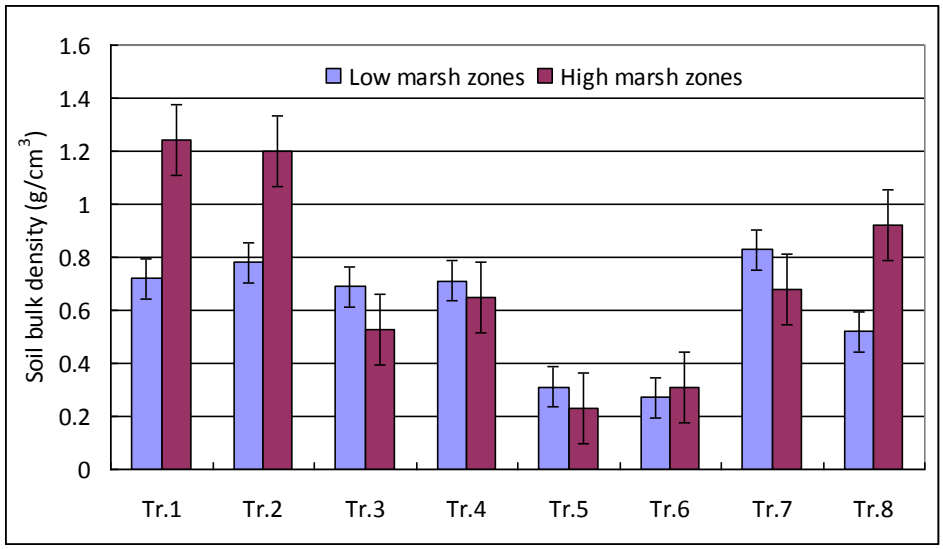

Fig. 5.33. Average soil bulk density in the low and high marsh zones in eight transects (±SE, n=120).

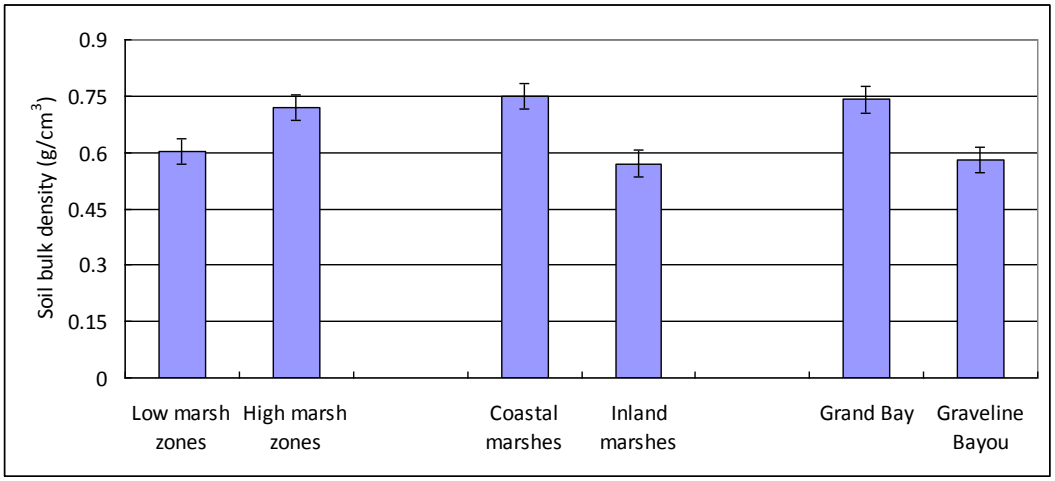

Fig. 5.34. Average soil bulk density compared for low marsh zones, high marsh zones, coastal marshes, inland marshes, Grand Bay and Graveline Bayou (±SE, n=120).

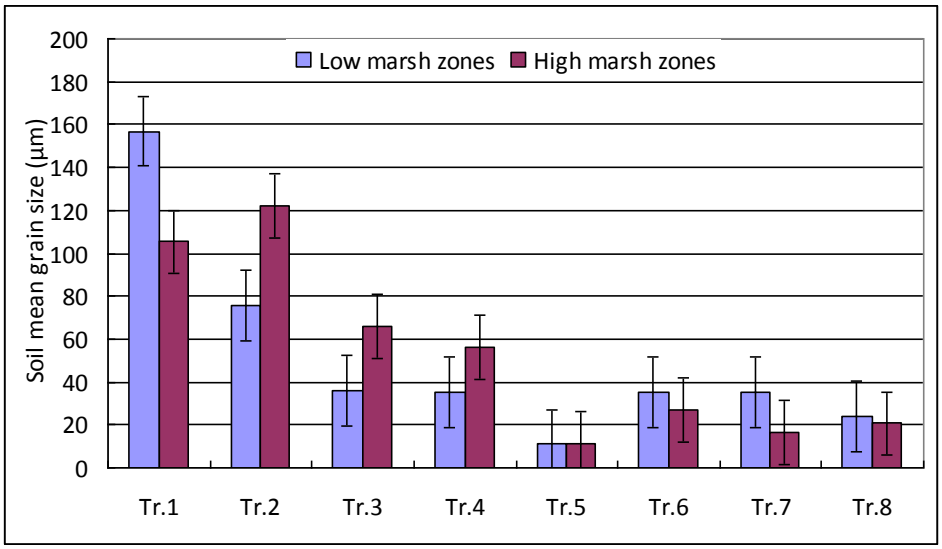

Fig. 5.35. Mean grain size in the low and high marsh zones in eight transects (±SE, n=120).

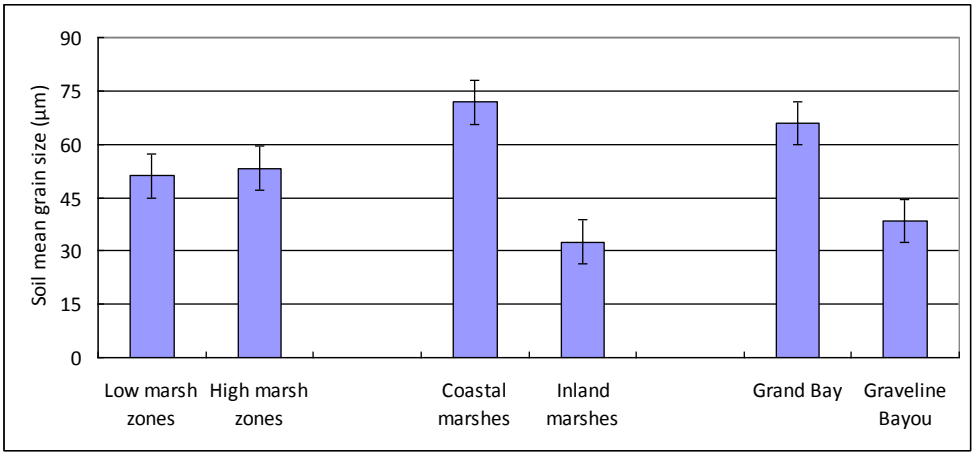

Fig. 5.36. Mean grain size compared for low marsh zones, high marsh zones, coastal marshes, inland marshes, Grand Bay and Graveline Bayou (±SE, n=120).

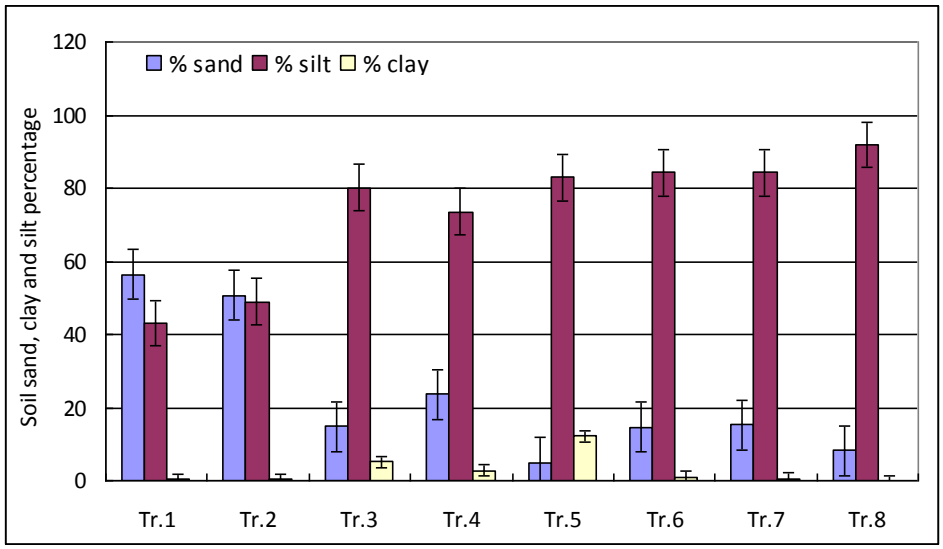

Fig. 5.37. Percentage of sand, clay and silt in the low marsh zones in eight transects (±SE, n=120).

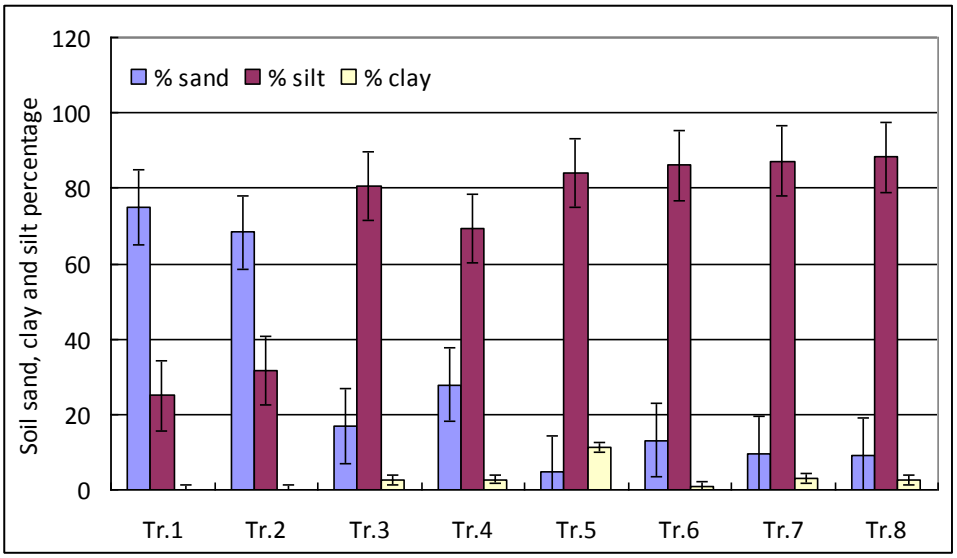

Fig. 5.38. Percentage of sand, clay and silt in the high marsh zones in eight transects (±SE, n=120).

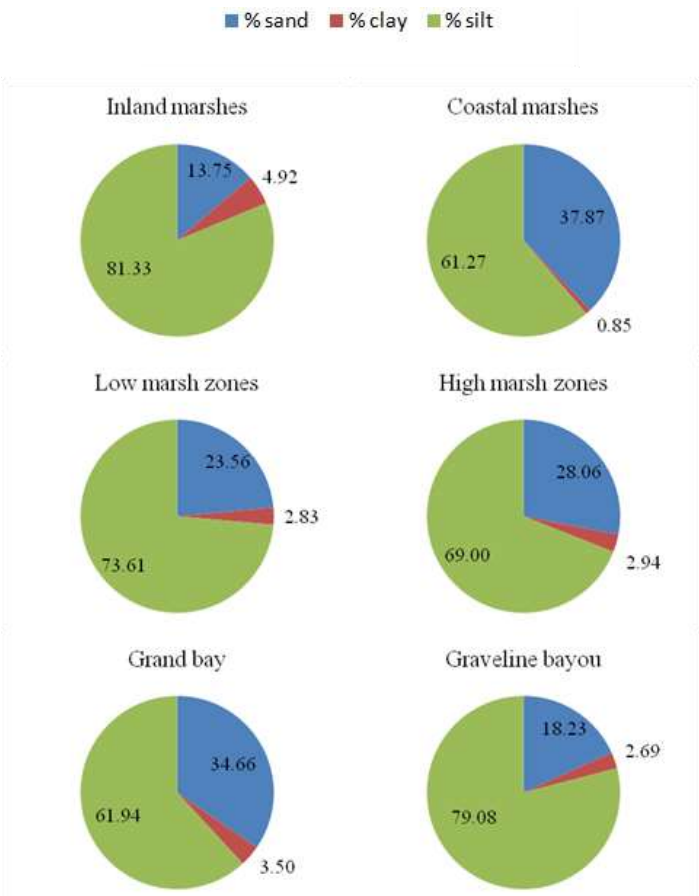

Fig. 5.39. Percentage of sand, clay and silt compared for low marsh zones, high marsh zones, coastal marshes, inland marshes, Grand Bay and Graveline Bayou.

5.2.5.3 **Plant parameters**

Percent cover

As in other marsh studies (Holland and Burk 1990), percent cover is used here to represent density. The low marsh zone and high marsh zone for both Transect 1 (west coast of Rigolets Island) and Transect 2 (East coast of Rigolets Island) are dominated by *Spartina alterniflora*. Three quadrats sampled in the low marsh zone for Transect 1 (west coast of South Graveline Bayou) have an average plant cover of 56.67% *Spartina alterniflora* and 43.33% open space. Another three quadrats in the high marsh zone for Transect 1 are occupied by 86.67% *Spartina alterniflora* and 13.33% open space. The low marsh zone for Transect 2 (east coast of Rigolets Island) is occupied by 70% *Spartina alterniflora* and 30% open space. The high marsh zone for Transect 2 is occupied by 73.33% *Spartina alterniflora* and 26.67% open space averaged in three quadrats. The low marsh zone for Transect 6 (west coast of South Graveline Bayou) is occupied by 80% *Spartina alterniflora* and 20% open space averaged in three quadrats. The high marsh zone for Transect 6 is occupied by 55% *Juncus roemerianus*, 10% *Spartina alterniflora*, 5% *Distichlis spicata* and 30% open space averaged in three quadrats. The low marsh zone for Transect 7 (east coast of South Graveline Bayou) has an average plant cover of 80% *Spartina alterniflora* and 20% open space. The high marsh zone

is occupied by 28.33% *Cladium mariscus*, 31.67% *Scirpus robustus*, 5% *Juncus roemerianus* and 35% open space averaged in three quadrats. The low marsh zones combined at these four coastal marsh transects have an average of 62.5% plant cover and high marsh zones have an average of 73.8% plant cover. When data from low marsh zone and high marsh zone are pooled at these four coastal marsh transects, the coastal marsh transects have an average of 68.1% plant cover.

The low marsh zone and high marsh zone for the four inland marsh transects are all dominated by *Juncus roemerianus*. The low marsh zone for Transect 3 (west inland of North Graveline Bayou) is occupied by 56.67% *Juncus roemerianus* and 10.33% *Spartina alterniflora*, and 33% open space averaged in three quadrats. The high marsh zone for Transect 3 is occupied by 90% *Juncus roemerianus*, 3.33% *Spartina alterniflora* and 6.67% open space averaged in three quadrats. The low marsh zone for Transect 4 (east inland of North Graveline Bayou) 74.67% *Juncus roemerianus*, 1% *Spartina alterniflora* and 24.33% open space averaged in three quadrats. The high marsh zone for Transect 4 is occupied by 33.67% *Juncus roemerianus* and 66.33% open space averaged in three quadrats. *Spartina alterniflora* The low marsh zone for Transect 5 (brackish marsh at Bayou Heron) is occupied by 80.67% *Juncus roemerianus*, 5% *Cladium mariscus*, 3% *Rumex verticillatus* and 11.33% open space averaged in three quadrats. The high marsh zone for Transect 5 is occupied by 89% *Juncus roemerianus*, 5% *Distichlis spicata* and 6% open space averaged in three quadrats. The low marsh zone for Transect 8 (Orange Grove at Grand Bay) is occupied by 100% *Juncus roemerianus* averaged in three quadrats. The high marsh zone for Transect 8 is occupied by 45% *Juncus roemerianus*, 25% *Distichlis spicata* and 15% *Cladium mariscus* averaged in three quadrats. The low marsh zones combined at these four inland marsh transects have an average of 82.84% plant cover and high marsh zones have an average of 76.5% plant cover. When data from low marsh zone and high marsh zone are pooled at these four inland marsh transects, the inland marsh transects have an average of 79.67% plant cover.

The average plant cover of the low and high marsh zones at the coastal marsh transects (Fig. 5.40) is lower than that at the inland marsh transects (Fig. 5.41). The plant average percent cover in the low marsh zones is lower than in the high marsh zones (Fig. 5.42). The plant average percent cover in the coastal is lower than in inland sites. On the other hand, when data for both the low and high marsh zones are combined into the Grand Bay and Graveline Bayou sites, the results (Fig. 5.42) show that the average plant percent cover at the Grand Bay is higher than at the Graveline Bayou.

Differences in the average plant covers between low and high marshes, between coastal and inland marshes and between Grand Bay and Graveline Bayou were compared using the two-way ANOVA test, and the results Table 5.10 show that there is significant difference in plant covers between coastal and inland marshes, but not between low and high marshes and between Grand Bay and Graveline Bayou. Note that Table 5.10 also provides similar comparision for other plant parameters, which will not be described in the following sections again to avoid redundancy.

Table 5.10. ANOVA test results of significant difference in plant parameters in marsh zones

Plant parameter	Low vs. high marsh zones	Coastal vs. inland marshes	Grand Bay vs. Graveline Bayou
Percent cover	No (p>0.05)	Yes (p=0.047<0.05)	No (p>0.05)
Vegetation height (Green *S. alterniflora*)	Yes (p=2.25 E-07 <0.05)	-	Yes (p=8.74 E-15 <0.05)
Vegetation height (Dead *S. alterniflora*)	Yes (p=6.7 E-13 <0.05)	-	Yes (p=4.44 E-07 <0.05)
Vegetation height (Green *J. roemerianus*)	No (p>0.05)	-	No (p>0.05)
Vegetation height (Dead *J. roemerianus*)	No (p>0.05)	-	No (p>0.05)
Rhizome Thickness (*S. alterniflora*)	No (p>0.05)	-	-
Rhizome Thickness (*J. roemerianus*)	No (p>0.05)	-	-
Stem Diameter (*S. alterniflora*)	Yes (p=5.07 E-04 <0.05)	-	No (p>0.05)
Stem Diameter (*J. roemerianus*)	No (p>0.05)	-	Yes (p=0.044 <0.05)
Density	Yes (p=2.75 E-05 <0.05)	Yes (p=7.3 E-15 <0.05)	No (p>0.05)
Aboveground biomass	No (p>0.05)	No (p>0.05)	No (p>0.05)
Belowground biomass	No (p>0.05)	No (p>0.05)	Yes (p=3.79 E-04 <0.05)

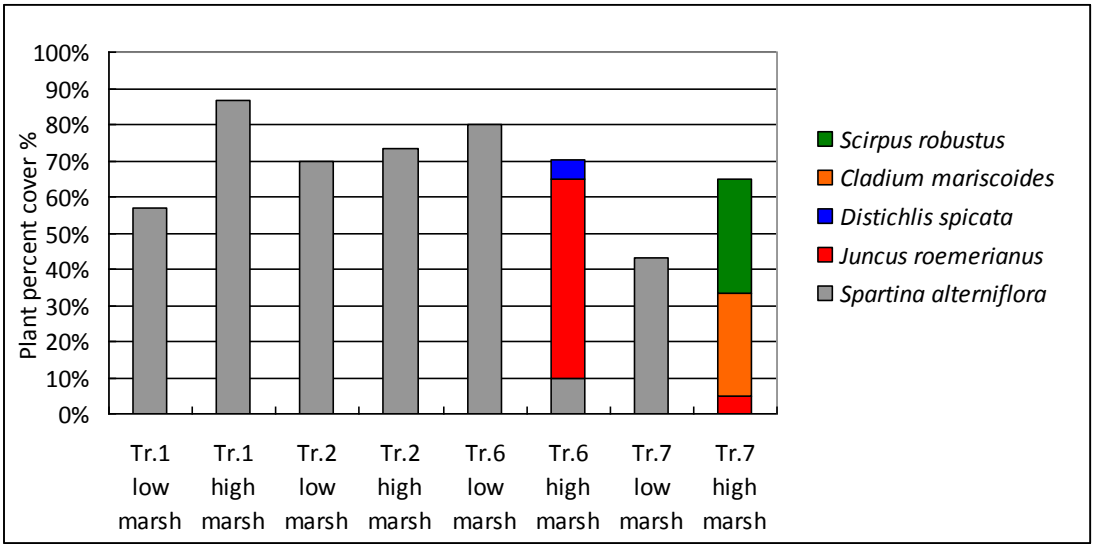

Fig. 5.40. Average space occupied by five species at the coastal sites on Transects 1, 2, 6, and 7.

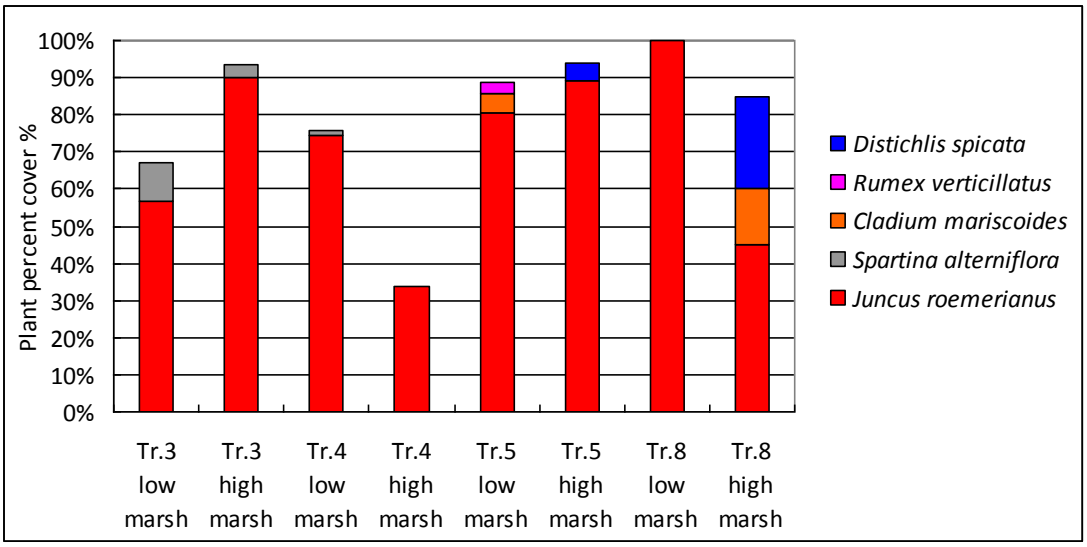

Fig. 5.41. Average space occupied by five species at the inland sites on Transects 3, 4, 5, and 8.

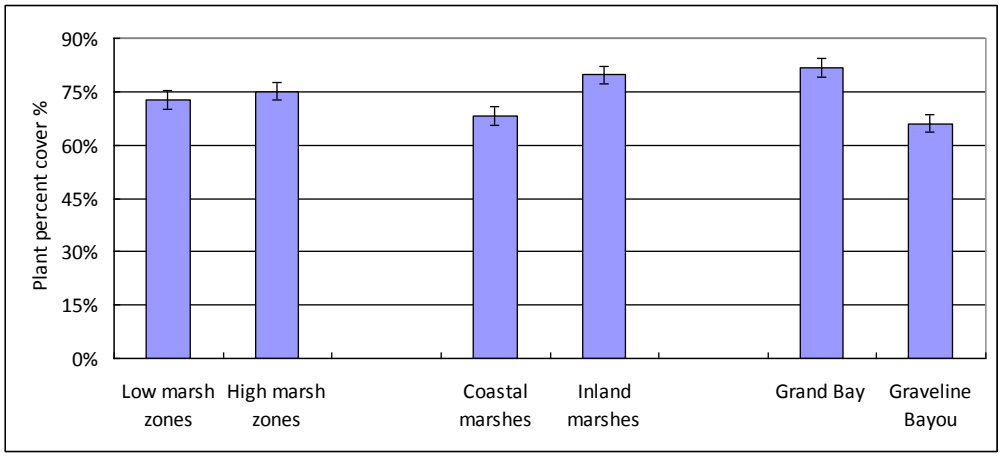

Fig. 5.42. Average percent cover (space occupied) compared for low marsh zones, high marsh zones, coastal marshes, inland marshes, Grand Bay and Graveline Bayou (±SE, n=32).

Vegetation heights

The results combined by the low and high marsh zones in Transects 1-8 (Fig. 5.43) show that the live standing shoot heights of *Spartina alterniflora* range from 0.45 m to 1.4 m and the average live standing shoot heights are 0.93 m in the low marsh zones. The dead standing shoot heights of *Spartina alterniflora* range from 0.3 m to 0.75 m and the average dead standing shoot heights are 0.53 m. The live standing shoot heights of *Juncus roemerianus* range from 0.78 m to 1.45 m in the low marsh zones. The average live standing shoot heights are 1.25 m. The dead standing shoot heights of *Juncus roemerianus* range from 0.67 m to 1.52 m. The average dead standing shoot heights are 1.14 m.

In the high marsh zones, the live standing shoot heights of *Spartina alterniflora* range from 0.78 m to 2.30 m and average live standing shoot heights are 1.01 m. The dead standing shoot heights of *Spartina alterniflora* range from 0.83 m to 1.45 m and the average dead standing shoot heights are 1.03 m in the high marsh zones. The live standing shoot heights

of *Juncus roemerianus* range from 1.4 m to 2.3 m and the average live standing shoot heights are 1.30 m in the high marsh zones. The dead standing shoot heights of *Juncus roemerianus* range from 0.8 m to 1.75 m and the average dead standing shoot heights are 1.07 m in the high marsh zones.

The average live and dead standing shoot heights of *Spartina alterniflora* in the low marsh zones are lower than those in the high marsh zones. The average live standing shoot heights of *Juncus roemerianus* in the low marsh zones are lower than those in the high marsh zones, but the average dead standing shoot heights in the low marsh zones are higher than in the high marsh zones.

Compared by different sampling seasons (Spring: March, April and May; Summer: June, July and August; Fall: September, October and November) in the low and high marsh zones in eight transects, the results (Fig. 5.44) show that the average live and dead standing shoot heights of both *Spartina alterniflora* and *Juncus roemerianus* in Summer are lowest of the three seasons sampled in the low marsh zones except the mean dead standing shoots heights of *Spartina alterniflora*. However, in the high marsh zones the average standing shoot heights of both *Spartina alterniflora* and *Juncus roemerianus* in Fall are lowest in three seasons.

The results combined by the coastal and inland marshes (Fig. 5.45) show that the live standing shoot heights of *Spartina alterniflora* range from 0.45 m to 1.4 m and the average live standing shoot heights are 0.97 m in the coastal marshes. The dead standing shoot heights of *Spartina alterniflora* range from 0.3 m to 1.45 m and the average dead standing shoot heights are 0.85 m in the coastal marshes. The live standing shoot heights of *Juncus roemerianus* range from 0.78 m to 2.3 m and the average live standing shoot heights are 1.28 m in the inland marshes. The dead standing shoot heights of *Juncus roemerianus* range from 0.67 m to 1.75 m and the average dead standing shoot heights are 1.13 m in the inland marshes. The average live standing shoot heights of *Spartina alterniflora* are higher than the average dead standing shoot heights. The average live standing shoot heights of *Juncus roemerianus* are higher than the average dead standing shoot heights as well.

Compared by different sampling seasons (Spring: March, April and May; Summer: June, July and August; Fall: September, October and November) in the coastal and inland marshes, the results (Fig. 5.46) show that the average live and dead standing shoot heights of *Spartina alterniflora* in Fall are lower than in Summer in the coastal marshes. The average live and dead standing shoot heights of *Juncus roemerianus* in Fall are lowest in three seasons in the inland marshes.

The results combined by the Grand Bay and the Graveline Bayou sites (Fig. 5.47) show that the live standing shoot heights of *Spartina alterniflora* range from 0.32 m to 1.32 m and the average live standing shoot heights are 0.84 m at the Grand Bay. The dead standing shoot heights of *Spartina alterniflora* range from 0.3 m to 1.45 m and the average dead standing shoot heights are 0.86 m at the Grand Bay. The live standing shoot heights of *Juncus roemerianus* range from 0.76 m to 2.3 m and the average live standing shoot heights are 1.28 m at the Grand Bay. The dead standing shoot heights of *Juncus roemerianus* range from 0.65 m to 1.75 m and the average dead standing shoot heights are 1.12 m at the Grand Bay. The live standing shoot heights of *Spartina alterniflora* range from 0.72 m to 1.62 m and the average live standing shoot heights are 1.22 m at the Graveline Bayou. The dead standing shoot heights of *Spartina alterniflora* range from 0.7 m to 0.88 m and the average dead standing shoot heights are 0.79 m at the Graveline Bayou. The live standing shoot heights of *Juncus roemerianus* range from 1.1 m to 1.4 m and the average live standing shoot heights are 1.21 m at the Graveline Bayou. The dead standing shoot heights of *Juncus*

roemerianus range from 0.98 m to 1.45 m and the average dead standing shoot heights are 1.11 m at the Graveline Bayou. *Spartina alterniflora* and *Juncus roemerianus* at the Grand Bay have higher standing shoot heights than at the Graveline Bayou except the mean live standing shoot heights of *Spartina alterniflora* are higher at the Graveline Bayou.

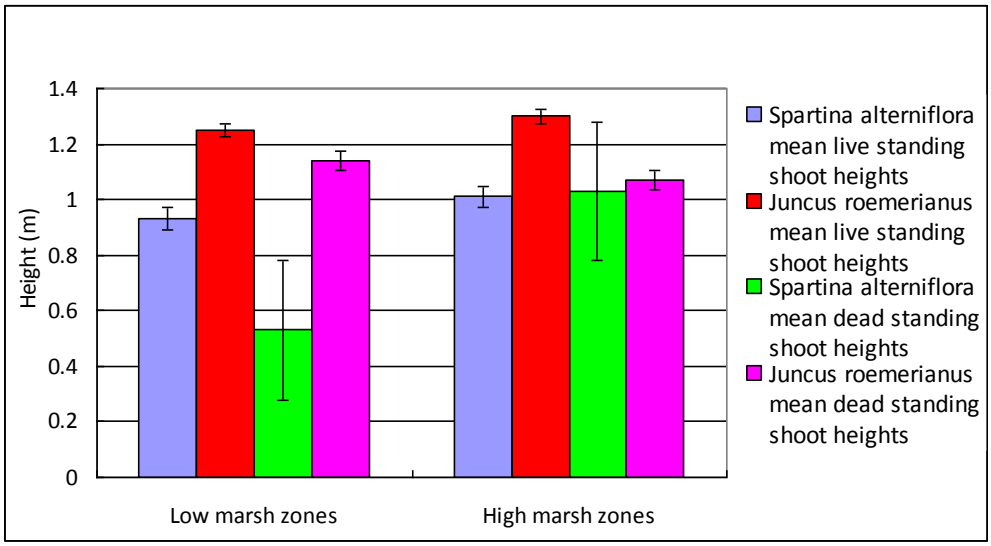

Fig. 5.43. *S. alterniflora* and *Juncus roemerianus* mean standing shoot heights compared between the low and high marsh zones (±SE, n=280)

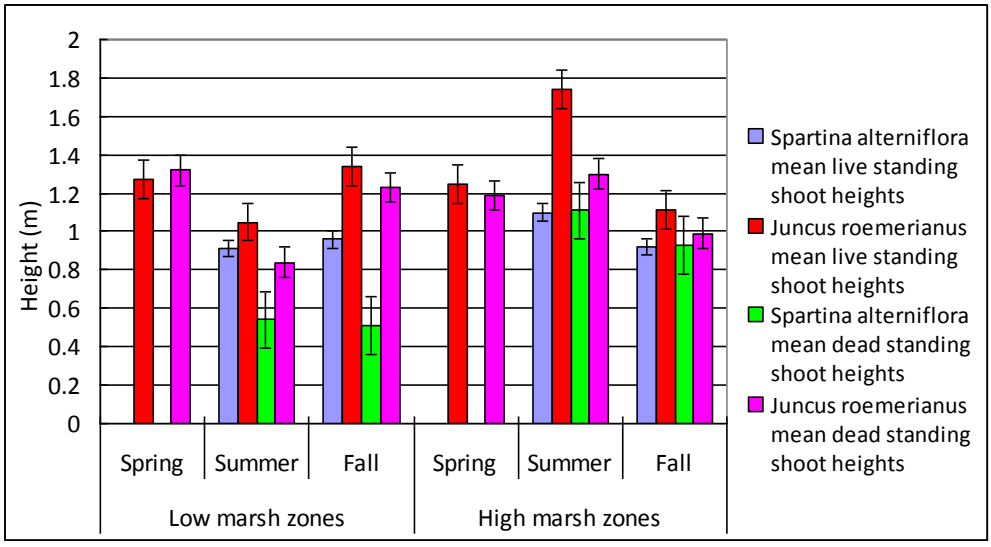

Fig. 5.44. Comparison of mean live and dead standing shoot heights of dominant plants in the low and high marsh zones in eight transects in different sampling seasons (±SE, n=280).

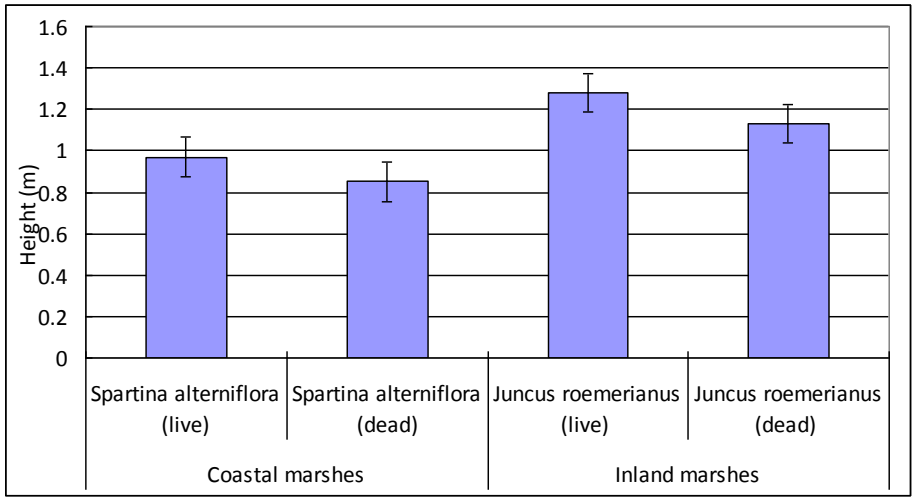

Fig. 5.45. *S. alterniflora* and *Juncus roemerianus* mean standing shoot heights compared between the coastal and inland marshes.

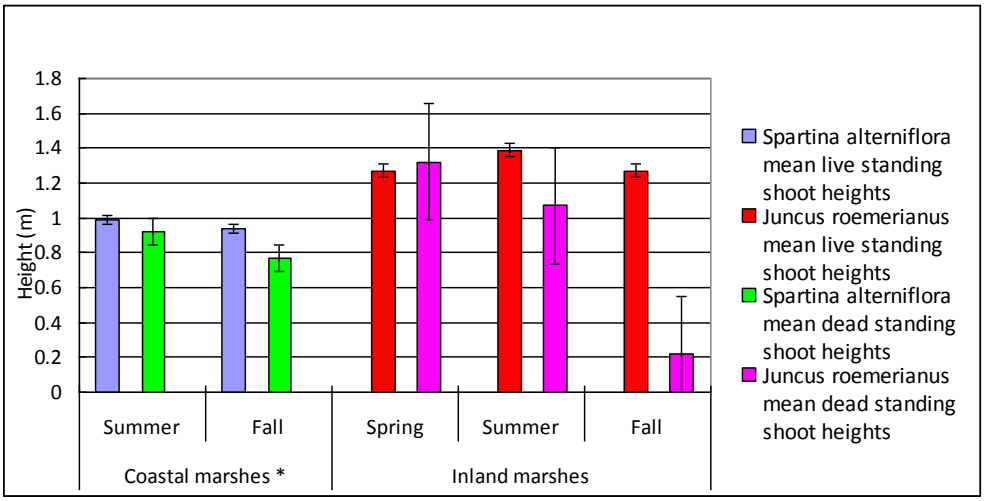

Fig. 5.46. Comparison of mean live and dead standing shoot heights of dominant plants in the coastal and inland marshes in different sampling seasons (±SE, n=280). [Boat access to coastal sites in Spring was not possible].

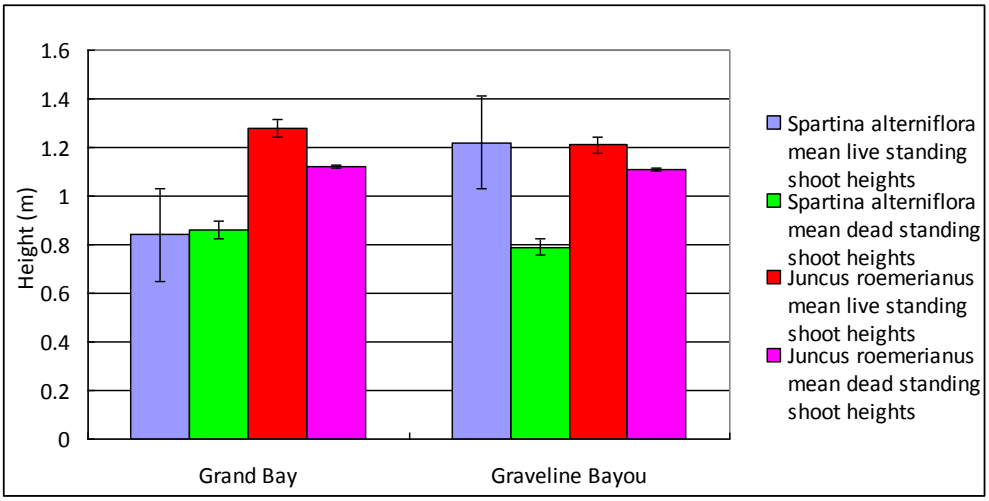

Fig. 5.47. Comparison of mean live and dead standing shoot heights of dominant plants at Grand Bay and Graveline Bayou (±SE, n=280).

Rhizome thickness and stem diameter

When data from the low and high marsh zones are combined in eight transects, the results (Fig. 5.48) show that the mean rhizome thickness of *Juncus roemerianus* are thicker than *Spartina alterniflora* in the low and high marsh zones. The mean rhizome thickness of both *Spartina alterniflora* and *Juncus roemerianus* in the high marsh zones are thicker than those in the low marsh zones. When data for the coastal and inland marshes are combined, the results (Fig. 5.49) show that the mean rhizome thickness of *Juncus roemerianus* in the inland marshes is thicker than *Spartina alterniflora* in the coastal marshes.

Compared by different sampling seasons (Spring: March, April and May; Summer: June, July and August; Fall: September, October and November) in the low and high marsh zones in eight transects, the results (Fig. 5.50) show that the mean rhizome thickness of *Spartina alterniflora* are thinnest in Fall in the low and high marsh zones. The mean rhizome thickness of *Juncus roemerianus* are thickest in Spring in three seasons in the low and high marsh zones.

Compared by different sampling seasons (Spring: March, April and May; Summer: June, July and August; Fall: September, October and November) in the coastal and inland marshes, the results (Fig. 5.51) show that the mean rhizome thickness of *Spartina alterniflora* are thinner than of *Juncus roemerianus* in all three seasons. The mean rhizome thickness of both *Spartina alterniflora* and *Juncus roemerianus* are thickest in Spring and thinnest in Fall.

Compared by the Grand Bay and Graveline Bayou sites, the results (Fig. 5.52) show that the mean rhizome thickness of *Spartina alterniflora* at the Grand Bay is thicker than that at the Graveline Bayou, but the mean rhizome thickness of *Juncus roemerianus* at the Grand Bay is similar to the Graveline Bayou. The mean rhizome thickness of *Juncus roemerianus* is thicker than *Spartina alterniflora* at both the Grand Bay and Graveline Bayou sites.

The mean stem diameters of both *Spartina alterniflora* and *Juncus roemerianus* in the low marsh zones are lower than those in the high marsh zones (Fig. 5.53). The mean stem diameter of *Spartina alterniflora* in the coastal marshes are higher than that of *Juncus roemerianus* in the inland marshes (Fig. 5.54).

When data for both the low and high marsh zones are combined into the Grand Bay and Graveline Bayou sites, the results (Fig. 5.55) show that the mean stem diameters of both

Spartina alterniflora and *Juncus roemerianus* at the Grand Bay are lower than at the Graveline Bayou.

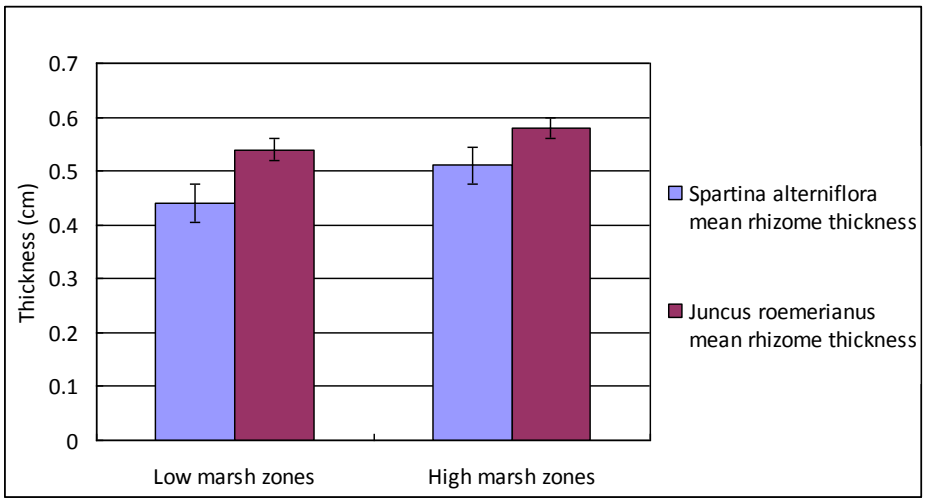

Fig. 5.48. Mean rhizome thickness of *Spartina alterniflora* and *Juncus roemerianus* compared for low and high marsh zones (±SE, n=102).

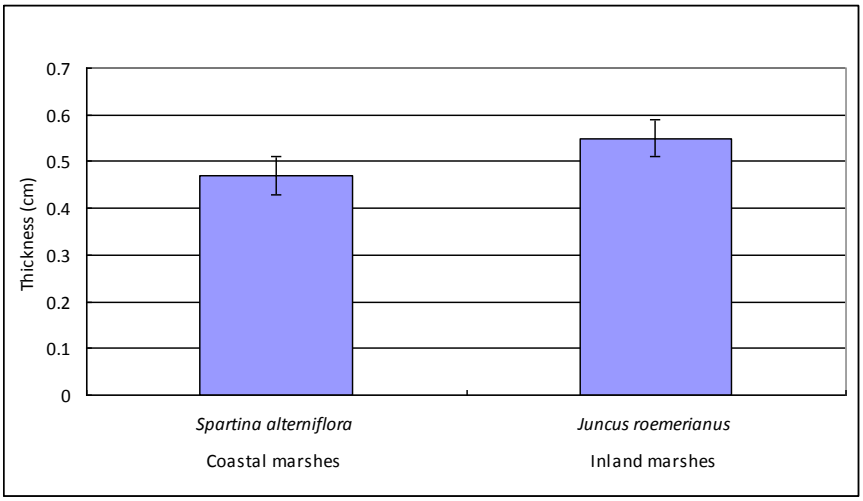

Fig. 5.49. Mean rhizome thickness of *Spartina alterniflora* and *Juncus roemerianus* compared for coastal and inland marshes.

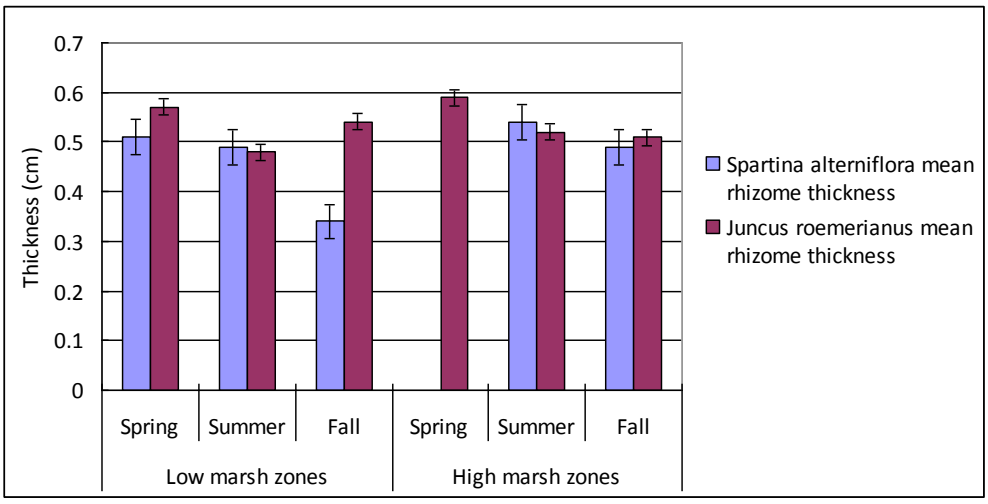

Fig. 5.50. ***S. alterniflora*** **and** ***Juncus roemerianus*** **mean rhizome thickness compared between the low and high marsh zones (±SE, n=102).**

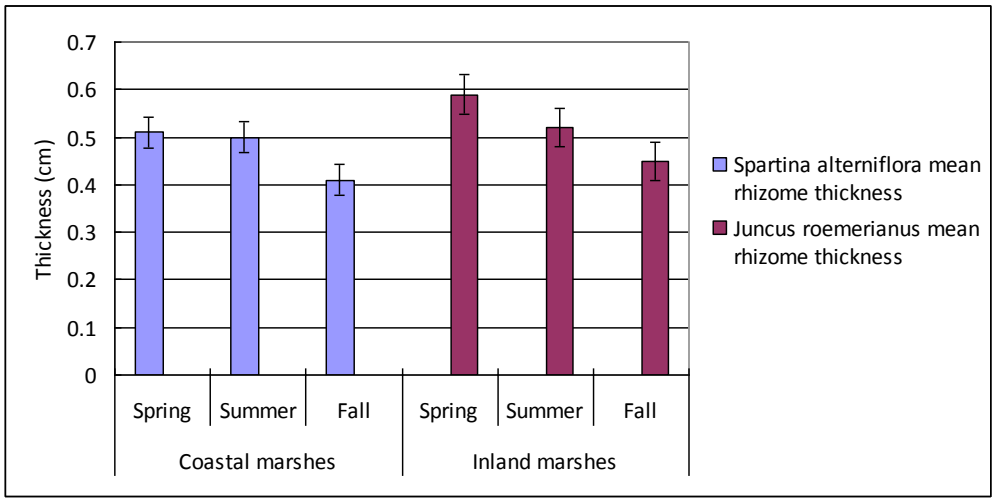

Fig. 5.51. ***S. alterniflora*** **and** ***Juncus roemerianus*** **mean rhizome thickness compared between the coastal and inland marshes (±SE, n=102).**

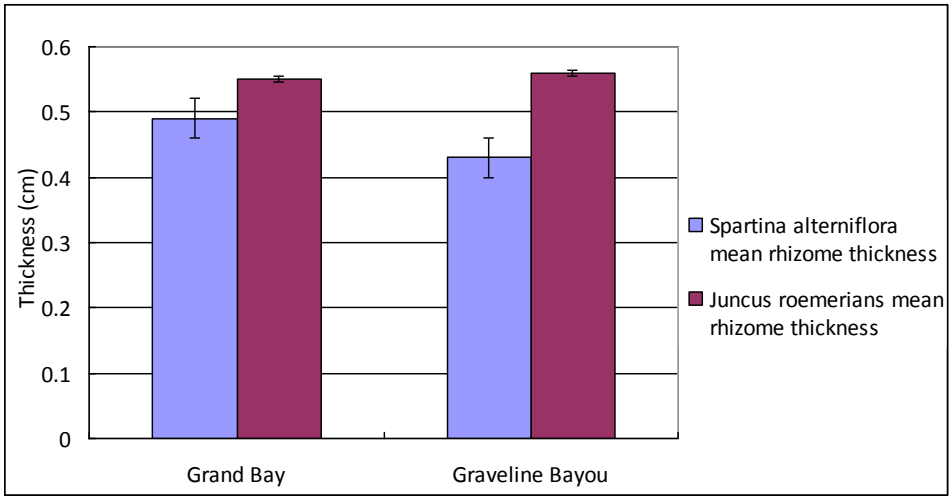

Fig. 5.52. S. alterniflora and Juncus roemerianus mean rhizome thickness compared for Grand Bay and Graveline Bayou (±SE, n=102).

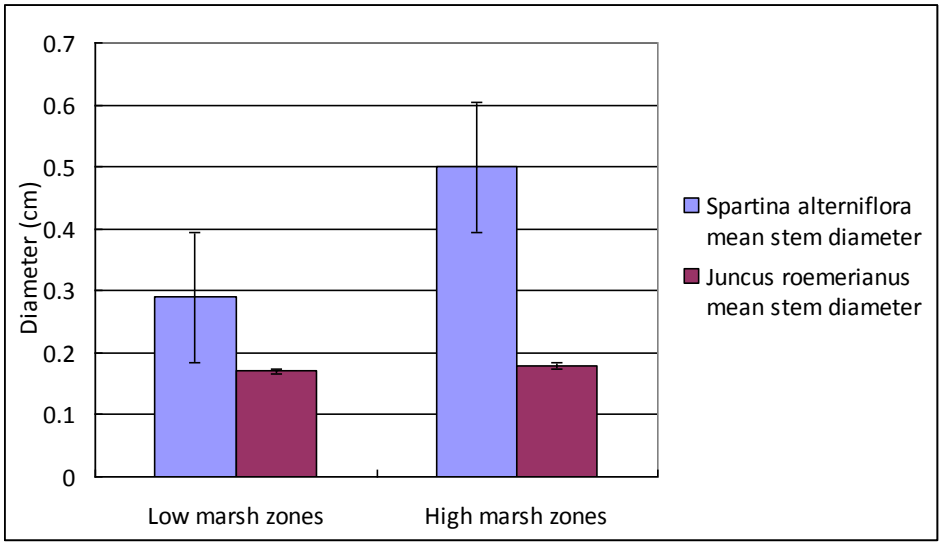

Fig. 5.53. Mean stem diameter of *Spartina alterniflora* and *Juncus roemerianus* compared for low and high marsh zones (±SE, n=66).

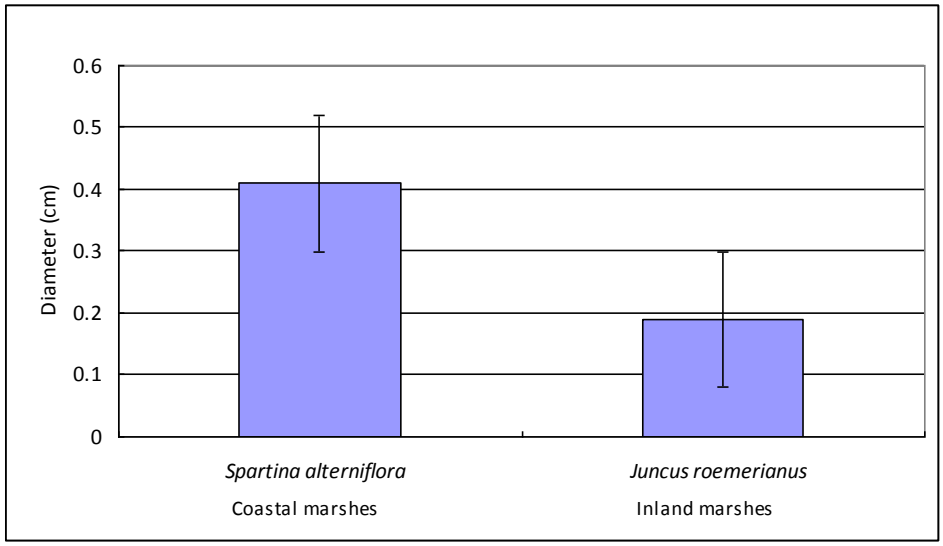

Fig. 5.54. Mean stem diameter of *Spartina alterniflora* and *Juncus roemerianus* compared for coastal and inland marshes.

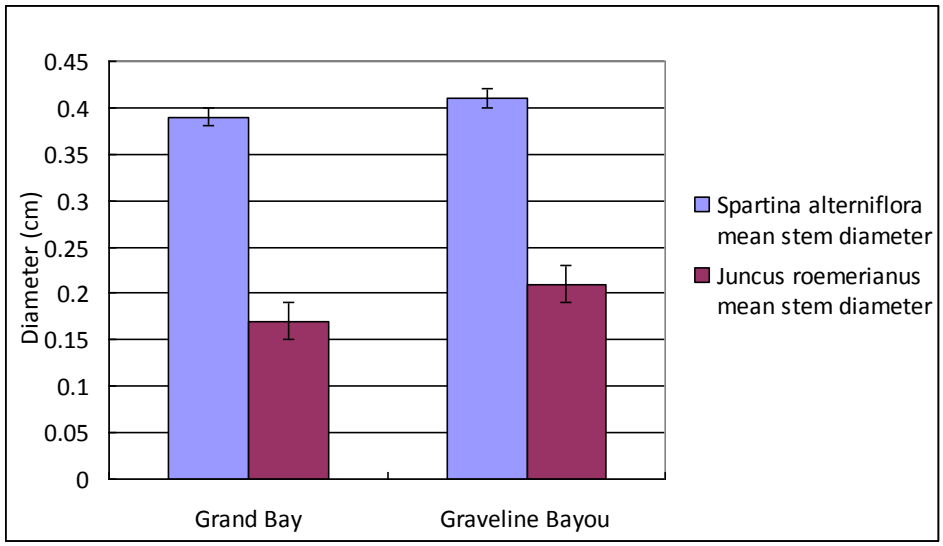

Fig. 5.55. Mean stem diameter of *Spartina alterniflora* and *Juncus roemerianus* compared for Grand Bay and Graveline Bayou.

Density

As in other marsh studies (Holland and Burk 1990), percent cover can be used here to represent density. Average plant density (units/m^2) was estimated by calculating the plant stem diameter of different plant species and multiplying its percent cover in each 0.25 m^2

quadrat. The results are shown in Fig. 5.56. When data for both the low and high marsh zones are combined into the Grand Bay and the Graveline Bayou, the results (Fig. 5.57) show that the average plant stem density at the Grand Bay is higher than at the Graveline Bayou.

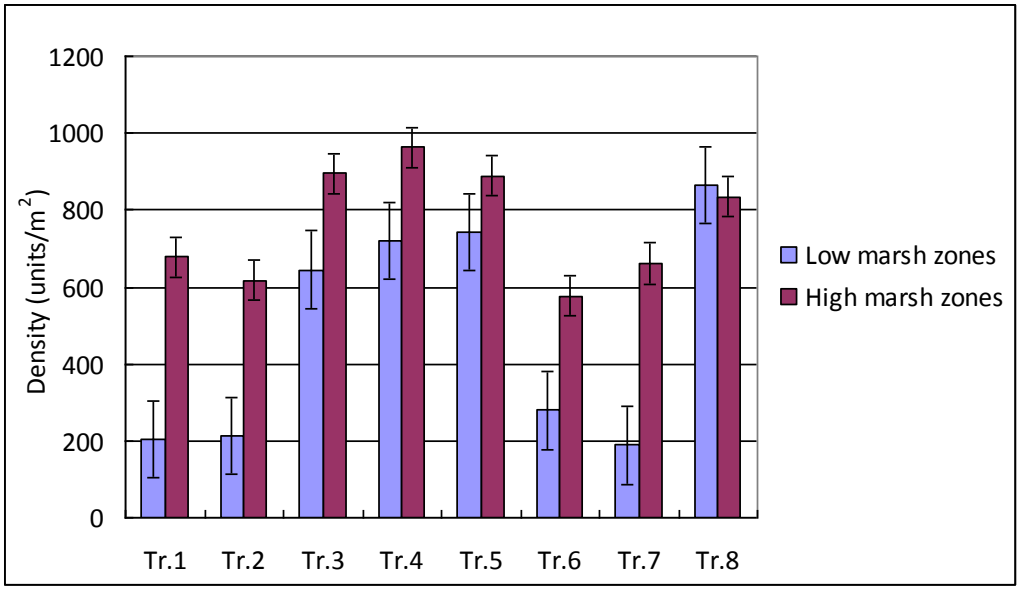

Fig. 5.56. Average plant density compared for low and high marsh zones in eight transects (±SE, n=66).

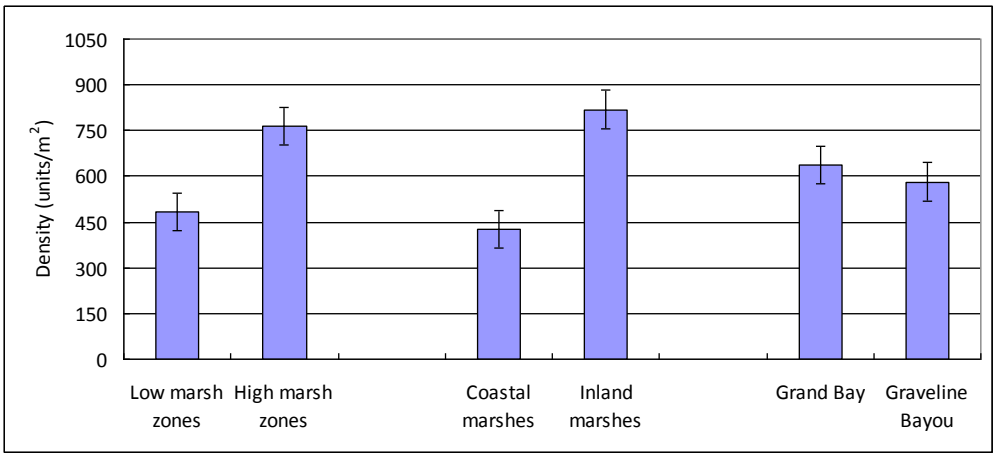

Fig. 5.57. Plant density compared for low marsh zones, high marsh zones, coastal marshes, inland marshes, Grand Bay and Graveline Bayou (±SE, n=66).

Above- and belowground biomass

Both average above- and belowground biomass in the low marsh zones combined on Transects 1-8 are lower than those in the high marsh zones (Fig. 5.58). The average belowground biomass in both low and high marsh zones is much higher than the average aboveground biomass.

When data for the eight transects are combined in the low and high marsh zones and compared by different sampling seasons (Spring: March, April and May; Summer: June, July and August; Fall: September, October and November), the results (Figs. 5.59 and 5.60) show that the average aboveground biomass in both low and high marsh zones is lowest in Fall. However, the average belowground biomass in both low and high marsh zones is lowest in Spring.

Both average above- and belowground biomass in the coastal marshes combined on Transects 1, 2, 6 and 7 are higher than those in the inland marshes combined on Transects 3, 4, 5 and 8 (Fig. 5.61).

When data for all the low and high marsh zones are combined into coastal and inland marshes and compared by different sampling seasons (Spring: March, April and May; Summer: June, July and August; Fall: September, October and November), the results (Figs. 5.62 and 5.63) show that the average aboveground biomass in the inland marshes is the lowest in Fall and highest in Summer. The average aboveground biomass in the coastal marshes is lowest in Spring and highest in Summer. The average belowground biomass in both coastal and inland marshes is lowest in Spring.

When data for all the low and high marsh zones are combined into the Grand Bay and the Graveline Bayou sites, the results (Fig. 5.64) show that the aboveground biomass at the Grand Bay is lower than that at the Graveline Bayou and the belowground biomass at the Grand Bay is much higher than that at the Graveline Bayou.

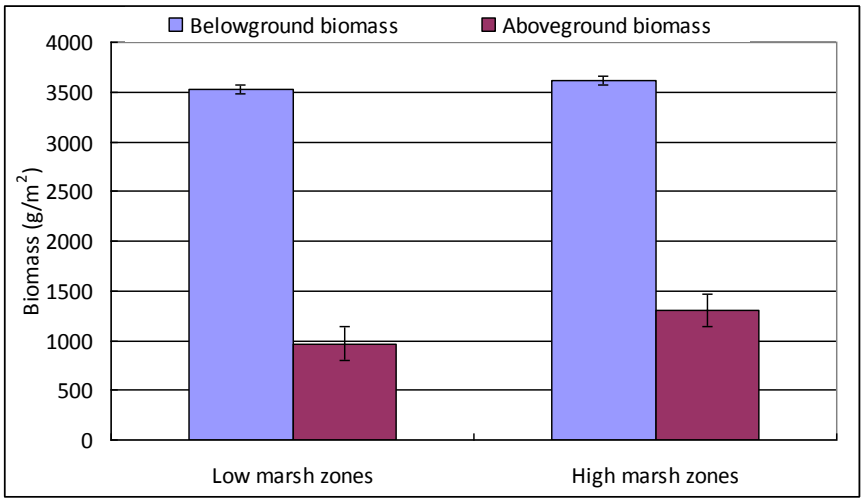

Fig. 5.58. Mean above- and belowground biomass sampled in all seasons compared for low and high marsh zones (±SE, n=150).

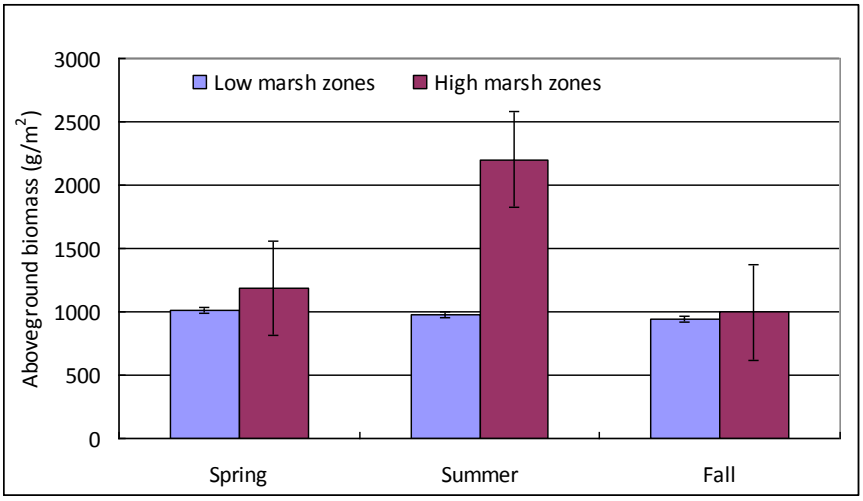

Fig. 5.59. Mean aboveground biomass compared in Spring, Summer and Fall between the low and high marsh zones (±SE, n=150).

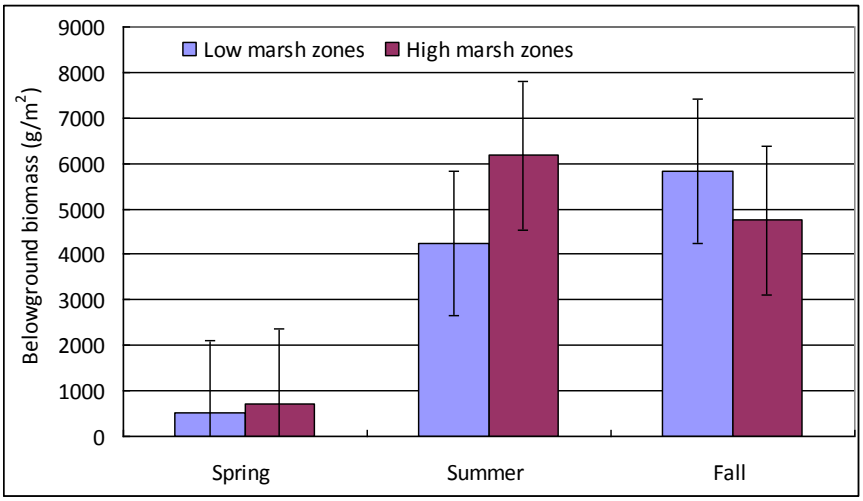

Fig. 5.60. Mean belowground biomass compared in Spring, Summer and Fall between the low and high marsh zones (±SE, n=150).

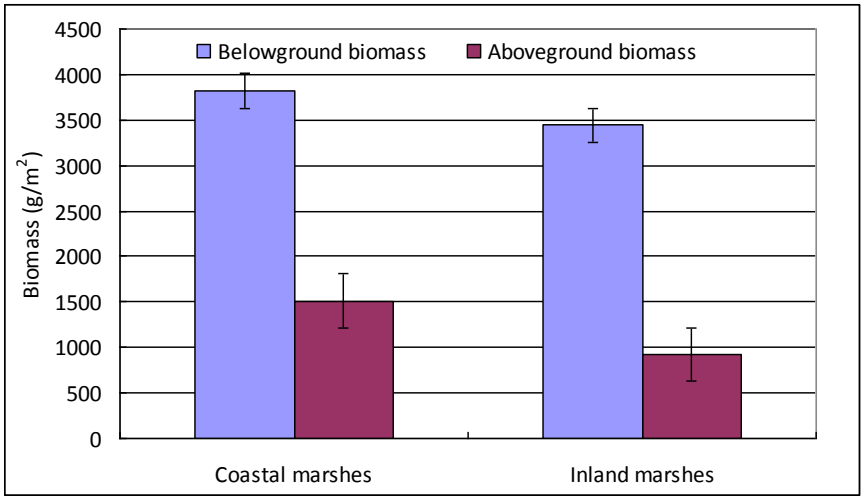

Fig. 5.61. Mean above- and belowground biomass sampled in all seasons compared for coastal and inland marshes (±SE, n=150).

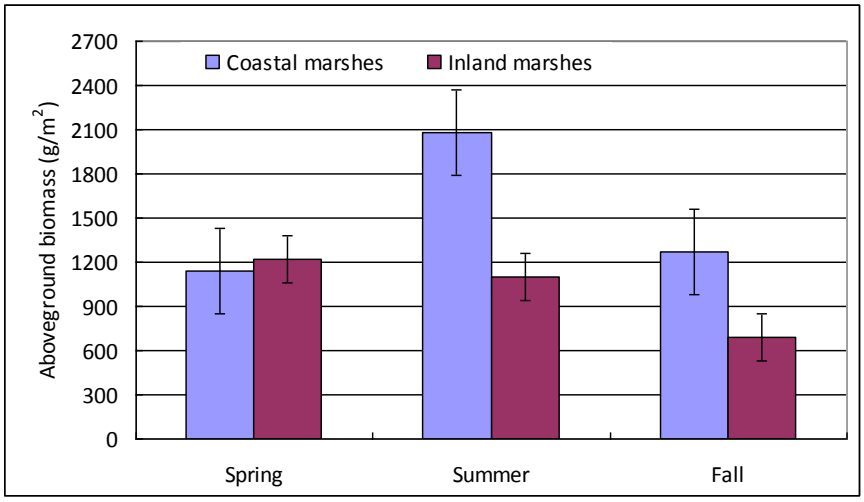

Fig. 5.62. Mean aboveground biomass compared in Spring, Summer and Fall between the coastal and inland marshes (±SE, n= 150).

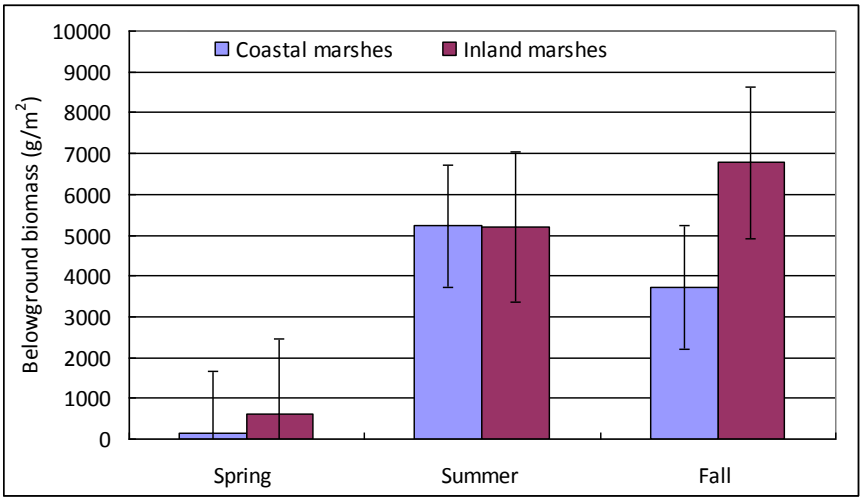

Fig. 5.63. Mean belowground biomass compared in Spring, Summer and Fall between the coastal and inland marshes (±SE, n=150).

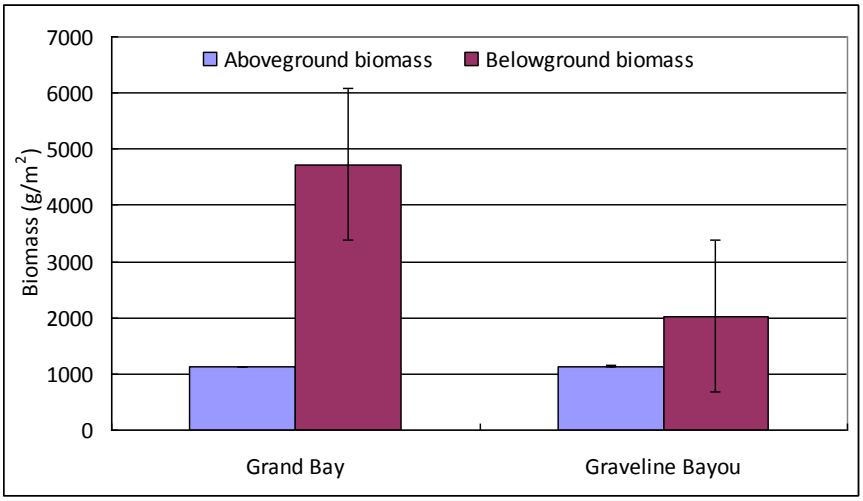

Fig. 5.64. Mean above- and belowground biomass compared for Grand Bay and Graveline Bayou (±SE, n=150).

5.2.5.4 **Plant response**

Environmental conditions have an essential effect on plant growth especially sediments. The high marsh zones contain greater organic matter content of sediments (Fig. 5.32) which affects the amount of nutrients and metals stored in the soil and this in turn has an impact on the plant. Plants in the high marsh zones have slightly higher primary productivity (Fig. 5.58). The bulk density and grain size of sediments are important factors for plants that grow in them. Higher percentage of silt and clay can be beneficial for plant growth because small-sized grains made up of silt and clay can hold more nutrients than coarse sandy soils due to their greater surface-to-volume ratio. However, waterlogged fine sediments which

have low oxygen can result in slower plant growth if the fine sediments are not well-drained. The plant communities can also be influenced by the slope of the marsh surface because each plant species is adapted to living in a certain amount of water and within a certain range of salinity. When salinity is outside the range of a particular plant, its productivity will decrease due to the salinity stress (Weis and Butler 2009).

Plant response in the low and high marsh zones

When data for all eight transects are combined by low and high marsh zones, the aboveground biomass in the high marsh zones changed significantly over seasons (Spring, Summer and Fall). The belowground plant biomass in both low and high marsh zones also changes significantly over seasons. In the high marsh zones, above- and belowground production was highest in Summer, but the belowground plant production in the low marsh zones was highest in Fall. However, *Juncus roemerianus* and *Spartina alterniflora* have higher rhizome thickness in Spring than Summer and Fall in both low and high marsh zones. Moreover, the mean rhizome thickness of *Juncus roemerianus* and *Spartina alterniflora* tends to decrease over Spring, Summer and Fall. Vegetation tend to begin decreasing rhizome thickness from Spring so that they can produce highest belowground productivity in Fall in the low marsh zones and highest above- and belowground productivity in Summer in the high marsh zones. Hurricane season in the Atlantic and the Eastern Pacific tends to begin in Summer and end in Fall (NOAA Coast Services Center website). Native vegetation tends to have lower heights and lower density in the low marsh zones where plants are regularly inundated by hurricanes and storm surges. Mean rhizome thickness of native vegetation tends to be thicker in Spring when hurricanes and storm surges rarely occur (NOAA Coast Services Center website). Plant density is recognized as a major factor determining the degree of competition between different plant species (Keddy 2010; Weis and Butler 2009). The high marsh zones tend to be dominated by more species of different plants which exhibit higher density than in the low marsh zones.

Plant response in the coastal and inland marshes

Although higher water salinity results in lower water dissolved oxygen, higher dissolved oxygen does not correlate to increased belowground biomass. Both above- and belowground plant biomass differs significantly over seasons (Spring, Summer and Fall). Aboveground plant production in both coastal and inland marshes is highest in Summer, and the standing shoot heights of *Juncus roemerianus* and *Spartina alterniflora* are highest then (Figs. 5.44 and 5.46). However, belowground productivity in the coastal marshes is highest in Summer and belowground productivity in the inland marshes is highest in Fall. *Juncus roemerianus* and *Spartina alterniflora* have higher rhizome thickness in Spring than Summer and Fall in both coastal and inland marshes (Figs. 5.50 and 5.51). Moreover, the mean rhizome thickness of *Juncus roemerianus* and *Spartina alterniflora* tends to decrease over Spring, Summer and Fall (Fig. 5.51). In addition, belowground biomass in both coastal and inland marshes is lowest in Spring with higher rhizome thickness, which means plant rhizomes are thicker when total plant biomass is less. Although coastal vegetation tend to have lower standing shoot heights and lower density, coastal vegetation can produce higher primary production especially belowground production in the high marsh zones.

Although there is no significant difference in elevation gradients between the coastal and inland marshes, native vegetation at lower elevation with lower density within the coastal and inland marshes tend to have lower above- and belowground primary

production (Figs. 5.59, 5.60 and 5.63). Lower production leads to lower soil stability. Where the natural pulses such as hurricanes, storm surges and flooding are moderate, productivity is highest. In general, net productivity in most types of wetlands increases with increasing pulse amplitude up to an optimum point beyond which too many pulses reduce productivity (Odum et al. 1995). More severe pulses tend to occur in the low marsh zones in the coastal marsh sites, so vegetation tends to exhibit decreased above- and belowground productivity there.

5.3 Summary

Two field campaigns were conducted to measure the marsh vegetation and soil properties in the Louisiana and Mississippi Gulf Coast. The first campaign focused on the biomechanical properties such as stiffness, height and diameter of *Spartina alterniflora*, *Juncus roemerianus* and several other species commonly found on the field sites at Terrebonne Bay and Breton Sound, LA that were used for wave and surge attenuation measurements in Chapter 4. Several other sites nearby were also sampled in order to establish a wide range of data coverage. The vegetation stiffness was measured using two methods: individual bending test and board drop test. It was found that the board drop test developed for inland grasses is not straightforward to be used for coastal marsh grasses which are stiffer and distribute more nonuniformly. The individual bending test was successful and provided a set of data that were used to establish the relationship of the stiffness and height/diameter ratio for these vegetation species. The data trendline showed that the plant stiffness increases with increase in stem height/stem diameter ratio for all plants sampled. An empirical regression function was established based on the data trend, which has a R^2 value of 0.85.

The stiffness measurements also showed that dormant plants of the same stem height/stem diameter ratio have a significantly lower stiffness modulus than their green equivalents. Another finding was that even though the invidual stems of *Juncus roemerianus* have smaller modulus of elasticity (E) than those of *Spartina alterniflora*, *Juncus* has larger *MEI* values than *Spartina* because it has higher density. This implies that *Juncus* can be more effective in attenuation of surge and waves if it can survive the storms. In addition, the seasonal variation of stem heights for *Spartina alterniflora* was also observed. It was found that both stem and total plant heights increase as the growing season progresses, whereas the difference between the total height and stem height decreases as the plant matures until the plant becomes dormant.

The second field campaign concerned the growth forms and productivities of *Spartina alterniflora* and *Juncus roemerianus*. Eight transects were established at Graveline Bayou in Gautier, MS and the Grand Bay National Estuarine Research Reserve in Pecan, MS. The vegetation height, diameter, coverage, and biomass in lower and higher marshes as well as in coastal and inland marshes were compared. It was found that the mean rhizome thickness of both *Juncus roemerianus* and *Spartina alterniflora* were thicker in the high marsh zones than in the low marsh zones. Although the mean rhizome thickness of both *Juncus roemerianus* and *Spartina alterniflora* in the high marsh zones did not differ significantly from those in the low marsh zones, the mean rhizome thickness of *Juncus roemerianus* changed significantly over Spring, Summer and Fall in both low and high marsh zones. The mean rhizome thickness of *Juncus roemerianus* is highest in Spring and lowest in Summer in the low marsh zones, but decreases over Spring, Summer, and Fall in the high marsh zones.

Vegetation tends to exhibit lower rhizome thickness in Spring and produce the highest belowground productivity in Fall in the low marsh zones and highest above- and belowground productivity in Summer in the high marsh zones. The above- and belowground biomass was higher in the high marsh zones than in the low marsh zones. Coastal vegetation grown at lower elevations tends to produce lower productivity.

It was also found that the above- and belowground biomass was lower in inland marshes than in coastal marshes. However, the difference is not significant. Aboveground plant production in both coastal and inland marshes is highest in Summer, and also the standing shoot heights of *Juncus roemerianus* and *Spartina alterniflora* are highest in Summer. However, belowground productivity in the coastal marshes is highest in Summer with lower rhizome thickness, and belowground productivity in the inland marshes is highest in Fall with lower rhizome thickness. In addition, belowground biomass in both coastal and inland marshes is lowest in Spring with higher rhizome thickness. Aboveground plant production is higher when plant standing shoot heights are higher, but belowground plant production is lower when plant rhizomes are thicker.

6. COMPUTATIONAL MODELING OF SURGE AND WAVES IN VEGETATED WATERS

As reviewed in Section 2.4, a variety of numerical models have been developed for surge and wave propagation in coastal waters in the literature. They can be classified as phase-resolving and phase-averaging models. Phase-resolving models often use the shallow water equations, Boussinesq equations or Navier-Stokes equations to compute the dynamic wave deformation processes in various levels of detail and accuracy. Normally the shallow water equations are applicable to long waves, while the Navier-Stokes equations and Boussinesq equations are valid for both long and short waves. The phase-averaging models often use the wave-action energy balance equation, perhaps coupled with phase-averaged current equations. These models may be 1-D, depth-averaged 2-D, vertical 2-D or 3-D. In order to demonstrate quantification of surge and wave attenuation by vegetation in as many typical models as possible, four models were selected in this study. The first model is a depth-averaged 2-D shallow water model, which is used for long waves such as tsunami wave propagation. The second model is a 1-D Boussinesq-type model, which is primarily used for short waves. The third model is a vertical 2-D model based on the Reynolds-averaged Navier-Stokes (RANS) equations. Because the Volume-of-Fluid (VOF) method is used, this vertical model is able to handle both long and short waves. The fourth model is a wave-action model for wave spectra. All four model selected can handle both breaking and non-breaking waves. Presented in the following sections are the mathematical formulations, numerical methods and validations of the four models, as well as differences in the drag coefficient values in these models.

6.1 A Depth-Averaged 2-D Shallow Water Model for Long Waves in Vegetated Waters

This section presents a depth-averaged 2-D shallow water flow model for investigating attenuation of long waves due to vegetation under non-breaking and breaking conditions. The effects of vegetation are modeled in the form of drag and inertia forces as source terms in the momentum equations. The governing equations are solved using an explicit finite-volume method with the HLL approximate Riemann solver for the convective fluxes at cell faces and a stable centered difference scheme for the surface gradient terms. The time discretization is first-order accurate, but a piecewise linear reconstruction of state variables at cell interfaces helps achieve second-order accuracy in space. The model was validated using several laboratory experiments including steady flow in a partially vegetated flume, dam-break wave over an obstacle, breaking and non-breaking solitary waves on a sloping beach, and tsunami wave runup over a partially vegetated sloping beach. The computed water surface elevations, flow velocities, wave heights and runups are in good agreement with experimental observations.

6.1.1 Mathematical Formulations

The shallow water equations, which are derived by depth-integration of the Navier-Stokes equations based on the hydrostatic pressure assumption, are often used as the governing equations of long waves in shallow water. To consider the wave propagation in a vegetation zone, the drag force and inertia forces of vegetation are added in the momentum

equations. The depth-averaged 2-D shallow equations with vegetation effects are then written in the conservative form as

$$\frac{\partial d}{\partial t}+\frac{\partial (Ud)}{\partial x}+\frac{\partial (Vd)}{\partial y}=0 \tag{6.1}$$

$$\frac{\partial}{\partial t}(Ud)+\frac{\partial}{\partial x}\left(U^2 d\right)+\frac{\partial}{\partial y}(UVd)=-\frac{1}{\rho}F_x-gd\frac{\partial \eta}{\partial x}+\frac{\partial}{\partial x}\left(\nu_t d\frac{\partial U}{\partial x}\right)+\frac{\partial}{\partial y}\left(\nu_t d\frac{\partial U}{\partial y}\right)-g\frac{n^2 m_b U\bar{U}}{d^{1/3}} \tag{6.2}$$

$$\frac{\partial}{\partial t}(Vd)+\frac{\partial}{\partial x}(UVd)+\frac{\partial}{\partial y}\left(V^2 d\right)=-\frac{1}{\rho}F_y-gd\frac{\partial \eta}{\partial y}+\frac{\partial}{\partial x}\left(\nu_t d\frac{\partial V}{\partial x}\right)+\frac{\partial}{\partial y}\left(\nu_t d\frac{\partial V}{\partial y}\right)-g\frac{n^2 m_b V\bar{U}}{d^{1/3}} \tag{6.3}$$

where t is the time, x and y are the horizontal (horizontal and lateral) coordinates, d is the total flow depth, U and V are the flow velocities in x and y directions, $\bar{U}=\sqrt{U^2+V^2}$, η is the water level above the still water, n is the Manning roughness coefficient, g is the gravitational acceleration, F_x and F_y are the components of forces acting on vegetation in x and y directions, ρ is the density of water, ν_t is the turbulent or eddy viscosity, and $m_b=\sqrt{1+\left(\partial z_b/\partial x\right)^2+\left(\partial z_b/\partial y\right)^2}$ considering the bed slope with z_b being the bed level. Fig. 6.1 shows the definition of the problem and some of the relevant variables.

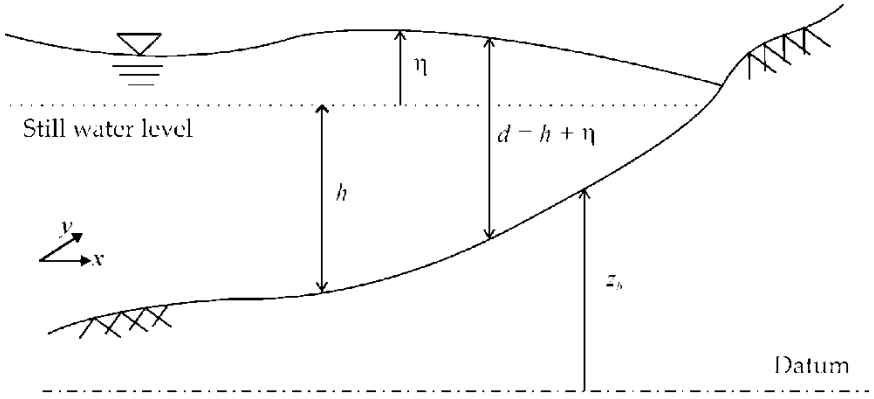

Fig. 6.1. Definition sketch of free surface flow problem

Consider a group of vegetation elements (stems) conceptualized as cylinders, as shown in Fig. 6.2. The forces acting on vegetation include the drag force and inertia force. The drag force is due to viscous effect and the wake formation downstream of the stem, and the inertia force is due to the fluid acceleration around the stem. These two forces can be expressed using the Morison equation (Morison et al. 1950):

$$F_i=\frac{1}{2}\rho C_D N_v A_v U_{vi}\sqrt{U_{vj}U_{vj}}+\rho C_M N_v V_v\frac{\partial U_{vi}}{\partial t} \tag{6.4}$$

where U_{vi} is the velocity acting on the vegetation element, C_D is the drag coefficient, C_M is the inertia coefficient, N_v is the vegetation density defined as number of vegetation elements per unit horizontal (bed) area, A_v is the projected area defined as the frontal area of a vegetation element projected to the plane normal to the streamwise flow direction, and V_v is

the volume of a vegetation element. The first term on the right-hand side of Eq. (6.4) denotes the drag force and the second term denotes the inertia force.

Because vegetation may be emergent or submerged, as shown in Fig. 6.2, the projected area and volume of the wetted portion should be used in Eq. (6.4). If the vegetation element is approximated as a cylindrical stem, the wetted projected area and volume are expressed as

$$A_v = D_v \min(h_v, d), \quad V_v = \frac{\pi D_v^2}{4} \min(h_v, d) \tag{6.5}$$

where D_v is the representative diameter of the vegetation element, and h_v is the vegetation height. For partially submerged vegetation, D_v represents the diameter of the wetted portion. For general vegetation, D_v can be interpreted as the nominal diameter of the stem that is related to the stem volume by $D_v = \sqrt{4V_v/\pi h_v}$. More details on how to approximate vegetation elements can be found in Wu (2007).

For emergent vegetation, the acting flow velocity U_{vi} used in Eq. (6.4) is the depth-averaged flow velocity U_i (i.e. U and V). For submerged vegetation, U_{vi} is the average velocity in the vegetation layer, as shown in Fig. 6.2. This velocity can be determined using Stone and Shen's (2002) method:

$$U_{vi} = \eta_v U_i \left(\frac{h_v}{d} \right)^{1/2} \tag{6.6}$$

where η_v is a coefficient of about 1.0.

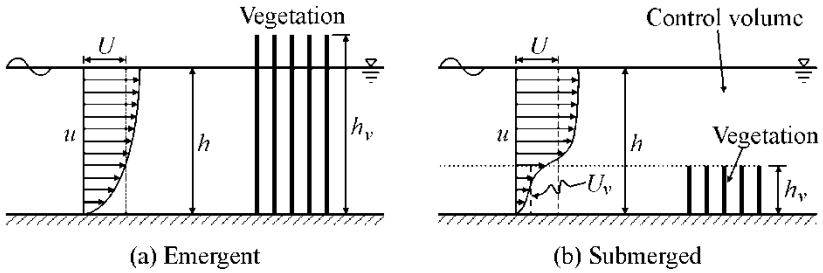

Fig. 6.2. Sketch of emergent and submerged vegetation elements

The eddy viscosity ν_t is determined using the modified mixing-length model (Wu 2007)

$$\nu_t = \sqrt{\left(\alpha_0 U_* d\right)^2 + \left(l_h^2 \left|\bar{S}\right|\right)^2} \tag{6.7}$$

where $\left|\bar{S}\right| = \left[2\left(\partial U/\partial x\right)^2 + 2\left(\partial V/\partial y\right)^2 + \left(\partial U/\partial y + \partial V/\partial x\right)^2 \right]^{1/2}$; α_0 is an empirical coefficient, set as $\kappa/6$; U_* is the bed shear velocity; and l_h is the horizontal mixing length, determined by $l_h = \kappa \min\left(c_m d, y\right)$, with y being the distance to the nearest wall and c_m an empirical coefficient between 0.2-1.2.

6.1.2 Numerical Solution Methods

6.1.2.1 Finite volume discretization

Eqs. (6.1)–(6.3) are written in the following compact form:

$$\frac{\partial \mathbf{\Phi}}{\partial t} + \frac{\partial \mathbf{F}(\mathbf{\Phi})}{\partial x} + \frac{\partial \mathbf{G}(\mathbf{\Phi})}{\partial y} = \mathbf{S}(\mathbf{\Phi}) \tag{6.8}$$

where $\mathbf{\Phi}$, $\mathbf{F}(\mathbf{\Phi})$, and $\mathbf{G}(\mathbf{\Phi})$ represent the vectors of unknown variables and fluxes:

$$\mathbf{\Phi} = \begin{bmatrix} d \\ Ud \\ Vd \end{bmatrix}, \quad \mathbf{F}(\mathbf{\Phi}) = \begin{bmatrix} Ud \\ U^2 d \\ UVd \end{bmatrix}, \quad \mathbf{G}(\mathbf{\Phi}) = \begin{bmatrix} Vd \\ UVd \\ V^2 d \end{bmatrix} \tag{6.9}$$

and $\mathbf{S}(\mathbf{\Phi})$ includes the remaining terms in each equation.

Consider the finite-volume mesh shown in Fig. 6.3. Each control volume (cell) is embraced by four faces. Non-staggered (collocated) grid system is used. The primary variables *h*, *U*, and *V* are defined at cell centers and represent the average values over each cell, while the fluxes are calculated at cell faces.

Integrating Eq. (6.8) over the (*i*, *j*) control volume, applying the Green theorem, and using the Euler scheme for the time derivative, one can derive the following discretized equation:

$$\mathbf{\Phi}_{i,j}^{n+1} = \mathbf{\Phi}_{i,j}^{n} - \frac{\Delta t}{\Delta x_{i,j}}\left(\mathbf{F}_{i+1/2,j}^{n} - \mathbf{F}_{i-1/2,j}^{n}\right) - \frac{\Delta t}{\Delta y_{i,j}}\left(\mathbf{G}_{i,j+1/2}^{n} - \mathbf{G}_{i,j-1/2}^{n}\right) + \Delta t\,\mathbf{S}_{i,j} \tag{6.10}$$

where Δt is the time step length, $\Delta x_{i,j}$ and $\Delta y_{i,j}$ are the cell lengths in x and y directions, $\mathbf{F}_{i+1/2,j}^{n}$ is the flux at face (i+1/2, j), and $\mathbf{G}_{i,j+1/2}^{n}$ is the flux at face (i, j+1/2).

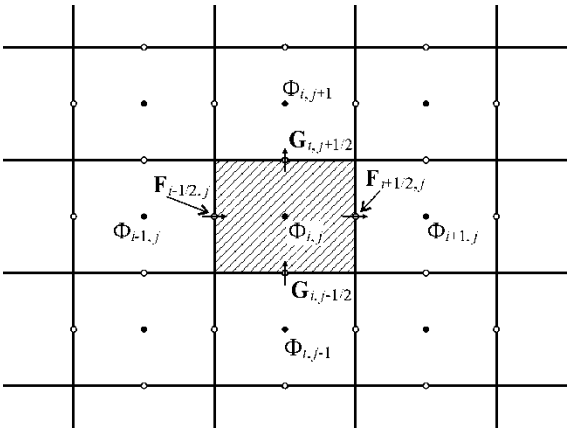

Fig. 6.3. 2-D finite-volume mesh

The discretized equation (6.10) has first-order accuracy in time, but its accuracy in space is determined by how to approximate the fluxes at cell faces and the source terms. The diffusion terms on the right-hand side of Eqs. (6.2) and (6.3) are discretized using the central

difference scheme at time level *n*. The bed friction and vegetation drag force terms are approximated by a semi-implicit scheme, and the intercell convective fluxes and the water surface gradient terms are approximated by second-order accurate methods, which are described in the next subsections. The present model has an overall accuracy of second order in space.

6.1.2.2 HLL approximate Riemann solver and MUSCL reconstruction

The HLL approximate Riemann solver (Harten et al. 1983) is used to determine the fluid mass and momentum fluxes at cell faces as follows:

$$\mathbf{F}_{\mathrm{HLL}} = \begin{cases} \mathbf{F}_L & \text{if } S_L \geq 0 \\ \dfrac{S_R\mathbf{F}_L - S_L\mathbf{F}_R + S_L S_R\left(\mathbf{\Phi}_R - \mathbf{\Phi}_L\right)}{S_R - S_L} & \text{if } S_L < 0 < S_R \\ \mathbf{F}_R & \text{if } S_R \leq 0 \end{cases} \tag{6.11}$$

where subscripts *L* and *R* denote the quantities evaluated at the left- and right-hand sides of each cell face, respectively; and S_L and S_R represent the wave speeds, separating constant states of the local Riemann problem solution at cell faces (Fig. 6.4). As suggested by Toro (2001), the wave speeds are estimated as

$$S_L = U_L - a_L\lambda_L, \quad S_R = U_R + a_R\lambda_R \tag{6.12}$$

where U_K (K = L, R) is the velocity, a_K is the celerity, and λ_K is given as

$$\lambda_K = \begin{cases} \sqrt{\dfrac{1}{2}\dfrac{\left(d_* + d_K\right)d_*}{d_K^2}} & \text{if } d_* > d_K \\ 1 & \text{if } d_* \leq d_K \end{cases} \tag{6.13}$$

with d_* being an estimate for the exact solution of d in the star region, evaluated as

$$d_* = \frac{1}{2}\left(d_L + d_R\right) - \frac{1}{4}\left(U_R - U_L\right)\left(d_L + d_R\right)/\left(a_L + a_R\right) \tag{6.14}$$

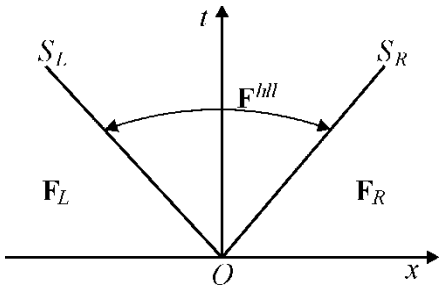

Fig. 6.4. Wave structures assumed in HLL approximate Riemann solver

If the left and right fluxes in Eq. (6.11) are determined by setting the intermediate states $\mathbf{\Phi}_L$ and $\mathbf{\Phi}_R$ as the cell-centered values, the scheme has first-order accuracy in space. A second-order accurate approximation can be obtained by reconstructing the left and right

states using the Monotonic Upstream Scheme for Conservation Laws (MUSCL) (van Leer 1979). A piecewise linear reconstruction is used, e.g. at face i+1/2,

$$f_L = f_i + \frac{\Delta x_i}{2}\left(\frac{\partial f}{\partial x}\right)_i, \qquad f_R = f_{i+1} - \frac{\Delta x_{i+1}}{2}\left(\frac{\partial f}{\partial x}\right)_{i+1} \tag{6.15}$$

where f is a state variable or flux. The gradient across cell i can be determined using the values in the neighboring cells $i \pm 1$. However, such gradient calculation often results in spurious oscillations in the solution. To eliminate such oscillations, the following slope limiter is used to determine the gradient:

$$\left(\frac{\partial f}{\partial x}\right)_i = \begin{cases} \max\left[0, \min\left(\beta\Delta_{i-1/2}, \Delta_{i+1/2}\right), \min\left(\Delta_{i-1/2}, \beta\Delta_{i+1/2}\right)\right], & \text{if } \Delta_{i+1/2} > 0 \\ \min\left[0, \max\left(\beta\Delta_{i-1/2}, \Delta_{i+1/2}\right), \max\left(\Delta_{i-1/2}, \beta\Delta_{i+1/2}\right)\right], & \text{if } \Delta_{i+1/2} < 0 \end{cases} \tag{6.16}$$

where $\Delta_{i-1/2} = \left(f_i - f_{i-1}\right)/\left(x_i - x_{i-1}\right)$ and $\Delta_{i+1/2} = \left(f_{i+1} - f_i\right)/\left(x_{i+1} - x_i\right)$. The parameter β =1 reproduces the MINBEE (or MINMOD) flux limiter, and β =2 reproduces the SUPERBEE flux limiter (Toro 2001). β =1 is used in this study.

The left and right states are usually estimated with the reconstruction method first and then used to obtain the left and right fluxes. In the present model, the left and right fluxes are directly obtained using the reconstruction method expressed in Eq. (6.15). These fluxes are in turn used as input to the Riemann solver.

The HLL approximate Riemann solver (6.11) was derived for the 1-D shallow water problem. Several approaches have been developed in the literature to extend this scheme to the 2-D shallow water problem (Toro 2001). These approaches treat the x- and y-direction convection terms as two 1-D Riemann problems and apply the HLL flux in both the x- and y-direction convection terms. Such treatments may experience strong numerical diffusion. To improve the accuracy, a hybrid approach is used here. The HLL flux is applied to determine only the x-direction convection flux in the U-momentum equation and the y-direction convection flux in the V-momentum equation, whereas the y-direction convection flux in the U-momentum equation and x-direction convection flux in the V-momentum equation are determined using a second-order upwind scheme called HLPA (Hybrid Linear/Parabolic Approach) proposed by Zhu (1991).

6.1.2.3 **Treatment of water surface gradient term**

Traditionally the water surface gradient term in the momentum equation is split into the depth gradient and bed slope terms, and the depth gradient term is added to the convection flux term (Toro 2001). To handle an uneven bed, the bed slope term needs to be specially treated; otherwise unphysical flow motions will be generated under still water conditions (Zhou et al. 2001). Recent study of Ying and Wang (2008) suggests an alternative method, in which the water surface gradient term is treated as a single term on the right-hand side of the momentum equation, as shown in Eqs. (6.2) and (6.3). Both splitting and single-term approaches have been proven to be efficient in many case studies of dam-break flow. Ying and Wang's method is adopted here to treat the water surface gradient term as follows:

$$gd\frac{\partial \eta}{\partial x} = gd_i^{n+1}\frac{\eta_{i+1/2}^{n+1} - \eta_{i-1/2}^{n+1}}{\Delta x_i} \tag{6.17}$$

where $\eta_{i+1/2}^{n+1} = \left(\eta_{i+1/2,L}^{n+1} + \eta_{i+1/2,R}^{n+1}\right)/2$, with $\eta_{i+1/2,L}^{n+1}$ and $\eta_{i+1/2,R}^{n+1}$ being the left and right water surface elevations at cell face i+1/2 determined using the MUSCL reconstruction method expressed in Eq. (6.15). A similar treatment applies to $\eta_{i-1/2}^{n+1}$. Eq. (6.17) has second-order accuracy in space. It is similar to but more stable than the center difference scheme.

Note that the water surface elevation of the new time level (n+1) is used in Eq. (6.17). This is achieved by solving the continuity equation first and then the momentum equations at each time step. This implicit treatment is found to be more stable.

In addition, to handle an uneven bed, the water level rather than the water depth is used for the state variables $\mathbf{\Phi}_L$ and $\mathbf{\Phi}_R$ in Eq. (6.11) when determining the mass flux for solution of the flow continuity equation.

6.1.2.4 **Treatment of bed friction and vegetation force terms**

The bed friction term, i.e. the last term on the right-hand side of Eqs. (6.2) and (6.3), is approximated by the following semi-implicit scheme:

$$g\frac{n^2 m_b \bar{U}}{d^{1/3}}(U,V) = g\left(\frac{n^2 m_b \bar{U}}{d^{1/3}}\right)_{i,j}^{n}\left(U_{i,j}^{n+1}, V_{i,j}^{n+1}\right) \tag{6.18}$$

The drag force, i.e. the first term in Eq. (6.4), can be rewritten in terms of depth-averaged flow velocities U and V by using Eq. (6.6), and then treated semi-implicitly as follows:

$$\frac{1}{2}\rho C_D N_v A_v \frac{h_v}{d}\bar{U}(U,V) = \frac{1}{2}\rho C_D N_v A_v h_v \left(\frac{\bar{U}}{d}\right)_{i,j}^{n}(U_{i,j}^{n+1}, V_{i,j}^{n+1}) \tag{6.19}$$

The bed friction and drag force terms are moved to the left-hand side of Eq. (6.10) for $U_{i,j}^{n+1}$ and $V_{i,j}^{n+1}$. This semi-implicit scheme is more stable than the fully explicit scheme for these two terms.

The time derivative of velocity in the inertia force term of Eq. (6.4) is discretized using the Euler scheme as used for the time derivative in Eq. (6.10). Thus, the inertia force term can be combined with the temporal terms in the momentum equations (6.2) and (6.3).

The coefficient m_b accounts for the effect of a sloping bed or bank, but it becomes indefinite in the case of a vertical bank. In such a case, the velocity normal to the bank is set as zero, and the bank friction to the velocity tangential to the bank line is added with the bed friction by multiplying Eq. (6.18) with a factor of $1+(n_w/n_b)^2 d_b/dn$. Here, n_w and n_b are Manning's coefficients for bank and bed, respectively, d_b is the flow depth at the bank, and dn is the near-bank grid spacing in the direction normal to the bank line. This factor considers the bank height as part of the wetted perimeter at the near-bank cell. In more general, one may also use the wall-function approach to handle the effect of vertical bank, as described by Wu (2007).

6.1.2.5 **Wetting and drying technique**

During the flood propagation in floodplains and channels with sloping boundaries, the water edges change with time and the computational nodes may become wet or dry at different time steps. In the present model, a threshold flow depth (a small value such as 0.001 m), denoted as d_{tol}, is used to judge drying and wetting. If the flow depth on a node is

larger than the threshold value, this node is considered to be wet; otherwise, this node is dry. The dry nodes are assigned zero velocity.

The HLL approximate Riemann solver usually needs to specially treat the wave speed estimates in Eq. (6.12) at the edge between dry and wet nodes. However, it is found that Eq. (6.13) can handle the problem at the water edge as well as inside the wet domain.

6.1.2.6 **Model stability**

Because the developed solution procedure is explicit, the computational time step should be limited by the Courant-Friedrichs-Lewy (CFL) stability condition:

$$\Delta t < \frac{\Delta x}{\left(|U| + \sqrt{gd}\right)/\Delta x + \left(|V| + \sqrt{gd}\right)/\Delta y} \tag{6.20}$$

6.1.3 Model Validations

6.1.3.1 **Steady flow in a flume partially covered with vegetation**

Steady, quasi-uniform flow in a flume partially covered with emergent vegetation along one side was studied experimentally by Tsujimoto and Kitamura (1995). The experimental setup is shown in Fig. 6.5. The flume was 12 m long and 0.4 m wide, with a slope of 0.0017. The vegetation zone was 0.12 m wide, consisting of bamboos with a diameter of 0.15 cm distributed in a parallel pattern. In the experiment runs A1 and B1, the average flow velocity was 0.32 and 0.276 m/s, the flow depth was 0.0457 and 0.0428 m, and the spacing of vegetation elements was 2.8 and 2.0 cm, respectively, as shown in Table 6.1.

The developed depth-averaged 2-D model was applied to simulate the flow pattern in the partially vegetated flume. The computational mesh was uniform, with grid spacing of 0.05 and 0.01 m in longitudinal and transverse directions. The Manning's n for the flume bed was estimated as 0.01-0.011. The drag coefficient C_d was set as 1.5 for both experimental runs. The coefficient c_m in the mixing-length turbulence model (6.7) was given as 0.6. Fig. 6.6 compares the measured and calculated depth-averaged flow velocities along the cross-section. The model reproduced well the lateral distribution of flow velocity. Due to the presence of vegetation, the flow in the vegetation zone was retarded, while the velocity of the main flow was increased.

Table 6.1. Flow and vegetation conditions in Tsujimoto and Kitamura's experiments

Experiment run No.	Flow velocity (m/s)	Flow depth (m)	Flume slope	Properties of model vegetation		
				Material	Diameter (cm)	Spacing (cm)
A1	0.32	0.0457	0.0017	Bamboo	0.15	2.8
B1	0.276	0.0428	0.0017	Bamboo	0.15	2.0

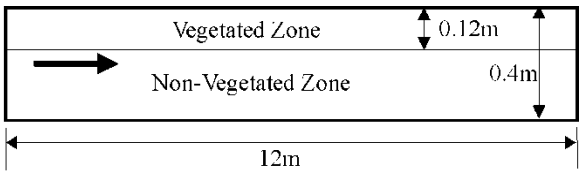

Fig. 6.5. Plan view of Tsujimoto and Kitamura's (1995) experiments

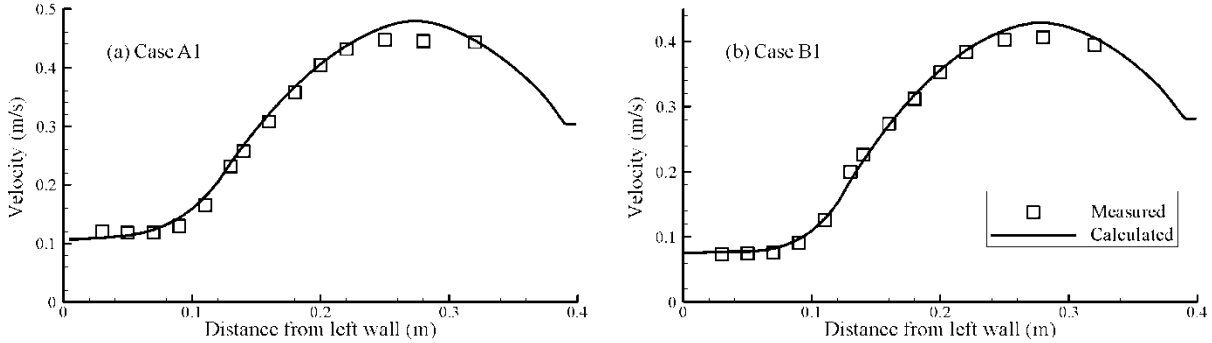

Fig. 6.6. Measured and calculated depth-averaged velocities along cross-section in a partially vegetated flume (Measurement by Tsujimoto and Kitamura, 1995)

6.1.3.2 Dam-break flow over a triangular obstacle

This test was carried out to reproduce the laboratory experiment of dam-break flow over a triangular hump recommended by the EU CADAM project. The physical experiment included complex hydraulic properties such as shocks, transitions between wet and dry beds, and flow over an obstacle. The experiment flume consisted of a reservoir with water up to 0.75 m contained by a dam at $x = 15.5$ m and a dry bed downstream within a rectangular channel of 22.5 m in length, as illustrated in Fig. 6.7. A symmetric triangular obstacle (6 m long, 0.4 m high) was placed on the channel with its vertex being located at 13 m downstream of the dam. In order to observe dam-break wave evolutions gage points were located at 2 m (G2), 4 m (G4), 8 m (G8), 10 m (G10), 11 m (G11), 13 m (G13) and 20 m (G20) from the dam. The gage point G13 was located at the vertex of the obstacle. The fixed boundaries were walls except the free outlet. The Manning's roughness coefficient was given as 0.0125 $m^{-1/3}s$, as suggested by Brufau et al. (2004).

In the computation, Δx = 0.1 m, Δt = 0.0005 s, and the threshold water depth d_{tol} for dry nodes was 0.00001 m. The simulation was carried out for 90 s. The temporal variations of water depth at the seven gage points are shown in Figs. 6.8(a)–(g). It can be seen that the predicted water depth evolutions and arrival time of the wave are quite comparable with the measured data at most of the gage points. The transition from wet to dry at Gage G13 was well predicted. Small discrepancy was observed at G20 (after the hump) between the calculated and measured values of water depth, which was also predicted by other researchers using different numerical schemes (e.g. Brufau et al. 2002, Liang and March 2009).

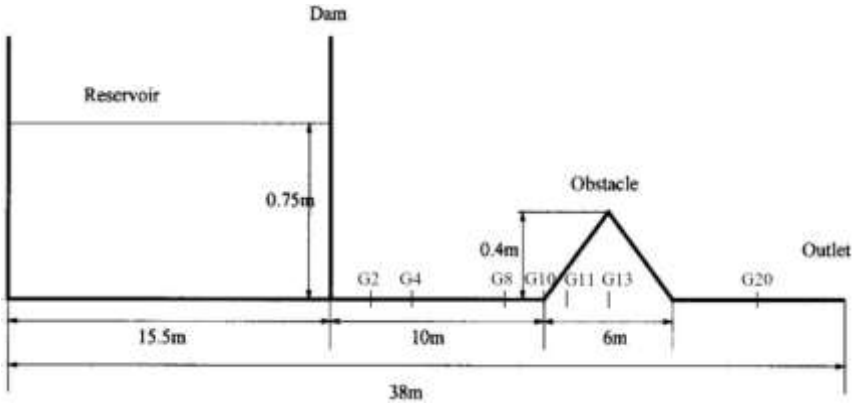

Fig. 6.7. Experiment setup for dam-break flow over a triangular hump

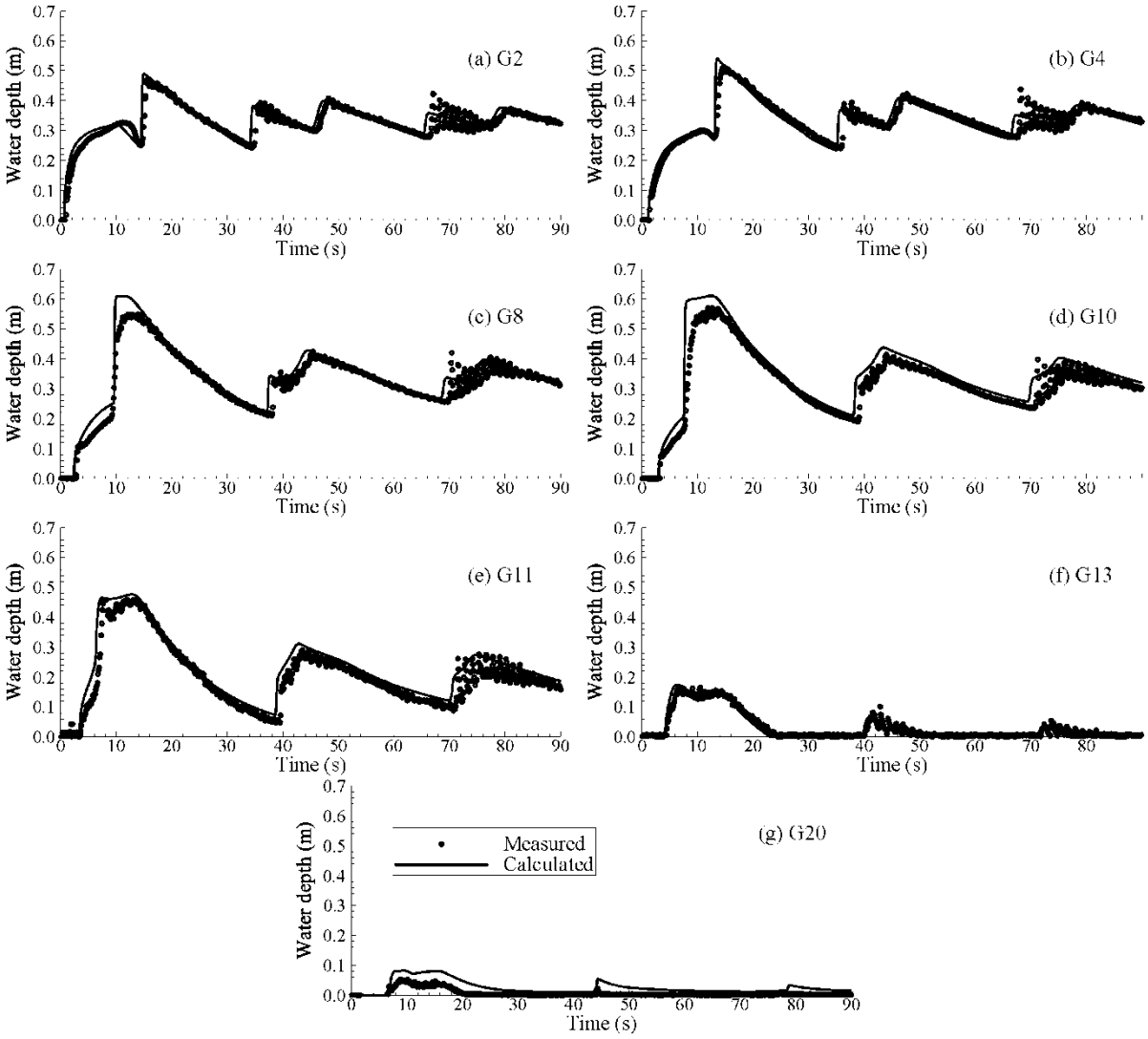

Fig. 6.8. Computed and measured water depths at gage stations: (a) G2; (b) G4; (c) G8; (d) G10; (e) G11; (f) G13; and (g) G20

6.1.3.3 **Solitary wave runup on a sloping beach**

Synolakis (1986) carried out a series of experiments to investigate runup/rundown and breaking of a solitary wave propagating on a sloping beach. The topography consisted of a plane beach with a slope of 1: $\cot\beta$ adjacent to a constant depth region, as shown in Fig. 6.9. Here, H = incident wave height, β = beach angle, and h = still water depth. These experimental results were extensively used to validate runup models (Li and Raichlen 2001, Delis et al. 2008, Mahdavi and Talebbeydokhti 2009, Zelt 1991, Titov and Synolakis 1995). The initial condition was still water in the computational domain, and a solitary wave of height H was specified at the seaside boundary:

$$\eta(x_0,t) = H\mathrm{sech}^2\left[\sqrt{\frac{3H}{4h^3}}(x_0 - Ct)\right] \tag{6.21}$$

where η is the water surface above the still water level, x_0 is the location of the seaside boundary ($x_0 = 0$), and C is the celerity of the solitary wave (Sorensen 2006):

$$C = \sqrt{gh}\left(1 + \frac{H}{2h}\right) \tag{6.22}$$

The following examples are presented to examine the accuracy of the model to predict runup of breaking and non-breaking waves. In the computation, the longitudinal grid spacing was 0.02 m, and the time step was 0.001 s. h = 1.0 m was used for experimental runs. The threshold water depth for dry bed definition is considered as 0.001 m. The Manning's roughness coefficient was set as 0.01 for the glass used in the experiments. The left boundary condition was kept sufficiently far away from the toe of the beach in order to avoid any interaction with the water waves during the runup process. For convenience, most of the results are reported in non-dimensional forms as

$$x^* = x/h,\ \ \eta^* = \eta/h,\ \ t^* = t\sqrt{g/h} \tag{6.23}$$

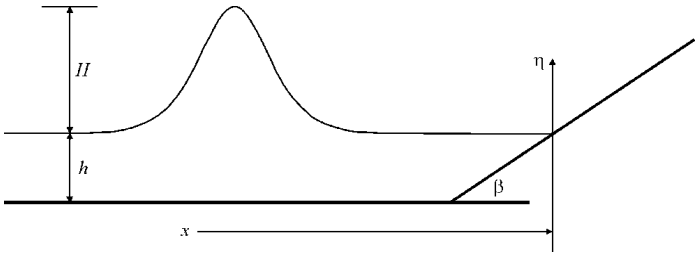

Fig. 6.9. Sketch for solitary wave runup on a sloping beach

Non-breaking wave runup over a sloping beach

For non-breaking solitary waves, two cases of H/h = 0.0185 and 0.04 on a beach of slope 1:19.85 were considered. According to Synolakis (1986), wave breaking occurs during rundown when H/h > 0.044. Thus, in both cases wave breaking did not occur although the second case was very close to the breaking condition. Figs. 6.10(a)–(j) show the water surface profiles in the case of H/h = 0.0185 in different times. At non-dimensional times t^* = 25, 30, and 35 the incident wave approached the shoreline, and by time t^* = 40 it started runup on the beach. The rundown took place around t^* = 60. Figs. 6.11(a)–(h) show the water surface

profiles for the case of H/h = 0.04. At times t^* = 20, 26, 32 the incident wave propagated to the shoreline, and it started runup and rundown approximately at t^* = 38 and 56, respectively. The experimental observation showed that the wave nearly broke down at t^* = 62, while the numerical results presented a similar feature, a hydraulic jump near the beach toe. One can see that the numerical model closely reproduced the experiment observations. The runup and rundown tongue thickness were also well predicted.

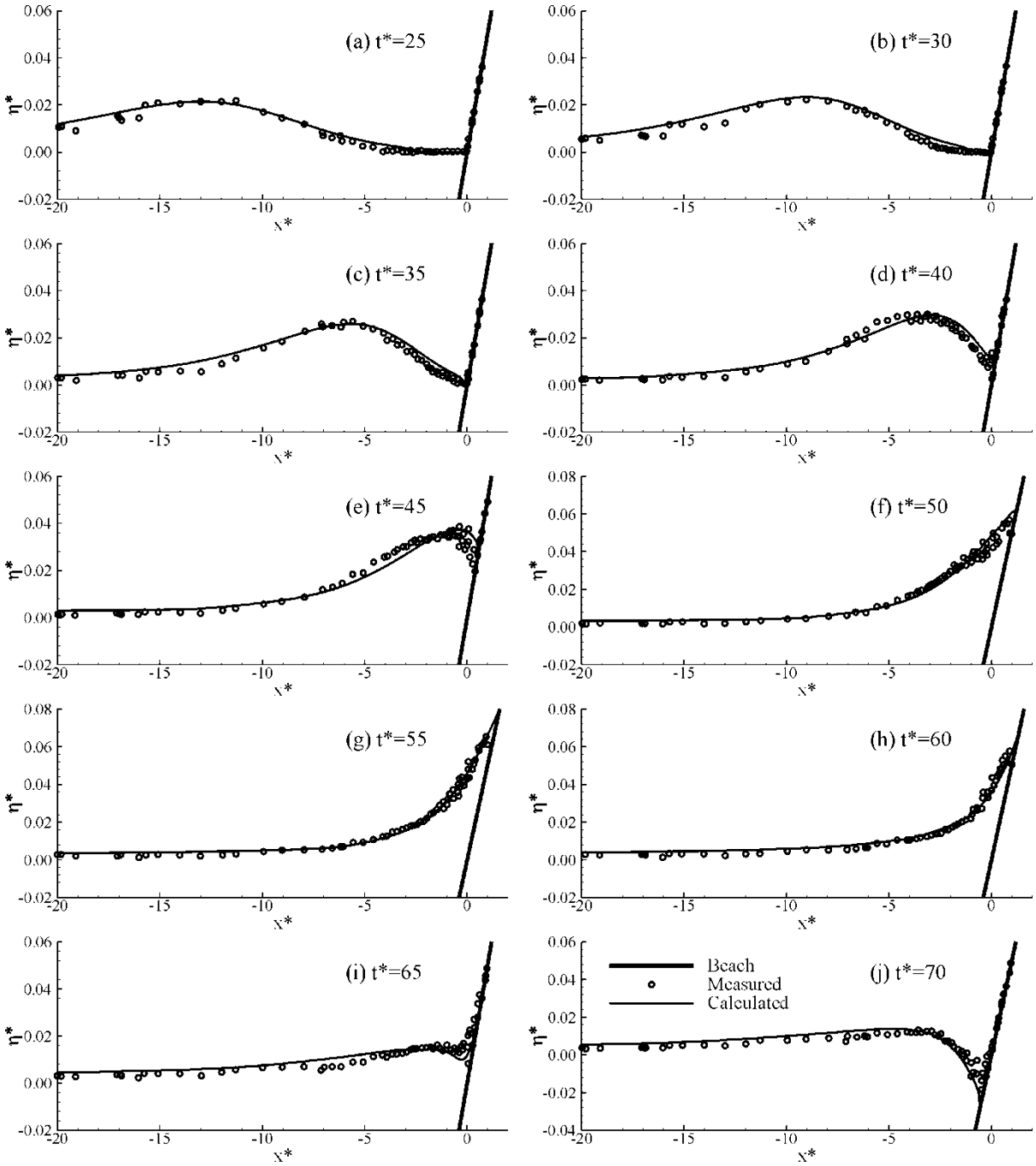

Fig. 6.10. Runup of *H/h* = 0.0185 non-breaking solitary wave on a 1:19.85 sloping beach

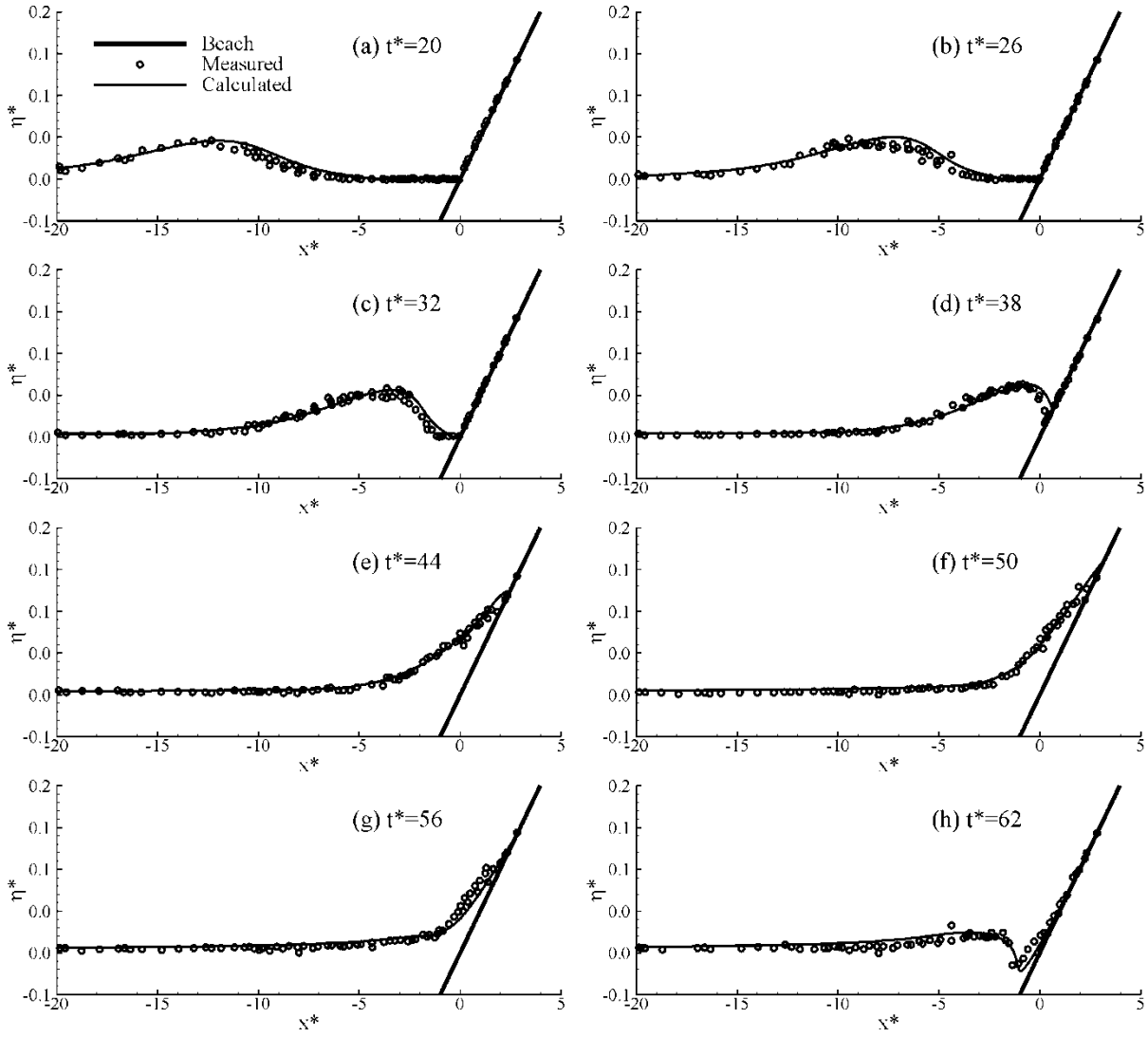

Fig. 6.11. Runup of *H/h* = 0.04 non-breaking solitary wave on a 1:19.85 sloping beach

Breaking wave runup over a sloping beach

The propagation of a breaking solitary wave with H/h = 0.3 on the same beach was computed using the developed model, and the results were examined against the experimental data of Synolakis (1986). Figs. 6.12(a)–(j) show the water surface profiles obtained at different times. At t^* = 15 and 20, the wave shoaled and the front face became steeper earlier than the experimental wave and changed to a bore type structure. This may be attributed to the limitation of the shallow water equations that do not include higher-order dispersive terms to account for the non-linear effects. The experimental wave broke around t^* = 20 and the computed wave represented this as a bore. The computed bore was slightly ahead of the experimental wave. The vertical front also indicated a sudden change in velocity from the bore to the undisturbed water. The breaking process terminated as the bore collapsed near the shoreline. Due to volume conservation, the computation fully recovered when breaking stopped at t^* = 25 and thereafter the attenuated wave formed a tongue propagating up the sloping beach at t^* = 30, 35, 40, and 45. After the wave reached the highest point around t^* = 45, rundown took place in which a thin layer of water

accelerated down the beach and discrepancies began to show at approximately $t^* = 50$ as the receding supercritical flow impacted the wave tail near the still water shoreline. The finite volume model approximated this flow pattern as a hydraulic jump and conserved the flow volume behind it. This study shows that the model is capable of simulating both breaking and non-breaking waves on a sloping beach.

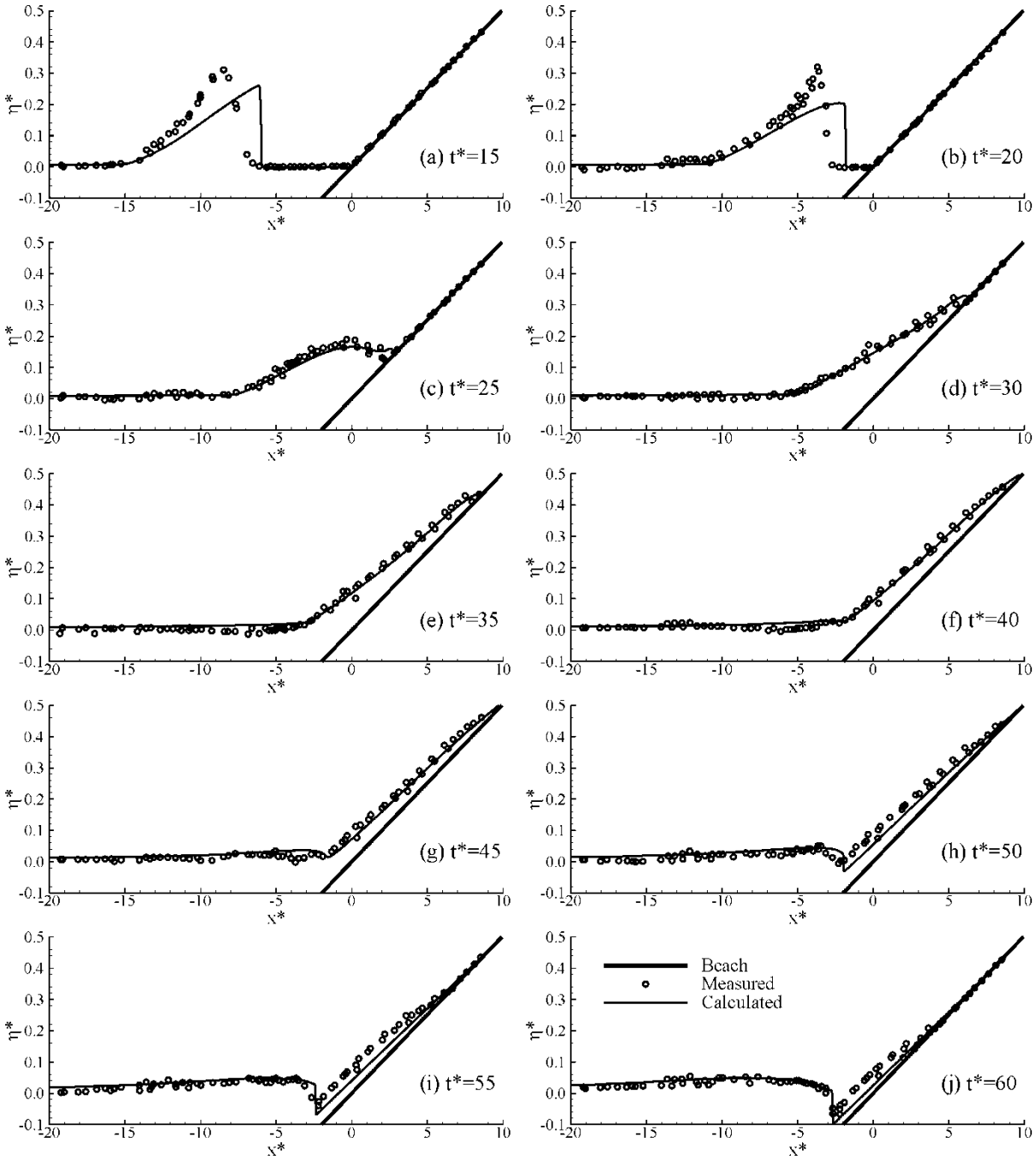

Fig. 6.12. Runup of *H/h* = 0.3 breaking solitary wave on a 1:19.85 sloping beach

Comparison of long wave runup on vegetated and non-vegetated sloping beaches

This numerical test was performed to test the ability of the model to predict qualitatively wave attenuation on a vegetated sloping beach. The geometry, the initial and boundary conditions were the same as those for the breaking wave of H/h = 0.3 shown in Fig. 6.12. Vegetation was assumed to be from -4 m to -2 m. The density of vegetation was N_v = 1,000 units/m^2 and diameter D_v = 0.01 m. The drag and inertia coefficients were specified as C_D = 1.0 and C_M = 2.0. Figs. 6.13(a)–(h) compare the water surface profiles with and without vegetation effects and demonstrate that the wave was significantly attenuated by vegetation. During t^* = 15 and 20 the wave shoaled and the front face became steep, but due to the presence of vegetation the wave height was significantly reduced. The maximum wave runup was also drastically reduced, which occurred at t^* = 45 when the propagating wave traveled maximum distance along the beach. In the case without vegetation, the thin layer of rundown wave developed supercritical flow and broke in the form of hydraulic jump at t^* = 50. However, such a phenomenon did not occur in the presence of vegetation. Therefore, vegetation on a sloping beach can reduce the energy of the propagating wave.

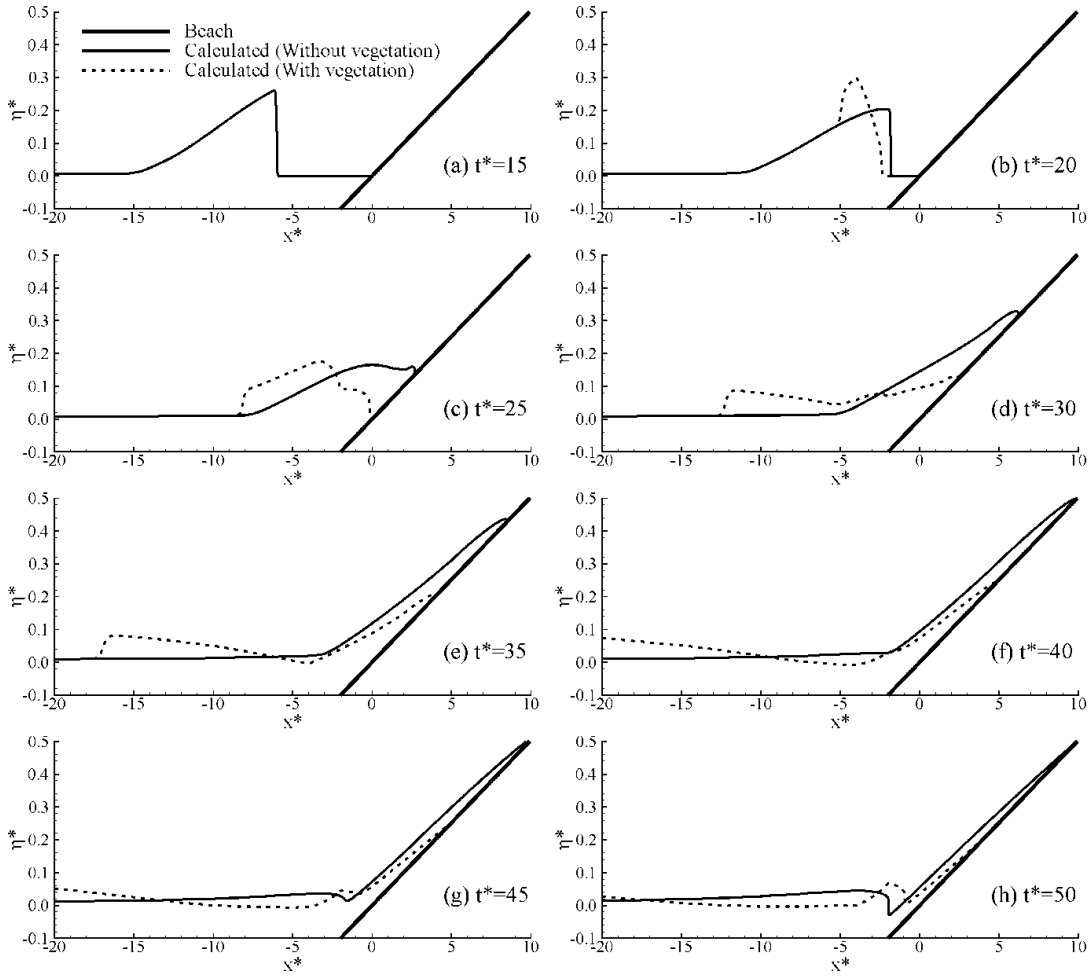

Fig. 6.13. Comparison of calculated runups of *H/h* = 0.3 breaking solitary wave on a 1:19.85 sloping beach with and without vegetation

6.1.3.4 Tsunami wave runup over a vegetated sloping beach

This test case considers the effects of an open gap, such as a road, in a coastal forest on long waves, such as tsunami wave. The laboratory experiment was carried by Thuy et al. (2010) at Saitama University, Japan. Fig. 6.14 shows the experimental setup of the wave flume, which was 15 m long and 0.4 m wide. The width was divided to an open gap zone and a vegetation zone, which were 0.07 and 0.33 m wide, respectively. The vegetation zone started at x = 10.36 m and ended at x = 11.36 m. The vegetation was modeled with wooden cylinders with a diameter of 5 mm in a staggered arrangement and a density of 2,200 units/m^2. The incident sinusoidal waves with a period of 20 s were generated on the offshore side, and the still water depth was 0.44 m.

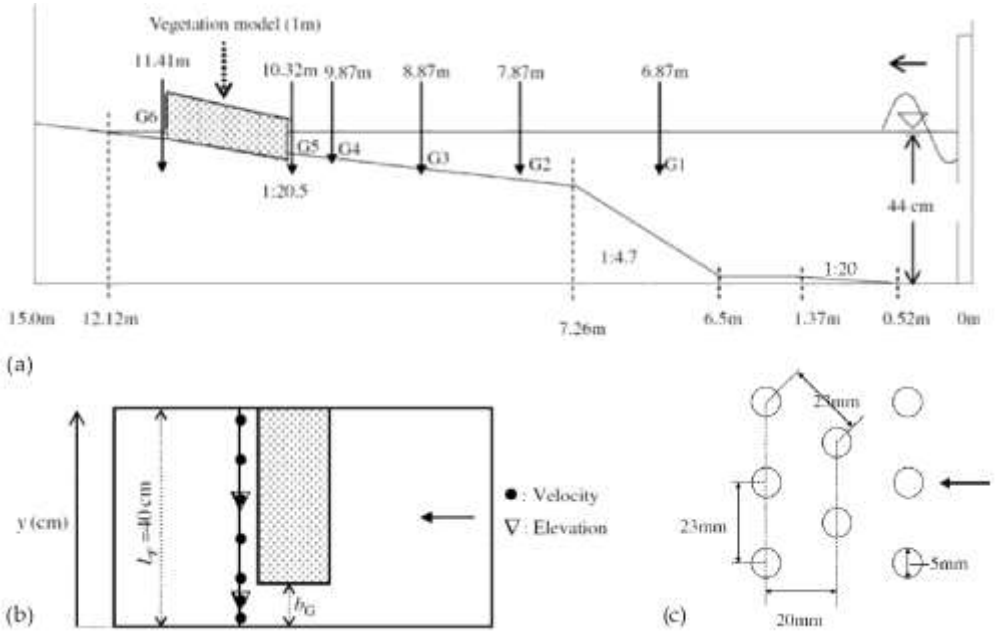

Fig. 6.14. Experimental setup of wave flume: (a) Longitudinal section, (b) plan view of vegetation zone and measurement points, and (c) vegetation arrangement (Thuy et al. 2009)

The simulation domain was represented with a uniform mesh consisting of 750×40 nodes in longitudinal and lateral directions, respectively. The time step was set by means of a Courant number of 0.25. After trial and error, it was found that an incident wave height of 1.6 cm gave the best fit between measured and calculated results at Gage 1. The drag coefficient C_D was 2.5, the Manning roughness coefficient n was 0.012, and the coefficient c_m in the mixing-length turbulence model was set as 0.2. Fig. 6.15 compares the measured and calculated wave characteristics in the case of full-width vegetation with no gap. Fig. 6.16 shows the time evolutions of velocities at the centers (y = 0.035 and 0.235 m) of gap and vegetation zone at Gage 6, and Fig. 6.17 compares the transverse distributions of measured and calculated maximum velocities along the cross-section at Gage 6, in the case of a 0.07 m wide gap existed. Thuy et al. (2010) pointed out that since the tsunami flow dominates in the x direction in their experiments, the velocity sign (+ or -) in Fig. 6.16 was defined by its

longitudinal component. The maximum velocities in Fig. 6.17 were averaged from the maximum velocities of five wave periods at the final developed stage. One can see that the calculated wave heights and flow velocities are in generally good agreement with the measured ones.

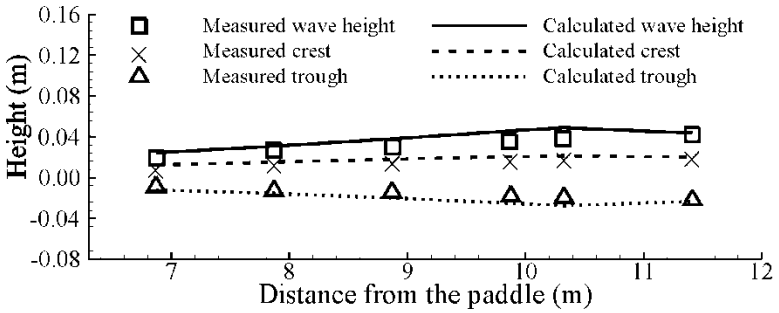

Fig. 6.15. Comparison of measured and calculated wave crests, heights, and troughs

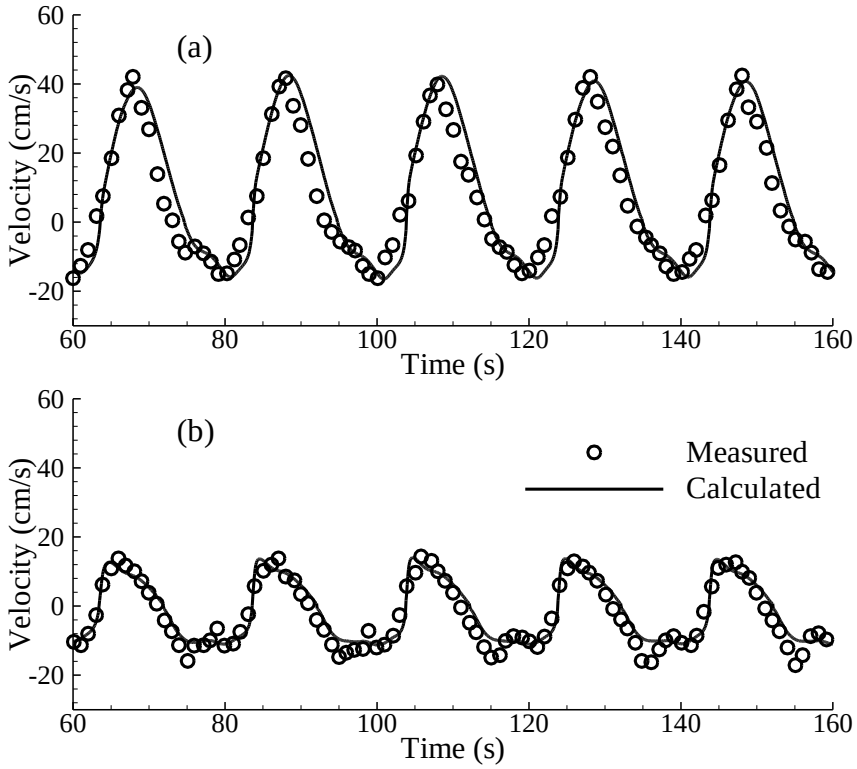

Fig. 6.16. Temporal variations of velocity at Gage 6: (a) at the gap center (y = 0.035 m), and (b) at the vegetation zone center (y = 0.235 m)

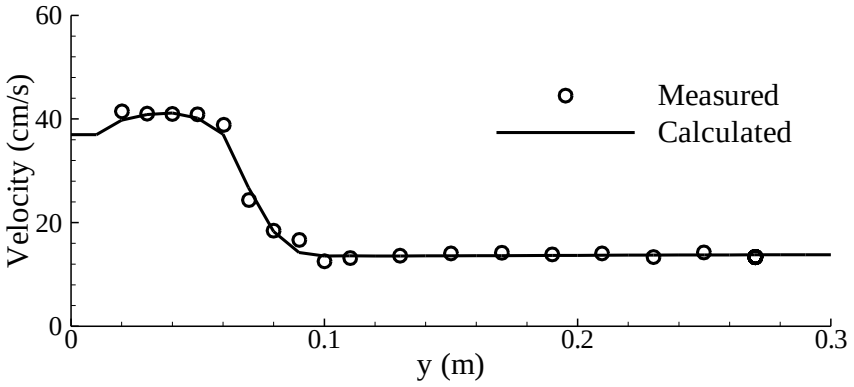

Fig. 6.17. Transverse distribution of maximum velocity across Gage 6

6.2 A 1-D Boussinesq Model for Short Waves in Vegetated Waters

In this section, a shock-capturing one-dimensional Boussinesq model has been used to study attenuation of short waves by vegetation. The Boussinesq equations presented by Madsen and Sørensen (1992) are modified to simulate wave propagation in vegetated waters. In order to consider the effect of vegetation, the drag force generated by vegetation is added as source term in the momentum equation. A hybrid finite-volume/finite-difference method is developed to solve the governing equations. The flux term is discretized by a finite-volume-based fourth-order accurate scheme, the dispersion and source terms are discretized by centered finite-difference schemes, and the unsteady term is discretized by the second-order MUSCL-Hancock scheme. The model has been verified and validated with analytical solutions and experiment data reported in the literature, as well as data measured through the experiments conducted at the National Sedimentation laboratory (NSL), Oxford, MS, USA as part of this project. The governing equations, numerical schemes, and validations of the model are described in the following subsections.

6.2.1 Governing Equations

The Boussinesq equations of Madsen and Sørensen (1992) are extended to consider the bottom shear stress and effects of vegetations as follows:

$$\frac{\partial \eta}{\partial t} + \frac{\partial (Ud)}{\partial x} = 0 \tag{6.24}$$

$$\frac{\partial (Ud)}{\partial t} + \frac{\partial \left(U^2 d\right)}{\partial x} + gd\frac{\partial \eta}{\partial x} + \frac{\partial \psi}{\partial x} + gdS_f + F_D = 0 \tag{6.25}$$

where U is the depth-averaged horizontal velocity, η is the free surface elevation above the still water, d is the entire water depth as shown in Fig. 6.1, S_f is the bed friction, F_D is the drag force per unit horizontal (bed) area induced by vegetation, and ψ includes the terms that model wave dispersion:

$$\frac{\partial \psi}{\partial x} = -\left(B + \frac{1}{3}\right)h^2 \frac{\partial^3 (Ud)}{\partial x^2 \partial t} - Bgh^3 \frac{\partial^3 \eta}{\partial x^3} - h\frac{\partial h}{\partial x}\left(\frac{1}{3}\frac{\partial^2 (Ud)}{\partial x \partial t} + 2Bgh\frac{\partial^2 \eta}{\partial x^2}\right) \tag{6.26}$$

where B is a free parameter that determines the dispersion properties of the system. Madsen and Sørensen (1992) suggested that $B = 1/15$.

By assuming that the bathymetry remains constant over time or changes much slower than the water surface, the continuity and momentum equations (6.24) and (6.25) can be rewritten in the conservative form as

$$\frac{\partial \mathbf{\Phi}}{\partial t} + \frac{\partial \mathbf{F}(\mathbf{\Phi})}{\partial x} = \mathbf{S} \tag{6.27}$$

where $\mathbf{\Phi}$ and $\mathbf{F(\Phi)}$ are vectors containing the conserved variables and fluxes, respectively, and $\mathbf{S}$ is the vector of source terms:

$$\mathbf{\Phi} = \begin{bmatrix} d \\ \Phi(Ud) \end{bmatrix}, \quad \mathbf{F} = \begin{bmatrix} Ud \\ U^2 d + \frac{1}{2} g d^2 \end{bmatrix}, \quad \mathbf{S} = \begin{bmatrix} 0 \\ gd\left(S_o - S_f\right) - F_D + S_d \end{bmatrix} \tag{6.28}$$

where

$$\Phi(Ud) = Ud - \left(B + \frac{1}{3}\right) h^2 \frac{\partial^2 (Ud)}{\partial x^2} - \frac{1}{3} h \frac{\partial h}{\partial x} \frac{\partial (Ud)}{\partial x}$$

$$S_o = -gd \frac{\partial z_b}{\partial x}$$

$$S_f = \frac{\mathrm{n}^2 U |U|}{d^{4/3}}$$

$$F_D = \frac{1}{2} C_D N_v A_v U |U|$$

$$S_d = Bgh^3 \frac{\partial^3 \eta}{\partial x^3} + 2Bgh^2 \frac{\partial h}{\partial x} \frac{\partial^2 \eta}{\partial x^2}$$

in which z_b is the bottom elevation measured from the datum, S_0 is the bed slope and S_d is the dispersion term. As defined in Section 6.1.1, n is the Manning's roughness coefficient, C_D is the drag coefficient, N_v is the number of stems per unit area, and A_v is the projected area of a stem normal to the flow direction given by Eq. (6.5).

Note that the inertia force is ignored after considering it is usually much smaller than the drag force. The drag force in this Boussinesg wave model has the same formulation as that in Eq. (6.4) used in the shallow water flow model.

6.2.2 Numerical Solution Methods

The Boussinesq equations given in Eqs. (6.24) and (6.25) are solved using a hybrid method in which a finite-volume scheme is applied to the conservative part and a finite-difference scheme is applied to the remaining terms. The hybrid method has fourth-order accuracy in space and second-order accuracy in time. Integrating Eq. (6.27) over a cell with a length of Δx and applying the divergence theorem yields

$$\int_{\Delta x} \frac{\partial \mathbf{\Phi}}{\partial t} dx + \oint_{\Gamma} \mathbf{F} \cdot \mathbf{n}_m d\Gamma = \int_{\Delta x} \mathbf{S} dx \tag{6.29}$$

where $\mathbf{n}_m$ is the outward pointing normal vector of side m. Eq. (6.29) can be further approximated as

$$\frac{\partial \mathbf{\Phi}}{\partial t}\Delta x + \sum_{m=1}^{M}\left(\mathbf{F}\cdot\mathbf{n}_m\right) = \mathbf{S}\Delta x \tag{6.30}$$

where M is the number of faces at each cell. The time integration, intercell fluxes and source terms of Eq. (6.30) are explained in the following subsections.

6.2.2.1 **Riemann fluxes and fourth-order MUSCL reconstruction**

In order to handle steep gradients of the variables, the solution of a local Riemann problem is required at each cell interface, and the HLL approximate Riemann solver (Harten et al. 1983) is herein used to compute the convective fluxes. The HLL Riemann flux is expressed in Eq. (6.11). Wei and Kirby (1995) point out that a fourth-order accurate treatment of the first derivatives is required, so that the truncation error in the numerical scheme is smaller than the dispersion terms present in the model. Therefore, the values of the state variables at cell interfaces are calculated using a fourth-order Monotonic Upstream Scheme for Conservation Laws (MUSCL) proposed by Yamamoto et al. (1998). The gradient across cell i is determined using the values of the neighbouring cells $i\pm1$. Evaluation of values at cell faces $i\pm1/2$ using the gradient may result in under/overshoots. The MUSCL scheme eliminates such spurious oscillations using a nonlinear limiter function.

The state values on the left- and right-hand sides of cell face $i+1/2$ can be computed as follows:

$$\begin{aligned}
\mathbf{\Phi}^{L}_{i+1/2} &= \mathbf{\Phi}_i + \frac{1}{6}\left[\Delta^*\overline{\mathbf{\Phi}}_{i-1/2} + 2\Delta^*\tilde{\mathbf{\Phi}}_{i+1/2}\right] \\
\mathbf{\Phi}^{R}_{i+1/2} &= \mathbf{\Phi}_{i+1} - \frac{1}{6}\left[2\Delta^*\overline{\mathbf{\Phi}}_{i+1/2} + \Delta^*\tilde{\mathbf{\Phi}}_{i+3/2}\right]
\end{aligned} \tag{6.31}$$

where

$$\begin{aligned}
\Delta^*\overline{\mathbf{\Phi}}_{i-1/2} &= \min\mathrm{mod}\left[\Delta^*\mathbf{\Phi}_{i-1/2},\, b_1\Delta^*\mathbf{\Phi}_{i+1/2}\right] \\
\Delta^*\tilde{\mathbf{\Phi}}_{i+1/2} &= \min\mathrm{mod}\left[\Delta^*\mathbf{\Phi}_{i+1/2},\, b_1\Delta^*\mathbf{\Phi}_{i-1/2}\right] \\
\Delta^*\overline{\mathbf{\Phi}}_{i+1/2} &= \min\mathrm{mod}\left[\Delta^*\mathbf{\Phi}_{i+1/2},\, b_1\Delta^*\mathbf{\Phi}_{i+3/2}\right] \\
\Delta^*\tilde{\mathbf{\Phi}}_{i+3/2} &= \min\mathrm{mod}\left[\Delta^*\mathbf{\Phi}_{i+3/2},\, b_1\Delta^*\mathbf{\Phi}_{i+1/2}\right]
\end{aligned}$$

with

$$\Delta^*\mathbf{\Phi}_{i+1/2} = \Delta\mathbf{\Phi}_{i+1/2} - \frac{1}{6}\left(\Delta\overline{\mathbf{\Phi}}_{i+3/2} - 2\Delta\overline{\mathbf{\Phi}}_{i+1/2} + \Delta\overline{\mathbf{\Phi}}_{i-1/2}\right)$$

$$\begin{aligned}
\Delta\overline{\mathbf{\Phi}}_{i-1/2} &= \overline{m}\left(\Delta\mathbf{\Phi}_{i-1/2},\, \Delta\mathbf{\Phi}_{i+1/2},\, \Delta\mathbf{\Phi}_{i+3/2}\right) \\
\Delta\overline{\mathbf{\Phi}}_{i+1/2} &= \overline{m}\left(\Delta\mathbf{\Phi}_{i+1/2},\, \Delta\mathbf{\Phi}_{i+3/2},\, \Delta\mathbf{\Phi}_{i-1/2}\right) \\
\Delta\overline{\mathbf{\Phi}}_{i+3/2} &= \overline{m}\left(\Delta\mathbf{\Phi}_{i+3/2},\, \Delta\mathbf{\Phi}_{i-1/2},\, \Delta\mathbf{\Phi}_{i+1/2}\right)
\end{aligned}$$

where $\overline{m}$ is defined as $\overline{m}(a,b,c) = \mathrm{sign}(a)\cdot\max\left[0, \min\left(|a|,\, b_2\cdot\mathrm{sign}(a)\cdot b,\, b_2\cdot\mathrm{sign}(a)\cdot c\right)\right]$.

This scheme is composed of two terms, the ordinary third-order term and a fourth-order term. b_1 = 4 and b_2 = 2 are specified. For smooth reconstruction of water surface at a cell interface, the surface gradient method (Zhou et al. 2001) is used, in which the water surface elevation rather than water depth is used as the state variable.

6.2.2.2 **Time integration**

The time discretization is generally based on a high-order predictor and corrector approach. The discretization proposed by Wei and Kirby (1995) uses the third-order Adams-Brashforth scheme for predictor and fourth-order Adams-Moulton for corrector. According to Shiach and Mingham (2009), the second-order accurate MUSCL-Hancock scheme provides sufficient accuracy with less computational cost and is thus adopted in this study. It uses two-stage predictor and corrector. The predictor step determines the intermediate values over a half time step as

$$\mathbf{\Phi}^{n+1/2} = \mathbf{\Phi}^{n} - \frac{\Delta t}{2\Delta x}\left[\sum_{m=1}^{M}\mathbf{F}\left(\mathbf{\Phi}_{m}\right)^{n}\cdot\mathbf{n}_{m}\right] \tag{6.32}$$

where n and n+1/2 denote the current and intermediate values, and Δt is the time step. The corrector step provides the full conservative solution over a time step, as given by

$$\mathbf{\Phi}^{n+1} = \mathbf{\Phi}^{n} - \frac{\Delta t}{\Delta x}\left[\sum_{m=1}^{M}\mathbf{F}\left(\mathbf{\Phi}_{m}^{L},\mathbf{\Phi}_{m}^{R}\right)^{n+1/2}\cdot\mathbf{n}_{m}\right] + \Delta t\left[gd\left(S_{o}-S_{f}\right)-F_{D}+S_{d}\right] \tag{6.33}$$

where $\mathbf{F}\left(\mathbf{\Phi}_{m}^{L},\mathbf{\Phi}_{m}^{R}\right)$ is the flux at cell face m, the values of which are obtained using the HLL approximate Riemann solver; and $\mathbf{\Phi}_{m}^{L}$ and $\mathbf{\Phi}_{m}^{R}$ are the values of the conserved variables at the cell face obtained using the fourth-order MUSCL reconstruction method proposed by Yamamoto et al. (1998).

6.2.2.3 **Evaluation of velocity**

The velocity function in Eq. (6.28) is discretized using the second-order accurate central differences for the first and second derivatives, resulting in the following tri-diagonal matrix form:

$$\Phi\left(Ud\right)_{i} = a_{i}\left(Ud\right)_{i-1} + b_{i}\left(Ud\right)_{i} + c_{i}\left(Ud\right)_{i+1} \tag{6.34}$$

where

$$a_{i} = -\frac{\left(B+1/3\right)d_{i}^{2}}{\Delta x^{2}} + \frac{d_{i}}{12\Delta x^{2}}\left(-d_{i-1}+d_{i+1}\right)$$

$$b_{i} = 1+\frac{2\left(B+1/3\right)d_{i}^{2}}{\Delta x^{2}}$$

$$c_{i} = -\frac{\left(B+1/3\right)d_{i}^{2}}{\Delta x^{2}} - \frac{d_{i}}{12\Delta x^{2}}\left(-d_{i-1}+d_{i+1}\right)$$

The coefficients in Eq. (6.34) are time independent, and hence are evaluated once and used throughout the simulation. In order to compute the flow velocity, the tri-diagonal matrix is efficiently solved using the Thomas algorithm.

6.2.2.4 **Source terms**

A cell-centered discretization is used for the bed slope, bed friction and vegetation terms. A fourth-order central difference approximation is used for the first spatial derivative, and second- and third-order central differences for the second and third spatial derivatives in the dispersion terms. The discretized source term takes the following form:

$$S_i = -gd_i\left(\frac{z_{bi+1/2}-z_{bi-1/2}}{\Delta x}\right) - gd_iS_f - F_D + \frac{Bgh_i^3}{2\Delta x^3}\left(-\eta_{i-2}+2\eta_{i-1}-2\eta_{i+1}+\eta_{i+2}\right) + \frac{Bgh_i^3}{6\Delta x^3}\left(h_{i-2}-8h_{i-1}+8h_{i+1}-h_{i+2}\right)\left(\eta_{i-1}-2\eta_i+\eta_{i+1}\right) \tag{6.35}$$

6.2.2.5 **Boundary conditions**

Various boundaries have been implemented in the developed Boussinesq wave model, including a non-reflecting wave boundary, a moving boundary due to wave runup and rundown over a sloping beach, and a sponge layer boundary to absorb wave energy at the end of the flume. The sponge layer boundary condition proposed by Larsen and Dancy (1983) is used here. Its details can be found in this reference and hence are not explained here. The non-reflecting wave boundary and moving boundary used in the present model are discussed briefly in the following subsections.

Non-reflecting boundary condition at wave entrance

When incident waves are imposed as a time series of water level, reflection may take place after they hit a land boundary at the other end of the domain. The reflected waves may interfere with the incident waves. In this case, a non-reflecting wave condition at the inlet boundary is required, so that the reflected waves can pass through without carrying any disturbance back into the computational domain. The second-order characteristic approach proposed by Hu et al. (2000) is implemented in the present model. The method is based on the long wave assumption and the inlet boundary has to be located beyond the break point, so that the flow at the boundary is subcritical.

Moving boundary on the shoreline

Wave runup and rundown on a sloping beach is a moving boundary problem that can be viewed as wetting and drying of boundary cells. The HLL solver is preferred in this case because it can conveniently describe the flux through the wet/dry interface. A local threshold water depth, d_{tol}, is used to determine wetting or drying. At each time step the cells are checked for dry and wet definition. The cells having water depths less than d_{tol} are defined as dry; otherwise the cells are wet. The moving boundary is defined as the line of separation between wet and dry cells. The dry cells that do not have any wet neighbouring cell are not considered in the computation at a time step.

Special attentions should be paid for two possible situations where a wet cell is adjacent to a dry cell. (A) If the water level of the wet cell is lower than the bed level of the dry cell, wetting is impossible and the mass flux and the dynamic component of the momentum are zero; thus, the wet cell velocity for the evaluation of the flux through the wet-dry interface is set as zero and the water level of the dry cell is temporarily set equal to the water level of the wet cell. (B) If the water level of the wet cell is higher than the water level of the dry cell, the flow may flood the dry cell. If the bed slope is steep, more water than is actually contained in the wet cell can be computed as flowing into the dry cell, resulting in negative water depth in the wet cell. Such situation may be handled using the approach suggested by Brufau et al. (2004), but that approach needs extra computations and book keeping of the variables that may not be necessary. For simplicity, if the water depth in a cell falls below the threshold water depth, then it will be reset to d_{tol} and the velocity is set as zero. This treatment may add extra mass in the system, but the added mass is found to be negligible (Hu et al. 2000, Que and Xu 2005).

6.2.3 Model Verifications and Validations

The proposed model was first verified in cases with analytical solutions for regular wave propagation without considering vegetation in the flow domain, and then validated by reproducing laboratory tests on waves in vegetated and non-vegetated water bodies. Details are introduced in the following subsections.

6.2.3.1 Demonstration of model capability of retaining solitary wave in a flat-bed channel

A solitary wave retains its amplitude, shape and speed as it travels down a flat-bed channel due to balance between the nonlinear terms that steepen the wave and the dispersion terms that flatten the wave. Wei and Kirby (1995) presented a classical example to test the model capability of simulating such a phenomenon. This example was applied to verify the present model. The initial values of η and u were defined by

$$\eta = A_1 \sec d^2\left[B\left(x - Ct\right)\right] + A_2 \sec d^4\left[B\left(x - Ct\right)\right]$$

$$u = A\sec d^2\left[B\left(x - Ct\right)\right]$$

where

$$A = \frac{C^2 - gh}{C}$$

$$B = \left(\frac{C^2 - gh}{4h^2\left[\left(\alpha + 1/3\right)gh - \alpha C^2\right]}\right)^{\frac{1}{2}}$$

$$A_1 = \frac{C^2 - gh}{3\left[\left(\alpha + 1/3\right)gh - \alpha C^2\right]}h$$

$$A_2 = -\frac{C^2 - gh}{2ghC^2}\frac{\left[(\alpha + 1/3)gh + 2\alpha C^2\right]}{3\left[(\alpha + 1/3)gh - \alpha C^2\right]}h$$

The channel was 450 m long, with a constant water depth h = 0.45. The channel was discretized using Δx = 0.01 m. The solitary wave with an amplitude of 0.45 m was generated at the inlet and traveled down the channel at a phase speed of C = 2.203 m/s. The solutions obtained using the present Boussinesq model at times t = 40, 80, 120, 160 and 200 s are shown in Fig. 6.18. The shape and amplitude of the computed solitary wave remain almost constant, indicating that the numerical scheme successfully retains the dispersion present in the governing equations. However, the results show that a train of small waves are generated behind the solitary wave. Such transformation is imputed to the low-order approximation of the velocity given to the model as initial condition, and can be avoided if high-order approximation of velocity is supplied (Tonelli and Petti 2010).

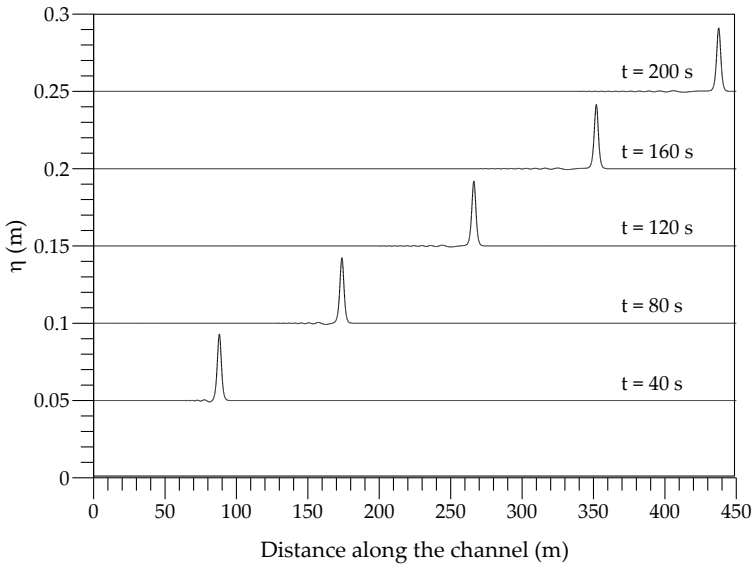

Fig. 6.18. Water surface profiles of the solitary wave at different elapsed times

6.2.3.2 **Verification against analytical solution of sine wave propagation**

To validate the drying/wetting boundary and non-reflective inlet boundary conditions implemented, the present model was applied to simulate runup/rundown motion of a monochromatic wave train on a sloping beach. A sine wave train with an amplitude of 0.003 m and a period of 10 s propagates in a channel with initial water depth of 0.5 m and climbs up a 1:25 sloping beach. This configuration has analytical solution, which was derived by Carrier and Greenspan (1958) using the hodograph transformation to solve the shallow water equations. This case was also used in Madsen et al. (1997), Kennedy et al. (2000), and Lynett et al. (2002). In the present numerical simulation, the domain was discretized using a grid size of 0.045 m, and a time step of 0.005 s was used. The threshold water depth d_{tol} = 0.000001 m. At the inlet, the non-reflective boundary condition was

imposed to reduce the wave reflectivity. Fig. 6.19 compares the calculated and analytical water surface profiles for the maximum and minimum runup. The agreement is good. This test proves the effectiveness of the boundary conditions and invokes the threshold water depth criterion for drying/wetting definition.

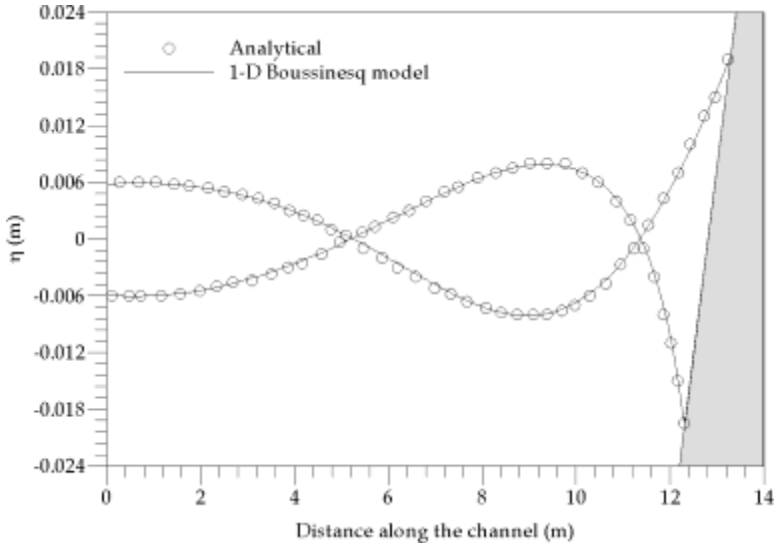

Fig. 6.19. Sine wave propagation in a straight channel

6.2.3.3 Validation using experiment data of regular wave propagation over a submerged bar

A classical case to test the Boussinesq-type wave model is the regular wave propagation over a submerged bar. This test was introduced by Dingemans (1987) and the same experiments were repeated by Beji and Battjes (1993). The experiments were conducted in a 23 m long straight flume with a submerged bar. The bar consisted of a 1:20 front slope and a 1:10 back slope separated by a level plane of 2 m in length, as shown in Fig. 6.20. The waves were generated with three different wave configurations (Table 6.2). Configurations A and C generated non-breaking waves, whereas Configuration B generated spilling breakers over the plane surface of the bar. The wave steepened along the front slope due to the nonlinear effect, whilst the back slope caused the wave train to break up into independent waves travelling at their own speeds. The gages placed at x = 2.0, 5.7, 10.5, 13.5, 15.7 and 19.0 m recorded water surface elevations over time.

The flume was discretized using a spatial step of $\Delta x = 0.01$ m. The regular waves were generated at the inlet boundary and a sponge layer was employed at the downstream end to reduce wave reflection. Figs. 6.21–6.23 compare the water surface elevations at different gages obtained from the experiments (Shiach and Mingham 2009) and the present model for the wave configurations A–C. It should be noted that the phase error recorded at Gage x = 5.7 m was attributed to an error in the recording of the experiments. At all other gages the model predicted the water surface elevations quite well.

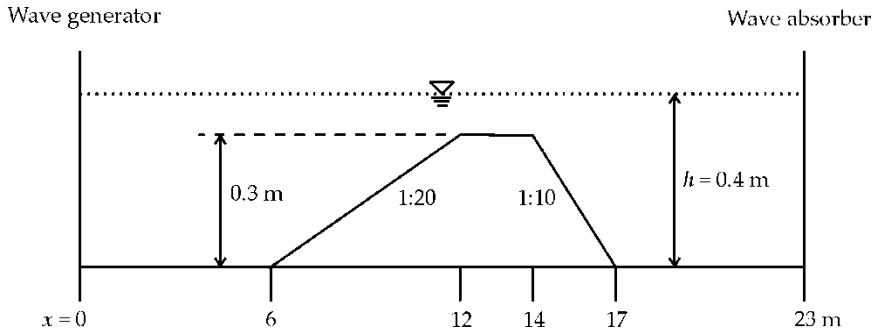

Fig. 6.20. Definition of bed topography for regular wave propagation over a submerged bar

Table 6.2. Laboratory wave configurations used by Beji and Battjes (1993)

Configuration	Wave height (m)	Period (s)	*d/L*
A	0.020	2.020	0.11
B	0.029	2.525	0.08
C	0.041	1.010	0.27

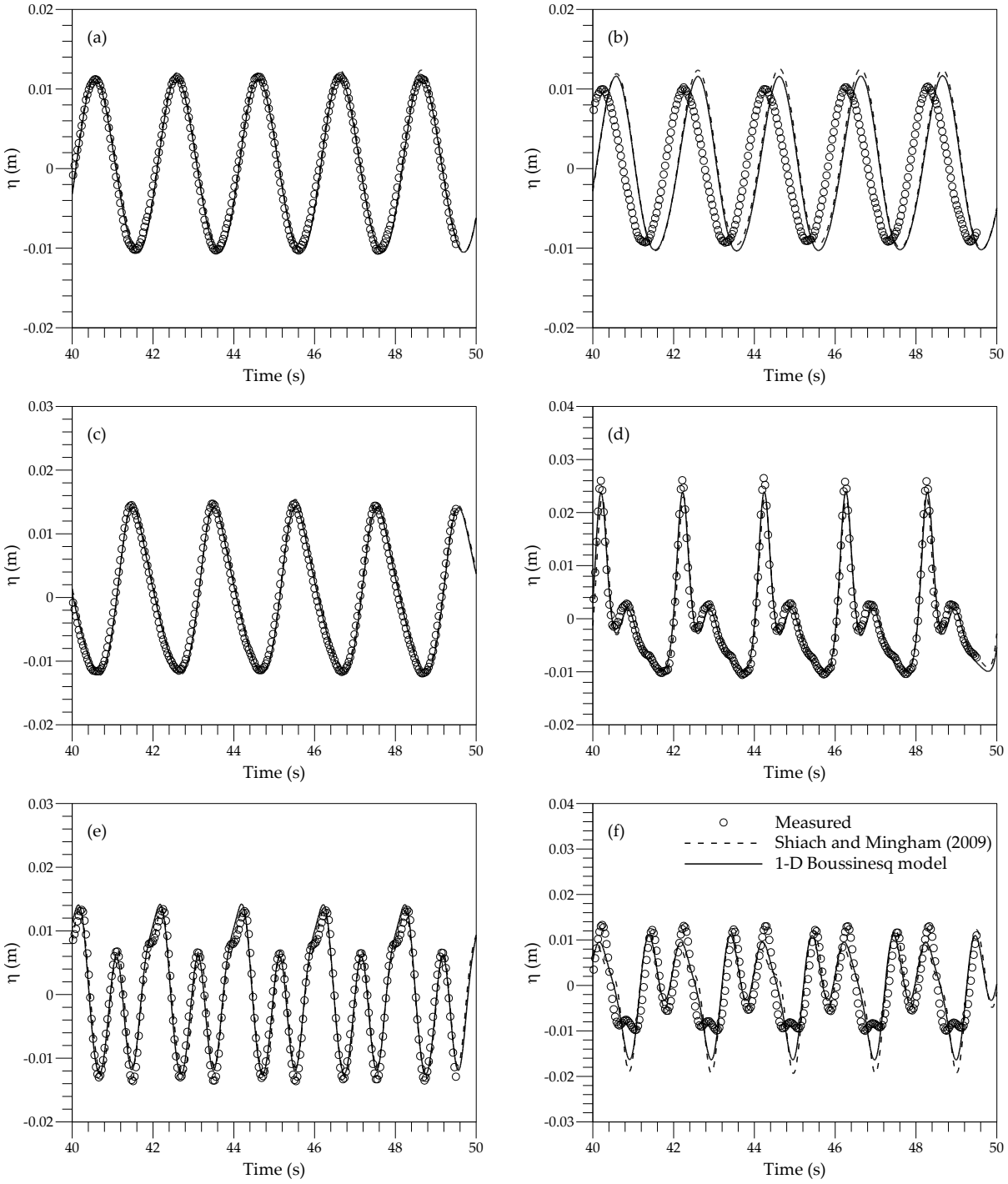

Fig. 6.21. Measured and calculated water surface elevations at gages: (a) x= 2.0 m, (b) 5.7 m, (c) 10.5 m, (d) 13.5 m, (e) 15.7 m and (f) 19.0 m for wave configuration A

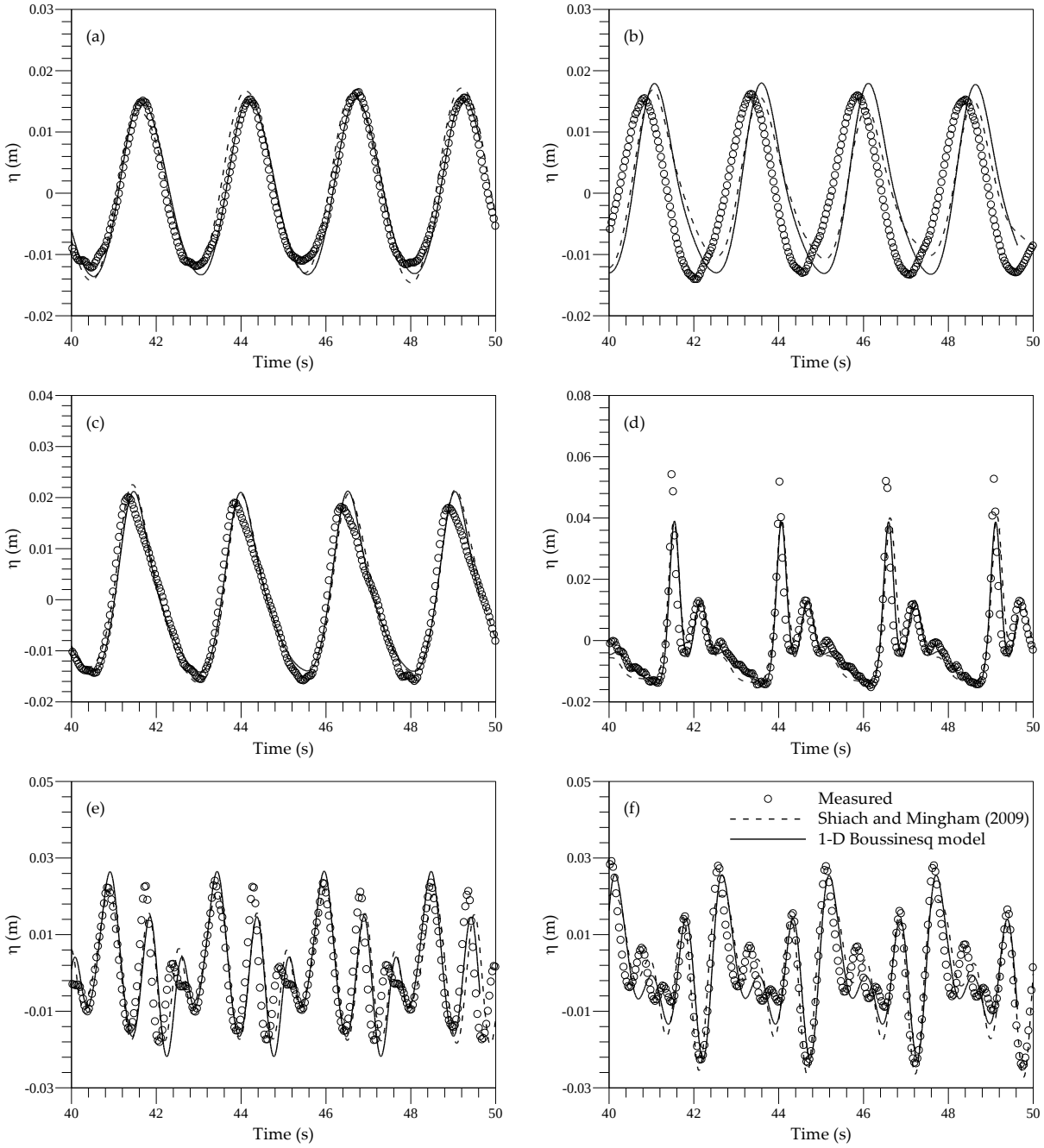

Fig. 6.22. Measured and calculated water surface elevations at gages: (a) *x*= 2.0 m, (b) 5.7 m, (c) 10.5 m, (d) 13.5 m, (e) 15.7 m and (f) 19.0 m for wave configuration B

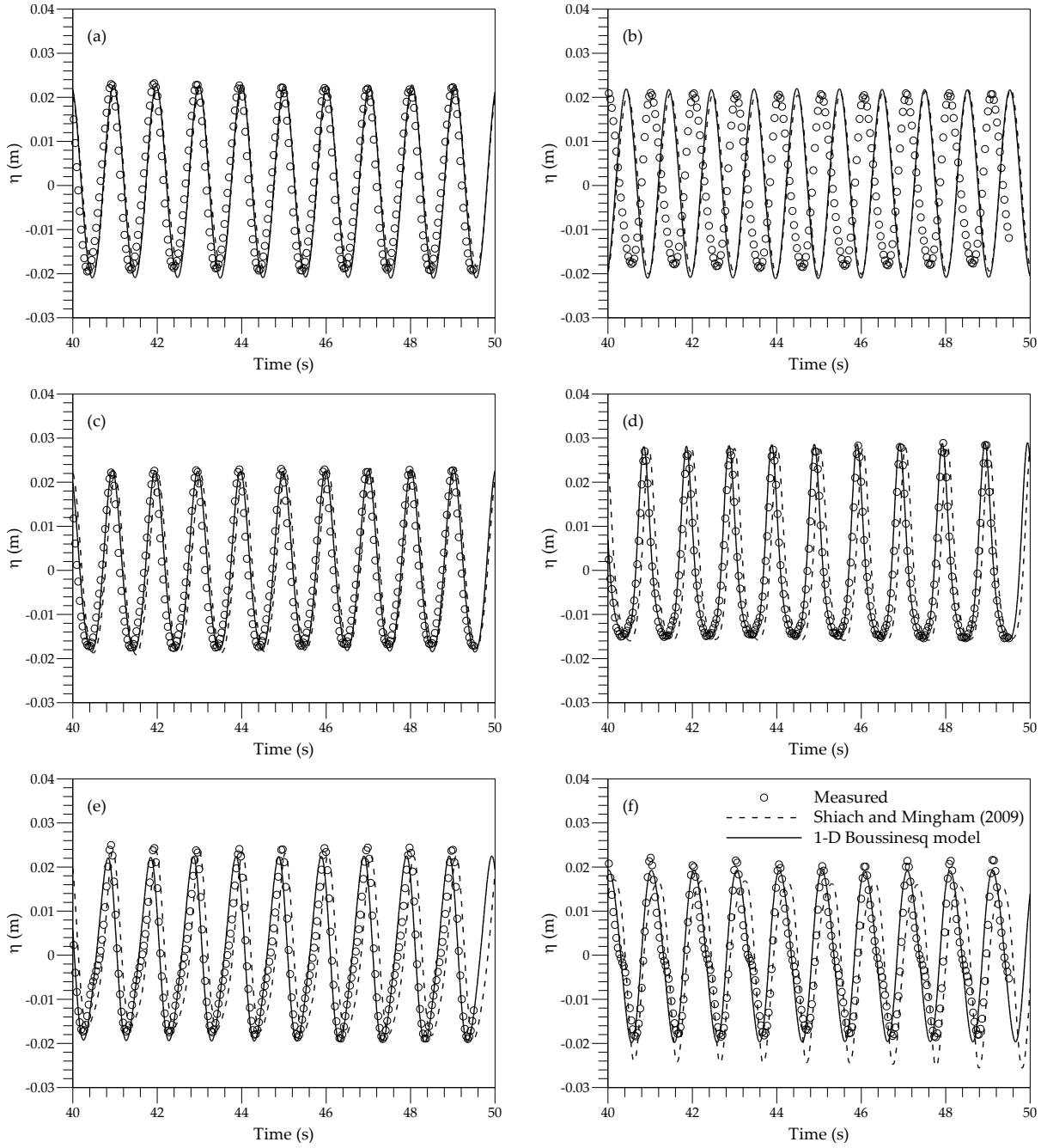

Fig. 6.23. Measured and calculated water surface elevations at gages: (a) x= 2.0 m, (b) 5.7 m, (c) 10.5 m, (d) 13.5 m, (e) 15.7 m and (f) 19.0 m for wave configuration C

6.2.3.4 **Validation using experiment data of waves in vegetated flume**

The experiments conducted by Asano et al. (1993) were used to test the accuracy of the developed Boussinesq wave model. The schematic view of the experimental setup is shown in Fig. 6.24. The experiments were conducted in a wave tank 27 m long, 0.5 m wide and 0.7 m high. The artificial vegetation was made of 0.25 m long, 0.052 m wide and 0.3 mm thick

polypropylene strips, with a specific gravity of 0.9. The strips were bound to a wire net at the bottom of the wave flume. The length of vegetation field was 8 m and the number density of strips placed uniformly was 1,110 and 1,490 m^{-2}. The total water depth in the tank ranged from 0.45 m to 0.52 m and the wave height from 0.036 m to 0.1934 m. The capacitance wave gages were used to measure the free surface oscillations at four locations. A series of 60 test runs were conducted, out of which two were chosen for testing the present model. The same two test runs were also considered by Li and Yan (2007) and their results are also presented here for comparison.

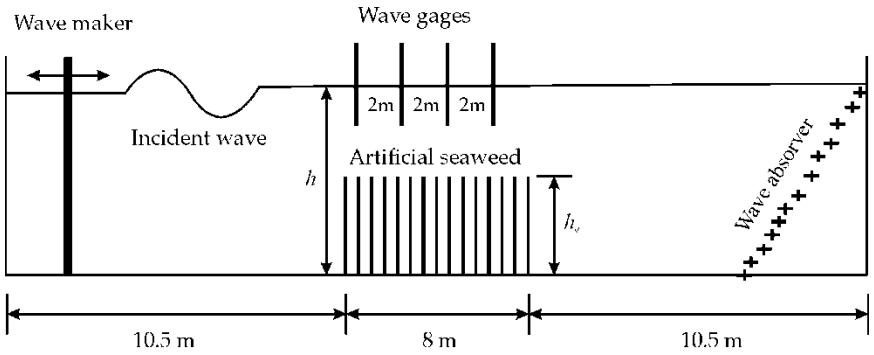

Fig. 6.24. Schematic diagram of the experimental setup of Asano et al. (1993)

The numerical model was set up to replicate the experimental conditions. The computational domain was 12 m long and 1 m wide, and $\Delta x = 0.01$ m was used. The non-reflecting boundary condition was specified at the inlet and a sponge layer of 2 m in length was provided at the downstream. At the inlet, a sine wave train was introduced and the simulation was carried out for long time so that a developed flow situation was achieved in the flow domain. The simulations were carried out for two different conditions: (a) H = 0.113 m, T = 1.25 s, h = 0.52 m and N_v = 1,110 units/m^2; and (b) H = 0.086 m, T = 2 s, h = 0.45 m and N_v = 1,490 units/m^2. The wave height at a point was obtained by subtracting the minimum water level from the maximum water level when the dynamic steady state was reached at that point. The longitudinal wave height profiles obtained from the present model, reported by Li and Yan (2007) and from the experiments are compared in Fig. 6.25. The origin in the plot is considered to be at the seaward side of the vegetation field. The model provides a reasonable estimate for the amount of wave height attenuation by vegetation. However, the reflection is prominent which needs to be improved.

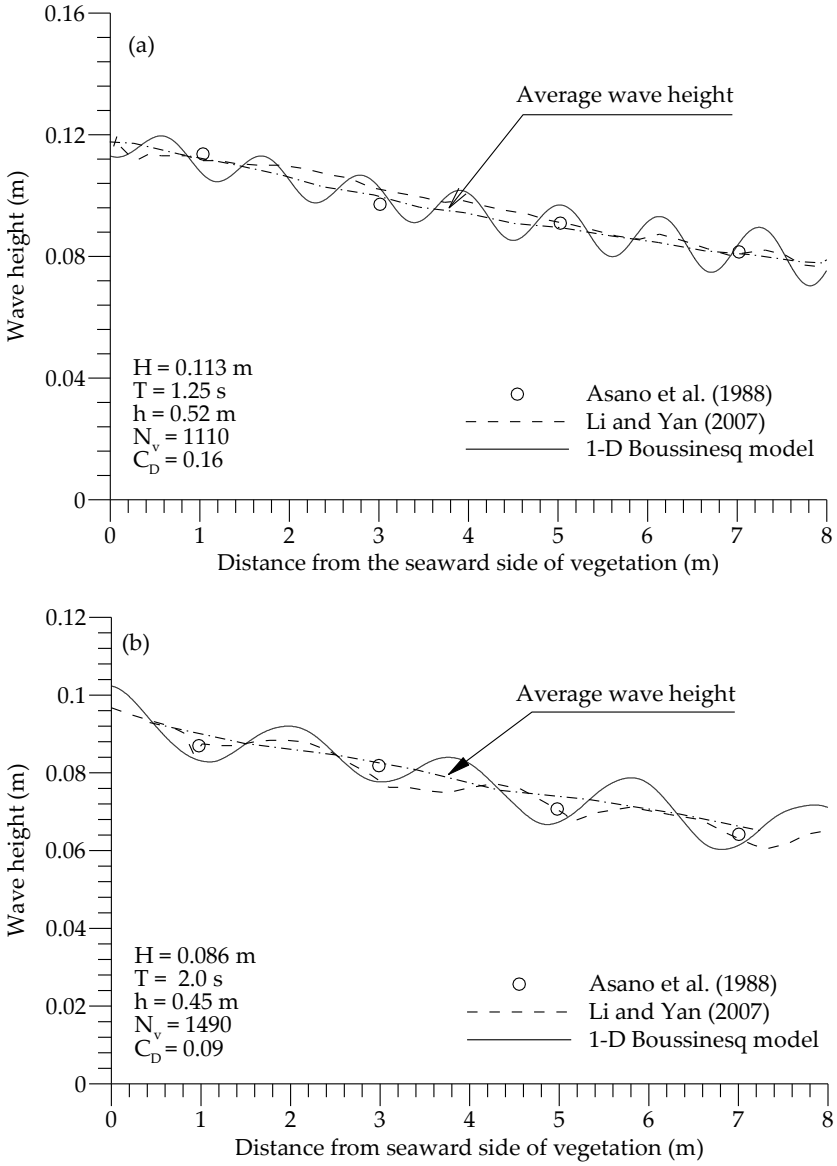

Fig. 6.25. Computed and measured wave heights along a vegetated channel

6.2.3.5 **Validation using experiment data obtained from the present project**

The developed 1-D Boussinesq wave model was tested with the measured data collected from a series of experiments on wave attenuation by vegetation conducted in a wave flume at the National Sedimentation Laboratory, Oxford, Mississippi as part of this SERRI project. The details of the experiments have been described in Chapter 3 of this report. The schematic experimental setup is shown in Fig. 3.2. The flume was 20.6 m long, 0.5 m wide and 1.22 m deep. The waves were generated at the inlet using an automatic wave generator controlled by a computer operated system. Regular and random waves of different amplitudes and periods were generated by the wave maker. At the downstream end, a wave absorber was used to avoid propagation of reflecting waves back into the flume. The vegetation species used include rigid model vegetation made of wooden circular cylinders,

flexible model vegetation made of rubber, and two live vegetation species collected from the Louisiana coast: *Spartina alterniflora* (green and dormant) and *Juncus roemerianus* (green). The rigid and flexible vegetation stems were fixed to a wire net at the bottom. The live vegetations were collected in a solid box and then placed in the flume. In all the cases the length of the vegetation field was L_V = 3.66 m. Five gages were placed at different locations to record the water surface elevations over time.

The numerical model was set up to replicate the experimental conditions. The inlet was placed at the location of the second gage and hence the computational domain was 7.2 m long. Since the wave flume bed was made of glass, the value of Manning's roughness coefficient at the bottom was considered as 0.012 $m^{-1/3}s$. The spatial domain was represented by a uniform mesh with $\Delta x = 0.01$ m. At the inlet waves were generated and a non-reflecting wave boundary condition was implemented. At the downstream, a 3 m long sponge layer was placed to reduce wave reflection.

The numerical investigations were carried out for two configurations of rigid model vegetation, one configuration of flexible model vegetation, and three configurations of live vegetation under three sets of wave heights, periods and still water levels, as shown in Table 6.3. Only regular waves were considered here. In the eighteen simulations, the drag coefficient, C_D, was the only one parameter that needs to be calibrated. By trial and error, the calibrated values of the drag coefficient for all the test cases were obtained by comparing computed and measured longitudinal profiles of wave heights along the channel. Table 6.3 lists the calibrated C_D values, and Figs. 6.26–6.28 show the attenuated wave heights along the vegetated channel. It can be seen that the developed 1-D Boussinesq wave model reproduced generally well the laboratory experiments. However, wave reflection from the downstream was not reduced completely. The model can be improved by implementing a better algorithm to define the flow condition in the sponge layer.

Fig. 6.29 and Table 6.3 show that the values of the drag coefficient in the 1-D Boussinesg model are mostly larger than those estimated using the analytical model of Dalrymple et al. (1984). The reason is that the analytical model use the local velocity squared to compute the drag force in Eq. (3.20), whereas the 1-D Boussinesq model uses the depth-averaged velocity squared for the drag force. The calibrated C_D in the depth-averaged model should be larger than that in the analytical model in order to get the same amount of total drag force and energy dissipation in a vertical line.

Table 6.3. Calibrated C_d values for the1-D Boussinesq model under regular waves

Experiment run No.	Wave conditions	Drag coefficient in different models	Rigid model (124363) N_v=350 h_v=0.63 m D_v=9.4 mm	Rigid model (126363) N_v=623 h_v=0.63 m D_v=9.4 mm	Flexible model N_v=350 h_v=0.48 m D_v=9.4 mm	Spartina (Dormant) N_v=545 h_v=0.62 m D_v=5.1 mm	Spartina (Green) N_v=405 h_v=0.59 m D_v=6.5 mm	Juncus (Green) N_v=2,857 h_v=1.03 m D_v=2.4 mm
501211001	h=0.50 m T=1.1 s H_{G2}=0.10 m	C_D in Eq. (3.20)	2.30	2.34	0.99	2.10	4.37	1.28
		C_D in Eq. (6.4)	4.15	4.50	1.20	4.15	9.45	2.55
600551101	h=0.60 m T=1.1 s H_{G2}=0.042 m	C_D in Eq. (3.20)	3.03	2.74	5.41	4.24	8.04	2.56
		C_D in Eq. (6.4)	2.15	4.45	3.45	6.15	10.45	3.50
700651201	h=0.70 m T=1.2 s H_{G2}=0.052 m	C_D in Eq. (3.20)	1.82	2.03	3.75		9.86	1.63
		C_D in Eq. (6.4)	2.10	3.12	2.50	2.45	9.50	2.65

Note: H_{G2} is the wave height measured at Gage 2 averaged over the runs with six vegetation configurations.

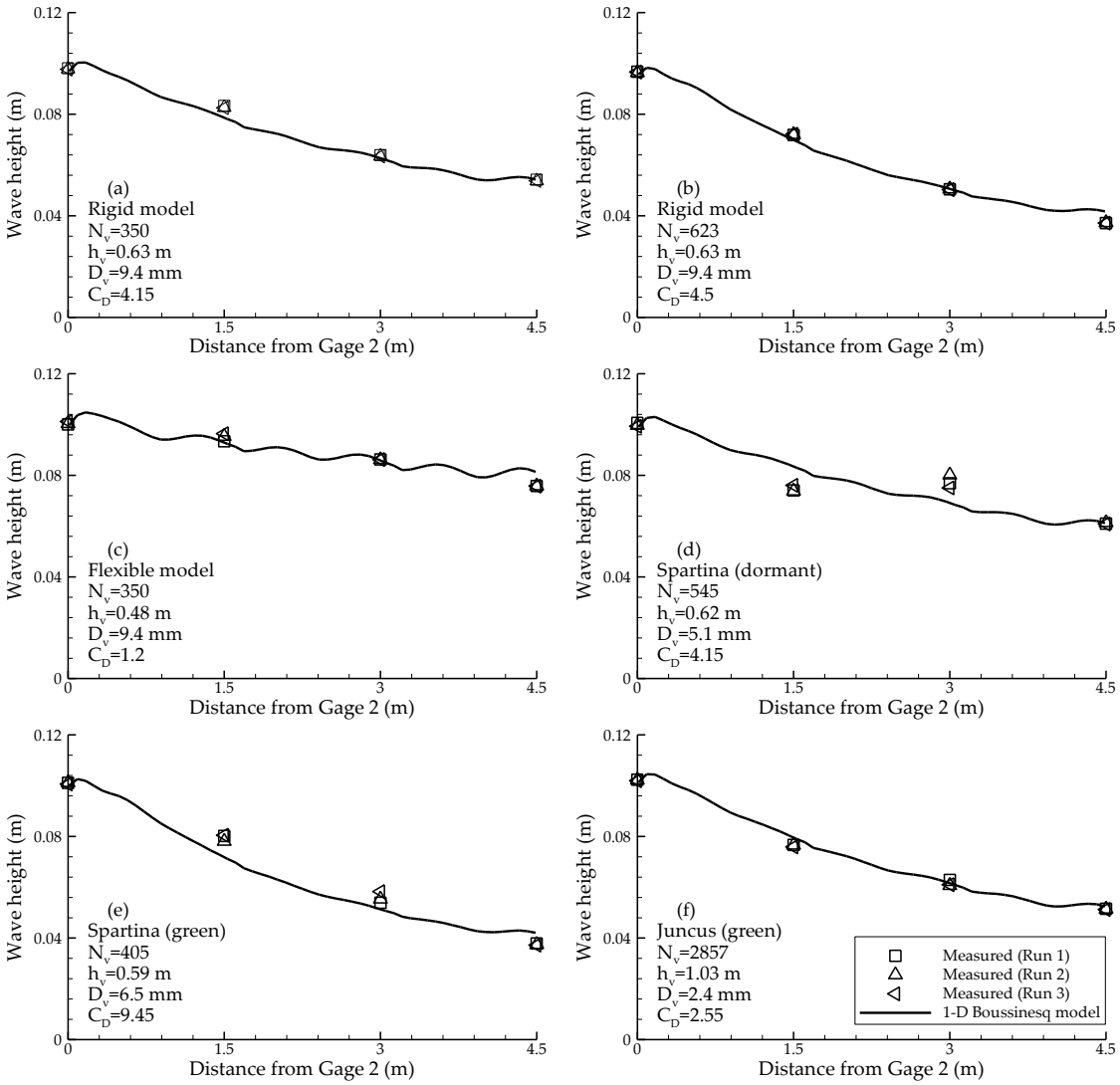

Fig. 6.26. Measured and calculated wave heights for regular wave experiment series No. 501211001 (h = 0.50 m, T = 1.1 s, H_{G2} = 0.10 m; simulations by the 1-D Boussinesq model)

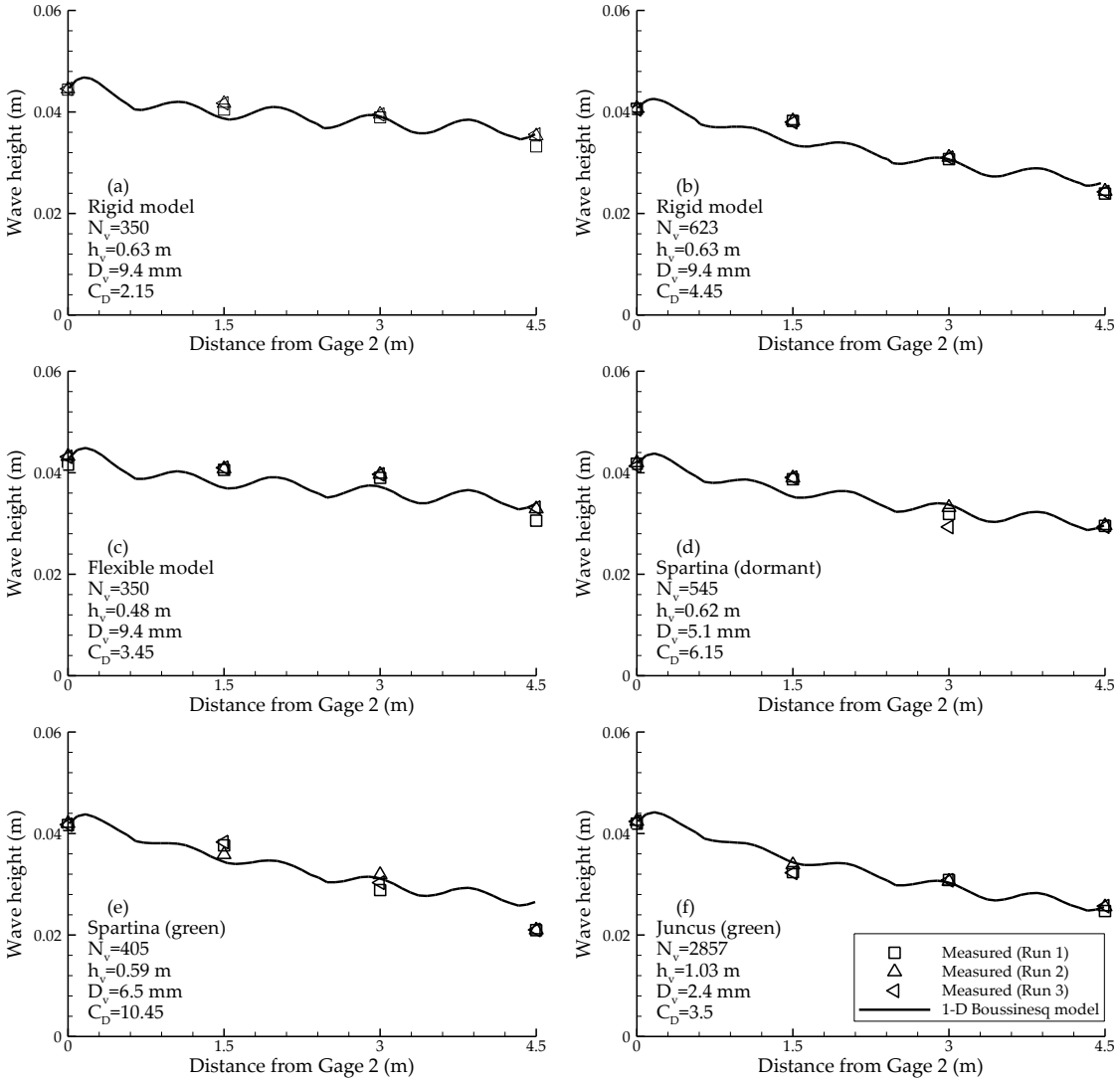

Fig. 6.27. Measured and calculated wave heights for regular wave experiment series No. 600551101 (*h* = 0.60 m, *T*=1.1 s, H_{G2} = 0.042 m; simulations by the 1-D Boussinesq model)

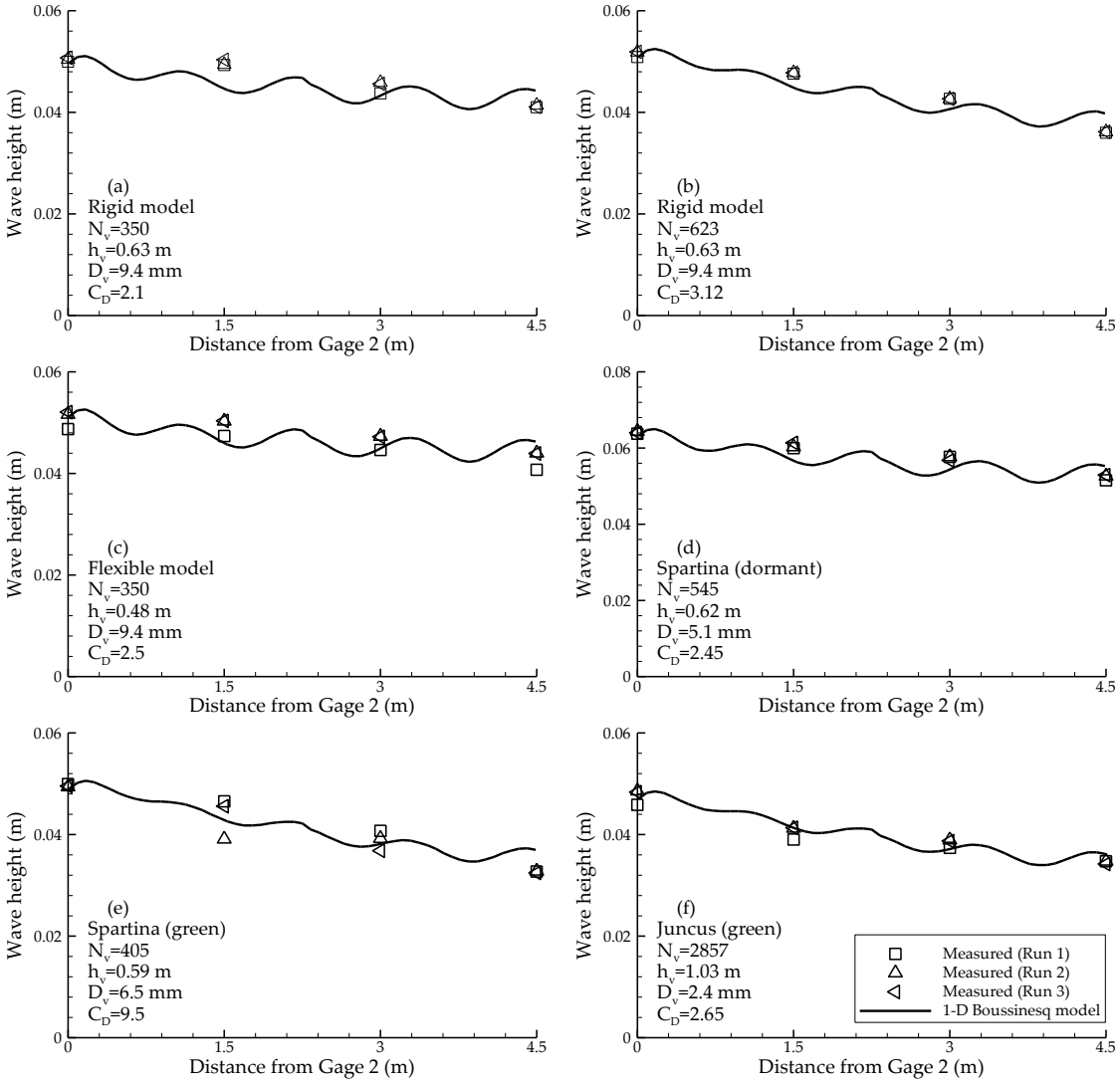

Fig. 6.28. Measured and calculated wave heights for regular wave experiment series No. 700651201 (h = 0.70 m, T = 1.2 s, H_{G2} = 0.052 m; simulations by the 1-D Boussinesq model)

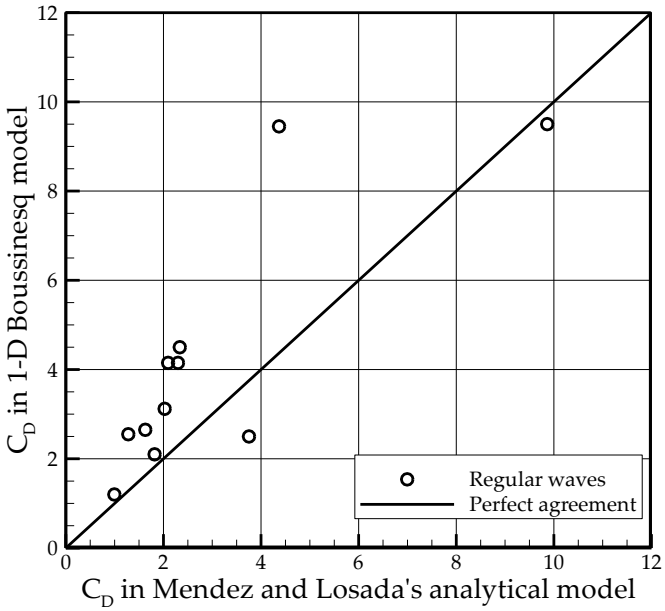

Fig. 6.29. Comparison of drag coefficients in the 1-D Boussinesq model and Mendez and Losada's (2004) analytical model

6.3 A Vertical 2-D VOF-Based RANS Model for Waves in Vegetated Waters

In this section, a vertical 2-D model has been applied in the simulation of wave propagation through vegetated and non-vegetated waters. The model is based on the finite difference code called SOLA-VOF, which solves the Reynolds-Averaged Navier-Stokes (RANS) equations and uses the fractional volume of fluid (VOF) to capture the free surface. The finite difference method on a staggered grid is adopted to solve the governing equations, and a specially designed algorithm is used to handle the coupling of velocity and pressure. The subgrid model is used for turbulence closure, and the effect of vegetation is simulated by adding the drag and inertia forces of vegetation into the flow momentum equations. The model has been tested by computing propagation of regular and random waves in vegetated channels, solitary wave runup over a vertical wall and on a sloping beach with and without effects of vegetation, as well as data collected from the experiments carried out as part of this project. The model reasonably well reproduces the experimental observations and demonstrates the wave energy dissipation and wave runup reduction by vegetation.

6.3.1 Mathematical Formulations

The governing equations used in this study are the vertical 2-D Reynolds-averaged continuity and Navier-Stokes (RANS) equations describing the conservation of mass and momentum. The momentum equations include additional source terms representing the spatially averaged resistance effects due to vegetation. The continuity and momentum equations in the Cartesian coordinate system are written in tensor form as

$$\frac{\partial u_i}{\partial x_i} = 0 \tag{6.36}$$

$$\frac{\partial u_i}{\partial t} + u_j \frac{\partial u_i}{\partial x_j} = g_i - \frac{1}{\rho}\frac{\partial p}{\partial x_i} + \frac{1}{\rho}\frac{\partial \tau_{ij}}{\partial x_j} + \frac{1}{\rho} f_i \tag{6.37}$$

where x_i is the coordinate in the ith direction, with i=1 for the longitudinal (x) direction and 2 for the vertical (y) direction (Fig. 6.30); u_i is the flow velocity in the ith direction (with u and v for velocity components in x- and y-directions, respectively); p is the pressure; g_i is the gravitational acceleration in the ith direction; ρ is the density of flow; f_i is the force experienced by the flow due to vegetation per unit volume; and τ_{ij} is the stress due to viscosity and turbulence, determined by

$$\tau_{ij} = \rho(\nu + \nu_t)\left(\frac{\partial u_i}{\partial x_j} + \frac{\partial u_j}{\partial x_i}\right) \tag{6.38}$$

where ν is the kinematic viscosity, and ν_t is the turbulent eddy viscosity. Using the Smagorinsky sub-grid scale (SGS) model (Breuer et al. 2003), the eddy viscosity is given by

$$\nu_t = (C_s \Delta)^2 \sqrt{2 S_{ij} S_{ij}} \tag{6.39}$$

where C_s is a coefficient between 0.1-0.15, Δ is a length scale equal to $(\Delta_1\Delta_2)^{1/2}$ with Δ_i being the grid spacing in the ith direction, and S_{ij} is the rate of strain $S_{ij} = \left(\partial u_i/\partial x_j + \partial u_j/\partial x_i\right)/2$.

Consider a group of vegetation elements conceptualized as cylinders, as shown in Fig. 6.2. The vegetation elements experience the drag force due to the viscous effect and pressure gradient and the inertia force due to the fluid acceleration around the stems. The resultant force on vegetation stems per volume (per unit depth per unit horizontal bed area) is given by $f_i = f_{Di} + f_{Ii}$, with the inertia force, f_{Ii}, is expressed as

$$f_{Ii} = \rho C_M N_v a_{tv} \frac{\partial u_i}{\partial t} \tag{6.40}$$

where a_v is the horizontal coverage area (or volume per unit height) of the stem. C_M and N_v are defined in Eq. (6.4). For a cylindrical stem, $a_{tv}=\pi(D_v)^2/4$, with D_v being the diameter of the stem.

The drag force, f_{Di}, has been evaluated in several vertical 2-D and 3-D models (Li and Yan 2007) as below:

$$f_{Di} = \frac{1}{2}\rho C'_{D(i)} N_v b_v u_i \sqrt{u_j u_j} \tag{6.41}$$

where b_v is the projection width (or area per unit height) of the vegetation stem. For a cylindrical stem, b_v is the diameter, D_v, of the stem. Note that subscript j in Eq. (6.41) follows the Einstein summation convention, but i does not.

The drag coefficient $C'_{D(i)}$ in Eq. (6.41) is treated to be isotropic in those models mentioned above, i.e. given the same value in the horizontal and vertical directions. However, this is a very crude assumption. Because the vegetation elements usually stand vertically, the resistance force in the horizontal direction is composed of form drag (pressure

gradient force) and skin friction, whereas the resistance force in the vertical direction is due to only skin friction. In the case of high Reynolds number, the form drag is dominant, so that the horizontal resistance is larger than the vertical resistance. Therefore, the drag coefficient $C'_{D(i)}$ should be anisotropic and have different values for horizontal and vertical directions. Nevertheless, because no measurement data are available to quantify such anisotropic feature, we still use the same value, denoted as C'_D, for the drag coefficient in horizontal and vertical directions in this study.

An alternative approach for the vegetation drag force is to consider only the horizontal component and ignore the vertical component, considering that the horizontal component might be much larger than the vertical one. In a 2-D vertical model, the horizontal drag force is determined as follows:

$$f_{Dx} = \frac{1}{2}\rho C_D N_v b_v u|u| \tag{6.42}$$

where u is the longitudinal component of velocity.

It has been found through the model test in Section 6.3.4 that the drag coefficient C_D in Eq. (6.42) has the same magnitude as that in Eq. (6.4) of the depth-averaged model, whereas C'_D is about 0.4-0.5 times C_D in Eq. (6.4) for the cases tested. The results from these two models will be compared in Section 6.3.4.

In order to capture the water surface elevation, a function F is firstly introduced by Hirt and Nichols (1981) that indicates the fraction of a mesh cell. F is governed by

$$\frac{\partial F}{\partial t} + \frac{\partial (u_i F)}{\partial x_i} = 0 \tag{6.43}$$

If F=1, the cell is full of fluid. If F=0, the cell is empty. If F is between 0 and 1, the cell must be a surface cell, as shown in Fig. 6.30(a).

The boundary conditions include the wave maker boundary at the inlet or seaside boundary, the Sommerfeld radiation conditions (Orlanski 1976) at the outlet boundary, and a sponge layer in the front of the outlet boundary to absorb the wave energy (Larsen and Daney 1983).

6.3.2 Numerical Solution Methods

The present vertical model is based on the existing model called SOLA-VOF (Hirt and Nichols, 1981). The governing equations are solved using a finite difference method on the staggered grid system. The momentum equations are discretized using an explicit scheme, with a hybrid upwind/central difference scheme for the convection terms and the second-order difference scheme for the diffusion terms. The coupling of velocity and pressure is achieved through an iteration procedure to make sure that the velocity field satisfies the continuity equation.

6.3.2.1 Discretization of continuity and momentum equations

The staggered grid system used is shown in Fig. 6.30(b). The velocities u and v are stored at cell faces, while the pressure p and other scalar variables are stored at cell centers.

The continuity equation is discretized as

$$D=\left(u_{i+1/2,j}^{n+1}-u_{i-1/2,j}^{n+1}\right)/\Delta x_i+\left(v_{i,j+1/2}^{n+1}-v_{i,j-1/2}^{n+1}\right)/\Delta y_j=0 \tag{6.44}$$

The momentum equations are discretized using an explicit scheme as (Torrey 1985)

$$u_{i+1/2,j}^{n+1}=u_{i+1/2,j}^{n}+\Delta t\left[g_x-\frac{\left(p_{i+1,j}^{n+1}-p_{i,j}^{n+1}\right)}{\rho\Delta x_{i+1/2}}-FUX_{i+1/2,j}-FUY_{i+1/2,j}+DIFFX_{i+1/2,j}\right] \tag{6.45}$$

$$v_{i,j+1/2}^{n+1}=v_{i,j+1/2}^{n}+\Delta t\left[g_y-\frac{\left(p_{i,j+1}^{n+1}-p_{i,j}^{n+1}\right)}{\rho\Delta y_{j+1/2}}-FVX_{i,j+1.2}-FVY_{i,j+1/2}+DIFFY_{i,j+1/2}\right] \tag{6.46}$$

where *FUX*, *FUY*, *FVX* and *FVY* are the convection terms, and *DIFFX* and *DIFFY* are the diffusion terms. The diffusion terms are discretized using the centered difference scheme with second-order accuracy, whereas the convection terms are discretized using a hybrid upwind/center difference scheme. The discretized convection terms in *x*-momentum equation are written as

$$FUX_{i+1/2,j}=u_{i+1/2,j}\left\{\Delta x_i\left(\frac{\partial u}{\partial x}\right)_{i+1}+\Delta x_{i+1}\left(\frac{\partial u}{\partial x}\right)_i+\alpha\cdot\mathrm{sign}(u)\left[\Delta x_{i+1}\left(\frac{\partial u}{\partial x}\right)_i-\Delta x_i\left(\frac{\partial u}{\partial x}\right)_{i+1}\right]\right\} \tag{6.47}$$
$$\Big/\left[\Delta x_i+\Delta x_{i+1}+\alpha\cdot\mathrm{sign}(u)\cdot\left(\Delta x_{i+1}-\Delta x_i\right)\right]$$

$$FUY_{i+1/2,j}=v_{i+1/2,j}\left\{\Delta y_j\left(\frac{\partial u}{\partial y}\right)_{i,j+1}+\Delta y_{j+1}\left(\frac{\partial u}{\partial y}\right)_{i,j}+\alpha\cdot\mathrm{sign}(v)\left[\Delta y_{j+1}\left(\frac{\partial u}{\partial y}\right)_{i,j}-\Delta y_j\left(\frac{\partial u}{\partial y}\right)_{i,j+1}\right]\right\} \tag{6.48}$$
$$\Big/\left[\Delta y_j+\Delta y_{j+1}+\alpha\cdot\mathrm{sign}(v)\cdot\left(\Delta y_{j+1}-\Delta y_j\right)\right]$$

where α is a weighting factor. Eqs. (6.47) and (6.48) represent the hybrid scheme combining the first-order upwind difference scheme and the second-order central difference scheme with the weighting factor α. The scheme reduces to the upwind difference scheme when α =1, and to the central difference scheme when α =0. Generally, α is between 0.2 and 0.5. The hybrid scheme takes advantages of both schemes, i.e., the upwind scheme is stable but usually introduces significant numerical diffusion and the central difference scheme is more accurate but generates numerical instability when the Peclet number is larger than 2.

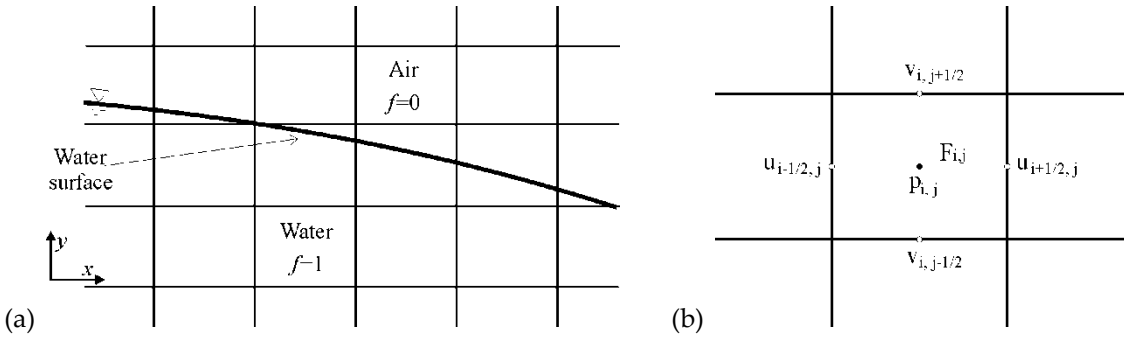

Fig. 6.30. (a) Volume-of-fluid function; and (b) staggered grid system

6.3.2.2 **Coupling of pressure and velocity**

Because the velocities appear in Eq. (6.44) are determined using Eqs. (6.45) and (6.46) which include the pressure of n+1 time level, an iteration procedure is required to solve the continuity and momentum equations together to achieve the coupling of pressure and velocity. The provisional velocity field predicted using Eqs. (6.45) and (6.46) with the most updated values of pressure p that are available does not fully satisfy the continuity equation, and the deviation is found as the divergence of the provisional velocity field. In order to satisfy the continuity equation, i.e. D = 0, the following pressure correction is imposed:

$$\Delta p = -D/(\partial D/\partial p) \tag{6.49}$$

where D is evaluated using Eq. (6.44) at each cell containing fluid, and the derivative is with respect to $p_{i,j}$. The cell pressure is then updated as

$$p_{i,j}^{n+1} + \Delta p \Rightarrow p_{i,j}^{n+1} \tag{6.50}$$

and the velocities are corrected as

$$\begin{aligned}
u_{i+1/2,j}^{n+1} + \frac{\Delta t}{\rho}\frac{\Delta p}{\Delta x_{i+1/2}} &\Rightarrow u_{i+1/2,j}^{n+1} \\
u_{i-1/2,j}^{n+1} - \frac{\Delta t}{\rho}\frac{\Delta p}{\Delta x_{i-1/2}} &\Rightarrow u_{i-1/2,j}^{n+1} \\
v_{i,j+1/2}^{n+1} + \frac{\Delta t}{\rho}\frac{\Delta p}{\Delta y_{j+1/2}} &\Rightarrow v_{i,j+1/2}^{n+1} \\
v_{i,j-1/2}^{n+1} - \frac{\Delta t}{\rho}\frac{\Delta p}{\Delta y_{j-1/2}} &\Rightarrow v_{i,j-1/2}^{n+1}
\end{aligned} \tag{6.51}$$

A similar procedure is used in cells containing a free surface, except that the D used in Eq. (6.49) is not determined using Eq. (6.44) but a relation that leads to the proper free surface boundary condition when driven to zero by the iteration (Hirt and Nichols 1981).

The above iteration procedure is continued until the divergence D is below a small tolerance. In some cases, convergence of this iteration can be accelerated by the successive over-relaxation (SOR). The relaxation coefficient factor of about 1.7 is often used.

6.3.2.3 **Approximation of volume-of-fluid function**

The donor-acceptor method developed by Hirt and Nichols (1981) can be used to discretize Eq. (6.43) and capture the free surface. Eq. (6.43) is discretized as

$$F_{i,j}^{n+1} = F_{i,j} - \Delta(Fu)\Delta t/\Delta x - \Delta(Fv)\Delta t/\Delta y \tag{6.52}$$

where the convection term is determined as

$$\Delta(Fu)\Delta t = \min\left\{F_{AD}|V_x| + F_f, F_D\Delta x_D\right\} \tag{6.53}$$

with $F_f = \max\left\{(1-F_{AD})|V_x| - (1-F_D)\Delta x_D, 0\right\}$ and $|V_x| = |u\Delta t|$. A and D are acceptor and donor cells in Eqs. (6.52) and (6.53), and AD denotes the value F at the cell upstream of the

donor cell. Once these are known, the fluid fluxes of the cell can be calculated geometrically. More details of free surface capturing used in the present model can be found in Hirt and Nichols (1981).

6.3.3 Model Validations Using Data Collected from the Literature

6.3.3.1 Regular wave propagation in vegetated channel

The developed vertical 2-D model was tested against the experiment data of Asano et al. (1993) in the case of regular wave propagation in a vegetated channel. The experiments were conducted in a wave flume of 27 m in length, 0.5 m in width, and 0.7 m in height. Vegetation was simulated by flexible polypropylene strips with a specific gravity of 0.9, length of 0.25 m, width of 0.052 m, and thickness of 0.3 mm. The vegetation zone was 8 m long. Two experimental runs were simulated using the developed model: (a) H = 0.113 m, T = 1.25 s, h = 0.52 m and N_v = 1,110 units/m^2; and (b) H = 0.086 m, T = 2 s, h = 0.45 m and N_v = 1,490 units/m^2. The numerical model was set up to replicate the experimental conditions. The computational domain was 14 m long. The grid spacing was 0.05 and 0.02 m in x and y directions, respectively, and the time step was 0.005 s. The waves were finite amplitude waves specified by the second-order Stokes theory. Because of flexible model vegetation, the drag coefficient was set as 0.225 and 0.09 for the two cases. The drag force was determined using Eq. (6.42). Fig. 6.31 shows the comparison of calculated and measured wave heights over the vegetation zone. The calculated wave height was determined as the difference between the maximum and minimum water levels at each point. It can be seen that the computed results agree well with the measured data. The model provided a reasonable estimate for the amount of wave height attenuation by vegetation.

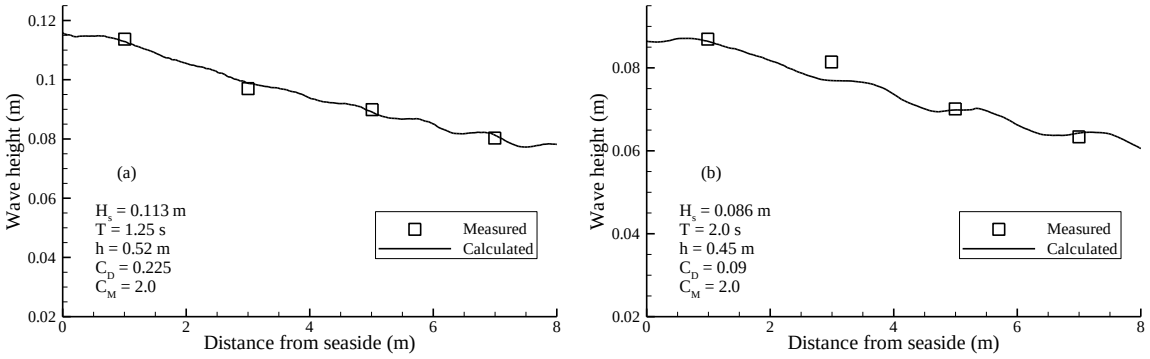

Fig. 6.31. Calculated and measured regular wave heights in a vegetated channel

6.3.3.2 Random wave propagation in vegetated channel

The numerical solution for random waves was compared with the experimental results for an artificial kelp field provided by Dubi and Torum (1997). The artificial kelp models were L. hyperborea with a plant area per unit height of b_v = 0.025 m and a height of 0.2 m. The vegetation field, located at the center of the flume, had a total length of 9.3 m. The number of uniformly distributed plants per unit horizontal area was N_v = 1,200 units/m^2. Two experimental runs (IR5WD63 and IR7WD68) were used for validating the present

model. The water depth was 0.6 m for both runs, and the other parameters are described in Fig. 6.32. The input irregular waves had the JONSWAP (Joint North Sea Wave Project) spectrum with a shape parameter of 3.3. Fig. 6.32 compares the computed results and measured data for root-mean-square wave height along the channel. Actually the drag coefficients depend on the flow conditions and plant type, especially flexible vegetation, and here they were set as constant representing average values (Mendez and Losada 2004). The drag force was determined using Eq. (6.42), with C_D equal to 0.28 and 0.18 for the two cases. The agreement is pretty good and shows that the model can correctly predict the root-mean-square height of random waves with vegetation effect.

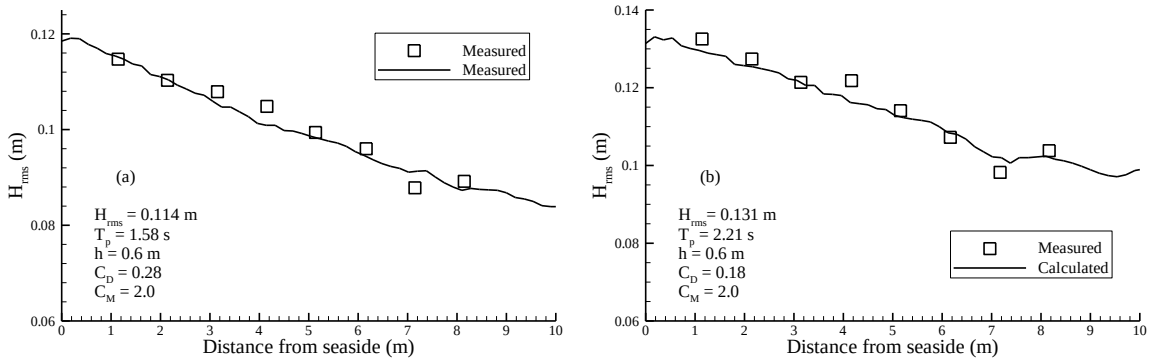

Fig. 6.32. Calculated and measured random wave heights in a vegetated channel

6.3.3.3 **Solitary wave runup over vertical wall**

The developed vertical 2-D model was used to simulate the solitary wave propagation through vegetated and non-vegetated channels and runup over a vertical wall at the downstream end. The experiments reported by Camfield and Street (1968) investigated this without vegetation effect in the channel. The still water depth was 0.35 m, and the wave height changed in different experimental runs. The 2-D model was tested using the experimental cases without vegetation and then applied to predict the wave runup with vegetation in the same channel. The computational domain was 8 m long, the grid spacing was 0.04 and 0.01 m in x and y directions, respectively, and the time step was 0.002 s. The vegetation elements used were rigid and had a diameter of 0.01 m and a height of 0.3 m. The vegetation zone was located from 5 to 7 m. The vegetation density was 1,000 units/m^2. The drag and inertia coefficients of vegetation were set as 1.0 and 2.0, respectively. The drag force was determined using Eq. (6.42).

Fig. 6.33 shows the computed flow pattern and water surface elevation at different elapsed times in the case of wave height of 0.14 m and without vegetation in the channel. The solitary wave traveled from the left side, touched the vertical wall at 4.4 s, and ran up against the vertical wall; it reached the maximum runup at 4.77 s, and then fell down from the wall and reflected back to the channel. The solitary wave runup evolution on the vertical wall was reasonably calculated by the developed model. Fig. 6.34 shows that the calculated wave runup results agree well with experiment data in cases without vegetation effect. Here, R is the runup of a solitary wave on a vertical wall, h is the still water depth, and H is the solitary wave height. Fig. 6.34 also shows the relation of R/h and H/h in the case with

vegetation in the channel. One can see that the presence of vegetation causes energy dissipation and decreases the wave runup height on the vertical wall.

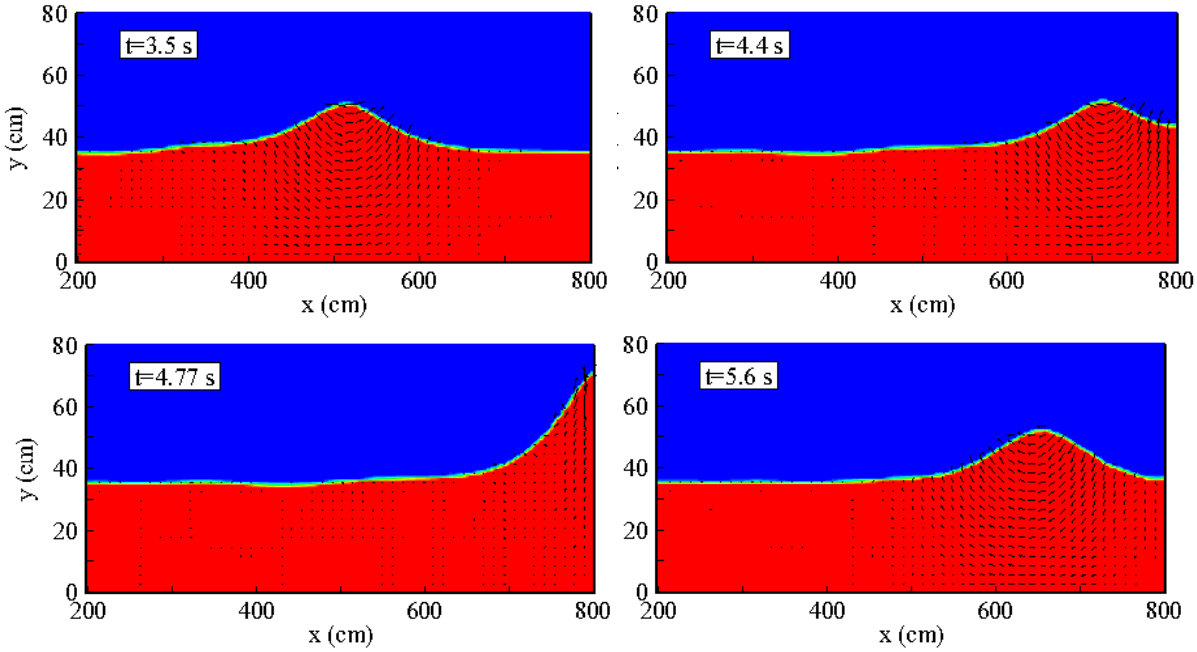

Fig. 6.33. Calculated flow pattern in the case of solitary wave runup over a vertical wall (Red color indicates zone of *F*=1, fully occupied by water, and blue color for *F*=0, fully empty)

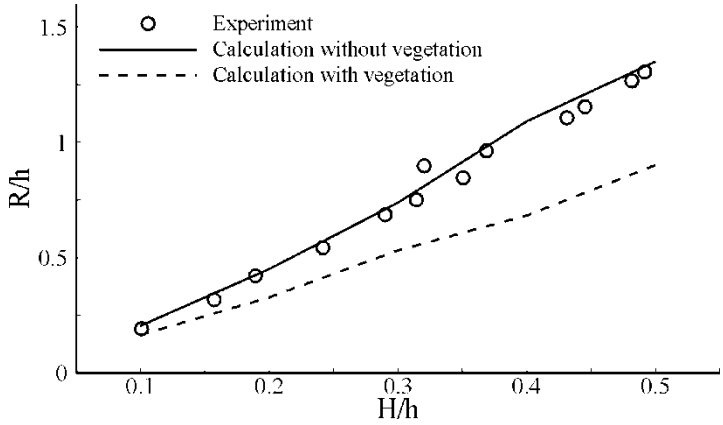

Fig. 6.34. Solitary wave runup over a vertical wall with and without vegetation effects

6.3.3.4 Solitary wave runup on vegetated and non-vegetated sloping beaches

The 2-D model was tested by simulating the solitary wave runup over vegetated and non-vegetated beaches. Firstly, the experiment data of breaking solitary wave runup of Synolakis (1986) was used to validate the model's ability to capture wave profile in the case of wave breaking. The beach had a slope of 1:20. In the case selected, the still water depth was 0.21 m, and the ratio of wave height to still water depth, H/h, was 0.28. The

computational domain was 14 m long and 0.5 m high. The slope started at 4 m from the seaside boundary. A uniform grid was used, with grid spacing of 0.025 and 0.005 m in x and y directions, respectively. The time step was 0.004 s. The calculated and measured water surface elevations at different elapsed times are shown in Fig. 6.35, in which the water surface elevation and the x-coordinate are normalized by the still water depth and the time is normalized as $t^* = t\sqrt{g/h}$. The wave shape became asymmetrical due to the effect of the sloping beach. Its front face became steeper and steeper, and ultimately broke. The wave height reached a maximum value at the breaking point and decreased after the wave broke. The breaking wave continued to run up the slope until it reached the maximum runup height. This demonstrates that the developed model can handle the breaking wave reasonably well.

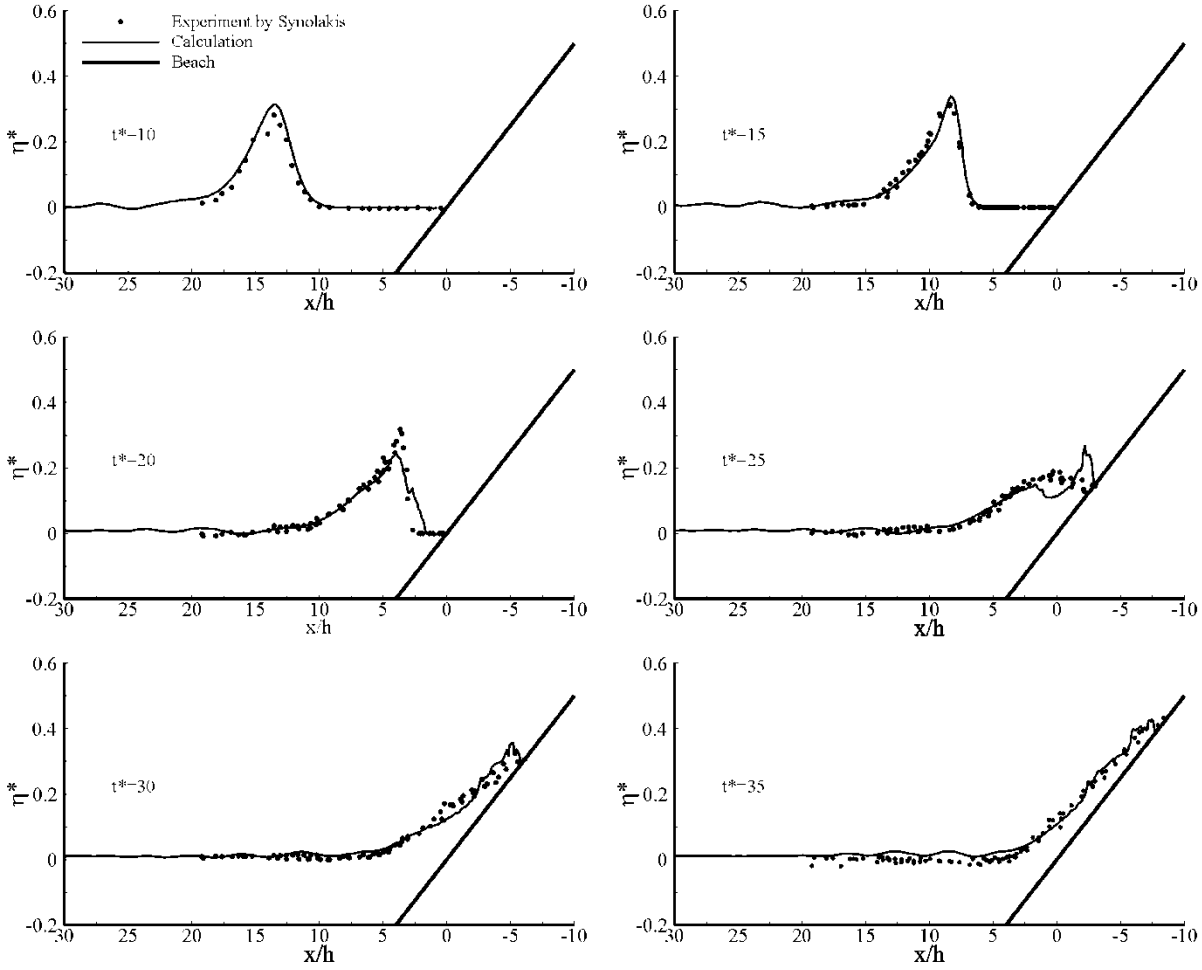

Fig. 6.35. Measured and calculated breaking solitary wave runup over a sloping beach

To investigate the effect of vegetation on wave runup, the vegetation zone was set up over the same beach, starting at 6.2 m from the seaside boundary with a length of 2.0 m. The vegetation elements were rigid, with a height of 0.2 m, a vegetation diameter of 0.01m, and a uniform vegetation density of 1,000 units/m^2. The drag and inertia coefficients were set as 1.0 and 2.0, respectively. The drag force was determined using Eq. (6.42). Fig. 6.36 compares

the calculated water surface profiles along the beach with and without vegetation for the same solitary wave. One can see that vegetation delays the wave propagation and reduce the wave runup.

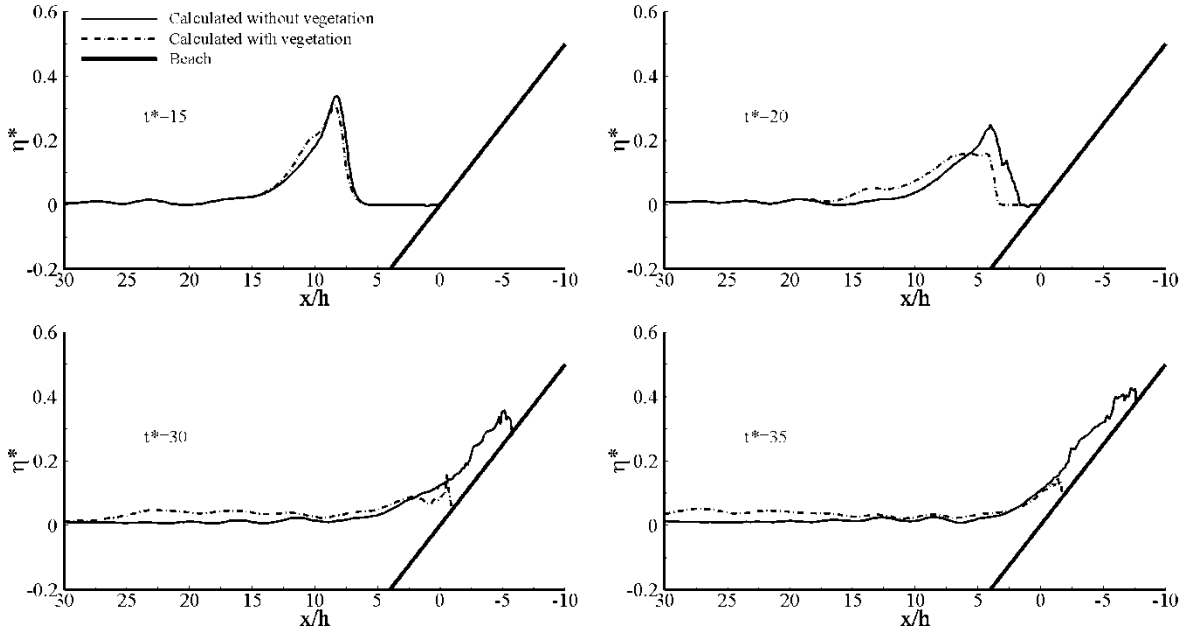

Fig. 6.36. Computed breaking solitary wave runup over a sloping beach with and without vegetation

6.3.3.5 **Random wave over vegetated sloping beach**

The laboratory data of Lovas (2000) were used to validate the vertical 2-D model for the transformation of random waves including dissipation by vegetation and breaking on a sloping channel. The walls and bottom of the flume were made of smooth concrete, and the experiments were carried out with a sandy 1:30 slope to simulate a surf zone. The detailed bed elevation and vegetation arrangement are shown in Fig. 6.37. The vegetation field, located at the center of the flume, had a total width of 7.27 m (Lovas 2000, Mendez and Losada 2004). The runs selected had a still water depth of 0.77 m, wave peak periods of 3.5 s, significant wave heights of 0.125 m and 0.2 m, and a vegetation density of 1,200 units/m^2. The drag force was determined using Eq. (6.42), with C_D being set as 0.2. The input for irregular waves was the JONSWAP spectrum. The comparison of calculated and measured root-mean-square wave height without and with vegetation is given in Fig.6.38. The computed results agree well with Lovas' experiment data and show the model can successfully predict the random wave over a sloping beach.

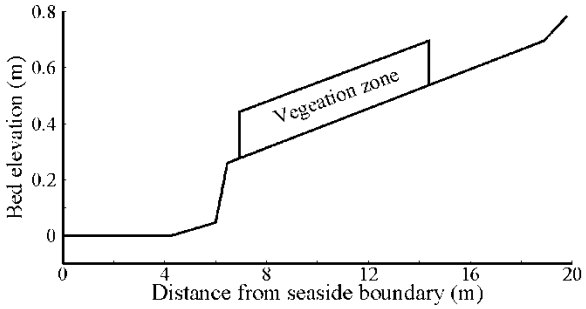

Fig. 6.37. Bed elevation of this experiment

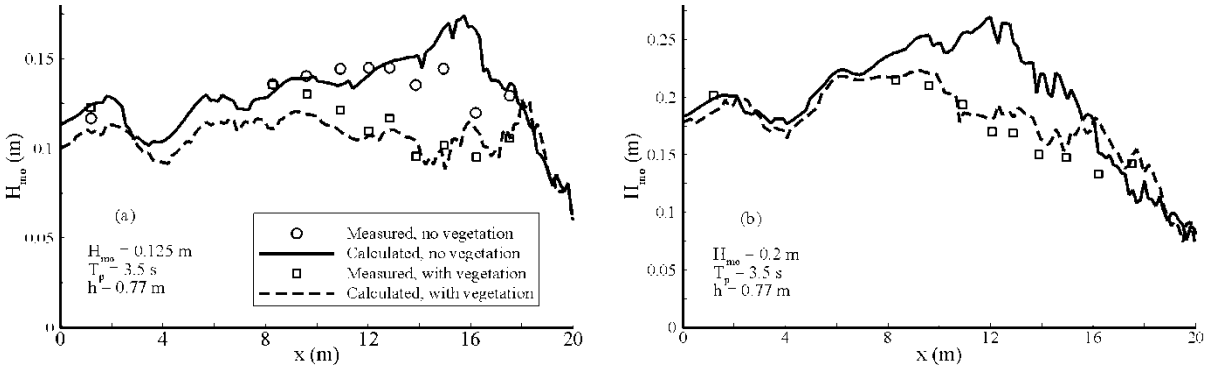

Fig. 6.38. Comparison of calculated and measured root-mean square wave height

6.3.4 Model Validations Using Data Obtained in the Present Project

The developed vertical 2-D flow model was tested using the laboratory experiment data of wave attenuation by vegetation measured in a wave flume at the National Sedimentation Laboratory, Oxford, Mississippi. The schematic experimental setup is shown in Fig. 3.2. The flume was 20.6 m long, 0.5 m wide, and 1.22 m deep. The details of experiment conditions are described in Chapter 3. The vegetation species used include rigid model vegetation made of wooden circular cylinders, flexible model vegetation made of rubber, and two live vegetation species collected from the Louisiana coast: *Spartina alterniflora* (green and dormant) and *Juncus roemerianus* (green). In all the cases the length of the vegetation field was L_V = 3.66 m.

The computational domain was 12 m long and started from 0.5 m seaward of Gage 2 (1 m seasward of the vegetation zone, or x = 10.5 m shown in Fig. 3.2). At the end of the domain, a 3 m long sponge layer was set up to reduce the wave reflection. The computational domain was represented by a uniform mesh with grid spacing Δx = 0.05 m and Δy = 0.02 m. The simulations included 36 experimental cases using 6 vegetation configurations under 4 sets of regular wave conditions and 2 sets of random wave conditions, as shown in Tables 6.4 and 6.5. For the regular waves, each simulation run used wave height and period measured at Gage 2 as the incident wave conditions, and the simulation period was about 20 s. The wave height at each computational grid was determined from the wave crest and trough at the developed stage (at the elapsed time approximately between 15-20 s). For the random waves, the input incident waves consisted

of a wave train of about 100-200 wave periods (about 150 s in total) generated by a random wave generator assuming the JONSWAP (Joint North Sea Wave Project) spectrum and using the root-mean-square wave height and peak wave period measured at Gage 2. The root-mean-square wave height at each computational grid was obtained from the time series of water levels obtained from the model simulation.

Both drag force models in Eqs. (6.41) and (6.42) were used in the simulations. The drag coefficients C_D and C_D' were calibrated by comparing the measured and calculated wave heights at the four measurement gages (Gages 2–5) in or near the vegetation zone. Table 6.4 lists the calibrated C_D and C_D' values, and Figs. 6.39-6.42 show the attenuated wave heights along the vegetated channel for the six vegetation configurations under four sets of regular waves. One can see that the vertical 2-D model reproduced well the experiments when the calibrated values of drag coefficient were used. The numerical simulations show that reflection occurred when the waves reached the vegetation zone. Reflection also occurred at the downstream end of the domain, even though the magnitude of reflective waves was reduced significantly by the sponge layer.

The wave heights computed using the drag force equations (6.41) and (6.42) are close to each other, but different values of drag coefficient should be used. Eq. (6.1) seems provides less reflection in the computed wave height profiles than Eq. (6.42). This may be due to the dissipation in the vertical momentum equation by vegetation friction is considered in Eq. (6.41), but not in Eq. (6.42). As shown in Fig. 6.45 and in Table 6.4, the drag coefficient $\boldsymbol{C'_D}$ in Eq. (6.41) is about 0.45 times the drag coefficient C_D in Eq. (6.42).

As shown in Fig. 6.46 and Table 6.4, the values of drag coefficient C_D used in vertical 2-D model with Eq. (6.42) are close to the estimates obtained using the analytical solution of Mendez and Losada (2004) given in Chapter 3. However, Fig. 6.47 shows the drag coefficient in the 1-D Boussinesq model in Section 6.2 is different from that used in the vertical 2-D model. In most of the cases tested, the values of C_D in 1-D model are larger than those used in the vertical 2-D model. The reason is that the vertical 2-D and Mendez and Losada's analytical model use the local velocity squared to compute the drag force in Eqs. (6.41) and (3.20), whereas the 1-D Boussinesq model uses the depth-averaged velocity squared for the drag force. The calibrated C_D in the depth-averaged model should be larger than that in the vertical 2-D model in order to get the same amount of total drag force and energy dissipation in the vertical line.

Table 6.4. Calibrated C_d values for the vertical VOF-based 2-D model under regular waves

Experiment No.	Wave conditions	Drag coefficient in different models	Rigid model (124363) N_v=350 h_v=0.63 m D_v=9.4 mm	Rigid model (126363) N_v=623 h_v=0.63 m D_v=9.4 mm	Flexible model N_v=350 h_v=0.48 m D_v=9.4 mm	Spartina (Dormant) N_v=545 h_v=0.62 m D_v=5.1 mm	Spartina (Green) N_v=405 h_v=0.59 m D_v=6.5 mm	Juncus (Green) N_v=2,857 h_v=1.03 m D_v=2.4 mm
500610701	h=0.50 m T=0.7 s H_{G2}=0.053 m	C_D in Eq. (3.20)	2.57	2.50	1.37	3.15	9.20	2.62
		C_D in Eq. (6.42)	1.9	1.95	0.75	2.7	9.4	2.4
		C'_D in Eq. (6.41)	0.83	0.85	0.3	1.1	4.0	0.97
501211001	h=0.50 m T=1.0 s H_{G2}=0.10 m	C_D in Eq. (3.20)	2.30	2.34	0.99	2.10	4.37	1.28
		C_D in Eq. (6.42)	2.0	2.05	1.05	2.0	4.25	1.15
		C'_D in Eq. (6.41)	0.95	1.02	0.47	1.0	2.1	0.56
700651201	h=0.70 m T=1.2 s H_{G2}=0.052 m	C_D in Eq. (3.20)	1.82	2.03	3.75		9.86	1.63
		C_D in Eq. (6.42)	1.35	2.3	3.2	2.4	9.5	1.0
		C'_D in Eq. (6.41)	0.6	1.0	1.4	1.1	4.3	0.45
701491101	h=0.70 m T=1.1 s H_{G2}=0.117 m	C_D in Eq. (3.20)	1.71	1.64	2.17	1.59	4.18	0.53
		C_D in Eq. (6.42)	1.8	1.9	2.4	1.3	4.8	0.42
		C'_D in Eq. (6.41)	0.8	0.85	1.2	0.55	2.2	0.19

Note: H_{G2} is the wave height measured at Gage 2 averaged over the runs with six vegetation configurations.

Table 6.5. Calibrated C_d values for the vertical VOF-based 2-D model under random waves

Experiment No.	Wave conditions	Drag coefficient in different models	Rigid model (124363)	Rigid model (126363)	Flexible model	Spartina (Dormant)	Spartina (Green)	Juncus (Green)
			N_v=350 h_v=0.63 m D_v=9.4 mm	N_v=623 h_v=0.63 m D_v=9.4 mm	N_v=350 h_v=0.48 m D_v=9.4 mm	N_v=545 h_v=0.62 m D_v=5.1 mm	N_v=405 h_v=0.59 m D_v=6.5 mm	N_v=2,857 h_v=1.03 m D_v=2.4 mm
R500611205	h=0.50 m T_p=1.2 s $H_{rms,G2}$=0.034 m	C_D in Eq. (3.22)	2.67	2.66	3.73	4.92	8.84	3.65
		C_D in Eq. (6.42)	2	2.6	4	4.5	9.4	3.4
R701091205	h=0.70 m T_p=1.2 s $H_{rms,G2}$=0.063 m	C_D in Eq. (3.22)	2.38	1.92	4.55	3.08	7.24	1.16
		C_D in Eq. (6.42)	1.8	1.7	2.3	2.1	7.4	0.85

Note: $H_{rms,G2}$ is the root-mean-square wave height measured at Gage 2 averaged over the runs with six vegetation configurations.

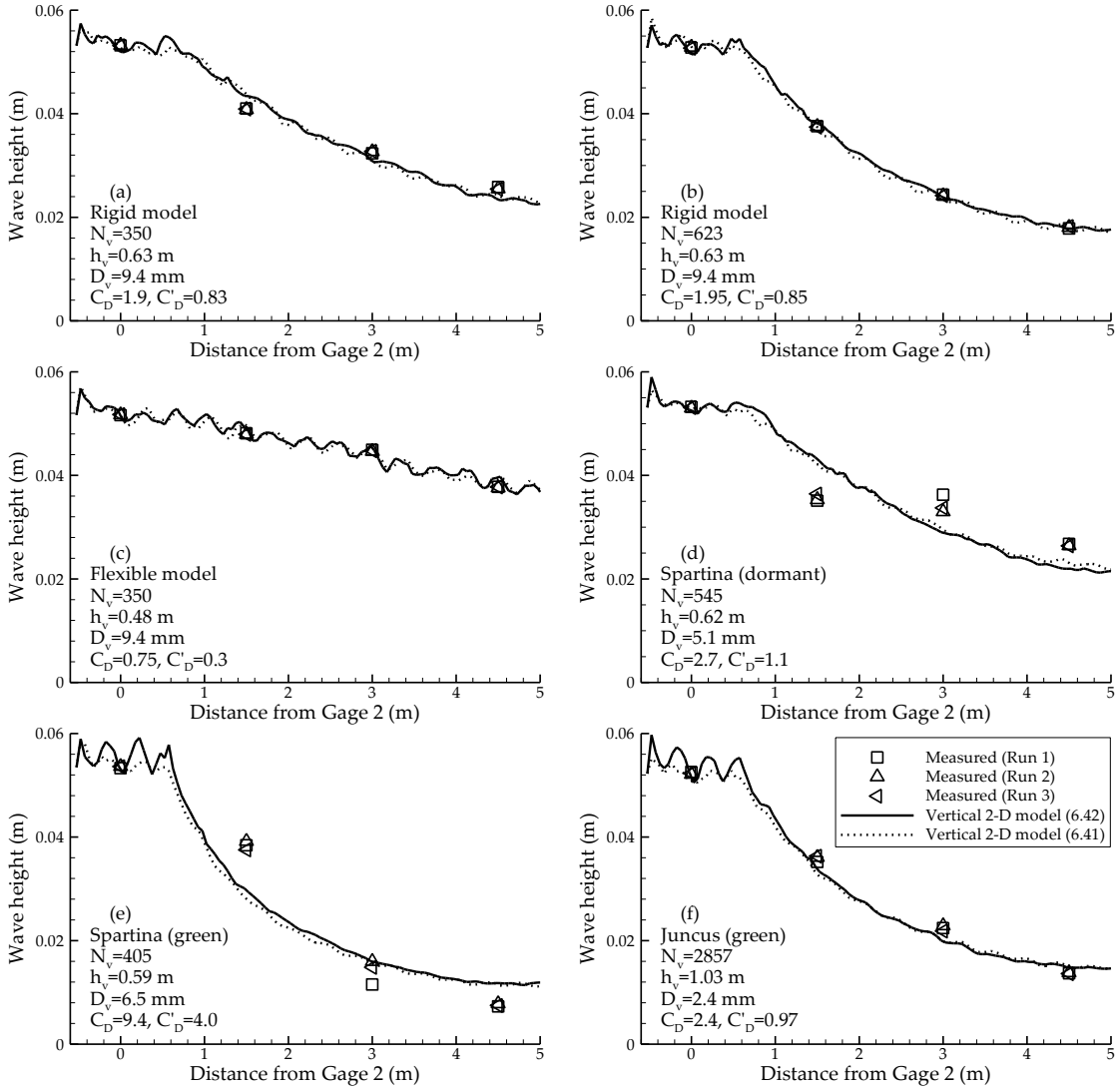

Fig. 6.39. Measured and calculated wave heights for regular wave experiment series No. 500610701 (h = 0.50 m, T = 0.7 s, H_{G2} = 0.053 m; simulations by the vertical 2-D model)

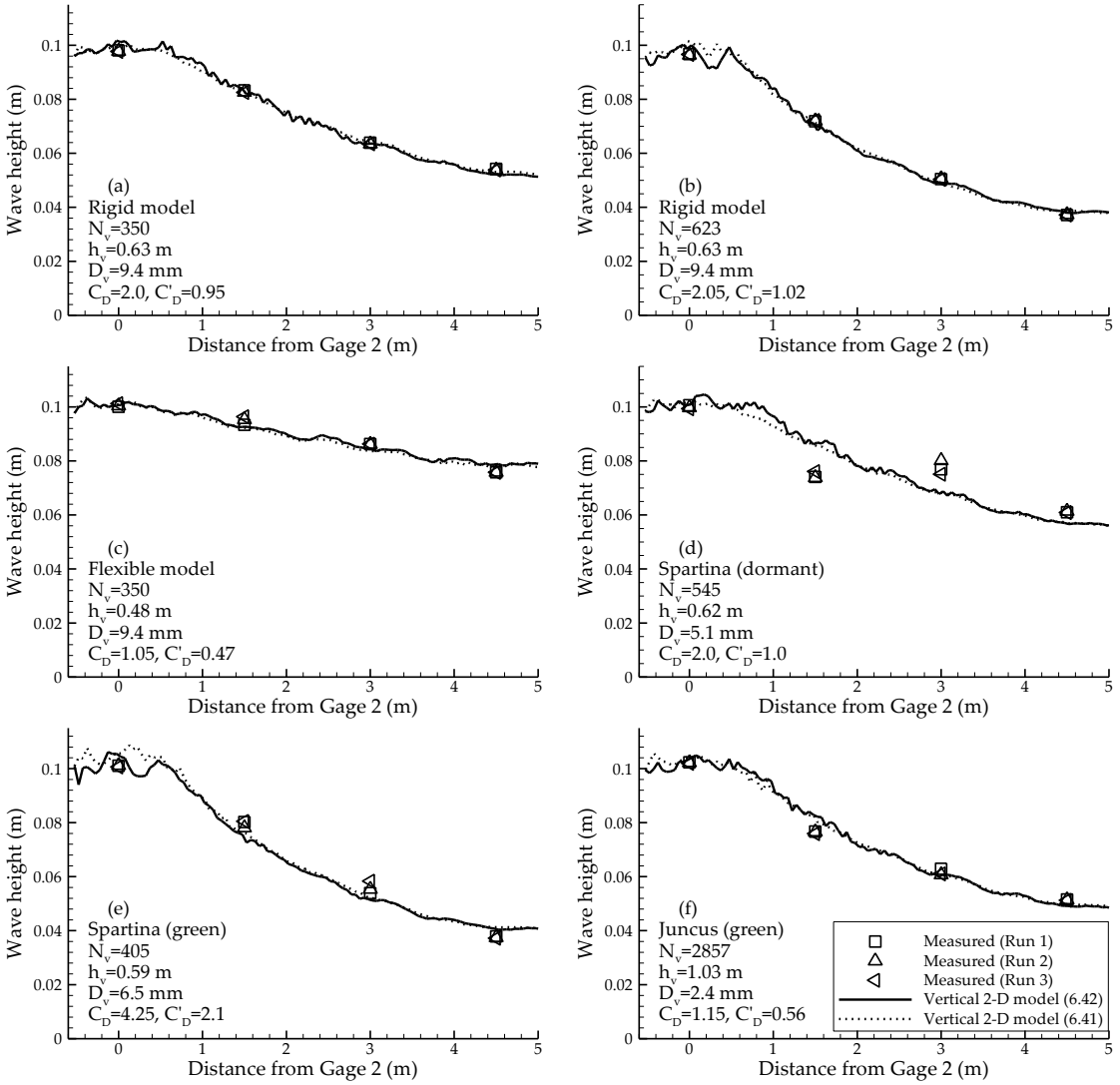

Fig. 6.40. Measured and calculated wave heights for regular wave experiment series No. 501211001 (h = 0.50 m, T = 1.0 s, H_{G2} = 0.10 m; simulations by the vertical 2-D model)

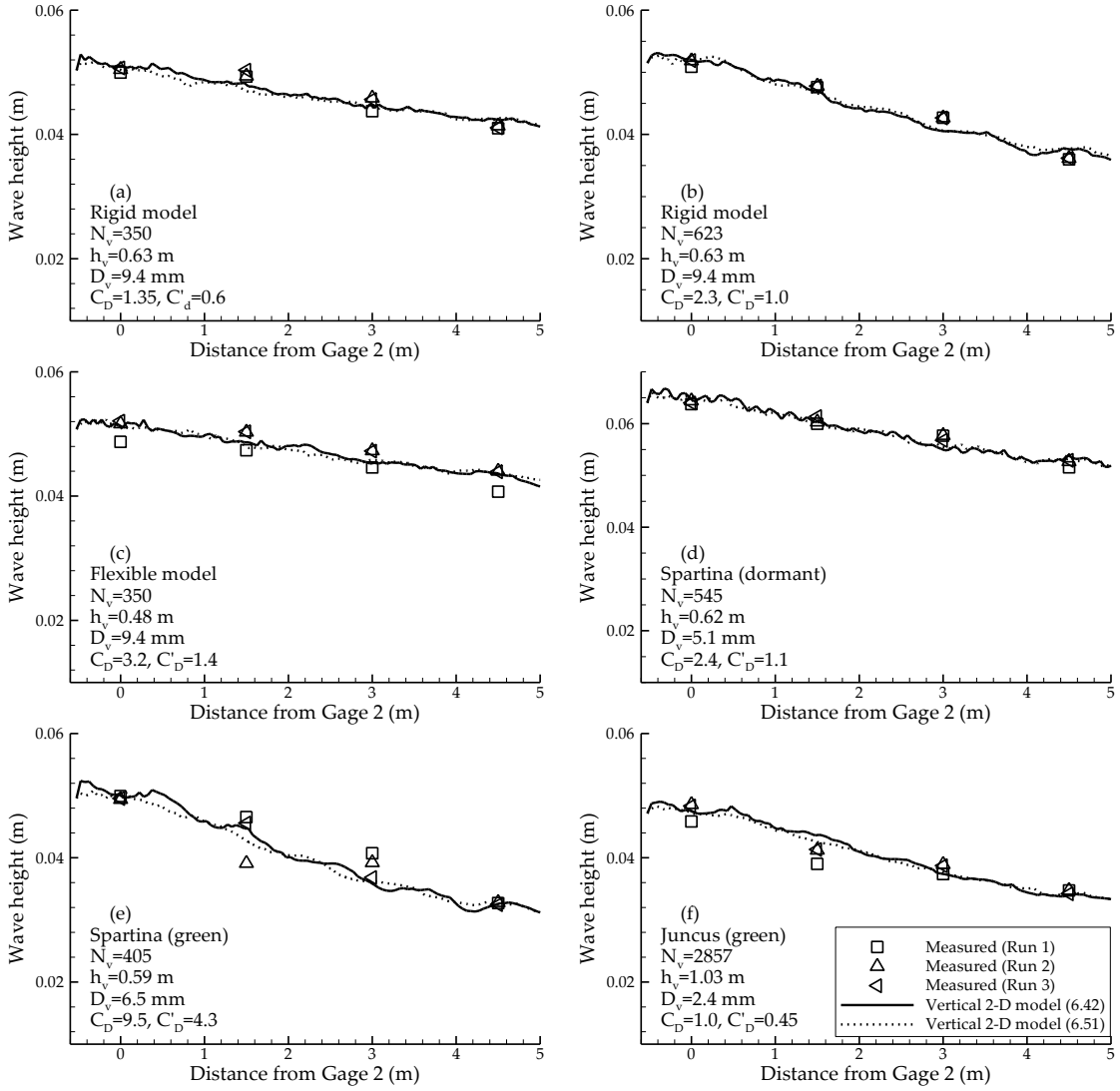

Fig. 6.41. Measured and calculated wave heights for regular wave experiment series No. 700651201 (h = 0.70 m, T = 1.2 s, H_{G2} = 0.052 m; simulations by the vertical 2-D model)

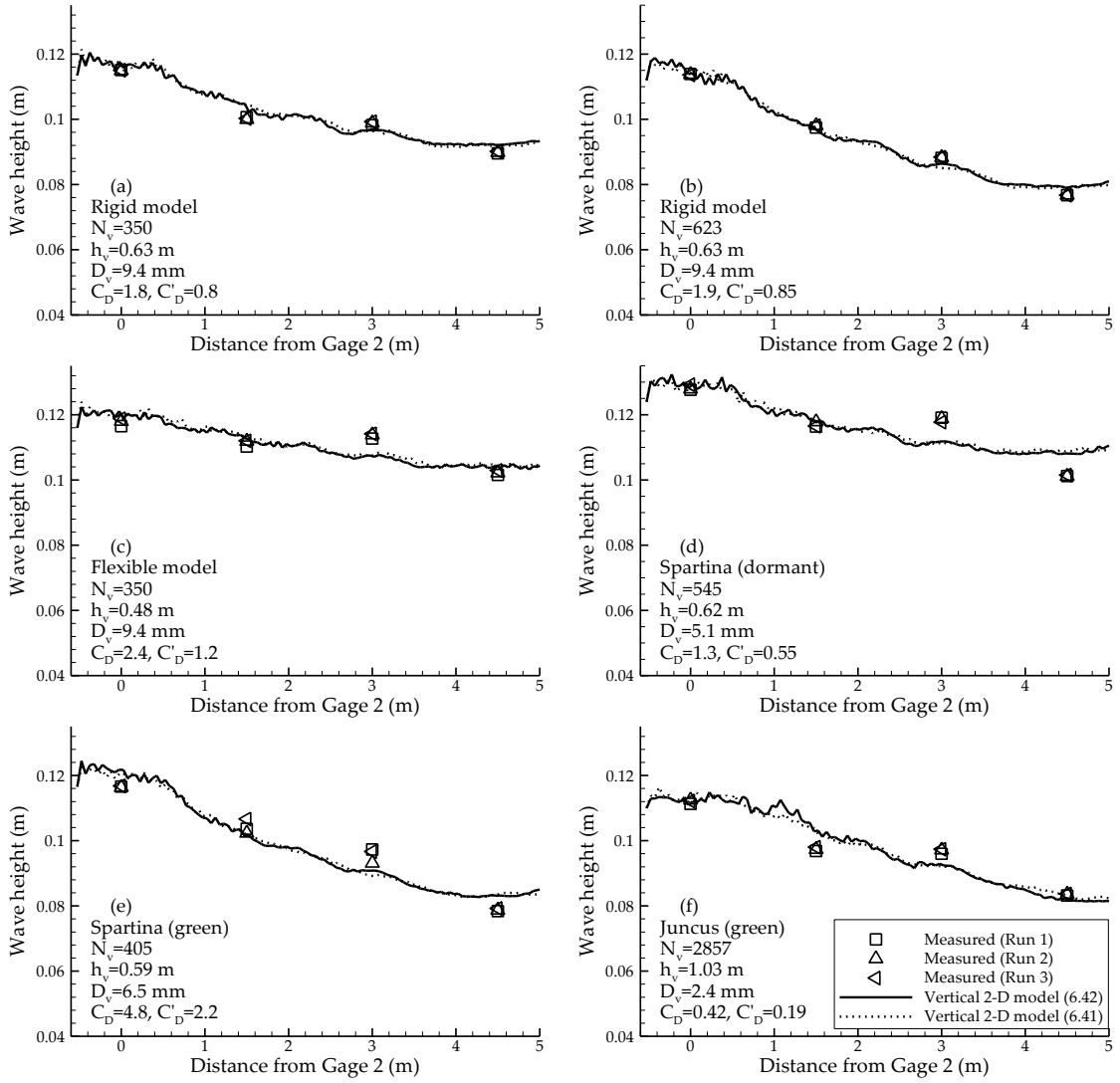

Fig. 6.42. Measured and calculated wave heights for regular wave experiment series No. 701491101 (h = 0.70 m, T = 1.1 s, H_{G2} = 0.117 m; simulations by the vertical 2-D model)

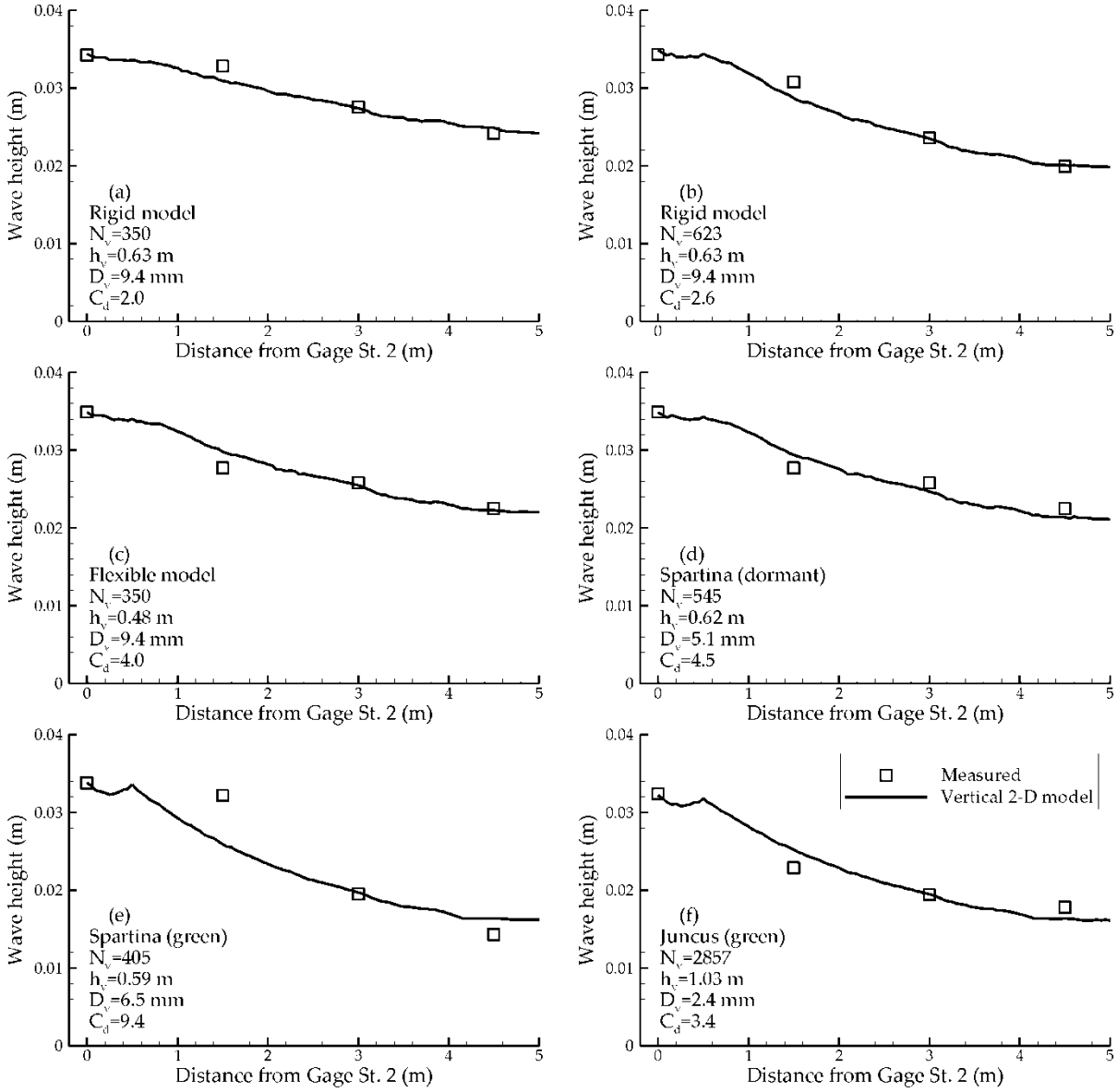

Fig. 6.43. Measured and calculated root-mean-square wave heights for random wave experiment series No. R500611201 (h = 0.50 m, T_p = 1.2 s, $H_{rms,G2}$ = 0.034 m; simulations by the vertical 2-D model)

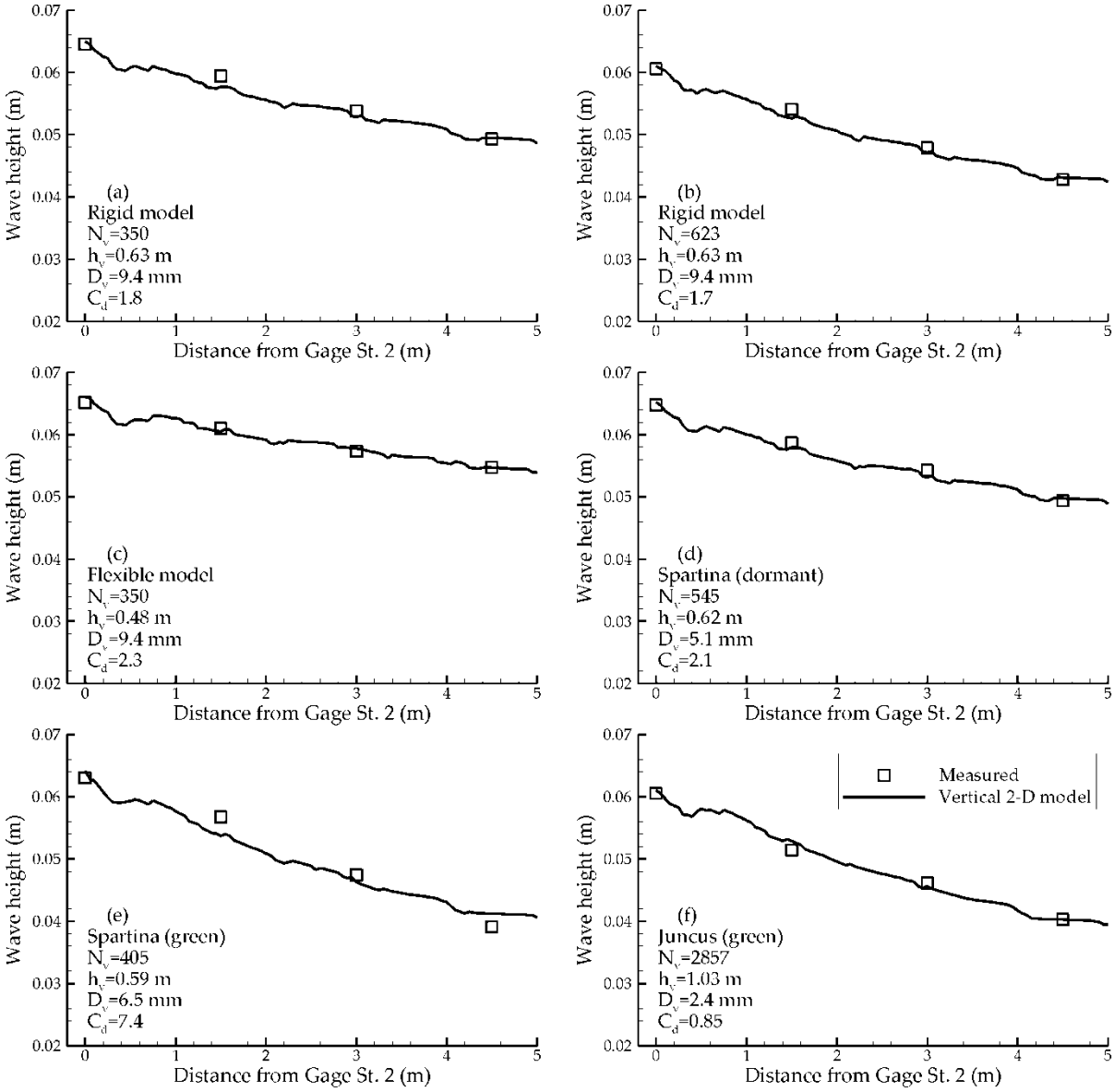

Fig. 6.44. Measured and calculated root-mean-square wave heights for random wave experiment series No. R701091201 (h = 0.70 m, T_p = 1.2 s, $H_{rms,G2}$ = 0.063 m; simulations by the vertical 2-D model)

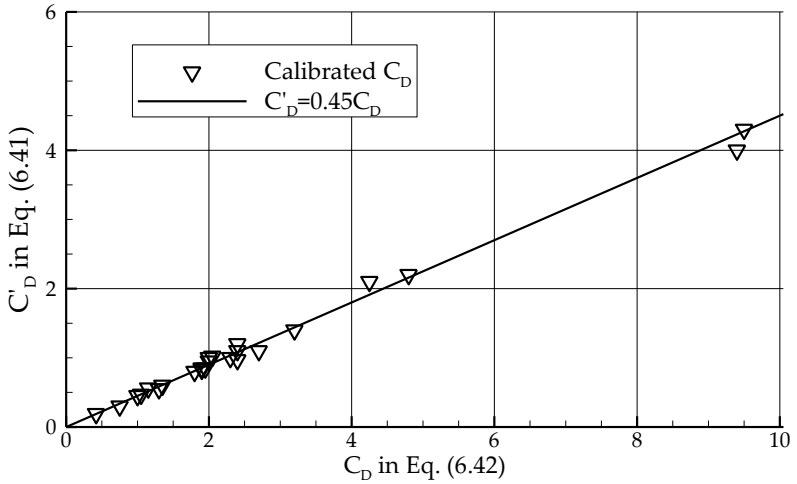

Fig. 6.45. Comparison of drag coefficients in the vertical 2-D models (6.41) and (6.42)

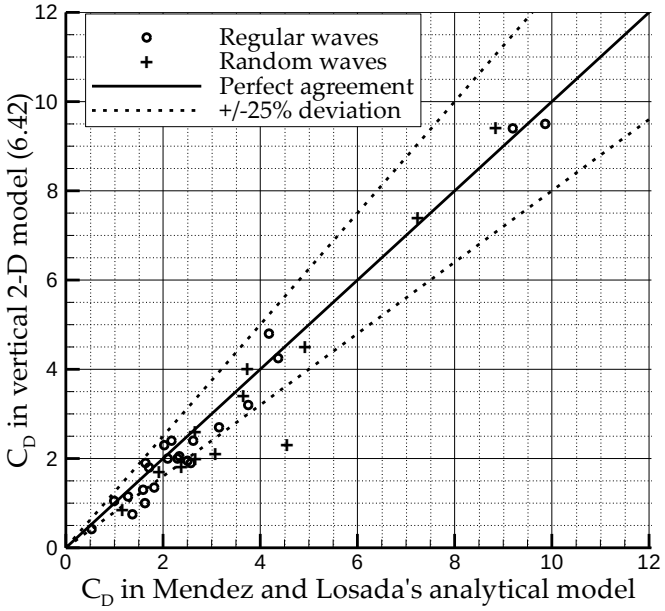

Fig. 6.46. Comparison of drag coefficients in the vertical 2-D model and Mendez and Losada's analytical model

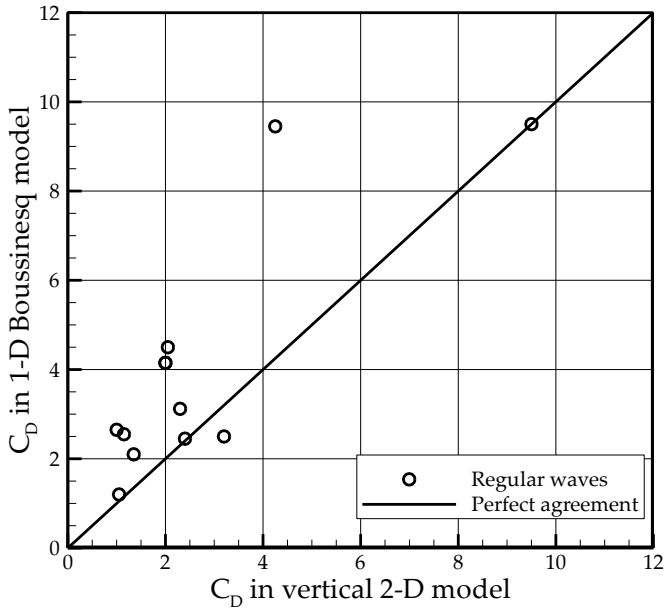

Fig. 6.47. Comparison of drag coefficients in the 1-D Boussinesq model and the vertical 2-D model with drag force model (6.42)

6.4 A Wave-Action Model for Simulating Wave Attenuation by Vegetation

This section describes a wave-action model applied to simulate directional random wave deformation/transformation through vegetation zones. The energy loss due to vegetation resistance is modeled by a vegetation drag model proposed by Dalrymple et al. (1984) and modified by Mendez and Losada (2004) for random wave conditions. The model is based on the directional wave-action balance equation, which is integrated into a coastal process model, CCHE2D-Coast. The wave-action model is capable of computing various random wave processes such as refraction, diffraction, breaking, wave-current interaction, bottom friction, etc. The newly developed capability in CCHE2D-Coast for simulation of wave attenuation effect due to vegetation resistance is validated by computing wave fields in four laboratory experiments in wave flumes with planted artificial vegetation, including two experiments conducted recently in the National Sedimentation Laboratory (NSL) sponsored by this project. Numerical results show that this model is capable of accurately simulating energy dissipations due to vegetation resistance and wave breaking, and reproducing wave parameters, wave energy spectra, and mean water elevations.

6.4.1 Mathematical Formulations

The spectral wave-action model is governed by a multidirectional wave-action balance equation to compute variations of wave-action density in time, space, wave directions, and frequency. The model formulation is based on the parabolic approximation equation including diffraction terms and energy dissipation terms due to wave breaking, bottom friction, and vegetation resistance. The model can simulate unsteady/steady state spectral transformation of directional random waves. The model takes into account the effect of an

ambient horizontal current or wave-current interaction and solves the wave-action balance equation of the wave-action density N as follows:

$$\frac{\partial N}{\partial t}+\nabla\bullet\left(\mathbf{c}N\right)+\frac{\partial(c_\theta N)}{\partial\theta}=\frac{\kappa}{2\sigma}\left[\frac{\partial}{\partial y}\left(CC_g\cos^2\theta\frac{\partial N}{\partial y}\right)-\frac{1}{2}CC_g\cos^2\theta\frac{\partial^2 N}{\partial y^2}\right]-\varepsilon_b N-Q_v+Q \tag{6.54}$$

where $N=N(x,y,\sigma,\theta,t)=E(x,y,\sigma,\theta,t)/\sigma$, E is the spectral wave density representing the wave energy per unit water surface area per frequency interval, σ=wave angular frequency (or intrinsic frequency), t = time, x, y = coordinates in two horizontal directions, $\nabla=(\partial/\partial x, \partial/\partial y)$, the gradient operator in the x-y plane, θ = wave angle relative to the positive x-direction, C, C_g = wave celerity and group velocity, respectively.

The first term on the left-hand side of Eq. (6.54) represents the local rate of change of action density in time. The second term represents propagation of wave action density in a horizontal x-y plane (with propagation velocities **c**). The third term represents depth-induced and current-induced refraction (with propagation velocity c_θ in θ space). The expressions for these propagation speeds are given by the linear wave theory (e.g., Holthuijsen et al. 1989) as

$$\mathbf{c}=C_g\mathbf{i}_\theta+\mathbf{U} \tag{6.55}$$

$$c_\theta=-\frac{1}{k}\frac{\partial\sigma}{\partial h}\frac{\partial h}{\partial n}-\frac{\partial\mathbf{U}}{\partial n}\bullet\mathbf{i}_\theta \tag{6.56}$$

where **U** =depth-averaged velocity vector, k = wave number, $\mathbf{i}_\theta$ = ($cos\theta$, $sin\theta$), a unit vector following the wave direction, h = water depth, n = wave crest direction.

The first term on the right-hand side of Eq. (6.54), introduced by Mase (2001), represents the energy dissipation due to the diffraction effect in the alongshore y-direction, which is implicitly perpendicular to wave direction. κ is an empirical coefficient. Mase (2001) suggested this empirical coefficient has a possible value within a range of 2.0–3.0. To specify an incident wave spectrum in the offshore, the TMA spectrum (Bouws et al. 1985) and the Bretschneider-Mitsuyasu (B-M) spectrum (Mitsuyasu 1970) can be selected in this model. The second term on the right-hand side represents wave energy loss due to wave breaking, where ε_b is a parameter for wave breaking energy dissipation. Similarly, the third term Q_v represents the wave energy loss due to vegetation resistance. The last term Q is source terms of wave energy due to wind forcing, bottom friction loss, nonlinear wave-wave interaction term, etc.

Based on the monochromatic linear wave theory and an assumption of impermeable bottom proposed by Dalrymple et al. (1984), Mendez and Losada (2004) established a relationship between the wave energy loss and vegetation parameters under a condition of random wave incidence. The Reyleigh probability density distribution function (Thornton and Guza 1983) is assumed to model random wave actions. As a result, the source term of the wave energy loss due to vegetation, Q_v, is obtained as follows:

$$Q_v=\frac{1}{\sigma 2\sqrt{\pi}}\rho C_D b_v N_v\left(\frac{kg}{2\sigma}\right)^3\frac{\sinh^3(k\alpha h)+3\sinh(k\alpha h)}{3k\cosh^3(kh)}H_{rms}^3 \tag{6.57}$$

where ρ = water density (kg/m^3), b_v = plant area per unit height of each vegetation stand normal to horizontal velocity (m), N_v = number of vegetation stems per unit horizontal area

(m^{-2}), C_D = drag coefficient of vegetation under random waves, g = gravitational acceleration (m/s^2), α = relative vegetation height, and H_{rms} = root-mean-square wave height (m). Because the random wave energy can be defined as $E = \frac{1}{8}\rho g H_{rms}^2$, the source term can be written as the local linear form of the wave action density, i.e., $Q_v = \varepsilon_v N$. Then the coefficient ε_v can be given as follows:

$$\varepsilon_v = \frac{4}{g\sqrt{\pi}} C_D b_v N_v \left(\frac{kg}{2\sigma}\right)^3 \frac{\sinh^3(k\alpha h) + 3\sinh(k\alpha h)}{3k\cosh^3(kh)} H_{rms} \tag{6.58}$$

According to Takayama et al. (1991), the wave energy dissipation due to wave breaking is calculated by assuming that (1) the probability distribution of breaking wave height can be represented by the Rayleigh distribution (Thornton and Guza 1983); (2) over a computational cell, the local bathymetry can be approximated as shore-parallel contours. Then, the local rate of wave breaking energy dissipation ε_b in a computational cell can be calculated as the time-averaged energy loss over a time that an individual wave travels through a cell from the seaward side to the inland side, i.e.

$$\varepsilon_b = \varepsilon_b' C / \sqrt{\Delta x \Delta y} \tag{6.59}$$

where Δx, Δy = the grid size in x- and y-directions, respectively. Based on the Rayleigh probability distribution of wave energy, Takayama et al. (1991) derived the coefficient ε_b' as follows:

$$\varepsilon_b' = 1 - \frac{1 - \left[1 + \frac{\pi}{4}\left(1.6\frac{H_{bO}}{H_{1/3}}\right)^2\right]\exp\left[-\frac{\pi}{4}\left(1.6\frac{H_{bO}}{H_{1/3}}\right)^2\right]}{1 - \left[1 + \frac{\pi}{4}\left(1.6\frac{H_{bi}}{H_{1/3}}\right)^2\right]\exp\left[-\frac{\pi}{4}\left(1.6\frac{H_{bi}}{H_{1/3}}\right)^2\right]} \tag{6.60}$$

where H_{bo}, H_{bi} = breaking wave heights at the offshore side and the onshore side of a computational cell, respectively, $H_{1/3}$ = the local significant wave height. The breaking wave height is calculated based on the wave breaking criterion proposed by Goda (1970), or the one extended by Sakai et al. (1988), i.e.,

$$H_b = \begin{cases} AL_0\left\{1 - \exp(-1.5\frac{\pi h}{L_0}(1 + 15\beta^{4/3})\right\} C(\varepsilon_d) & \beta \geq 0 \\ AL_0\left\{1 - \exp(-1.5\frac{\pi h}{L_0})\right\} & \beta < 0 \end{cases} \tag{6.61}$$

where H_b = breaking wave height, L_0 = wave length of the wave at the offshore side of the computational cell, A = empirical coefficient (0.12–0.18), β = sea bed slope, and $C(\varepsilon_d)$ is a coefficient given by Sakai et al. (1988):

$$C(\varepsilon_d) = \begin{cases} 0.506 & \varepsilon_d \geq 0.0024 \\ 1.13 - 260\varepsilon_d & 0.0024 > \varepsilon_d \geq 0.0005 \\ 1.0 & \varepsilon_d < 0.0005 \end{cases} \tag{6.62}$$

where $\varepsilon_d = |\mathbf{U}| L_0 \beta^{1/4} / (g^2 T^3)$, with T =the significant wave period for random waves.

This wave-action model can also take into account the wave-current interaction. Under the circumstance of co-existence of wave and current, wave frequency is changed with water depth and velocities. According to the small-amplitude wave theory, the resulting wave number can be calculated by the dispersion equation with the Doppler frequency shift. For the description on the wave-current interaction, one may refer to Ding and Wang (2010). The source term Q in Eq. (6.54) includes the wave energy dissipation due to bottom friction and the wave energy input induced by winds. The energy loss by bottom friction is calculated by a drag law model (Collins 1972). In this study, the energy input by wind forcing is not considered in the laboratory experiments.

6.4.2 Numerical Approaches

In CCHE2D-Coast, by means of finite difference schemes, the wave-action balance equation (6.54) is numerically discretized in a geophysical domain which takes into account non-uniform grid size and a general quadrilateral mesh shape. In addition, the wave spectra are discretized into a number of frequency bins, based on the equal energy dividend, by which each frequency bin represents an individual wave. The bins for wave directions are also discretized to cover a half-plane wave direction (θ) domain from $+\pi/2$ to $-\pi/2$. A first-order upwinding finite difference scheme is applied to discretize the second, third, and fourth terms which represent the propagation of wave action in the horizontal plane and wave refraction due to varying water depth. The central difference scheme is applied to discretize the first term in the right-hand side for the diffraction term. A semi-implicit treatment is applied to the source terms for vegetation resistance, wave breaking, and bottom friction in order to increase the stability of the numerical model. Finally, the discretized wave-action balance equation is solved by means of the parabolic approximation, in which the waves are assumed to have a principal propagation direction from offshore toward onshore. An iterative solver, the Gauss-Seidel algorithm, is used to solve the discretized wave-action balance equations in every y-θ plane arranged from offshore to onshore. The computed wave actions in all the frequency bins add up to the total wave energy, which can be used to calculate statistical wave parameters such as wave heights, mean wave directions, and peak/mean periods.

Moreover, this integrated coastal process model (CCHE2D-Coast) has been built in a well-established numerical software package called CCHE2D (CCHE2D 2011), which is a general numerical tool to analyze 2-D shallow water flows, sediment transport, and water quality, with natural flow boundary conditions. Similar to the CCHE2D hydrodynamic model, the wave and hydrodynamic models in CCHE2D-Coast are discretized in a non-orthogonal grid system so that the models have more flexibility to simulate physical variables in complex coastal zones with irregular coastlines. This coastal process model has been validated by simulating waves, wave-induced currents, and morphological changes in coastal applications in various laboratory and field scales (e.g., Ding et al. 2006, Ding and Wang 2008&2010).

6.4.3 Boundary Conditions

Boundary conditions for simulating wave deformation over a computational domain covering ocean, coast and estuary are comprised of offshore wave spectra determined by

incident wave parameters (i.e., wave heights, peak or significant periods, and mean directions). The present wave spectral model supports two kinds of offshore (deepwater) wave spectrum inputs, i.e., the TMA spectrum (Bouws et al. 1985) and the Bretschneider-Mitsuyasu (B-M) spectrum (Mitsuyasu 1970). The multi-directional spreading function is given by a directional function proposed by Mitsuyasu (1970). The boundary condition at the onshore side is the non-reflective condition, namely, the waves reaching the shoreline are absorbed completely.

6.4.4 Model Validations Using Data Collected from the Literature

6.4.4.1 Non-breaking random waves through a vegetation zone

Mendez and Losada (2004) presented an analytical solution for a non-breaking wave through a vegetation zone in a straight flume in which the still water depth is uniform. The root-mean-square wave height evolution is described with Eq. (3.21). Mendez and Losada (2004) have calibrated the bulk drag coefficient C_D by comparing analytical solutions with the experimental data obtained by Dubi (1995).

The experiments were carried out in a 33-m-long, 1-m-wide and 1.6-m-high flat-bed wave flume. The width of the channel was partitioned to give a width of 0.5 m. The vegetation field, located at the center of the flume, had a total width of b = 9.3 m. The artificial kelp models were *L. hyperborean* with a plant area per unit height of b_v = 0.025 m and a height of d_v = 0.2 m. The number of uniformly distributed plants per unit horizontal area was N_v = 1,200 units/m^2. At the end of the wave flume, a wave absorber was installed to reduce reflection.

Dubi (1995) carried out a total of 154 runs with varying water depths h = 0.4–1.0 m, wave peak periods T_p = 1.26–4.42 s, and root-mean-square wave heights H_{rms} = 0.045–0.17 m. The input for irregular waves was the JONSWAP (Joint North Sea Wave Project) spectrum with shape parameter γ = 3.3. There were eight wave gages installed in the wave flume for measuring free surface oscillations, including one set up at the front face of the vegetation field. Among the experimental runs, a total of six experimental cases as shown in Table 6.6 were selected for validation of the wave action model. The values of the bulk drag coefficient C_D were adopted from the model calibration results of Mendez and Losada (2004). The vegetation zone with a domain size of 9.0 m long and 0.5 m wide was discretized into a grid of 181×11 with a uniform grid spacing of 0.05 m. A total of 200 frequency bins cover a wide range of frequency from 0.001 to 10 Hz. In order to be comparable with the analytical solution given by Mendez and Losada (2004), in the numerical simulations by the wave-action model, the effects of wave diffraction, breaking, bottom friction, and unsteadiness were neglected.

Table 6.6. Experimental parameters in validation cases

Case No.	$H_{rms,o}$ (m)	T_p (s)	h (m)	C_D
1	0.084	3.79	0.4	0.21
2	0.150	2.53	0.5	0.08
3	0.114	1.58	0.6	0.28
4	0.131	2.21	0.6	0.18
5	0.161	1.89	0.7	0.18
6	0.187	2.53	1.0	0.09

*Note: $H_{rms,o}$ = incident root-mean-square wave heights.

By using the present wave-action model, the computed root-mean-square wave heights (H_{rms}) for the six cases are compared with their analytical solutions given by Eq. (3.21) and the experimental data observed by Dubi (1995). Figs. 6.48 plot all the longitudinal profiles of the wave heights obtained from the three approaches. Since the computed wave parameters are uniformly distributed in the transverse direction of the computational wave flume, the longitudinal profiles are located at the center of the flume. The comparisons shown in the figures imply that the numerical wave heights are in excellent agreement with the analytical solutions. Despite some discrepancies in Case 1, the numerical results are also in good agreement with the experimental gage data.

6.4.4.2 **Breaking random waves on a vegetated sloping beach**

The laboratory data of Lovas (2000) were used to validate the numerical model for the transformation of random waves including dissipation by vegetation and breaking. The experimental setup was carried out in a 40-m-long and 5-m-wide wave flume at SINTEF (Norway). The width of the channel was partitioned to give a width of 0.6 m. To model a real beach, sand was put on top of the concrete (slope 1:30). Above the mean water level shoreline, the slope was increased (1:10) towards the dune foot. The front of the sand dune was shaped with a slope of 1:1.5 and a height of 30 cm.

Five thousand *L. hyperborea* model plants were prepared on a sandy 1:30 slope (see Fig. 6.49(a)). The sand used in the experiment had a median size of 0.22 mm and its density was 2,650 kg/m^3. The vegetation field, located at the center of the flume, had a total length of 7.27 m (Lovas and Torum 2001). The maximum number of uniformly distributed plants per unit horizontal area was N = 1,200 units/m^2. For the validation of the root-mean-square wave height evolution, 13 runs were analyzed, with varying water depths h = 0.69–0.77 m, wave peak periods T_p = 2.5 and 3.5 s, significant wave heights H_{mo} = 0.12–0.22 m and varying N (0, 600 and 1,200 units/m^2). The input for irregular waves was the JONSWAP spectrum with shape parameter γ = 7.0. For each run, free surface oscillations were measured at 10 wave gages, the first defining the offshore wave conditions and the other nine over the sloping beach.

A total of 3 experimental cases were used to validate the wave-action model, of which the model input parameters are listed in Table 6.7. The vegetation zone with a domain size of 20.0 m long and 0.6 m wide was discretized into a grid of 201×7 with a uniform grid spacing of 0.1 m. A total of 200 frequency bins cover a wide range of frequency from 0.001 to 10 Hz. In the numerical simulations by the wave-action model, the effects of wave diffraction, bottom friction, and unsteadiness were neglected.

The bulk drag coefficient C_D given in Table 6.7 was determined using the formulation proposed by Mendez and Losada (2004):

$$C_D = \frac{\exp(-0.0138Q)}{Q^{0.3}}, \quad 7 \le Q \le 172 \tag{6.63}$$

where $Q = K/a^{0.76}$, K = Keulegan-Carpenter number, $K=u_c T_p/b_v$, u_c = maximum horizontal velocity at the middle of the vegetation.

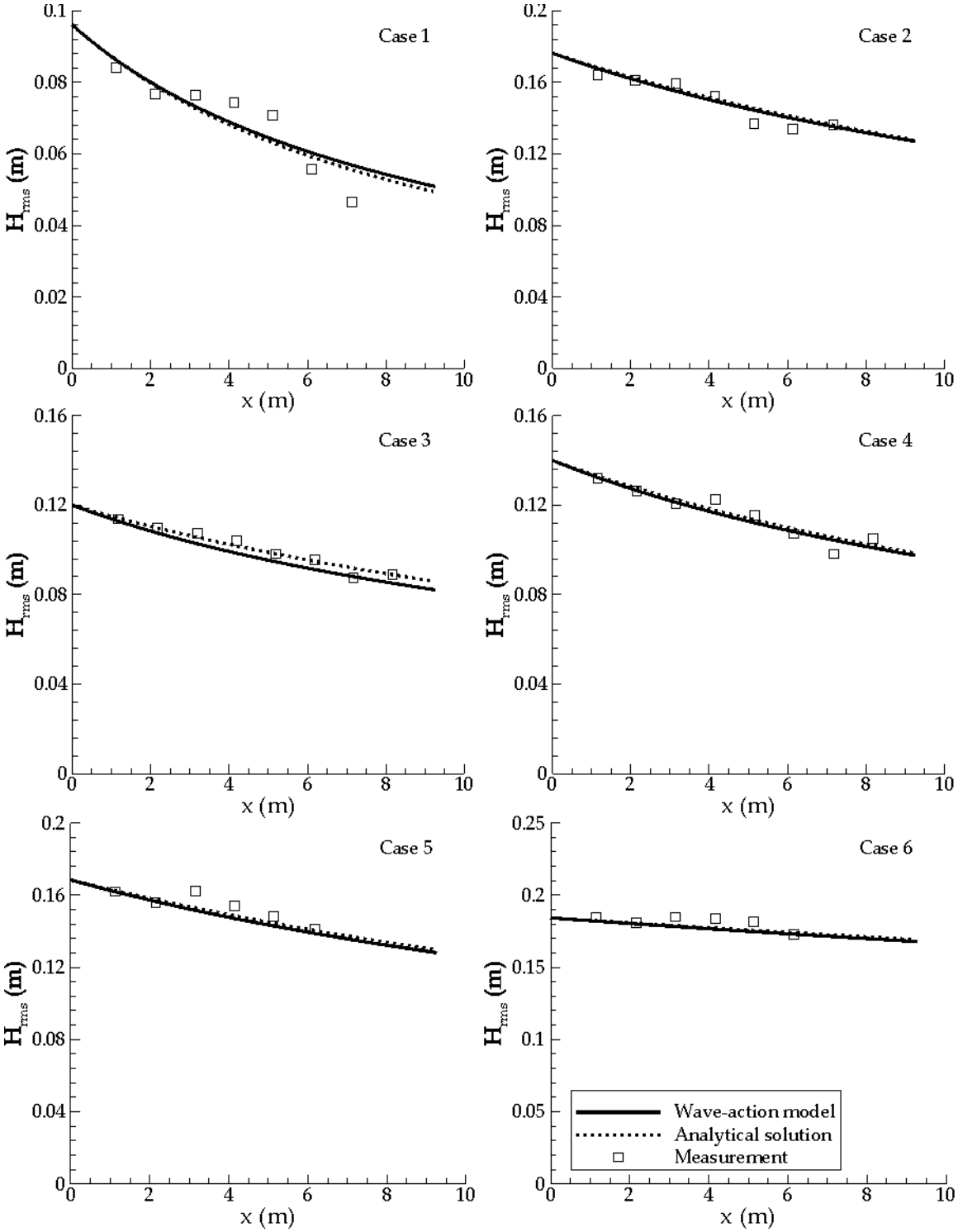

Fig. 6.48. Numerical, experimental, and analytical results of H_{rms} profiles

Table 6.7. Breaking random waves

Case No.	$H_{rms,o}$ (m)	T_p (s)	h (m)	C_D
1	0.18	3.5	0.69	0.079
2	0.22	2.5	0.77	0.115
3	0.125	3.5	0.77	0.136

Numerical simulations of wave fields by CCHE2D-Coast were carried out under two types of conditions: (1) without vegetation in the flume, and (2) with vegetation. By doing so, the wave breaking model can be validated independently, and the energy dissipation effect due to vegetation resistance can be identified in the case that waves are breaking in a vegetation zone. Fig. 6.49 gives longitudinal profiles of significant wave heights computed under the two conditions. Through comparisons of significant wave heights from experiments (Lovas 2000) and simulations, it is found that both the wave breaking model and the vegetation model work very well, so that the integrated wave model reproduced the wave deformations in the flume under the condition of only wave breaking and the combined breaking and vegetation resistance.

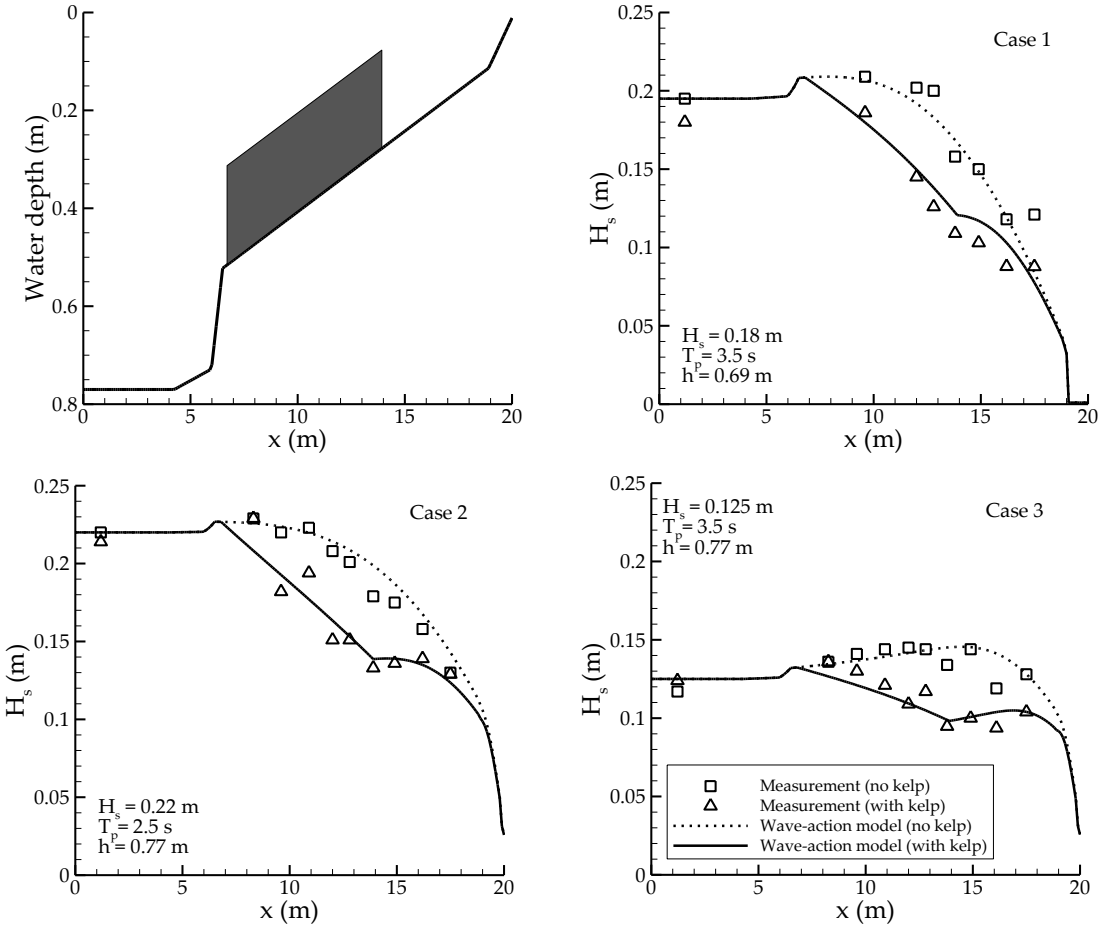

Fig. 6.49. Computed and observed significant wave heights

Fig. 6.50 further presents two spectra of wave-action density N in a frequency-direction space at the middle of the vegetation zone (x = 13.8m). In comparison with the density distribution without vegetation, Fig. 6.50(b) shows that the vegetation indeed reduced the wave-action density in the frequency-direction space, the wave heights therefore are attenuated accordingly.

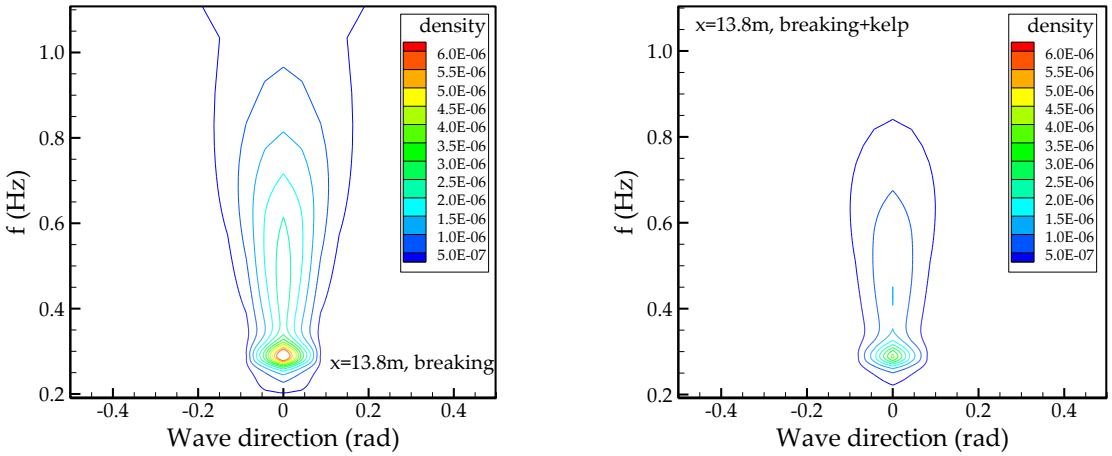

(a) Density N without vegetation (b) Density N with vegetation

Fig. 6.50. Computed wave-action density N

6.4.5 Model Validations Using Data Obtained by the Present Project

6.4.5.1 Random waves in a flat-bottom vegetated flume

This model validation case was to simulate the random wave transformation/deformation in a flat wave flume built in the National Sedimentation Laboratory, Oxford, Mississippi, in which the laboratory experiments were sponsored by the current DHS-SERRI program.

The experiments were conducted in a flume of 20.6 m in length, 0.69 m in width, and 1.22 m in height. The details of the experiment setup, vegetation species and wave conditions used are described in Chapter 3. In the experiments, regular waves and random waves were generated by the wave maker. The wave height data at each gage was used as a measure of wave attenuation due to vegetation. For the random wave cases, the JONSWAP spectrum was used to generate the random waves, in which the spectral peak enhancement factor γ=3.3. The measured frequency crossed a range from 0.0 Hz up to 15.0 Hz. However, the wave energy at a frequency higher than 10.0 Hz was very small. A large number of experimental cases using various configurations of rigid and flexible model and live vegetation under regular and random waves were investigated in the laboratory experiments. Six cases using rigid model vegetation under random waves were selected for validation of the wave-action model, of which the offshore wave parameters are listed in Table 6.8.

The numerical model was set up to replicate the experimental conditions. The computational domain was 17.55 m long and 0.69 m wide, starting from Gage 1 in Fig. 3.2.

Since the wave flume bed was made of glass, the value of Manning's roughness coefficient on the bottom was given as 0.012. The inlet was placed at the location of the first gage in order to use the measured wave parameters and spectra as the offshore incident wave conditions (boundary conditions). The spatial domain was represented by a uniform mesh with $\Delta x = \Delta y = 0.05$ m. Therefore, the total grid number was 352×15 (longitudinal × transverse). A total of 200 frequency bins were used to cover a wide range of frequency from 0.001 to 10 Hz. In the numerical simulations by the wave-action model, the effects of vegetation attenuation and bottom friction were included; the effects of wave diffraction and unsteadiness were neglected. A non-reflective boundary condition was specified on the right side of the flume (i.e. downstream) to model the effect of the absorber in the experiments.

Table 6.8. Wave and vegetation properties in the simulation cases

Case No.	$H_{rms,o}$ (m)	T_p (s)	h (m)	C_D by (12)	Calibrated C_D
1	0.0174	1.60	0.50	0.494	3.35
2	0.0376	1.20	0.50	0.388	2.80
3	0.0227	1.80	0.60	0.447	3.25
4	0.0615	1.20	0.60	0.293	2.55
5	0.0157	1.40	0.70	0.557	3.45
6	0.0219	1.80	0.70	0.446	2.95

*Note: D_v = 0.00953 m, N_v = 623 units/m², and h_v = 0.63 m.

In the simulations of the wave fields under random incident waves, the drag coefficient C_D is the only one parameter which needs to be calibrated. Unfortunately, the test runs using the wave-action model show that the values of C_D estimated by Mendez-Losada's formulation (6.65) give significantly overpredicted wave heights (or underestimated vegetation attenuation effect), in comparison with their observations. By trial and error, the calibrated values of the drag coefficient for all the six cases are obtained and listed in Table 6.8.

It is obvious that the estimated values by Eq. (6.63) are much less than the final calibrated ones. Using the calibrated drag coefficients, the best computed longitudinal profiles of root-mean-square wave heights (H_{rms}) in the six cases are shown in Fig. 6.51. The computed wave height profiles reproduced well the wave attenuation effect due to the artificial vegetation in the test section of the experiments.

To get insight into the deformation of the wave spectra in the wave flume, the distributions of the wave energy density $E(f)$ in the five wave gages were compared with their observed spectra. As shown in Figs. 6.52–6.57, the computed wave spectra by the wave-action model are in excellent agreement with their experimental observation spectra. No matter how the wave energy varies in the offshore, from the small offshore incident wave in Case 1 to the large one in Case 4, the computed wave spectra accurately reproduced the reduction effect of wave energy due to vegetation attenuation along the wave flume. It reveals that the developed wave-action model is capable of not only accurately predicting statistical wave parameters such as significant wave heights but also correctly simulating the wave energy variations in frequency. The latter one assures that the wave-action model has been established on a solid foundation of wave mechanics theory.

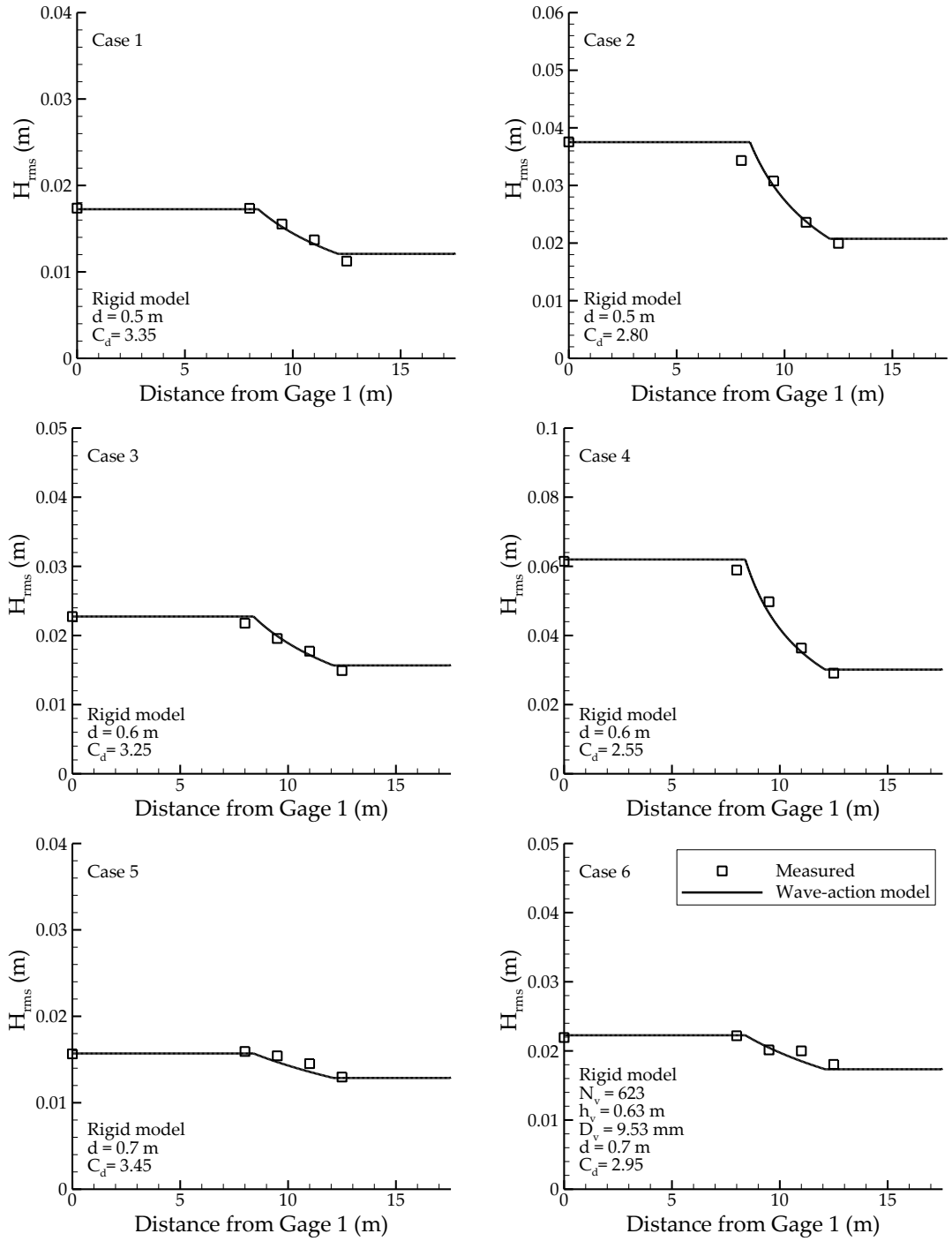

Fig. 6.51. Comparisons of root-mean-square wave heights (H_{rms})

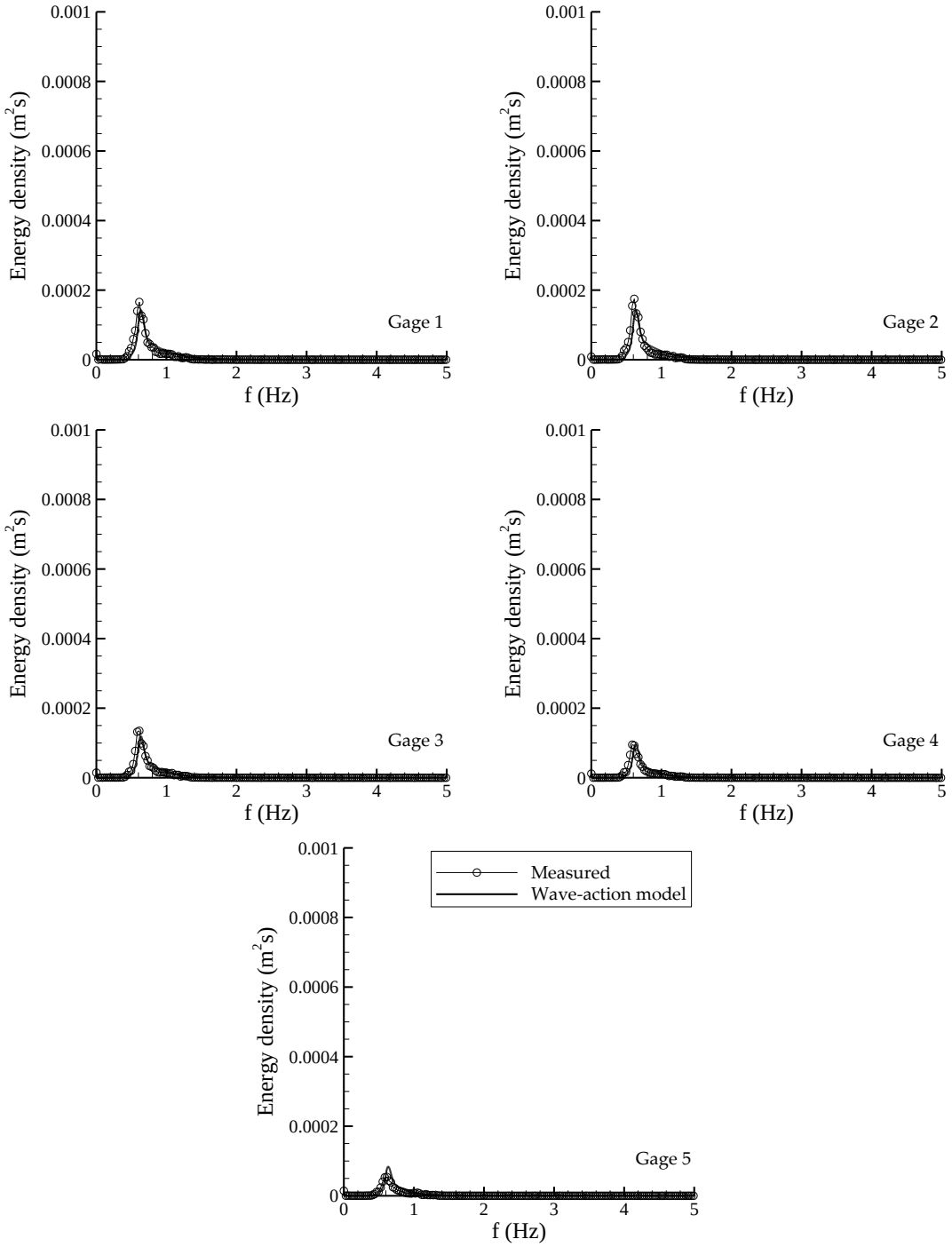

Fig. 6.52. Comparisons of wave energy density in Case 1

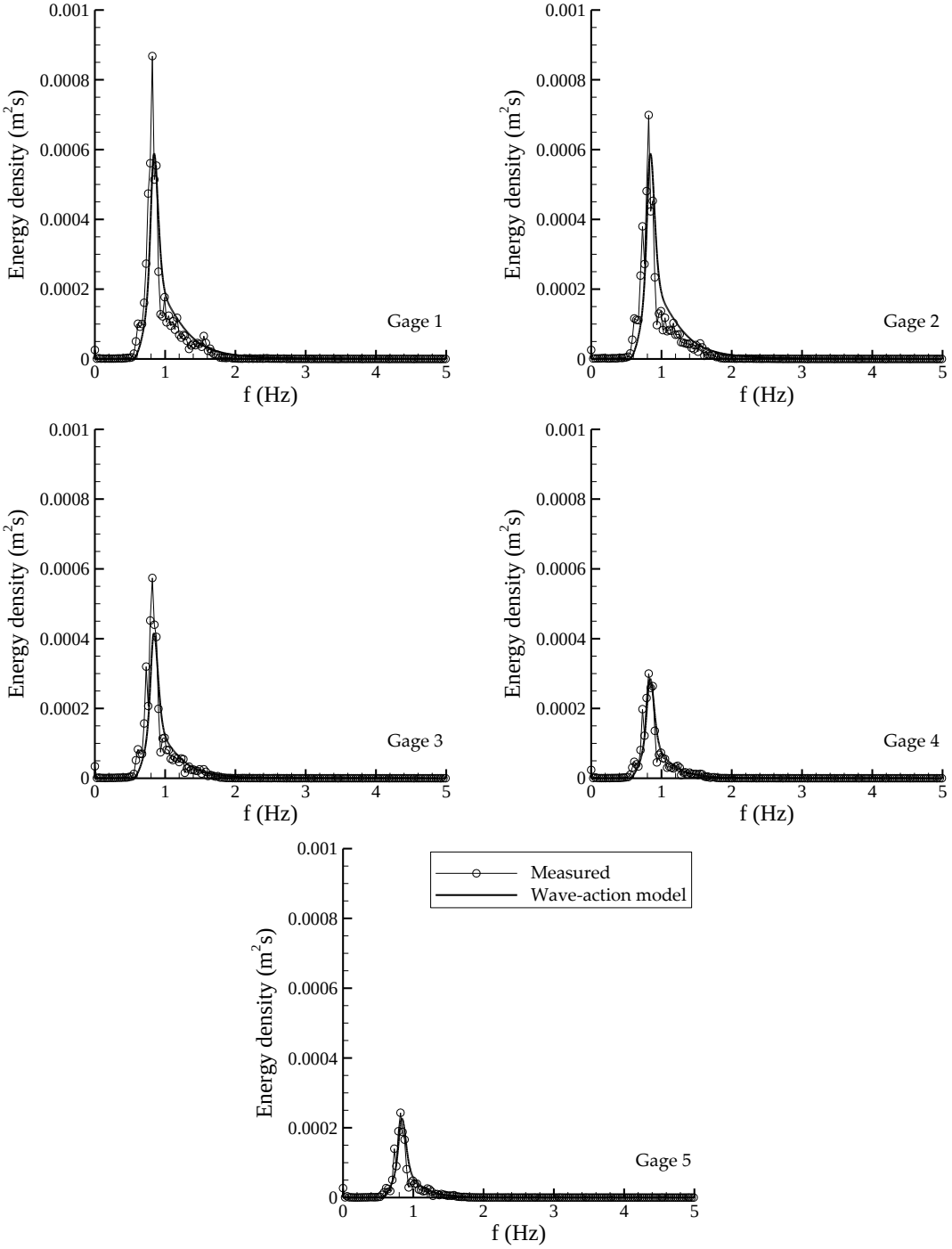

Fig. 6.53. Comparisons of wave energy density in Case 2

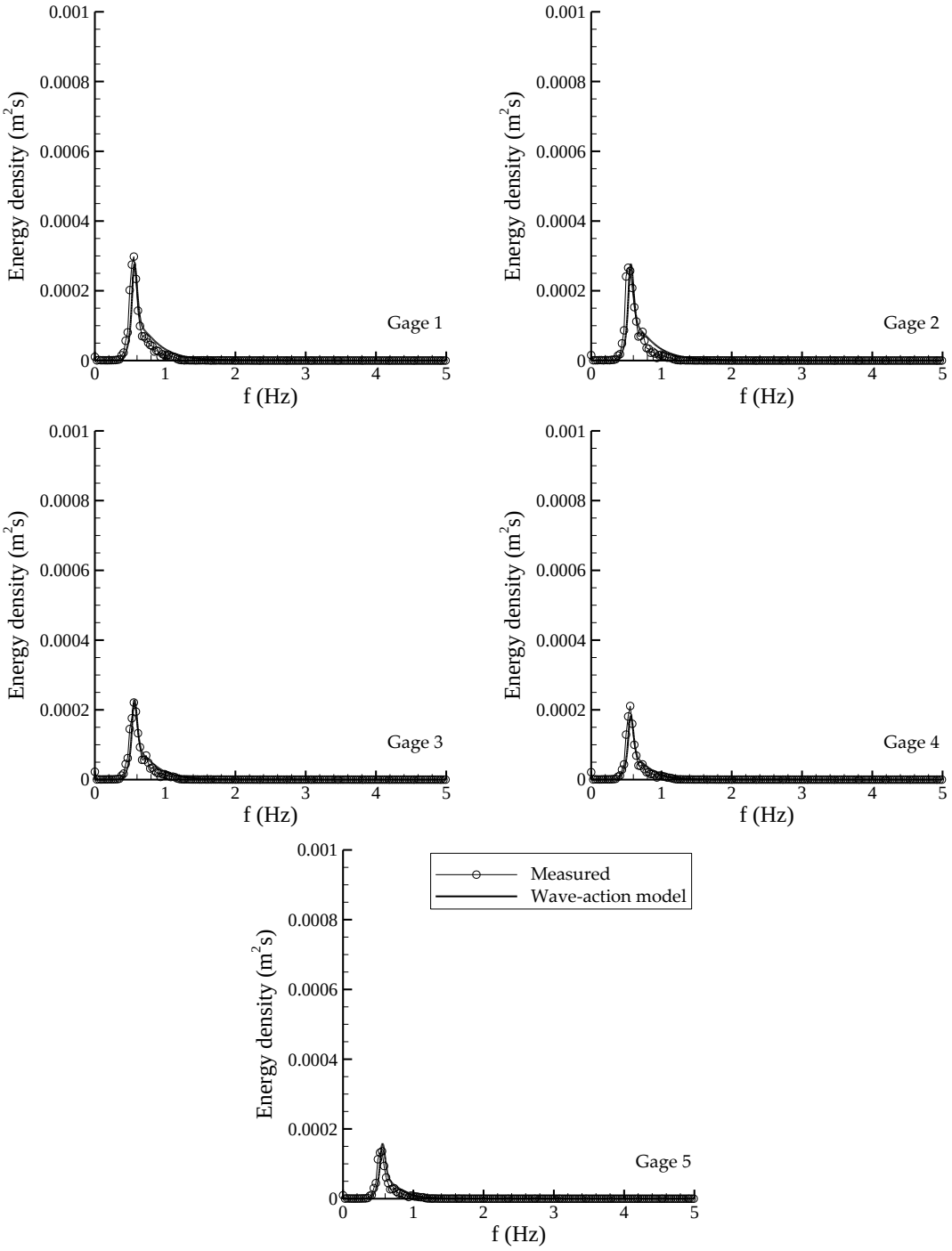

Fig. 6.54. Comparisons of wave energy density in Case 3

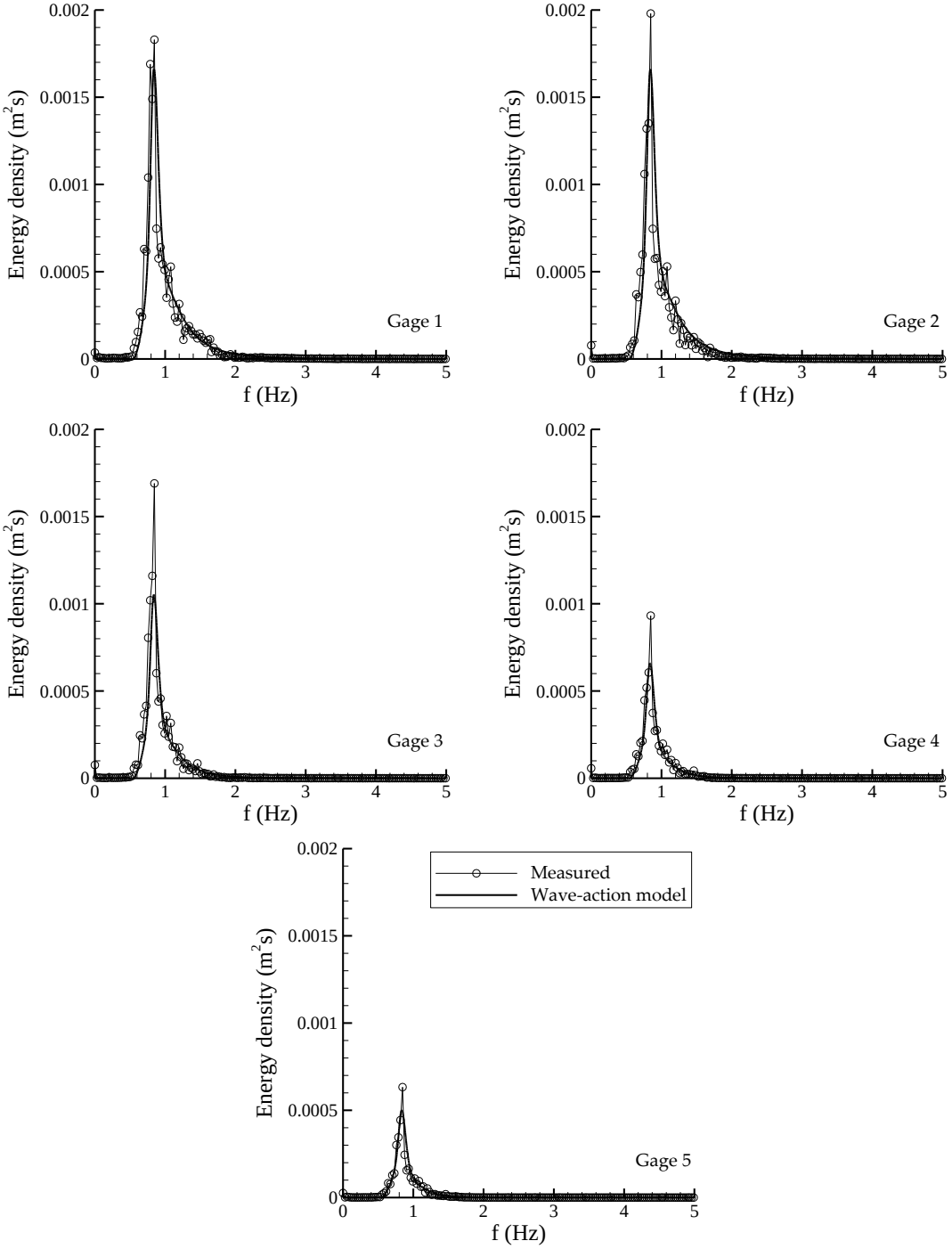

Fig. 6.55. Comparisons of wave energy density in Case 4

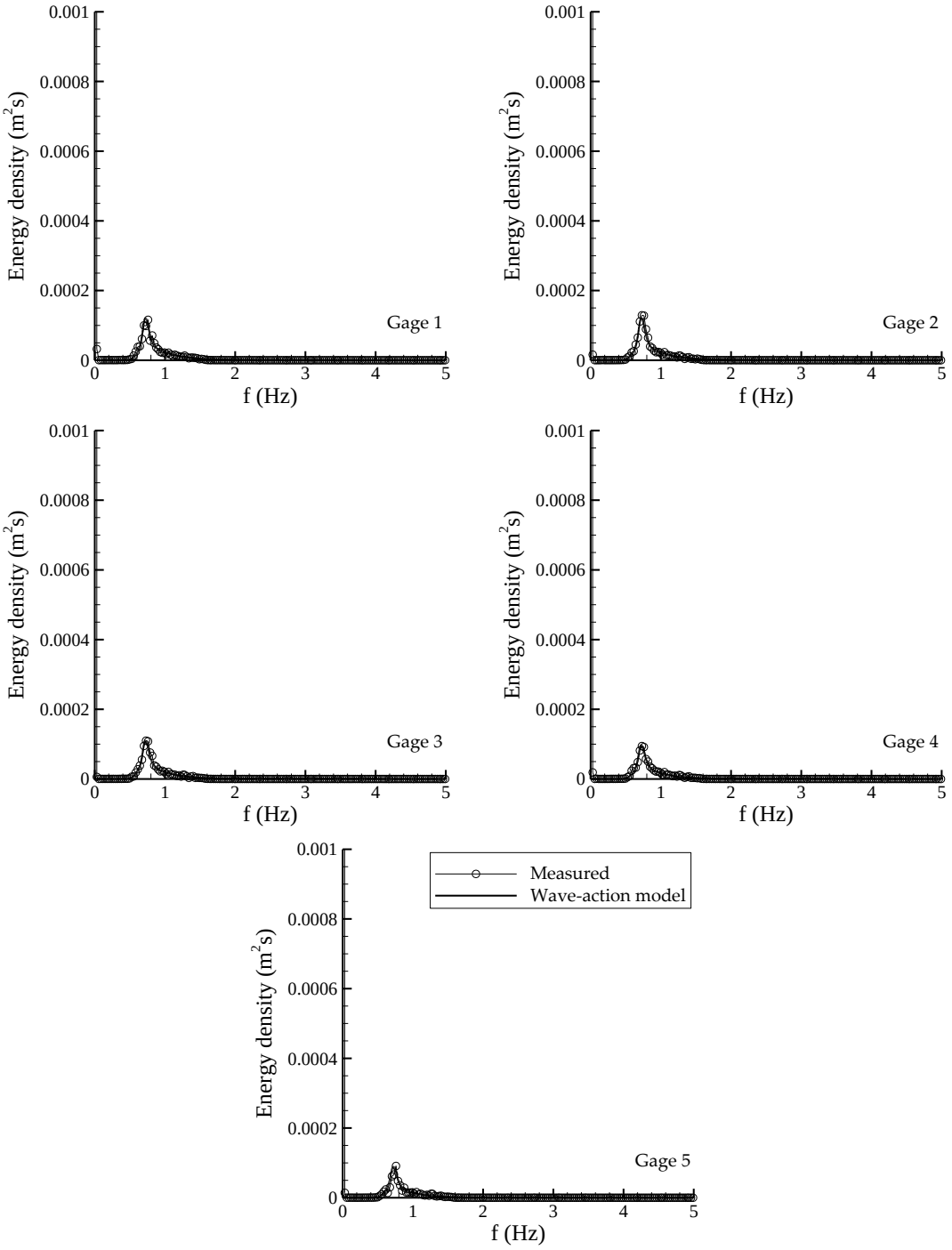

Fig. 6.56. Comparisons of wave energy density in Case 5

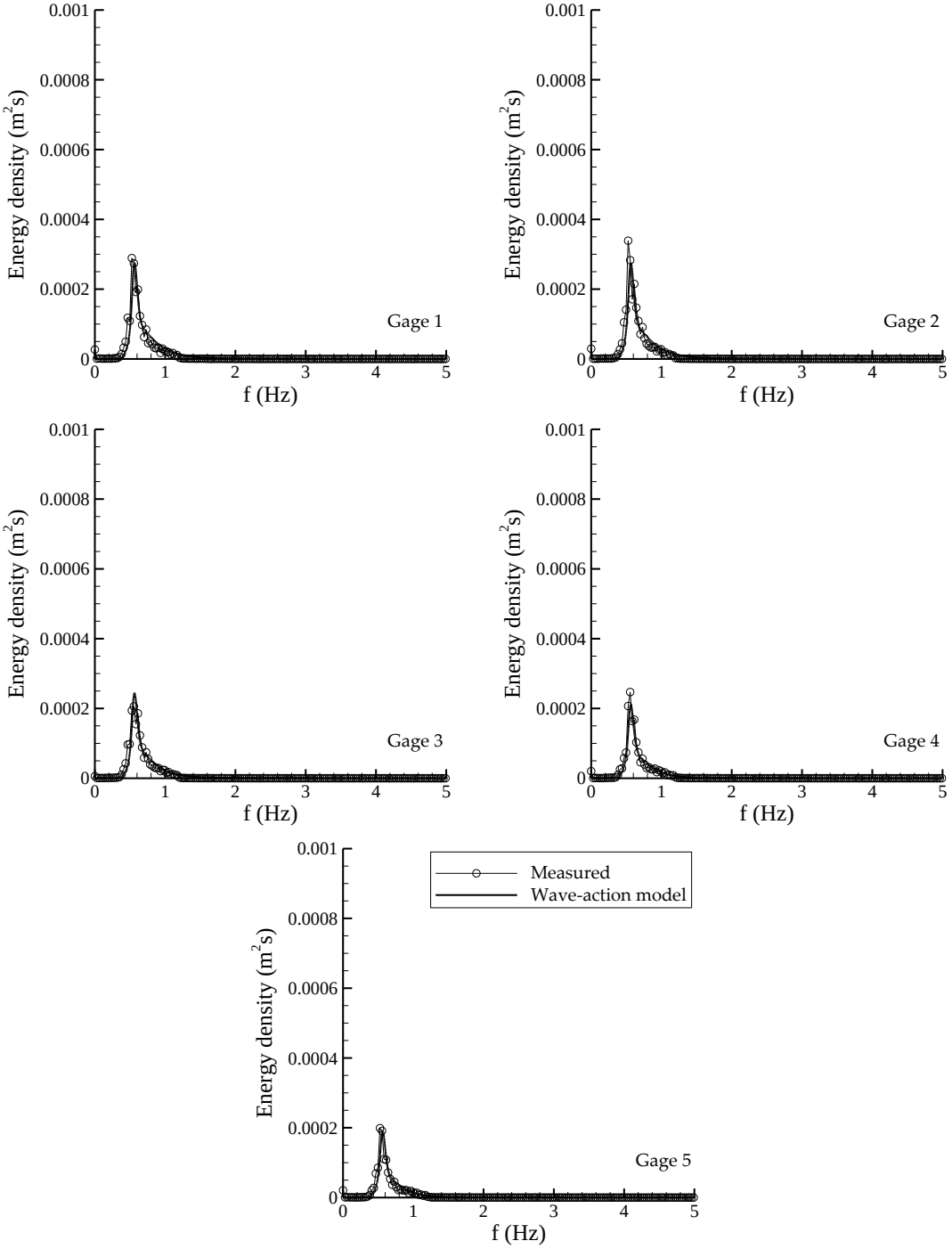

Fig. 6.57. Comparisons of wave energy density in Case 6

6.4.5.2 **Wave runup on a vegetated sloping beach**

This validation case was to simulate the random wave deformation and wave runup in a wave flume with a slope experimentally investigated at the National Sedimentation Laboratory, Oxford, Mississippi, as part of this project. The experimental setup in the laboratory is shown in Fig. 3.9. The dimensions of the flume were 20.6 m long, 0.69 m wide and 1.22 m deep. A wave generator was installed at the left-hand side of the flume. A slope of 1/21 was installed on the right-hand side of the flume, in which the slope toe was located at x=7.2 m. The vegetation zone was placed on the slope in a range from 11.60 to 15.16 m. The vegetation stems were rigid wooden cylinders of 0.2 m in height and 3.175 mm in diameter. The density of the stems was 3,150 units/m^2. The still water depth at the offshore (i.e., the flat bed section) was 0.4 m.

The computational domain was the same as the previous flat bed wave flume i.e., 17.55 m long and 0.69 m wide. The value of Manning's roughness coefficient on the bottom was specified as 0.012. The spatial domain was represented by a uniform mesh with $\Delta x = \Delta y =$ 0.05 m. Thus, the total grid number was 352×15 (longitudinal × transverse). A total of 200 frequency bins covered a wide range of frequency from 0.001 to 10 Hz. In the numerical simulations by the wave-action model, the effects of vegetation attenuation, wave breaking, and bottom friction were included, but the effects of wave diffraction and unsteadiness were neglected.

In order to compute the wave runup on the sloping beach, the wave simulation was coupled with a hydrodynamic model implemented in CCHE2-Coast. For the details of the hydrodynamc model, one may refer to Ding and Wang (2008). This hydrodynamic model simulates the wave-induced current, including the radiation stresses driven by wave actions and drag forcing due to vegetation. The drag force $\mathbf{F}_D$ on the current from vegetation is written as

$$\mathbf{F}_D = \frac{1}{2}\rho C_{Df} b_v N_v h \,|\mathbf{U}_c|\,\mathbf{U}_c \tag{6.64}$$

where $\mathbf{U_c}$ = depth-averaged velocity of the current, and C_{Df} = drag coefficient on the current due to vegetation resistance, which can be calculated by Mendez's formula (Mendez et al 1999):

$$C_{Df} = \left(\frac{2200}{\mathrm{Re}}\right)^{2.2} + 0.08, \qquad 200 \le \mathrm{Re} \le 15500 \tag{6.65}$$

where Re = $u_b b_v/\nu$, with u_b=the orbital velocity of wave at the bottom and ν = the kinematic viscosity of water.

The wave-action model coupled with the hydrodynamic model was used to simulate the wave fields and wave setup/runup driven by the random incident waves generated by the wave maker in the experiments. The parameters for the random wave cases are listed in Table 6.9. The case reference numbers were used in the experiments. Each case had two runs: one was carried out without vegetation installed, and the other one with the rigid vegetation.

Table 6.9. Parameters for cases of wave propagation on a sloping beach

Case	Case Ref. #	H_{s0} (m) (no	H_{s0} (m) (with	T_p(s)	Calibrated

No.		vegetation)	vegetation)		C_D
1	r400391205	0.0353	0.0365	1.20	2.50
2	r400571605	0.0460	0.0469	1.60	1.90
3	r400581205	0.0527	0.0527	1.20	2.00
4	r400981805	0.0771	0.0788	1.80	1.58

For computing wave fields with the wave runup effect, the wave-action model was run once every 30 min, and the hydrodynamic model was performed to simulate a time-dependent current field by including the radiation forcing and drag forcing. After two iterations of the wave-current interaction, the wave field and the current field were viewed as the steady results to compare with the experimental observations.

As shown in Fig. 6.58, the computed significant wave heights for all the eight cases (with and without vegetation installed) are compared with measurements. By comparing wave heights at the cases without vegetation, the computed wave heights (dashed lines) are in excellent agreement with the measurements from the wave flume. It indicates that the current wave breaking model described previously has an excellent accuracy to simulate breaking wave energy and wave heights in the beach with a slope.

After the successful validation of the wave breaking model, the wave-current coupled model was used to simulate wave fields and flow fields by considering the cases with vegetation installed on the slope. As shown in Fig. 6.58, the computed wave heights (solid lines) started to receive the vegetation resistance at the location of the beach toe at x = 7.2 m, and quickly dropped along the wave flume. By trial and error, the parameter, C_D, was calibrated in every case. The calibrated C_D values are listed in Table 6.9. The computed wave heights (solid lines) with the calibrated values almost exactly fit the measurement points over the vegetation zone. The computation accuracy for wave fields is excellent.

The wave setup and runup were computed by using the hydrodynamic model which contains the wave radiation forcing, turbulence, bottom friction stresses driven by combined wave and current, and drag forcing on the current due to vegetation resistance. The shortwave-period-averaged water elevations and currents were obtained by iteratively running the wave-action model and the hydrodynamic model. The wave fields were updated every 30 min during the wave-current interactions. A steady flow was confirmed after having run the hydrodynamic model for one hour. Two runs for each case listed in Table 6.9 were carried out: one was for exclusion of vegetation and the other one for including vegetation. The computed mean water elevations (MWEs) for all the four cases under the conditions with and without vegetation are shown in Fig. 6.59. At the left-hand side, the figures represent the comparisons of MWEs in the wave flume without vegetation. The error bars are the standard deviations of the observed MWEs in the experiments. The coupled wave-current models give excellent predictions about the wave setup, setdown, and runup. At the right-hand side of **Fig**. 6.59, the models also reproduced the MWEs under the vegetation resistance for Cases 1, 2, and 3. The computed MWEs for Case 4 indicate the overpredictions by the models. By considering the wave runup when vegetation existed was less than 2 mm and the experimental errors showing in the error bars, the predicted wave setup and runup at Case 4 are still plausible. Meanwhile, the values of drag coefficient C_{Df} were directly calculated by using Mendez's formulation in Eq. (6.65). The predictions would be better if the drag coefficients on the current could be adjusted manually, as done for the drag coefficient in the wave action model. Moreover, since the vegetation was uniformly installed in the wave flume and the waves were normal to the beach bathymetry contours,

the computed shortwave-period-averaged current velocities were very weak, in which the longitudinal components were less than 1 mm/s.

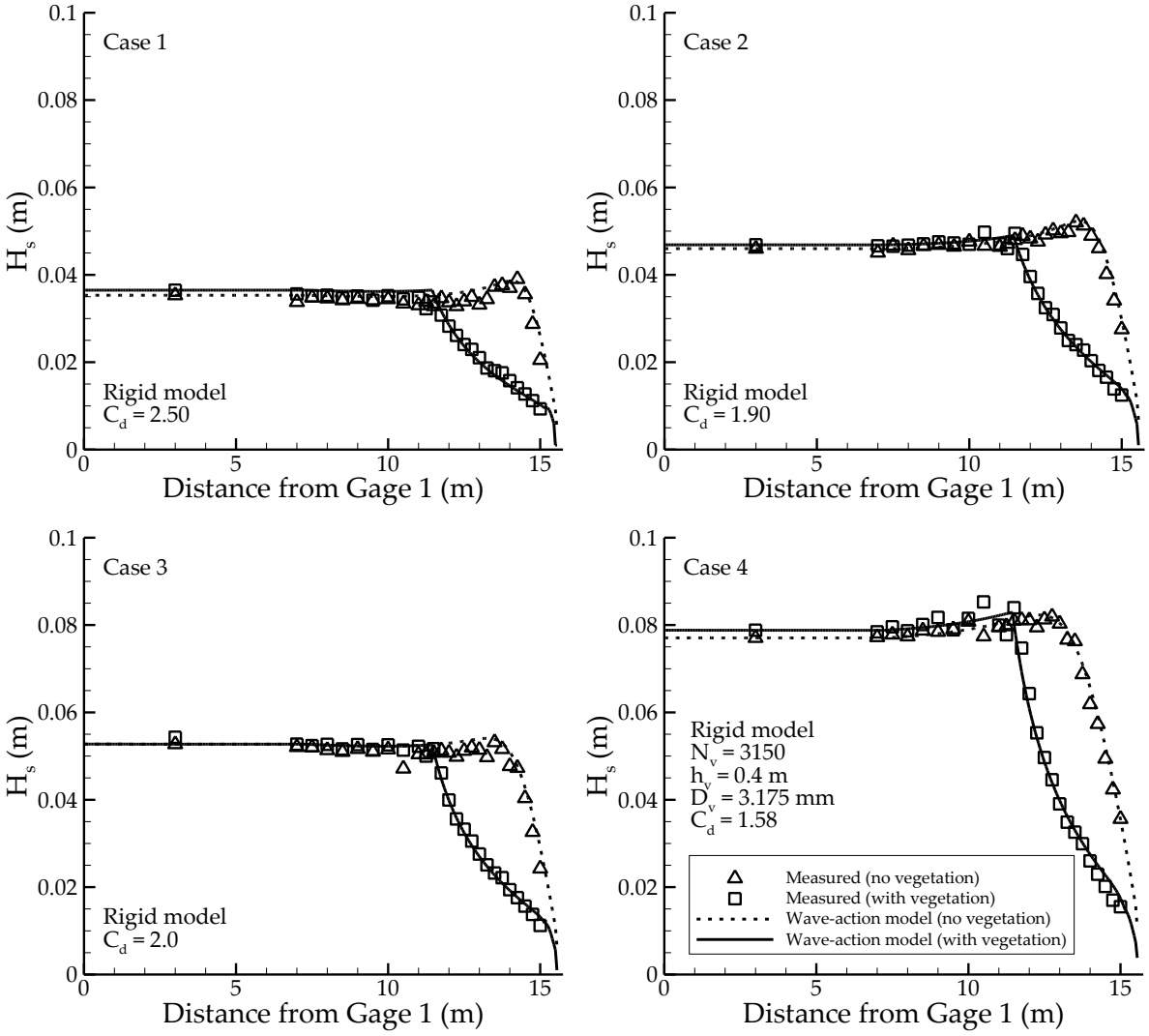

Fig. 6.58. Comparisons of significant wave heights with and without vegetation

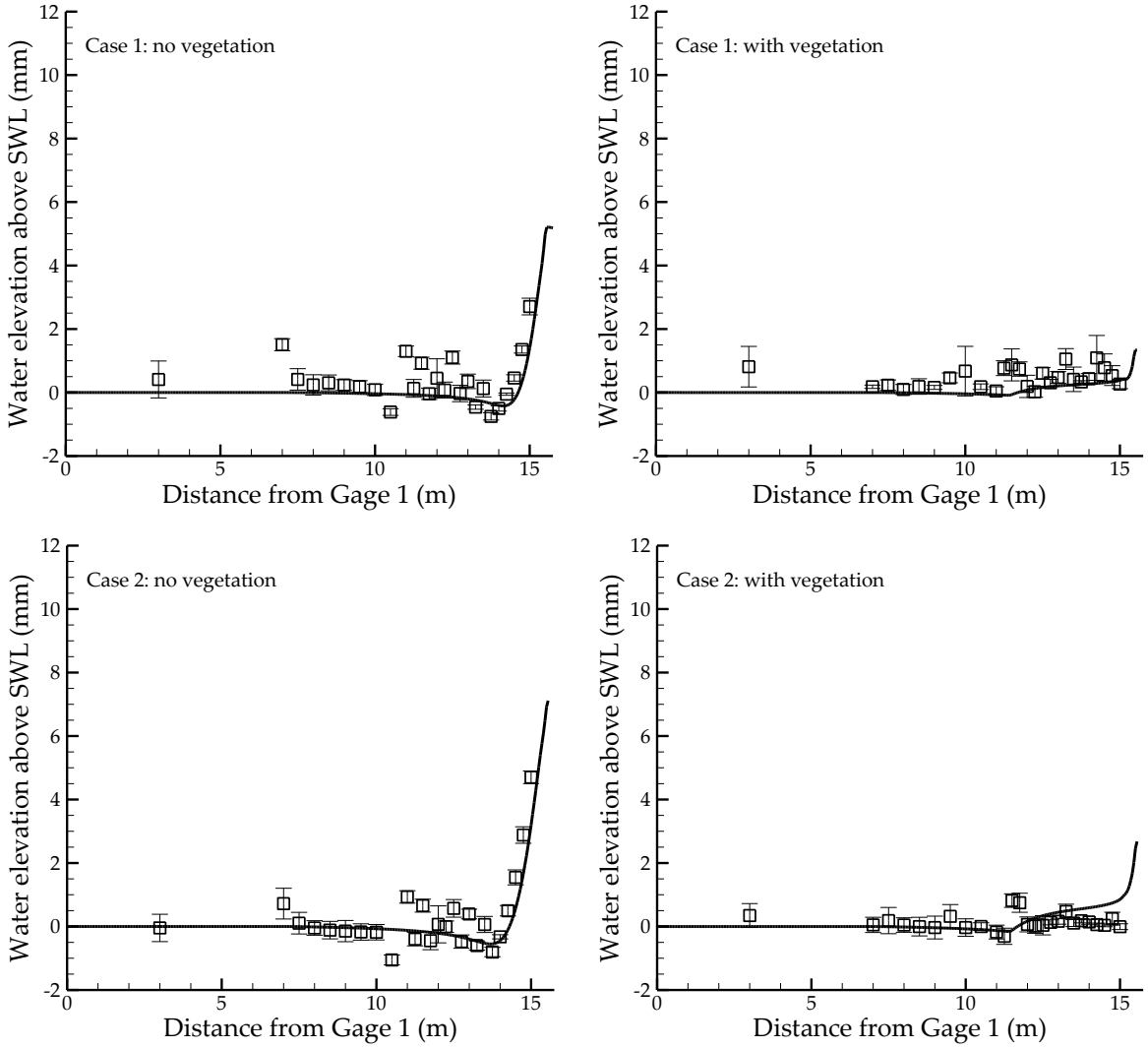

Fig. 6.59. Comparisons of mean water elevations with and without vegetation

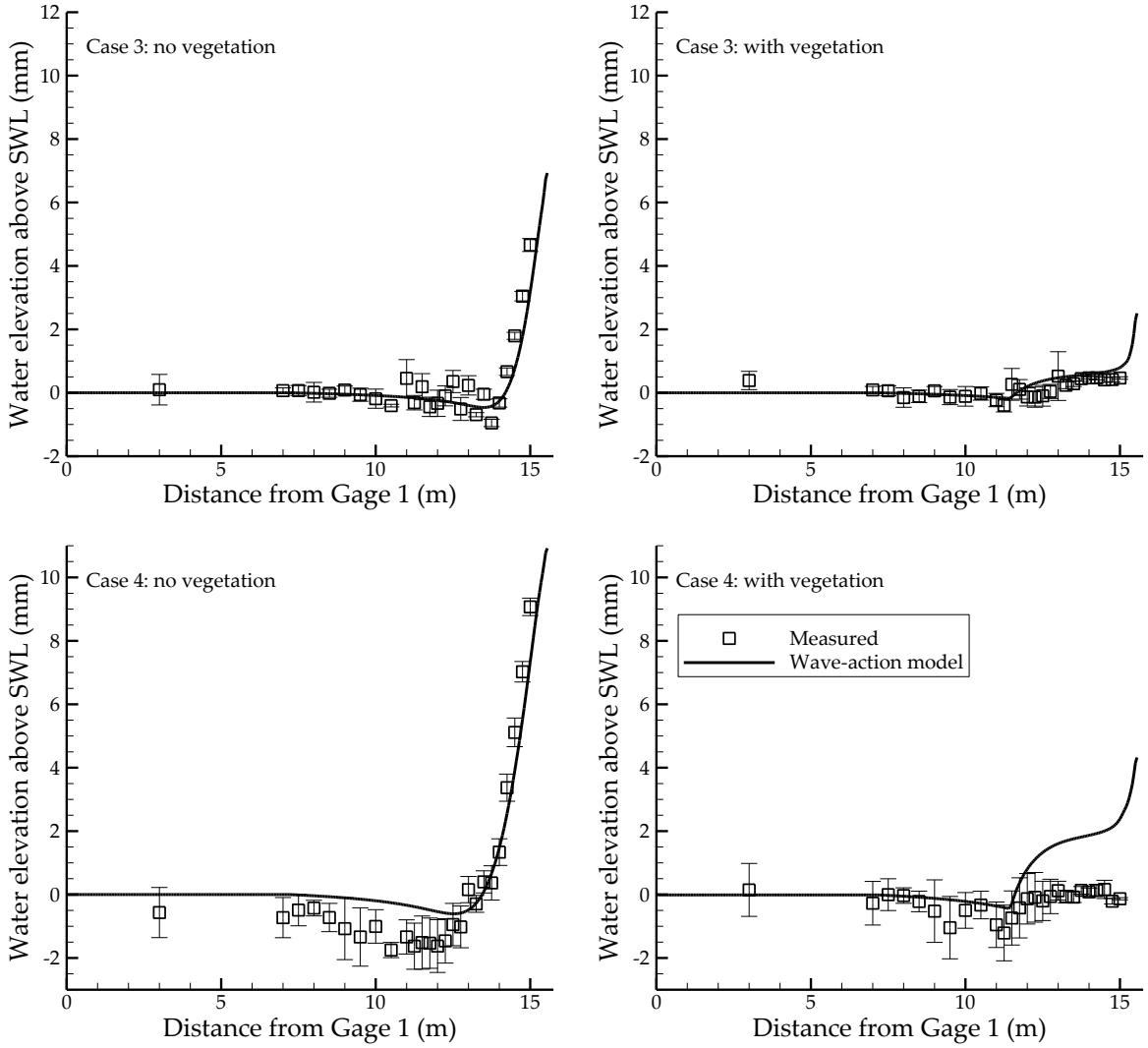

Fig. 6.59. Comparisons of mean water elevations with and without vegetation (continued)

As shown in Fig. 6.60, the computed wave energy density distributions at the gage stations at x = 8.0, 10.0, 12.0, and 14.0 m in Case 4 are compared with the observations from the experiments. At the left-hand side of the figure, no vegetation was installed. At the right-hand side, the rigid vegetation was placed in the flume. The computed energy density profiles in the cases both with and without vegetation are in good agreement with the measured energy density. Only the computed energy density at x = 14.0 m gives a discrepancy with the observations.

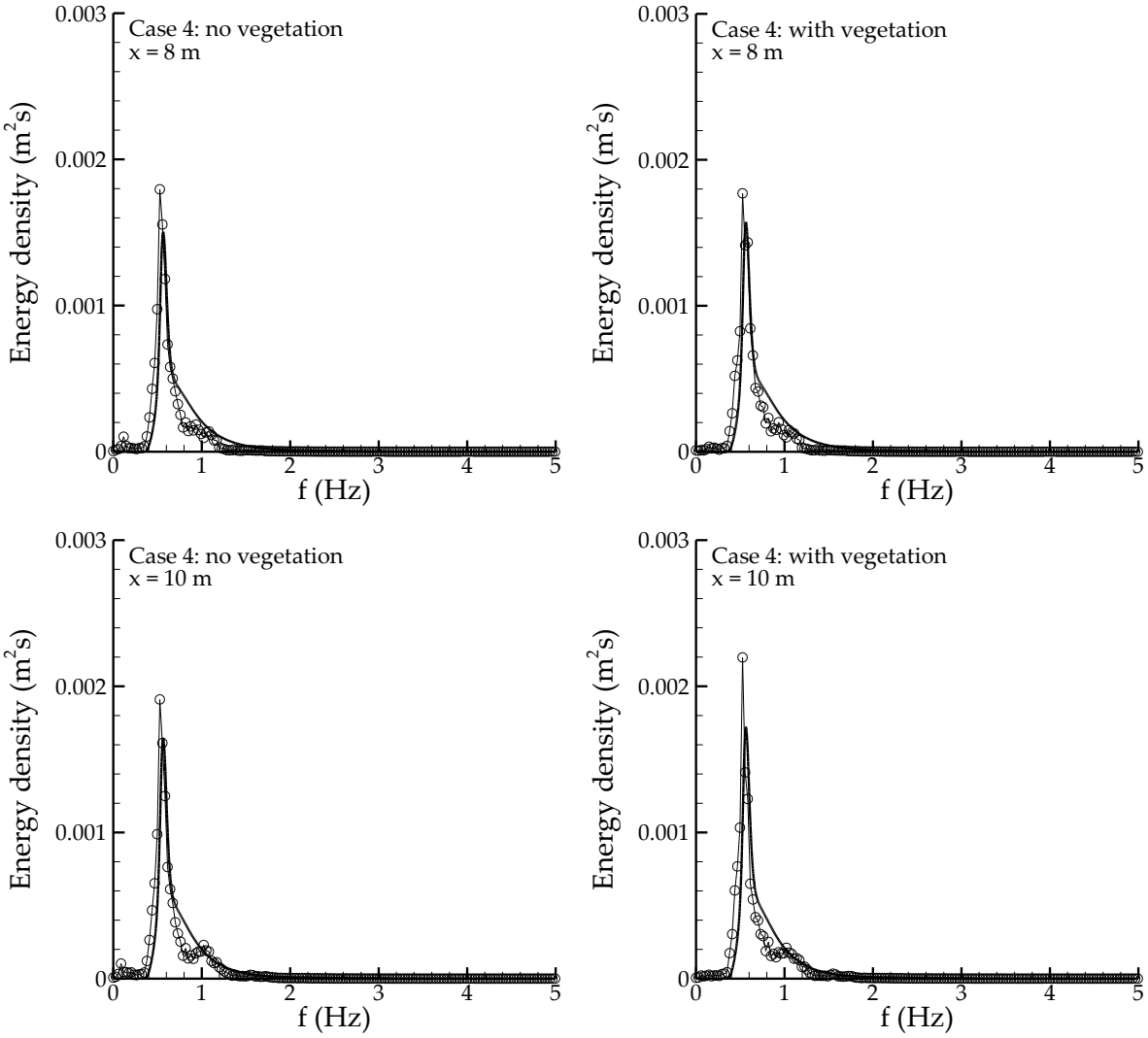

Fig. 6.60. Comparison of wave energy densities at with and without vegetation in Case 4

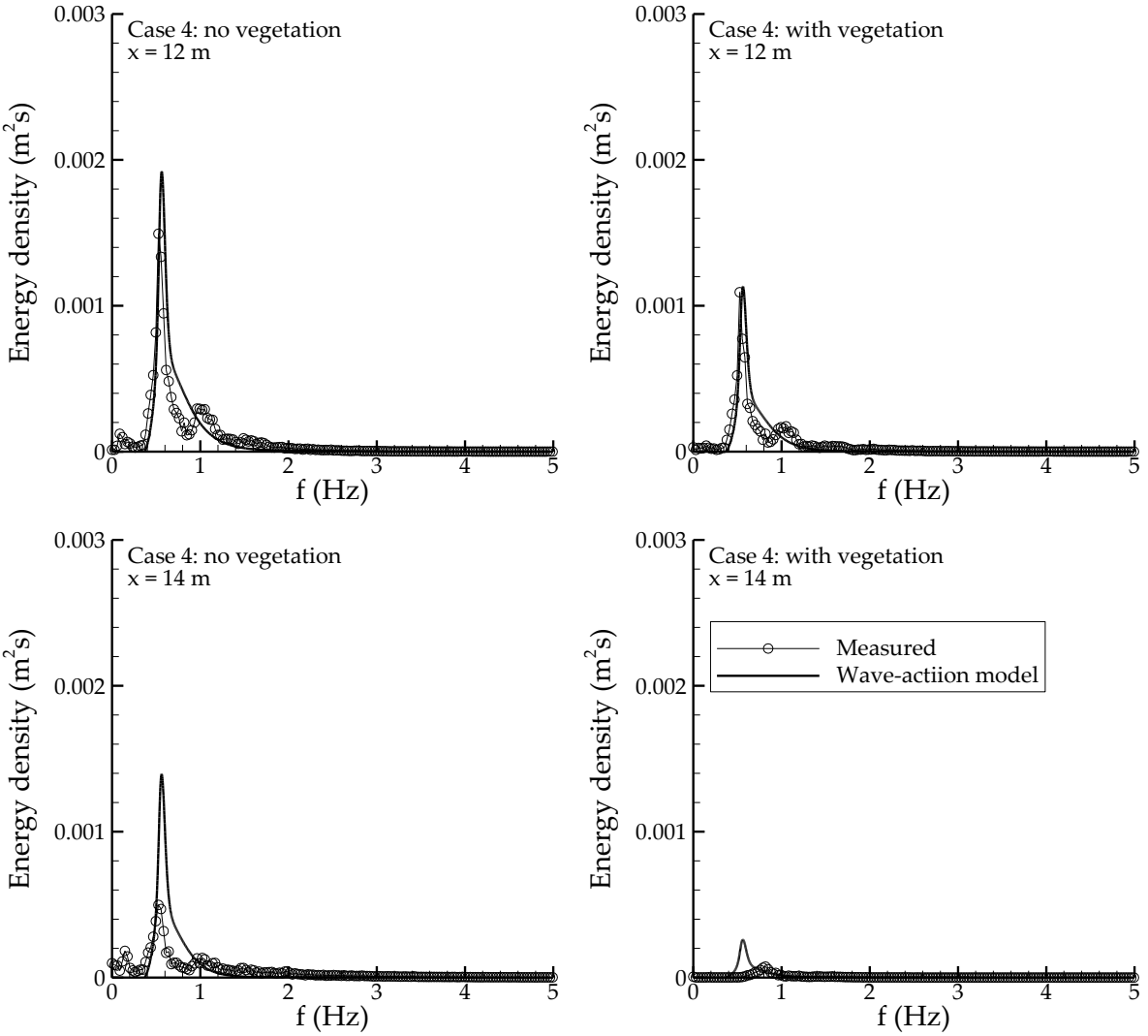

Fig. 6.60. Comparison of wave energy densities at with and without vegetation in Case 4 (continued)

6.5 Summary

Four numerical models were selected to demonstrate the modeling of surg and wave propagation in vegetated water bodies. The used models included a depth-averaged two-dimensional shallow water model for long waves such as tsunami wave, a one-dimensional Boussinesq model for short waves such as wind waves, a vertical two-dimensional model based on the Navier-Stokes equations for both long and short waves, and a wave-action model for wave energy spectra. Each selected model represents a type of models that are often used in coastal engineering.

The depth-averaged 2-D shallow water model used in this study adopts an explicit finite-volume method with the HLL approximate Riemann solver for the convective fluxes at cell faces and a stable centered difference scheme for the surface gradient terms. The model is first-order accurate in time and second-order accurate in space. The used one-dimensional Boussinesq model uses a hybrid finite-volume/finite-difference method to

solve the governing equations. The flux term is discretized using a finite-volume-based fourth-order accurate scheme, the dispersion and source terms are discretized with centered finite-difference schemes, and the unsteady term is discretized using the second-order MUSCL-Hancock scheme. The selected vertical 2-D model solves the Reynolds-Averaged Navier-Stokes (RANS) equations and uses the fractional volume of fluid (VOF) to capture the free surface. These three models are phase-resolving models that compute the wave dynamic deformation processes under non-breaking and breaking conditions. The effects of vegetation are taken into account in these models by adding the drag and/or inertia forces in the momometum equations.

The selected wave-action model adopts the directional wave-action balance equation to simulate random wave deformation/transformation through vegetation zones. The energy loss due to vegetation resistance is modeled by a vegetation drag model proposed by Dalrymple et al. (1984) and modified by Mendez and Losada (2004) for random wave conditions. The wave-action model is capable of computing various random wave processes such as refraction, diffraction, breaking, wave-current interaction, bottom friction, etc. This wave-action model is a phase-averaging model that determines the characteristic wave height, period and spectrum distribution.

All the four models were tested using the analytical solutions and experiment data reported in the literature, as well as data measured through the experiments conducted at the National Sedimentation laboratory (NSL), Oxford, MS as part of this project. The calculated water surface elevation, flow velocity, wave height, setup and runup are in good agreement with experimental observations. The calibrated values of drag coefficient in the vertical model agree generally well with those estimated using the analytical model of Dalrymple et al. (1984) and Mendez and Losada's (2004), because both types of models use the local velocity squared to determine the drag force of vegetation. However, the drag coefficient in a depth-averaged model needs to use larger values than the vertical 2-D model and the analytical model, because the depth-averaged model uses the depth-averaged velocity squared to determine the drag force. This implies that the regression equations of drag coefficient derived in Chapter 3 can be approximately applied in a vertical 2-D (or 3-D) model, but need to be modified when applied in a depth-averaged 1-D/2-D model.

7. CONCLUSIONS

Vegetation in wetlands, coastal fringes and stream floodplains can reduce surge and waves induced by hurricanes and severe storms while stabilizing marsh soils and providing ecological benefits. However, there is limited knowledge and few models that address the effects of vegetation on surge and waves. The main objective of this project was to conduct laboratory experiments and field investigations in order to gain a better understanding of the underlying mechanisms of surge and wave interaction with marsh grasses while developing/validating more reliable models to quantify the reduction of surge and waves by vegetation. The project was divided into three interrelated tasks: laboratory experiments, field investigations, and computational modeling.

The laboratory experiments were conducted in a 20.6 m long, 0.69 m wide and 1.22 m deep wave flume in the USDA-ARS National Sedimentation Laboratory (NSL), Oxford, Mississippi to investigate wave attenuation by full-scale rigid and flexible model vegetation as well as live vegetation under monochromatic and random wave conditions. The live vegetation species included *Spartina alterniflora* (dormant and green) and *Juncus roemerianus* (green), which are commonly found in Mississippi and Louisiana costs. The experiments used two bed topography configurations: a flat bed and a sloping beach. In the flat-bottom experiments, the total number of combined wave and vegetation configurations was 1,041 for regular waves and 476 for irregular waves. Each configuration was repeated three times for regular waves and up to five times for irregular waves to obtain more statistically reliable data sets. The water surface elevations were recorded by wave gages, and also by a new technique using a consumer grade digital video camera in some of the experiments. Drag coefficients of each of the tested vegetation species were calibrated from the collected wave gage data and video images, and regression equations were derived for the drag coefficient as functions of the Reynolds number and Keulegan-Carpenter number.

In the sloping beach experiments, rigid wooden dowels with a 1:3 model to prototype scale were used as the model vegetation and tested under regular and irregular waves. There were 144 experiments covering 24 different regular wave conditions and 70 experiments covering 24 different irregular wave conditions. Water surface elevation measurements were augmented by repeating experiments with the wave staffs at different locations. Video data analysis was also used to obtain complete water surface profiles during the sloping beach phase of the experimental work. Time-series of water surface elevations, average wave heights, mean water levels, and wave spectra for vegetated and non-vegetated beach experiments were compared to identify the influence of vegetation on wave breaking and wave setup. The experiments showed that wave setup and runup are reduced significantly by vegetation.

Field investigations were conducted to collect data on surge and wave attenuation by vegetation under tropical storm and winter cold front conditions. Considerable effort was devoted to selecting sites at Terrebonne Bay, LA, where permission was obtained to access a privately-owned wetland suitable for the project. An array of instruments was developed and deployed, including 9 wave gages and one water level gage, at a fixed location in Terrebonne Bay to measure wave attenuation in shallow water and over salt marshes in the hurricane and cold-front active seasons in 2009 and 2010. In addition to the instrument array at the fixed location, five portable, self-recording wave gages were successfully deployed twice in Breton Sound and Terrebonne Bay in rapid response to Tropical Storm Ida in 2009 and Tropical Storm Bonnie in 2010. The data collection on the fixed site of

Terrebonne Bay encountered many unexpected factors that were beyond our our control. However, valuable surge and wave attenuation data during the two tropical storms and wave climate data for Terrebonne Bay were collected, and the lessons learned through the field campaign are useful for future studies.

Field investigations were also conducted to measure the heights, diameters, densities, stiffnesses (modulus of elasticity), growth forms, and productivities of *Spartina alterniflora* and *Juncus roemerianus*, as well as the associated soil properties. These two species were the main focus of the present study, and several other species were also studied less extensively. The stiffnesses of these vegetation species at Terrebonne Bay, Breton Sound and Barataria Bay, LA and Graveline Bayou, MS were measured using individual plant bending test and board drop test. The relationship of the stiffness and height/diameter ratio of these vegetation species was established using the measured data. It was shown that the plant stiffness increases with the increase in stem height/stem diameter ratio for all green plants sampled, and the dormant plants of the same stem height/stem diameter ratio have a significantly lower stiffness modulus than their green equivalents. It was found that both stem and total plant heights increase as the growing season progresses, whereas the difference between the total height and stem height decreases as the plant matures until the plant becomes dormant.

To investigate the growth forms and productivities of *Spartina alterniflora* and *Juncus roemerianus*, eight transects were established at Graveline Bayou and the Grand Bay National Estuarine Research Reserve, MS. The vegetation height, diameter, rhizome thickness, percent cover, above-/belowground biomass in the lower and higher marshes as well as in coastal and inland marshes were compared. The associated soil properties, such as soil moisture, organic matter, bulk density, mean grain size and size composition were also measured. It was found that the mean rhizome thicknesses of both *Juncus roemerianus* and *Spartina alterniflora* were thicker in the high marsh zones than in the low marsh zones. The mean rhizome thickness of *Juncus roemerianus* is highest in Spring and lowest in Summer in the low marsh zones, but decreases over Spring, Summer, and Fall in the high marsh zones. The above- and belowground biomass is lower in inland marshes than in coastal marshes. Aboveground plant production in both coastal and inland marshes is highest in Summer, and the standing shoot heights of *Juncus roemerianus* and *Spartina alterniflora* are highest in Summer. However, belowground productivity in the coastal marshes is highest in Summer with lower rhizome thickness, and belowground productivity in the inland marshes is highest in Fall with lower rhizome thickness.

Four numerical models were used to quantify the effects of vegetation on surge and waves, including a depth-averaged two-dimensional shallow water model for long waves such as a tsunami wave, a one-dimensional Boussinesq model primarily for short waves, a vertical two-dimensional model based on the Navier-Stokes equations for both long and short waves, and a wave-action model for wave energy spectra. These four models represent the most common types of models being used by coastal engineering. The first three models are phase-resolving models and all adopt numerical schemes that can handle both non-breaking and breaking waves; thus they can compute the wave dynamic deformation processes. The fourth model is a phase-averaging model that determines the characteristic wave height, period and spectrum distribution.

All the four models were tested using the analytical solutions and experiment data reported in the literature, as well as data measured through the experiments conducted at the National Sedimentation laboratory (NSL), Oxford, MS as part of this project. The

calculated water surface elevation, flow velocity, wave height, setup and runup are in good agreement with experimental observations. However, it was observed that the calibrated values of drag coefficient might have different values in different models. The vertical model and the analytical model of Dalrymple et al. (1984) and Mendez and Losada (2004) yield approximately the same values of drag coefficient, because both types of models use the local velocity squared to determine the drag force of vegetation. A depth-averaged model needs to use larger values than the vertical 2-D model and the analytical model, because the depth-averaged model uses the depth-averaged velocity squared to determine the drag force.

Laboratory and field data have been included in the appendices and the empirical formulas and numerical models have been documented in this report. Included also is a comprehensive literature review conducted by this research team, which identifies what had been done and what needed to be done related to this topic. The documented formulas, models, data and references will be very useful for other researchers who are interested in this topic.

In addition, the team built a portable demonstration wave tank for educational purposes at the USDA-ARS National Sedimentation Laboratory, Oxford, MS. The wave tank is 4' long 6"wide and 8" deep, made of transparent polycarbonate sheets. A hand driven piston-type wave paddle was built to generate waves. This wave tank had been successfully used for laboratory demonstrations/tours to K-12 students from nearby schools. It is anticipated that students numbering, at least, in the hundreds will view and use this demonstration in the future. Moreover, totally four graduate students have been funded by this project and, upon graduation, they will become well-trained coastal engineers and/or scientists.

In the future, efforts will be continued by expanding and enhancing the field and laboratory experiments, data collection and analysis, and computational modeling. More laboratory experiments with a wider range of vegetation submergence ratio will be conducted, and the erosion at marsh edges will be investigated. The field campaign will be improved by considering different sites and using different data collection strategies to overcome the difficulties encountered in Phase I. The developed empirical relations of drag coefficient will be augmented to include a wider range of wave and vegetation parameters. These formulas will be tested in a variety of computational models using the laboratory and field data collected in Phases I-II of this project as well as from the literature.

8. REFERENCES

Adams, L.G., K. Baggett, J. Boyd, B. Bradley, S.A. Brown, J. Buchanan, J. Clark, K. Harvey, S. Johnston, K. McGee, F. Nation, D. Reid, D. Ruple, M. Sedlecky, L. Skupien, C. Snyder, S. H. Walker, and A. Underwood. 2008. *Selected Plants of Coastal Mississippi & Alabama Grand Bay National Estuarine Research Reserve and Weeks Bay National Estuarine Research Reserve*. National Oceanic and Atmospheric Administration (NOAA) and Office of Ocean and Coastal Resource Management.

Anastasiou, C.J., and J.R. Brooks. 2003. Effects of soil pH, redox potential, and elevation on survival of Spartina patens planted at a west central Florida salt marsh restoration site. *Wetlands* **23**(4): 845-859.

APHA, AWWA, WPCF. 1989. *Standard Methods for the Examination of Water and Wastewater*, 17th edition. Washington, DC: American Public Health Association.

Asano, T. 2006. Wave attenuation and sediment deposition due to coastal vegetation. *Journal of Global Environment Engineering* **11**: 29-44.

Asano, T., H. Deguchi, and N. Kobayashi. 1993. Interaction between water waves and vegetation. *Proceedings of the 23rd International Coastal Engineering Conference (ICEC'93).*

Asano, T., S. Tsutsui, and T. Sakai. 1988. Wave damping characteristics due to seaweed. *Proceedings of the 25th International Coastal Engineering Conference (ICEC' 88).*

ASTM Standard D2974-00. 2000. *Standard Test Methods for Moisture, Ash, and Organic Matter of Peat and Other Organic Soils.* ASTM International, West Conshohocken, PA, DOI: 10.1520/D2974-07A, *www.astm.org*.

ASTM Standard D422-63, 1963. 2002. *Standard Test Method for Particle-Size Analysis of Soils.* ASTM International, West Conshohocken, PA, DOI: 10.1520/D0422-63R07, *www.astm.org*.

ASTM Standard D4318-05. 2005. *Standard Test Methods for Liquid Limit, Plastic Limit, and Plasticity index of Soils.* ASTM International, West Conshohocken, PA, DOI: 10.1520/D4318-10, *www.astm.org*.

Atkinson, R.B., J.E. Perry, G.B. Noe, W.L. Daniels, and J. Jr. Cairns. 2010. Primary productivity in 20-year old created wetlands in Southwestern Virginia. *Wetlands* **30**: 200-210.

Augustin, L.N., , J.L. Irish, and P.L. Lynett. 2009. Laboratory and numerical studies of wave damping by emergent and near-emergent wetland vegetation. *Coastal Engineering* **56**(3): 332-340.

Avila, L.A., and J. Cangialosi . 2009. *Tropical Cyclone Report. Hurricane Ida.* Report TCR-AL112009. National Hurricane Center.

Baldwin, A.H., and I.A. Mendelssohn. 1998. Effects of salinity and water level on coastal marshes: an experimental test of disturbance as a catalyst for vegetation change. *Aquatic Botany* **61**(4): 255-268.

Barfield, B.J., E.W. Tollner, and J.C. Hayes. 1979. Filtration of sediment by simulated vegetation, I. Steady-state flow with homogeneous sediment. *Transactions, Soil and Water Division, ASCE,* No. **4451**: 540-556.

Baumann, R.H., J.W. Day, and C.A. Miller. 1984. Mississippi Deltaic wetland survival: sedimentation versus coastal submergence. *Science* **224**(4653): 1093-1095.

Beji, S., and J.A. Battjes. 1993. Experimental investigations of wave propagation over a bar. *Coastal Engineering* **19** (1–2): 151–162.

Black, C.A. 1965. *Methods of soil analysis: Part 1. Physical and mineralogical properties*. Madison, WI: American Society of Agronomy.

Bokaian, A. and F. Geoola. 1984. Wake-induced galloping of two interfering circular cylinders. *Journal of Fluid Mechanics* **146**: 383-415.

Bouws, E., H. Gunther, W. Rosenthal, and C.L. Vincent. 1985. Similarity of the wind wave spectrum in finite depth water, 1-Spectral form. *Journal of Geophysical Research* **90**(C1): 975-986.

Bretschneider, C. L., and R. O. Reid. 1954. *Modification of Wave Height Due to Bottom Friction, Percolation, and Refraction*. U.S. Army Corps of Engineers, Beach Erosion Board, Washington D.C.

Brocchini, M., R. Bernetti, A. Mancinelli, and G. Albertini. 2001. An efficient solver for nearshore flows based on the WAF method. *Coastal Engineering* **43**(2): 105-129.

Brufau, P., P.A. García-Navarro, M.E. Vázquez-Cendón. 2004. Zero mass error using unsteady wetting-drying conditions in shallow flows over dry irregular topography. *International Journal for Numerical Methods in Fluids* **45**: 1047-82.

Brufau, P., M.E. Vázquez-Cendón, and P.A. García-Navarro. 2002. Numerical model for the flooding and drying of irregular domains. *Int. J. Numer. Methods Fluids* **39**:247-275.

Bunya S., J.C. Dietrich, J.J. Westerink, B.A. Ebersole, J.M. Smith, J.H. Atkinson, R. Jensen, D.T. Resio, R.A. Luettich, C. Dawson, V.J. Cardone, A.T. Cox, M.D. Powell, H.J. Westerink, and H.J. Roberts. 2010. *A High-Resolution Coupled Riverine Flow, Tide, Wind, Wind Wave, and Storm Surge Model for Southern Louisiana and Mississippi. Part I: Model Development and Validation.* Monthly Weather Review 138(2):345–377

Burgin, A.J., W.H. Yang, S.K. Hamilton, and W.L. Silver. 2011. Beyond carbon and nitrogen: how the microbial energy economy couples elemental cycles in diverse ecosystems. *Frontiers in Ecology and Environment* **9**(1): 44-52.

Byrd, K.B. and M. Kelly. 2006. Salt marsh vegetation response to edaphic and topographic changes from upland sedimentation in a Pacific Estuary. *Wetlands* **26**(3): 813-829.

Camfield, F.E. 1983. Wind wave growth with high friction. *Journal of Waterway, Port, Coastal and Ocean Engineering* **109**(1): 115–117.

Camfield, F., and R. Street. 1968. The effects of bottom configuration on the deformation, breaking and run-up of solitary waves. *Proc. 10th Conference on Coastal Eng.*, 173-189.

Carrier, G.F., and H.P. Greenspan. 1958. Water waves of finite amplitude on a sloping Beach. *Journal of Fluid Mechanics* **4**: 97-109.

CCHE2D. 2011. http://www.ncche.olemiss.edu/software/cche2d, accessed on Jan. 11, 2011.

Center for Applied Research and Environmental Systems (CARES) Website. 2010. The Cooperative Soil Survey. Soil Bulk Density-Physical Properties. *http://soils.missouri.edu/index.asp*.

Chapman, V.J. 1960. *Salt Marshes and Salt Deserts of the World*. NY: Interscience

Chen, S.-N., P.S. Lawrence, W.K. Evamaria, S. Fengyan, and W.N. 2007. A Nearshore model to investigate the effects of seagrassbBed geometry on wave attenuation and suspended sediment transport. *Estuaries and Coasts* **30**(2): 296-310.

Cho, H.J., and C.A. May. 2006. An initial restoration tool for submersed aquatic vegetation. *National Wetlands Newsletter* **28**(6): 10-20.

Choi, S.-U. and H. Kang. 2001. Reynolds Stress Modeling of Vegetated Open Channel Flows. *Proceedings of the XXIX IAHR Congress Conference Proceedings*.

Christmas, J.Y., L.N. Eleuterius, W.W. Langley, H.M. Perry, and R.S. Waller. 1973. *Cooperative Gulf of Mexico Estuarine Inventory and Study Mississippi. Phase III: Sedimentology*. Ocean Springs, MS: Mississippi Marine Conservation Commission. Gulf Coast Research Laboratory.

Collins, J.I. 1972. Prediction of shallow water spectra. *Journal of Geophysical Research* **77**(15): 2693-2707.

Corps of Engineers, US Army Engineer District, New Orleans. 1963. *Interim Survey Report, Morgan City, Louisiana and Vicinity, Serial No. 63*. New Orleans, LA: US Army Engineer District,

Cronk, J.K., and M.S. Fennessy. 2001. *Wetland Plants: Biology and Ecology*. Boca Raton, FL: Lewis Publishers.

Crowell, M., S. Edelman, K. Coulton, and S. McAfee. 2007. How many people live in coastal areas? *Journal of Coastal Research* **23**(5): iii-vi.

Cui, J., and V.S. Neary. 2002. Large eddy simulation (LES) of fully developed flow through vegetation. *Proceedings of the 5th International Conference on Hydroinformatics (IAHR).*

Dalrymple, R.A., J.T. Kirby, and P.A. Hwang. 1984. Wave Diffraction Due to Areas of Energy Dissipation. *J. Waterway, Port, Coastal and Ocean Engineering* **110**(1): 67–79.

Dalrymple, R.A. 1985. *Physical Modeling in Coastal Engineering*. A.A.Balkema, Rotterdam, The Netherlands.

Darby, F.A. and R.E. Turner. 2008. Below- and aboveground biomass of *Spartina alterniflora*: response to nutrient addition in a Louisiana salt marsh. *Estuaries and Coasts* **31**: 326-334.

De La Cruz, A.A. 1973. The role of tidal marshes in the productivity of coastal waters. *Association of Southeastern Biologists (ASB) Bulletin* **20**(4): 147-156.

De La Cruz, A.A., and B.C. Garbriel. 1973. Calorie, elemental and nutritive value changes in decomposing Juncus roemerianus leaves. *Association of Southeastern Biologists (ASB) Bulletin* **20**: 47.

De La Cruz, A.A., and C.T. Hackney. 1977. Energy value, elemental composition, and productivity of belowground biomass of a *Juncus* tidal marsh. *Ecology* **58**: 1165-1170.

Dean, G.D. and R.A. Dalrymple. 1991. *Water Wave Mechanics for Engineers and Scientists*. Singapore: World Scientific.

Dean, R. G., and Bender, C. J. 2006. Static wave setup with emphasis on damping effects by vegetation and bottom friction. *Journal of Coastal Engineering* **53**:149-156.

Dean, R.G.. and T.L. Walton. *Handbook of Coastal Engineering*. Singapore: World Scientific.

Delis, A. I., M. Kazolea, and N.A. Kampanis. 2008. A robust high-resolution finite volume scheme for the simulation of long waves over complex domains. *International Journal for Numerical Methods in Fluids* **56**: 419-452.

Ding, Y., and S.S.Y. Wang. 2008. Development and application of coastal and estuarine morphological process modeling system. *Journal of Coastal Research, Special Issue No.* **52**: 127-140.

Ding, Y., and Wang, S.S.Y. 2010. Modeling of wave-current interaction using a multidirectional wave-action balance equation. *Proceeding of the 32nd International Conference on Coastal Engineering (ICEC'10)*.

Ding, Y., S.S.Y. Wang, and Y. Jia. 2006. Development and validation of a quasi three-dimensional coastal area morphological model. *Journal of Waterway, Port, Coastal and Ocean Engineering* **132**(6): 462-476.

Dingemans, M.W. 1987. *Verification of Numerical Wave Propagation Models with Laboratory Measurements, Report H228 Part 1*. The Netherlands: Delft Hydraulics.

Dodd, N. 1998. Numerical model of wave run-up, overtopping, and regeneration. *Journal of Waterway, Port, Coastal and Ocean Engineering* **124**: 73-81.

Dubi, A., and A. Torum. 1995. Wave damping by kelp vegetation. *Proceedings of the 24th International Coastal Engineering Conference (ICEC'95).*

Dubi, A., and A. Torum. 1997. Wave energy dissipation in kelp vegetation. *Twenty-Fifth Coastal Engineering Conference.*

Dubi, A.M. 1995. *Damping of Water Waves by Submerged Vegetation: A Case Study on Laminaria Hyperborea*. PhD thesis. Norway: University of Trondheim.

Eastgate, W.I. 1966. *Vegetated Stabilization of Grassed Waterways and Dam Bywashes*. Masters in Engineering Science Theis. St. Lucia, Queensland, Australia: Department of Civil Engineering, University of Queensland,

Edwards, K.R., and C.E. Proffitt. 2003. Comparison of wetland structural characteristics between created and natural salt marshes in Southwest Louisiana, USA. *Wetlands* **23**(2): 344-356.

Eleuterius, L.N. 1972. The marshes of Mississippi. *Southern Appalachian Botanical Society* **37**(3): 153-168.

Eleuterius, L.N. 1975. The life of the salt marsh rush, Juncus roemerianus. *Bulletin of The Torrey Botanical Club* **102**(3): 135-140.

Eleuterius, L.N. 1976. The distribution of Juncus roemerianus in the salt marshes of North America. *Chesapeake Science* **17**(4): 289-292.

Eleuterius, L.N. 1990. *Tidal Marsh Plants*. Gretna, LA: Pelican Publishing Company, Inc.

Elwany, M.H.S., and R.E. Flick. 1996. Relationship between kelp beds and beach width in Southern California. *Journal of Waterway, Port, Coastal and Ocean Engineering* **122**(1): 34–37.

Elwany, M.H.S., W.C. O'Reilly, R.T. Guza, and R.E. Flick. 1995. Effects of Southern California kelp beds on waves. *Journal of Waterway, Port, Coastal and Ocean Engineering* **121**(2): 143– 150.

Erduran, K. S., and V. Kutija. 2003. Quasi-three-dimensional numerical model for flow through flexible, rigid, submerged and non-submerged vegetation. *Journal of hydrodynamics* **5**(3): 189-202.

Erduran, K.S., S. Ilic, and V. Kutija. 2005. Hybrid finite-volume finite-difference scheme for the solution of Boussinesq equations. *International Journal for Numerical Methods in Fluids* **49**: 1213-1232.

Fathi-Moghadam, M., and N. Kouwen. 1997. Nonrigid, nonsubmerged, vegetative roughness on floodplains. *Journal of Hydraulic Engineering* **123**(1): 51-57.

Feagin, R.A., S.M. Lozada-Bernard, T.M. Ravens, I. Möller, K.M. Yeager, and A.H. Balrd. 2009. Does vegetation prevent wave erosion of salt marsh edges? *Proceedings of the National Academy of Sciences (PNAS'09).*

Fonseca, M.S., and J.A. Calahan. 1992. A preliminary evaluation of wave attenuation by four species of seagrass. *Estuarine, Coastal and Shelf Science* **35**: 565– 576.

Foster, W.A. 1968. *Studies on the Distribution and Growth of Juncus Roemerianus in Southeastern Brunswick County, North Carolina.* M.S. Thesis. MI: University of Michigan.

Freeman, G. E., W. J. Rahmeyer, and R. R. Copeland. 2000. *Determination of Resistance due to Shrubs and Woody Vegetation.* ERDC/CHL TR-00-25. Vicksburg, MS: Coastal and Hydraulics Laboratory, ERDC, US Army Corps of Engineers.

Freeman, G.E. 1997. *Analysis and Prediction of Plant Ptiffness Modulus for Selected Plants.* Federal Contract No. DACW-39-97-M-1413. Vicksburg, MS: U.S. Army Engineer Waterways Experiment Station.

Freeman, G.E., W.J. Rahmeyer, and R.R. Copeland. 2000. *Determination of Resistance due to Shrubs and Woody Vegetation.* Report No. ERDC/CHL TR-00-25. Coastal and Hydraulics Laboratory, Engineer Research and Development Center, US Army Corps of Engineers.

Furukawa, K., E. Wolanski, and H. Mueller. 1997. Currents and sediment transport in mangrove forests. *Estuarine, Coastal and Shelf Science* **44**(30: 301-310.

Gacia, E., and C.M. Duarte. 2001. Sediment retention by a Mediterranean Posidonia oceanica meadow: the balance between deposition and resuspension. *Estuarine, Coastal and Shelf Science* **52**: 505–514.

Gambi, M.C., A.R.M. Nowell, and P.A. Jumars. 1990. Flume observations on flow dynamics in *Zostera marina* (eelgrass) beds. *Marine Ecology Progress Series* **61**: 159– 169.

Georgiou, I.Y., D.M. Fitzgerald, and G.W. Stone. 2005. The impact of physical processes along the Louisiana coast. *Journal of Coastal Research* **44:** 72-89.

Ghisalberti, M., and H.M. Nepf. 2004. The limited growth of vegetated shear layers. *Water Resources Research* **40**: W07502.

Goda, Y. 1970. A synthesis of breaker indices. *Transactions of Japan Society of Civil Engineers* **13:** 227–230.

Grand Bay National Estuarine Research Reserve (GNDNERR) website. 2010. Mississippi Department of Marine Resources Grand Bay National Estuarine Research Reserve. *http://grandbaynerr.org*.

Graumann, A., T. Houston, J. Lawrimore, D. Levinson, N. Lott, S. Stephens, and D. Wuerts. 2005. *Hurricane Katrina: A Climatological Perspective – Preliminary Report.* Technical Report No. 2005-01. Washington, D.C.: NOAA's National Climate Data Center.

Gulf Ecological Management Sites (GEMS) website. 2010. Mississippi Department of Marine Resources. Coast Preserves Program. GEMS- Graveline Bay. *http://www.dmr.state.ms.us*.

Hall, G. and Cratchley, R. 2006. *Sediment Erosion, Transport and Deposition during the July 2001 Mawddach Extreme Flood Event.* Sediment Dynamics and the Hydromorphology of Fluvial Systems. Bangor: IAHS Publication 306.

Harada, K., and F. Imamura. 2005. Effects of coastal forest on tsunami hazard mitigation – a preliminary investigation, tsunamis: Case studies and recent developments. *Advances in Natural and Technological Hazards Research*: 279-292.

Harper, R.M. 1918. Some dynamic studies of Long Island vegetation. *Plant World* **21**: 38-46.

Harten, A., P.D. Lax, and B. van Leer. 1983. On upstream differencing and Godunov-type schemes for hyperbolic conservation laws. *SIAM Review* **25**(1): 35–61.

Hartley, S., R. Pace III, J.B. Johnston, M. Swann, C. O'Neil, L. Handley, and L. Smith. 2000. *A GAP Analysis of Louisiana: Final Report and Data.* US Department of the Interior, US Geological Survey.

Heald, E.J. 1969. *The Production of Organic Detritus in a South Florida Estuary*. Ph.D. Thesis. FL: University of Miami.

Heuscher, S.A., C.C. Brandt, and P.M. Jardine. 2005. Using soil physical and chemical properties to estimate bulk density. *Soil Science Society of America* **69**: 1-7.

Hieu, P.D., K. Tanimoto, and V.T. Ca. 2004. Numerical simulation of breaking waves using a two-phase flow model. *Applied Mathematical Modeling* **28**: 983-1005.

Hirt, C.W., and B.D. Nichols. 1981. Volume of fluid (VOF) method for the dynamics of free boundaryies. *J. Comp. Phys.* **39**(1): 201–225.

Hitchcock, A.S., and A. Chase. 1950. *Manual of the Grasses of the United States. Descriptions of Genera and Species.* NY: Dover Publications, Inc.

Holland, M.M., and C.J. Burk. 1990. The marsh vegetation of three Connecticut River oxbows: a ten-year comparison. *RHODORA* **92**(871): 166-204.

Holthuijsen, L.H., N. Booij, and T.H.C. Herbers. 1989. A prediction model for stationary, short-crested waves in shallow water with ambient currents. *Coastal Engineering* **13:** 23-54.

Horneck, D.A., and R.O. Miller. 1998. *Determination of Total Nitrogen in Plant Tissue*. Handbook of reference methods for plant analysis. Boca Raton, FL: CRC Press.

Howarth, R., F. Chan, D.J. Conley, J. Garnier, S.C. Doney, R. Marino, and G. Billen. 2011. Coupled biogeochemical cycles: Eutrophication and hypoxia in temperate estuaries and coastal marine ecosystems. *Frontiers in Ecology and Environment* **9**(1): 18-26.

Howes, B.L., J.W.H. Dacey, and D.D. Goehringer. 1986. Factors controlling the growth form of Spartina alterniflora: feedbacks between aboveground production, sediment oxidation, nitrogen and salinity. *Journal of Ecology* **74**: 881-898.

Hu, K., C.G. Mingham, and D.M. Causon. 2000. Numerical simulation of wave overtopping of coastal structures using the non-linear shallow water equations. *Coastal Engineering* **41**: 433–465.

Hughes, S.A. 1993. *Physical Models and Laboratory Techniques in Coastal Engineering*. Singapore: World Scientific.

IAHR/PIANC. 1986. *List of Sea State Parameters*. Supplement to Bulletin No. 52 of the Permanent International Association of Navigation Congresses, Brussels.

Iwata, K., K. Kawasaki, and D. Kim. 1996. Breaking limit, breaking and post breaking wave deformation due to submerged structures. *Proceedings of the 25th International Coastal Engineering Conference (ICEC'96).*

Jarvela, J. 2004. Determination of flow resistance caused by non-submerged woody vegetation. *International Journal of River Basin Management* **2**(1): 61–70.

Johnson, M. 1970. *Preliminary Report on Species Composition, Chemical Composition, Biomass, and Production of Marsh Vegetation in the Upper Patuxent Estuary, Maryland*. MD: Office of Water Resources. Natural Resources Institute, University of Maryland.

Keddy, P.A. 2010. *Wetland Ecology: Principles and Conservation*. Cambridge, UK: Cambridge University Press.

Kennedy, A.B., Q. Chen, J.T. Kirby, and R.A. Dalrymple. 2000. Boussinesq modeling of wave transformation, breaking and runup. Part I: 1D. *J. Water., Port, Coast., Ocean Eng*. **126**:39–47.

Kennedy, A.B., U. Gravois, B. Zachry, R.A. Luettich, T. Whipple, R. Weaver, J. Fleming, Q.J. Chen, and R. Avissar. 2010. Rapidly Installed Temporary Gauging for Hurricane Waves and Surge, and Application to Hurricane Gustav. *Continental Shelf Research* **30**(16): 1743-1752.

Ketabdari, M.J., M.R.H. Nobari, and M. M. Larmaei. 2008. Simulation of waves group propagation and breaking in coastal zone using a Navier Stokes solver with an improved VOF free surface treatment. *Applied Ocean Research* **30:** 130-143.

Kirby, C.J.Jr. 1971. *The Annual Net Primary Production and Decomposition of the Salt Marsh Grass Spartina Alterniflora Loisel in the Barataria Bay Estuary, Louisiana*. Ph.D. Thesis. LA: Louisiana State University.

Knutson, P.L., R.A. Brochu, W.N. Seelig, and M. Inskeep. 1982. Wave damping in Spartina alterniflora marshes. *Wetlands* **2**: 87-104

Kobayashi, N., A.W. Raichlen, and T. Asano. 1993. Wave attenuation by vegetation. *Journal of Waterway, Port, Coastal and Ocean Engineering* **199**(1):30–48.

Kothe, D.B. and R.C. Mjolsness. 1992. Ripple: A new model for incompressible flows with free surfaces. *AIAA Journal* **30**(11): 2694-2700.

Kouwen N. 1988. Field estimation of the biomechanical properties of grass. *Journal of Hydraulics Engineering* **26**(5): 559–568.

Kouwen, N., and Fathi-Moghadam, M. 2000. Friction factors for coniferous trees along rivers. *Journal of Hydraulic Engineering* **126**(10): 732–740.

Kouwen, N., and R.M. Li. 1980. Biomechanics of vegetative channel linings. *J. Hydr. Div.*, ASCE, **106**(HY6): 1085-1103.

Kouwen, N., T. Unny, and H.M. Hill. 1969. Flow retardance in vegetated channels. *Journal of Irrigation and Drainage Division* **95**(IR2): 329-342.

Kutija, V., and H.T.M. Hong. 1996. A numerical model for assessing the additional resistance to flow introduced by flexible vegetation. *J. Hydr. Res*. **34**(5): 99-114.

Lachat Instruments. 1995. *Total Phosphorus in Kjeldahl Digests, QuikChem Method 10-115-05-1-C.* Milwaukee, WI: Lachat Instruments.

Larsen, J., and H. Dancy. 1983. Open boundaries in short wave simulations - a new approach. *Coastal Engineering* **7**: 285-297.

Le Mehaute, B. 1972. Progressive Wave Absorber. *Journal of Hydraulic Research* **10**(2): 153-169.

Liang, Q., and F. Marche. 2009. Numerical resolution of well-balanced shallow water equations with complex source terms. *Adv. Water Resour*. **32**:873-884.

Li, C.W., and K. Yan. 2007. Numerical Investigation of Wave–Current–Vegetation Interaction. *Journal of Hydraulic Engineering* **133**(7): 794-803.

Li, R.M., and H.W. Shen. 1973. Effect of tall vegetation on flow and sediment. *Journal of the Hydraulic Division* **99**(5): 793–814.

Li, Y., and F. Raichlen. 2001. Solitary wave run-up on plane slopes. *Journal of Waterway, Port, Coastal and Ocean Engineering* **127**: 33-44.

Lightbody, A.F. and H.M. Nepf. 2006. Prediction of velocity profiles and longitudinal dispersion in emergent salt marsh vegetation. *Limnology and Oceanography* **51**(1): 218-228

Lima, S.F., C.F. Neves, and N.M.L. Rosauro. 2006. Damping of gravity waves by fields of flexible vegetation. *Proceedings of the 30th International Coastal Engineering Conference (ICEC'06).*

Lin, L., and R.-Q. Lin. 2004. Wave breaking function. *Proceedings of the 8th International Workshop on Wave Hindcasting and Prediction (IWWHP'04).*

Lin, P., and P.L.F. Liu. 1998. A numerical study of breaking waves in the surf zone. *Journal of Fluid Mechanics* **359:** 239-264.

Lin, P., and W.L. Xu. 2006. NEWFLUME: a numerical water flume for two-dimensional turbulent free surface flows. *Journal of Hydraulic Research* **44**(1): 79-93.

Lin, R.-Q., and L. Lin. 2004. Wind input function. *Proceedings of the 8th International Workshop on Wave Hindcasting and Prediction (IWWHP'04).*

Lindner, K. 1982. Der Stroemungswiderstand von Pflanzenbestaenden. *Mitteilungen 75*, Leichtweiss-Institut fuer Wasserbau, TU Braunschweig.

Longuet-Higgins, M.S. 1952. On the statistical distribution of the heights of sea waves. *Journal of Marine Research* **11**(3): 245-266.

Lopez, F. and M. Garcia. 1997. *Open Channel Flow through Simulated Vegetation: Turbulence Modeling and Sediment Transport*. Wetlands Research Technical Report WRP-CP-10: U.S. Army Corps of Engineers, Waterways Experiment Station.

Lopez, F., and M. Garcia. 2001. Mean flow and turbulence structure of open-channel flow through non-emergent vegetation. *Journal of Hydraulic Engineering* **127**(5): 392-402.

Lovas, S.M. 2000. *Hydro-Physical Conditions in Kelp Forests and the Effect on Wave Damping and Dune Erosion: A Case Study on Laminaria Hyperborea*. PhD thesis. Norway: University of Trondheim.

Lovas, S.M., and A. Torum. 2001. Effect of the kelp Laminaria hyperborea upon sand dune erosion and water particle velocities. *Coastal Engineering* **44:** 37– 63.

Lynett, P.J., T.R. Wu, and P.L.-F. Liu. 2002. Modeling wave runup with depth-integrated Equations. *J. Coast. Eng*. **46**:89–107.

Madsen, P.A. 1983. Wave reflection from a vertical permeable wave absorber. *Coastal Engineering* 7: 381-396.

Madsen, P.A., and O.R. Sørensen. 1992. A new form of the Boussinesq equations with improved linear dispersion characteristics. Part 2. A slowly-varying bathymetry. *Coastal Engineering* **18**: 183–204.

Madsen, P.A., O.R. Sørensen, and H.A. Schaffer. 1997. Surf zone dynamics simulated by a Boussinesq-type model: Part I. Model description and cross-shore motion of regular waves. *Coastal Engineering* **32**: 255– 287.

Madsen, P.A., R. Murray, and O.R. Sørensen. 1991. A new form of Boussinesq equations with improved linear dispersion characteristics. *Coastal Engineering* **15**: 371–388.

Magi, M., Y. Mazda, Y. Ikeda, and T. Kurokawa. 1996. Wave reduction in a mangrove area near the mouth of Shiira River on the Iriomote Island, Japan. *Mangrove Science* **1**: 35–42.

Mahdavi, A., and N. Talebbeydokhti. 2009. Modeling of non-breaking and breaking solitary wave run-up using FORCE-MUSCL scheme. *Journal of Hydraulic Research* **47**(4): 476-185.

Mase, H. 2001. Multi-directional random wave transformation model based on energy balance equation. *Coastal Engineering Journal* **43**(4): 317-337.

Massel S.R.,K. Furukawa, and R.M. Brinkman. 1999. Surface wave propagation in mangrove forests. *Fluid Dynamics Research* **24**: 219–249.

Mazda, Y., E. Wolanski, B. King, A. Sase, D. Ohtsuka, and M. Magi. 1997. Drag force due to vegetation in mangrove swamps. *Mangroves and Salt Marshes* **1**: 193–199.

Mazda, Y., N. Kanazawa, and E. Wolanski. 1995. Tidal asymmetry in mangrove creeks. *Hydrobiologia* **295**: 51-58

McKee, K.L., and J.A. Cherry. 2009. Hurricane Katrina sediment slowed elevation loss in subsiding brackish marshes of the Mississippi River Delta. *Wetlands* **29**(1): 2-15.

Meijer, M.C. 2005. *Wave Attenuation over Salt Marsh Vegetation, a Numerical Implementation of Vegetation in SWAN*. Thesis project. The Netherlands: Delft University of Technology.

Mendelssohn, I.A. and D.M. Burdick. 1988. *The Relationship of Soil Parameters and Root Metabolism to Primary Production in Periodically Inundated Soils. The Tolerance of Plant Species to Wetland Soils.* The ecology and management of wetlands. Volume I. Croom Helm, Portland, OR: Timber Press.

Mendelssohn, I.A., and K.L. McKee. 1989. *The Use of Basic Research in Wetland Management Decisions.* Marsh Management in Coastal Louisiana: Effects and Issues. U.S. Fish and Wildlife Service. Washingon, D.C.: Biology of Reproduction **89**(22).

Méndez, F.J., and I.J. Losada. 2004. An empirical model to estimate the propagation of random breaking and nonbreaking waves over vegetation fields. *Coastal Engineering* **51**: 103-118.

Mendez, F.J., I.J. Losada, and M.A. Losada. 1999. Hydrodynamics induced by wind waves in a vegetation field. *Journal of Geophysical Research* **104**(C8): 18383–18396.

Metzler, K., and R. Rosza. 1982. Vegetation of fresh and brackish tidal marshes in Connecticut. *Newsletter of the Connecticut Botanical Society* **10**(1): 1-3.

Mitsch, W.J., and J.G. Gosselink. 2009. *Wetlands*, 4th edition. NY: John Wiley & Sons, Inc.

Mitsch, W.J., J.G. Gosselink, C.J. Anderson, and L. Zhang. 2009. *Wetland Ecosystems*. Hoboken, NJ: John Wiley & Sons, Inc.

Mitsuyasu, H. 1970. On the growth of spectrum of wind-generated waves. *Proceedings of the 17th Japanese Conference on Coastal Engineering* (JSCE'70).

Möller, I., T. Spencer, and J.R. French. 1996. Wind wave attenuation over saltmarsh surfaces: preliminary results from Norfolk England. *Journal of Coastal Research* **12**(4): 1009– 1016.

Möller, I., T. Spencer, J.R. French, D.J. Leggett, and M. Dixon. 1999. Wave transformation over salt marshes: a field and numerical modelling study from North Norfolk England. *Estuarine, Coastal and Shelf Science* **49**: 411 – 426.

Möller,I. 2006. Quantifying saltmarsh vegetation and its effect on wave height dissipation: results from a UK East coast saltmarsh. *Estuarine, Coastal and Shelf Science* 69: 337–351.

Morgan, M.H. 1961. *Annual Angiosperm Production on a Salt Marsh*. M.S. Thesis. DL: University of Delaware.

Morison, J.R., M.P. O'Brien, J.W. Johnson, and S.A. Schaaf. 1950. The force exerted by surface waves on piles. *Petroleum Transactions (American Institute of Mining Engineers)* **189**: 149–154.

Mork, M. 1996. *Wave Attenuation due to Bottom Vegetation*. Oslo, Norway: Kluwer Academic Publishers.

Naot, D., I. Nezu, and H. Nakagawa. 1996. Hydrodynamic Behavior of partly vegetated open-channels. *Journal of Hydraulic Engineering* **122**(11): 625 – 633.

National Oceanic and Atmospheric Administration (NOAA) Coast Services Center website. United States Department of Commerce. National Oceanic and Atmospheric Administration. National Ocean Service. *http://www.csc.noaa.gov/.*

Neary, V.S. 2003. Numerical solution of fully-developed flow with vegetative resistance. *Journal of Engineering Mechanics* **129**(5): 558-563.

Nepf, H.M. 1999. Drag, turbulence and diffusion in flow through emergent vegetation. *Water Resources Research* **35**: 479–489.

Newell, R.I.E., and E.W. Koch. 2004. Modeling seagrass density and distribution in response to changes in turbidity stemming from bivalve filtration and seagrass sediment stabilization. *Estuaries* **27**: 793–806

Niering, W.A., and R.S. Warren. 1980. Vegetation patterns and processes in New England Salt marshes. *Bioscience* **30**(5): 301-307.

Nixon, S.W., and C.A. Oviatt. 1973. Ecology of a New England salt marsh. *Ecological Monographs* **43**(4): 463-498.

Nwogu, O. 1993. An alternative form of the Boussinesq equations for nearshore wave propagation. *Journal of Waterway, Port, Coastal and Ocean Engineering* **119**(6): 618–638.

Odum, E.P. 1971. *Fundamentals of Ecology*, 3rd edition. Phila: W. B. Saunders Co.

Odum, E.P., and M.E. Fanning. 1973. Comparison of the productivity of Spartina alterniflora and Spartina cyosuroides in Georgia coastal marshes. *Bulletin of the Georgia Academy of Science (SAUS)* **31**: 1-12.

Odum, W.E. 1978. The importance of tidal freshwater wetlands in coastal zone management. *Symposium on Technical, Environmental, Socioeconomic and Regulatory Aspects of Coastal Zone Management*.

Odum, W.E., E.P. Odum, and H.T. Odum. 1995. Nature's Pulsing Paradigm. *Estuaries* **19**(4): 547-555.

Odum, W.E., M.L. Dunn, and T.J. Smith III. 1978. *Habitat Value of Tidal Fresh Water Wetlands.* Wetland functions and values: The state of our understanding. Minneapolis, MN: American Water Resources Association.

Orlanski, I. 1976. Simple boundary-condition for unbounded hyperbolic flows. *J. Computational Physics* **21**(3): 251-269.

Otvos, E.G. 1985. *Coastal Evolution- Louisiana to Northwest Florida: Guidebook.* New Orleans: American Association of Petroleum Geologists Annual Meeting.

Ozeren, Y., and D.G. Wren. 2011. *Experimental Investigation of Surge and Wave Reduction by Vegetation (Phase I).* Oxford, MS: National Sedimentation Laboratory Research Report No. 73.

Ozeren, Y., D.G. Wren, and C.V. Alonso. 2009. *Development of Wave-Energy Absorbers for Cost-Effective Protection of Levees in Irrigation Reservoirs*. Oxford, MS: USDA-ARS, National Sedimentation Lab., Tech. Rep. No. 65.

Pennings, S.C., M.B. Grant and M.D. Bertness. 2005. Plant zonation in low-latitude salt marshes: disentangling the roles of flooding, salinity and competition. *Journal of Ecology* **93**: 159-167.

Peregrine, D.H. 1967. Long waves on a beach. *Journal of Fluid Mechanics* **27**(4): 815–827.

Petryk, S., and G. Bosmajian. 1975. Analysis of flow through vegetation. *Proceedings of the American society of Civil Engineering, Journal of the Hydraulics Division.*

Price, W.A., K.W. Tomlinson, and J.N. Hunt. 1968. The effect of artificial seaweed in promoting the build-up of beaches. *Proceedings of the 11th International Coastal Engineering Conference (ICEC'68).*

Putnam, J.A., and J.W. Johnson. 1949. The dissipation of wave energy by bottom friction. *EOS Transactions, American Geophysical Union* **30:** 67-74.

Quartel, S., A. Kroon, P.G.E.F. Augustinus, P.V. Santen, N.H. Tri. 2007. Wave attenuation in coastal mangroves in the Red River Delta, Vietnam. *Journal of Asian Earth Sciences* **29**: 576-584.

Que, Y.-T., and K. Xu. 2005. The numerical study of roll-waves in inclined open channels and solitary wave runup. *International Journal for Numerical Methods in Fluids* **50**: 1003–1027.

Ree, W.O., and V.J. Palmer. 1949. *Flow of Water in Channels Protected by Vegetative Linings*. Technical Bulletin No. 967. Washington, D.C.: USDA, Soil Conservation Service.

Resio, D.T. 2007. *White Paper on Estimating Hurricane Inundation Probabilities*. Vicksburg, MS: US Army Engineering Research and Development Center,

Resio, D.T. and J.J. Westerink. 2008. Modeling the physics of storm surge. *Physics Today* **61**(9): 33-38.

Roe, P.L. 1981. Approximate Riemann solvers, parameter vectors and difference schemes. *Journal of Computational Physics* **43**: 357-372.

Roland. R.M., and S.L. Douglass. 2005. Wave tolerance of *spartina alterniflora* in coastal Alabama. *Journal of Coastal Research* **21:** 453-463.

Sakai, S., K.Hirayama, H. Sakai. 1988. A new parameter for wave breaking with opposing current on sloping sea bed. *Proceedings of the 21st Conference on Coastal Engineering*, ASCE, Costa del Sol-Malaga, Spain, **2**: 1035–1044.

Sasser, C.E., J.M. Visser, E. Mouton, J. Linscombe, and S.B. Hartley. 2008. *Vegetation Types in Coastal Louisiana in 2007.* U.S. Geological Survey Open-File Report 2008–1224, 1 sheet, scale 1:550,000.

Schelske, C.L., and E.P. Odum. 1961. Mechanisms maintaining high productivity in Georgia estuaries. *Proceedings of the Gulf and Caribbean Fisheries Institute (GCFI'61)*.

Schmid, K. 2000. *Shoreline Erosion Analysis of Grand Bay Marsh*. Open file report. Jackson, MS: Mississippi Department of Environmental Quality, Office of Geology.

Schutten, J., J. Dainty, and A.J. Davy. 2004. Wave-induced hydraulic forces on submerged aquatic plants in shallow lakes. *Annals of Botany* **93**: 333-341

Shiach, J.B., and C.G. Mingham. 2009. A temporally second-order accurate Godunov-type scheme for solving the extended Boussinesq equations. *Coastal Engineering* **56**: 32-45.

Shimizu, Y. and T. Tsujimoto. 1994. Numerical analysis of turbulent open-channel flow over vegetation layer using a k-turbulence model. *Journal of Hydroscience and Hydraulic Engineering* **11**(2): 57-67.

Sleath, J.F.A. 1984. *Sea Bed Mechanics*. New York: John Wiley and Sons.

Smalley, A.E. 1959. The growth cycle of Spartina and its relation to the insect populations in the marsh. *Proceedings of the Salt Marsh Conference (SMC'59)*.

Smith, J.M., R.E. Jensen, A.B. Kennedy, J.C. Dietrich, and J.J. Westerink. 2010. Waves in Wetlands: Hurricane Gustav. *Proceedings of 32nd International Conference on Coastal Engineering (ICEC'10).*

Sorensen, R.M. 2006. *Basic Coastal Engineering*, 3rd edition. USA: Springer.

Stewart, S.R. 2010. *Tropical Cyclone Report. Tropical Storm Bonnie*. Report TCR-AL032010. National Hurricane Center.

Stone, B.M., and H.T. Shen. 2002. Hydraulic resistance of flow in channels with cylindrical roughness. *Journal of Hydraulic Engineering* **128**(5): 500–506.

Straub, L.G., C.E. Bowers, and J. B. Herbrich. 1956. Laboratory tests of permeable wave absorbers. *Proceedings of 6th International Conference on Coastal Engineering (ICEC'56).*

Struve, J., A. Falconer, and Wu, Y. 2003. Influence of model mangrove trees on the hydrodynamics in a flume. *Estuarine, Coastal and Shelf Science* **58**(1): 163–171.

Su, X., and C. W. Li. 2002. Large eddy simulation of free surface turbulent flow in partly vegetated open channels. *International Journal for Numerical Methods in Fluids* **39**(10): 919-937.

Svendsen, I.A. 2006. *Introduction to Nearshore Hydrodynamics.* Singapore: World Scientific.

Synolakis, C.E. 1986. *The Run-up of Long Waves*. PhD Thesis. Pasadena, CA: California Institute of Technology.

Takayama, T., N. Ikeda, T. Hiraishi. 1991. Wave transformation calculation considering wave breaking and reflection. *Report of Port and Harbor Research Institute* **30**(1): 21–67.

Teal, J.M. 1962. Energy flow in the salt marsh ecosystem of Georgia. *Ecology* **43**: 614-624.

Teeter, A.M., B.H. Johnson, C. Berger, G. Stelling, N.W. Scheffner, M.H. Garcia, and T.M. Parchure. (2001). Hydrodynamic and sediment transport modeling emphasis on shallow-water, vegetated areas (lakes, reservoirs, estuaries and lagoons). *Hydrobiologia* **444**: 1– 23.

Temple, D.M. 1987. Closure of 'Velocity distribution coefficients for grass-lined channels'. *Journal of Hydraulic Engineering* **113**(9): 1224–1226.

Teo, F.Y., A. Falconer, B. Lin. 2009. Modelling effects of mangroves on tsunamis. *Proceedings of the Institution of Civil Engineers, Water Management* 162: 3-12

Thornton, E.B., and R.T. Guza. 1983. Transformation of wave height distribution. *Journal of Geophysical Research* **88**(C10): 5925–5938.

Thuy, N. B., K. Tanimoto, and N. Tanaka. 2010. Flow and potential force due to runup tsunami around a coastal forest with a gap, experiments and numerical simulations. *Science of Tsunami Hazards* **29**(2), 43-69.

Timoshenko, S. 1955. *Strength of Materials; Part 1: Elementary Theory and Problems*. Van Nostrand, New York.

Tiner, R.W. 2005. Assessing Cumulative Loss of Wetland Functions in the Nanticoke River Watershed Using Enhanced National Wetlands Inventory Data. *Wetlands* **25**(2): 405-419.

Titov, V.V., and C.E. Synolaki. 1995. Modeling of breaking and non-breaking long-wave evolution and run-up using VTCS-2. *J. Water., Port, Coast., Ocean Eng*. **121**:308-461.

Tonelli, M. and M. Petti. 2009. Hybrid finite volume – finite difference scheme for 2DH improved Boussinesq equations. *Coastal Engineering* **56**: 609-620.

Tonelli, M., and M. Petti. 2010. Finite volume scheme for the solution of 2D extended Boussinesq equations in the surf zone. *Ocean Engineering* **37**: 567-582.

Toro, E.F. 2001. *Shock-Capturing Methods for Free-Surface Shallow Flows*. Wiley, England.

Troch, P., and J.D. Rouck. 1999. An active wave generating–absorbing boundary condition for VOF type numerical model. *Coastal Engineering* **38:** 223-247.

Tsai, C.H., M.C. Huang, F.J. Young, Y.C. Lin, and H.W. Li. 2005. On the recovery of surface wave by pressure transfer function. *Ocean Engineering* **32**: 1247–1259.

Tsujimoto, T., and T. Kitamura. 1995. Lateral bed-load transport and sand-ridge formation near vegetation zone in an open channel. *Journal of Hydroscience and Hydraulic Engineering* **13**(1): 35-45.

U.S. Army Corps of Engineers. 1965. *Morgan City and Vicinity*, Louisiana. House Document No. 167.

USDA Plants Database. 2010. Natural Resources Conservation Service. United States Department of Agriculture. *http://plants.usda.gov*.

Villea, F.J. 2005. Mississippi GAP analysis project. *GAP Analysis Bulletin 13*. US Department of the Interior, US Geological Survey.

Van Leer, B. 1979. Towards the Ultimate Conservative Difference Scheme, V. A Second Order Sequel to Godunov's Method. *J. Comput. Phys*. **32**:101–136.

Waits, E.D. 1967. *Net Primary Productivity of an Irregularly Flooded North Carolina Salt Marsh.* Ph.D. Thesis. NC: North Carolina State University.

Wamsley, T.V., M.A. Cialone, J.M. Smith, J.H. Atkinson, and J.D. Rosati. 2010. The potential of wetlands in reducing storm surge. *Ocean Engineering* **37**(1): 59-68.

Wamsley,T.V., M.A. Cialone, J.M. Smith, B.A. Ebersole, and A.S. Grzegorzewski. 2009. Influence of landscape restoration and degradation on storm surge and waves in southern Louisiana. *Journal of Natural Hazards* **51**(1): 207-224.

Wang, H., D. Y. Lee, and A. Garcia. 1986. Time-series surface wave recovery from pressure gauge. *Coastal Engineering* **10**(4)**:** 379-393.

Warren, R.S., and W.A. Niering. 1993. Vegetation change on a northeast tidal marsh: interaction of sea-level rise and marsh accretion. *Ecology* **74**(1): 96-103.

Wei, G., and J.T. Kirby. 1995. Time-dependent numerical code for extended Boussinesq equations. *Journal of Waterway, Port, Coastal and Ocean Engineering* **121**(5): 251-261.

Wei, G., J.T. Kirby, S.T. Grilli, and R. Subramanya. 1995. A fully nonlinear Boussinesq model for surface waves: part 1. highly nonlinear unsteady waves. *Journal of Fluid Mechanics* **294**: 71–92.

Wei, Y, X.Z. Mao, and K.F. Cheung. 2006. Well-balanced finite-volume model for longwave run-up. *Journal of Waterway, Port, Coastal and Ocean Engineering* **132**: 114-124.

Weis, J.S., and C.A. Butler. 2009. *Salt Marshes: A Natural and Unnatural History*. New Brunswick, NJ and London: Rutgers University Press.

Wendt, K. 1997. *Determination of Total Kjeldahl Nitrogen by Flow Injection Analysis Colorimetry (Block Digestor Method), Quikchem Method 10-107-06-2-E*. Milwaukee, WI: Lachat Instruments.

Whigham, D., and R. Simpson. 1977. Growth, mortality, and biomass partitioning in freshwater tidal wetland populations of wild rice (Zizania aquatica var. aquatica). *Bulletin of the Torrey Botanical Club* **104**(4): 347-351.

Williams, R.B., and M.B. Murdoch. 1969. The potential importance of Spartina alterniflora in conveying zinc, manganese, and iron into estuarine food chains. *Proceedings of the 2nd National Symposium in Radioecology (NSR'69)*.

Wolanski, E., M. Jones, and J.S. Bunt. 1980. Hydrodynamics of a tidal creek mangrove swamp system. *Australian Journal of Marine and Freshwater Research* **31**: 431–450.

Wolanski, E., Mazda, Y., Furukawa, K., Ridd, P., Kitheka, J., Spagnol, S., and Stieglitz T. 2001. *Oceanographic Processes of Coral Reefs*. London, UK: CRC Press.

Woodrey, M.S., and J. Walker. 2009. *Selected Birds of the Grand Bay National Estuarine Research Reserve and Vicinity.* Moss Point, MS: Department of Marine Resources,

Wu, F.C., H.W. Shen, and Y.J. Chou. 1999. Variation of roughness coefficient for unsubmerged and submerged vegetation. *Journal of Hydraulic Engineering* **125**(9): 934–942.

Wu, W. 2007. *Computational River Dynamics*. Taylor & Francis, London, UK.

Wu, W., F.D.Jr. Shields, S.J. Bennett, and S.S.Y. Wang. 2005. A depth-averaged 2-D model for flow, sediment transport and bed topography in curved channels with riparian vegetation. *Water Resources Research* **41:** W03015.

Wu, Y., A. Falconer, and J. Struve. 2001. Mathematical modeling of tidal currents in mangrove fields. *Environmental Modelling and Software* **16**(1): 19–29.

Xiao, H., and W. Huang. 2008. Numerical modeling of wave runup and forces on an idealized beachfront house. *Ocean Engineering* **35**: 106-116.

Yamamoto, S., S. Kano, and H. Daiguji. 1998. An efficient CFD approach for simulating unsteady hypersonic shock–shock interference flows. *Computers & Fluids* **27**(5–6): 571–580.

Zhou, J.G., D.M. Causon, C.G. Mingham, and D.M. Ingram. 2001. The surface gradient method for the treatment of source terms in the shallow water equations. *Journal of Computational Physics* **168**(1): 1–25.

Southeast Region Research Initiative
National Security Directorate
P.O. Box 6242
Oak Ridge National Laboratory
Oak Ridge, TN 37831-6252

www.serri.org